Lavery, Christopher Allan (2016) *Exploring the role of miR-34a in regulating adipose inflammation during obesity.* PhD thesis.

http://theses.gla.ac.uk/7796/

Copyright and moral rights for this work are retained by the author

A copy can be downloaded for personal non-commercial research or study, without prior permission or charge

This work cannot be reproduced or quoted extensively from without first obtaining permission in writing from the author

The content must not be changed in any way or sold commercially in any format or medium without the formal permission of the author

When referring to this work, full bibliographic details including the author, title, awarding institution and date of the thesis must be given

Glasgow Theses Service
http://theses.gla.ac.uk/
theses@gla.ac.uk

Exploring the Role of miR-34a in Regulating Adipose Inflammation During Obesity

Christopher Allan Lavery
B.Sc (Hons), MRes

Submitted in the fulfilment of the requirements of the degree of Doctor of Philosophy in the College of Medical, Veterinary and Life Sciences, University of Glasgow

British Heart Foundation Glasgow Cardiovascular Research Centre, Institute of Cardiovascular and Medical Sciences, College of Medical, Veterinary and Life Sciences, University of Glasgow

June 2016

© C. A. Lavery 2016

Abstract

Background: Obesity is not a new disease, with roots that can be traced back to 400 BC. However, with the staggering increase in individuals that are overweight and obese since the 1980s, now over a quarter of individuals in Europe and the Americas are classed as obese. This presents a global health problem that needs to be addressed with novel therapies.

It is now well accepted that obesity is a chronic, low-grade inflammatory condition that could predispose individuals to a number of comorbidities. Obesity is associated with cardiovascular diseases (CVDs) and type 2 diabetes (T2D) as part of "the metabolic syndrome," and as first identified by Dr Vauge, central distribution of white adipose tissue (WAT) is an important risk factor in the development of these diseases. Subsequently, visceral WAT (vWAT) was shown to be an important factor in this association with CVDs and T2D, and increasing inflammation. As the obese WAT expands, mainly through hypertrophy, there is an increase in inflammation that recruits numerous immune cells to the tissue that further exacerbate this inflammation, causing local and systemic inflammatory and metabolic effects. One of the main types of immune cell involved in this pathogenic process is pro-inflammatory M1 adipose tissue macrophages (ATMs).

MicroRNAs (miRNAs) are a species of small RNAs that post-transcriptionally regulate gene expression by targeting gene mRNA, causing its degradation or translational repression. These miRNAs are promiscuous, regulating numerous genes and pathways involved in a disease, making them useful therapeutic targets, but also difficult to study. miR-34a has been shown to increase in the serum, liver, pancreas, and subcutaneous (sc)WAT of patients with obesity, non-alcoholic fatty liver disease (NAFLD) and T2D. Additionally, miR-34a has been shown to regulate a number of metabolic and inflammatory genes in numerous cell types, including those in macrophages. However, the role of miR-34a in regulating vWAT metabolism and inflammation is poorly understood.

Hypothesis: miR-34a is dysregulated in the adipose tissue during obesity, causing dysregulation of metabolic and inflammatory pathways in adipocytes and

ATMs that contribute to adipose inflammation and obesity's comorbidities, particularly T2D.

Method/Results: The role of miR-34a in adipose inflammation was investigated using a murine miR-34a$^{-/-}$ diet-induced obesity model, and primary *in vitro* models of adipocyte differentiation and inflammatory bone marrow-derived macrophages (BMDMs). miR-34a was shown to be ubiquitously expressed throughout the murine epididymal (e)WAT of obese high-fat diet (HFD)-fed WT mice and *ob/ob* mice, as well as omental WAT from patients with obesity. Additionally, miR-34a transcripts were increased in the liver and brown adipose tissue (BAT) of *ob/ob* and HFD-fed WT mice, compared to WT controls.

When miR-34a$^{-/-}$ mice were fed HFD *ad libitum* for 24 weeks they were significantly heavier than their WT counterparts by the end of the study. *Ex vivo* examinations showed that miR-34a$^{-/-}$ eWAT had a smaller adipocyte area on chow, which significantly increased to WT levels during HFD-feeding. Additionally, miR-34a$^{-/-}$ eWAT showed basal increases in cholesterol and fatty acid metabolism genes *Cd36*, *Hmgcr*, *Lxrα*, *Pgc1α*, and *Fasn*. miR-34a$^{-/-}$ iBAT showed basal reductions in *Cebpα* and *Cebpβ*, with increased *Pgc1α* expression during HFD-feeding. The miR-34a$^{-/-}$ liver additionally showed increased basal transcript expression of *Pgc1α*, suggesting miR-34a may broadly regulate PGC1α. Accompanying the *ex vivo* changes in cholesterol and fatty acid metabolism genes, *in vitro* miR-34a$^{-/-}$ white adipocytes showed increased lipid content.

An F4/80^{high} macrophage population was identified in HFD-fed miR-34a$^{-/-}$ eWAT, with increased *Il-10* transcripts and serum IL-5 protein. Following these *ex vivo* observations, BMDMs from WT mice upregulated miR-34a expression in response to TNFα stimulation. Additionally, miR-34a$^{-/-}$ BMDMs showed an ablated CXCL1 response to TNFα.

Conclusion: These findings suggest miR-34a has a multi-factorial role in controlling a susceptibility to obesity, by regulating inflammatory and metabolic pathways, potentially through regulation of PGC1α.

Table of Contents

Abstract 2

Table of Contents 4

List of Tables 6

List of Figures 7

Publications 10

Acknowledgments 11

Author's Declaration 12

Common Definitions/Abbreviations 13

Chapter 1: Introduction 15
- **1.1 Obesity Overview** 16
- **1.2 Adipose Tissue** 34
- **1.3 microRNAs** 62
- **1.4 General Aims** 83

Chapter 2: Materials and Methods 84
- **2.1 General Lab Practise** 85
- **2.2 Biological Models** 87
- **2.3 Molecular Methods** 93
- **2.4 Histology Analysis** 116
- **2.5 Flow Cytometry** 123
- **2.6 Confocal Fluorescent Microscopy** 125
- **2.7 Statistics** 125

Chapter 3: Profiling miR-34a Expression In Models of Obesity 126
- **3.1 Introduction** 127
- **3.2 Aims** 129
- **3.3 Methods** 130
- **3.4 Results** 134
- **3.5 Discussion** 150

Chapter 4: miR-34a$^{-/-}$ Mice Are Susceptible to Diet-Induced Obesity 157
- **4.1 Introduction** 158
- **4.2 Aims** 161
- **4.3 Methods** 162
- **4.4 Results** 166
- **4.5 Discussion** 189

Chapter 5: Examining The Role of miR-34a in Macrophages *in vitro* 201
- **5.1 Introduction** 202
- **5.2 Aims** 205
- **5.3 Methods** 206
- **5.4 Results** 211
- **5.5 Discussion** 227

Chapter 6: Examining the Role of miR-34a in Adipocytes *in vitro* 234
- **6.1 Introduction** 235
- **6.2 Aims** 237
- **6.3 Methods** 238
- **6.4 Results** 242
- **6.5 Discussion** 264

Chapter 7: General Discussion and Conclusion 272
List of References 281

List of Tables

Table 1.1: The Role of Adipokines In Inflammation, T2D, and CVDs During Obesity 44
Table 1.2: Validated miR-34a Targets Involved In Metabolism and Immune System Function 78
Table 2.1: Qiagen miScript RT II Kit Protocol cDNA Synthesis Reaction Mix. 102
Table 2.2: Qiagen miScript RT II Kit Protocol RT PCR Conditions. 102
Table 2.3: TaqMan® MicroRNA Reverse Transcription Kit Reaction Master Mixes. 103
Table 2.4: TaqMan® MicroRNA Reverse Transcription Kit PCR Cycling Conditions. 103
Table 2.5: Qiagen microRNA SYBR Green qPCR Reaction Master Mix. 104
Table 2.6: Qiagen microRNA SYBR Green qPCR Cycling Conditions. 105
Table 2.7: TaqMan® qPCR Master Mix for Gene and Mature miRNA Expression. 106
Table 2.8: TaqMan® qPCR Cycling Conditions for Gene and miRNA Expression. 106
Table 2.9: BigDye Terminator Sequencing PCR master mix 109
Table 2.10: BigDye Terminator Sequencing PCR Cycling Conditions 110
Table 2.11: Custom IDT Genotyping Primers For miR-34a$^{-/-}$ mice 112
Table 2.12: PCR Master Mix For Genotyping miR-34a$^{-/-}$ Mice 112
Table 2.13: PCR Cycling Conditions For Genotyping miR-34a$^{-/-}$ Mice 113
Table 2.14: OpenArray® Megaplex™ Reverse Transcription PCR Master Mix 113
Table 2.15: OpenArray® Megaplex™ Reverse Transcription PCR Cycling Conditions 114
Table 2.16: OpenArray® Megaplex™ Pre-Amplication PCR Master Mix 114
Table 2.17: OpenArray® Megaplex™ Pre-Amplification PCR Cycling Conditions 115
Table 2.18: Shandon Excelsior Paraffin Processing Steps for Tissues 117
Table 2.19: Haematoxylin & Eosin Staining Protocol 118
Table 2.20: ISH Depariffinisation, Dehydration, and SSC Wash Steps 120
Table 2.21: List of Flow Cytometry Antibodies and Supplier Information Used Throughout 124
Table 3.1: Bariatric Surgery Patient Profile 131
Table 3.2: Manufacturer Information For miRNA qRT-PCR Primer Assays 131
Table 4.1: List of Life Technologies TaqMan® Probes Used In This Chapter 164
Table 4.2: Fasting Serum Lipid Measurements From miR-34a$^{-/-}$ and WT Mice During HFD-feeding 169
Table 5.1: TaqMan™ Gene Expression Assays Used in This Chapter 209
Table 5.2: Manufacturer Information For miRNA qRT-PCR Primer Assays 209
Table 6.1: TaqMan™ Gene Expression Assays Used in This Chapter 240
Table 6.2: Manufacturer Information for miRNA qRT-PCR Primer Assays 241

List of Figures

Figure 1.1: The Prevalence of Obesity Worldwide in 2014. 17
Figure 1.2: Percentage of Adult UK Population that are Overweight and Obese from 1980-2013 18
Figure 1.3: Diagram of the Major White and Brown Adipose Depots in Humans and Mice 35
Figure 1.4: Diagram of the Biochemical Mechanism for Triglyceride Storage and Release in Adipocytes 38
Figure 1.5: A Simplified View of Adipose Inflammation During Obesity 49
Figure 1.6: Diagram of the Biochemical Process of Mitochondrial Thermogenesis 60
Figure 1.7: Simplified Diagram of miRNA Processing and mRNA Silencing 64
Figure 1.8: Distribution of Validated miR-34a Targets Among Cell and Tissue Types 79
Figure 2.1: Validation of RNA Extraction Method From White Adipose Tissue 95
Figure 2.2: Representative Dissociation Curves From Qiagen SYBR Green qPCR. 105
Figure 2.3: Example of Images Generated During Fiji Image Analysis of Adipocyte Area and number. 122
Figure 3.1: Diagram of Life Technologies' pcDNA™ 3.3-TOPO® Plasmid For Cloning 133
Figure 3.2: miR-34a Expression Profile Across Murine Tissues 134
Figure 3.3: *in situ* Hybridisation Optimisation For eWAT 136
Figure 3.4: Characterisation of miR-34a Distribution In Genetically Obese *ob/ob* Mice eWAT 137
Figure 3.5: Characterisation of miR-34a Distribution In Diet-Induced Obese Mice eWAT and Obese Patient omental WAT 138
Figure 3.6: miR-34a Expression Increases In the iBAT and Liver, and Decreases In the eWAT of *ob/ob* Mice, During Weight-Gain 139
Figure 3.7: miR-34a* Expression Follows A Similar Profile to miR-34 In *ob/ob* Mice During Weight-Gain 140
Figure 3.8: miR-34a Expression In WT Tissues From Diet-Induced Obese Mice and Omental WAT From Obese Patients 141
Figure 3.9: miR-34a qRT-PCR Quality Control 143
Figure 3.10: Profiling The miR-34 Family Using The TaqMan™ System In Diet-Induced Obese Mice 145
Figure 3.11: OpenArray® miRNAs Showing The Greatest Change In Obese eWAT 148
Figure 3.12: OpenArray® miRNAs Showing The Greatest Change In Obese eWAT Cont. 149
Figure 4.1: *In vivo* miR-34a$^{-/-}$ Obesity Study Design 162
Figure 4.2: *In vivo* miR-34a$^{-/-}$ Metabolic Cage Study Design 162
Figure 4.3: Representative Gel Images of *in vivo* miR-34a$^{-/-}$ Obesity Study Genotyping 163
Figure 4.4: miR-34a$^{-/-}$ Mice Are More Susceptible to Diet-Induced Obesity, Without Glucose Handling Effects 167
Figure 4.5: miR-34a$^{-/-}$ Mice Showed No Change in Serum Adipokines or Total Body Fat Percentage 168

Figure 4.6: miR-34a$^{-/-}$ eWAT Showed A Greater Hypertrophic Response to HFD-Feeding 170
Figure 4.7: miR-34a$^{-/-}$ Adipose Tissue Metabolic Gene Changes 172
Figure 4.8: Profile of Metabolic Genes Within the miR-34a$^{-/-}$ Liver 173
Figure 4.9: Quantification of Inflammatory Genes in eWAT and Liver From HFD-fed miR-34a$^{-/-}$ Mice 175
Figure 4.10: Serum Cytokine Expression in HFD-fed miR-34a$^{-/-}$ Mice. 176
Figure 4.11: Representative Flow Cytometry Plots and Gating Strategy for eWAT Macrophages 178
Figure 4.12: Representative Flow Cytometry Plots of eWAT Macrophage Markers, Continued 179
Figure 4.13: Flow Cytometry Quantification of Macrophage Markers From Cells Isolated from eWAT 180
Figure 4.14: Representative Flow Cytometry Plots and Gating Strategy for eWAT Lymphocytes 182
Figure 4.15: Lymphocyte and Neutrophil Quantification and Representative Flow Cytometry Plots 183
Figure 4.16: Spleen Lymphocyte Gating Strategy and Representative Flow Cytometry Plots 185
Figure 4.17: Spleen Leukocyte Quantification and Flow Cytometry Gating Strategy for Macrophages and Neutrophils 186
Figure 4.18: Representative Flow Cytometry plots for Splenic Macrophage and Neutrophil Populations 187
Figure 4.19: Weight Differences Between miR-34a$^{-/-}$ and WT Mice are Not Due to Differences in Food and Water Consumption 188
Figure 4.20: Summary of Chapter Conclusions 200
Figure 5.1: Assessment of BMDM Culture Purity by Flow Cytometry 206
Figure 5.2: Expression of miR-34 Family in BMDMs Stimulated With TNFα 211
Figure 5.3: Gating Strategy and Representative Flow Cytometry Plots for Macrophage Markers on WT and miR-34a$^{-/-}$ BMDMs Stimulated With TNFα 213
Figure 5.4: Representative Flow Cytometry Plots for Macrophage Markers on WT and miR-34a$^{-/-}$ BMDMs Stimulated With TNFα, Continued 214
Figure 5.5: Flow Cytometry Quantification of Macrophage Markers on WT and miR-34a$^{-/-}$ BMDMs Stimulated With TNFα 215
Figure 5.6: Gene Expression Changes Between WT and miR-34a$^{-/-}$ BMDMs Stimulated With TNFα 217
Figure 5.7: WT and miR-34a$^{-/-}$ BMDM Supernatant Cytokine Luminex Results 219
Figure 5.8: WT and miR-34a-/- BMDM Supernatant Obesity Proteome Array Results 220
Figure 5.9: Transfection Optimisation in WT BMDMs 222
Figure 5.10: Transcript Expression of The miR-34 Family In miR-34a-mimic Transfected WT BMDMs 224
Figure 5.11: Transcripts Expression of M1/M2 Marker Genes in miR-34a-mimic Transfected WT BMDMs 225
Figure 5.12: Supernatant Cytokine Luminex Results from miR-34a-mimic Transfected WT BMDMs 226
Figure 5.13: Theoretical Mechanism for miR-34a's Regulation of TNFα Signalling in Macrophages 233
Figure 6.1: Diagram of the *in vitro* Primary Pre-Adipocyte Differentiation Protocol 238

Figure 6.2: Representative Flow Cytometry Plots Showing *in vitro* Adipocyte Culture Purity 239
Figure 6.3: Primary White Pre-Adipocyte Differentiation Profile 243
Figure 6.4: Representative Oil Red "O" Images of Brown Pre-Adipocyte Differentiation 245
Figure 6.5: Genetic Markers of Brown Pre-Adipocyte Differentiation 246
Figure 6.6: miR-34 Family Expression During White Pre-Adipocyte Differentiation *in vitro* 248
Figure 6.7: Comparison of Differentiation Markers in WT and miR-34a$^{-/-}$ White Pre-Adipocyte *in vitro* 249
Figure 6.8: Examination of Altered miR-34a$^{-/-}$ eWAT Genes During White Pre-Adipocyte Differentiation *in vitro* 250
Figure 6.9: miR-34 Family Expression Over Brown Adipocyte Differentiation *in vitro* 252
Figure 6.10: Comparison of Differentiation Markers in WT and miR-34a$^{-/-}$ Brown Pre-Adipocytes *in vitro* 253
Figure 6.11: *in vitro* WT and miR-34a$^{-/-}$ Brown Pre-Adipocyte Phenotype At Day 8 254
Figure 6.12: Confocal Images of MitoTracker Staining Optimisation in Pre-Adipocytes 256
Figure 6.13: Confocal Images of BODIPY Staining Optimisation in Pre-Adipocytes 257
Figure 6.14: Flow Cytometry Quantification of MitoTracker Titration in Pre-Adipocytes 258
Figure 6.15: Representative Dot-Plot Overlays of Flow Cytometry Quantification of Lipid and Mitochondria Content in Pre-Adipocytes 259
Figure 6.16: Flow Cytometry Quantification of Lipid and Mitochondrial Content in Pre-Adipocytes 260
Figure 6.17: Luminex Quantification of Supernatant Adipokines During Pre-Adipocyte Differentiation 262
Figure 6.18: Obesity Proteome Array Analysis of Adipokines in Day 8 Pre-Adipocytes 263
Figure 7.1: Theoretical Mechanism in miR-34a$^{-/-}$ Mice Predisposing them to Obesity 280

Publications

Manuscripts

Christopher. A. Lavery, Mariola Kurowska-Stolarska, William M. Holmes, Iona Donnelly, Muriel Caslake, Andrew Collier, Andrew. H. Baker, Ashley. M. Miller. (2016) miR-34a$^{-/-}$ mice are susceptible to diet-induced obesity. **Obesity**. Vol. 24 (8): pp. 1741-1751.

Miller AM, Gilchrist DS, Nijjar J, Araldi E, Ramirez CM, **Lavery CA**, Fernández-Hernando C, McInnes IB and Kurowska-Stolarska M. (2013) MiR-155 has a protective role in the development of non-alcoholic hepatosteatosis in mice. **PLoS ONE**. 8: e72324.

Parker, A. L., White, K. M., **Lavery, C. A.**, Custers, J., Waddington, S. N., & Baker, A. H. (2013). Pseudotyping the adenovirus serotype 5 capsid with both the fibre and penton of serotype 35 enhances vascular smooth muscle cell transduction. **Gene Therapy**, 1–7.

Poster Abstracts

Christopher. A. Lavery, Mariola Kurowska-Stolarska, Iona Donnelly, Andrew. H. Baker, Ashley. M. Miller. (2015). miR-34a Has A Role In Weight Gain, During Murine Diet-Induced Obesity. **European Atherosclerosis Society National Congress**.

C. A. Lavery, M. Kurowska-Stolarska, I. Donnelly, J. Cooney, M. Caslake, A. H. Baker, A. M. Miller. (2015) The Role of miR-34a In Murine Diet-Induced Obesity. **Keystone Conference: The Crossroads Between Lipid Metabolism and Type 2 Diabetes**.

Acknowledgments

I would first like to thank my supervisor Dr Ashley M. Miller for her continued guidance and support throughout my studies, and for all the opportunities afforded to me, including presenting work at international conferences. Additionally, I would like to thank the British Heart Foundation for their support and funding, without it this research would not have been possible. I would also like to thank my provisional supervisor Dr Ian Salt.

I would like to thank Dr Mariola Kurowska-Stolarska for her kind donation of a miR-34a$^{-/-}$ breeding pair, which made most of the experiments in this thesis possible, and for her technical assistance with miR-34a manipulation and profiling. Mr Jim Mullin and Dr William Holmes from the Glasgow Experimental MRI Centre, University of Glasgow for running the MRS and advice on data analysis. Mrs Josephine Cooney for acquiring cholesterol and lipid measurements on serum samples, and Professor Muriel Caslake for providing access to Josephine and the blood chemistry analyser. Professor Andrew Collier MD for organising the acquisition of human adipose samples from bariatric surgery patients, as part of a pilot study, and to Mr Majid Ali MD for performing the bariatric surgeries and collecting the adipose samples, both from Ayr Hospital, NHS: Ayrshire & Arran, Ayr.

A special thank you to Iona Donnelly for her assistance with flow cytometry, Luminex, *in vivo* tissue collections, cell isolation, and general advice and support. Additionally, Dr Scott Johnstone for his assistance with confocal microscopy and Dr Lorraine Work for her help with OpenArray. Wendy Beattie, Gregor Aitchison, and Nicola Britton for their technical support and lab banter, which helped get me through the long days in the lab and showed me that you do not always have to be too serious whilst doing science! My friends and office colleagues Valters, Estrella, Josie, and Izah for listening to my complaints, their support, and cups of tea!

I would especially like to thank my family for all their support and advice, even though they did not know what I was talking about half the time. Finally, but not least, I would like to thank my wonderful girlfriend Sarah for her support and understanding through my write-up and long days in the lab.

Author's Declaration

I declare that this thesis has been entirely written by myself and that the results presented within are entirely my own work, unless explicitly stated otherwise. I also confirm that this thesis has not been previously submitted for a higher degree. The research was carried out at the Institute of Cardiovascular and Medical Sciences, University of Glasgow, under the supervision of Dr A.M. Miller and Professor A.H. Baker.

Christopher A. Lavery

Common Definitions/Abbreviations

Acronyms

ACC	Acetyl-CoA carboxylase
ARG1	Arginase 1
ATM	Adipose tissue macrophage
BAT	Brown adipose tissue
CCL/CCR	CC chemokine ligand/receptor
CD	Cluster of differentiation
cDNA	Complementary deoxyribonucleic acid
CEBP	CCAAT/enhancer binding protein
CHI3L3	Chitinase-like 3
COSHH	Control of Substances Hazardous to Health
CPT1A	Carnitine palmitoyltransferase 1A
CROT	Carnitine O-octanoyltransferase
Ct	Cycle Threshold
CVD	Cardiovascular disease
CXCL/CXCR	CXC chemokine ligand/receptor
CYP7A1	Cytochrome P450, family 7, subfamily A, polypeptide 1
DMSO	Dimethyl sulfoxide
DNA	Deoxyribonucleic acid
dNTPs	Deoxynucleotides
FA	Fatty acids
FABP	Fatty acid binding protein
FAS	Fatty acid synthase
FFA	Free fatty acids
GTC	Guanidinium thiocyanate
HFD	High fat diet
HMGCR	3-hydroxy-3-methylglutaryl-CoA reductase
IL	Interleukin
IP	Intraperitoneal
ISH	*In situ* hybridisation
KO	Knock-out
LPL	Lipoprotein lipase
LXR	Liver X receptor
MHC	Major histocompatibility complex
miR/miRNA	MicroRNA
NOS	Nitric oxide synthase
ORO	Oil red “O”
PBS	Phosphate Buffered Saline
PBS-T	Phosphate Buffered Saline-Tween
PCK	Phosphoenolpyruvate carboxykinase
PCR	Polymerase chain reaction
PFA	Paraformaldehyde
PGC1	Peroxisome proliferator-activated receptor gamma, coactivator 1
PPAR	Peroxisome proliferator-activated receptor
qPCR	Quantitative polymerase chain reaction
RETNLA	Resistin-like alpha
RNA	Ribonucleic acid
RQ	Relative quantification
rRNA	Ribosomal ribonucleic acid
RT	Reverse Transcription
qRT-PCR	Quantitative reverse transcription polymerase chain reaction
SAT	Subcutaneous adipose tissue

scWAT	Subcutaneous white adipose tissue
SIRT	Silent mating type information regulation 2, S. cerevisiae, homolog
SREBF	Sterol regulatory element binding transcription factor
T2D	Type 2 diabetes
Taq polymerase	Thermus aquaticus polymerase
TBE Buffer	Tris-Borate EDTA buffer
TG	Triglyceride
TLR	Toll-like receptor
TNF	Tumour necrosis factor
UCP	Uncoupling protein
VAT	Visceral adipose tissue
vWAT	Visceral white adipose tissue
WAT	White adipose tissue
WT	Wild type

Abbreviations

dH_2O	Distilled water
CO_2	Carbon dioxide
N_2	Nitrogen
EtBr	Ethidium Bromide
EDTA	Ethylenediaminetetraacetic acid
HCL	Hydrogen Chloride
NaOH	Sodium Hydroxide
Tris-HCL	Tris hydrogen chloride
$Na_2HPO_4 \cdot H_2O$	Sodium phosphate dibasic dihydrate
$NaH_2PO_4 \cdot H_2O$	Sodium phosphate monobasic dihydrate
NaCl	Sodium Chloride
KCl	Potassium Chloride

Symbols

M	Molar
mM/mmol	Millimolar
μM	Micromolar
nM	Nanomolar
pM	Picomolar
μm	Micrometers
nm	Nanometers
kg	Kilograms
g	Grams
mg	Milligrams
μg	Micrograms
ng	Nanograms
pg	Picograms
ml	Milliliters
μl	Microliters
Hz	Hertz
V	Volts
mV	Millivolts
kb	Kilobases
bp	Base pairs
nt	Nucleotides

Chapter 1: Introduction

1.1 Obesity Overview

Obesity is not a new disease; it has roots that can be traced back through human history to prehistoric times 30,000 years ago. The Ancient Greek physician Hippocrates (Hippocrates II) was the first to describe co-morbidities of obesity in 400 BC, observing associations with infertility and premature death. He was also the first to suggest that changes in diet could improve health, and identified that maintaining the energy balance between dietary intake and energy output, through exercise, were important factors in maintaining a healthy weight. As early as 129-circa 200 AD the physician, surgeon, and philosopher, Galen (Claudius Galenus) wrote one of the earliest recorded case studies for the treatment of obesity with a regime of diet and exercise. However, it was not until the 1600s that Tobias Venner started using the term “obesity” medically to replace corpulent, for grossly overweight individuals. An in depth look at the history of obesity is reviewed here (Haslam 2007; 2011). General management of obesity has not changed much since Galen’s time, with the exception of gastric bypass/banding surgery and the anti-obesity drug Orlistat, but there have been great advances in the development of therapies for the comorbidities of obesity, including metformin and statins. However, there is a lack of therapies that specifically target the underlying inflammation, making it vital to explore novel therapies for treating obesity-induced inflammation.

1.1.1 Obesity Epidemiology

Obesity is medically defined as the abnormal accumulation of body fat and characterised by a body mass index (BMI: body mass (kg) ÷ height $(m)^2$) ≥30 kg/m^2, with individuals that are overweight in the range of BMI 25-30 kg/m^2. Although obesity, with its various names, has been known about for millennia, it was not until recent history that it became an endemic problem of the western world, representing a major public health concern (Figure 1.1). In the United Kingdom (UK) alone, the percentage of adults that were overweight and obese almost doubled (36 to 62.1%) from 1980 to 2013 (Figure 1.2). The most recent statistics show that in 2014 69% of men and 61% of women (≥16 years of age) in Scotland were overweight/obese, with 26% of men and 29% of women showing

obesity. In the same year, self-reported data from Wales showed that 61% of men and 54% of women (≥16 years of age) were overweight/obese, with 21% of men and 22% of women obese. In England a year before (2013), 67% of men and 57% of women (≥16 years of age) were overweight/obese, with 26% of men and 24% of women obese. Finally, between 2013-2014, 67% of men and 56% of women were overweight/obese in Northern Ireland, with 25% of men and 23% of women showing obesity (Townsend et al. 2015). Overall, these statistics show that between 2013-2014 approximately a quarter of the population in the UK were classed as obese.

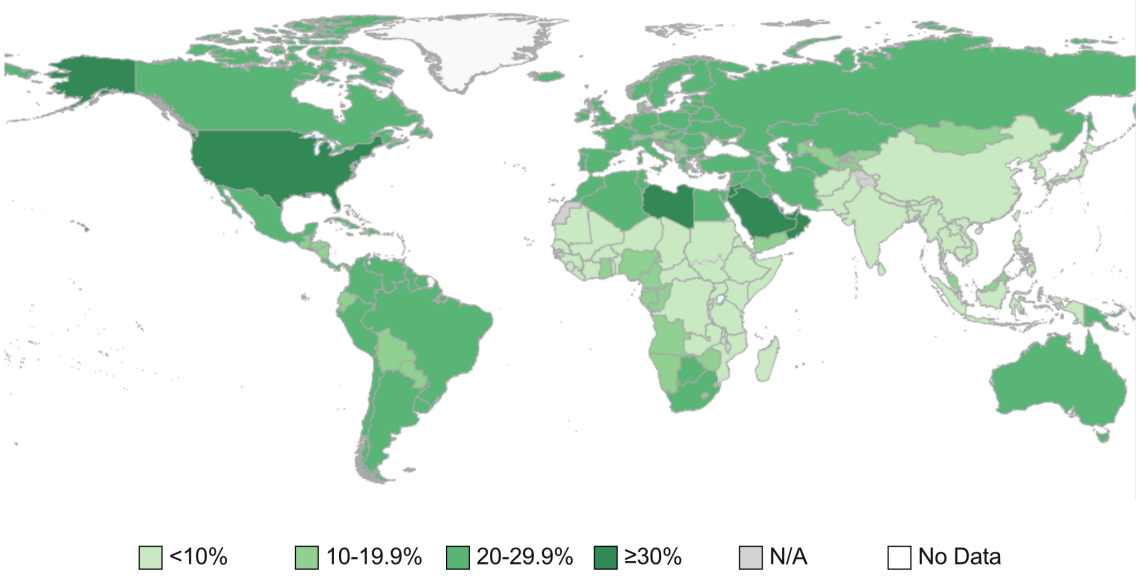

Figure 1.1: The Prevalence of Obesity Worldwide in 2014.
Showing the percentage of adults (18+ years) with obesity (BMI ≥30 kg/m^2) for each country worldwide in 2014. Graphic is taken from World Health Organization (WHO) Global Health Obervatory (GHO) data for obesity (URL: (Boutant et al. 2015), Accessed: 18/03/14)

Furthermore, The Scottish Government estimated that in 2014 the co-morbidities of overweight and obese individuals cost the National Health Service (NHS) £363-600 million, with the total cost (indirect and direct) to the economy estimated at £0.9-4.6 billion (The Scottish Government 2015). With these facts in mind, not only is obesity a major health concern, but it also puts a great burden on the economy and health services with its associated co-morbidities. In an attempt to slow the obesity epidemic, the World Health Organization (WHO) halved the recommended daily allowance (RDA) of added dietary sugars from 10% to 5% (approximately 25 g) of total energy intake in 2014. Additionally, the UK

government recently announced a “sugar tax” on high-sugar drinks from April 2018. Therefore, it is of paramount importance that new management strategies and novel therapies are developed for obesity.

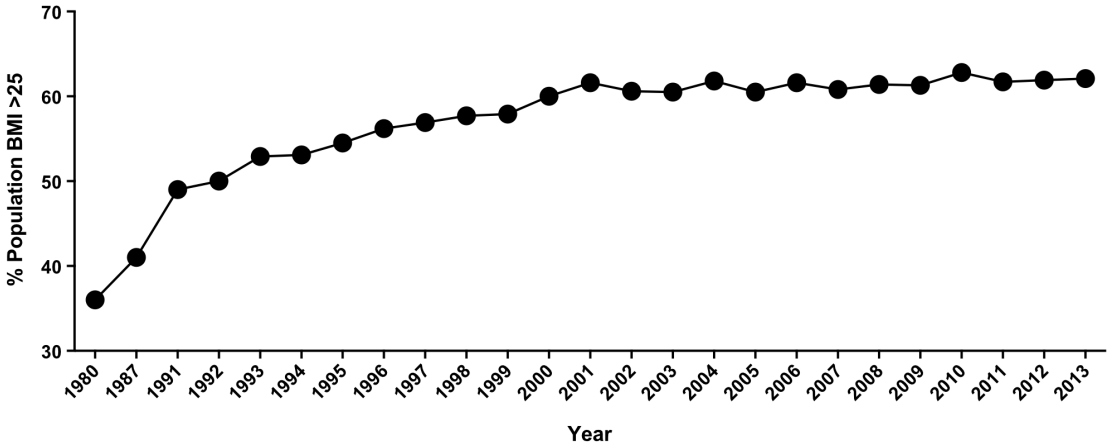

Figure 1.2: Percentage of Adult UK Population that are Overweight and Obese from 1980-2013
Showing historical data of the percentage of adults (15+ years) in the United Kingdom population that are overweight and obese (BMI >25). Data is taken from The Organisation for Economic Co-operation and Development (OECD) health risks section (URL: https://data.oecd.org/healthrisk/overweight-or-obese-population.htm, Accessed: 18/03/16).

1.1.2 Risk Factors for Obesity Development

Obesity, as Hippocrates correctly identified, is caused by an imbalance in energy homeostasis over time towards greater energy input, over expenditure. However, there is a complex mixture of environmental, genetic, physiological, and psychological factors that contribute to individuals overeating and energy imbalance. It is widely accepted that changes in our environment that have affected our lifestyle and food supply are the main causes of the obesity epidemic, creating an “obesogenic” environment that promotes overeating and lower energy expenditure. These environmental changes include: 1) mass production of highly processed foods that are energy-dense and highly gratifying, which are readily and cheaply available for convenience (Swinburn et al. 2011). 2) Increases in portion sizes and in food marketing strategies that promote purchasing less nutritious foods and in greater quantities (Swinburn et al. 2011; Llewellyn and Wardle 2015). 3) Reductions in physically demanding occupations and everyday tasks, along with reductions in the distances walked to school/work with advances and proliferation of transportation technology, have made the population more sedentary (Wareham 2007). However, in 2014 The Scottish Government reported

that 68% of adults met the moderate/vigorous physical activity (MVPA) guidelines of 150 min/week moderate exercise or 75 min/week vigorous exercise, which had remained constant since 2012. This is despite no change in the number of obese adults over the same period (The Scottish Government 2015). This suggests that dietary intake of energy is a greater contributing factor to the obesity epidemic, though these statistics of physical activity are self-reported, so should be treated with some caution. Additionally, these levels of physical activity may not equate to the same energy expenditure as used historically during everyday tasks. In fact, a review of the evidence suggested that 45-60 minutes of moderate-intensity exercise/day was required to stave off becoming overweight or obese (Saris et al. 2003).

Therefore, much research has focused on why individuals overeat. There are controversial suggestions that dietary increases in the fructose-containing disaccharide sucrose (cane sugar) and high fructose corn syrup could contribute to the obesity epidemic and its comorbidities. Some studies showed that fructose reduced the serum concentrations of the satiety hormone leptin in subjects and had addictive qualities by activating reward regions of the brain, reviewed here (Stanhope 2015). There is also a hereditary component to obesity, with monozygotic twin studies showing that >70% of BMI and waist circumference was inherited, even when twins were adopted separately and raised in different environments (Allison et al. 1996; Wardle et al. 2008). It was also shown that adopted monozygotic twins had BMIs that more closely resembled those of their biological parents, than their adopted parents (Sørensen et al. 1989). There have been a number of genetic variants identified affecting genes involved in eating behavior: e.g. *Leptin Receptor (LEPR)*, *Melanocortin 4 Receptor (MC4R)*, *Proprotein Convertase Subtilisin Kexin type 1 (PCSK1)*, *Melanocortin 2 Receptor Accessory Protein (MRAP)2*, *SH2 Domain-Containing Protein 1B (SH2B1)*, *Brain-Derived Neurotrophic Factor (BDNF)*, and *Fat Mass And Obesity Associated (FTO)*; however, these collectively only account for <5% of the incidences of human obesity, reviewed here (van der Klaauw and Farooqi 2015). Epigenetic modifications could also have a role in predisposing individuals to obesity, with maternal obesity during pregnancy associated with an increased risk of obesity development in offspring. Though, studies looking directly at the epigenetic effects

of maternal obesity in humans have been limited, reviewed here (Gaillard 2015). Furthermore, the composition of the gut microbiota has been suggested to predispose individuals to the development of obesity in an obesogenic environment, reviewed here (Rosenbaum et al. 2015).

1.1.3 Comorbidities

Obesity is associated with numerous co-morbidities. One systematic review and meta-analysis showed that being overweight or obese was associated with type 2 diabetes (T2D), numerous cancers: breast (postmenopausal), colorectal, endometrial, esophageal, kidney, ovarian, pancreatic, and prostate; cardiovascular diseases (CVDs): hypertension, coronary heart disease (CHD), congestive heart failure, pulmonary embolism, and stroke; as well as asthma, gallbladder disease, osteoarthritis, and chronic back pain (Guh et al. 2009). Besides these inflammatory conditions, obesity is also associated with disability, sleep apnoea, menstrual irregularities, and psychological disorders: depression, eating disorders, and social stigma (Bean et al. 2008). However, here the focus will mainly be on T2D and CVDs.

1.1.3.1 Type-2 Diabetes

T2D or diabetes mellitus type 2, meaning “sweet/honey urine,” is characterised by hyperglycaemia, decreased insulin-mediated glucose uptake (insulin resistance), and pancreatic β-islet cell dysfunction. Hyperglycaemia and insulin resistance precede the development of T2D, and β-islet cells respond to these by cellular hypertrophy and increased insulin secretion, leading to hyperinsulinaemia. Once the β-islet cells can no longer compensate for the level of insulin resistance they become dysfunctional and insulin production decreases, leading to T2D. Numerous factors have been suggested to contribute to β-islet cells dysfunction, including lipotoxicity (ectopic lipid deposition), glucotoxicity, oxidative stress, endoplasmic reticulum (ER) stress, and inflammation. These factors can also lead to increased β-islet cell death (Donath and Shoelson 2011).

1.1.3.2 Cardiovascular Disease

CVDs are a collection of diseases that affect the heart and blood vessels, including CHD, stroke, pulmonary embolism, and peripheral artery disease (PAD). The main cause of CVD associated with obesity is the development of atherosclerotic plaques in the vasculature that restrict blood flow and can rupture, forming a thrombus that can block blood vessels and restrict blood flow to tissues. This can cause cardiomyocyte death in the case of CHD and neuronal death in stroke, leading to a reduced quality of life or death. These atherosclerotic plaques are caused by ectopic lipid deposition in the blood vessels and contain numerous inflammatory immune cells, including macrophages that become "foam cells" with lipid accumulation, which contribute to atherosclerosis development and plaque rupture (Libby et al. 2011). Obesity is a risk factor for atherosclerosis development due to its association with dyslipidaemia and hyperglycaemia/insulin resistance, which form "the metabolic syndrome" (section 1.1.3.3). The risk of CVD increases exponentially as BMI increases, especially at a BMI ≥27 kg/m^2, with a family history of central obesity moderately increasing an individual's CVD risk. Additionally, Individuals with T2D are at very high risk of CVD, and increasing total serum cholesterol and low-density lipoprotein (LDL) levels represents a further substantial risk for CVD development (Reiner et al. 2011). Individuals with central obesity show increased levels of atherosclerosis, with women generally showing a lower incidence due to their peripheral gynoid distribution of adipose (see section 1.1.4), but this protective effect is reduced in women with central obesity (McGill et al. 2002; Tankó et al. 2003a; 2003b). Increasing BMI has also been correlated with reduced plaque calcification and plaque stability, making the atherosclerotic plaques more likely to rupture (Ghoorah et al. 2016).

1.1.3.3 The Metabolic Syndrome

Obesity forms part of "the metabolic syndrome," which is a clustering of interconnected risk factors for CVDs and T2D that are found together. The metabolic syndrome includes: hyperglycaemia, hypertension, dyslipidaemia (increased serum triglycerides (TGs) and decreased high-density lipoprotein (HDL) cholesterol), and central obesity, with some definitions also including insulin resistance (Kahn et al. 2005; Alberti et al. 2009). However, there are multiple

clinical criteria for diagnosing the metabolic syndrome, introducing inconsistencies between studies (Alberti et al. 2009). The concept of a metabolic or insulin resistance syndrome was introduced by a number of investigators when they observed a correlation between these risk factors and insulin resistance between the late 1960s-80s (Avogaro et al. 1967; Haller 1977; Singer 1977; Stern and Haffner 1986). However, it was not until 1988 that Professor Gerald Reaven, in his Banting Medal lecture, proposed that these risk factors could be the underlying cause of many CVDs, coining the term “syndrome X” for this association (Reaven 1988). One of the consequences of the metabolic syndrome is non-alcoholic fatty liver disease (NAFLD), caused by adipose accumulation in the liver (steatosis), which can progress onto non-alcoholic steatohepatitis (NASH). Furthermore, NAFLD is a risk factor for CVDs, by contributing to systemic inflammation (e.g. increasing tumour necrosis factor (TNF)α and interleukin (IL)-6 levels), T2D development, and dyslipidaemia, reviewed here (Edens et al. 2009).

1.1.4 The Importance of Adipose Distribution

In terms of obesity as a risk factor for CVD and T2D, the distribution of adiposity is an important factor, with central or abdominal obesity presenting a greater risk than peripheral obesity. During post-mortem dissections Giovanni Battista Morgagni (1765) and William Wadd (1829) were the first to identify that abdominal obesity was associated with sudden, premature death (Haslam 2011). Then in 1956 Dr Jean Vague showed that obesity in the upper portions of the body, which he termed “android,” strongly correlated with T2D, atherosclerosis, and gout, but not obesity in the lower portions, termed “gynoid” (Vague 1956). Vague also noted that males had a greater frequency of android obesity, whereas females had a greater frequency of gynoid obesity, until post-menopausal age. These observations identified sex differences in fat distribution, but also in T2D and CVD risk during obesity, even though these sex differences in fat distribution had been identified far earlier (Stern and Haffner 1986; Haslam 2011). Later studies showed the relationship between central obesity and T2D and CVDs, over peripheral obesity (Albrink and Meigs 1964; Feldman et al. 1969; Blair et al. 1984). Vague’s dichotomy of upper and lower obesity subtypes was re-introduced in the mid 1980s when researchers from the United States and Sweden introduced the

concept of the waist-to-hip ratio (WHR = waist circumference (cm) ÷ hip circumference (cm)) over BMI, as a better independent risk factor of metabolic disease and CVDs (Kissebah et al. 1982; Krotkiewski et al. 1983; Lapidus et al. 1984; Larsson et al. 1984; Ohlson et al. 1985). The researchers showed that a higher WHR was strongly correlated with increased dyslipidaemia, hypertension, CVDs, and T2D. Subsequently a WHR of 0.95 for men and 0.80 for women were set as the upper limits defining abdominal obesity (Misra and Vikram 2003). However, in 1994 Pouliot et al. showed that waist circumference provided a better predictor of abdominal obesity and visceral adiposity, with a stronger association with serum insulin levels, than WHR (Pouliot et al. 1994). Additionally, other studies have shown that waist circumference measurements are a better predictor of CVD and T2D risk than BMI alone (de Koning et al. 2007; Vazquez et al. 2007). One study of 168,000 primary care patients in 63 countries showed that waist circumference had a greater positive correlation with CVD and T2D than BMI, and even showed a significant correlation with CVD and T2D in lean patients (Balkau et al. 2007). A review of the evidence for WHR and waist circumference by the WHO recommended waist circumference over WHR, due to its ease of measurement. The guidelines for indicating increased disease risk suggest a cut-off for waist circumference, in individuals with a BMI ≥25, of >102 cm for men and >88 cm for women. The WHO does point out that these guidelines may be more appropriate for Caucasians, with limited evidence showing differences between different ethnic groups (World Health Organization 2011).

What makes central obesity a major risk factor for CVDs, T2D, and metabolic syndrome is its association with increased visceral distribution of adipose tissue. The measurement of waist circumference itself cannot indicate visceral adiposity, with the inability to discriminate between the contributions of liver steatosis, and subcutaneous and visceral adipose to central obesity. However, numerous studies on large patient cohorts from the Framingham Heart Study (FHS) and Jackson Heart Study (JHS) using computed tomography (CT) scanning convincingly showed that increased visceral adiposity is strongly correlated with CVD risk factors, T2D, and inflammation (Pou et al. 2007; Rosito et al. 2008; Preis et al. 2010; Tadros et al. 2010; Liu et al. 2010a; 2010b; 2011a). These studies showed that the volume of abdominal visceral adipose tissue (VAT)

was positively correlated with insulin resistance; risk of T2Ds, hypertension, and metabolic syndrome; increased fasting plasma glucose and TGs, and lower HDL cholesterol. VAT was shown to be a stronger correlate than abdominal subcutaneous adipose tissue (SAT) (Preis et al. 2010; Liu et al. 2010b). Additionally, they showed that increased abdominal VAT had a stronger correlation than fatty liver, for metabolic syndrome and diabetes; increased fasting serum glucose, TGs, and haemoglobin A1C, and decreased HDL cholesterol (Liu et al. 2011a). Whilst examining the local effects of VAT depots on the vasculature, the researchers showed that increased pericardial adipose (surrounding the heart) correlated with coronary artery calcification, and increased intrathoracic adipose correlated with abdominal aortic calcification, indicating atherosclerosis (Rosito et al. 2008; Liu et al. 2010a). Finally, they showed that abdominal VAT was a stronger correlate with systemic measurements of inflammation and oxidative stress than abdominal SAT, such as: serum C-reactive protein (CRP), IL-6, monocyte chemoattractant protein-1 (MCP-1/CCL2), and urinary isoprostanes (marker of oxidative stress) (Pou et al. 2007; Tadros et al. 2010). Another independent study showed that abdominal VAT was positively associated with systemic markers of inflammation in T2D patients with obesity, including CRP, CCL2, plasminogen activator inhibitor type 1 (PAI-1), intracellular adhesion molecule (ICAM)-1, and vascular cell adhesion molecule (VCAM)-1 (Sam et al. 2009). These associations of VAT with inflammation are important in contributing to the co-morbidities of obesity, which will be the focus of the later sections. It is hypothesised that the anatomical location of VAT contributes to the systemic effects of obesity, as intra-abdominal VAT has direct drainage through the portal vein to the liver. This allows the flow of free fatty acids (FFAs) (see section 1.2.1.4) and inflammatory adipokines (see section 1.2.1.5) to the liver, contributing to NAFLD and systemic inflammation, along with local inflammatory effects on organs in the torso (Ibrahim 2010).

On the other hand, subcutaneous distribution of adipose has been shown to elicit protective effects. For example, women tend to show a more favorable CVD risk profile than men, with generally lower levels of VAT in favor of SAT, and when these differences in VAT area are controlled for, the CVD risk profile between sexes is similar (Lemieux et al. 1994). Additionally, peripheral fat mass

distribution over central distribution has been shown to provide greater protection from atherosclerosis in women (Lissner et al. 2001; Tankó et al. 2003a; 2003b). There is evidence that the protective distribution of adipose tissue in women is hormonally controlled. Metabolic studies on transsexuals undergoing hormone replacement therapy (HRT) have shown that a female-to-male transition (with testosterone) causes a loss of gluteal-femoral fat and gain of VAT, whereas the opposite was observed during male-to-female transition (with oestrogen) (Elbers et al. 1997; 1999; 2003). Additionally, VAT was shown to express a higher density of androgen receptors than SAT (Freedland 2004), with oestrogen receptors in SAT of men showing a greater binding capacity for oestrogen (Pedersen et al. 1996). In men, testosterone has been suggested to be protective, with correlations being observed between the reduction in testosterone over age and the accumulation of VAT, which can be reduced by testosterone administration. However, the opposite appears true in women, where VAT accumulation is associated with increased testosterone. Reduced oestrogen levels, especially in post-menopausal women are also associated with increased VAT (Freedland 2004). Further risk factors for VAT development include age, smoking, genetic predispositions, and stress, with VAT showing a higher expression of glucocorticoid receptors (Rebuffé-Scrive et al. 1985; Ibrahim 2010; Després 2012).

1.1.5 Inflammation and Obesity

It is now well accepted that obesity is a chronic inflammatory disease, associated with low-grade inflammation and altered metabolism, a state termed “metaflammation” by Gregor et al. to differentiate it from classical inflammation (Gregor 2011). The connection between inflammation and metabolism in obesity was first made by Hotamisligil and colleagues, who showed that during rodent obesity TNFα is expressed in adipose tissue, primarily by adipocytes, and contributes to local adipocyte and peripheral insulin resistance (Hotamisligil et al. 1993). These observations were followed by reports showing increased TNFα expression in adipose tissue from individuals with obesity, which correlated with hyperinsulinaemia and reduced adipose tissue lipoprotein lipase (LPL) activity. Weight loss was shown to reduce adipose tissue TNFα expression in these individuals (Hotamisligil et al. 1995; Kern et al. 1995). Subsequently TNFα was

also shown to induce lipolysis in adipocytes, inhibit *in vitro* differentiation of pre-adipocytes, and block insulin signaling by causing serine phosphorylation of the insulin receptor, contributing to adipose insulin resistance (Fantuzzi 2005; Gregor 2011). Inflammation is seen in other tissues such as the vasculature, pancreas, liver, brain, and maybe muscle during obesity, but in this thesis we are focusing on the adipose (section 1.2) (Gregor 2011).

TNFα is not the only inflammatory marker seen during obesity. In obese serum a number of other markers and mediators of inflammation can be seen, including fibrinogen, CRP, sialic acid, serum amyloid A (SAA), PAI-1, retinol binding protein 4 (RBP4), IL-1β, IL-6, IL-18, CCL2, and CXCL8 (Fantuzzi 2005; Shoelson et al. 2006; 2007; Galic et al. 2010). An increase in blood leukocytes (white blood/immune cells) is also observed that, along with many of these inflammatory markers, is correlated with insulin resistance and T2D (Shoelson et al. 2006). This increased level of systemic inflammation within the circulation could be an important contributing factor to the pathogenesis of atherosclerosis, which has a large inflammatory component, and hence increased CVD (Libby et al. 2011). Additionally, many of these inflammatory mediators and cytokines are produced by the adipose tissue, including TNFα, IL-1β, IL-6, CCL2, CXCL8, SAA, PAI-1, and RBP4 (Fantuzzi 2005; Shoelson et al. 2007; Galic et al. 2010). In fact, the adipose tissue has been estimated to produce about one third of the circulating IL-6 (Fantuzzi 2005). Additionally, RBP4 secreted by adipocytes was shown to induce systemic insulin resistance in mice, by inhibiting insulin signalling in skeletal muscle and increasing hepatic glucose output (Yang et al. 2005). However, in humans, RBP4 protein was shown to increase in the serum of individuals with obesity, but not in the abdominal SAT (Yang et al. 2005; Hoggard et al. 2012). These inflammatory mediators can contribute to adipose inflammation and the infiltration of immune cells, which can further exacerbate local and systemic inflammation and insulin resistance, talked about in more detail in sections 1.2.1.4, 1.2.1.5, and 1.2.1.6.

1.1.6 Cholesterol Metabolism

The dyslipidaemia associated with obesity is a major risk factor for CVD development. Results from the Framingham Heart Study, Seven Countries Study, and Copenhagen General Population Study/Copenhagen Heart Study/Copenhagen Ischemic Heart Disease Study have shown that increases in BMI are associated with increases in serum TGs, LDL cholesterol, and total cholesterol with a reduction in HDL cholesterol (Garrison et al. 1980; Tervahauta et al. 1993; Molenaar et al. 2008; Ingelsson et al. 2009; Varbo et al. 2015). Correlations have been observed between reduced HDL cholesterol and increased LDL cholesterol, with increased CVD risk (Kannel 1985; Varbo et al. 2015). In particular, there is an abundance of evidence for "the LDL hypothesis," which states that increased LDL cholesterol is causal in the development of atherosclerosis (Jarcho and Keaney 2015). The Cholesterol Treatment Trialists' (CTT) collaborators showed that a plasma LDL cholesterol reduction of 1 mmol/L over 5 years reduced overall major vascular events by 21%, in patients treated with statins (Baigent et al. 2005). Furthermore, results from the Improved Reduction of Outcomes: Vytorin Efficacy International Trial (IMPROVE-IT) showed that statin-independent reductions in LDL with ezetimibe, through reduced intestinal cholesterol absorption, significantly improved cardiovascular outcome (Cannon et al. 2015).

There are two main sources of cholesterol in humans, dietary intake and *de novo* synthesis, with the latter showing the biggest contribution to overall body cholesterol (approximately 70%). One of the main sites of cholesterol biosynthesis is liver hepatocytes (Ikonen 2008). All nucleated cells can synthesise cholesterol, even adipocytes, with cholesterol content and synthesis being shown to increase with adipocyte hypertrophy. However, the rate of cholesterol synthesis in adipose tissue is only about 4% that of the liver, making it a minor contributor to total body cholesterol (Kovanen et al. 1975). Cholesterol is synthesised from acetyl-CoA through the mevalonate pathway. The rate-limiting step in this pathway is the conversion of 3-hydroxy-3-methyl-glutaryl-coenzyme A (HMG-CoA) to mevalonate, which is catalysed by HMG-CoA reductase (HMGCR). Mevalonate is then converted to cholesterol through a number of other enzymatic steps that produce

isopentenylpyrophosphate, squalene, lanosterol, and 7-dehydrocholesterol as intermediate compounds. The resulting cholesterol can then be hydroxylated to produce oxysterols or acylated with fatty acid (FA) to produce cholesteryl esters. Cholesterol and cholesteryl esters can then be packaged into lipoproteins for transport around the body by intestinal enterocytes and liver hepatocytes (Ikonen 2008).

Dietary cholesterol along with TGs are packed into chylomicrons by enterocytes of the small intestine and released into the circulation. The chylomicrons are processed by peripheral tissues, such as adipocytes (section 1.2.1.1), using lipoprotein lipase (LPL) to hydrolyse the TGs into free-fatty acids (FFAs) for uptake. This produces chylomicron remnants with apoproteins that are transported to and internalised by liver hepatocytes using the LDL receptor (LDLR). The hepatocytes then package lipids into very low density lipoproteins (VLDLs), which are processed by peripheral tissues into cholesterol-rich LDL. LDL can then be internalised by peripheral tissues using LDLR to deliver cholesterol to the cell. Liver-derived HDL can collect excess cholesterol from peripheral tissues and return it to the liver in a process called “reverse cholesterol transport.” The returned cholesterol can then be secreted into the small intestine by the liver in bile as cholesterol or bile acids, which can be reabsorbed by enterocytes or excreted. The classic pathway of bile acid synthesis is catalysed by the rate-limiting enzyme cholesterol 7α-hydroxylase (CYP7A1), which produces cholic acid from cholesterol (Ikonen 2008).

These processes of cholesterol synthesis, uptake, and processing can be transcriptionally controlled by sterol regulatory element binding proteins (SREBPs) and liver X receptors (LXRs) (Ikonen 2008). SREBPs are encoded by two genes: SREB transcription factor 1 (*SREBF1*) and *SREBF2*, with the former encoding 2 proteins, SREBP1a and SREBP1c, and the latter just one, SREBP2. SREBP1c is the SREBP1 isoform predominantly expressed in the liver, adipose, and muscle, and SREBP2 is predominantly expressed in the liver. SREBP1c mainly activates genes involved in FA and TG synthesis (section 1.2.1.1), whereas SREBP2 mainly activates LDLR and genes involved in cholesterol synthesis (e.g. HMGCR), increasing cellular cholesterol (Horton et al. 2002). SREBP is present in the ER

and is activated during times of low sterol production by proteolytic cleavage; the processed fragment then translocates to the nucleus (Ikonen 2008). LXRs consist of 2 isotypes: LXRα (NR1H3), which is mainly expressed in the liver, adipose tissue, and macrophages, and LXRβ (NR1H2), which is expressed ubiquitously (Calkin and Tontonoz 2012). LXRs are activated by oxysterols and promote reverse cholesterol transport, increasing secretion of cholesterol in the bile (Ikonen 2008; Calkin and Tontonoz 2012). Additionally, LXRs activate SREBP1c, increasing FA synthesis, which increases cellular oleate that can be used to produce cholesteryl esters for transport and storage (Horton et al. 2002). LXRs have also been shown to increase serum HDL and HDL return to the liver, serum VLDL levels, and the degradation of LDLR expression on peripheral cells, reducing peripheral LDL uptake (Calkin and Tontonoz 2012).

1.1.7 Current Obesity Therapies

There are few clinical therapies that target obesity itself to reduce weight and in the process improve metabolic and inflammatory phenotypes. The main treatment for obesity is lifestyle modification involving changes in physical activity and diet to shift the energy balance to greater energy expenditure, hence inducing weight loss. This can also be accompanied by behavioral therapy to help patients stick to diet and exercise regimes (Fabricatore and Wadden 2003). However, lifestyle changes reduce weight by only 5-10% in most cases, with the majority relapsing after 3-6 months. There are other pharmacological and surgical treatments that can be used if patients struggle to lose weight, although these are limited. For patients with severe obesity (BMI ≥40 kg/m^2 or ≥35 kg/m^2 with comorbidities), bariatric surgery may be suggested as a therapeutic option (Fabricatore and Wadden 2003; Svane and Madsbad 2014). This is a collection of surgical procedures that limit the stomach size to reduce overeating and aid weight loss. The most common bariatric surgery procedures are laparoscopic sleeve gastrectomy (SG), laparoscopic adjustable gastric banding (LAGB), and laparoscopic Roux-en-Y gastric bypass (RYGB). Collectively, these bariatric procedures result in weight loss of 20-30% over 15-20 years and have a low rate of complications, but RYGB shows the highest mortality. Additionally, bariatric

surgery has been shown to significantly improve patients CVD risk (Svane and Madsbad 2014).

The only weight loss medication approved in the European Union (EU) is orlistat, which inhibits pancreatic lipase, reducing dietary fat absorption. Orlistat has limited efficacy, but has a well-established safety record with minor side effects. However, it is only prescribed in individuals with obesity (BMI ≥30 kg/m^2) or those that have a BMI ≥28 kg/m^2 and obesity comorbidities. There are a few other weight loss medications that have been approved outside the EU including locaserin and liraglutide. Locaserin acts centrally in the brain as an agonist of the serotonin receptor 5-HT_{2C}, inducing satiety by activating pro-opiomelanocortin (POMC) neurones and reducing ghrelin-induced food intake. Liraglutide is a long-acting glucagon-like peptide (GLP)1 mimic, causing anti-hyperglycaemia effects through stimulation of glucose-mediated insulin secretion and inhibition of glucagon secretion from the pancreas. GLP1 also decreases appetite by reducing gastric emptying. Although both locaserin and liraglutide show efficacy in inducing weight loss, clinical trials have shown a high drop-out rate due to common uncomfortable side-effects of dizziness, headaches, nausea, and vomiting (Rankin and Wittert 2015).

Patients with obesity are usually also on other pharmacological therapies to manage obesity comorbidities, particularly dyslipidemia and hyperglycaemia/T2D. However, not all individuals with obesity will have these comorbidities, as some have “metabolically healthy obesity” (Kim et al. 2015c). The frontline therapy for patients with dyslipidaemia is a statin, such as lovastatin, parvastatin, and simvastatin. Statins inhibit HMGCR (section 1.1.6) reducing cholesterol synthesis and hepatic cholesterol, which triggers the up-regulation of hepatic LDLR expression, clearing more LDL from the blood. They may also decrease hepatic synthesis and secretion of lipoproteins. Apart from their LDL-lowering effects statins have also been shown to modestly increase plasma HDL and decrease TGs. Statins are very effective and can cut CHD risk by 30% over a 5-year period in high risk patients, and were shown to reduce serum CRP levels and incidence of transplant rejection (Maron et al. 2000). The frontline pharmacological therapy for T2D is metformin, which lowers blood glucose by reducing hepatic glucose

secretion and increasing insulin sensitivity of peripheral tissues, mainly muscle, increasing glucose uptake from the blood. Metformin induces these effects through activation of liver kinase B1 (LKB-1) that then inactivates adenosine monophosphatase co-activator, transducer of regulated CREB protein 2 (TORC2), downregulating the transcription of gluconeogenic enzymes (Mazzola 2012; Rojas and Gomes 2013). Additionally, metformin can help weight maintainance or cause some weight loss (Mazzola 2012). Treatment of patients with metformin has been shown to reduce CVD mortality, particularly atherosclerosis and myocardial infarction (Rojas and Gomes 2013).

1.1.8 Murine Models of Obesity

Animal models of disease represent an invaluable tool for studying human diseases. They allow investigators the ability to examine the effects of manipulating particular molecules and pathways on multiple biological systems within the animal, and the effect this has on the overall disease phenotype. Additionally, they allow for greater control over environmental variables, including diet (e.g. fat, carbohydrate, and protein content), activity, light-dark cycles, ambient temperature, and pathogen exposure. This makes them useful for controlling and studying physiology, studying immune function, and elucidating mechanisms. Importantly, they can give insights into therapies for human diseases, through controlled administration of small molecules or other therapeutics, or surgical procedures. The use of smaller mammals, such as mice, allows for the study of chronic diseases and their development over a reasonable time frame, with greater numbers for statistical power, and at lower costs. Their shorter generation times and large litters also allow for quicker generation of colony numbers, and of transgenic animals with the appropriate genotype. A further advantage of mice is the relative ease of genetic manipulation for producing knock-out (KO) and knock-in transgenic animals, with the ability to produce full-body, tissue-specific, and conditional transgenics, allowing studies on specific gene functions (Rosenthal and Brown 2007). This level of genetic manipulation *in vivo* was generally reserved for mice, until the advent of clustered regularly interspaced short palindromic repeats (CRISPR)/Cas9 technology. However, animal models are not perfect. Each have their own pitfalls, and it can be argued that the best models for

human disease are humans, although they come with their own obvious ethical and logistical issues. The standard animal models used in obesity research fall into two main categories: diet-induced obesity and genetic obesity.

1.1.8.1 Diet-Induced Obesity

Diet-induced obesity in mice is considered more reflective of human obesity. As only a small percentage of human obesity cases are related to genetic variations and the majority of free-living humans develop obesity through obesogenic diets and a sedentary lifestyle (section 1.1.2). Therefore, feeding mice an obesogenic diet with restricted physical activity follows the same developmental line as human obesity. The main obesogenic diet is a high-fat diet (HFD), which contains approximately 30-78% of the calories from fat (mainly saturated fats) and higher cholesterol levels (Hariri and Thibault 2010). Previous research has shown that high-fat : low-carbohydrate diets are more effective than low-fat : high-carbohydrate diets (Takahashi et al. 1999). These HFDs induce increased body weight, white adipose tissue (WAT) weight, liver weight and triglycerides, fasting blood glucose (FBG), glucose tolerance, insulin resistance, serum cholesterol, and white adipocyte hypertrophy and hyperplasia (Bourgeois et al. 1983; Takahashi et al. 1999; Eisinger et al. 2014). However, there are mouse strain-specific differences in their susceptibility to diet-induced obesity through HFD feeding. A comparison between different mouse strains on HFD showed that BALB/c are resistant to weight gain, glucose tolerance, and insulin resistance, with 129X1 and DBA/2 mice showing the greatest susceptibility, and C57BL/6 and FVB/N mice showing a more moderate susceptibility (Montgomery et al. 2013). Out of these strains only 129X1 was shown to have increased serum TGs on HFD, which points out that these models still do not fully replicate human obesity. It is worth noting that there are also strain-specific differences in immune function of mice strains. For example, C57BL/6 mice tend to show a bias towards a T helper cell 1 (Th1)-type immune response, whereas BALB/c mice show a bias towards a T helper cell 2 (Th2)-type immune response, reviewed here (Sellers et al. 2012). C57BL/6 mice have also been shown to develop obesity on a normal diet while they age, with a slow, gradual accumulation of fat over time, mimicking human obesity (Lutz and Woods 2012).

1.1.8.2 Genetic Models of Obesity

The most commonly-used mouse models of obesity are the leptin-deficient obese (*ob/ob*) mouse and leptin receptor-deficient diabetic (*db/db*) mouse (Lutz and Woods 2012). Both of these genotypes were shown to cause almost identical phenotypes when expressed on the same inbred murine background. Furthermore, parabiosis experiments by Coleman and colleagues during the 1960s-70s showed that *ob/ob* mice lack a secreted satiety factor and *db/db* mice cannot respond to this factor due to a defect in the satiety centre (Coleman 1978).

The *ob/ob* mouse was discovered by Ingalls et al. in 1950 when a spontaneous mutation occurred. They observed that these mice weighed twice that of their WT counterparts at 3 months of age (Ingalls et al. 1950). Then the seminal paper by Mayer et al. in 1951 showed that these mice also had increased FBG levels and insulin resistance (Mayer et al. 1951). However, the gene product of *ob*, leptin, was not discovered until 1994 by the Friedman laboratory (Zhang et al. 1994). The authors sequenced the *ob* gene and discovered that a single nucleotide substitution introduced a stop codon into the gene, prematurely terminating gene translation; this gene was shown to be specifically expressed by WAT. Further work by Friedman and others showed that circulating leptin increases proportionally to WAT mass and acts on the hypothalamus to decrease food intake and increase energy expenditure (Friedman 1997). *ob/ob* mice are characterised by expressing symptoms of: excessive eating (hyperphagia), hyperinsulinaemia, hyperglycaemia, obesity, hypogonadism, sterility, hypertrophy and hyperplasia of pancreatic islets of Langerhans, stunted growth (growth hormone deficiency), hypothermia, hormonal abnormalities, and reduced movement (Coleman 1978; Friedman 1997). These symptoms are reversed by administration of recombinant leptin (Friedman 1997).

The *db/db* mouse was discovered by Hummel et al. in 1966 after a spontaneous mutation occurred, and were shown to have a similar phenotype to *ob/ob* mice, but more severe hyperglycaemia (in a different mouse strain) (Hummel et al. 1966; Coleman and Hummel 1967). However, it was not known that the *db* gene coded for the leptin receptor until its discovery in 1995 by Tartaglia et al. (Tartaglia et al. 1995). One difference these mice have over *ob/ob*,

is that they express high levels of circulating leptin (Coleman 1978). Both of these genotypes have the advantage that they rapidly produce an extreme obese phenotype and can be used to examine the effects of treatments on eating behavior. However, they are not truly reflective of the human population, where obesity tends to develop gradually over time and the majority have normal leptin signaling, apart from the development of leptin resistance (Friedman 1997). The abnormality in leptin signaling may also obscure other metabolic changes from interventions. There are other genetic models of obesity downstream of the brain leptin receptor, including murine KOs of POMC, AgRP, MC4R, MC4R, and MC4/MC3 receptor, reviewed here (Lutz and Woods 2012).

1.2 Adipose Tissue

The main proponent of weight gain and pathology during obesity is adipose tissue, particularly WAT. However, there are two known types of adipose tissue: WAT and brown adipose tissue (BAT), with somewhat contrasting roles. WAT has a major role as a highly plastic store of lipids that helps maintain energy balance within the body. BAT is highly metabolically active and oxidises lipids to produce heat, maintaining body temperature homeostasis through non-shivering thermogenesis. These tissues are mainly composed of white and brown adipocytes, respectively, but WAT also contains the more recently discovered beige/brite adipocytes that express attributes of both white and brown adipocytes (Cannon and Nedergaard 2012a).

There are numerous anatomical locations of WAT and BAT around the body (Figure 1.3). WAT is mainly distributed subcutaneously (scWAT) in the hypodermis and viscerally (vWAT), surrounding the internal organs within the torso (Wronska and Kmiec 2012). There are two main scWAT depots in rodents: anterior and posterior (Figure 1.3B). The anterior depot mainly occupies the dorsal region and includes the interscapular, subscapular, axillo-thoracic, and superficial cervical areas. The posterior depot is situated at the base of the hind legs and runs across the dorso-lumbar, inguinal, and gluteal areas. The vWAT depots in rodents are spread through the thoracic and abdominal cavities, with the former including the mediastinic depot. In the abdomen, there are the mesenteric, retroperitoneal,

perirenal, omental (very little in mice), and perigonadal depots. The perigonadal depot surround the ovaries, uterus, and bladder in females and is named periovarian adipose tissue. In males, this depot surrounds the epididymis, and is named epididymal adipose tissue (eWAT). All of these adipose depots mentioned above can contain both WAT and BAT, with the proportions varying depending on: species, strain, age, and environmental/nutritional conditions. However, the main BAT depots are usually found in the anterior subcutaneous (interscapular, subscapular and axillo-thoracic), visceral mediastinic, visceral perirenal areas, and cervical (Cinti 2005).

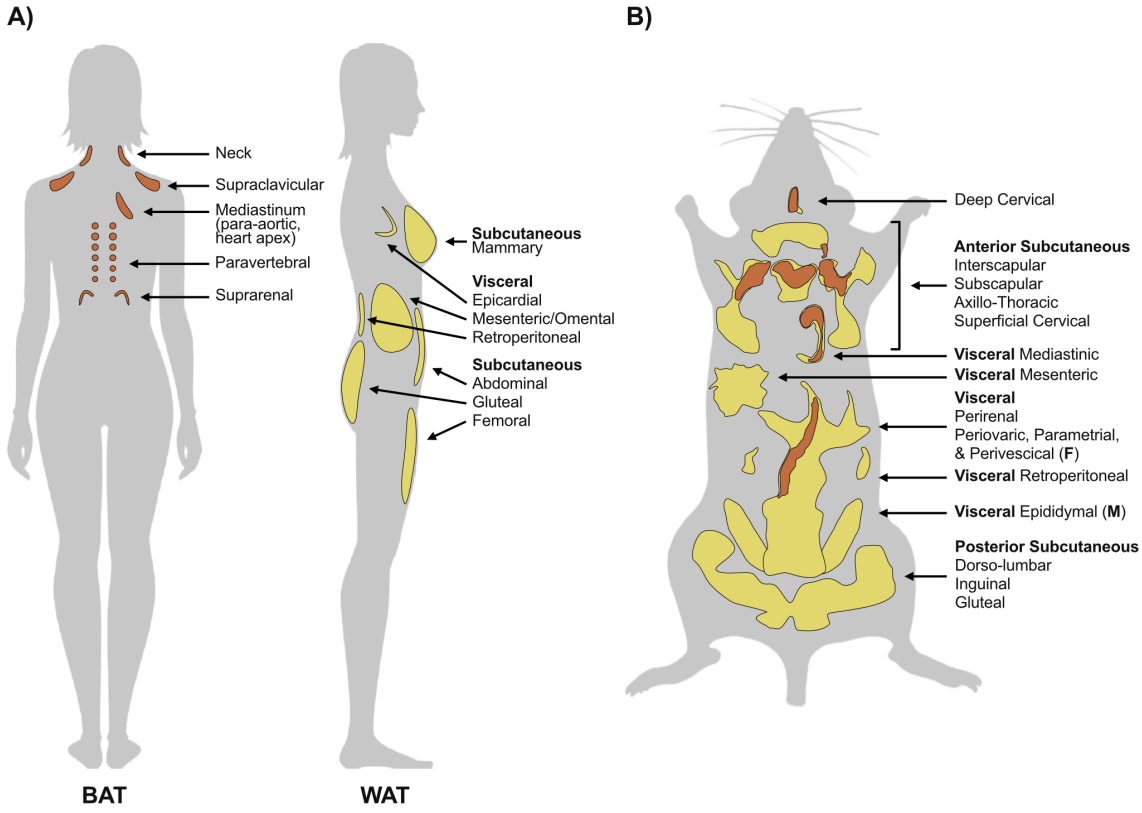

Figure 1.3: Diagram of the Major White and Brown Adipose Depots in Humans and Mice
(A) Showing the major brown adipose tissue (BAT) and white adipose tissue (WAT) depots in humans. (B) Showing the major BAT and WAT depots in mice, with female (F) and male (M) specific depots indicated. BAT is indicated by the colour brown and WAT by the colour yellow. Diagrams are adapted from (Cinti 2005; Nedergaard et al. 2007; Wronska and Kmiec 2012).

Most of these adipose depots are also conserved in humans, but there are a few key differences (Figure 1.3A). In humans, the BAT depots are found in similar regions in newborns, but there is loss of the interscapular BAT depot shortly after birth. In adults, this leaves BAT depots in the neck (cervical), supraclavicular,

paravertebral, mediastinum (para-aortic and heart apex), and suprarenal areas (Nedergaard et al. 2007). Furthermore, the WAT distribution in humans is similar to that in mice; however, mice lack the subcutaneous abdominal depot, have a greatly reduced visceral omental depot, and lack visceral epicardial adipose tissue. Humans also have an additional visceral pararenal depot and lack the visceral perigonadal depots, but both mice and humans have mammary adipose tissue (Wronska and Kmiec 2012). Both WAT and BAT are highly vascularised and innervated by nerves, mainly consisting of noradrenergic fibres; however, BAT shows a denser vascularisation and nerve innervation than WAT (Cinti 2005).

1.2.1 White Adipose Tissue

WAT is mainly composed of unilocular white adipocytes, with one large lipid droplet, containing neutral lipids consisting of steryl esters, like cholesteryl ester, and TGs. These act as an important medium for neutralising the toxic effects of FFAs by esterification of FAs with glycerol to make TGs (providing energy storage) and esterification of sterols with FAs to make steryl esters (allowing storage of new membrane components). This TG store provides an important source of energy for cells, which can be densely packed due to the hydrophobic nature of TGs. The FAs in these molecules can be oxidised in the mitochondria to release energy, with complete oxidation giving off approximately 38 KJ/g, more than double that of carbohydrate or protein (Sturley and Hussain 2012). Because white adipocytes have the infrastructure to store large amounts of lipid, this makes them important storage vessels of energy reserves for managing energy homeostasis. WAT shows great plasticity with the ability to expand and contract depending on energy demands. However, WAT also contributes to maintaining body temperature by providing insulation, provides cushioning to protect body tissues and organs from mechanical damage, and can direct physiological and immunological function by secreting a number of hormones and cytokines called adipokines (section 1.2.1.3) (Wronska and Kmiec 2012).

1.2.1.1 Overview of Biochemical Control of Lipid Storage

TGs accumulate in white adipocytes for storage by two main pathways: uptake of FFA from plasma or *de novo* lipogenesis (from non-lipid precursors). A

number of proteins and enzymes are involved in these processes (Figure 1.4). FAs are delivered to adipocytes in the form of TGs contained within gut-derived chylomicron lipoproteins or liver-derived VLDL. These large lipoprotein molecules are processed within the luminal space of adipose tissue capillaries to release FAs from the lipoprotein TGs by LPL. LPL is synthesised and secreted by adipocytes before it is translocated to the capillary endothelium, where it is bound by glycosaminoglycans (e.g. heparin sulphate proteoglycans) facilitating LPL-dependent lipolysis of the lipoproteins. LPL is also increased in the fed-state and decreases during fasting. The liberated FAs move through the endothelial lining towards the adipocytes; however, adipocytes are not 100% efficient at capturing FFAs, leaving some to become bound to serum albumin for transport to other tissues. The FFAs can passively diffuse across the adipocyte cell membrane, but they are also actively transported by plasma membrane fatty acid-binding protein (FABPpm), fatty acid transport proteins (FATP)-1, and fatty acid translocase (FAT/CD36). The uptake of these FFAs across the cell membrane is linked to their conversion to acyl-CoA by acyl-CoA synthetases (ACSs), with FATP-1 constitutively associating with ACS-1/ACS long-chain family member-1 (ACSL1). ACSs are a family of isozymes specific for short, medium, and long-chain FAs that catalyse the conversion of FAs to acyl-CoA. Additionally, FATP-1 is upregulated by insulin to increase FA uptake (Lafontan 2008).

The major site of *de novo* lipogenesis is the liver; however, adipose tissue can carry out lipogenesis from non-lipid substrates to store the energy as lipid, generally after a carbohydrate-rich meal (Figure 1.4). Cytosolic glucose goes through glycolysis to produce pyruvate, which is converted to acetyl-CoA by pyruvate dehydrogenase that then enters the Krebs (citric acid/TCA) cycle in the mitochondrion matrix. Excess citrate from Krebs cycle is transported into the cytoplasm and converted to acetyl-CoA by adenosine triphosphate (ATP)-citrate lyase (ACL), which is then converted to malonyl-CoA by acetyl-CoA carboxylase (ACC)α, the rate-limiting enzyme for FA synthesis in adipose. Both acetyl-CoA and malonyl-CoA from these enzymatic processes are then converted to the FA palmitic acid by fatty acid synthase (FAS/FASN), which can be converted to other FFAs by other processes. These FFAs are then converted to acyl-CoA by ACSs (Saponaro et al. 2015; Solinas et al. 2015).

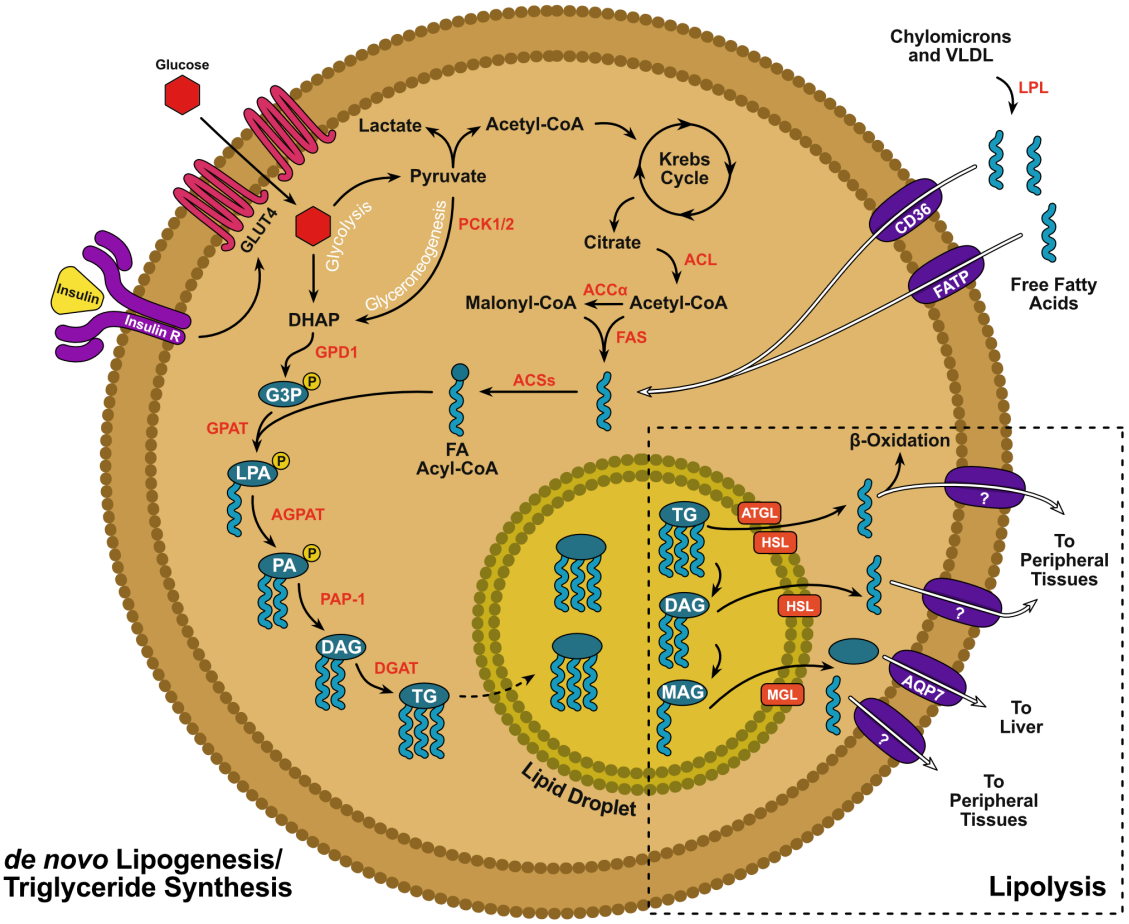

Figure 1.4: Diagram of the Biochemical Mechanism for Triglyceride Storage and Release in Adipocytes
Showing an overview of the biochemical processes involved in de novo lipogenesis, de novo triglyceride synthesis, and lipolysis in adipocytes. These processes are detailed in the main body text, and the information for this diagram was adapted from (Coleman 2004; Lafontan 2008; Rutkowski et al. 2015; Saponaro et al. 2015). Insulin R (insulin receptor), AQP7 (aquaporin 7).

Once the FFAs from the circulation or *de novo* lipogenesis are in the cytosol, they need esterification with glycerol-3-phosphate (G3P) for storage in the lipid droplet (Figure 1.4). However, adipocytes lack the enzyme glycerol kinase, found in the liver, that generates G3P from glycerol by phosphorylation. Therefore, to generate G3P, dihdroxyacetone-3 phosphate (DHAP) produced during glycolysis is converted to G3P by glycerophosphate dehydrogenase (GPD1). DHAP can also be produced through glyceroneogenesis, where pyruvate, lactate, and amino acids can be converted to DHAP by the assistance of phosphoenolpyruvate carboxykinase (PEPCK), which has a cytoplasmic (PCK1) and mitochondrial (PCK2) isoform. PCK1/2 are the rate-limiting enzymes that assist in the formation of DHAP by catalysing the conversion of oxaloacetate to phosphoenolpyruvate. The first, rate-limiting step in *de novo* TG synthesis is catalysed by the acyl-

CoA:glycerol-3-phosphate acyltransferase (GPAT) enzymes in either the mitochondria (GPAM & GPAT2) or ER (GPAT3 & GPAT4), which acylates (adds an acyl-CoA FA) G3P to form lysophosphatidic acid (LPA). In adipocytes LPA is then further acylated to phosphatidic acid (PA) in a reaction catalysed by acylglycerol-3-phosphate acyltransferase (AGPAT)-1 or -2 in the ER, other cell types also use AGPAT-3, 4, and 5. Next, PA is dephosphorylated to produce diacylglycerol (DAG) by phosphatidic acid phosphatase (PAP)-1/LPIN1 in the ER. Finally, DAG is acylated to produce triacylglycerol/triglyceride (TAG/TG) by diacylglycerol O-acyltransferase (DGAT)-1 and -2 in the ER. The finished TGs are then transported to the lipid droplet for storage (Coleman 2004; Rutkowski et al. 2015).

To convert the TGs stored in the adipose lipid droplet back into FFAs for beta-oxidation, or for release into the circulation for metabolism by other cells, they go through lipolysis (Figure 1.4). The reaction is catalysed by lipases recruited to the lipid droplet: hormone sensitive lipase (HSL), adipose triglyceride lipase (ATGL), and monoacylglycerol lipase (MGL). HSL is a hydrolase that can bind multiple substrates: TG, DAG, cholesterol ester, and retinyl ester, which catalyses the hydrolysis (breakdown) of TG into DAG and DAG into monoacylglycerol (MAG). ATGL also catalyses the hydrolysis of TG to DAG, but with specificity for TGs. Finally, MAG is hydrolysed to a FFA and glycerol by MGL. This whole process produces 3 FFAs and 1 glycerol for every TG, which can then be exported from the adipocyte and released into the circulation, allowing uptake of FFAs by peripheral tissues and glycerol uptake by the liver. The FFAs are shuttled around the adipocyte by fatty acid binding proteins (FABPs), such as FABP4, which is primarily expressed in adipocytes (Lafontan 2008; Saponaro et al. 2015).

This balance between *de novo* lipogenesis/*de novo* TG synthesis and lipolysis is hormonally regulated. For example, insulin promotes lipid synthesis and adipogenesis, and inhibits lipolysis; whereas glucagon and catecholamines (e.g. noradrenaline/norepinephrine & adrenaline/epinephrine) inhibit FA synthesis and promote lipolysis (Saponaro et al. 2015). Insulin signaling has been shown to promote exocytosis of the predominant adipocyte glucose transporter: glucose transporter type 4 (GLUT-4), to the cell membrane, enhancing glucose uptake into

the cell (Stöckli et al. 2011). This would then regulate the rate of glycolysis and hence regulate *de novo* lipogenesis and TG synthesis. Additionally, the production of lactate from glycolysis can inhibit lipolysis (Ahmed et al. 2010), and insulin can inhibit lipolysis by blocking phosphorylation of HSL (Strålfors et al. 1984). GLUT-4 expression has also been linked to increasing expression of carbohydrate-responsive-element-binding protein (ChREBP) through increased glucose uptake, which enhances lipogenesis by increasing *Accα* and *Fasn* transcripts (Herman et al. 2012). SREBP-1c/*SREBF1*) is also expressed in adipose, which in the liver increases expression of ACCα, FAS, and glycolytic genes (e.g. $_{L}$-pyruvate kinase ($_{L}$-PK)), but plays a more minor role in adipose (Shimano et al. 1999; Dentin et al. 2004; Herman et al. 2012). LXRs activate SREBP-1c in hepatocytes (Ou et al. 2001), and have also been shown to increase the expression of GLUT4, promoting glucose uptake, and enhancing lipolysis and beta-oxidation in adipocytes (Calkin and Tontonoz 2012). Importantly, the production of malonyl-CoA during *de novo* lipogenesis inhibits carnitine palmitoyl transferase-1 (CPT-1), which mediates the rate-limiting step of beta-oxidation by transporting fatty acyl-CoAs through the outer mitochondrial membrane, thereby preserving a lipogenic state (Rutkowski et al. 2015). Furthermore, peroxisome proliferator-activated receptor (PPAR)ɣ has been shown to up-regulate transcripts of many genes involved in FA synthesis, FA transport/uptake, FA storage, FA oxidation and glucose storage in WAT and BAT (Way et al. 2001). There is sympathetic nervous system (SNS) control over these processes too, with noradrenaline/adrenaline stimulation of β1-, β2-, and β3-adrenergic receptors expressed on adipocytes activating HSL and promoting lipolysis in white adipocytes. Conversely, noradrenaline/adrenaline stimulation of α2-adrenergic receptors on white adipocytes inhibits lipolysis (Lafontan and Langin 2009).

1.2.1.2 Adipocyte Differentiation

All adipocytes are derived from a mesenchymal stem cell (MSC) in a process called adipogenesis, which is the common precursor for osteoblasts, myocytes, and chondrocytes as well (Cristancho and Lazar 2011). Adipogenesis is separated into 2 main stages, the “determination phase”: where the stem cell is committed to the adipocyte lineage and forms a pre-adipocyte, and the “terminal differentiation

phase": where the pre-adipocyte differentiates and expresses the characteristics of a mature adipocyte (Moreno-Navarrete and Fernández-Real 2012). Here, the focus will be on the latter phase, as in this thesis pre-adipocytes were isolated from the stromal vascular fraction (SVF) of mature fat pads and differentiated *in vitro* with adipogenic stimuli. The SVF contains fibroblasts that have adipogenic potential (pre-adipocytes) and those that are non-adipogenic, along with endothelial cells, erythrocytes, and immune cells (Cristancho and Lazar 2011). Using mouse studies, WAT pre-adipocyte fibroblasts were shown to reside near adipose blood vessels (perivascular) and express the phenotype: Lin^- $CD29^+$ $CD34^+$ $Sca\text{-}1^+$ $CD24^+$ *in vivo* (Rodeheffer et al. 2008; Tang et al. 2008). Many *in vitro* models of adipogenesis require confluence to differentiate properly (Green and Meuth 1974), and a common pre-adipocyte cell line that is used in many studies is mouse 3T3-L1 cells.

For these pre-adipocytes to become fully differentiated into a mature adipocyte they need to activate peroxisome proliferator-activated receptor (PPAR)ɣ, the so-called "master" regulator of adipogenesis. Additionally, CCAAT/enhancer-binding protein (C/EBP)α, C/EBPβ, and C/EBPɣ, along with PPARɣ, make up the primary drivers of terminal differentiation. Once fully differentiated they will also express a number of genes and proteins important for their mature functions, such as FABP4, GLUT4, HSL, adiponectin, and leptin (Cristancho and Lazar 2011). Additionally, insulin receptor expression and insulin sensitivity increases (Moreno-Navarrete and Fernández-Real 2012). The first stage of differentiation is marked by a morphological change in the pre-adipocyte as the cell loses its spindly fibroblast shape and takes on a round shape, through reorganisation of the cytoskeleton. This process has been shown to be mediated by ectoderm-neural cortex-1 (ENC-1) *in vitro*, where ENC-1 transcripts are transiently increased at the beginning of differentiation, preceding the expression of PPARɣ and C/EBPα genes, and ENC-1 protein is co-localised with actin filaments (Zhao et al. 2000). After this morphological change the adipocyte then begins to accumulate lipid droplets.

Within the first 24 hours of differentiation synthesis of both C/EBPβ and C/EBPɣ are increased (Moreno-Navarrete and Fernández-Real 2012). However,

C/EBPβ is already present in low levels at histone regions of silenced adipogenic genes (Cristancho and Lazar 2011). When differentiation is initiated C/EBPβ is phosphorylated by mitogen-activated protein kinase (MAPK) and glycogen synthase kinase (GSK)3β, activating C/EBPβ (Moreno-Navarrete and Fernández-Real 2012). C/EBPβ then promotes the acetylation of histones at adipogenic gene sites and recruits additional transcription factors, including signal transducer and activator of transcription 5A (STAT5A), glucocorticoid receptor (GR), retinoid X receptor (RXR), C/EBPɣ, and co-activators, which form the transcriptional activation complex (Cristancho and Lazar 2011). These adipogenic gene sites include those for PPARɣ and C/EBPα promoting their transcription, which can then auto-regulate their own transcription, with PPARɣ, C/EBPα, and C/EBPβ cooperating together to further enhance PPARɣ gene transcription (Cristancho and Lazar 2011; Moreno-Navarrete and Fernández-Real 2012). PPARɣ has two protein isoforms: PPARɣ1 that is ubiquitously expressed, with the highest expression in adipocytes (particularly during adipocyte differentiation), and PPARɣ2 that is specific to adipocytes. Together, both PPARɣ and C/EBPα are estimated to promote around 60% of all the genes activated over terminal differentiation. In mature adipocytes, PPARɣ, C/EBPα, and C/EBPβ are essential for continual expression of PPARɣ and C/EBP target genes (e.g. Adiponectin, HSL, and FABP4) (Cristancho and Lazar 2011). However, only PPARɣ has been shown to induce adipogenesis, which can promote adipogenesis in the absence of C/EBPα, but not vice versa (Moreno-Navarrete and Fernández-Real 2012). Both glucocorticoid and cyclic adenosine monophosphate (cAMP) agonists (e.g. 3-isobutyl-1-methylxanthine (IBMX) and dexamethasone, respectively) can increase the expression of C/EBPβ and promote adipogenesis. However, thiazolidinediones (glitazones), such as rosiglitazone, are PPARɣ agonists that can also promote adipogenesis (Cristancho and Lazar 2011).

1.2.1.3 Adipokines

Adipose is not just a passive lipid storage vessel as once thought, but can direct inflammatory and metabolic process by producing a number of inflammatory mediators and cytokines, as mentioned in section 1.1.5. Some of these can be produced by adipocytes themselves (e.g. TNFα, IL-6, CCL2, and PAI-1), but most

are also produced by other cells resident within the adipose tissue (e.g. macrophages) (Shoelson et al. 2007). The idea that adipose is an important endocrine organ was first introduced when Friedman's group and Coleman identified that leptin could be produced from adipocytes to signal satiety to the central nervous system (Zhang et al. 1994). They had identified the first adipokine, with the category soon growing to include leptin, adiponectin, resistin, visfatin, visceral adipose-tissue-derived serine protease inhibitor (VASPIN), and RBP4 which are thought to link obesity, inflammation, and insulin resistance (Table 1.1) (Tilg and Moschen 2006). Leptin and adiponectin are primarily produced by adipocytes and are the most abundant adipokines, making them the primary adipokines (Tilg and Moschen 2006; Shoelson et al. 2007).

Adiponectin is the most abundant adipokine found in human serum, with levels in the range of 5-10 mg/ml, but circulating levels decrease with the development of obesity and insulin resistance. It binds to two known receptors: ADIPOR1 that is expressed ubiquitously and ADIPOR2 that is mainly expressed in the liver. Adiponectin is mainly regarded as an anti-inflammatory adipokine, with its transcription inhibited by pro-inflammatory cytokines, such as TNFα and IL-6, and synthesis promoted by weight loss and PPARɣ. However, adiponectin has been shown to further increase CXCL8 expression from lipopolysaccharide (LPS)-stimulated macrophages, suggesting a pro-inflammatory role too. On the other hand, adiponectin overexpression decreases the development of diet-induced obesity and insulin resistance and has many anti-inflammatory functions (Table 1.1) (Tilg and Moschen 2006).

Leptin signals through the leptin receptor (Ob-R) and its main role is the suppression of appetite and increase of energy expenditure, with serum levels increasing proportionally to the size of the adipose tissue and BMI. However, the increased levels of leptin during obesity are also associated with leptin resistance (Friedman 1997). Leptin has additional roles in promoting angiogenesis and haematopoiesis, but has also been shown to have a number of pro-inflammatory functions (Table 1.1) (Ibrahim 2010). Despite the effect of expanding adipose on leptin levels, pro-inflammatory cytokines (e.g. TNFα and IL-1) were shown to increase leptin synthesis (Friedman 1997; Tilg and Moschen 2006).

Adipokine	Levels In Obesity	Pro/Anti-Inflammatory	Effect on Immune system	Effect on Obesity Comorbidities
Adiponectin	Decreased	Anti-inflammatory	↓ Endothelial adhesion molecules ↓ NF-κB ↓ Mac TNFα, IL-6, IFNɣ ↓ Mac phagocytosis ↑ Mac IL-10, IL-1RA ↓ B-cell lymphopoiesis ↓ T-cell Responses	↓ Insulin resistance, T2D ↓ NAFLD (↓ hepatic TNFα, SREBP1C. ↑β-oxidation, AMPK) Anti-atherosclerotic Cardio-protective
Leptin	Increased	Pro-inflammatory	↑ Mac TNFα, IL-6, IL-12 ↑ Neutrophil activation ↑ Neutrophil ROS ↑ Chemotaxis (CCL2) ↑ NK-cell function ↑ Lymphopoiesis ↑ T-cell proliferation ($CD4^+CD8^-$, $CD4^+CD8^+$) ↑ Thymocyte survival ↑ T_H1 response (IL-2, IFNɣ) ↓ T_H2 response (IL-4)	↓ Insulin resistance
Resistin	Variable (↑, –, ↓)	Pro-inflammatory	↑ TNFα, IL-1, IL-6, IL-12 (various cells) ↑ NF-κB ↑ Endothelial adhesion molecules (VCAM1, ICAM1) and CCL2	↑ Insulin resistance, T2D (mice) Pro-atherosclerotic ↑ NAFLD (↓AMPK)
Visfatin (PBEF)	Increased	Pro-inflammatory	↑ IL-6, CXCL8 ↓ Neutrophil apoptosis	↓ Insulin resistance, T2D

Table 1.1: The Role of Adipokines In Inflammation, T2D, and CVDs During Obesity
Adapted from (Fantuzzi 2005; Tilg and Moschen 2006; Galic et al. 2010). NF-κB: nucelar factor-κB, TNF: tumour-necrosis factor, IL: interleukin, IL-1RA: IL-1 receptor antagonist, IFNɣ: interferon-ɣ, CCL: CC chemokine ligand, CXCL: CXC chemokine ligand, ROS: reactive oxygen species, NK: natural killer, VCAM: vascular cell-adhesion molecule, ICAM: intercellular adhesion molecule, T2D: type 2 diabetes, NAFLD: non-alcoholic fatty liver disease, SREBP1C: sterol-regulatory-element-binding protein 1C, AMPK: AMP-activated protein kinase.

When resistin (FIZZ3) was discovered it was shown to induce insulin resistance in mice, and hence named resistin. In mice, resistin is primarily produced by adipocytes; however, in humans it has been shown to be produced by adipocytes, pancreatic cells, muscle cells, and macrophages (Tilg and Moschen 2006). Resistin's importance in humans is not clear, with resistin protein not being well conserved between mice and humans, and serum levels not always

correlating with T2D during obesity (Tilg and Moschen 2006; Galic et al. 2010). However, resistin has been shown to have a pro-inflammatory role (Table 1.1) in humans and resistin's mRNA expression is increased by LPS, TNFα, IL-1, and IL-6 in human peripheral-blood mononuclear cells (PBMCs). Furthermore, resistin synthesis is inhibited by PPARɣ activation (Tilg and Moschen 2006).

Visfatin was discovered to be produced by vWAT and to reduce insulin resistance by activation of the insulin receptor, without blocking insulin binding. It was then discovered that visfatin was identical to pre-B-cell colony-enhancing factor (PBEF). Despite its role in insulin signaling, visfatin has also been shown to have pro-inflammatory functions (Table 1.1) (Fantuzzi 2005; Tilg and Moschen 2006).

1.2.1.4 Adipose Expansion During Obesity

During over-nutrition there is expansion of the WAT through hypertrophy (increased cell size) or hyperplasia (increased cell number). Current evidence suggests that WAT expands through hypertrophy up to a certain limit, which is then followed by hyperplasia during over-nutrition (Hirsch and Batchelor 1976; Prins and O'Rahilly 1997; van Harmelen et al. 2003; Jo et al. 2009; Sun et al. 2011). Hyperplasia occurs through the differentiation of perivascular pre-adipocytes (Lin^- $CD29^+$ $CD34^+$ $Sca\text{-}1^+$ $CD24^+$) present within the WAT (Rodeheffer et al. 2008; Tang et al. 2008). The mechanism of adipocyte differentiation is described in section 1.2.1.2, but it worth noting that whether adipogenesis occurs in adult humans is still controversial (Cristancho and Lazar 2011). However, studies have shown mechanistic differences in tissue expansion between scWAT and vWAT. Using adipocyte-specific, doxycycline-inducible LacZ reporter transgenic mice it was shown that eWAT expanded by hypertrophy after 35 days on a HFD and by hyperplasia after 56 and 89 days, whereas scWAT showed only hypertrophy over the same period (Wang et al. 2013). A previous mouse study showed that scWAT expands primarily through hyperplasia, with a greater precursor content that has a greater prolific capacity when stimulated by calorie intake than vWAT, which primarily expanded through hypertrophy (Joe et al. 2009). Both studies showed that vWAT showed greater hypertrophy even under normal diet conditions, suggesting that vWAT is more hypertrophic than scWAT,

but will expand further through hyperplasia once the adipocytes get to a certain size. In fact, there are limiting factors on how big adipocytes can get, including the level of vascularisation of the tissue, the limits of oxygen diffusion to the cells, and the extracellular matrix infrastructure, with depot-specific limits of hypertrophy seen in rats (DiGirolamo et al. 1998; Halberg et al. 2009). Additionally, human CT scans have shown that vWAT expands mainly by hypertrophy during weight gain and has a higher rate of lipid uptake than scWAT. Isolated visceral adipocytes were also more responsive to lipolysis signals from norepinephrine *in vitro* (Mårin et al. 1992). As discussed in section 1.1.4, vWAT is correlated with numerous risk factors for the development of the metabolic syndrome. This connection between increased visceral adiposity and the metabolic syndrome could be due to vWAT's propensity to expand by hypertrophy, which is associated with "pathological" adipose expansion defined as: rapid growth with hypertrophy, increased macrophage infiltration, fibrosis, and limited angiogenesis. This is in contrast to "healthy" adipose expansion, with enlargement through recruitment of stromal cells and adipocyte precursors (hyperplasia), which differentiate into mature adipocytes, low inflammation, appropriate vascularisation, and limited extracellular matrix (ECM) deposition (Sun et al. 2011). However, the mechanisms underlying abdominal and visceral adiposity's association with the metabolic syndrome and other comorbidities are still poorly understood.

scWAT is thought to act as a "metabolic sink" that expands to accommodate the growing energy storage demands during a positive energy balance (increased intake : reduce expenditure), storing the excess FFAs as TGs. However, during physiological stress from excessive calorie intake (i.e. during obesity) and/or psychological stress there is impairment of scWAT's ability to effectively store lipids, through hypertrophic or hyperplastic limits, which causes deposition of lipids in other tissues (Després and Lemieux 2006; Després et al. 2008; Ibrahim 2010). This causes visceral fat deposition and ectopic deposition of fat in undesirable locations, such as the liver, heart, skeletal muscle, pancreas, kidney, and vasculature. This is known as the "lipid spillover hypothesis" (Després and Lemieux 2006; Després et al. 2008). The excess lipids in the circulation and other tissues can cause lipotoxicity, contributing to the metabolic syndrome phenotype. The increased circulating FFAs induce reduced muscular insulin-stimulated

glucose uptake, hepatic and peripheral insulin resistance, and increase plasma VCAM, ICAM, PAI-1, and CCL2 levels, contributing to atherosclerosis. Accumulation of FFAs in the liver were shown to increase hepatic TG and VLDL synthesis (contributing to dyslipidaemia), inflammation, insulin resistance, and induce the development of NAFLD (Samuel et al. 2004; Saponaro et al. 2015). The accumulation of visceral adipose in the pericardium or TGs within the cardiomyocytes of the heart myocardium, is linked with cardiomyocyte dysfunction and coronary artery disease (CAD). Within the skeletal muscle, accumulation of intramyocyte lipid induces impairment of glucose metabolism, mitochondrial dysfunction, decreased ATP synthesis, and decreased nitric oxide production. Finally, accumulation of FFAs in the pancreas causes dysregulated insulin secretion, β-cell dysfunction, and is associated with β-cell death, contributing to the development of T2D (Saponaro et al. 2015).

One of the biggest contributing factors to the pathology of obesity is adipocyte hypertrophy. Increases in adipocyte size were shown to increase systemic insulin resistance (Kubota et al. 1999). However, this increase in size has also been shown to induce insulin resistance in adipocytes *in vitro*, reducing insulin-mediated glucose uptake and GLUT4 trafficking to the plasma membrane (Kim et al. 2015a). This systemic and local insulin-resistance would limit the anti-lipolytic effects of insulin on adipocytes, further promoting the release of FFAs into the circulation and exacerbating systemic insulin resistance and obesity's comorbidities. *In vivo* mouse studies promoting the storage of FFAs as triglycerides in adipocytes, through glyceroneogenesis induced by overexpressing or activating PEPCK, have shown reduced FFA release from adipocytes and increased hypertrophy, with normalisation of leptin levels, systemic glucose tolerance and insulin sensitivity, and skeletal muscle insulin sensitivity (Franckhauser et al. 2002; Tordjman et al. 2003). Furthermore, white adipocytes from VAT are more sensitive to catecholamine-induced lipolysis, but less sensitive to the anti-lipolytic effects of insulin, prostagladins, and adenosine, than those from SAT (Arner 1997). This could be a contributing factor to VAT's association with metabolic syndrome. However, even if the adipocyte was still responsive to the anti-lipolytic and pro-lipogenic/TG synthesis signals, the lipid load on the cell causes cellular stress that results in mitochondrial dysfunction, with reductions in

PPARγ coactivator (PGC)-1α mRNA and membrane potential, increasing reactive oxygen species (ROS) generation (Gao et al. 2010). These ROS can lead to oxidative stress and may promote inflammation. There is also ER stress related to mitochondrial dysfunction, which results in an increased release of FFAs (Deng et al. 2012; Kusminski and Scherer 2012). Furthermore, due to the excess FFAs within adipocytes there is production of ceramides (a sphingolipid), mainly from long-chain fatty acyl-CoAs. These are associated with cellular stress and apoptosis during ectopic deposition, and insulin resistance in adipocytes (Holland and Summers 2008).

As the WAT increases in size there is deposition of ECM to cope with the increasing hypertrophy of the adipocytes, and as the adipose expands further the adipocytes reach the limits of oxygen diffusion from the capillaries. This is due to insufficient vascularisation of the tissue and limits of capillary spacing, which induces hypoxia in the "core" of the adipocyte mass (Sun et al. 2011; Rutkowski et al. 2015). The reduced oxygen concentration within the tissue activates hypoxia inducible factor (HIF)-1α in adipocytes, which cannot induce an effective angiogenesis response in the adipose tissue. This results in an alternative response that enhances ECM component synthesis and causes tissue fibrosis. Due to the increased fibrosis and hypoxic environment adipocytes become necrotic, which prompts tissue inflammation and the infiltration of macrophages and other immune cells (Figure 1.5) (Sun et al. 2013).

1.2.1.5 Macrophages and Adipose Inflammation

Macrophages are phagocytic cells that form part of the innate immune system and have important roles in driving inflammation and activating other branches of the immune system through antigen presentation and cytokine release. However, they also play an important role in normal physiological tissue remodeling and maintenance. Macrophages play a vital role in the remodeling process of adipose tissue and inflammation (Figure 1.5). Their association with the pathology of obesity was first identified in 2003 by Weisberg et al. and Xu et al (Weisberg et al. 2003; Xu et al. 2003b; Sun et al. 2011). They showed a large infiltration of macrophages into the adipose tissue of obese mice that was proportional to the size of the adipocytes, and an increase in associated markers

of inflammation (e.g. TNFα, inducible nitric oxide synthase (iNOS), IL-6, and CCL2). Weisberg showed that the percentage of F4/80^{+} macrophages increased from approximately 12% in the lean adipose to 41% in the obese adipose, and suggested they were M-CSF-dependent macrophages recruited from the bone marrow (Weisberg et al. 2003). This was subsequently proved in human obese WAT, where a greater accumulation of macrophages were observed in the omental adipose than the subcutaneous (Cancello et al. 2006). The authors also showed a correlation between increased macrophage infiltration in the omental adipose and an increase in serum glucose, insulin, and TG levels.

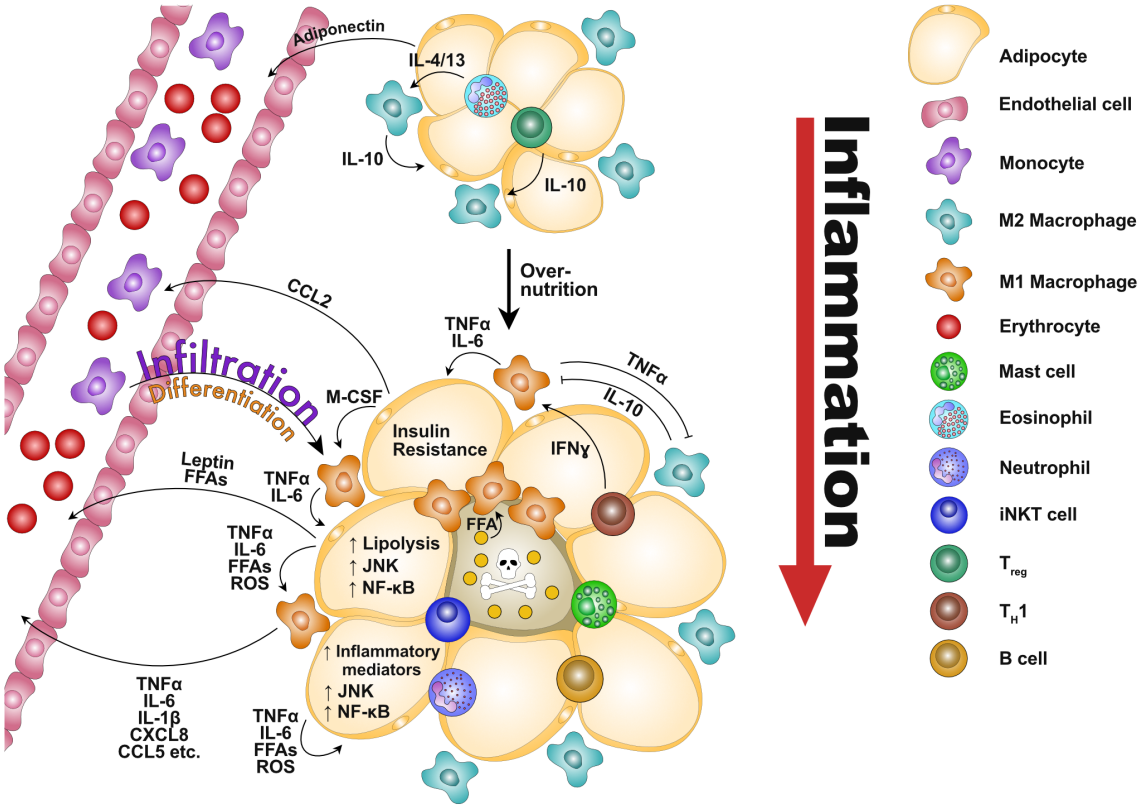

Figure 1.5: A Simplified View of Adipose Inflammation During Obesity
This figure mainly focuses on the inflammatory functions of macrophages in the obese adipose tissue. The lean adipose tissue contains resident macrophages (ATMs) of an M2 phenotype that suppress inflammation by the production of interleukin (IL)-10 and play important functions in physiological tissue expansion. Resident eosinophils that maintain the M2 ATMs by the production of IL-4/13 and T_{regs} that can produce IL-10 are also present. Additionally, adipocytes produce the anti-inflammatory adipokine adiponectin. During over-nutrition there is hypertrophy of the adipocytes resulting in a hypoxic core within the tissue that induces adipocyte death and the release of free fatty acids (FFAs). The lipid overload on the adipocyte also induces reactive oxygen species (ROS) generation and additional FFAs from ER-stress. FFAs can induce inflammatory pathways in adipocytes (c-jun N-terminal kinase (JNK) and nuclear factor (NF)-κB signaling) through toll-like receptor 4 (TLR)4. This results in the production of numerous inflammatory cytokine and adipokines, including CCL2, which recruits inflammatory monocytes to the tissue that are differentiated into macrophages by macrophage-colony stimulating factor (M-CSF) produced by adipocytes and polarised to an inflammatory M1 ATM phenotype due to the inflammatory environment. The M1 ATMs then produce other inflammatory cytokines (e.g. tissue necrosis factor (TNFα) and IL-6) that increase insulin resistance, lipolysis, and inflammatory signaling in adipocytes, further exacerbating the inflammatory environment. The increase in FFAs from adipocytes activates M1 ATMs through TLR4 and 2, increasing inflammation. FFAs and leptin are also released into the circulation, promoting ectopic lipid deposition, systemic inflammation and insulin

resistance. Further inflammatory cytokines and chemokines are also released into the circulation by M1 ATMs promoting systemic inflammation, insulin resistance, and recruiting other immune cells that can further promote inflammation; for example T_H1 lymphocytes promote M1 ATM differentiation through interferon (IFN)-γ.

Both adipocytes and macrophages express toll-like receptor (TLR)4, which is well known for recognising the gram-negative bacterial membrane component lipopolysaccharide (LPS) (Shoelson et al. 2006). However, saturated FFAs have also been shown to bind and activate TLR4 (Shi et al. 2006). These cells also express the receptor for advanced glycation end products (RAGE), which binds glycosylated proteins (AGEs) produced during hyperglycaemia (Bierhaus et al. 2005). Both of these receptors signal through nuclear factor (NF)-κB and c-jun N-terminal kinase (JNK), inducing the expression of pro-inflammatory cytokines and chemokines (Shi et al. 2006; Nguyen et al. 2007). Additionally, signalling through both JNK and NF-κB increase in WAT with tissue expansion and are linked to inducing insulin resistance (Shoelson et al. 2006). The increased saturated FFAs within the WAT during increased lipolysis and necrosis of adipocytes activate TLR4 on adipocytes, inducing the expression of inflammatory cytokines and chemokines, including the CC chemokine CCL2 (Shi et al. 2006; Nguyen et al. 2007). CCL2 is a chemoattractant for circulating monocytes through the CC chemokine receptor (CCR)2 expressed on these cells. CCR2 ablation reduces adipose macrophage infiltration and *TNFα* mRNA, increases adiponectin, and improves systemic glucose homeostasis during obesity (Weisberg et al. 2006). Therefore, CCL2 causes the recruitment of monocytes into the WAT, which is assisted by the adipose-mediated up-regulation of the adhesion molecules intercellular adhesion molecule (ICAM)-1 and platelet/endothelial cell adhesion molecule (PECAM)-1 on endothelial cells, likely through increased leptin levels (Curat et al. 2004). Once the monocytes have migrated into the WAT, they then differentiate into adipose tissue macrophages (ATMs). Recently, the neuronal chemotropic protein, netrin-1, was shown to act as a retention signal for ATMs during obesity (Ramkhelawon et al. 2014).

The ATMs themselves are activated by FFAs through TLR4 and TLR2 causing them to release pro-inflammatory cytokines such as TNFα, IL-6, IL-1β, and CCL2, and matrix metalloproteinase (MMP)-9 and cyclooxygenase (COX)-2

(Nguyen et al. 2007). Along with the CCL2 released by the ATMs themselves, ATM-derived TNFα further increases CCL2 release from adipocytes, increasing the influx of ATMs (Suganami et al. 2005). Furthermore, TNFα and IL-6 were shown to increase lipolysis from adipocytes during chronic exposure, which would further aid the recruitment of ATMs into the WAT, exacerbate the inflammatory environment, and increase plasma FFA levels (Langin and Arner 2006; Lafontan 2008). ATMs were shown to be the major source of TNFα within the WAT and contribute around half of WAT IL-6 (Fantuzzi 2005). Numerous other inflammatory mediators and adipokines are produced within the WAT that exacerbate local and systemic inflammation, including the cytokines TNFα, TNFβ, Interferon (IFN)-ɣ, IL-1β, IL-6, IL-12, and IL-18; the chemokines CCL2, CCL3 (MIP-1α), CCL4 (MIP-1β), CCL5 (RANTES), CCL20 (MIP-3α), CXCL2 (MIP-2), and CXCL8; and the hormones/other proteins leptin, resistin, PAI-1, angiotensinogen, visfatin, RBP4, SAA, COX2, vascular endothelial growth factor (VEGF), and Insulin-like growth factor binding proteins (IGFBPs). However, the exact contribution of adipocytes and ATMs to the production/secretion of these adipokines is unclear, as many of them can be produced by both cells, with leptin and adiponectin the exceptions (Shoelson et al. 2006; 2007). The variety of chemokines released can also contribute to the recruitment of other immune cells to the WAT (section 1.2.1.6) (Figure 1.5).

There is evidence that the ATMs (~90%) localise to the necrotic cells within the WAT during obesity to clear the adipocyte cell debris, and form crown-like structures (CLS) exclusively around singular necrotic adipocytes. These CLS can contain as many as 15 macrophages and their formation is associated with the increased necrosis during adipocyte hypertrophy (Cinti et al. 2005; Nishimura et al. 2008). The ATMs scavenge the lipids released from the necrotic adipocytes, but lipids (particularly saturated FFAs) induce apoptosis in macrophages (Bird 2010). Therefore, the multinucleated giant cells (MGCs) also found around the necrotic adipocytes in CLS may be due to lipid-containing ATMs being engulfed by other ATMs; this is usually an indicator of chronic inflammation (Cinti et al. 2005). The recruited ATMs within these CLS were shown to have a pro-inflammatory M1 or “classically activated” phenotype, which contrasts with the resident-ATMs in lean adipose that show an anti-inflammatory M2 or “alternatively activated” phenotype

(Lumeng et al. 2007a). These M1 ATMs were F4/80$^+$ CD11b$^+$ CD11c$^+$ CCR2$^+$ and expressed higher levels of numerous M1-associated genes, including *Il-6* and *Nos2*, with higher TLR4 surface expression. The resident M2 ATMs were F4/80$^+$ CD11b$^+$ CD11c$^-$ CCR2$^-$ and expressed higher levels of numerous M2-associated genes, including *Il-10*, *arginase (Arg)1*, *mannose receptor, C type (Mrc)2*, *chitinase 3-like (Chi3l)3*, and *macrophage galactose N-acetyl-galactosamine-specific lectins (Mgl)1* and *2*, but both equally expressed *Tnfα* (Lumeng et al. 2007a; 2007b; 2008). *In vitro* data showed that IL-10 reduced the secretion of CCL2 and inhibited TNFα-induced insulin resistance in adipocytes, suggesting that the resident M2 ATMs are protective during obesity (Lumeng et al. 2007a). Additionally, conditioned media from M1 bone marrow-derived macrophages (BMDMs) incubated with adipocytes, induced insulin resistance and inhibition of differentiation, not seen with M2 BMDMs (Lumeng et al. 2008). The influx of M1 ATMs during obesity was shown to be dependent on CCR2 expression using KO mice (Lumeng et al. 2007b), whereas the recruitment of resident M2 ATMs to the WAT is CCR2 and CCL2-independent, and they are located within the interstitial spaces between adipocytes (Lumeng et al. 2008). More recent evidence shows that the resident M2 ATMs can be maintained within lean WAT by IL-4 induced proliferation, which is released by eosinophils (Kraakman et al. 2014). In mice, the influx of M1 ATMs was shown to peak after around 12 weeks on HFD, but were observed after only 8 weeks (Li et al. 2010; Shaul et al. 2010).

The pro-inflammatory M1 ATMs recruited to the WAT during obesity therefore appear to have an important role in the pathogenesis of obesity, contributing to adipocyte insulin resistance and the inflammatory environment through the release of pro-inflammatory cytokines and ROS (Figure 1.5). In fact, the accumulation of CD11c$^+$ CD206$^+$ ATMs in WAT has been correlated with insulin resistance in obese patients (Wentworth et al. 2010). Others have shown that with the reduction in adipose inflammation during weight loss, M1 ATMs have a reduced inflammatory phenotype showing reductions in *Tnfα*, *Il-1β*, and *Galectin-3* mRNA and galectin-3 surface expression (Li et al. 2010). This suggests that M1 ATMs modify their phenotype based on the inflammatory environment. Additionally, there is some heterogeneity in the M1 ATM population with the identification of MGL1$^-$ CD11c$^+$ and MGL^{med} CD11c$^+$ subtypes; MGL^{med} CD11c$^+$

ATMs show a phenotype mid-way between MGL^+ $CD11c^-$ M2 ATMs and $MGL1^-$ $CD11c^+$ ATMs (Shaul et al. 2010). Both the $CD11c^+$ M1 ATM subtypes also showed an increase in M2-associated genes and a decrease in M1-associated genes with the increasing chronicity of inflammation. This was accompanied by indications of a switch from glycolytic to oxidative metabolism (associated with M2 macrophages), with increased *Pparγ* and *Pgc1α* mRNA (Shaul et al. 2010; Kelly and O'Neill 2015). Using live imaging and cell tracking it was shown that M2 ATMs proliferate in the CLS during obesity and then migrate to the interstitial space (Haase et al. 2014). Therefore, infiltrating M1 ATMs may polarise to an M2 phenotype during chronic adipose inflammation in an attempt to resolve inflammation. The promotion of an M2 phenotype in ATMs could provide therapeutic benefits in reducing inflammation and insulin resistance. Research from the Chawla group showed that M2 ATMs, in an IL-4/13-dependent manner, can release catecholamines during cold stimulation that induce lipolysis from WAT and adaptive thermogenesis in BAT, and can induce WAT "browning" (Nguyen et al. 2011; Qiu et al. 2014). This induction of a more favourable metabolic phenotype that increases metabolic rate could be another benefit of promoting an M2 ATMs phenotype for the treatment of obesity.

1.2.1.6 Adipose-Associated Immune Cells

Apart from ATMs, other immune cells are recruited to the WAT during obesity that modulate adipocyte metabolism and the inflammatory environment (Figure 1.5). Numerous T cell (lymphocyte) subsets have been identified in obese WAT, including T regulatory cells (T_{regs}), T helper (T_H)1, T_H2, T_H17, cytotoxic T cells (T_c), and invariant natural killer T (iNKT) cells, but $CD3^+$ T cell subsets make up <5% of the cells in the eWAT SVF in lean mice (Feuerer et al. 2009; Kraakman et al. 2014). T_{regs} are $CD4^+$ $Foxp3^+$ cells that form a mechanism of peripheral tolerance, which can inhibit inflammatory pathways in innate and adaptive immune cells and promote an M2 macrophage phenotype (Winer et al. 2009). These T_{regs} constituted more than 50% of the $CD4^+$ T cells in lean eWAT, which increased with age in the eWAT, but not scWAT, and were located at the CLS. Using genetic and diet-induced obese mice these adipose T_{regs} were shown to be protective against systemic and adipose insulin resistance, and decreased inflammatory gene

expression, primarily through the production of IL-10. However, during murine and human obesity these protective adipose T_{regs} decline (Feuerer et al. 2009). The more anti-inflammatory $CD3^+$ $CD4^+$ T_H2 cells secrete IL-4 and IL-13 that can induce M2 macrophage polarisation. Additionally, T_H2 cells were shown to reduce body weight, adipocyte hypertrophy and improve fasting blood glucose, insulin, and glucose tolerance after reconstitution in HFD-fed T cell deficient Rag1 mice (Winer et al. 2009). However, during obesity the majority of the $CD3^+$ $CD4^+$ T cells show a T_H1 phenotype in WAT, secreting IFN-ɣ that induces M1 macrophage polarisation, with the greatest accumulation seen in the vWAT over scWAT (Feuerer et al. 2009; Winer et al. 2009). This would counteract the anti-inflammatory effects from T_{regs} and T_H2 cells. T_H17 cells are another pro-inflammatory T cell subset that secretes IL-1, IL-6, IL-17, and TNFα. These T_H17 cells, however, make up a minority of the $CD4^+$ T cell population during obesity and only show an increase in scWAT, but not vWAT (Winer et al. 2009). T_c cells are $CD3^+$ $CD4^-$ $CD8^+$ T cells that are pro-inflammatory and have an important role in the induction of apoptosis of infected and malignantly transformed cells. These T_c cells increase in the eWAT of HFD-fed mice after only 2 weeks of the diet and locate in CLS, preceding the infiltration of ATMs after 6 weeks. It was also shown that $CD3^+$ $CD4^+$ $CD8^-$ T cells and $CD4^+$ $CD25^+$ $FoxP3^+$ T_{regs} decreased after 6 and 11 weeks, respectively (Nishimura et al. 2009). Reconstitution of HFD-fed Rag1 mice with $CD8^+$ T cells did not reduce their body weight or improve their metabolic profile (Winer et al. 2009). However, depletion of $CD8^+$ T cells during the development of, and in already established, diet-induced murine obesity reduced systemic insulin resistance and glucose tolerance, along with decreasing M1 ATM infiltration and pro-inflammatory cytokine mRNA in eWAT. The authors additionally showed through adoptive transfer and co-culture experiments that $CD8^+$ T cells were important for the recruitment, differentiation, and activation of M1 ATMs in obese eWAT, which also induced $CD8^+$ T cell proliferation (Nishimura et al. 2009).

iNKT (type 1 NKT) cells are a subset of NKT cells that express an invariant T cell receptor (TCR), forming a population of innate T cells. The specific TCRs on iNKT cells recognise glycolipids (e.g. α-galactosylceramide (α-GC)) presented on CD1d. Once activated, iNKT cells show important anti-tumor functions through cytotoxic activity and release both T_H1 and T_H2 cytokines, including TNFα, IFN-ɣ,

IL-4, IL-10 and IL-13 (Lynch et al. 2009; 2012). iNKT cells are present in both human omental and mouse eWAT, and decrease with increasing BMI and weight gain. Additionally, in both of these models weight loss restores the iNKT cell population (Lynch et al. 2009; 2012). Human omental iNKT cells were shown to increase cytotoxicity and both IFN-ɣ and IL-4 when stimulated with α-GC (Lynch et al. 2009). Adoptive transfer of iNKT cells into diet-induced obese mice caused a decrease in body weight, adipocyte size, $CD11c^+$ macrophages, fasting blood glucose and systemic glucose tolerance and insulin resistance, without inducing weight loss or hypoglycaemia in lean mice. The authors show that these protective effects could be due to iNKT cell production of IL-10 and IL-4 (Lynch et al. 2012).

T cells are not the only lymphocytes that have been implicated in modulating adipose inflammation and metabolism during obesity. B cells (B lymphocytes) also contribute to the pathogenesis of obesity, increasing in vWAT during murine diet-induced obesity. They traditionally produce antibodies to protect the host from pathogens. However, these adipose B cells were shown to produce IgG autoantibodies during obesity that located to CLS in vWAT and were released into the circulation, contributing to systemic insulin resistance and glucose intolerance. Additionally, adipose B cells were shown to activate $CD4^+$ T_H1 cells, $CD8^+$ T_c cells, and M1 ATMs in obese vWAT, contributing to local and systemic inflammation, insulin resistance, and glucose intolerance (Winer et al. 2011). Recent studies have shown that during inflammation B cells are present in primitive lymphoid tissues called fat-associated lymphoid clusters (FALCs), associated with vWAT. These FALCs may be important areas of lymphoid immune responses during obesity. The function, composition, and distribution of these FALCs remains unknown; however, they contain a high number of B1 cells, T cells, innate lymphoid cells (ILCs), and stromal cells (Moro et al. 2010; Bénézech et al. 2015). CXCL13 produced from the FALC was shown to be an important recruitment and retention signal, allowing the B cells to proliferate and differentiate into antibody-producing plasma cells or germinal centre B cells upon antigen stimulation. Additionally, FALC formation is dependent on iNKT cell production of IL-13 and macrophage TNFα (Bénézech et al. 2015).

Apart from macrophages, other innate immune cells reside in WAT during the lean and obese state, including Dendritic cells (DCs), eosinophils, neutrophils, and ILCs. DCs are important innate immune cells that survey the body for pathogens and prime the adaptive immune response. During diet-induced obesity DCs have been found to increase in murine eWAT (Bertola et al. 2012; Reynolds et al. 2012). These DCs were shown to be split into two subsets within the eWAT that were $CD11c^{high}$ $F4/80^{low}$ $CX3CR1^{+}$ and $CD11c^{high}$ $F4/80^{-}$ $CX3CR1^{-}$. The former was shown to differentiate more *in vitro* OVA-activated $CD4^{+}$ T cells to T_H17 cells, with the latter inducing differentiation of both T_H1 and T_H17 cells in small amounts (Bertola et al. 2012). The accumulation of $CD1c^{+}$ DCs and $CD11c^{+}$ $F4/80^{-}$ DCs have been correlated with increased systemic and adipocyte insulin resistance in humans and mice with obesity, respectively (Bertola et al. 2012; Reynolds et al. 2012). Eosinophils are innate immune cells that are involved in allergies and protection from helminths, which produce IL-4 and IL-13. Eosinophils were present in eWAT, mesenteric WAT, scWAT, and BAT, but made up only 4-5% of the SVF cells within the lean murine eWAT, which decreased in diet-induced obese and *ob/ob* eWAT with weight gain. However, they were shown to be the major IL-4 producing cell within the lean eWAT and were shown to be important for the maintenance of M2 ATMs within the eWAT through the production of IL-4 and IL-13. Additionally, hypereosinophilia improved peripheral glucose tolerance and reduced WAT size (Wu et al. 2011). Neutrophils are usually the first infiltrating immune cell during a classical inflammatory response, and are important mediators of host defence against pathogens through phagocytosis and the release of cytokines, chemokines, and proteases (e.g. elastase), among others. Murine diet-induced obesity has been shown to increase the infiltration of neutrophils into the eWAT after as little as 3 days on HFD. These neutrophils' production of elastase has been shown to contribute to systemic insulin resistance and local adipose insulin resistance, inflammation, neutrophil infiltration, and M1 ATM infiltration (Talukdar et al. 2012).

Another branch of the innate immune system that has become an area of great interest is ILCs. ILCs express a classic lymphoid cell morphology, but do not express cell lineage markers that identify other immune cells, and can regulate immune responses and lymphoid tissue development by the production of a

diverse range of cytokines. They consist of the cytotoxic natural killer (NK) cells and non-cytotoxic group 1, group 2, and group 3 ILCs (including lymphoid tissue inducer (LTi) cells) (Artis and Spits 2015). A number of studies have shown a role for group 2 ILCs (ILC2s) in the adipose tissue. For example, ILC2s were shown to enhance B1 cell proliferation and antibody production in FALCs through the production of IL-5 and IL-6 (Moro et al. 2010). Additionally, ILC2s that produce IL-5 and IL-13 have been found in murine vWAT that enhance eosinophil and M2 ATM accumulation, reducing weight gain, adiposity, and insulin resistance during HFD-induced obesity (Hams et al. 2013; Molofsky et al. 2013). These ILC2s have also been shown to promote “browning” of the WAT by inducing the differentiation of uncoupling protein 1 (UCP1)-expressing beige adipocytes from pre-adipocytes (Brestoff et al. 2014; Lee et al. 2014).

1.2.2 Brown Adipose Tissue

BAT mainly consists of brown adipocytes that are multilocular, with many small lipid droplets. Near the lipid droplets are dense networks of large mitochondria with laminar cristae, which give brown adipocytes their colour. Their main function is to produce heat through adaptive thermogenesis, which is mediated through the expression of the uncoupling protein (UCP)1 (Frontini and Cinti 2010). They are cold-activated, with one of the main pathways of activation involving SNS induction of noradrenaline that binds β-adrenergic receptors on brown adipocytes. This heat generation from BAT is crucial for small mammals’ survival in cold environments and during hibernation (Harms and Seale 2013). However, the role of BAT in maintaining human body temperature is still not widely accepted, but it has been shown that BAT can be activated in humans by cold conditions, resulting in an increased metabolic rate and greater utilisation of radiolabeled acetate by the BAT and a small increase in FA uptake (Cannon and Nedergaard 2012b). The fuel for brown adipocyte thermogenesis primarily comes from FFAs released from the lipid droplets or taken from the circulating TG-rich lipoproteins and FFAs (see section 1.2.1.1), but glucose can also be used as an energy source for thermogenesis (Bartelt et al. 2011; Cannon and Nedergaard 2012b). This “fat burning” property of BAT has brought a lot of attention to the

possibility of enhancing brown adipocyte metabolism or BAT expansion, and "browning" of WAT, as a therapeutic approach to the obesity epidemic.

1.2.2.1 Differentiation

Unlike white adipocytes, brown adipocytes are more closely related to skeletal muscle than white adipocytes. Both brown adipocytes and skeletal muscle are derived from a common precursor that expresses the muscle markers myogenic factor 5 (MYF5) and paired box 7 (PAX7) (Cristancho and Lazar 2011). The SVF of BAT also contains pre-adipocytes that can be differentiated *in vitro* to produce mature brown adipocytes, but these pre-adipocytes are not as well defined as those for white adipocytes (Klaus et al. 1995). Unlike white adipocytes, brown pre-adipocytes can differentiate *in vitro* without classical stimulation, e.g. PPARɣ agonists or β-adrenergic stimulation. For example, undifferentiated brown pre-adipocytes express low levels of UCP1 protein, which increases with respiration when cultured with insulin (Klaus et al. 1995). Additionally, confluence of the brown pre-adipocytes in insulin-supplemented media induces differentiation, as well as UCP1 transcript up-regulation; these subsequently decrease in post-confluence (Rehnmark et al. 1990). Like white pre-adipocytes, PPARɣ is essential for brown pre-adipocyte terminal differentiation to a mature adipocyte, and both PPARɣ and C/EBPs are required to induce the expression of adipogenic genes (Cristancho and Lazar 2011). However, another essential zinc finger-containing transcription factor is PR domain containing 16 (PRDM16), which is important for promoting brown adipocyte characteristics over those of skeletal muscle. Loss of PRDM16 in brown pre-adipocytes causes them to default to myocyte differentiation (Seale et al. 2008).

PRDM16 promotes brown pre-adipocyte terminal differentiation by associating with C/EBPβ and enhancing its transcriptional activity, which can then promote transcription of PPARɣ and the important brown adipocyte gene PGC-1α (Kajimura et al. 2009). PPARɣ can then associate with PRDM16 to promote its own transcription, but also the transcription of brown adipocyte-specific genes such as UCP1 and cell death-inducing DFFA-like effector A (CIDEA), and common adipocyte genes, such as FABP4 and adiponectin (Seale et al. 2008). PRDM16

also associates with C/EBPα and C/EBPɣ, as well as PPARα, which is thought to regulate UCP1 transcription (Seale et al. 2008; Kajimura et al. 2009). White adipocyte-specific genes (e.g. resistin) are also inhibited by PRDM16 in association with C-terminal-binding protein (CtBP)-1 and CtBP-2. These are displaced from the PRDM16 complex by PGC-1α and PGC-1β to further enhance the activation of brown adipocyte genes, including PGC-1α (Kajimura et al. 2008). Both PGC-1α and PGC-1β are involved in brown pre-adipocyte differentiation, but they are not essential for brown adipocyte terminal differentiation. PGC-1α and β ablation/inhibition in brown pre-adipocytes did not caused a loss of differentiation capacity. However, both are required for mature brown adipocytes to express the full brown adipocyte phenotype with thermogenic capacity. In mature brown adipocytes, only PGC-1α is required to increase UCP1 expression after cAMP stimulation, but both PGC-1α and β are required for full respiratory capacity and maintaining mitochondrial density (Uldry et al. 2006). Brown pre-adipocytes from the SVF already express PPARɣ, FABP4, C/EBPα, and C/EBPβ, indicating that they are already partially differentiated. However, they have no detectable PGC-1α and UCP1 transcripts, these appear upon stimulation of differentiation with a PPARɣ agonist, such as Rosiglitazone (Rehnmark et al. 1993; Petrovic et al. 2008). The pre-adipocytes accumulate lipid droplets during differentiation and become responsive to β-adrenergic stimulation (e.g. with noradrenaline), which increases oxygen consumption and PGC-1α and UCP1 expression (Rehnmark et al. 1990; Petrovic et al. 2008). Both thiazolidinediones (e.g. Rosiglitazone) and the activation of bone morphogenetic protein 7 (Bmp7), which increases PRDM16 mRNA, can promote brown adipocyte gene expression (Harms and Seale 2013).

1.2.2.2 Thermogenesis

Thermogenesis is a defining characteristic of brown adipocytes that is dependent on UCP1 (also called thermogenin), which mediates the uncoupling of the mitochondrial respiratory (electron transport) chain (Figure 1.6) (Matthias et al. 2000). UCP1 expression is unique to brown adipocytes and beige adipocytes, its structure comprising 6 transmembrane domains that are split into thirds consisting of two α-helices linked by a polar domain; each third is joined by hydrophilic segments. UCP1 functions as a proton transporter, located in the inner

mitochondrial membrane, and makes up around 8% of total mitochondrial protein (Cannon and Nedergaard 1985; Rousset et al. 2004). The mitochondrial respiratory chain consists of 5 complexes located in the inner membrane of the mitochondria, which generate a proton gradient in the intermembrane space through complex I (Nicotinamide adenine dinucleotide (NADH) dehydrogenase), III (cytochrome bc_1), and IV (cytochrome c oxidase), pumping protons out of the mitochondrial matrix (Figure 1.6). This electrochemical proton gradient provides "free" energy that allows complex V (ATP synthase) to phosphorylate ADP to ATP by the reentry of protons through complex V. The electrons required to mediate this process are produced from the conversion of NADH to NAD^+ by complex I, succinate to fumarate by complex II (succinate dehydrogenase), and O_2 to H_2O by complex IV (Figure 1.6).

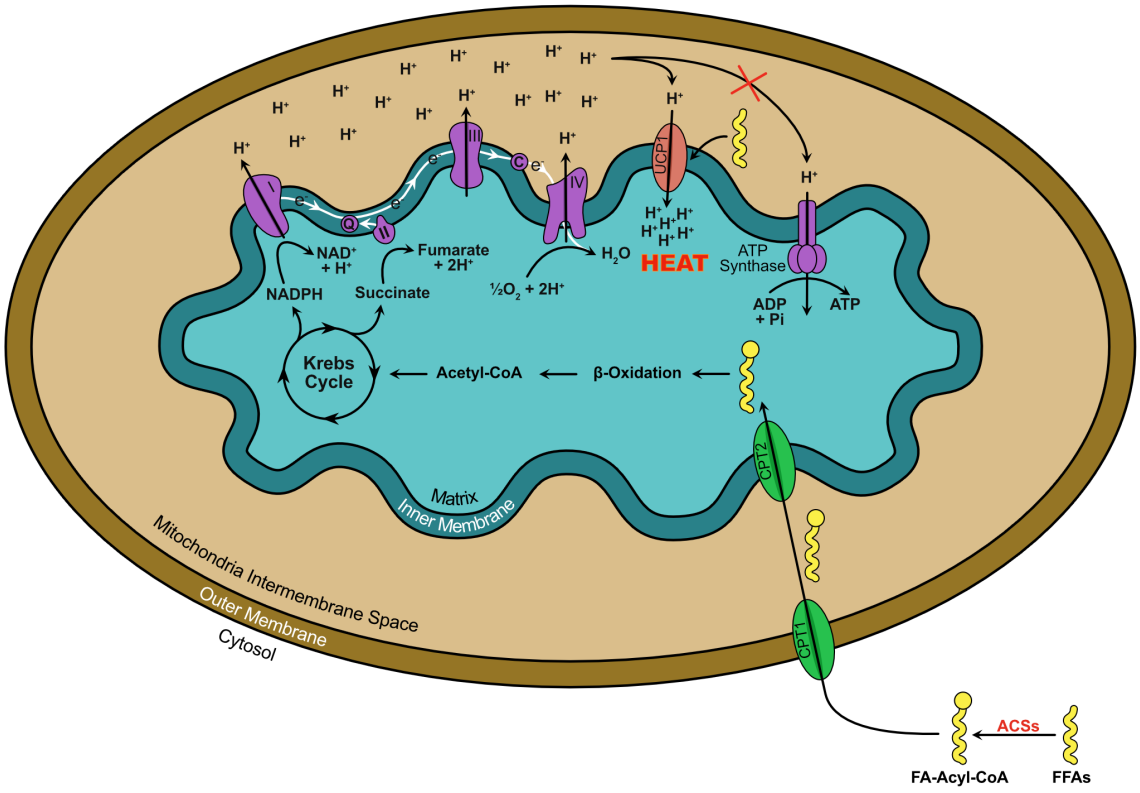

Figure 1.6: Diagram of the Biochemical Process of Mitochondrial Thermogenesis
The flow of electrons in the electron transport chain is shown by the white arrows. Complex I, II, III, and IV are labelled with the roman numeral. Acronyms: adenosine diphosphate (ADP), adenosine triphosphate (ATP), phosphate (Pi), acyl-CoA synthetases (ACSs), CoA (coenzyme A), free fatty acids (FFAs), Nicotinamide adenine dinucleotide phosphate (NADPH), ubiquinone (Q), uncoupling protein 1 (UCP1), and protons (H^+).

Both NADH and succinate are produced from the Krebs cycle, with additional NADH produced by β-oxidation of FFAs and glycolysis (Sazanov 2015). UCP1

"uncouples" the proton gradient from complex V causing a proton leak, facilitating the rapid flow of protons back through to the mitochondrial matrix where they oxidise substrates and dissipate the produced energy as heat (Figure 1.6). UCP1 is activated by FFAs produced by lipolysis of TGs in the lipid droplet and taken up from the circulation, but inhibited by purine nucleotides (Cannon and Nedergaard 1985; Rousset et al. 2004).

During cold exposure there is increased blood flow to the BAT to help with heat exchange and deliver oxygen to the tissue (Cannon and Nedergaard 2012b). Prolonged cold exposure has also been shown to induce brown adipocytes to produce VEGF, increasing the tissue vasculature (Harms and Seale 2013). Cold exposure has been shown to increase UCP1 transcripts through PGC-1α enhancing PPARɣ/RXRα and thyroid hormone receptor (TR)β/RXRα transactivation of the UCP1 gene promoter. Additionally, PGC-1α increases mitochondrial biogenesis and gene expression of the complex IV subunits COX II and COX IV (Puigserver et al. 1998). PGC-1α is essential for cold or β-agonist (cAMP-mediated) induction of UCP1 transcription (Uldry et al. 2006). However, c/EBPβ is also a transcriptional regulator of UCP1 and is essential for the thermogenic functions of brown adipocytes, its expression increasing after noradrenaline stimulation (Rehnmark et al. 1993; Carmona et al. 2005). As mentioned above, the main pathway that stimulates thermogenesis in brown adipocytes is stimulation with noradrenaline from tissue-innervating nerve fibres. The main adrenergic receptor involved in this process is the β3-adrenergic receptor, which is specifically expressed on white and brown adipocytes (Cannon and Nedergaard 2004). However, the α1-adrenergic receptor also increases UCP1 gene expression, but to a lesser degree than β3-adrenergic receptor stimulation (Rehnmark et al. 1990). Despite nerve fibre release of noradrenaline, catecholamines are also produced by cold-stimulated M2 ATMs, inducing thermogenesis (Nguyen et al. 2011). Activation of the adrenergic receptors induces the activation of adenylyl cyclase (that converts ATP to cAMP), which activates protein kinase A (PKA). PKA then induces lipolysis by the activation of HSL and through the phosphorylation (inhibition) of perilipin, which protects the lipid droplet from HSL activity (Cannon and Nedergaard 2004). PKA also activates cAMP response element-binding protein (CREB) and p38 mitogen-activated

protein kinase (MAPK). p38 MAPK activates PGC-1α and activating transcription factor (ATF)2 through phosphorylation, which along with CREB increase the transcription of thermogenic genes, including PGC-1α itself and UCP1 (Harms and Seale 2013). Additionally, adrenergic receptor stimulation increases LPL and CD36 expression, enhancing the clearance of lipoproteins from the circulation and increasing cytosol FFAs (Bartelt et al. 2011). The increased cytosolic FFAs then activate UCP1. Apart from inducing thermogenesis, prolonged β-adrenergic stimulation also induces the proliferation and differentiation of brown adipocyte precursors (Cannon and Nedergaard 2004).

Cold is not the only stimulus for brown adipocyte thermogenesis, with excessive calorie consumption in mice increasing thermogenesis, showing that this process can be diet-induced (Rothwell and Stock 1979). Although β-adrenergic stimulation activates brown adipocyte thermogenesis, a number of other endogenous stimuli have been identified, including thyroid hormone, which directly activates brown adipocyte thermogenesis by stimulating the cAMP pathway (Puigserver et al. 1998; de Jesus et al. 2001). Fibroblast growth factor (FGF)21, which is synthesised by brown adipocytes after β-adrenergic stimulation, but also produced by the liver, increases thermogenesis in brown adipocytes by increasing expression of PGC-1α, UCP1, and other thermogenic genes (Hondares et al. 2010; 2011). Finally, natriuretic peptides induce thermogenesis by inducing lipolysis and thermogenic gene expression by production of cyclic GMP (cGMP) that activates cGMP-dependent protein kinase (PKG), this uses a similar pathway to cAMP-PKA (Bordicchia et al. 2012).

1.3 microRNAs

microRNAs (miRNAs/miRs) are a species of small RNAs that regulate gene expression post-transcriptionally by targeting mRNA and are in a family of small RNAs that also include small interfering (si)RNA and PIWI-interacting (pi)RNA. Mature miRNA strands are approximately 22 nucleotides (nt) long, are non-protein coding, and silence target mRNA by primarily binding to the 3’ untranslated region (UTR) of mRNA and inducing translational repression or mRNA degradation (Ha and Kim 2014). These regulatory processes act to “fine tune” the expression of

genes. They were first discovered in Caenorhabditis (C.) elegans by Lee and colleagues in 1993, who showed that a 22 nt RNA transcript of *lin-4* was derived from the 5' end of a larger 61 nt transcript. Additionally, the 5' end of the smaller *lin-4* transcript was complementary to a base sequence that was repeated 7 times in the 3' UTR of *lin-14* (Lee and Feinbaum 1993). *lin-4* is essential for normal *C. elegans* development and this report described the novel mechanism by which *lin-4* inhibited the expression of LIN-14 protein and identified *lin-4* as the first miRNA (Wightman et al. 1993). 7 years later the second miRNA was discovered, *let-7*, which also showed important regulatory functions for *C. elegans* development (Reinhart et al. 2000). However, *let-7* was also the first miRNA shown to be expressed in humans (Pasquinelli et al. 2000). From there, numerous other miRNAs have been discovered in animals and plants, with miRBase cataloging 2,588 miRNAs in humans and 1,915 in mice (http://www.mirbase.org, Accessed: 09/05/16) (Kozomara and Griffiths-Jones 2013). It has been estimated that greater than 60% of the protein-coding genes in humans are regulated by miRNAs (Ha and Kim 2014).

1.3.1 miRNA Processing

The biogenesis of mature miRNAs is controlled by numerous enzymes both in the nucleus and cytoplasm of cells (Figure 1.7). The majority of mammalian miRNA genes are found in the introns of other non-protein-coding or protein-coding genes; however, some miRNA genes are also found in exons. In some cases, the miRNA genes are found in the introns of the gene they regulate. It is not always the case that only one miRNA is encoded in a genomic region; multiple miRNA loci can be clustered together and co-transcribed to produce multiple mature miRNAs at once. In the nucleus, miRNA genes are transcribed to RNA by RNA polymerase (Pol) II and transcription is controlled by numerous transcription factors (e.g. p53, MYC, ZEB1 and ZEB2) and epigenetic regulators (e.g. histone modifications and DNA methylation). This produces the primary miRNA (pri-miRNA) transcript, which is typically greater than 1 kb in length and forms a stem-loop structure containing the mature miRNA sequence. The pri-miRNA structure usually consists of a terminal loop with a double-stranded (ds) stem (around 33-35 bp long) and single-stranded (ss)RNA regions at the 5' and 3' ends (Figure 1.7).

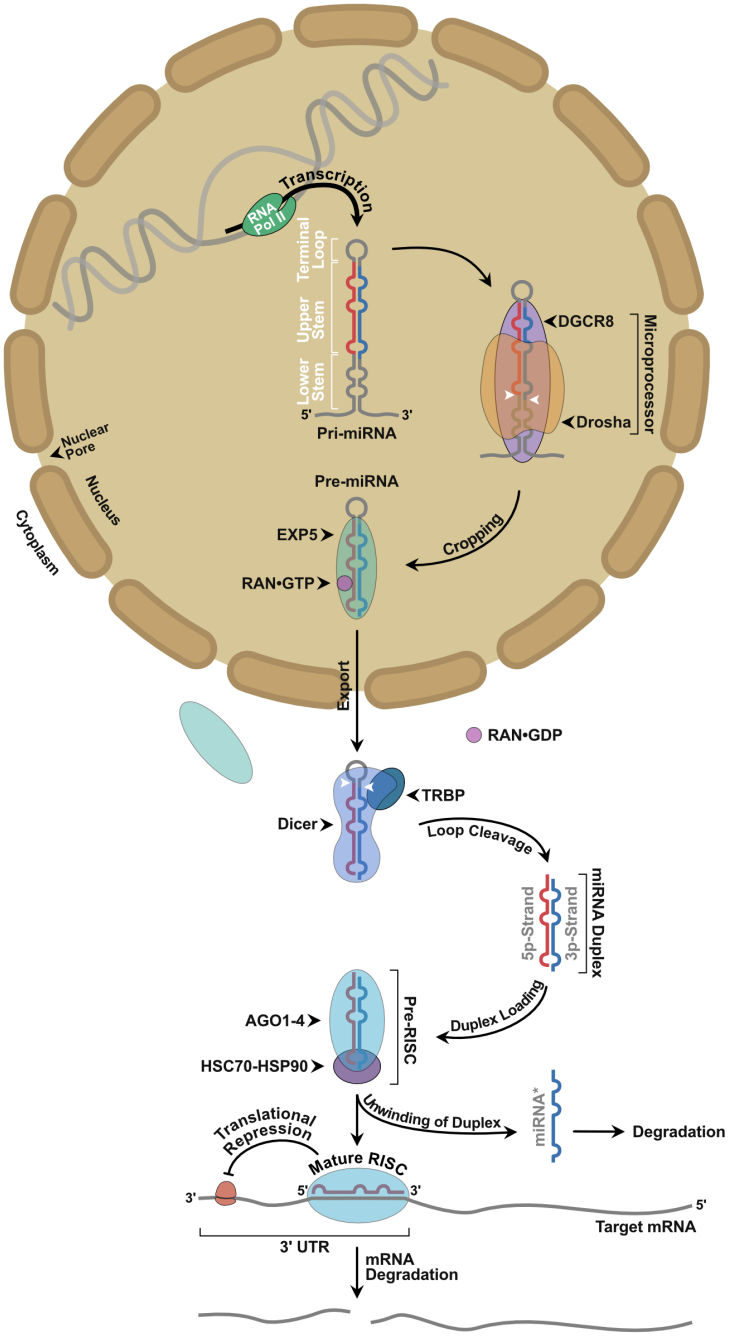

Figure 1.7: Simplified Diagram of miRNA Processing and mRNA Silencing
White arrows indicate sites of enzymatic RNA cleavage. Acronyms: RNA pol (polymerase) II, DGCR8 (DiGeorge syndrome critical region 8), EXP (exportin)5, TRBP (TAR RNA-binding protein), AGO (argonaut), RAN•GTP (GTP-binding nuclear protein Ran), HSC (heat-shock cognate)70, HSP (heat-shock protein)90, RISC (RNA-induced silencing complex), UTR (untranslated region). Information from (Ha and Kim 2014).

The 5' and 3' ssRNA regions along with some of the dsRNA stem of the pri-miRNA are then removed by the Microprocessor complex, forming a small (around 65 nt) RNA hairpin structure called pre-miRNA. The Microprocessor complex consists of the dsRNA-specific RNase III-type endonuclease Drosha and the cofactor DiGeorge syndrome critical region 8 (DGCR8). Drosha has two RNase III

domains (RIIIDa and RIIIDb), which dimerise to form a processing unit, and a dsRNA-binding domain (dsRBD) at the carboxyl (C)-terminus. The dsRBD of Drosha holds the pri-miRNA in place, but for a stable interaction DGCR8 is also required, which binds to the pri-miRNA with its two dsRBDs while its C-terminus binds Drosha. Drosha cleaves the pri-miRNA at specific sites on the 5' and 3' strand of the dsRNA stem, which are determined by the secondary structure of the pri-miRNA. The cuts are made by the RIIIDs approximately 22 bp away from the junction between the dsRNA stem and terminal loop (apical junction) and 11 bp from the junction between the dsRNA stem and ssRNA region (basal junction). The RIIIDs of Drosha make staggered cuts producing a two-nt 3' overhang, with RIIIDa cutting the 3' strand and RIIIDb cutting the 5' strand (Figure 1.7) (Ha and Kim 2014).

The resulting pre-miRNA from Drosha processing is exported into the cytoplasm through a nuclear pore by exportin 5 (EXP5). This is mediated by EXP5 forming a transport complex with the pre-miRNA and GTP-binding nuclear protein Ran (RAN•GTP). The 3' overhang created by Drosha is an important step for EXP5 recognition, which recognises a 3' overhang of 1-8 nts in length on a dsRNA stem >14 bp. After successful recognition of the pre-miRNA the transport complex passes through the nuclear pore into the cytosol and GTP is hydrolysed, dismantling the transport complex and releasing the pre-miRNA (Figure 1.7). Once in the cytoplasm, the pre-miRNA is processed by the RNase III-type endonuclease Dicer to produce a small miRNA duplex consisting of the mature 5' (5p) and 3' (3p) miRNA strands. Like Drosha, Dicer has two RIIIDs at its C-terminus that dimerise to form a processing unit for cleavage of the pre-miRNA. Additionally, Dicer has an N-terminal helicase domain that binds the pre-miRNA terminal loop and a PIWI-Argonaut (AGO)-ZWILLE (PAZ) domain that binds the pre-miRNA termini to hold it in place. Again the secondary structure of the pre-miRNA is important for Dicer processing, with Dicer showing a preference for dsRNAs with a two-nt 3' overhang (produced by Drosha). This is due in part to the PAZ domain requiring a two-nt 3' overhang to simultaneously hold both the 5' and 3' ends of the pre-miRNA. The region between the dimerised RIIIDs and PAZ domain is thought to act like a "molecular ruler," allowing the production of small RNAs of a consistent size. Dicer cleaves the terminal loop by making a cut 21-25 nts from the 3' terminus of the

dsRNA stem and another 22 nts from the 5' terminus producing the miRNA duplex (Figure 1.7). A number of other proteins also regulate Dicer function, such as TAR RNA-binding protein (TRBP) that is thought to stabilise the interaction of pre-miRNAs with Dicer, and KH-type splicing regulatory protein (KSRP), which helps Dicer processing of pre-miRNAs by binding to the terminal loop (Ha and Kim 2014).

Alternative Drosha and Dicer processing is also thought to contribute to the production of isomiRs derived from the same pri-miRNA. These isomiRs mainly consist of nucleotide additions or subtractions at the 3' end of the miRNA sequence, but can also consist of nucleotide additions or subtractions at the 5' end, although less common (Chiang et al. 2010; Newman et al. 2011). A number of mechanisms have been shown to alter miRNA processing and target specificity, including single nucleotide polymorphisms (SNPs) in miRNA genes, RNA tailing with adenylation or uridylation of the 3' end of the pre-miRNA or mature miRNA, RNA editing with the replacement of adenosine bases for inosine, and RNA methylation (Ha and Kim 2014).

1.3.2 miRNA Gene Silencing

The post-transcriptional gene silencing capabilities of miRNAs are mediated through loading of the mature miRNA template into an AGO protein with the target mRNA, forming the RNA-induced silencing complex (RISC) (Figure 1.7). Mature miRNAs target mRNA by binding to regions, usually found in the 3' UTR of mRNA, that are complementary to the "seed sequence" of the miRNA, located at the 5' end in nt position 2-7. However, nt 8 and 13-16 also assist base pairing with the target mRNA, but nts 13-16 are not as important. miRNAs that share the same seed sequence are considered to belong to the same family and are indicated by the use of a letter suffix (e.g. miR-34a, miR-34b, and miR-34c). There are 4 AGO proteins (AGO1-4) in humans and mice that can all induce mRNA translational repression and decay; however, only AGO2 can cleave target mRNAs that perfectly match the miRNA template. AGO2 cleaves target mRNAs at nts 10-11, with the 5' end of the mature miRNA acting as a template, using an active site in its PIWI domain at the C-terminus (Ha and Kim 2014).

The miRNA duplex, processed by Dicer, is loaded into AGO proteins to form the pre-RISC (Figure 1.7). The passenger strand (miRNA*) is quickly removed from the RISC to produce a mature RISC (Ha and Kim 2014). Which strand is selected (5p or 3p) to be the mature miRNA strand is determined by the stability of the base pairs at the 5' ends of the miRNA duplex, with an unstable 5' terminus typically being more favourable (Khvorova et al. 2003; Schwarz et al. 2003). However, AGO proteins also show a preference for miRNA strands that have a uracil (U) base at the first nt position. The passenger strand is removed from the pre-RISC by either AGO2 cleavage of the passenger strand (if there is base matching at the centre of the duplex), or more commonly, by unwinding of the intact passenger strand. Unwinding is promoted by base pair mismatches at nt positions 2-8 and 12-15, with this process being assisted by a chaperone complex consisting of heat shock cognate 70 (HSC70) and heat shock protein 90 (HSP90). The released passenger strand is usually quickly degraded, but can be involved in silencing activity in certain situations. The mature RISC containing the mature miRNA template is then free to bind target mRNA and inhibit its translation through inhibition of the translational machinery or cleavage of the mRNA by AGO2 (if there is central complementarity with the mRNA) (Figure 1.7) (Ha and Kim 2014).

1.3.3 microRNAs in Obesity and Cardiovascular Diseases

With the role of miRNAs as "fine tuners" of gene expression a lot of attention has been paid to miRNAs in the regulation of CVDs and other obesity co-morbidities. After their discovery in humans in 2000, it was not until 2005 that findings showed miRNAs regulate processes in the cardiovascular system, with the discovery that the muscle-specific miR-1 is important for cardiac development in mice due to its targeting of the hand transcription factor (Hand)2 mRNA (Zhao et al. 2005). However, it was not until 2006 that miRNAs were correlated with CVDs, when Rooij et al. showed that a number of expression changes in miRNAs were associated with pathological cardiac hypertrophy in mice and humans (van Rooij et al. 2006). Among these altered miRNAs the authors showed that miR-23a, 23b, 24, 195, and 214 (up-regulated during cardiac hypertrophy) could induce cardiomyocyte hypertrophy *in vitro*, and that miRNAs miR-150 and 181b (down-regulated during cardiac hypertrophy) reduced cardiomyocyte hypertrophy *in vitro*.

Around the same time, evidence started to emerge that miRNAs could also be important regulators of obesity's comorbidities, with the discovery that liver-specific miRNA miR-122 contributes to the development of diet-induced hepatic steatosis in mice (Esau et al. 2006).

Over the last decade, since correlations were drawn between miRNAs and pathogenesis in CVDs and obesity, countless other studies have explored the role of other miRNAs in these diseases. To name a few, miR-24 has been shown to potentially have a role in regulating hypertension by targeting *CYP11B1* and *CYP11B2* mRNA in adrenocortical cells, reducing the production of aldosterone and cortisol (Robertson et al. 2013). A number of miRNAs have been implicated in vascular remodeling during pulmonary arterial hypertension (PAH), including miR-143-3p, miR-145, and miR-451 (Caruso et al. 2012; Grant et al. 2013; Deng et al. 2015). Additionally, while not involved in PAH development, miR-214 is involved in PAH-associated right ventricular hypertrophy (Stevens et al. 2016). miRNAs have also been implicated in vascular remodeling in the context of coronary artery therapies. For example, miR-21 was shown to be involved in saphenous vein graft failure by promoting neointima formation in a porcine coronary artery bypass grafting (CABG) model (McDonald et al. 2013). Furthermore, both miR-21-5p and miR-21-3p were shown to promote in-stent restenosis in a murine stent model, with miR-21 KO mice (lacking the stem-loop) showing reduced vascular neointima formation, and increased levels of M2 macrophages (McDonald et al. 2015). miR-21 has also been implicated in atherosclerosis, which is the major cause of CVD and the cause that has the greatest association with obesity. miR-21 is up-regulated in human atherosclerotic plaques, and enhances endothelial cell VCAM-1 and CCL2 expression, and monocyte adhesion *in vitro*; this could enhance macrophage recruitment to the plaque (Raitoharju et al. 2011; Zhou et al. 2011). There are, of course, numerous other miRNAs that have roles in atherosclerosis, including miR-10, miR-17-3p, miR-3, miR-92a, miR-126, miR-155, miR-181b, and *let-7g* in endothelial cell inflammation; miR-1, miR-33, miR-132, miR-208, miR-221, miR-222*, let-7d*, and *let-7g* in vascular smooth muscle cell (VSMC) proliferation; and miR-30c, miR-33a, miR-33b, miR-106, miR-144, and miR-758 in lipid metabolism (Aryal et al. 2014).

Interestingly, despite miR-21's role in vascular pathology, it has also been implicated in the development of obesity. Pharmacological inhibition of miR-21 induced a reduction in weight, eWAT adipocyte size, serum TGs, eWAT leptin and CCL2 secretion in *db/db* mice (Seeger et al. 2014). On the other hand, miR-155 has been shown to be protective against the development of non-alcoholic hepatosteatosis in HFD-fed mice, through potentially targeting LXRα (Miller et al. 2013). However, miR-155 has also been shown to inhibit brown adipocyte differentiation and thermogenesis, and WAT "browning" by targeting CEBPβ, suggesting that it may contribute to obesity development in an obesogenic environment (Chen et al. 2013). Intriguing research from the Olson group showed how miRNAs can "fine tune" cardiac tissue regulation of global energy metabolism, highlighting miRNAs' importance in this bridge between obesity and CVDs (Grueter et al. 2012). They showed that heart-specific miR-208a targets MED13 in the heart, to inhibit numerous thyroid hormone- and nuclear receptor-responsive genes in the heart. Pharmacological anti-miR inhibition of miR-208a in HFD-fed mice induced resistance to weight gain, improve insulin sensitivity and glucose tolerance, as well as reduced WAT and BAT mass, and reduced adipocyte hypertrophy, which was reiterated in MED13 over-expressing TG mice (Grueter et al. 2012). Other miRNAs of importance are the miR-33 family (miR-33a and 33b), which were shown to be important therapeutic targets for treating dyslipidaemia. miR-33a and 33b are encoded in the introns of the *SREBF2* and *SREBF1* genes, respectively. They collaborate to increase intracellular cholesterol and lipid levels by targeting numerous mRNAs for proteins associated with cholesterol synthesis, transport, and secretion, and fatty acid oxidation and insulin signaling (Rayner et al. 2011; Abente et al. 2016). A pre-clinical trial in non-human primates using locked nucleic acid (LNA) anti-miR-33 (targeting both miR-33a and b) showed promising results. The LNA anti-miR-33 increased HDL and reduced VLDL in the serum, whilst increasing the expression of multiple genes involved in FA oxidation and reducing those involved in FA synthesis in the liver (Rayner et al. 2011). Numerous other miRNAs have also been shown to regulate pathways involved in obesity comorbidities, including miR-1, miR-24, miR-27a, miR-27b, miR-107, miR-205, miR-206, miR-378, miR-378*, miR-485-5p, and miR-613 in hepatic lipogenesis; and miR-93, miR-99a, miR-122, miR-130a-3p, miR-181, miR-190b, miR-221, and miR-802 in hepatocyte and adipocyte insulin resistance (Abente et

al. 2016). Additionally, countless miRNAs have been implicated in regulating adipogenesis, including let-7, miR-15a, miR-17, miR-21, miR-24, miR-27, miR-31, miR-92, miR-103, miR-107, miR-125b, miR-138, and miR-143 (McGregor and Choi 2011).

These studies highlight that miRNAs are intimately involved in the regulation of many disease mechanisms in obesity and CVDs. However, this thesis mainly focuses on miRNA regulation of the link between inflammatory and metabolic pathways in the adipose tissue and ATMs (briefly summarised in section 1.3.3.1). In particular, this thesis explores miR-34a's role in regulating these pathways (section 1.3.4), discussed below.

1.3.3.1 miRNAs In Macrophages and Adipose Inflammation

There has been limited investigation of miRNA regulation of macrophage metabolic and inflammatory functions, with even less known about miRNA regulation of these processes in the context of adipose inflammation. Only miR-223 and miR-671-5p have been shown to regulate macrophage inflammatory processes in adipose tissue, to date (Zhuang et al. 2012; Lien et al. 2014). miR-223 promotes an M2 macrophage phenotype in murine BMDMs *in vitro* by targeting Pknox1, which promotes an M1 phenotype under a polarising stimulus (e.g. IL-4 or LPS) and increases protein levels in miR-223 KO vWAT. Additionally, HFD-fed miR-223 KO mice showed exacerbated systemic insulin resistance, with the vWAT having increased mass, inflammation, and M1 ($CD11c^+$ $CD206^-$) ATM infiltration, with a corresponding decrease in M2 ($CD11c^-$ $CD206^+$) ATMs (Zhuang et al. 2012). On the other side, *in vitro* co-culture experiments with human orbital fat-derived stem cells (OFSCs) and LPS-stimulated RAW264.7 macrophages showed that OFSC miR-671-5p expression regulated the anti-inflammatory effects of OFSCs on LPS-stimulated macrophages. The authors showed that miR-671-5p targeted soluble TNF receptor II (sTNFRII) and IL-1RA mRNA, reducing OFSCs' anti-inflammatory effect on macrophages (Lien et al. 2014). Although OFSCs are not fully committed to the adipocyte lineage, both of these studies do highlight the possibility of miRNAs regulating adipose inflammation by targeting genes in both adipocytes and macrophages. In fact, further evidence showed that adipocyte miR-130a and miR-130b can be stimulated by TNFα through the activation of the

NF-κB subunit p65, which binds to the promoter region of miR-130a/b. The authors showed that miR-130a/b was increased in the WAT of HFD-fed mice and targeted PPARɣ in 3T3L1 white adipocytes, with TNFα-induced down-regulation of PPARɣ also down-regulating its target genes: FABP4, LPL, and the protective adipokine adipsin (Kim et al. 2013a). Additionally, in primary human adipocytes miR-145 was shown to increase TNFα secretion and lipolysis, through autocrine TNFα-stimulation. This increased HSL activation and reduced phosphodiesterase 3B (PDE3B) mRNA, which inactivates cAMP-mediated lipolysis. The authors further showed that miR-145 increased NF-κB p65 activation and targeted ADAM17, which processes TNFα to produce soluble TNFα, increasing the amount of the more biologically active membrane-bound TNFα (Lorente-Cebrián et al. 2014). Therefore, these studies show that miRNAs can regulate adipose inflammation and the adverse metabolic effects of inflammation on adipocytes.

In other contexts, a number of other miRNAs were shown to regulate macrophage phenotype. miR-142-5p and miR-130a-3p counter-regulate the pro-fibrosis actions of murine M2 (IL-4/13 stimulated) macrophages, through targeting suppressor of cytokine signaling (SOCS)1 and PPARɣ, respectively. miR-142-5p inhibition of SOCS1 expression in macrophages up-regulates macrophage pro-fibrosis genes (e.g. *transforming growth factor* (*Tgf)-β*) and decreases fibroblast collagen deposition during *in vitro* co-culture, whilst also exacerbating liver and lung fibrosis in mice. On the other hand, miR-130a-3p inhibition of PPARɣ expression had an opposite and protective effect (Su et al. 2015). Along with its roles in vascular inflammation and obesity, intracellular miR-21 directly influences macrophage polarisation. However, there are some conflicting studies surrounding miR-21's regulation of macrophage polarisation, with one study showing that it promotes an M2 phenotype and another suggesting it inhibits this (Caescu et al. 2015; Wang et al. 2015). The first study shows that miR-21 can be activated by phosphoinositide 3-kinase (PI3K) and MAPK1 (ERK2) and 3 (ERK1) signaling by the activation of the macrophage colony stimulating factor receptor (M-CSF-R) on murine BMDMs *in vitro*. The authors further show that miR-21 targets numerous pro-inflammatory (M1) genes (e.g. IL-1β, IL-6, CCL2, and CXCL10) in BMDMs; miR-21 LNA knock-down decreased a number of M2 markers (e.g. Arg1, CD206, IL-4R, and Retnla), showing miR-21 promotes an M2 macrophage phenotype

(Caescu et al. 2015). However, the other study showed that peritoneal macrophages from miR-21 KO mice have enhanced mRNA expression of M2 markers (e.g. Arg1, IL-10, Chi3l3, and Retnla) and miR-21-mimic increases the mRNA expression of TNFα and IL-1β in WT macrophages. They also showed that miR-21 targets STAT3, which promotes an M2 macrophage phenotype (Wang et al. 2015). Thus, the role of miR-21 in macrophage inflammatory responses is currently unclear. A final miRNA of interest is miR-155, especially since it has already been shown to be protective in non-alcoholic hepatosteatosis; however, studies have shown that miR-155 promotes an M1 macrophage phenotype (O'Connell et al. 2007; Martinez-Nunez et al. 2011; Xu et al. 2013). A number of pro-inflammatory stimuli (TNFα, IFNβ, IFNɣ, and LPS) up-regulate miR-155 expression in murine BMDMs, this is thought to be mediated through the JNK signaling pathway (O'Connell et al. 2007). miR-155 also directly targets *Il13rα1* mRNA, reducing IL-13Rα1 protein and STAT6 activation through the type II IL-4 receptor reducing IL-13 signaling, a M2 polarising cytokine (Martinez-Nunez et al. 2011). Furthermore, miR-155 was shown to promote an M1 macrophage phenotype (increasing TNFα, IL-6, and nitric oxide production) in BMDMs by targeting SOCS1 when stimulated with *Staphylococcus aureus*, a pathway inhibited by Akt signalling (Xu et al. 2013). A number of other miRNAs also regulate macrophage polarisation, including miR-9, miR-125b, and miR-127 by promoting an M1 phenotype; and miR-124, miR-125a-5p, miR-132, miR-146a, and *let-7c* by promoting an M2 phenotype in macrophages (Essandoh et al. 2016).

Therefore, these studies show that miRNAs have important regulatory roles in macrophage responses and in adipose inflammation. However, the full extent of miRNA's regulation of these processes is still to be clarified.

1.3.4 miR-34a

1.3.4.1 miR-34 Family

miR-34 was first cloned in 2001 by Lau et al. in *C. elegans*. They also showed that it was conserved in *Drosophila* and humans (Lau et al. 2001). Subsequently, it was discovered that miR-34 was a miRNA family consisting of 3 members: miR-34a, miR-34b, and miR-34c. In mammals, these miRNAs are

encoded by two different genes, with miR-34a encoded on chromosome 1p36.23 within exon 2 of its own primary transcript, whereas miR-34b and c are clustered together on chromosome 11q23.1 and encoded within intron 1 and exon 2, respectively, on the same primary transcript, therefore sharing the same promoter (Bommer et al. 2007; He et al. 2007; Welch et al. 2007; Rokavec et al. 2014a). Because miR-34b and c share the same promoter they share the same expression profile in mice, with expression in the lungs and brain, although with higher abundance in the former. On the other hand, miR-34a shows a different expression profile, with broader expression in the heart, lungs, liver, kidney, spleen, skeletal muscle, brain, small/large intestines, and stomach, but with the highest abundance in the brain (Bommer et al. 2007). The testis is one of the only organs that expresses high levels of all 3 family members (Dutta et al. 2007). Despite miR-34a, b, and c all being in the same miRNA family, only miR-34a and c share identical seed sequences, while the seed sequence of miR-34b differs by one base (Rokavec et al. 2014a).

The miR-34 family was brought into the limelight by the discovery that the whole family is regulated by the tumour-suppressor p53, which binds to the promoter of the miR-34 genes and directly induces their transcription (Bommer et al. 2007). Additionally, all of the miR-34 family were shown to induce cell cycle arrest and cellular senescence in numerous tumour cells, but miR-34a showed the greatest induction by p53. miR-34a was found to mediate these effects partly through targeting cyclin-dependant kinase 4 (CDK4) and MET (He et al. 2007). Since these discoveries the miR-34 family has been shown to regulate multiple genes involved in cancer progression through numerous pathways, including cell cycle, invasion apoptosis, epithelial-mesenchymal transition (EMT), stemness, differentiation, and metabolism (Rokavec et al. 2014a).

1.3.4.2 miR-34a In Cardiovascular Diseases and Obesity

Apart from miR-34a's protective role in cancer, it has also been implicated in CVDs. For example, miR-34a is up-regulated in human atherosclerotic plaques from various arteries of individuals that are overweight with hypertension and dyslipidaemia (Raitoharju et al. 2011). Additionally, miR-34a was shown to increase during neointima formation in a saphenous vein graft used in a porcine

CABG model (McDonald et al. 2013). There is also evidence that miR-34a has an important role in the regeneration of cardiac tissue. Following myocardial infarction (MI), miR-34a transcripts increase in the adult murine heart, and inhibit cardiomyocyte proliferation and promote cardiomyocyte apoptosis, preventing cardiac regeneration post-MI, and increasing fibrotic remodeling of the heart (Boon et al. 2013; Yang et al. 2015). The authors further showed that these effects can be mediated through miR-34a targeting: *B-cell/CCL lymphoma (Bcl)2*, *Cyclin D1*, and *silent mating type information regulation 2, S. cerevisiae, homolog (Sirt)1* transcripts (Yang et al. 2015). Furthermore, miR-34a transcripts increase in the murine heart with age and contribute to age-related cardiomyocyte death by targeting phosphatase 1 nuclear targeting subunit (PNUTS), causing telomere shortening, DNA damage responses and apoptosis. This lead to increased cardiac fibrosis and reduced cardiac contractility (Boon et al. 2013). Interestingly, these adverse effects of miR-34a on cardiomyocytes are suppressed by delivery of bone marrow-derived mononuclear cells (BMCs) to the murine myocardium, through BMC production of IGF-1 blocking miR-34a transcript processing (Iekushi et al. 2012). Patients with MI also have more miR-34a in their BMCs, which promotes hydrogen peroxide-induced cell death of these cells *in vitro* (Xu et al. 2012). Additionally, both atherosclerosis and neointima formation are associated with macrophage infiltration. Therefore, these studies suggest that miR-34a could have important regulatory functions in macrophages associated with CVDs.

Importantly, miR-34a is a candidate biomarker for T2D, with a meta-analysis of T2D studies showing that miR-34a is consistently up-regulated in the blood, liver, and pancreas of both humans and mice (Zhu and Leung 2015). Additionally, miR-34a transcript expression has been shown to increase in human scWAT linearly with increasing BMI, but the same relationship was not observed in omental adipose (Klöting et al. 2009; Ortega et al. 2010). A similar observation was made in mice, with murine WAT miR-34a transcripts increasing during HFD-feeding, but the authors did not indicate which specific depot was used (Fu et al. 2014). Examination of the adipocytes themselves showed that miR-34a transcripts increased over *in vitro* differentiation of human subcutaneous white adipocytes (Ortega et al. 2010). Another report showed that miR-34a overexpression reduced proliferation and differentiation of primary, human white adipose derived stem cells

(ADSCs) into adipocytes by regulating senescence and cell cycle progression. The authors additionally showed that miR-34a overexpression in ADSCs during differentiation increased the secretion of CCL2, CCL5, CXCL8, and IL-6, and reduced the transcript expression of *PPARγ* and *ADIPOQ* (adiponectin) (Park et al. 2015). Interestingly, leptin reduces miR-34a expression in breast cancer cell lines (Avtanski et al. 2015a), suggesting that miR-34a expression could be regulated by adipocytes. These studies suggest that miR-34a could have a role in regulating adipocyte function and adipogenesis during obesity. However, few studies have looked at miR-34a in adipose tissue and even fewer in vWAT.

In contrast, more attention has been given to exploring miR-34a in the liver during obesity. A number of studies in mice and humans have shown that hepatic miR-34a expression increases with the development of NAFLD during obesity (Cheung et al. 2008; Li et al. 2009; Cermelli et al. 2011; Yamada et al. 2013). The level of miR-34a expression in human serum and liver correlates with the severity of NAFLD, with higher transcript levels observed with progression to NASH (Cheung et al. 2008; Cermelli et al. 2011). However, one study only observed this trend in the serum of male patients with NAFLD; whilst the female NAFLD patients showed increased miR-34a transcripts they did not correlate with disease severity (Yamada et al. 2013). These studies suggest that miR-34a is involved in the pathogenesis of NAFLD and, in fact, inhibition of miR-34a in rodents reduces hepatocyte apoptosis, increases hepatic FA oxidation, reduces hepatic lipid accumulation and inflammation, and improves systemic insulin resistance (Lee et al. 2010; Castro et al. 2012; Fu et al. 2012; Choi et al. 2013).

In hepatitis C patients, serum levels of miR-34a positively correlate with increased hepatitis C severity, blood glucose levels, and insulin resistance (Cermelli et al. 2011). Furthermore, non-obese type 1 diabetic (T1D) mice showed increased hepatic expression of miR-34a (Li et al. 2009). This suggests that miR-34a is involved in diabetes, or at least hyperglycaemia. Corollary, patients that are overweight with T2D show increased serum levels of miR-34a, compared to those who are overweight without T2D (Kong et al. 2011). *In vitro*, increased expressed of miR-34a in primary beta-islet cells reduces insulin secretion and promotes inflammation-induced (IL-1β and palmitate) cell death (Lovis et al. 2008; Roggli et

al. 2010). In rats and humans, the declining proliferative capacity of beta-islet cells with age has also been correlated with increased miR-34a transcripts, which also induced beta-islet cell apoptosis (Tugay et al. 2016). Therefore, these studies suggest that miR-34a can regulate the development of diabetes.

1.3.4.3 miR-34a Targets In Adipocyte Metabolism and Inflammation

The vast majority of validated miR-34a targets regulate aspects of cancer development (Figure 1.8) (Rokavec et al. 2014a); however, there are a number of validated targets that are also involved in adipocyte metabolism and inflammation (Table 1.2). One of the most regularly studied miR-34a target is SIRT1. SIRT 1 is a NAD^+-dependent deacetylase that interacts with a variety of other proteins, including AMP-activated protein kinase (AMPK), PGC1α, PPARα, PPARɣ, and NF-κB. Due to the variety of proteins deacetylated by SIRT1, it has been shown to inhibit inflammation and glycolysis, whilst promoting oxidative metabolism (Kauppinen et al. 2013). SIRT1 also regulates adipogenesis through deacetylation of PPARɣ, which represses PPARɣ activity and inhibits white adipocyte differentiation, while promoting PRDM16 docking and WAT browning (Han et al. 2010; Harms and Seale 2013; Mayoral et al. 2015; Kim et al. 2015b). PPARɣ can regulate this process by inhibiting SIRT1 expression (Kauppinen et al. 2013). Additionally, SIRT1 promotes increased thermogenesis in brown adipocytes (Boutant et al. 2015). Yamakuchi et al. was the first to show that SIRT1 was a direct target of miR-34a and that the inhibition of SIRT1 transcripts by miR-34a enhances activity of p53, inducing a positive-feedback loop, as SIRT1 inhibits p53 activity through deacetylation (Yamakuchi et al. 2008). In a murine diet-induced obesity model of NAFLD, liver SIRT1 levels decreased with HFD-feeding due to the increased expression of miR-34a, which is inhibited by farnesoid X receptor (FXR). miR-34a inhibition improved the HFD liver phenotype by decreasing hepatic and plasma TG levels, as well as gene transcripts involved in ER stress, inflammation (*Tnfa* and *Il-6*), lipogenesis, and *Cd36*, whilst increasing β-oxidation gene transcripts and improving systemic insulin resistance (Lee et al. 2010; Choi et al. 2013). The authors showed that not only could miR-34a regulate SIRT1 transcript expression directly, but that miR-34a also targets nicotinamide phosphoribosyltransferase (NAMPT), which is the rate-limiting enzyme in NAD^+

biosynthesis from nicotinamide, reducing NAD+ levels and SIRT1 activity (Choi et al. 2013). SIRT1 is also observed to decrease in the skeletal muscle and WAT of diet-induced obese mice, suggesting miR-34a could be regulating SIRT1 and metabolism in these tissues too (Coste et al. 2008; Fu et al. 2014). In fact, one study showed that miR-34a inhibits browning of WAT and BAT formation in murine diet-induced obesity by directly targeting SIRT1, FGFR1, and the FGFR co-receptor β-Klotho (βKL) transcripts, reducing FGF21 induction of browning and thermogenesis (e.g. reduced *Ucp1* and *Pgc1α* mRNA) in adipocytes (Fu et al. 2014). βKL was previously shown to be a direct target of miR-34a, causing the inhibition of FGF19 signalling in hepatocytes and suppressing the protective effects of FGF19 on NAFLD development in a murine diet-induced obesity model (Fu et al. 2012). FGF19 is released when bile acids are absorbed in the intestines and signals through hepatic FGFR4 and βKL. FGF19 regulates hepatic bile acid synthesis, and protein and glycogen metabolism independently of insulin (Kir et al. 2011). Furthermore, miR-34a can directly target PPARα in hepatocytes, which the authors suggest contributes to liver steatosis through decreased β-oxidation in HFD-fed mice. The author also observed increased expression of β-oxidation gene transcripts and AMPK activation during miR-34a inhibition *in vitro* and *in vivo* (Ding et al. 2015).

Gene	**Full Name**	**Immune Sys/ Metabolism**	**Cellular Process**	**Reference**
ACSL1	Acyl-CoA synthetase long-chain family member 1	Metabolism	TG Synthesis	(Kaller et al. 2011; Li et al. 2011a)
ACSL4	Acyl-CoA synthetase long-chain family member 4	Metabolism	TG Synthesis	(Kaller et al. 2011)
AXL	AXL receptor tyrosine kinase	Immune Sys	Efferocytosis (apoptotic cell clearance)	(McCubbrey et al. 2016)
βKL	β-Klotho	Metabolism	FGFR signaling (co-receptor)	(Fu et al. 2012; 2014)
CCL22	CC chemokine ligand 22	Immune Sys	Chemokine, cell migration (CCR4)	(He et al. 2015)
DGKζ	Diacylglycerol kinase	Immune Sys	GPCR/IL-R signaling, T cell activation	(Shin et al. 2013)
E2F3	E2F transcription factor 3	Immune Sys	Granulocyte/myeloid cell transition	(Pulikkan et al. 2010)
FGFR1	Fibroblast growth factor receptor 1	Metabolism	FGFR signaling	(Fu et al. 2014)

Gene	Full Name	Immune Sys/ Metabolism	Cellular Process	Reference
FOXP1	Forkhead box p1	Immune Sys	Transcriptional repressor, B cell differentiation	(Rao et al. 2010; Craig et al. 2011).
GPI	Glucose-6-phosphate isomerase	Metabolism	Glycolysis	(Kim et al. 2013b)
HK1	Hexokinase 1	Metabolism	Glycolysis	(Kim et al. 2013b)
HK2	Hexokinase 2	Metabolism	Glycolysis	(Kim et al. 2013b)
IL6R	Interleukin 6 receptor (soluble & membrane bound)	Immune Sys	Inflammatory cytokine signaling (IL-6)	(Rokavec et al. 2014b; Li et al. 2015)
LDHA	Lactate dehydrogenase A	Metabolism	Glycolysis	(Kaller et al. 2011)
LEF1	Lymphoid enhancer-binding factor	Immune Sys	Transdifferentiation of pre-B cells to macrophages	(Rodriguez-Ubreva et al. 2014)
NAMPT	Nicotinamide Phosphoribosyltransferase	Metabolism	NAD^+ production, SIRT1 activation	(Choi et al. 2013)
NOTCH1	Notch homolog 1, translocation-associated	Immune Sys	Development/cell fate decisions of immune cells, TLR & NF-κB signaling	(Jiang et al. 2012)
PDGFRα	platelet-derived growth factor receptor α	Metabolism	Cell proliferation (beta islet cells)	(Tugay et al. 2016)
PDK1	Pyruvate dehydrogenase kinase isoform 1	Metabolism	Glycolysis	(Kim et al. 2013b)
PPARα	Peroxisome proliferator-activated receptor α	Metabolism	FA (β)-oxidation, cell proliferation, differentiation	(Ding et al. 2015)
SIRT1	Silent mating type information regulation 2, *S. cerevisiae*, homolog 1	Metabolism	Proliferation/differentiation (including adipocytes) and FA metabolism	(Yamakuchi et al. 2008)
ULBP2	UL16 binding protein 2	Immune Sys	Cell marker of stress, ligand for NK cell & CTL receptor (NKG2D)	(Heinemann et al. 2012)
VAMP2	Vesicle-associated membrane protein	Metabolism	Targeting/fusion of transport vesicles, insulin secretion	(Lovis et al. 2008; Roggli et al. 2010)

Table 1.2: Validated miR-34a Targets Involved In Metabolism and Immune System Function
Abbreviations: immune system (immune sys), fatty acid (FA), triglyceride (TG), fibroblast growth factor receptor (FGFR), CC chemokine receptor (CCR), interleukin (IL) receptor (R), G-protein-coupled receptor (GPCR), Toll-like receptor (TLR), nucelar factor-κB (NF-κB), natural killer (NK) cell, cytotoxic T lymphocyte (CTL), killer cell lectin-like receptor subfamily K, member 1 (NKG2D), and nicotinamide adenine dinucleotide (NAD^+/NADH).

To date, no other studies have directly looked at miR-34a function in adipocytes (Figure 1.8). However, a number of studies have shown that miR-34a targets genes in FA and glycolytic metabolism that are relevant to adipocyte

function: ACSL1 and ACSL4 in TG synthesis; glucose-6-phosphate isomerase (GPI), hexokinase (HK)1, HK2, lactate dehydrogenase A (LDHA), and pyruvate dehydrogenase kinase isoform (PDK)1 in glycolysis; and PPARα in β-oxidation (Table 1.2). Through the regulation of these genes and SIRT1 it suggests that miR-34a could have an important role in adipocyte metabolism during obesity. Additionally, C/EBPα has been shown to promote the expression of miR-34a, suggesting that miR-34a expression could be induced during adipogenesis (Pulikkan et al. 2010).

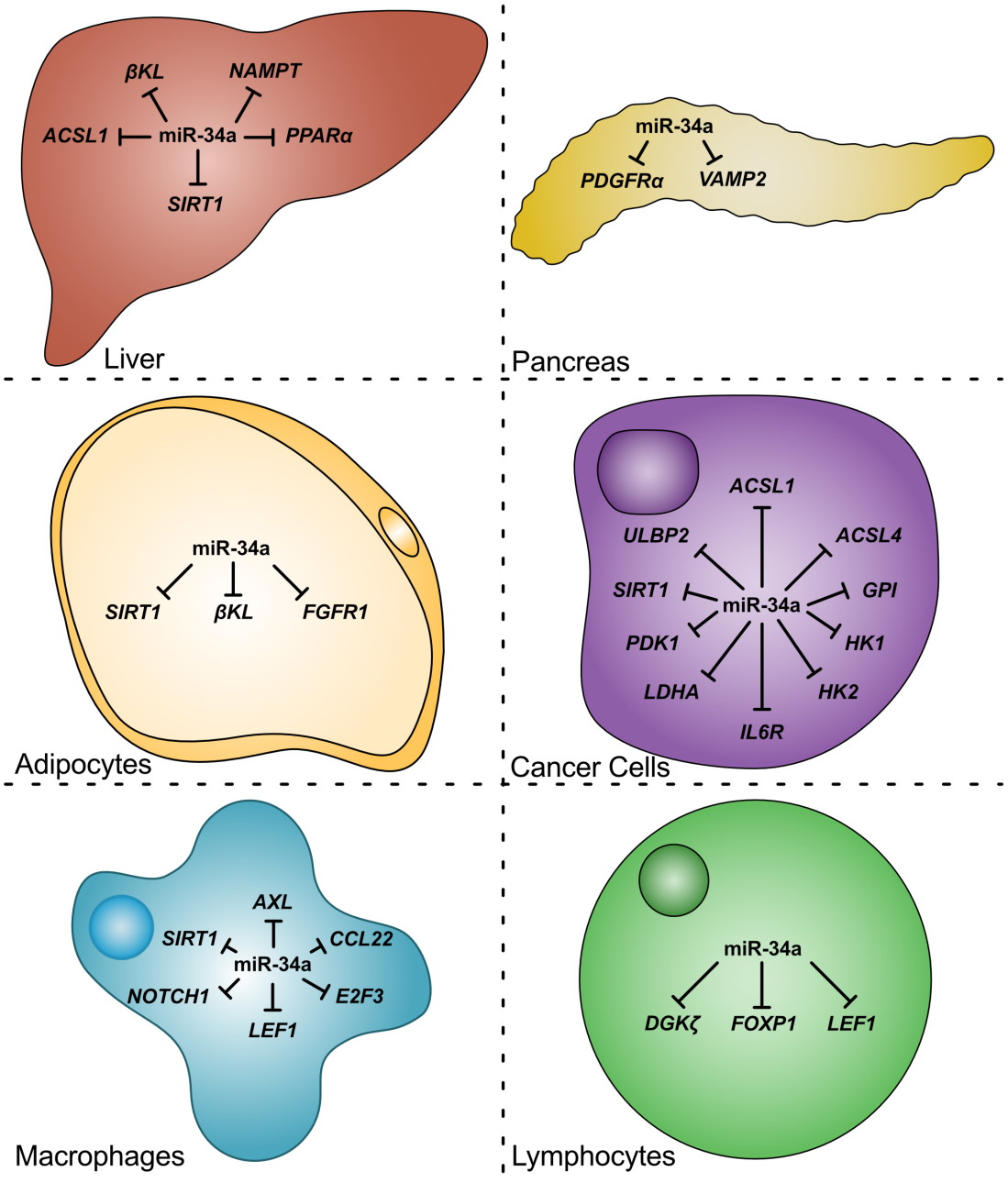

Figure 1.8: Distribution of Validated miR-34a Targets Among Cell and Tissue Types
Showing the tissue/cell distribution of the validated miR-34a targets involved in metabolism and immune function shown in Table 1.2.

Another tissue that miR-34a has been poorly examined in during obesity is the pancreas (Figure 1.8). However, saturated FAs (e.g. palmitic acid and stearic acid) and inflammatory cytokines (e.g IL-1β) were shown to induce pancreatic beta-islet cell death, and this process is regulated by miR-34a (Lovis et al. 2008; Roggli et al. 2010; Lu et al. 2016). During stearic acid stimulation, miR-34a transcripts are up-regulated by protein kinase-like ER kinase (PERK) activation of p53, which allows miR-34a to directly target the anti-apoptotic genes for B cell CLL/lymphoma 2 (BCL-2) and BCL-2-like 2 (BCL-L2), promoting beta-islet apoptosis (Lu et al. 2016). Pro-apoptosis and anti-proliferative functions of miR-34a on beta islet cells are also mediated through miR-34a targeting platelet-derived growth factor receptor (PDGFR)α (Tugay et al. 2016). Additionally, miR-34a inhibits insulin secretion from beta-islet cells by directly targeting the vesicle docking/fusion protein vesicle-associated membrane protein (VAMP)2 (Lovis et al. 2008; Roggli et al. 2010).

The inflammatory environment in adipose tissue during obesity is of great interest, as the cross-talk between metabolic tissues and the immune system is pinnacle to the development of obesity's co-morbidities. Therefore, finding novel mechanisms that can regulate this process is important. As mentioned above, only a few studies have examined miRNA regulation of these processes in the adipose, and currently no studies have directly looked at miR-34a's regulation of inflammatory networks in the adipose tissue. However, there is evidence that miR-34a can regulate inflammatory pathways (Table 1.2, Figure 1.8). For example, *C. parvum*-induced inflammation in mice increased miR-34a transcript expression in the spleen, suggesting that miR-34a could be involved in regulating immune function, with the spleen showing a dense population of lymphocytes and innate immune cells (Mathé et al. 2012). There are some conflicting studies, making it unclear whether miR-34a is pro- or anti-inflammatory, but miR-34a's regulatory roles may also be context dependent. LPS stimulation reduces miR-34a transcript expression in RAW264.7 macrophages *in vitro*, increasing the expression of TNFα, IL-6, and CCL22 (Jiang et al. 2012; He et al. 2015). The authors showed that miR-34a directly targets notch homolog 1, translocation-associated (NOTCH1) gene transcripts, which can activate NF-κB, reducing the expression of TNFα and IL-6 (Jiang et al. 2012). Furthermore, miR-34a inhibits IL-6 signaling in cancer

cells through directly targeting the gene transcripts of soluble and membrane-bound IL-6 receptor (IL-6R), a process which can be inhibited by IL-6 signaling activating STAT3 to inhibit miR-34a transcription in a feedback loop (Rokavec et al. 2014b; Li et al. 2015). Interestingly, STAT3 was identified as a potential direct target of miR-34a during AGO pull-down, suggesting that miR-34a also inhibits the IL-6 signaling pathway (Lal et al. 2011). A correlation was also observed between the increase in miR-34a transcripts and insulin-like growth factor (IGF)-1 levels in alveolar macrophages during murine lung fibrosis (Honeyman et al. 2013). Finally, transfection of pre-miR-34a into human hepatocytes increases expression of MMP2 and 9, usually associated with an M2 macrophage phenotype (Meng et al. 2012). Therefore, these studies suggest that miR-34a promotes an anti-inflammatory phenotype.

On the other hand, CCL22 is a chemoattractant for T_{regs} and CCL22 gene transcripts are a direct target of miR-34a (Yang et al. 2012; He et al. 2015). miR-34a inhibits TGF-β-induced CCL22 recruitment of T_{regs}, in an *in vitro* and *in vivo* portal vein tumor thrombus (PVTT) model. Additionally, an AGO pull-down study suggests TGF-β, FGFs, FGFRs, and insulin receptor are direct targets of miR-34a, but these results were not validated (Lal et al. 2011). *In vitro* studies using Jurkat T cells have shown that miR-34a enhances T cell activation (increased CD69 expression and ERK1/2 activation (phosphorylation)) by targeting diacylglycerol kinase (DGK)ζ (Shin et al. 2013). Finally, *in vitro* studies in alveolar macrophages show that miR-34a inhibits apoptotic cell clearance (efferocytosis) by reducing apoptotic cell binding, partly through directly targeting AXL receptor tyrosine kinase (AXL) and SIRT1 gene transcripts (McCubbrey et al. 2016). Therefore, these studies suggest that miR-34a promotes a pro-inflammatory phenotype.

A few studies have also implicated miR-34a in macrophage and B cell differentiation. The T1D resistance locus Idd9.3, which encodes miR-34a, has been shown to inhibit B cell lymphopoiesis when expressed in non-obese diabetic (NOD) mice, implicating miR-34a in B cell lymphopoiesis (Berry et al. 2014). Furthermore, miR-34a inhibits B cell differentiation of pro-B cells to pre-B cells by targeting gene transcripts of the transcription factor forkhead box (FOX)P1, reducing the percentage of mature B Cells ($CD19^+$ IgM^+) in murine bone marrow,

but not T cell ($CD3\varepsilon^+$) numbers (Rao et al. 2010). The inhibition of FOXP1 by miR-34a was shown to inhibit malignant transformation of the low-grade, gastric mucosa-associated lymphoid tissue (MALT) B cell lymphoma to the high-grade, gastric diffuse large B-cell lymphoma (gDLBCL) *in vitro* and *in vivo* (Craig et al. 2011; 2012). Interestingly, *in vitro* studies looking at miRNAs in haematopoiesis show that miR-34a enhances transdifferentiation of murine bone marrow-derived pre-B cells into macrophage-like cells ($Mac\text{-}1^+$) by targeting lymphoid enhancer-binding factor (Lef)1 (Rodriguez-Ubreva et al. 2014). Additionally, miR-34a directly targets E2F transcription factor (E2F)3 gene transcripts, blocking myeloid cell differentiation during granulopoiesis in human acute myeloid leukaemia (AML) blast cells, a process regulated by C/EBPα transactivation of miR-34a transcription (Pulikkan et al. 2010).

1.3.5 Therapeutic Potential of miR-34a

In the previous section (1.3.4.3) studies showed that miR-34a has important regulatory functions in both metabolic and inflammatory pathways. This highlights the possibility that miR-34a could also regulate similar processes in obese adipose tissue. The current literature suggests that inhibition of miR-34a would promote an improved metabolic phenotype, but what effect that would have on immune function is not as clear with some studies suggesting miR-34a is pro-inflammation and others anti-inflammation. However, the miR-34 family has already been shown to have clinical therapeutic potential, with a miR-34 mimic (MRX34) being the first miRNA to reach phase 1 clinical trials in 2013. MRX34 is a dsRNA mimic that is encapsulated in liposomal nanoparticles that mainly accumulate in the liver, and was trialled in liver cancer patients with unresectable primary liver cancer and metastatic cancer. The liposome charge changes when entering the tumour microenvironment from anionic to cationic, due to the reduced pH, providing specificity for tumour delivery (Agostini and Knight 2014). The trial finished at the end of 2015, but no data from the trial is expected to be released until mid-2017. It will be interesting to see how effective MRX34 was and if there were any off-target effects on FA/glucose metabolism and inflammatory pathways. The success of this trial, and subsequent phase 2 and 3 trials, could open the door for miR-34a therapies in other diseases, such as obesity.

1.4 General Aims

The overall hypothesis of this thesis is that miR-34a is dysregulated in the adipose tissue during obesity, causing dysregulation of metabolic and inflammatory pathways in adipocytes and ATMs that contribute to adipose inflammation and obesity's comorbidities, particularly T2D.

The main aims of this thesis are:

- To examine the expression of miR-34a in vWAT and BAT in murine models of obesity and miR-34a localisation in obese murine and human WAT.

- To explore the role of miR-34a during murine, diet-induced obesity using an *in vivo* miR-34a$^{-/-}$ (KO) model, by examining the metabolic and immune phenotypes (esp. ATMs) within the adipose tissue.

- To explore the role of miR-34a on primary BMDM polarisation and metabolic and inflammatory functions *in vitro*.

- To characterise the expression of miR-34a during adipocyte differentiation and examine the function of miR-34a in adipocyte metabolism *in vitro*.

Chapter 2: Materials and Methods

In this chapter, the general methods and practises for the following chapters have been outlined, with each results chapter having its own materials and methods.

2.1 General Lab Practise

2.1.1 Regulations

All experiments were carried out in accordance with the stipulated Control of Substances Hazardous to Health (COSHH) guidelines for each protocol, and chemicals were of the highest grade available. The appropriate protective equipment was used where required, and basic lab safety consisted of wearing a cuffed, high-collar lab coat (Howie) and nitrile gloves (Semper). When using acids and other materials that present a splash hazard, safety glasses (Fisher Scientific) were worn. Additionally, a fume hood (Laboratory Systems: FC.C4/3) was used for procedures that presented an aerosol risk. In accordance with local legislation, all waste chemicals were disposed of in the appropriate manner.

2.1.2 Equipment

StarLab ErgoONE P1000, P200, P20, and P2.5 pipettes with disposable pipette tips (Mettler Toledo) were used for dispensing volumes between 0.1 μl to 1000 μl. For dispensing replicate volumes needed for polymerase chain reactions (PCRs), electronic Picus P10 and P120 pipettes (Sartorius) were used. For volumes above 1 ml a Gilson Pipette Boy and disposable 5 ml, 10 ml, and 25 ml stripettes (Costar) were used. Solutions were prepared in disposable plastics for volumes up to 50 ml, using 15 ml and 50 ml centrifuge tubes (Corning), 5 ml and 20 ml “Universal” tubes (Sterilin), 0.5 ml, 1.5 ml, and 2 ml microcentrifuge tubes (Greiner Bio-one), and 0.2ml PCR tubes (StarLab: I1402-8100). Otherwise, solutions were prepared in reusable 250 ml, 500 ml, 1 l, or 2 l glass bottles (Fisher Scientific). All glassware was washed in Decon 75 (Decon Laboratories Ltd), rinsed in distilled water (dH_2O), and dried at 37°C in a drying cupboard (Leec). Solutions and equipment requiring sterilisation were autoclaved by a Priorclave Tactrol 2; however, solutions that couldn’t be autoclaved were sterile filtered using 250 ml (Thermo Scientific: 126-0020) or 500 ml (Millipore-Merck: SCGPU05RE)

filter cups, or a 0.2 μm syringe filter (SartoriusStedim: 16534) and syringe (BD Biosciences).

Reagents and materials were weighed using a Sartorius Extend fine balance (ED224S) for measurements down to 0.0001 g, or an Ohaus Portable Advance balance for measurements down to 0.01 g, unless indicated otherwise. Most reagents were dissolved or diluted in dH_2O for aqueous solutions, unless indicated otherwise. Where constant heat and stirring were required to aid dissolution, a Jenway 1000 Hotplate & Stirrer and magnetic stirrer were used. pH was adjusted using 1 M or 0.5 M Sodium Hydroxide solutions (NaOH; Fisher Chemical: S/4920/53), or 1 M or 0.5 M Hydrogen Chloride solutions (HCL; Fisher Chemical: H/1200/PB17), and a Jenway 3510 digital pH meter, calibrated using pH 7 and 9 buffers (VWR).

Experiments requiring samples and reagents to be mixed were homogenised by inversion, flicking, or use of an IKA Lab Dancer Vortexer. Microcentrifuge tubes were centrifuged using an Eppendorf 5415 D microcentrifuge, whilst larger tubes and reaction plates were centrifuged in a Thermo Scientific Centra GP8R centrifuge and Sigma-Aldrich 4K15 centrifuge for tissue culture samples. All samples were centrifuged at room temperature, unless stated otherwise; however, for temperatures below 21°C an Eppendorf 5415 R microcentrifuge was used. Incubations of samples and solutions above 37.5°C were carried out using a Clifton water-bath, unless stated otherwise.

Ribonucleic acid (RNA) work was carried out on the bench, unless phenol-based lysis buffers were used, in which case a suitable fume hood was used. All surfaces and equipment were cleaned with RNaseZap Solution (Life Technologies: AM9780), before work began, and certified RNA and ribonuclease (RNase)-free plastics and reagents were used. These included RNase-free microcentrifuge tubes (Greiner), P20-P1000 (Mettler Toledo: GP-20F, GP-200F, GP-1000F) and P10 (Sarstedt: 70.1130.210) filtered pipette tips, and RNase-free water (Qiagen: 129115).

2.1.3 Animal work

All work on animals was carried out in a registered animal facility, in accordance with UK Home Office guidelines and personal and project licenses. Each facility was temperature and humidity controlled to keep a constant condition of 22-23°C. Additionally, lighting was kept on a 12-hour light-dark cycle (7am-7pm) to limit circadian effects. The appropriate lab coats, nitrile gloves, shoe covers, and face-masks were worn whilst working within the facility.

2.1.4 Human Samples

All human samples were collected and analysed following strict protocols approved by a UK National Health Service (NHS) ethics committee. The correct informed consent was obtained from patients before samples were collected, and samples were stored in an appropriate manner.

2.2 Biological Models

2.2.1 Animal Studies

2.2.1.1 Tissue Collection

All studies were carried out on mice, and in most cases animals were euthanized by cervical dislocation. However, terminal carbon dioxide (CO_2) or terminal anaesthesia by intraperitoneal (IP) injection of Avertin (100%(w/v) 2,2,2-Tribromoethanol (Sigma-Alrich: T48402-5G), 2-methyl-2-butanol stock (Sigma-Alrich: 240486-5ML), diluted 1:40 in Dulbucco's phosphate buffered saline (DPBS; Life Technologies: 14190-094)) was used where indicated. Anaesthesia was checked using the paw withdrawal reflex, and Avertin was administered up to 800 μl IP, until the mouse showed no reflex. Whilst using Avertin, the mice were exsanguinated by cardiac puncture to collect whole blood.

Wild type (WT) C57BL/6 mice and Leptin deficient, obese *ob/ob* (B6.V-Lep^{ob}/OlaHsd) mice were obtained from Harlan Laboratories. Micro RNA(miRNA/miR)-$34a^{-/-}$ (knock-out (KO); B6.Cg-$Mir34a^{tm1Lhe}$/J) mice and their WT control (C57BL/6J) mice were kindly donated by Dr Mariola Kurowska-Stolarska

and bred in-house, but were originally obtained from The Jackson Laboratory. Tissues were harvested from mice between 6 to 31 weeks of age.

2.2.1.2 Fasting Blood Glucose Measurements

ob/ob, miR-34a$^{-/-}$, or WT mice were fed either a normal chow diet (containing Fenbendazole, Harlan Laboratories) or high-fat diet (HFD; 0.15% cholesterol and 21% lard, Special Diet Services) for up to 24 weeks. To track body weight, mice were weighted using a 1 decimal place balance. Fasting blood glucose measurements were taken using an Accu-Chek® Mobile glucose monitor (Roche: Model U1), with an upper-limit of 33.33 mmol/L. The mice were fasted overnight for 16-18 hours, restrained, and a sterile scalpel blade was used to make a small nick at the end of the tail. The surrounding area was massaged to encourage formation of a blood droplet and blood glucose was measured.

Glucose tolerance tests (GTTs) were carried out using the same method with an I.P. injection of glucose solution at 1 g or 2 g per kg of body weight, after a baseline fasting blood glucose measurement. Stock glucose solutions were used at 0.22 g/ml or 0.4 g/ml of glucose (Sigma-Alrich: G7021-100G) in 0.9% sterile saline solution (NaCl (VWR: 27810.295) and dH_2O), respectively. Blood glucose concentrations were measured from 0 to 90 or 120 minutes, in 30-minute increments. The primary incision was re-used for measurements to limit stress to the animal.

2.2.1.3 Metabolic Cage Studies

Metabolic cage studies were used to monitor mouse food and water consumption and excretion. Before mice were placed in the metabolic cages (Techniplast: 3700M022), the weights of all collection containers and full water bottles (200 ml) and food dishes were recorded. Mice were placed in the metabolic cage a week before the experiment began for 3 hours, to acclimatise them to the cages. On the day of the experiment the mice were placed in the metabolic cages for 24 hours with water and their assigned diet. At the end of the experiment, all the collection containers, water bottle and food dish were re-weighed to assess

consumption and output. The urine and water bottle volume was also recorded. The mice were then sacrificed and tissues were collected.

2.2.1.4 Body Fat Percentage MRS

Mouse body fat percentage was measured by whole body Magnetic Resonance Spectroscopy (MRS) as previously described (Miller et al. 2010). Measurements were made using a 7 Tesla (T) Bruker Biospec system (Karlsruhe), with a 15 cm diameter proton birdcage radio frequency coil, both transmitting and receiving at a proton resonance of 300 MHz. A large Radio Frequency (RF) coil was used to ensure a uniform B_1 field (RF field that excites proton spins) over the whole animal. A 75 μs RF pulse was used to induce the free induction decay (FID), with the mean of 4 signals used (50 kHz sweep width, Repetition time (Tr) = 15 s, 8192 point digitization). This was done while mice were terminally anaesthetised using Avertin. Mr Jim Mullin or Dr William M. Holmes at the Glasgow Experimental MRI Centre conducted the MRS. Data was analysed using Paravision v4.0 software, where the proton spectra were obtained by Fourier transformation and automatic phasing of the signal. A 3000 Hz range on each peak was used for area under the curve (AUC) analysis by integration. This gave integration ratios for the fat (AUC_{lipid}) to water (AUC_{H2O}) peaks, with the water peak value set to 1. Percentage body fat was calculated using the following equation:

$$\% \text{ Body Fat} = (AUC_{lipid} \div (AUC_{H2O} + AUC_{lipid})) \times 100$$

2.2.2 *In vitro* Cultures

All *in vitro* cultures were carried out in sterile tissue culture hoods (Thermo Scientific), with sterile plastic/glassware and reagents. All equipment that could not be autoclaved was cleaned with 70% ethanol. All cells were cultured at 37°C with 5% CO_2 in tissue culture incubators (C&M Scientific).

2.2.2.1 Adipocyte Culture

Primary white and brown adipocytes were grown using the following protocol. Epididymal white adipose tissue (eWAT) and interscapular brown adipose tissue (iBAT) from 5-12 week old mice were collected in wash media:

Dulbecco's modified Eagle medium (DMEM; Life Technologies: 41966-029) supplemented with 1% penicillin/streptomycin (pen-strep; Life Technologies: 15140-122). The tissue was dissociated using sterile scissors and incubated in sterile Hepes isolation buffer containing 0.2% Collagenase II (Sigma-Aldrich: C6885), with constant rotation at 37°C for 30 minutes. HEPES isolation buffer consisted of: 100 mM HEPES (VWR: 441485H), 120 mM NaCl, 4.80 mM KCl (BDH Chemical: 101984L), 1 mM $CaCl_2$•$2H_2O$ (Sigma-Aldrich: C7902-500G), 4.5 mM Glucose, and 1.5% Albumin (Sigma-Aldrich: A9418-500G) in dH_2O, adjusted to pH 7.4. Digested material was filtered (70 µm filter; Corning: 352350) and incubated at 4°C for 15 minutes to separate the mature adipocytes from adipocytes precursors in the stromal vascular fraction (SVF). The bottom SVF layer was aspirated and washed with wash media, centrifuging at 600 x g for 10 minutes. Cells were plated at 0.5-1x10^6 cells/well in 8-well chamber slides (Corning: 354118) or 24-well culture plates (Costar: 3524). Cells were cultured in DMEM supplemented with: 10% foetal calf serum (FCS; Life Technologies: 10270-106), 4 mM L-Glutamine (Life Technologies: 25030-024), 1% pen-strep, 10 µg/ml Insulin (Sigma-Aldrich: I9278), 25 µg/ml sodium Ascorbate (Sigma-Aldrich: A4034-100G), 10 mM Hepes (Life Technologies: 15630-049), and 1 µM Rosiglitazone (Enzo Life Sciences: ALX-350-125-M025). Every 48-hours the media was changed, or supernatants and RNA cell-lysates were collected, using Qiazol (section 2.3.1.3). Brown adipocyte phenotype was checked, by quantifying UCP1 expression following a 4-hour stimulation with 0.1 μM nor-adrenaline (Sigma-Aldrich: A0937-1G).

2.2.2.2 Bone Marrow-Derived Macrophage Culture

Bone marrow was isolated from the femur and tibia of female, WT and miR-34a$^{-/-}$ mice, by flushing bones with Roswell Park Memorial Institute medium (RPMI) 1640 (Life Technologies: 31870-025) wash media, including 1% pen-strep. Flow-through was passed through a 70μm filter and washed twice with wash media, centrifuged at 478 x g for 5 minutes. Cells were resuspended in 2ml Red Blood Cell Lysis Buffer (Sigma-Aldrich: R7557) for 2 minutes, before being washed again as before. Cells were cultured at 2x10^6 cells per 90 mm petri dish (Thermo Scientific), in RPMI 1640 culture media (10% FCS, 1% pen-strep, 2nM L-

glutamine) with 50 ng/ml macrophage-colony stimulating factor (M-CSF; PeproTech: 315-02). Cells were differentiated to macrophages over 6 days, with the media changed every 3 days. Macrophage phenotype was checked by flow cytometry analysis (section 2.5) of percentage $CD45^+$ $F480^+$ cells.

Mature macrophages were harvested using 5 ml Cell Dissociation Solution (Sigma-Aldrich: C5914) and a cell scraper (Greiner: 541080). The plates were washed with an additional 5 ml DPBS and the macrophage solution was centrifuged at 478 x g for 5 minutes. Cells were resuspended in culture media and plated at $0.5x10^6$ cells/well in 24-well culture plates for experiments.

2.2.3 Serum and *in vitro* Culture Supernatant Analysis

Serum was isolated from whole blood left to clot at room temperature for 2 hours and centrifuged at 16100 x g for 15 minutes. The top straw-coloured serum layer was then collected and aliquoted. *In vitro* culture supernatants were collected at time points over culture or at the end of the experiment. Both serum and supernatant samples were stored at -80℃ until analysis.

2.2.3.1 Serum Lipid and Cholesterol Measurements

Serum lipid and cholesterol was measured using an ILAB 600 clinical chemistry analyser, operated by Mrs Josephine Cooney. Colourimetric kits were used with the ILAB to measure serum triglycerides (TGs; Randox: TR210), glycerol (Randox: GY105), total cholesterol (Randox: CH200) and high-density lipoproteins (HDLs; Roche: 03045935). These kits work by measuring the amount of hydrogen peroxide that is produced from the enzymatic breakdown of each molecule, which results in a colour change. The ILAB was calibrated using the appropriate kit calibrators, and checked against kit quality controls prior to sample analysis. True TG values were calculated by the equation below and negative results were removed from downstream analysis.

$$\text{True TGs} = \text{TGs mmol/L} - \text{glycerol mmol/L}$$

2.2.3.2 Cytokine and Adipokine Luminex

Serum and *in vitro* culture supernatant adipokine and cytokine protein was measured by a Mouse Adipokine Milliplex (Millipore-Merck: MADKMAG-71K), and Mouse Cytokine 20-Plex Panel (Applied Biosystems: LMC0006), respectively. Both of these are Luminex xMAP® (multiple analyte processing) technologies, which use 5.6 μm polystyrene beads, containing red and infrared fluorophores of different intensities. These make up the "bead regions" allowing each bead to be uniquely identified. Each bead is conjugated to a capture antibody specific for the analyte of interest, allowing the analyte to be identified by the bead. A second protein-specific biotinylated antibody is added, which binds the analyte. The concentration of analyte is then quantified by a Streptavidin-fluorescent protein (e.g. R-Phycoerythrin (RPE) or just PE) conjugate, which binds to the secondary antibody biotin molecule.

Plates were analysed by a Bio-Rad Bio-Plex 100 Luminex analyser with Bio-Plex Manager v5.0 software. Cytokine and adipokine concentrations were determined using standard curves for each analyte, produced using serially diluted kit standards. Standards and controls were run in technical duplicates, with samples run unduplicated. For values that were out of range (OOR) at the low end, these were replaced with either half the lowest standard or lowest extrapolated value for statistics, whichever was lower.

2.2.3.3 Obesity Proteome Array

Obesity-associated proteins were measured in *in vitro* culture supernatants, using a Mouse Adipokine Array Kit (R&D Systems: ARY013). This consists of membranes pre-coated with capture antibodies for 38 analytes, which are detected by a secondary biotinylated antibody. Streptavidin-horseradish peroxidase (HRP) is then added and binds to biotin, causing a specific chemiluminescent signal to be produced upon substrate addition. This signal is proportional to the quantity of protein. 3 biological replicates were pooled together for each group, with 1 group per membrane. Membranes were imaged upon development using a FujiFilm LAS-3000 and LAS-3000 software. Exposures from 30 seconds to 12 minutes were taken, with the best exposure used for analysis.

Spots were analysed using Image Studio Lite v4.0.21 (LI-COR), with the negative control spots being used as the background for each membrane. Technical duplicates were averaged and normalised to the background value for each membrane, and the 6 positive reference spots were all averaged together.

2.3 Molecular Methods

2.3.1 RNA Extraction

Extracting RNA from fatty tissues presents some challenges. Generally, the RNA yields are lower from fat tissue and the lipids in the cells can interfere with RNA binding to purification columns. Therefore, the best method for optimal RNA yields was investigated. The resulting RNA extraction protocol was used throughout.

2.3.1.1 Phenol-Chloroform Extraction Principles

The RNA extraction method from both tissues and cells involves an initial phenol-chloroform extraction process and purification of the RNA using Qiagen spin columns. The phenol-based cell lysis buffer QIAzol (Qiagen: 79306) was used to liberate the RNA from cells and prevent RNA degradation, by inhibiting RNase activity. QIAzol contains the cationic detergent guanidinium thiocyanate (GTC), which dissolves cell membranes and inactivates RNases, through disruption of protein-nucleic acid interactions. Additionally, low pH phenol in QIAzol increases RNA recovery from the aqueous phase, by separating out deoxyribonucleic acid (DNA) and proteins. With the addition of the organic solvent chloroform and centrifugation, the solution separates into an upper aqueous and lower phase, separated by a white interphase of precipitated proteins. This interphase is rich in RNases. As chloroform cannot mix with the cell lysate, it forms the lower phase (containing DNA), with the RNA contained within the upper aqueous phase. GTC is also present within the aqueous phase, inhibiting RNase activity (Bird 2005; Chomczynski and Sacchi 2006; Vomelová et al. 2009). Therefore, the aqueous phase is collected and mixed with ethanol to precipitate the RNA and facilitate binding to the silica-based membrane within the RNA spin columns. A number of ethanol-based buffers and ethanol solutions are then used to wash away

contaminants, while retaining the RNA in the column. Finally, water is added to dissolve the RNA and elute it from the column.

2.3.1.2 Development of Extraction Protocol

For optimal purification of RNA from WAT different standard column purification methods were examined: RNeasy Mini Kit (Qiagen: 74104) using 100% ethanol for precipitation, miRNeasy Mini Kit (Qiagen: 217004), and RNeasy Lipid Tissue Mini Kit (Qiagen: 74804) (Figure 2.1). RNA was extracted from 6-week old, WT C57BL/6 mouse eWAT using these methods and QIAzol-chloroform extraction. RNA quality and concentration were examined using the NanoDrop spectrophotometer, Agilent Bioanalyzer, and a 1% agarose ethidium bromide gel with 1 kb ladder, described in section 2.3.2. The lipid method gave cleaner 28s and 18s ribosomal (r)RNA bands, better RNA quality and better RNA Integrity Numbers (RINs) (Figure 2.1a). However, it showed fainter small RNA bands (containing miRNAs). The lipid kit used 70% ethanol for precipitation; therefore, we examined using the same method with the RNeasy kit and different precipitating alcohols. Both 80% and 100% ethanol gave similar results; however, using 80% ethanol resulted in a modest increase in mean RNA quality and quantity: 189.8 Vs 105.1 ng/μl. To check miRNAs could still be detected, expression of the WAT abundant miR-103 was examined by Qiagen qRT-PCR (see section 2.3.4), with 100% ethanol only showing a marginal increase in expression (Figure 2.1b) (Xie et al. 2009). Therefore, 80% ethanol was chosen for future extractions (section 2.3.1.3).

A)

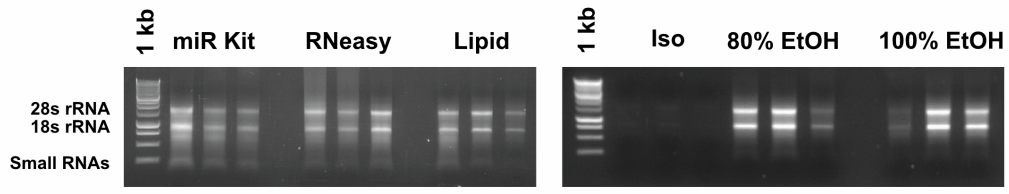

		miR Kit	RNeasy	Lipid	Isopropanol	80 % Ethanol	100 % Ethanol
B6-1	ng/µl	238.2	177.6	112.5	11.9	164	32.7
	260/280	2	1.97	2.01	1.5	2.07	1.93
	260/230	1.66	0.73	1.94	0.83	1.91	0.7
	RIN	7.3	6.3	7.2			
B6-2	ng/µl	114.9	130.4	86.4	19.8	359.9	172.6
	260/280	1.94	1.85	2.08	1.61	2.06	2.08
	260/230	1.43	0.65	2.02	0.69	2.16	1.98
	RIN	7.7	7.5	7.7			
B6-3	ng/µl	116	118.2	45.7	22.2	45.5	110
	260/280	1.85	2.01	1.85	1.49	2.01	2.05
	260/230	1.19	0.85	1.12	0.68	0.56	1.59
	RIN	6.9	8.3	8.1			

B)

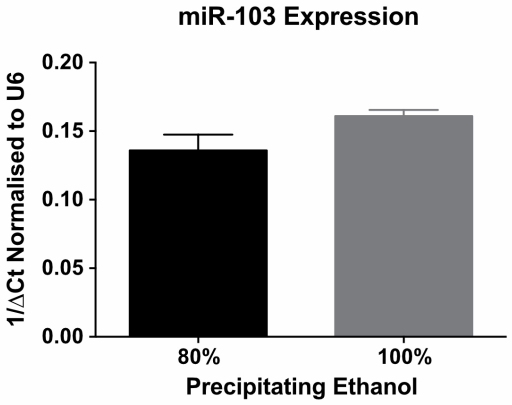

Figure 2.1: Validation of RNA Extraction Method From White Adipose Tissue
A) Showing the comparison between RNA quality and concentration extracted from 6 week old, WT C57BL/6 epididymal white adipose tissue (eWAT), using the standard method with the miRNeasy, RNeasy, and RNeasy Lipid Qiagen Kits (left). Samples were run on a 1% EtBr gel with 1 Kb ladder, and analysed by a NanoDrop spectrophotometer and Agilent Bioanalyzer (RINs), shown in the tables. The lipid method showed the best quality, so different precipitation methods were examined to retain the small RNAs (right). n=3 for all. B) The expression of miR-103 (Qiagen qRT-PCR) was examined in these precipitation methods to verify miRNAs could be detected; Mean values of n=3 (80%) and n=2 (100%) with SEM, normalised to RNU6B expression.

2.3.1.3 RNA Extraction Protocol

Tissues for RNA extraction were snap frozen in liquid nitrogen (N_2) on collection and then stored at -80°C, to preserve RNA. For extraction of RNA from cells, they were first washed in 500 µl-1 ml sterile PBS per well and 1 ml QIAzol Lysis Reagent was then added. The well was scrapped with a pipette tip, to remove residual cells, and the QIAzol-cell suspension was then aspirated and stored at -80°C until extraction. To extract RNA from tissues, ≤100 mg of tissue

was placed in an RNase-free 2 ml microcentrifuge tube with 1 ml QIAzol and 2 stainless steel homogenisation beads (Qiagen: 69989), whilst still frozen. These were then homogenised in a Tissue Lyser LT (Qiagen) at 25 Hz for 3x2 minutes. Cell lysates were vortexed for 15 seconds to homgenise samples. Tissue lysates (in a fresh tube) or cell lysates were incubated at room temperature for 5 minutes, before being mixed with 200 µl chloroform, by hand, and incubated at room temperature for 3 minutes. Samples were centrifuged at 16100 x g for 15 minutes at 4°C, and the top aqueous layer was aspirated.

RNA was precipitated from the aqueous layer using 1.5X volume 80% HPLC grade ethanol (Diluted in dH_2O; Sigma: E7023-500ml) and added to RNeasy Mini Kit (74104, Qiagen) spin columns, 700 μl at a time. The columns were centrifuged at 12000 x g for 1 minute and flow-through discarded. Columns were washed with 350 μl buffer RW1, centrifuging at 12000 x g for 1 minute, and 80 μl of DNase solution (diluted 1:8 in RDD buffer; Qiagen: 79254) was added to the column membrane for 15 minutes at room temperature. This digested genomic DNA to prevent contamination of downstream PCR reactions. Once elapsed, the column was again washed with RW1, as above. Two washes with 500 μl buffer RPE were then carried out, inverting the columns a couple of times and incubated for 2-3 minutes at room temperature. On the first wash, samples were centrifuged at 12000 x g for 1 minute, and on the second at 16100 x g for 2 minutes. A final wash with 500 μl 80% ethanol was carried out, incubating columns for 2-3 minutes at room temperature after inversion and centrifuging at 16100 x g for 2 minutes. To dry the columns completely for elution, they were centrifuged empty with the lid open at 16100 x g for 2 minutes. In fresh collection tubes, 20 μl RNase-free water was added to the column membrane and incubated for 1 minute at room temperature, before centrifuging at 16100 x g for 1 minute to elute the RNA. The RNA concentration was quantified using the NanoDrop Spectrophotometer (section 2.3.2.1), and RNA was stored at -80°C, unless used for downstream assays immediately.

2.3.2 Measuring Quality and Concentration of RNA

After RNA was extracted it was analysed for quality and concentration using all or some of these methods.

2.3.2.1 NanoDrop Spectrophotometer

Thermo Scientific's NanoDrop ND-1000 spectrophotometer, with NanoDrop 1000 v3.7.1 software was routinely used to measure the concentration of RNA in samples and give some basic quality information. First, 1.5 μl of the elution buffer (usually RNase-free water) was dispensed onto the NanoDrop pedestal to give a "blank" background measurement. Next, the pedestal was cleaned with tissue and 1.5 μl of the sample was dispensed onto the pedestal for a sample measurement. The NanoDrop has a working range of 2 ng/μl to 3700 ng/μl double stranded (ds)DNA, and correlates concentration with calculated absorbance using the Beer-Lambert Law. For nucleic acids the following equation is used:

$$\text{Conc}_{\text{nucleic acids}} = (\text{Absorbance}_{\text{AU}} \times \text{Extinction coefficient}_{\text{ng-cm}/\mu\text{l}}) / \text{Path length}_{\text{cm}}$$

The path length is 0.1-0.02 cm for this model and the extinction coefficients are 50, 33, and 40 ng-cm/μl for dsDNA, single-stranded (ss)DNA, and RNA, respectively. Absorbance is measured at 260nm for concentrations and 260/280 nm and 260/230 nm ratios are used to assess RNA quality. Pure DNA has 260/280 values of ~1.8, and RNA has values ~2. Low values can indicate protein, phenol, or other contaminants, which absorb near 280 nm. However, the base composition of the nucleic acids will also affect this ratio. The 260/230 ratio is a secondary measure of nucleic acid purity, with acceptable ranges usually between 1.8-2.2.

2.3.2.2 Agilent Bioanalyzer

In some cases, total RNA quality was assessed using an Agilent Bioanalyser 2100 and a Eukaryote Total RNA Nano Series II chip. Glasgow Polyomics at the University of Glasgow carried out the analysis. The samples are separated by electrophoresis on an electronic chip, and nucleic acid fragments are detected using an intercalating, fluorescent dye, by laser excitation. These are run

with an RNA ladder for fragment sizing and a size marker for alignment. Resulting gel-like densitometry images (bands) and electropherograms (peaks) show defined bands or peaks for 18S and 28S ribosomal (r)RNA. The ratio between these rRNA species and the RNA integrity number (RIN) are used to assess RNA quality. The RIN values are calculated from the entire electrophoretic signal, giving a value from 1 (completely degraded) to 10 (perfect).

2.3.3 Agarose Gel Electrophoresis

Agarose gel electrophoresis was used to quickly assess RNA quality, but also for separation and sizing of DNA PCR products throughout. Agarose gels were prepared with UltraPure™ Agarose (Life Technologies: 16500-500) and 1X Tris-Borate Ethylenediaminetetraacetic acid (EDTA) (TBE) buffer (Life Technologies: 15581-044), melted in a Prestige SM23 microwave. Whilst still molten, 0.2 µg/ml ethidium bromide (EtBr; Sigma, E1510) was added to the gel and poured into a mould to set. The gels were run in a Bio-Rad mini-sub cell GT tank with Bio-Rad Power PAC 300, at between 85-100 V. Samples were loaded with 6X Blue/Orange Loading Dye (Promega: G190A) and run with a 1 kb (Promega: G571A), 100 bp (Promega: G210A), or 10 bp (Life Technologies: 10488-019) DNA ladder. For assessing RNA quality, a 1% agarose gel with EtBr was used, and DNA PCR products were sized using 2-5% gels. Images were taken with UV transillumination on a Bio-Rad Molecular Imager® Chemi Doc™ XRS+ imager with Quantity One v4.6.8 software.

2.3.4 Analysis of Gene Transcripts By qRT-PCR

2.3.4.1 Principles of qRT-PCR

Quantitative reverse transcription polymerase chain reaction (qRT-PCR) is a molecular technique, which allows the quantification of gene expression by analysing the abundance of gene transcripts. This works in a similar manner to quantitative PCR (qPCR), but has an additional complementary DNA (cDNA) synthesis step. This is achieved by using a heat-stable reverse transcriptase to convert the RNA sequence into a complementary DNA sequence, which can be duplicated and amplified in the qPCR reaction by DNA polymerases. Within the

qPCR reaction, using fluorescent dyes or probes, a fluorescent signal is produced that is proportional to the amount of DNA product formed, and this is correlated with the amplification cycle number when a set fluorescent signal is reached. This process is a modification of PCR, originally developed by the Nobel laureate Kary Mullis et al. in the 1980s (Saiki et al. 1985), and further development on the quantitative processes developed by Higuchi et al. in the early 1990s (Higuchi et al. 1992; 1993). Higuchi et al. described a process whereby the amount of DNA produced during PCR amplification could be measured by the increasing fluorescence of ethidium bromide (EtBr), as it intercalated with more DNA strands.

The reverse transcription (RT-PCR) reaction involves an initial primer-binding step for the RNAs of interest, followed by extension of the primer with the enzyme reverse transcriptase, to produce a cDNA strand, and finally denaturing of the reverse transcriptase at a high temperature. This produces a double-stranded RNA-DNA hybrid, which can then be used in the qPCR reaction. Reverse transcriptase can produce cDNA without primers, but with poor efficiency. Therefore, three main priming strategies are used: oligo-dT primers, random sequence primers, and gene specific primers. Oligo-dT primers consist of a short sequence of thymidine bases, which bind to the poly-Adenosine(A) tail on eukaryotic mRNAs, allowing the whole transcript to be reverse transcribed. Random sequence primers are short, random base sequences of all possible sequences, typically six (random hexamers) or nine (random nonamers) bases long. These primers should allow reverse transcription of all the RNA species present. Gene-specific primers are primers designed for the transcript of interest, which should only produce cDNA of that specific RNA.

The cDNA is then added into a reaction mix for qPCR, containing a forward and reverse primer for the sequence to be amplified; the four deoxyribonucleotides (dNTPs) for adenosine, thymidine, cytosine, and guanine; a thermostable DNA polymerase, usually a Thermus aquaticus (Taq) polymerase; and magnesium ions to help primer annealing. qPCR involves temperature cycling to amplify the DNA strands, which can have an initial high temperature stage to activate the DNA polymerase. The cycling conditions have a high temperature denaturing step, which separates the DNA strands, followed by a reduction in temperature to allow

primmer annealing, and finally a slight increase in temperature to allow extension of the primers by the polymerase using the dNTPs. However, in some cases the same temperature is used for both primer annealing and extension, such as in TaqMan® qPCR. As each new double-stranded DNA (dsDNA) molecule is created, there is an exponential increase in fluorescence produced by a dye or probe. This is quantified by measuring at what PCR cycle a set fluorescent threshold is reached, called a cycle threshold (Ct) value (Kubista et al. 2006).

2.3.4.1.1 The Qiagen miScript System

Qiagen's miScript kits allow the synthesis of cDNA from only the mature miRNAs, small nucleolar RNAs, and small nuclear RNAs, or alternatively all the RNAs in the sample, using the Qiagen miScript Reverse Transcription II Kit (218161). This is achieved by using either the HiSpec or HiFlex buffer, respectively. The HiSpec buffer contains oligo-dT primers and a poly(A)polymerase, allowing the oligo-dTs to bind the miRNAs by polyadenylation. Additionally, the oligo-dTs have a 3' degenerate anchor and a 5' universal tag sequence, to increase specific amplification of the mature miRNAs during the qPCR step. The HiFlex buffer is the same as the HiSpec buffer, but has additional random primers for reverse transcription of the other RNA species.

Mature miRNAs were quantified using the Qiagen miScript SYBR Green PCR Kit (218073) and specific mature miRNA forward primer (miScript Primer Assay). The kits contain a universal reverse primer that binds to the oligo-dT universal tag sequence, and HotStarTaq® DNA polymerase and SYBR Green I in the QuantiTect® SYBR Green PCR Master Mix. In this case, the SYBR Green dye fluoresces when it binds to dsDNA, regardless of the sequence. Hence the greater number of dsDNA molecules, the greater the fluorescent signal. However, the dye binds to all dsDNA molecules, meaning you can get an erroneous fluorescent signal from primer-dimers (Kubista et al. 2006).

2.3.4.1.2 Life Technologies' TaqMan® System

For quantifying mRNA, cDNA produced from the miScript RT kit and TaqMan® Gene Expression assays were used. However, the TaqMan® MicroRNA

Reverse Transcription Kit (Life Technologies: 4366597) and TaqMan® MicroRNA Assays' RT primer were used to synthesise cDNA from miRNAs in some experiments. This RT process uses a specific stem-looped primer for the miRNA of interest, which should allow specific amplification of only that miRNA cDNA. During the qPCR reaction specific forward and reverse primers, along with a specific TaqMan® probe, in the TaqMan® Assays, allows amplification and quantification of the miRNA cDNA. For enhanced specificity, the reverse primer anneals to a sequence in the stem-looped primer and the TaqMan® probe anneals across the primer-cDNA boundary (Chen 2005).

Gene expression TaqMan® does not need a specific primer RT step, but works under the same principles. The TaqMan® probe is an oligonucleotide with a fluorescent dye at one end and a quencher at the other, which absorbs the fluorescent signal on excitation and dissipates it as heat. As the DNA polymerase adds dNTPs to produce a new DNA strand, it cleaves the fluorescent dye (usually FAM or VIC) from the probe allowing the release of a fluorescent signal. This is mediated by increased distance of the dye from the quencher (usually MGB) (Kubista et al. 2006).

2.3.4.2 Reverse Transcription cDNA Synthesis

cDNA was created from template RNA, for downstream qPCR analysis of transcript expression, following these methods.

2.3.4.2.1 Qiagen miScript RT II Protocol

cDNA synthesis for gene and miRNA expression, using Qiagen qPCR protocol, was carried out using the Qiagen miScript Reverse Transcription II Kit. First, ≤1 μg template RNA was added to each sample well of a 96-well PCR plate (Starlab: E1403-5200) or 0.2 ml PCR tubes, diluted in RNase-free water to 12 μl. Next, a master mix was created for all the samples (Table 2.1) and added to each sample well, bringing the total well volume to 20 μl.

Component	Volume Per Reaction
Template RNA (≤1μg)	≤12 μl
RNase-free Water	RNA made up to 12 μl
5X miScript HiFlex Buffer	4 μl
10X miScript Nucleics Mix	2 μl
miScript Reverse Transcriptase Mix	2 μl
Total Well Volume	**20 μl**

Table 2.1: Qiagen miScript RT II Kit Protocol cDNA Synthesis Reaction Mix.

The miScript HiFlex Buffer was used over the HiSpec Buffer, to give both messenger RNA (mRNA) and miRNA species. The plate was then covered with a plate seal (Thermo Scientific: AB-0558), gently mixed and centrifuged at 1000 x g for 1 minute. Any bubbles were removed by flicking the wells, with re-centrifugation. The plate/tubes were incubated in a PTC-225 Peltier Thermal Cycler (MJ Research) with the conditions detailed in Table 2.2. The resulting cDNA was stored at -20°C, unless used immediately for downstream assays, in which case, it was stored at 4°C until use.

Stage	Temperature	Time
Reverse transcription	37°C	60 min
RT Denaturing	95°C	5 min
Storage	4°C	Forever

Table 2.2: Qiagen miScript RT II Kit Protocol RT PCR Conditions.

2.3.4.2.2 Life Technologies' TaqMan® MicroRNA RT Protocol

Template RNA was diluted to 2 ng/μl in RNase-free water for use in the reaction. A reaction master mix was then created using the TaqMan® MicroRNA Reverse Transcription Kit and 12.5 μl was added to each well of a 96-well PCR plate or 0.2 ml PCR tubes. The reagent volumes in the master mix changed depending on weather a single or multiple miRNAs were being investigated in a sample. For single miRNAs the standard master mix was used (Table 2.3).

However, for multiple miRNAs a multiplex RT reaction was created (Table 2.3) using an RT primer pool. The primer pool contains the RT primers for all the miRNA assays at 0.5X, by a 1:10 dilution in 1X Tris-EDTA (TE) buffer (10 mM Tris HCL (Sigma-Aldrich: T-3253) and 1 mM EDTA (Sigma-Aldrich: 27285), made to pH 8). 2.5 µl of the diluted RNA was added to the master mix in the PCR plate wells or tubes to make a total of 5 ng RNA per well/tube.

Component	Standard	Multiplex
RT primer/primer pool	3.00 µl	6.00 µl
dNTPs	0.15 µl	0.30 µl
Reverse transcriptase	1.00 µl	2 µl
10X RT Buffer	1.50 µl	1.50 µl
RNase Inhibitor	0.19 µl	0.19 µl
RNase-free Water	6.66 µl	2.51 µl
Template RNA (2ng/µl)	2.50 µl	2.50 µl
Total	**15 µl**	**15 µl**

Table 2.3: TaqMan® MicroRNA Reverse Transcription Kit Reaction Master Mixes.

Next, the plate was sealed, gently mixed, and centrifuged at 1000 x g for 1 minute. Bubbles were removed and the plate/tubes were put in the thermocycler, as in the Qiagen protocol above. The cycling conditions were the same for both standard and multiplex reactions, shown in Table 2.4. The multiplex reaction was a modification of a Life Technologies protocol (4465407).

Stage	Temperature	Time
Primer annealing	16°C	30 min
Reverse transcription	42°C	30 min
RT Denaturing	85°C	5 min
Storage	4°C	Forever

Table 2.4: TaqMan® MicroRNA Reverse Transcription Kit PCR Cycling Conditions.

2.3.4.3 Quantitative PCR Reactions

Here, the protocols for Qiagen miRNA and TaqMan® Gene and miRNA expression qPCR are detailed. Reactions were set up in duplicate for each sample and non-template controls were used for each primer assay. Gene expression assays designed across exon boundaries were picked, where available, to prevent cross-reactivity with any remaining genomic DNA. The primer assays used are detailed in each results chapter. All data was acquired using Sequence Detection Software (SDS) 2.3 software and a 7900HT Fast Real-Time PCR System (Life Technologies).

2.3.4.3.1 Qiagen miScript SYBR Green qPCR

Mature miRNA transcripts were quantified using the Qiagen miScript SYBR Green PCR Kit and miScript Primer Assays. Sample cDNA template, from the Qiagen cDNA reaction, was diluted to 3 ng/μl for use in the qPCR reaction and a PCR master mix was created (Table 2.5). The reaction was prepared in an optical 384-well PCR plate (Life Technologies: 4309849), with 9 μl of master mix added to each well.

Component	Volume/Reaction
2X SYBR Green PCR Master Mix	5 μl
10X miScript Universal Primer	1 μl
10X miScript Primer Assay	1 μl
RNase-free Water	2 μl
cDNA Template	1 μl
Total Well Volume	**10 μl**

Table 2.5: Qiagen microRNA SYBR Green qPCR Reaction Master Mix.

The plate was centrifuged briefly to pull down the solution and 1 μl of cDNA was added to each well to yield 3 ng of cDNA per well and make the total well volume to 10 μl. The plate was sealed with Optical Adhesive Film (Life Technologies: 4311971), briefly mixed and centrifuged at 1000 x g for 1 minute. Bubbles were

removed by flicking each well and re-centrifugation. The plate was then loaded into the qPCR machine and run with the cycle conditions in Table 2.6.

Stage	Temperature	Time
Polymerase Activation	95°C	15 min
Amplification (40 cycles)		
Denaturing	94°C	15 sec
Annealing	55°C	15 sec
Extension (data collection)	70°C	30 sec

Table 2.6: Qiagen microRNA SYBR Green qPCR Cycling Conditions.

A dissociation step was added to check that primer-dimers were not formed. The results were examined to make sure only a single peak was formed with a high DNA strand melting temperature (T_m) (Figure 2.2). This indicates that there are large ds-DNA molecules present and not small ones, indicative of primers binding together.

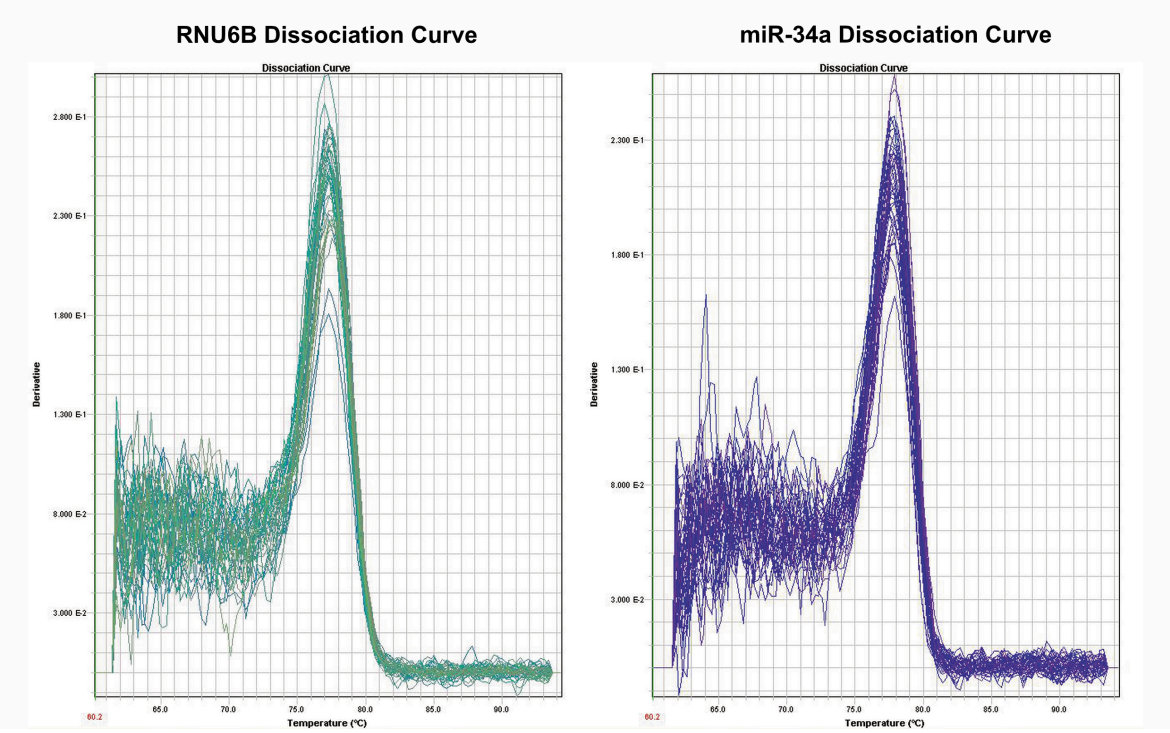

Figure 2.2: Representative Dissociation Curves From Qiagen SYBR Green qPCR.

2.3.4.3.2 Life Technologies TaqMan® qPCR

Gene expression was analysed using Life Technologies' TaqMan® Gene Expression Master mix (4369016) and TaqMan® Gene Expression Assays. Mature miRNA transcripts were analysed using Life Technologies' TaqMan® Universal Master mix 2, no UNG (4440040) with TaqMan® microRNA Assays. For gene expression, Qiagen sample cDNA templates were diluted to 1-10 ng/μl and TaqMan® microRNA RT cDNA was used undiluted for mature miRNA transcript analysis. For both, a master mix was created (Table 2.7) and 9 μl for gene expression, or 9.3 μl for mature miRNA expression, was added per well of a 384-well PCR plate.

Component	1X Gene Exp	1X miR Exp
2X TaqMan® Master Mix	5 μl	5 μl
TaqMan® Assay	0.5 μl	0.5 μl
RNase-free Water	3.5 μl	3.8 μl
cDNA Template	1 μl	0.7 μl
Total Well Volume	**10 μl**	**10 μl**

Table 2.7: TaqMan® qPCR Master Mix for Gene and Mature miRNA Expression.

The plate was centrifuged briefly and 1 μl (gene expression) or 0.7 μl (miRNA expression) cDNA was added to each well, giving a total volume of 10 μl per well. The plate was prepared as described above and loaded into the qPCR machine with the cycle conditions in Table 2.8.

Stage	Temperature	Time
Polymerase Activation	95°C	10 min
Amplification (40 cycles)		
Denaturing	95°C	15 sec
Annealing/Extension	60°C	1 min

Table 2.8: TaqMan® qPCR Cycling Conditions for Gene and miRNA Expression.

2.3.4.4 qPCR Data Analysis

Once qPCR data was collected, it was organised and the endogenous control Ct values were checked to make sure the standard deviation (SD) was ≤1 across samples. Technical duplicate Ct values were averaged and the genes of interest were normalised to the endogenous control, giving a ΔCt value calculated as follows:

$$\Delta Ct = Ct_{\text{gene of interest}} - Ct_{\text{endogenous control}}$$

The ΔCt values were then used to calculate relative quantification (RQ) values or inverse values (1/ΔCt) for plotting on a graph. Calculating these values is advantageous, because they change the negative relationship between Ct values and expression level to a positive one. RQ values were calculated as follows:

$$\Delta\Delta Ct = \Delta Ct_{\text{sample of interest}} - \Delta Ct_{\text{calibrator sample}}$$

$$RQ = 2^{-\Delta\Delta Ct}$$

For 1/ΔCt values standard error of the mean (SEM) could be used to calculated error bars. However, for RQ values the SEM has to be transformed the same way as RQ. This was calculated as follows:

$$RQ_{min} = RQ - (2^{-(\Delta\Delta Ct + SEM)})$$

$$RQ_{max} = (2^{-(\Delta\Delta Ct - SEM)}) - RQ$$

Statistics were calculated off the ΔCt or 1/ΔCt values.

2.3.5 Cloning and Sequencing

To identify the product from qPCR reactions, cloning of the qPCR product into a plasmid vector and subsequent DNA sequencing was carried out. The protocol is outlined below.

2.3.5.1 Cloning

Taq polymerase in the qPCR reaction adds a single deoxyadenosine base (A) to the 3' end of the PCR product. This allows the cloning of this sequence into a TA plasmid vector with single deoxythymidine overhangs, such as the linerarised pcDNA™ 3.3-TOPO® vector. Therefore, we cloned the qPCR product into this vector using the pcDNA™ 3.3-TOPO® TA Cloning Kit (Life Technologies: K8300-01). A qPCR product was created using the miRNA TaqMan® protocol outlined in section 2.3.4.3.2 above. The PCR product was then combined with the vector using the following cloning reaction. 4 μl of PCR product, yielding 8 ng DNA, was combined with 1 μl salt solution and 1 μl TOPO® vector. For a negative control the PCR product was replaced with 4 μl dH_2O. These reactions were mixed and centrifuged briefly, before being incubated at room temperature for 20 minutes and then at 4°C until use.

To transform One Shot® TOP10 *Escherichia coli* (*E. Coli;* included in cloning kit), 2 μl of the above cloning reactions or 1 μl of pUC19 positive control plasmid, was gently mixed with a vial of *E. Coli* (50 μl). These were incubated at 4°C for 30 minutes and heat-shocked for 30 seconds at 42°C, before being immediately transferred back to 4°C. 250 μl S.O.C. Medium at room temperature was added to the transformation reactions and shaken horizontally at 180 rpm for 2 hours at 37°C in a shaking incubator (New Brunswick Scientific: Innova 44). Following incubation, 10, 30, and 50 μl of each transformation reaction was spread on pre-warmed (37°C) ampicillin (100 μg/ml; Life Technologies: 11593027) lysogeny broth (LB; Life Technologies: 22700-025) selection plates. Plates were incubated overnight at 37°C. Colonies were picked at a ratio of 2:1 of the negative control and 10 ml of 100 μg/ml ampicillin LB broth (Life Technologies: 12780-052) was inoculated with each colony in separate tubes. Inoculated broth was incubated at 180 rpm overnight at 37°C in the shaking incubator.

2.3.5.2 Mini Prep Plasmid DNA Isolation

Plasmid DNA was isolated from the colonies grown above using the PureLink® Quick Plasmid Miniprep Kit (Life technologies: K2100-11), following the standard protocol. 5 ml of the LB broth preparation, grown overnight, was

centrifuged at 600 x g for 5 minutes to pellet the bacteria. This was resuspended in 250 µl resuspension buffer R3 (50 mM Tris-HCL, 10 mM EDTA), containing 20 mg/ml RNase A, before 250 µl Lysis Buffer L7 (200 mM NaOH, 1% w/v SDS) was added. Samples were mixed by inversion and incubated for 5 minutes at room temperature. DNA was precipitated by mixing samples with 350 µl precipitation buffer N4 and centrifuging at 12000 x g for 10 minutes. The supernatant containing the DNA precipitate was added to the spin column for binding, centrifuging at 12000 x g for 1 minute. The flow-through was discarded for this and the following steps. Columns were washed with 500 µl of wash buffer W10, with a 1-minute incubation at room temperature and centrifugation at 12000 x g for 1 minute. A final wash was carried out with 700 µl wash buffer W9, centrifuging at 12000 x g for 1 minute. This was followed by an empty spin at 12000 x g for 1 minute. Finally, DNA was eluted in 70 µl 1X TE buffer by incubating the column for 1 minute at room temperature and centrifuging at 12000 x g for 2 minutes. The eluted DNA concentration was measured using the NanoDrop spectrophotometer (section 2.3.2.1) and was stored at 4°C for short-term storage, or -20°C for long-term.

2.3.5.3 Sequencing

The plasmid DNA was sequenced using the BigDye Terminator v3.1 Cycle Sequencing Kit (Life technologies: 4337457) and sequencing primers from the pcDNA™ 3.3-TOPO® TA Cloning Kit. A sequencing PCR amplification reaction was carried out, using 200 ng total plasmid DNA (Table 2.9).

Component	Volume/Reaction
BigDye Terminator Seq. Buffer	4 µl
Ready Reaction Mix	1 µl
Reverse Primer (2 µM)	2 µl
Forward Primer (2 µM)	2 µl
RNase-free Water	7 µl
DNA Template (200 ng)	4 µl
Total Well Volume	**20 µl**

Table 2.9: BigDye Terminator Sequencing PCR master mix

16 μl of master mix was added to each well of a 96-well PCR plate, followed by 4 μl of DNA. The plate was then sealed, gently mixed and centrifuged at 1000 x g for 1 minute. Any bubbles were removed by flicking and re-centrifugation. The plate was incubated in a PTC-225 Peltier Thermal Cycler, following the cycle conditions in Table 2.10. The plate was then stored at 4°C until use.

Stage	Temperature	Time
Amplification (25 cycles)		
Denaturing	96°C	45 sec
Annealing	50°C	25 sec
Extension	60°C	4 min
Final Step		
Annealing	50°C	25 sec
Extension	60°C	4 min

Table 2.10: BigDye Terminator Sequencing PCR Cycling Conditions

Next, The PCR product was “cleaned” for sequencing. 10 μl CleanSEQ (Beckman Coulter: A29154) and 62 μl 85% ethanol was added to each well of the PCR plate. The plate was sealed, vortexed and centrifuged briefly, before being put on the plate magnet for 2 minutes. The plate contents were decanted (whilst on the magnet) and 150 μl 85% ethanol was added to each well. The plate was sealed, vortexed, and centrifuged briefly, before being placed on the magnet for 2 minutes. Whilst on the magnet, the plate contents were again decanted. The plate with the magnet was centrifuged briefly upside down on tissue, to remove excess ethanol. To completely remove any ethanol the plate was air-dried for 10 minutes. 40 μl RNase-free water was then added to each well to elute the DNA from the magnetic beads and the plate was vortexed. Finally, the plate was put on the magnet for 2 minutes and 20 μl of each sample was put into a 96-well sequencing plate (Thermo Scientific: BC-1100). The sequencing plate was analysed using an 3730 DNA Analyzer (Life Technologies) and Run 3730 Data Collection v3.0 Software.

2.3.6 Genotyping

At sacrifice, miR-34a$^{-/-}$ and WT mice from *in vivo* studies were genotyped, to make sure that they were all allocated into the correct groups for downstream analysis. Tail tips were collected at sacrifice and stored at -80°C until analysis. The genotyping protocol is described below.

2.3.6.1 DNA Extraction

DNA was extracted from the tail tips using a QIAamp DNA Mini Kit (Qiagen: 51306). Firstly, 0.4-0.6 cm of tail tips were incubated with 200μl proteinase K-ATL buffer solution (20 μl proteinase K : 180 μl ATL buffer) at 55°C overnight. The following day, samples were vortexed for 15 seconds and 400 μl Buffer AL was added. The resulting mixture was added to the DNeasy Mini spin column and centrifuged at 6000 x g for 1 minute, with the flow-through discarded. The column was then washed with 500 μl AW1 buffer at 6000 x g for 1 minute, and 500 μl AW2 buffer at 16100 x g for 1 minute. The column was then placed in a fresh 2 ml collection tube and centrifuged at 16100 x g for 1 minute, as a dry spin. Finally, DNA was eluted into a fresh nuclease-free 1.5 ml microcentrifuge tube with 50 μl RNase-free dH_2O, centrifuged at 6000 x g for 1 minute. The DNA concentration was measured using the NanoDrop spectrophotometer (section 2.3.2.1) and samples stored at -20°C, until use.

2.3.6.2 Amplifying Sequence By PCR

The WT and transgenic sequences were amplified using custom DNA primers from Integrated DNA Technologies, the GoTaq Flexi DNA polymerase kit (Promega: M8301), and dNTPs mix (New England Bioscience: N0447S). The custom DNA primer sequence was obtained from Jackson Labs for genotyping their miR-34a$^{-/-}$ mice. The primer sequences can be seen in Table 2.11.

Primer	Sequence
Common Forward	ACT GCT GTA CCC TGC TGC TT
Wild-Type Reverse	GTA CCC CGA CAT GCA AAC TT
miR-34a$^{-/-}$ Reverse	GCA GGA CCA CTG GAT CAT TT

Table 2.11: Custom IDT Genotyping Primers For miR-34a$^{-/-}$ mice

A PCR reaction master mix was created for each sample, shown in Table 2.12. 47.5 µl of master mix was added to each well of a 96-well PCR plate or 0.2 ml PCR tubes. To this, 2.5 µl of template DNA was added to make a total volume of 50 µl and the plate/tubes were sealed, gently mixed, and centrifuged at 1000 x g for 1 minute to settle everything to the bottom.

Component	Volume/Reaction
5X Green GoTaq Flexi Buffer	10 µl
$MgCl_2$ Solution (25 mM)	2 µl
dNTPs (10 mM)	1 µl
GoTaq DNA polymerase (5 U/µl)	0.25 µl
WT Reverse Primer (10 µM)	1.25 µl
miR-34a$^{-/-}$ Reverse Primer (10 µM)	1.25 µl
Common Forward Primer (10 µM)	2.5 µl
RNase-free Water	29.25 µl
DNA Template	2.5 µl
Total Well Volume	**50 µl**

Table 2.12: PCR Master Mix For Genotyping miR-34a$^{-/-}$ Mice

Bubbles were removed by flicking the wells/tubes and re-centrifugation. Samples were incubated in a PTC-225 Peltier Thermal Cycler, following the conditions outlined in Table 2.13. The PCR product was stored at 4°C for immediate use, or -20°C for long-term storage. The PCR product was run out on a 2% agarose gel containing 0.2 µg/ml ethidium bromide at 85 V for ~50 minutes, with a 1 kb ladder. Images were taken as described in section 2.3.3.

Stage	Temperature	Time
Denaturing	94°C	3 min
Amplification (30 cycles)		
Denaturing	94°C	45 sec
Annealing	60°C	30 sec
Extension	72°C	90 sec
Extension	72°C	10 min
Storage	4°C	Forever

Table 2.13: PCR Cycling Conditions For Genotyping miR-34a$^{-/-}$ Mice

2.3.7 Open Array

To examine the differential expression of miRNAs within WAT during diet-induced obesity, a Life Technologies miRNA Open Array® was carried out. This works using the same chemistry as the TaqMan® miRNA system, described in section 2.3.4.1.2, but allows the simultaneous analysis of hundreds of miRNAs.

First, a RT reaction was carried out to make cDNA for all the miRNAs of interest. Using the TaqMan® MicroRNA Reverse Transcription Kit (in section 2.3.4.2.2) and RT primers from the Rodent Megaplex™ Primer Pools Set (Life Technologies: 4444766), a reaction master mix was created (Table 2.14). Two master mixes were created, 1 for primer pool A and 1 for primer pool B.

Component	Volume/Reaction
Megaplex™ RT Primers (10X**)**	0.8 µl
dNTPs (100 mM)	0.2 µl
Reverse Transcriptase (50 U/µl)	1.5 µl
10X RT Buffer	0.8 µl
$MgCl_2$ (25 mM)	0.9 µl
RNase Inhibitor (20 U/µl)	0.1 µl
RNase-free Water	0.2 µl
RNA Template	2.5 µl
Total Well Volume	**7 µl**

Table 2.14: OpenArray® Megaplex™ Reverse Transcription PCR Master Mix

4.5 µl of each master mix was added to each well of a 96 well PCR plate, making a primer pool A and B well for each sample. To each of these wells 3 µl of 33.5 ng/µl RNA sample was added, to make 100.5 ng total RNA per primer pool well. The plate was then sealed and centrifuged at 1000 x g for 1 minute, before being incubated on a PTC-225 Peltier Thermal Cycler, following the conditions outlined in Table 2.15. The cDNA PCR product was stored at 4°C for immediate use, or -20°C for long-term storage.

Stage	Temperature	Time
Amplification (40 cycles)		
Annealing	16°C	2 min
Extension	42°C	1 min
Denaturing	50°C	1 sec
RT Denaturing	85°C	5 min
Storage	4°C	Forever

Table 2.15: OpenArray® Megaplex™ Reverse Transcription PCR Cycling Conditions

Second, the cDNA product was pre-amplified using the specific forward and reverse Megaplex™ PreAmp Primers, from the primer pool set above, and TaqMan® PreAmp Master Mix (Life Technologies: 4391128). 2 separate PCR master mixes were created for PreAmp primer pools A and B (Table 2.16), mirroring RT primer pools A and B above.

Component	Volume/Reaction
TaqMan® PreAmp Master Mix (2X)	12.5 µl
Megaplex™ PreAmp Primers (10X**)**	2.5 µl
RNase-free Water	7.5 µl
RNA Template	2.5 µl
Total Well Volume	**25 µl**

Table 2.16: OpenArray® Megaplex™ Pre-Amplication PCR Master Mix

In a new 96 well PCR plate, 22.5 µl of master mix was added to each well and 2.5 µl of cDNA was added to each well, retaining set A and B for each sample. The plate was then sealed, centrifuged, and incubated as above, following the cycling conditions outlined in Table 2.17. The pre-amplified cDNA product was then diluted 1:20 in 0.1X TE buffer (pH 8).

Stage	Temperature	Time
Initial Denaturing/Activation	95°C	10 min
	55°C	2 min
	72°C	2 min
Amplification (12 cycles)		
Denaturing	95°C	15 sec
Annealing/Extension	60°C	4 min
Polymerase Denaturing	99.9°C	10 min
Storage	4°C	Forever

Table 2.17: OpenArray® Megaplex™ Pre-Amplification PCR Cycling Conditions

Finally, 12.5 µl of the diluted, pre-amplified cDNA product was mixed with 36.75 µl of TaqMan® OpenArray® Real-Time PCR Master Mix (Life Technologies: 4462159) in a fresh 96 well PCR plate. 5 µl from each well was then transferred to 8 wells in the OpenArray® 384-Well Sample Plate (Life Technologies: 4406947), forming a set of 8 wells for each sample (A and B). This plate was then sealed and centrifuged briefly for loading onto the TaqMan® OpenArray® Rodent MicroRNA cards (Life Technologies: 4461105). The OpenArray® cards were loaded using the OpenArray@ AccuFill™ System (Life Technologies) and sealed into their cycling case using the OpenArray® Case Sealing Station. The array cards were then analysed using the NT Cycler OpenArray® machine (Life Technologies) and OpenArray® Real-Time qPCR Software. The same data analysis principles were applied from section 2.3.4.4.

2.4 Histology Analysis

To assess cell and tissue morphology, as well as localisation and quantification of specific molecules, a number of staining techniques were used. These are described below.

2.4.1 Preparing Tissues and Sections

Tissues for paraffin embedding were fixed in 4% paraformaldehyde (PFA) for 2-4 days at room temperature. 4% PFA was prepared by dissolving PFA powder (Sigma-Aldrich: P6148-500G) in 0.1M phosphate buffer (7.7% 1M sodium phosphate dibasic dihydrate ($Na_2HPO_4 \cdot H_2O$; Sigma-Aldrich: 71643-1KG) + 2.3% 1M sodium phosphate monobasic dihydrate ($NaH_2PO_4 \cdot H_2O$; Sigma-Aldrich: 04269) in dH_2O). Tissues were stored in 70% ethanol (VWR:20821.330, diluted in dH_2O) until processing, using a Shandon Excelsior (Thermo Scientific) processor. The processing steps are outlined in Table 2.18, with Xylene (UN1307) and ethanol (UN1170) from Genta Medical, and paraffin from Thermo Scientific (8331). Once tissues were processed, they were embedded in paraffin blocks, using a Shandon Histocentre 3 (Thermo Scientific). The paraffin blocks were left to harden and stored at room temperature until use. Paraffin sections were cut using a Shandon Finesse 325 Microtome (Thermo Scientific) and MX35 Premier microtome blades (Thermo Scientific). Sections were mounted on adhesive slides (Tissue-Tek: 9721).

Step	Reagent	Time
1	70% Ethanol	30 min
2	95% Ethanol	30 min
3	100% Ethanol	30 min
4	100% Ethanol	30 min
5	100% Ethanol	45 min
6	100% Ethanol	45 min
7	100% Ethanol	1 hour
8	100% Ethanol/Xylene	30 min
9	Xylene	30 min
10	Xylene	30 min
11	Paraffin	30 min
12	Paraffin	30 min
13	Paraffin	45 min
14	Paraffin	45 min

Table 2.18: Shandon Excelsior Paraffin Processing Steps for Tissues

For frozen sections, tissues were embedded in OCT (Tissue-Tek: 4583) on collection, using dry ice to freeze blocks, before being snap frozen in liquid N_2 and stored at -80°C. Frozen sections were cut using a Cryotome E (Thermo Scientific) with Leica microtome blades (631-1080) and mounted on the same slides as above.

2.4.2 Haematoxylin and Eosin Staining

To assess gross tissue structure of tissues, Haematoxylin and Eosin (H&E) staining was carried out on paraffin or frozen sections. To fix frozen sections prior to staining, they were air dried for 1 hour, before being fixed in acetone (VWR: 20066.330) for 10 minutes. Sections were then air dried, before being washed in DPBS for 5 minutes. Paraffin sections were deparaffinised and rehydrated before staining, by the following steps. Sections were placed in Histoclear (National Diagnostics: HS-200) for 7 minutes, twice, and taken down a gradient of 100%, 95%, and 70% ethanol and finally to dH_2O, with a 7-minute incubation at each

stage. The H&E staining protocol is outlined in Table 2.19, where Cell Path acidified Harris modified Haematoxylin (RBA-4202-00A) and Tissue-Tek Eosin Solution (8702) was used. Slides were mounted with DPX (Sigma-Aldrich: 06522-500ML). Haematoxylin stains acidic and negatively charged structures, such as the nucleic acids of the nucleus, making it a useful nuclear stain. Whereas eosin stains basic and positively charged structures, such as cytoplasmic proteins.

Step	Reagent	Time
1	Harris Modified Haematoxylin	1 min
2	Running Scot's tap water	5 min
3	70% Ethanol	1 min
4	Eosin solution	3 min
5	95% Ethanol	30 sec
6	95% Ethanol	30 sec
7	100% Ethanol	1 min
8	100% Ethanol	5 min
9	Histoclear	5 min
10	Histoclear	8 min

Table 2.19: Haematoxylin & Eosin Staining Protocol

2.4.3 Masson's Trichrome Staining

Masson's Trichrome staining was used to analyse fibrosis in tissues, by staining collagen deposition. Frozen sections were air-dried for 1 hour and placed in Bouin's solution (Sigma-Aldrich: HT10-1-32) overnight. Sections were then rinsed in Scott's tap water for 5 minutes and stained with Harris Haematoxylin for 15 minutes, before again being rinsed in tap water for 5 minutes. Following this, sections were placed in Collagen stain (0.6% m/v Chromotrope 2R, 0.3% m/v Fast Green FCF, 0.6% m/v phosphotungstic acid, 1% v/v glacial acetic acid, and dH_2O) for 20 minutes, rinsed in dH_2O, and dehydrated with 100% ethanol. Slides were finally mounted with DPX.

2.4.4 Oil Red "O" Staining

Oil Red "O" (ORO) staining was used to identify and quantify lipid content within cells and tissues. Chamber slide-cultured cells (section 2.2.2.1) were washed in DPBS and fixed in 4% PFA for 10 minutes. Fixed cells were stained using ORO working solution (1% Oil Red "O" powder (Sigma-Aldrich: O0625-25G) in Isopropanol (Sigma-Aldrich: 24137-2.5L-R), with 1% corn dextrin type III (Sigma-Aldrich: D2256-500G)) for ≥20 minutes. Slides were washed in water and counterstained with Harris Haematoxylin briefly, before being washed again in water and mounted using Aquatex (Merck: HC958756). Once the mount had secured the cover slip, the slide was sealed with clear nail polish.

2.4.5 *In situ* Hybridisation

2.4.5.1 Principles of Exiqon ISH

A one-day *in situ* hybridisation (ISH) protocol was performed with double labeled digoxigenin (DIG) miRNA probes. The protocol involves the unmasking of miRNAs using Proteinase-K, allowing the DIG-labelled Locked Nucleic Acid (LNA) probes to hybridise to the miRNA target. DIG can then be bound by DIG-specific antibody Fab fragments, conjugated to Alkaline Phosphatase (AP). AP converts a soluble substrate (Roche: 11697471001) containing 4-nitro-blue tetrazolium (NBT) and 5-bromo-4-chloro-3′-indolyphosphate (BCIP), into a dark-blue precipitate. This allows localisation of miRNA expression within the tissue or cells.

2.4.5.2 ISH Protocol

Sections were cut using fresh microtome blades and RNase-free equipment and workspace was used throughout. RNase-free, Diethylpyrocarbonate (DEPC; Sigma-Aldrich: 159220-100G) treated dH_2O was used to make up all solutions and for the section water bath. An adapted protocol from the Exiqon miRCURY LNA™ microRNA ISH Optimization Kit, previously described by Mariola Kurowska-Stolarska et al. (Kurowska-Stolarska et al. 2011), was followed and is described below.

Sections were deparaffinised in Xylene and ethanol (EtOH) as shown in Table 2.20, before being incubated with 15 μg/ml proteinase-K (Exiqon: 90010) for 10 minutes at 37°C. Sections were then washed twice in PBS and dehydrated as show in Table 2.20, and air-dried for 15 minutes. Hybridisation was performed at 55°C for 1 hour, with 50-6.25 nM Exiqon LNA double DIG-labeled probes for miR-34a (38487-15; ACAACCAGCTAAGACACTGCCA) or scramble control (90010; GTGTAACACGTCTATACGCCCA), or 1 nM 5'-DIG-labeled U6 small nuclear (sn)RNA positive control (90010; CACGAATTTGCGTGTCATCCTT). Following hybridisation, sections were washed in Saline-Sodium Citrate (SSC) buffer (Sigma-Aldrich: S6639-1L) at 55°C as shown in Table 2.20, with the last 0.2X SSC wash incubated at room temperature (RT).

Depariffinise	**Time**	**Dehydrate**	**Time**	**SSC Wash**	Time
1. Xylene	5 min	1. 70% EtOH	Dip x10	1. 5X SSC	5 min
2. Xylene	5 min	2. 70% EtOH	1 min	2. 1X SSC	5 min
3. Xylene	5 min	3. 96% EtOH	Dip x10	3. 1X SSC	5 min
4. 99.9% EtOH	Dip x10	4. 96% EtOH	1 min	4. 0.2X SSC	5 min
5. 99.9% EtOH	Dip x10	5. 99.9% EtOH	Dip x10	5. 0.2X SSC	5 min
6. 99.9% EtOH	5 min	6. 99.9% EtOH	1 min	6. 0.2X SSC	5 min (RT)
7. 96% EtOH	Dip x10				
8. 96% EtOH	5 min				
9. 70% EtOH	Dip x10				
10. 70% EtOH	5 min				
11. PBS	2-5 min				

Table 2.20: ISH Depariffinisation, Dehydration, and SSC Wash Steps

Sections were then blocked with DIG blocking solution (Roche: 11585762001) for 15 minutes at room temperature, in a humidifying chamber. AP-conjugated, sheep anti-DIG Fab fragments (1:800; Roche: 11093274910) in the blocking solution with 2% sheep serum (Jackson Immunoresearch: 013-000-121-JIR) was then added to the sections for 1 hour at room temperature, in the humidifying chamber. Next, slides were washed 3x3 minutes in PBS tween (PBS-T; Thermo Scientific: 28352) and incubated with AP substrate containing 0.2 mM

Levamisol hydrochloride (Sigma-Aldrich: 31742) for 1-2 hours at 30°C. The reaction was stopped by incubating slides 2x5 minutes with KTBT stop solution, containing 50 mM Tris-HCL, 150 mM NaCl, and 10 mM KCl. Finally, slides were washed with dH_2O for 2x1 minute, counterstained for nuclei using Nuclear Fast Red (Vector Labs: H-3403) for 1 minute at room temperature, rinsed in Scott's tap water for 10 minutes and dehydrated as shown in Table 2.20. Slides were mounted with Eukitt mount (Sigma-Aldrich: 03989).

2.4.6 Imaging Stains

Images of stained tissues and cells were taken using one of the following microscopes, which is specified in each results chapter. An Olympus BX41 microscope, with 10, 40, and 100X Olympus Uplan FLN Objective, and QCapture Pro 6.0 Software was used in most cases. Otherwise, an EVOS XL Core microscope (Life Technologies), with 1.25X Olympus Plan Apo N, and 10X and 40X Olympus Uplan FLN Objectives was used.

2.4.7 Quantification of Images

To quantify adipocyte area and number in WAT, the following method was used on H&E stained tissues. Images of anonymised WAT sections were taken by an EVOS XL Core microscope with 40X Objective, and analysed using Fiji 2 image analysis software (SciJava consortium). The following process was then used for quantification. Images were split into 3 colour channels using H&E Color Deconvolution function, colours were "Inverted" in channels 1 and 2, and converted to 16-bit images. Both these channels were merged using the Image Calculator, with "Add" blend mode. The combined image then had a Threshold adjustment applied with the "Precentile" preset and "Dark background" option checked. The Set Measurements function was used to specify particle measurements of "Area," constrained by the Threshold adjustment using "Limit to threshold" option and "Display label" was checked. The cells were then analysed using the Analyze Particles function, which was set to measure particles in the range of 2000-infinity pixels, with a circularity of 0-1, and only count full cells using "Exclude on Edges" option. The "Display results" option was also selected to show the outline of the counted particles. A table of results and image of counted cells

was then generated (Figure 2.3). The number of counts was taken as the cell number and the area value in pixels was converted to μm^2 using the image scale. This protocol was adapted from steps suggested by Mr Cameron James Nowell (Monash University, Australia), and works in a similar manner to work described by Osman S Osman et al. (Osman et al. 2013). A custom JavaScript Macro was written to batch-process the images for unbiased and high-throughput analysis. The average was taken from ≥5 random fields for each section.

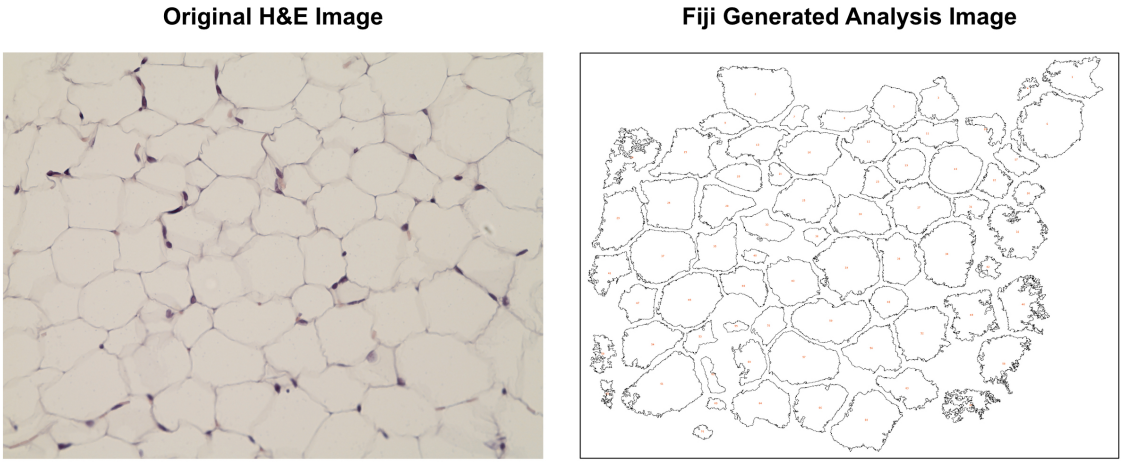

Figure 2.3: Example of Images Generated During Fiji Image Analysis of Adipocyte Area and number.

ORO staining was also quantified by Fiji 2 software. Images of anonymised slides were taken at 40X on the Olympus BX41 microscope, unless otherwise stated. Images of 5 random fields were taken for each section and each image was split into its RGB channels using the Color Deconvolution function. The red and blue channels were converted to 16-bit images and the red channel had colours “Inverted”. ORO staining was quantified using a Threshold adjustment with the “Minimum” preset and “Dark background” option checked. Then the Set Measurements function was used to specify particle measurements of “Area,” constrained by the Threshold adjustment using “Limit to threshold” option. The staining was then analysed using the Analyze Particles function, which had the “Summarize” and “Clear results” options checked, with others as default. This generated a result for the pixel area of the ORO stained regions, which was normalised to cell number, calculated as follows. The blue channel had a 2 sigma Gaussian blur applied and nuclei were counted using the Find Maxima function, with a Noise tolerance of 55 and “Light background” and “Count” options checked.

This process was put into the same custom JavaScript Macro used above, to batch-analyse images. The average was taken from ≥5 random fields for each section.

2.5 Flow Cytometry

2.5.1 Principles of Flow Cytometry

Cells are stained with fluorophore-conjugated antibodies for the specific antigen of interest, or fluorescent dyes, before being loaded into the flow cytometry machine. Cells are hydrodynamically focused into single file using sheath fluid and fluidics, before passing through a laser beam. As the cell passes through the laser beam, there is increasing light scattering depending on the size and granularity of the cell, represented as forward scatter (FSC) and side scatter (SSC), respectively. This allows the cells to be separated using these parameters for selection of different populations. These can then be further subdivided into other populations, based on the fluorescence intensity from the fluorescently labelled molecules, as the laser excites them.

2.5.2 General Flow Cytometry Protocol

Cells were counted using 1:10 Trypan blue and $0.5x10^6$ cells were used per Fluorescence-Activated Cell Sorting (FACS) tube (Elkay Labs: 2052-I1R), unless specified. Cells were washed in 1 ml FACS buffer (DPBS, 2% FCS, and 2 mM EDTA (Sigma-Aldrich: 27285)), centrifuged for 5 minutes at 510 x g. Cells were then incubated with 50 µl Fc-block (eBioscience: 14-0161-81), diluted to 0.01 μg/μl in FACS buffer, at 4°C for 15 minutes. Cells were stained with 2 μl (0.4μg) anti-mouse, fluorophore-conjugated antibodies (Table 2.21) added to the Fc-block, or were left unstained, for 30 minutes at 4°C in darkness. After incubation, cells were washed in 1 ml FACS buffer, centrifuged for 5 minutes at 510 x g, and resuspended in 300 µl FACS buffer for acquisition. If it was not practical to analyse the samples that day, they were fixed using 100 μl 4% FACS-fix (Thermo Scientific: 28908) for 10 minutes and washed in 300 μl FACS buffer, as above. They were then resuspended in 300 μl FACS buffer and stored at 4°C in darkness, until acquisition.

For each multi-stain tube Fluorescence Minus One (FMO) controls were produced, consisting of a separate tube for each stain containing all the stains except the one being examined. Voltages and compensation setting were set up using unstained and single-stained tubes. In some cases, compensation beads (BD Biosciences: 552845) were used for compensation setup, which were stained in 100 μl FACS buffer at room temperature for 30 minutes, covered. Cell marker expression was quantified using Diva v6.1.3 software and a BD Canto 2. Flow cytometry Plots, gating, and post-acquisition compensation was generated using FlowJo v.10.0.7 software, with gates set on FMO controls.

Antibody	Supplier	Cat no.	Antibody	Supplier	Cat no.
F480-APC	eBio	17-4801-82	CD4-PE	BD	553048
CD45-APC-Cy7	BD	561037	TLR2-PE	eBio	12-9021-82
CD86-PE-Cy7	BD	560582	CX3CR1-PE	R&D	FAB5825P
CD11b-PE-Cy7	BD	561098	CD8a-APC	eBio	17-0081-82
CD80-PerCP-Cy5.5	BD	560526	MHC Class II	BD	558593
CD69-PerCP-Cy5.5	BD	561931	CD31	BD	558738
CD19-PerCP-Cy5.5	BD	551001			
Ly-6g/c-PerCP-Cy5.5	BD	561103			
CD3-FITC	BD	555274			
CD11c-FITC	BD	557400			
CD206-PE	BioLeg	141706			

Table 2.21: List of Flow Cytometry Antibodies and Supplier Information Used Throughout
eBio = eBioscience, BD = BD Biosciences, BioLeg = BioLegend.

For flow cytometry analysis of lipid and mitochondrial content, the Fc-block step was omitted and cells were resuspended in 450 μl FACS buffer. Cells were then incubated with 0.1 μg/ml BODIPY 493/503 (Applied biosystems: D-3922) or 50-200 nM MitoTracker Deep Red FM (Applied biosystems: M22426), at 37°C for 30 minutes in darkness. These cells were washed and resuspended for analysis, as above.

2.6 Confocal Fluorescent Microscopy

Cells were grown in 8-well chamber slides as described in Section 2.2.2.1 above, with 500 μl culture media in each well. For mitochondrial staining, 50 μl of media was removed from each well and replaced with 50 μl of MitoTracker Deep Red FM at a final concentration of 200 nM, 100 nM, or 50 nM, or 50 μl of culture media as an unstained control. The slides were then incubated for 30 minutes at 37°C, covered. Once the incubation time had elapsed the media was removed from all the wells and replaced with either fresh culture media or BODIPY 493/503-supplemented media for lipid staining. If BODIPY was used, 500 μl culture media containing 100, 10, or 1 μg/ml BODIPY was added to each well, or pure culture media as an unstained control. The slides were incubated for 15 minutes at room temperature, covered. This was then replaced with 500 μl fresh culture media, before being replaced with 200 μl 4% PFA, for 1 hour at room temperature to fix cells. Finally, cells were washed in PBS and mounted using VECTASHEILD HardSet mount with DAPI (Vector Labs: H-1500), for nuclear staining. Slides were sealed with clear nail polish and stored at 4°C until imaging.

Images were taken on a Zeiss LSM 510 Meta Confocal Microscope, with 40X (Zeiss) and 63X (Zeiss) objective lenses. Settings were set on the highest concentration wells for each stain and modified using the unstained wells to reduce background and non-specific staining.

2.7 Statistics

All graphs were produced using Numbers (Apple Inc. v3.2) or Prism (GraphPad Software, Inc. v4) and data is graphed as mean values of ≥3 biological replicates, averaged from ≥2 technical repeats, unless otherwise indicated. Error bars are calculated as SEM or RQmax and RQmin. Statistics were calculated by student's t test, or One-way or Two-way ANOVA using Prism, and for all graphs * = $p<0.05$, ** = $p<0.01$, *** = $p<0.001$, and **** = $p<0.0001$.

Chapter 3: Profiling miR-34a Expression In Models of Obesity

3.1 Introduction

The expression profile and role of miR-34a in visceral white adipose tissue (vWAT) during obesity is very poorly understood. Due to the invasive procedure required to collect vWAT depots in humans, along with the difficulty in getting biopsies from healthy controls, the majority of human obesity studies examine subcutaneous (sc)WAT depots. The few studies that have been published examining miR-34a in human obesity are correlative microarray studies, mainly examining miRNA expression in serum and scWAT. These studies have shown correlations between miR-34a and obesity, with overweight (BMI≥25), type 2 diabetic (T2D) patients showing increased serum miR-34a transcripts, compared to overweight, non-diabetics (Kong et al. 2011). Additionally, a positive correlation has been observed between increasing body mass index (BMI) and miR-34a transcripts in human scWAT, with no correlation observed in omental vWAT (Klöting et al. 2009; Ortega et al. 2010). During the course of subcutaneous white adipocyte differentiation *in vitro*, an increase in miR-34a has also been observed (Ortega et al. 2010). However, no studies have looked directly at the localisation of miR-34a expression within the vWAT and the particular cell types that express miR-34a. This localisation data could help to identify the individual cell types that express miR-34a within vWAT and also potentially those that contribute to pathology in obesity. Therefore, due to the difficulties obtaining human vWAT, examining miR-34a expression in animal models of obesity may provide a better indication of its role in human vWAT. Furthermore, during the time the experiments in this chapter were conducted, there were no publications examining miR-34a in brown adipose tissue (BAT). With the protective functions of BAT during obesity, examination of miR-34a expression and function in this tissue is also of interest.

In contrast, the expression of miR-34a in the liver during obesity has been well studied. Reports have shown a correlation between hepatic miR-34a expression and the obesity comorbidity, non-alcoholic fatty liver disease (NAFLD). Using a microarray screen, Cheung et al. showed that hepatic miR-34a transcripts were up-regulated in nonalcoholic steatohepatitis (NASH) patients, validated by qRT-PCR (Cheung et al. 2008). Another microarray study further showed that miR-34a was up-regulated in the livers of obese, hyperglyceamic *ob/ob* mice, with

fatty liver, and non-obese, STZ-induced type 1 diabetic C57BL/6 mice (Li et al. 2009). Subsequent studies, using murine diet-induced obesity models of NAFLD, also showed increases in hepatic miR-34a transcripts on high-fat diet (HFD) with hepatic lipid accumulation (Lee et al. 2010; Fu et al. 2012; Choi et al. 2013). Human studies have found that serum miR-34a expression increases proportionally with the severity of NAFLD, increasing with the progression to NASH (Cermelli et al. 2011; Castro et al. 2012; Yamada et al. 2013). However, this correlation has been shown to be sex-dependent, with one study showing that although serum miR-34a transcripts were increased in both male and female patients with NAFLD, only male patients showed increased serum miR-34a as severity increased (Yamada et al. 2013). Additionally, hepatic inflammation in hepatitis C patients has been correlated with increased serum miR-34a transcripts, which increased with hepatitis C severity, blood glucose levels, and insulin resistance (Cermelli et al. 2011). A meta-analysis of published miRNA T2D studies, found that miR-34a is consistently up-regulated in the blood, liver, and pancreas in both human and mouse T2D models (Zhu and Leung 2015). This led the authors to suggest that miR-34a would be a useful T2D biomarker. Therefore, these studies strongly suggest that miR-34a is up-regulated in the liver during obesity.

Therefore, it was hypothesised that miR-34a expression is altered in the epididymal (e)WAT, liver, and BAT during murine diet-induced obesity. In this chapter the localisation and transcript expression of miR-34a in murine eWAT from models of obesity and patient omental WAT was examined. Additionally, miR-34a expression in the liver and BAT was examined in these murine obesity models.

3.2 Aims

- Examine the localisation of miR-34a expression within murine eWAT and human omental WAT.

- Quantify the expression of miR-34a transcripts in various non-obese WT murine tissues, including eWAT, liver, and BAT.

- Quantify the expression of miR-34a transcripts in eWAT, liver, and BAT during murine models of obesity.

3.3 Methods

For specific details of individual methods please refer to Chapter 2: Materials and Methods.

3.3.1 Mouse Studies

The mouse tissues examined in this chapter are from 6 to 12-week old, male, wild type (WT) C57BL/6 mice, or 6 to 12-week-old leptin deficient, male *ob/ob* mice, on normal chow diet for 6 weeks. 7-week-old WT C57BL/6 or miR-34a$^{-/-}$ ((KO) B6.Cg-Mir34a^{tm1Lhe}/J) mice, fed either chow or HFD *ad libitum* for 24 weeks, were also used. These mice are described further in section 2.2.1. Mice were euthanised using Avertin or cervical dislocation at the end of the study and tissues were collected as described in section 2.2.1.1. Serum, lungs, heart, kidney, liver, thigh muscle, pancreas, testicle, spleen, eWAT, and intrascapular (i)BAT were collected. miR-34a$^{-/-}$ mice were genotyped as described in section 2.3.6.

3.3.2 Human Patient Samples

In collaboration with Professor Andrew Collier MD (Consultant Diabetologist) at Ayr Hospital, omental WAT biopsies were collected by Mr Majid Ali MD (Bariatric Surgeon), from 6 obese (BMI = 42.13±3.24) patients with T2D and/or sleep apnoea, undergoing bariatric surgery. Prior to surgery, patients were put on a low calorie (800-1000 kcal/day) liver diet, to shrink the size of the liver and avoid surgical complications. All Patients were being treated with Metformin and patient baseline demographics are shown in Table 3.1. Written, informed consent was obtained from all patients before inclusion in the study, and the study was approved by the West of Scotland Research Ethics Service (REC Ref 12/WS/0158). The tissue was collected in a falcon tube and transported back to the University of Glasgow in a Dewar flask of 37°C water. The tissue was then snap frozen in liquid N_2 and stored at -80°C, fixed in 4% paraformaldehyde (PFA) for 48 hours, or else the stromal vascular fraction (SVF) was isolated following the protocol in section 2.2.2.1.

Patient	Sex	Age (Yrs)	BMI (kg/m^2)	HbA1c (%)	Chol (mmol/L)	HDL (mmol/L)	TG (mmol/L)	Hb (g/dL)
1	F	54	42.5	6.5	5.2	1.51	0.68	14.2
2	F	53	45.8	7.4	4.9	1.88	0.66	12.6
3	F	62	36.5	8.7	3.6	1.29	0.86	13.0
4	M	44	40.7	6.9	3.5	1.18	3.03	12.4
5	F	49	43.2	6.8	6.9	1.38	3.06	13.7
6	F	39	44.1	8.7	4.9	1.53	1.64	14.9
SD		**8.08**	**3.24**	**0.97**	**1.24**	**0.24**	**1.13**	**0.98**
SEM		**3.30**	**1.32**	**0.40**	**0.51**	**0.10**	**0.46**	**0.40**
Avg		**50.17**	**42.13**	**7.50**	**4.83**	**1.46**	**1.66**	**13.47**

Table 3.1: Bariatric Surgery Patient Profile
BMI = body mass index, HbA1c = glycated haemoglobin, HDL = high density lipoprotein, TG = triglyceride, and Hb = haemoglobin.

3.3.3 *in situ* Hybridisation

Tissues for *in situ* hybridisation (ISH) staining were fixed in 4% PFA for 48 hours and embedded in paraffin, as described in section 2.4.1. Tissue sections were cut and processed for ISH as described in section 2.4.5.2. Images of the mounted slides were taken with a 10 or 40X Olympus Uplan FLN objective, on an Olympus BX41 microscope with QCapture Pro 6.0 Software.

3.3.4 miRNA Transcript Expression

RNA was extracted and quantified as described in sections 2.3.1.3 and 2.3.2.1, respectively. qRT-PCR analysis of miRNA transcripts was quantified using either the Qiagen miScript system or Life Technologies' TaqMan® microRNA system, as described in section 2.3.4.

TaqMan® microRNA		Qiagen miScript	
Primer Assay	**Cat no.**	**Primer Assay**	**Cat no.**
miR-34a	000426	Mm_miR-34a_1	MS00001428
miR-34a-3p	465771_mat	Mm_miR-34a*_1	MS00025697
miR-34b-5p	002617	Hs_RNU6B_3	MS00029204
miR-34b-3p	002618		
miR-34c	000428		
miR-34c*	002584		
U6	001973		

Table 3.2: Manufacturer Information For miRNA qRT-PCR Primer Assays

For each system, Qiagen miScript primer assays or Life Technologies' TaqMan® microRNA assays were used, shown in Table 3.2. The quality of DNA products from qRT-PCR reactions were assessed by running them out on a 4% agarose gel with 0.2 µg/ml ethidum bromide (EtBr), at 85 V, as described in section 2.3.3.

3.3.5 Open Array miRNA Profiling

miRNAs were profiled in the eWAT from WT C57BL/6 mice that had been fed a chow or HFD for 24 weeks. RNA was extracted from eWAT as described in section 2.3.1.3 and quantified as described in section 2.3.2.1. The RNA from 3 samples were pooled together for each group: chow (WTC1), HFD (WTH2)-mild, and HFD (WTH1)-substantial, and the Open Array protocol was carried out as described in section 2.3.7. The HFD groups were segregated based on diet response, using week-24 weight: WTH2-mild (38.43±0.45 g) and WTH1-substantial (42.9±0.06 g), with WT chow control mice weighing: 33.23±0.45 g. Data was normalised to RNU6B and the mean was calculated from two separate arrays run in parallel for each primer assay. Primer assays that produced no data were excluded from further analysis. Change in assay expression over the WT control sample was calculated as follows:

$$\text{Change} = \Delta Ct \text{ HFD group assay} - \Delta Ct \text{ WTC1 assay}$$

Data was analysed using DataAssist™ software (Life Technologies) and Apple Numbers v.3.6.1 (California, USA).

3.3.6 qRT-PCR Product Cloning and Sequencing

The miR-34a qRT-PCR DNA product from microRNA TaqMan® was cloned into a TA plasmid vector and sequenced following the protocol in section 2.3.5. The plasmid map is shown in Figure 3.1. Sequences were analysed and aligned using CLC Sequence Viewer v7.6.1 (CLC Bio), and sequence traces were examined and exported using 4Peaks v1.8 (Nucleobytes). The cloned sequences were identified from each colony and aligned to get a consensus sequence from 5 colonies. This consensus sequence was used for alignment of target sequences. miR-34 family sequences were obtained from miRBase (University of Manchester,

UK; http://www.mirbase.org, Accessed: 27/11/15) (Kozomara and Griffiths-Jones 2013).

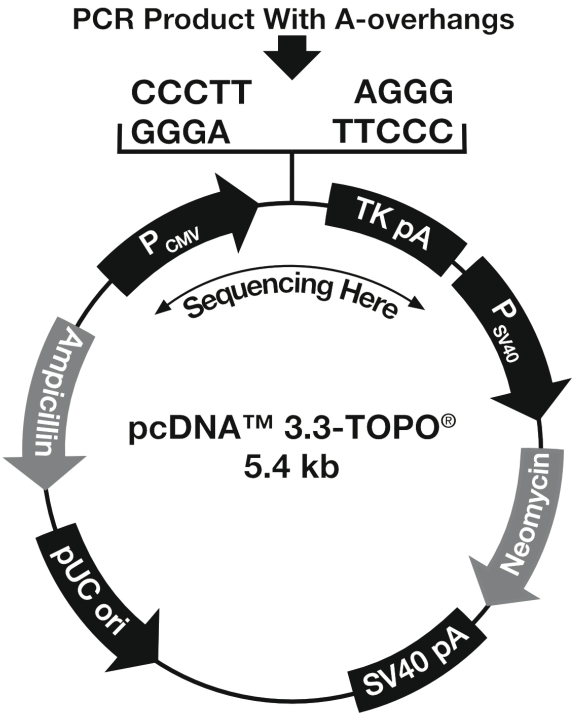

Figure 3.1: Diagram of Life Technologies' pcDNA™ 3.3-TOPO® Plasmid For Cloning
Diagram adapted from Life Technologies' pcDNA™ 3.3-TOPO® TA Cloning Kit manual (K8300-01). P_{CMV} = cytomegalovirus promoter, TK pA = reverse primer binding site, P_{SV40} = early promoter, SV40 pA = SV40 polyadenylation signal, pUC ori = pUC origin.

3.4 Results

3.4.1 Characterising miR-34a Expression Across WT Murine Tissue

First, the expression of miR-34a was examined across WT murine tissues, in 6-week-old C57BL/6 mice by qRT-PCR (Figure 3.2). Due to issues finding a stable reference gene for pancreatic tissue, the data is represented as 1/Ct values for a full comparison of the different tissues. From the tissues examined, kidney tissue showed the highest levels of miR-34a expression (Ct = 26.66±0.15), with serum showing the lowest (Ct = 32.92±0.83). Grouping tissues by miR-34a expression, the kidney, heart, lung, iBAT, and eWAT showed the highest (Ct = 26.66±0.15 to 27.60±0.19), followed by the liver, skeletal muscle, and spleen (Ct = 28.19±0.38 to 28.23±0.86). The pancreas and serum showed significantly less miR-34a than the rest of the tissues, with serum levels significantly lower than that in the kidney (P=0.0113), heart (P=0.005), iBAT (P=0.0036), eWAT (P=0.0241), and skeletal muscle (P=0.0246). Pancreas levels (Ct = 31.48±0.80) were significantly less than that in the kidney (P=0.0208), heart (P=0.0246), lung (P=0.0003), iBAT (P=0.0337), Liver (P=0.0461), and spleen (P=0.0171).

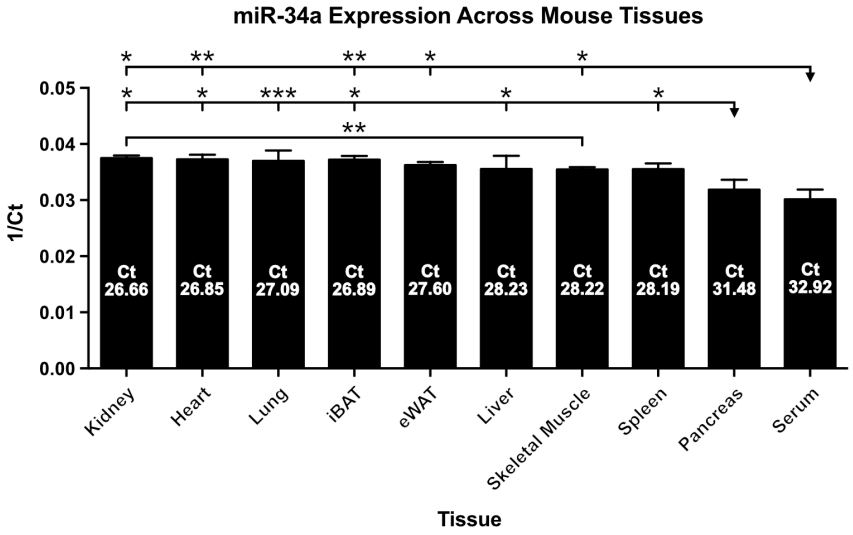

Figure 3.2: miR-34a Expression Profile Across Murine Tissues
Showing qRT-PCR expression data for miR-34a across different tissues from 6-week-old, WT C57BL/6 mice, using the Qiagen miScript System. Data is represented as mean 1/Ct with SEM, and 3 ng total RNA was used for each reaction. The raw, average Ct values are shown on each bar, n=5. *P<0.05, **P<0.01, ***P<0.001, ****P<0.0001 One-way ANOVA, with Tukey's multiple comparisons post-test.

3.4.2 miR-34a Localisation Within vWAT

To examine the localisation of miR-34a expression within the vWAT, tissues from murine obesity models and patients were stained for ISH. The eWAT from 6-12 week old *ob/ob* Vs. WT C57BL/6 mice and WT C57BL/6 mice fed chow Vs. HFD for 24 weeks, and omental vWAT from obese patients undergoing bariatric surgery, were examined. However, some optimisation of the ISH staining protocol was required, which is detailed in section 3.4.2.1, below.

3.4.2.1 miR-34a ISH Optimisation

To achieve appropriate ISH staining within the eWAT, which was not overexposed, allowing the identification of darker areas of staining, a number of probe concentrations and AP substrate developing times were evaluated (Figure 3.3). The standard miR-34a ISH protocol suggested a probe concentration of 50 nM with a developing time of 2 hours for the AP substrate. However, this produced very dark staining in some areas, obscuring tissue structures and making it difficult to identify areas of low and high staining. Subsequent ISH staining halved both the probe concentration (25 nM) and developing time (1 hour). This improved miR-34a staining, but still produced areas of very dark staining. Next, the probe concentration was halved (12.5 nM) and halved again (6.25 nM). The probe concentration of 12.5 nM worked well, showing better contrast between areas of dark and light staining. However, 6.25 nM produced light staining, resulting in the loss of staining in some areas. Therefore, a probe concentration of 12.5 nM and a developing time of 1 hour was chosen for future WAT miR-34a ISH staining.

3.4.2.2 miR-34a Is Ubiquitously Expressed Throughout Murine eWAT and Human Omental WAT

Using the optimised ISH staining protocol for miR-34a, localisation of miR-34a was examined within murine eWAT and human omental WAT. Little difference was observed in miR-34a staining between WT and *ob/ob* mouse eWAT at both 6 and 12 weeks of age (Figure 3.4). However, dark staining was observed on the inner and outer layer of blood vessels, parts of the epididymis, and white adipocyte nuclei. Overall, miR-34a appears to be ubiquitously expressed throughout the eWAT. Similar staining was observed in chow and HFD-fed WT C57BL/6 mice

eWAT, and obese human omental WAT (Figure 3.5). Only a slight increase in staining intensity was observed in HFD-fed WT eWAT Vs. WT chow eWAT.

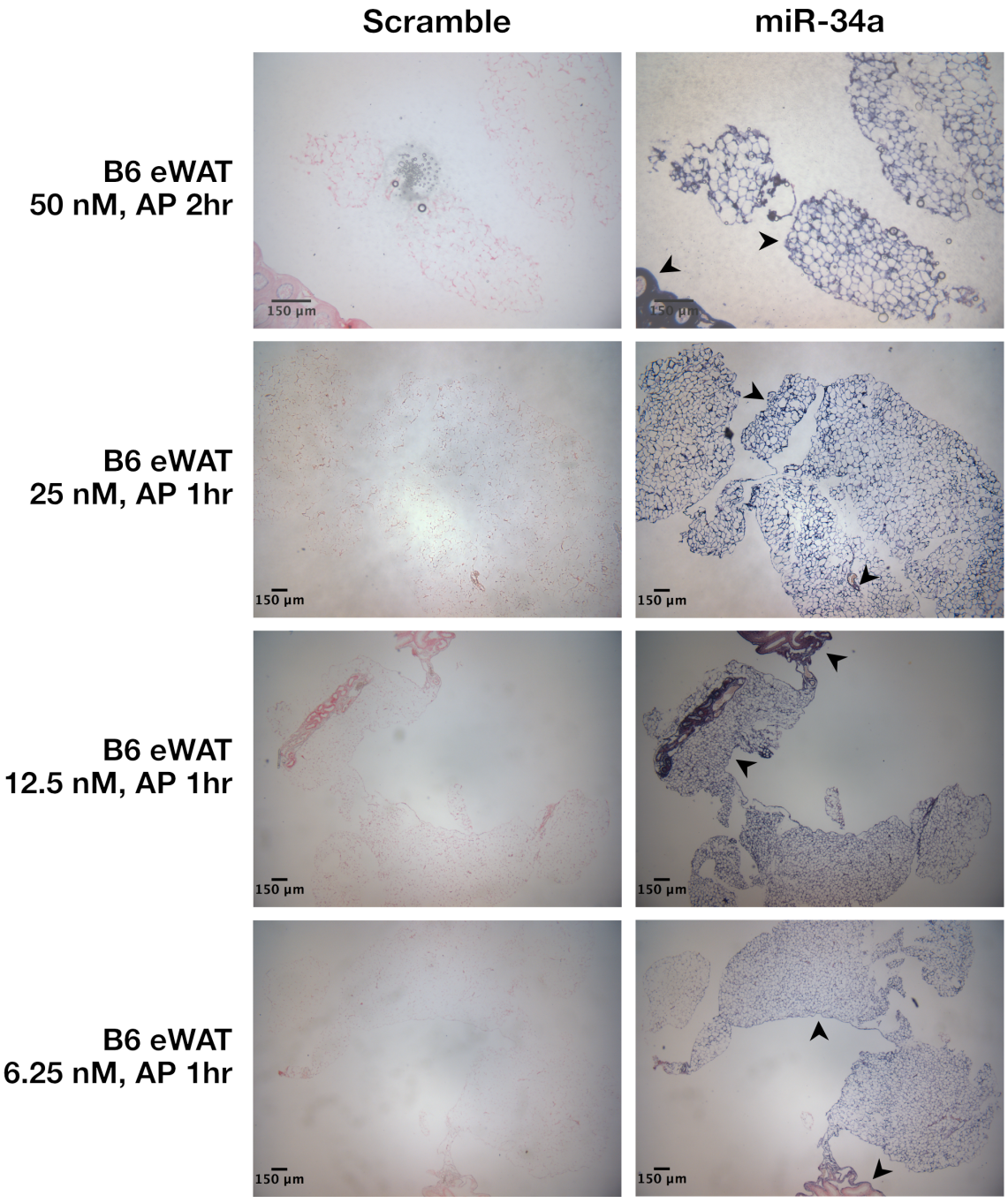

Figure 3.3: *in situ* Hybridisation Optimisation For eWAT
Representative images of different ISH staining conditions for miR-34a in epididymal white adipose tissue (eWAT) from WT C57BL6 at 6 weeks of age, fed a normal chow diet. Both scramble negative control (red/pink) and miR-34a (purple) probe was used at concentrations of 50-6.25 nM, with an AP substrate developing time of 1-2 hours. Images were taken at 4 and 10X and were selected from an image set with n=2 for each condition. Scale bar = 150 μm and points of interest are indicated by arrows.

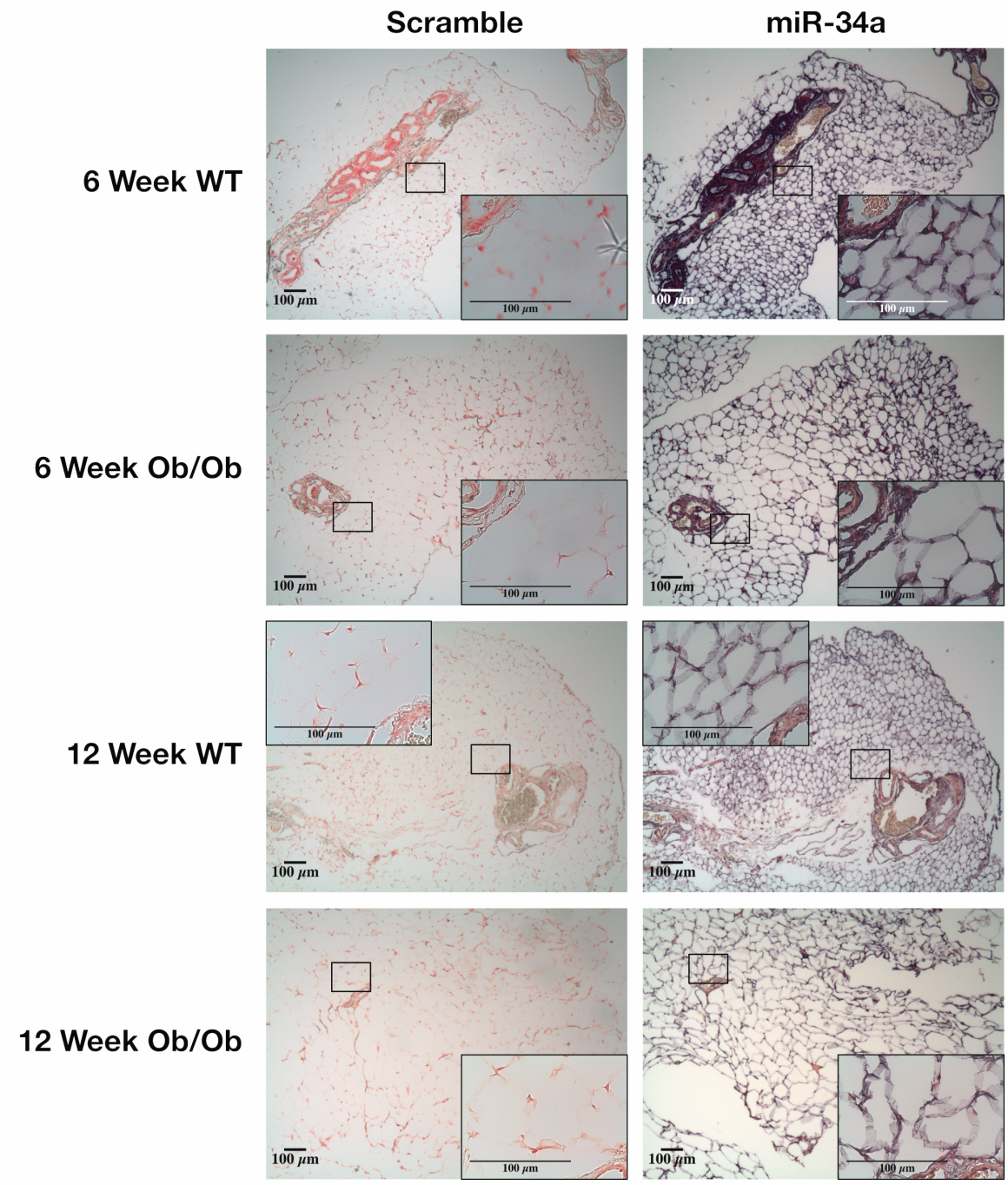

Figure 3.4: Characterisation of miR-34a Distribution In Genetically Obese *ob/ob* Mice eWAT
Representative images of ISH staining for miR-34a in epididymal white adipose tissue (eWAT) from WT C57BL6 and *ob/ob* mice at 6 or 12 weeks of age, fed a normal chow diet. Both scramble negative control (red/pink) and miR-34a (purple) probes were used at 12.5 nM, with an AP substrate developing time of 1 hour. Images were taken at 4 and 40X, with the higher magnification image location shown by the black box. Images were selected from an image set with n=5 for each group. Scale bar = 100 μm.

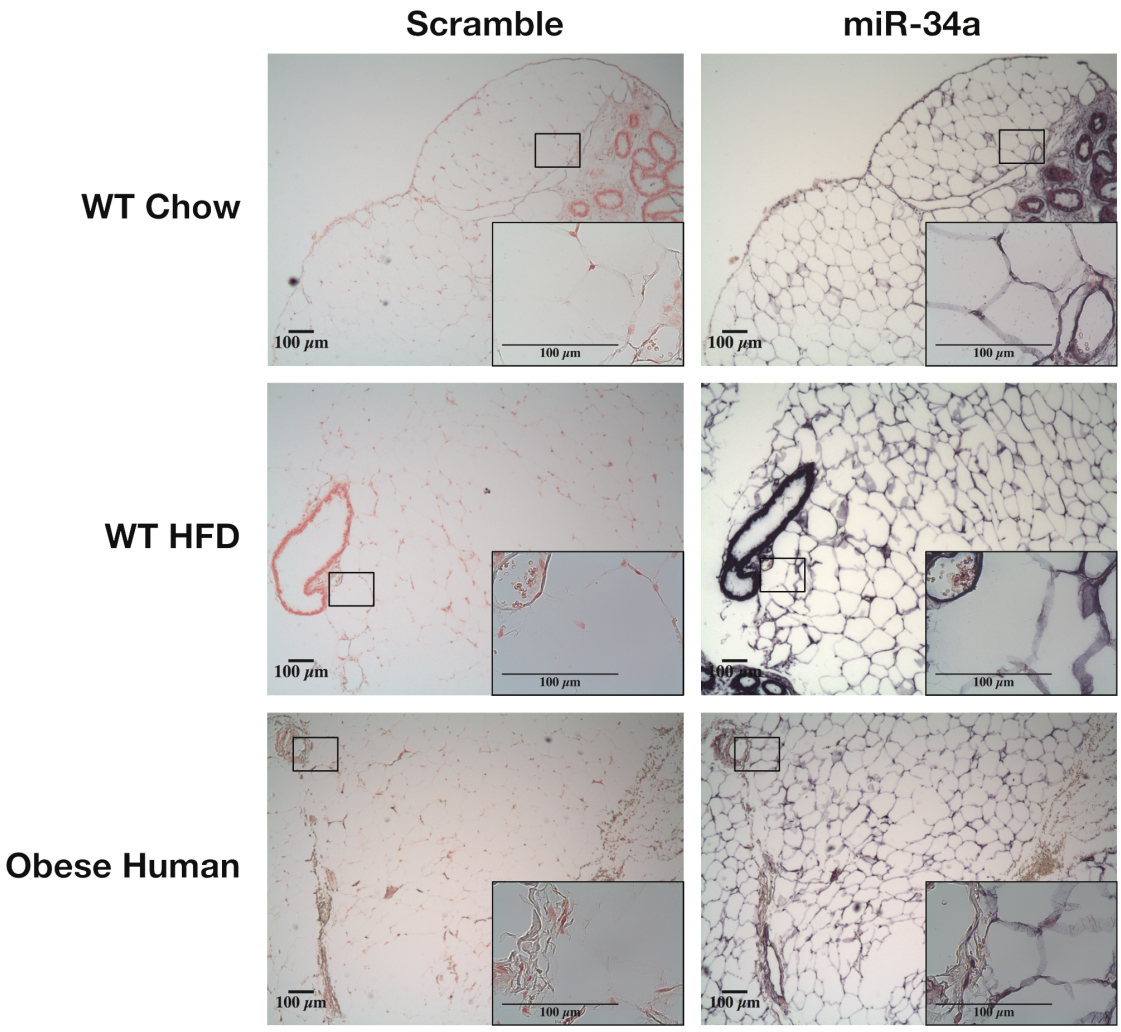

Figure 3.5: Characterisation of miR-34a Distribution In Diet-Induced Obese Mice eWAT and Obese Patient omental WAT
Representative images of ISH staining for miR-34a in epididymal white adipose tissue (eWAT) from WT C57BL6 mice fed a chow or HFD for 24 weeks, and omental WAT from obese, T2D patients. Both scramble negative control (red/pink) and miR-34a (purple) probes were used at 12.5 nM, with an AP substrate developing time of 1 hour. Images were taken at 4 and 40X, with the higher magnification image location shown by the black box. Images were selected from an image set with n≥3 for each group.

3.4.3 Quantification of miR-34a Expression in *ob/ob* Tissues

To quantify miR-34a expression in *ob/ob* adipose and liver during weight gain, tissues were collected from *ob/ob* and WT C57BL/6 mice on a chow diet, at 6, 9, and 12 weeks of age. Over this 6-week period (age 6-12 weeks), *ob/ob* mice were significantly heavier ($P<0.0001$) than their WT counterparts (*ob/ob*: 27.5±0.28 – 42.8±1.96 g Vs. WT: 19.7±0.42 – 28±0.32 g), by area under the curve (AUC) analysis (Figure 3.6A). Surprisingly, qRT-PCR analysis of miR-34a levels in *ob/ob* eWAT showed a decrease ($P=0.0308$) at 12 weeks of age, compared to WT (Figure 3.6B). Furthermore, an increase in miR-34a expression was observed at 12 weeks of age in *ob/ob* iBAT ($P=0.0033$), compared to WT (Figure 3.6C).

Interestingly, miR-34a expression in the *ob/ob* liver increased at 9 weeks of age (P=0.0014), but not 12 weeks of age (P=0.0726), compared to WT (Figure 3.6D). The star strand for miR-34a (miR-34a*/miR-34a-3p) was also examined in these tissues, to see if it followed the same expression pattern. Interestingly, miR-34a* was also decreased in *ob/ob* eWAT, but at 9 weeks of age (P=0.0006), compared to WT (Figure 3.7A). Additionally, miR-34a* showed similar expression to the mature strand in *ob/ob* iBAT, increasing at 12 weeks of age (P=0.0121), compared to WT (Figure 3.7B). Finally, miR-34a* expression increased at 12 (P=0.0499), and not 9 (P=0.4721), weeks of age in the *ob/ob* liver, compared to WT (Figure 3.7C).

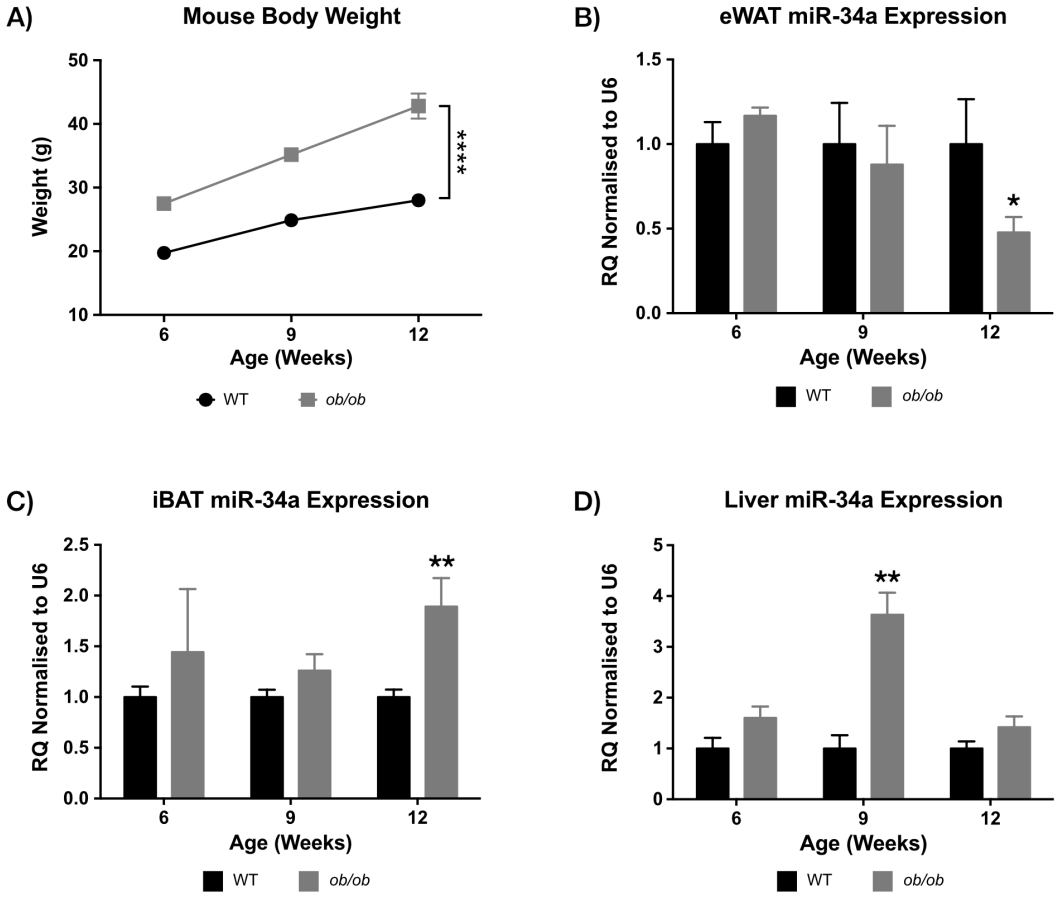

Figure 3.6: miR-34a Expression Increases In the iBAT and Liver, and Decreases In the eWAT of *ob/ob* Mice, During Weight-Gain

(A) Showing weight gain in WT C57BL/6 and *ob/ob* mice on a normal chow diet, at 6-12 weeks of age; n=5. Represented as mean values with SEM, and statistics were calculated off AUC analysis for each group. (B-D) qRT-PCR data using the Qiagen miScript system, showing miR-34a expression in the epididymal white adipose tissue (eWAT; B), intrascapular brown adipose tissue (iBAT; C), and liver (D) in the same animals as shown in (A); n=5. Data represented as relative quantification (RQ) values of WT, normalised to RNU6B, with RQ_{min} and RQ_{max} values. *P<0.05, **P<0.01, ****P<0.0001 unpaired, Student's t-test.

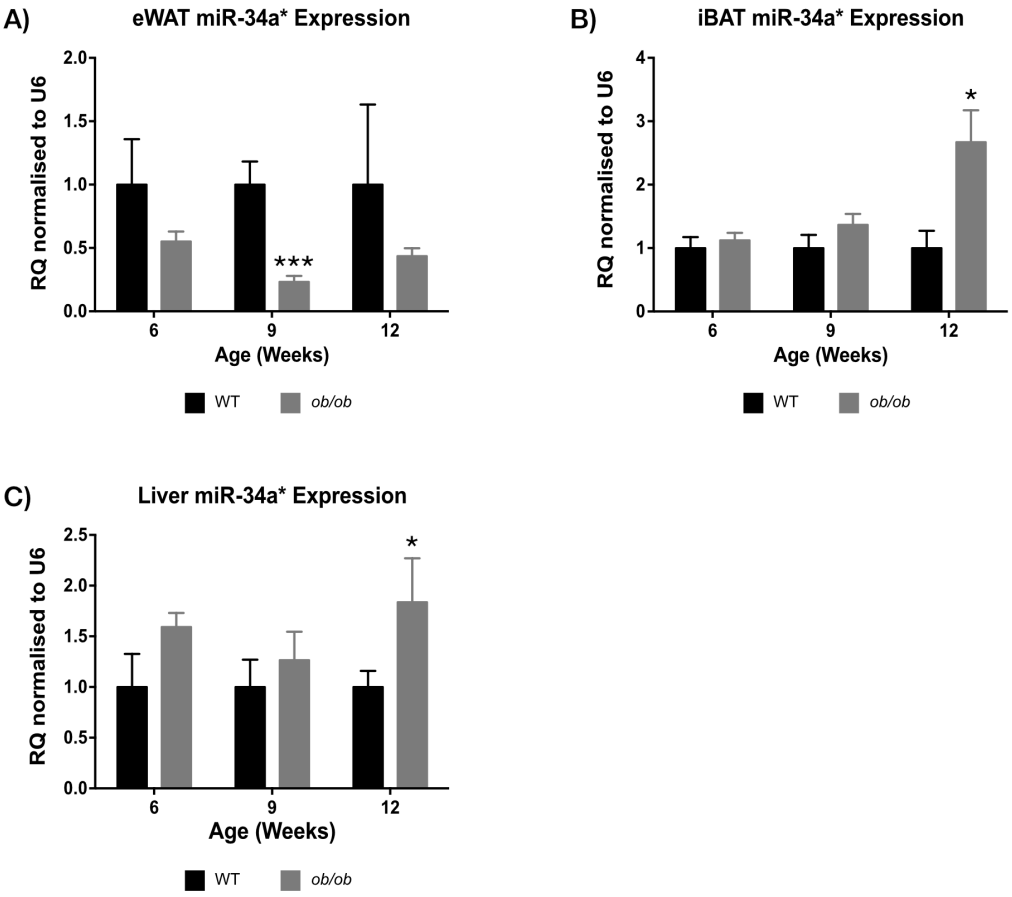

Figure 3.7: miR-34a* Expression Follows A Similar Profile to miR-34 In *ob/ob* Mice During Weight-Gain
(A-C) qRT-PCR data using the Qiagen miScript system, showing miR-34a* expression in the epididymal white adipose tissue (eWAT; A), intrascapular brown adipose tissue (iBAT; B), and liver (C) in the same animals as shown in (Figure 3.6A); n=5. Data represented as relative quantification (RQ) values of WT, normalised to RNU6B, with RQ_{min} and RQ_{max} values. *P<0.05, ***P<0.001 unpaired, Student's t-test.

3.4.4 Quantification of miR-34a Expression in Diet-Induced, Obese Mice

To validate the changes in miR-34a and 34a* expression observed in *ob/ob* mice, using a more representative model of human obesity, expression in a murine, diet-induced obesity model was examined. The expressions of both miR-34a and 34a* were examined in WT C57BL/6 mice fed chow or HFD for 24 weeks (Figure 3.8). Correlating with observations in *ob/ob* mice, an increase in miR-34a transcripts were observed in the iBAT (P=0.0048) and liver (P=0.0086) of HFD-fed WT mice (Figure 3.8A). Interestingly, no change was observed in eWAT miR-34a transcripts, in these mice (P=0.7875). Additionally, no change in miR-34a* transcripts were observed in the eWAT (P=0.2808), iBAT (P=0.1984), or liver (P=0.9416) of HFD-fed WT mice (Figure 3.8B). To explore if there was differential expression of miR-34a in the pre-adipocyte and leukocyte rich SVF of obese

human vWAT, the SVF from omental WAT of obese patients were examined (Figure 3.8C). The SVF showed higher expression of miR-34a (Ct = 27.58±1.72), compared to whole WAT (Ct = 33.21±0.11), but not to a statistically significant degree (P=0.5560).

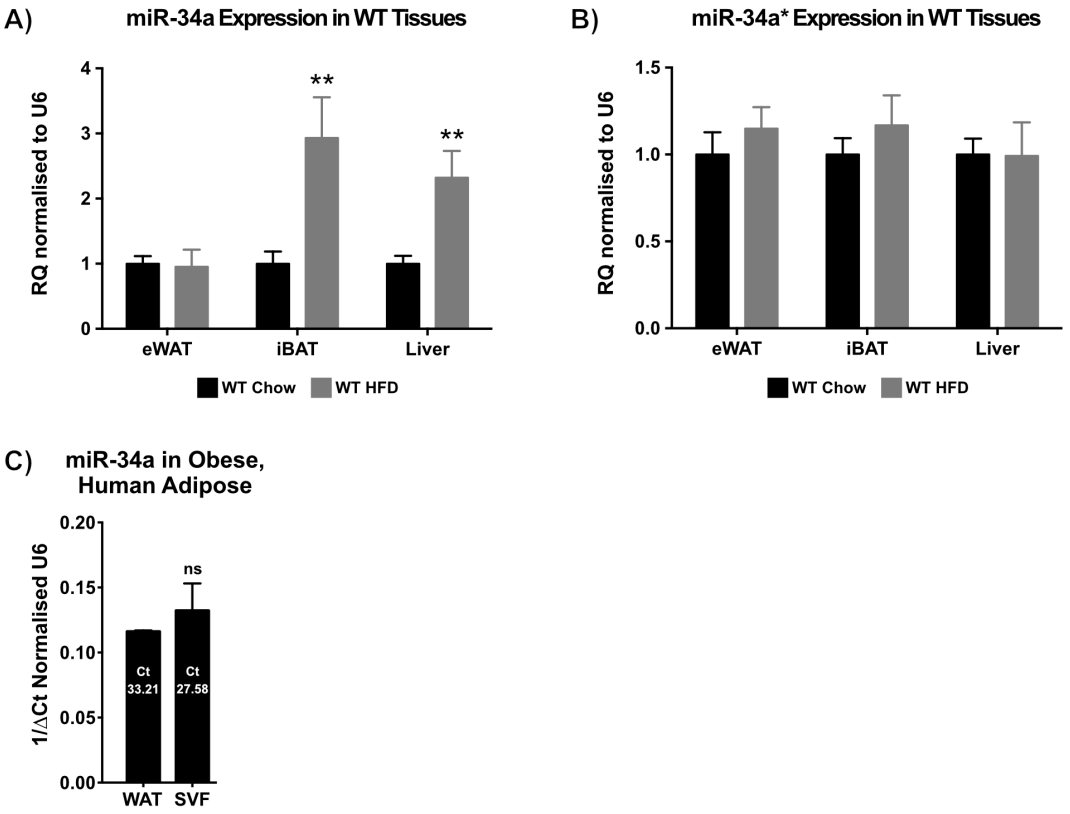

Figure 3.8: miR-34a Expression In WT Tissues From Diet-Induced Obese Mice and Omental WAT From Obese Patients
(A-B) Qiagen qRT-PCR data showing miR-34a (A) and miR-34a* (B) expression in the epididymal (e)WAT, intrascapular (i)BAT, and liver from WT C57BL/6 mice fed a chow diet or HFD for 24 weeks. Data is represented as relative quantification (RQ) of WT chow controls, normalised to RNU6B expression, with RQ_{min} and RQ_{max} values. Statistics were calculated off ΔCt values; n=5-6. (C) Qiagen qRT-PCR data comparing miR-34a expression in the whole omental WAT, with the stromal vascular fraction (SVF) of the tissue, from obese, T2D patients. Data is represented as 1/ΔCt, normalised to RNU6B, with SEM and overlaid mean CT values; WAT: n=5 and SVF: n=3. ns = not significant, **P<0.01 unpaired, Student's t-test.

3.4.4.1 miRNA qRT-PCR Protocol Quality Control

Whilst checking the deletion of miR-34a and 34a* from miR-34a$^{-/-}$ mice at the transcript level, it was discovered that, although there were reductions in the transcripts of both miR-34a and 34a* in these mice, they were still detectable (Figure 3.9A). These mice should express neither of these miRs, as the miR-34a stem-loop has been deleted from their genome. All the qRT-PCR analysis up to this point was carried out with the Qiagen miScript system. This showed that miR-34a transcripts were reduced from: ΔCt = 7.51±0.09 to 13.47±0.53 and miR-34a* from: ΔCt = 12.82±0.12 to 16.87±0.81, in the testicles of miR-34a$^{-/-}$ mice. The

testicle was used as a positive control; as previous studies have shown high expression of the miR-34 family in this tissue (Dutta et al. 2007). Therefore, the use of Life Technologies' microRNA TaqMan™ system was explored, which produced better results, but still had similar issues with low level detection of miR-34a (Ct = 35.5±0.23) and 34a* (Ct = 36.13±0.36) in miR-34a$^{-/-}$ mice (Figure 3.9B-C). In the comparison between the two systems, it appears that the TaqMan™ system produces a similar profile of expression, which is shifted back a couple of cycles. Comparing the difference between the WT and miR-34a$^{-/-}$ expression of miR-34a showed that miScript detected a difference of 6.83±0.26 ($P<0.0001$), with TaqMan™ detecting 8.99±0.18 ($P<0.0001$) (Figure 3.9B). For miR-34a*, miScript detected a difference of 4.96±0.05 ($P<0.0001$), compared to TaqMan™ detecting 4.11±0.30 ($P=0.0007$) (Figure 3.9C). The mice used for these analyses were genotyped to confirm their KO status (Figure 3.9D). Since the expression of miR-34a and 34a* was low (Ct: 35-36) in miR-34a$^{-/-}$ mice using microRNA TaqMan™, the qRT-PCR DNA product was run on a gel to check if there was a visible product from the miR-34a$^{-/-}$ samples (Figure 3.9E). Unfortunately, in the miR-34a$^{-/-}$ samples a faint band was visible for miR-34a at the same size as the WT product (<100 bp), and a faint larger-sized band (~100 bp) was visible for miR-34a* in these samples. Therefore, cloning and sequencing of the qRT-PCR product from the miR-34a$^{-/-}$ sample KOC1, for both miR-34a and 34a* was attempted. The product from miR-34a qRT-PCR was successfully cloned and colonies were selected for sequencing. Disappointingly, many attempts failed to clone the product from the miR-34a* qRT-PCR. Once sequenced, the consensus sequence from all the colonies was aligned with the sequence of the whole miR-34 family (Figure 3.9F), as it has been previously shown that microRNA TaqMan™ primers can bind other family members (Chen 2005). Only miR-34a-5p and miR-34c-5p fully aligned with the sequence, with a few mismatches. However, the sequence mismatches for miR-34c-5p may match the miR-34c-5p sequence. As the sequencing trace shows two peaks at each of these regions, one of which corresponds with the correct base for the miR-34c-5p sequence, except for the first adenine base. Therefore, the miR-34a TaqMan™ primer may produce a background signal representing miR-34c-5p, prompting examination of the whole miR-34 family from here on.

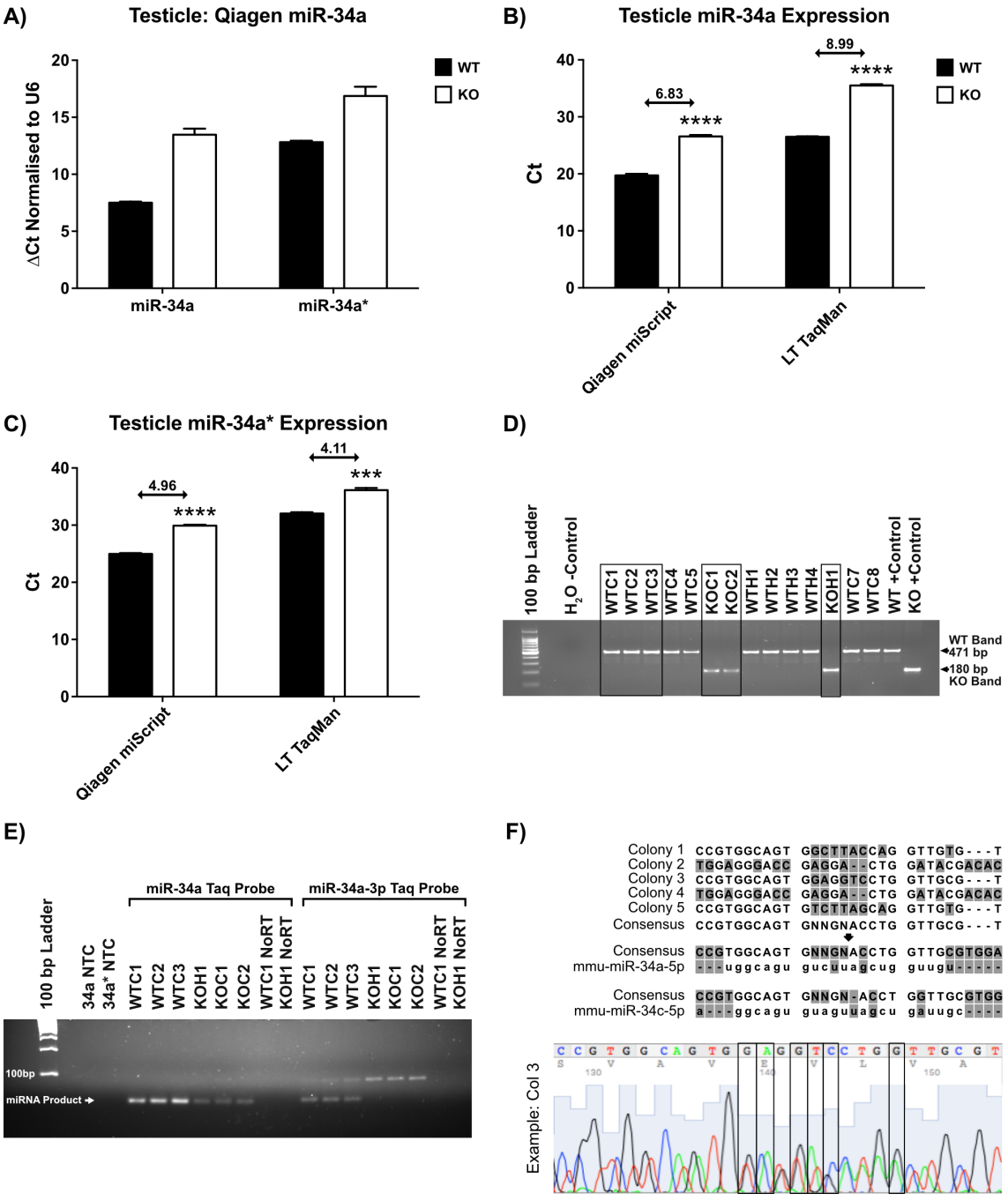

Figure 3.9: miR-34a qRT-PCR Quality Control

(A) qRT-PCR data showing expression of miR-34a and miR-34a* in the testicles of WT and miR-34a$^{-/-}$ (KO) C57BL/6 mice fed chow for 24 weeks, using the Qiagen miScript system. Data represented as ΔCt values normalised to RNU6B, with SEM; WT: n=3 and KO: n=2. (B-C) qRT-PCR data comparing the expression of miR-34a (B) and miR-34a* (C) in the testicles of WT Vs. KO mice using the Qiagen miScript and Life Technologies (LT) TaqMan™ systems. Data is represented as Ct values with SEM and shows the mean Ct difference between WT and KO samples; n=3. (D) Representative image of genotyping gel results, PCR product was run on a 2% agarose gel with 0.2 µg/ml EtBr, at 85 V. Mice used in (A-C) are highlighted using the black boxes. (E) Representative image of the qRT-PCR product from the Life Technologies TaqMan™ system shown in (B-C), run on a 4% agarose gel with 0.2 µg/ml EtBr, at 85 V. NTC = non-template control, NoRT = no reverse transcriptase control. (F) Sequencing results from the Life Technologies TaqMan™ miR-34a qRT-PCR product observed in the KO samples in (B-C, E). 5 Colonies were picked from the cloning process with the sample KOC1 and sequenced, before the sequences were aligned to find a consensus sequence. The sequences of all the miR-34 family were aligned with this consensus sequence, but only miR-34a-5p and miR-34c-5p fully aligned, with some mismatches (grey boxes). An example sequence trace for colony 3 is shown, with miR-34c-5p mismatches highlighted by the black boxes. ***P<0.001, ****P<0.0001 unpaired, Student's t-test.

3.4.4.2 Repeat of miR-34a Expression in Diet-induced, Obese Murine Tissues Using The microRNA TaqMan™ System

The expressions of miR-34a and 34a* were re-examined using Life Technologies' TaqMan™ system in WT C57BL/6 mouse tissues, fed chow or HFD for 24 weeks (Figure 3.10). Correlating with the Qiagen miScript data, miR-34a was unchanged in the eWAT (P=0.6619), but increased in both the iBAT (P=0.0433) and liver (P=0.0088) of HFD-fed WT mice (Figure 3.10A, C, E). Additionally, miR-34a* was unchanged in the eWAT (P=0.4196) (Figure 3.10A). Surprisingly, miR-34a* transcripts were increased in both the iBAT (P=0.0399) and liver (P=0.0247) of HFD-fed WT mice (Figure 3.10C, E). To account for a background signal produced by the TaqMan™ primers for miR-34a and miR-34a*, the whole miR-34 family was examined in these tissues (Figure 3.10B, D, F). Furthermore, the other miR-34 family members (miR-34b, 34b*, 34c, and 34c*) were also examined in miR-34a$^{-/-}$ mice on chow Vs. HFD, to look for signs of regulation of these family members by miR-34a/34a*. In the eWAT, iBAT, and liver, none of the other miR-34 family members were altered in either WT or KO tissues (Figure 3.10B, D, F).

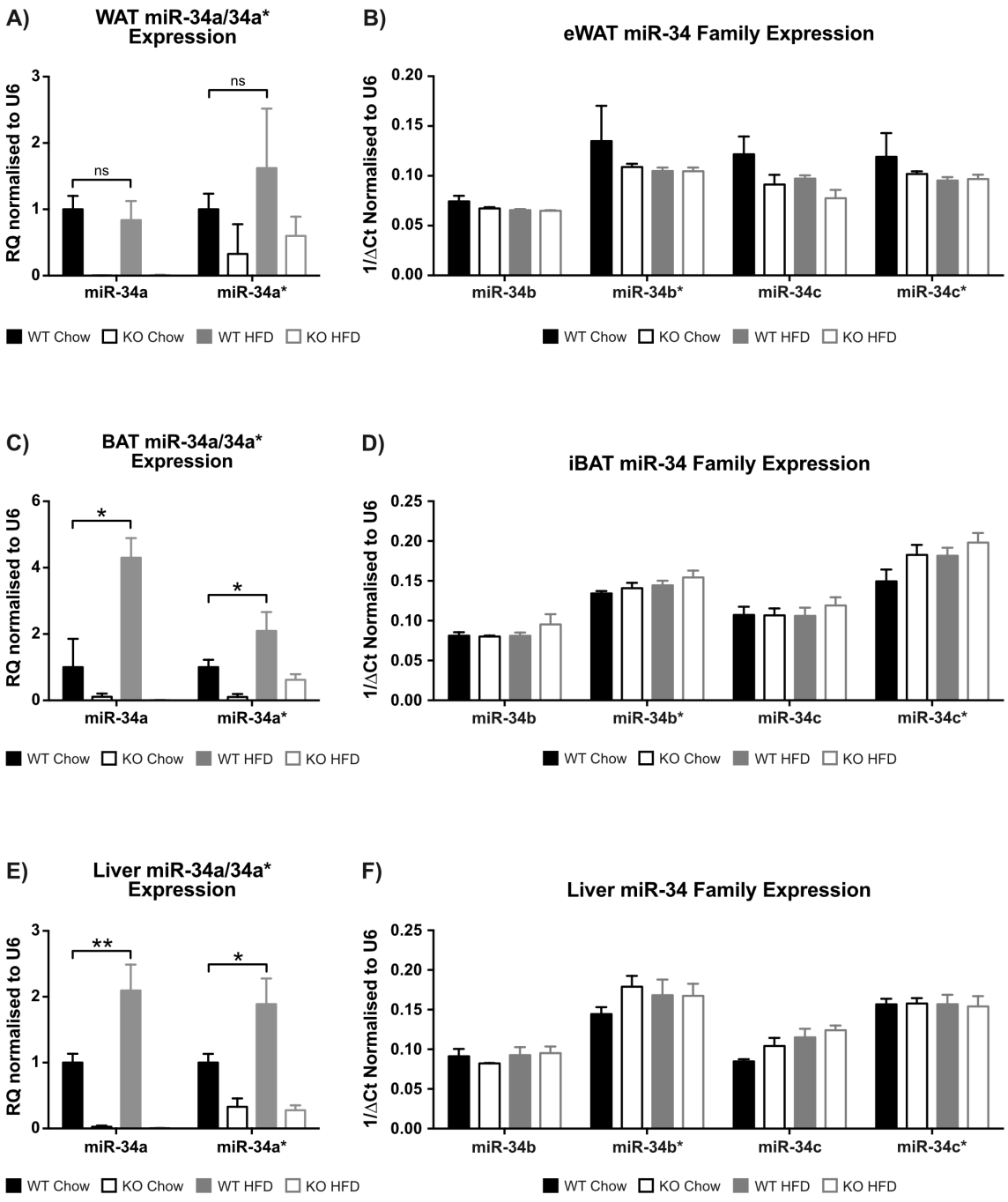

Figure 3.10: Profiling The miR-34 Family Using The TaqMan™ System In Diet-Induced Obese Mice

(A, C, E) qRT-PCR data showing the expression of miR-34a and miR-34a* in the epididymal (e)WAT (A), intrascapular (i)BAT (C), and liver (E) of WT C57BL/6 or miR-34a$^{-/-}$ (KO) mice fed chow Vs. HFD for 24 weeks. Data is represented as relative quantification (RQ) of WT chow, normalised to RNU6B, with RQ_{min} and RQ_{max} values, and statistics were calculated off ΔCt values using an unpaired student's t-test for WT data. (B, D, F) qRT-PCR data showing expression of the rest of the miR-34 family in eWAT (B), iBAT (D), and liver (F) in the same mice as (A, C, E). Data is represented as 1/ΔCt with SEM, and statistics were calculated by One-way ANOVA, with Bonferroni's multiple comparisons post-test. For all graphs eWAT: n=3-4, iBAT: n=6, and liver: n=5-6. *P<0.05, **P<0.01, ns = not significant.

3.4.5 Pilot OpenArray® Study of miRNAs in diet-induced, obese murine eWAT

In order to examine broad miRNA expression in adipose tissue, access to 3 spare Rodent MicroRNA OpenArray® Plates was kindly granted by a colleague (Dr Lorraine Work), who did not require them. This allowed a pilot study to be carried out looking at global miRNA expression in mouse eWAT. Constrained by only being able to analyse 3 samples, the RNA from 3 eWAT samples for each group were pooled together, from WT mice fed chow or HFD for 24 weeks. The HFD samples were split into a mild weight gain (WTH2: 38.43±0.45 g) and substantial weight gain (WTH1: 42.9±0.06 g) group, based on week 24 body weight, which was compared with a normal chow group (WTC1: 33.23±0.45 g). The top increased miRNAs, compared to WTC1, in both HFD groups are shown in Figure 3.11A-B and decreased miRNAs in Figure 3.11C-D. Interestingly, miR-34c* ranked as the second highest (ΔCt change: -6.80) and highest increased (ΔCt change: -7.02) miRNA in the mild (Figure 3.11A) and substantial (Figure 3.11B) HFD groups, respectively. miR-34c* was only surpassed by miR-190 (ΔCt change: -9.82) in the mild HFD group. Furthermore, miR-34b* and miR-34c were among the greatest increased miRNAs in both the mild and substantial HFD groups (Figure 3.11A-B), but only showed a modest increase of ~1 cycle with weight gain (miR-34b*: ΔCt 2.27 – 3.2; miR-34c: ΔCt 14.64 – 13.24) (Figure 3.12A). On the other hand, miR-34a barely increased during HFD feeding, showing a change below the ΔCt≤-1 cut-off (ΔCt change for mild: -0.34 & substantial: -0.36). However, miR-34a showed a high level of expression in the eWAT across groups (ΔCt: 8.06 – 8.42) (Figure 3.12A). Furthermore, miR-34b was only detectable in the substantial HFD group at lower levels (ΔCt: 19.1) (Figure 3.12A). The top decreased miRNAs were miR-1981 and miR-674 from the mild and substantial HFD group, respectively (Figure 3.11C-D).

Comparing the top ranked miRNAs that increased or decreased by greater than 2 ΔCt, compared to WTC1 control, between the two HFD groups showed some overlapping miRNAs (Figure 3.12B-C). The common increased miRNAs were: miR-34c, miR-34b*, miR-34c*, miR-135a, miR-190, miR-200b, miR-200b*, miR-200c, miR-375, and miR-429 (Figure 3.12B). The common decreased

miRNAs were: miR-18a*, miR-467b, miR-706, and miR-1981 (Figure 3.12C). Looking at changes in these miRNAs with weight gain (mild to substantial HFD groups), miR-190 (ΔCt change: -9.82 – -4.33) showed a large decrease in expression (Figure 3.12D (left)). miR-34c (ΔCt change: -2.20 – -3.61) and miR-200b (ΔCt change: -3.10 – -4.25) increased in the same data set, and the other miRNAs showed little change. Out of the common decreased miRNAs, miR-18a (ΔCt change: 2.31 – 3.22) and miR-467b (ΔCt change: 2.43 – 4.16), further decreased in expression (Figure 3.12D (right)).

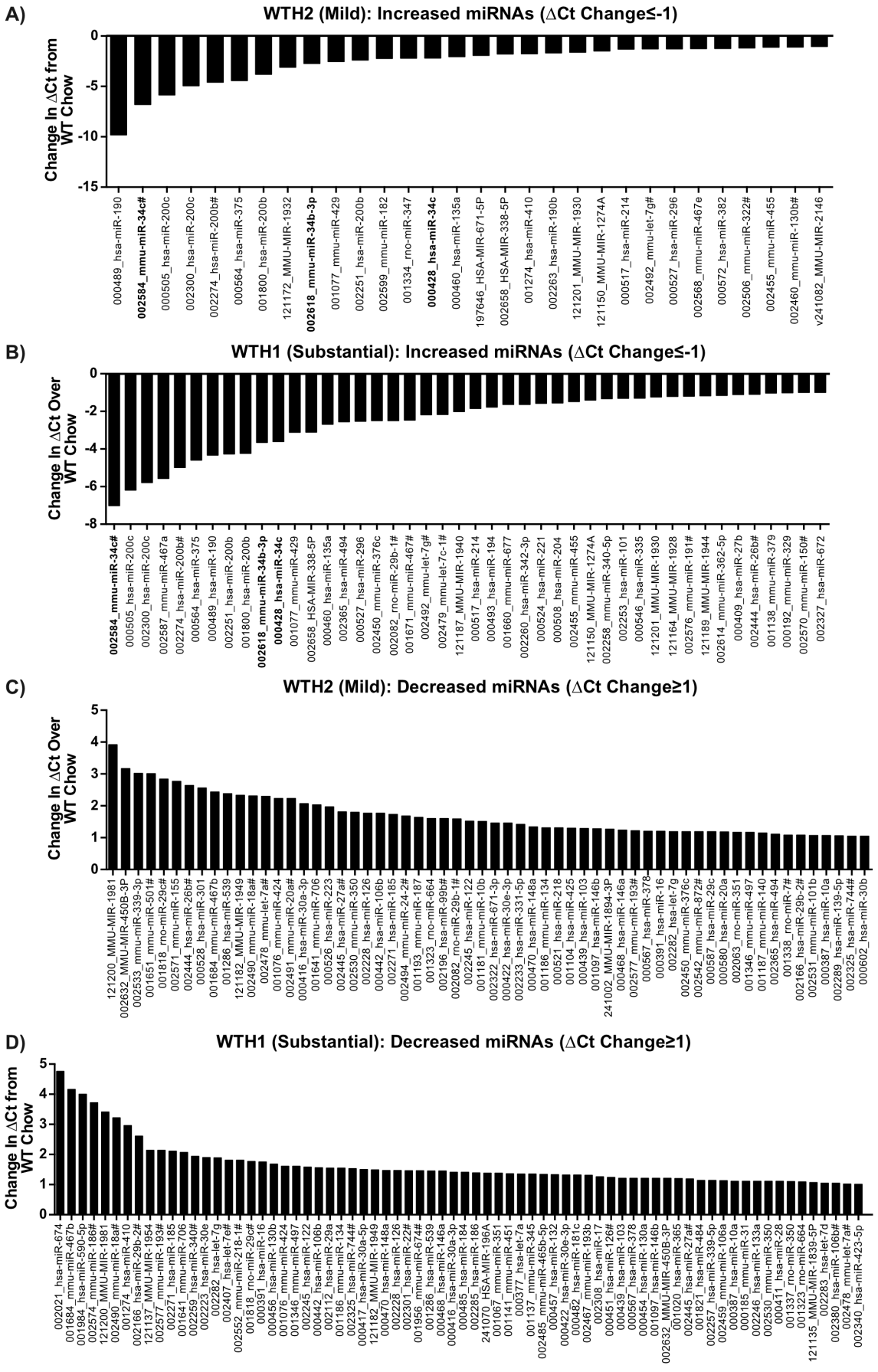

Figure 3.11: OpenArray® miRNAs Showing The Greatest Change In Obese eWAT
(A-D) OpenArray® results showing the top increased (change in ΔCt≤-1) and decreased (change in ΔCt≥1) miRNAs in eWAT from WT HFD-fed (24 weeks) mice showing mild (WTH2: 38.43±0.45 g) and substantial (WTH1: 42.9±0.06 g) weight gain, compared to chow-fed WT controls (33.23±0.45 g). Data is represented as

the change in ΔCt from WT chow group to WT HFD group, normalised to RNU6B expression, with expression for each miRNA averaged from 2 arrays; n=1 from 3 pooled samples. miR-34 family members are highlighted in bold.

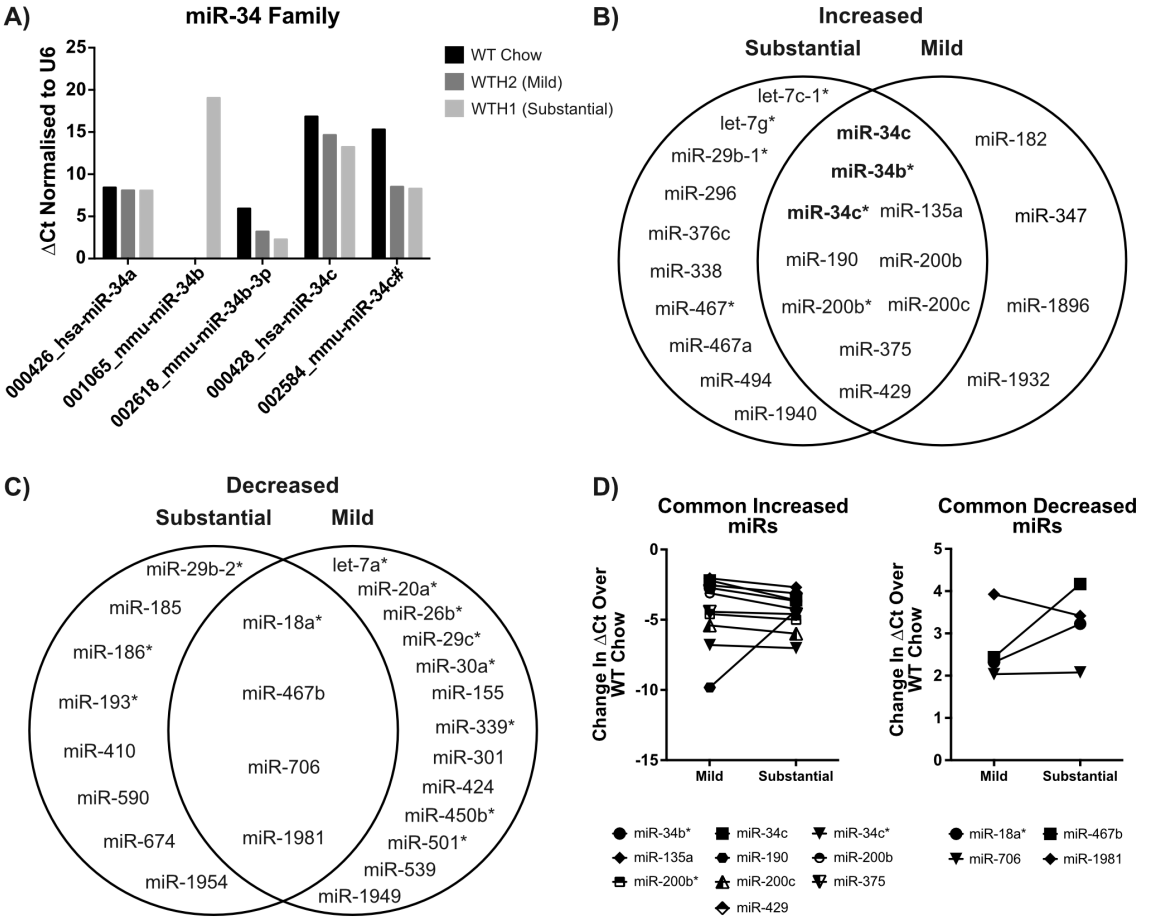

Figure 3.12: OpenArray® miRNAs Showing The Greatest Change In Obese eWAT Cont.
(A) Comparison of the expression of the miR-34 family between WT chow and HFD groups, from Figure 3.11A-B. Data is represented as ΔCt values, normalised to RNU6B, and empty values for miR-34b were replaced with an arbitrary value of ΔCt = 40. (B-C) Venn diagram showing the overlap in miRNA expression between the mild (WTH2) and substantial (WTH1) weight gain, HFD-fed groups, of the miRNAs that increased or decreased more than a ΔCt of 2, compared to WT chow. Data taken from Figure 3.11A-D. (D) Comparison between the expression of the overlapping miRNAs in (B-C). Data is represented as the change in ΔCt from WT chow group to WT HFD group, normalised to RNU6B expression, with each miRNA data point joined by a line. miR-34 family members are highlighted in bold throughout.

3.5 Discussion

In this chapter it has been shown that miR-34a is ubiquitously expressed throughout the obese murine and human visceral WAT, and that miR-34a transcripts increase in the iBAT and liver of murine models of obesity. It has also highlighted the importance of examining all the miRNAs in a family, whilst using qRT-PCR technology. Whilst profiling the expression of miR-34a in various murine tissues the kidney, heart, lung, iBAT, and eWAT showed the highest expression, with the pancreas and serum showing the lowest expression. The role of miR-34a in the kidney has not been explored in obesity or metabolic syndrome, but it has been shown to be protective in renal cell carcinoma models (Yamamura et al. 2012; Weng et al. 2014). In the heart, miR-34a has been shown to regulate cardiac regeneration and aging, decreasing cardiac regeneration and function post-myocardial infarction, and increasing age-associated cardiomyocyte apoptosis and telomere shortening (Boon et al. 2013; Yang et al. 2015). One of these studies supports the data here, by showing higher levels of miR-34a transcripts in the left ventricle than in the lung, skeletal muscle, and liver (Yang et al. 2015). However, a previous report showed higher miR-34a transcript expression in the lung than heart and kidney. The transcript expression of miR-34a in these tissues was significantly higher than that in the liver, but miR-34a transcripts in the liver were still higher than those in the skeletal muscle, correlating with the data here (Bommer et al. 2007). On the contrary, Yang et al. showed that skeletal muscle expression of miR-34a was higher than that in the liver, and Bommer et al. showed that splenic miR-34a transcripts were higher than both of these tissues (Bommer et al. 2007; Yang et al. 2015). miR-34a mimics have also been shown to reduce cancer progression in mouse models of non-small cell lung cancer (NSCLC) (Kasinski and Slack 2012; Xue et al. 2014). The role of miR-34a in WAT and BAT is still poorly understood, but it has been suggested to inhibit browning of WAT and BAT formation by suppressing fibroblast growth factor (FGF)21 signaling and SIRT1 function (Fu et al. 2014). The low expression of miR-34a in the pancreas could be protective in preserving glucose homeostasis, as miR-34a has been associated with inflammation-induced and age-related destruction of beta-islet cells, with a decline in insulin secretion (Lovis et al. 2008; Roggli et al. 2010; Tugay et al. 2016). This suggests that there could

be tissue specific functions of miR-34a. However, due to the difficulty in finding a stable reference gene for pancreatic tissue, variations in miR-34a expression between replicates could change the overall mean and inaccurately represent pancreatic expression. The pancreas is notorious for showing rapid degradation of RNA, which could explain these difficulties in finding a stable reference gene, even though miRNAs remain stable during total RNA degradation (Jung et al. 2010). To counteract this, the data could have been normalised to the mean of multiple reference genes (Nolan et al. 2006) or the "relative expression ratio" method (Pfaffl 2001) could have been used. Additionally, some of the expression differences between tissues could be due to use of the Qiagen miScript system for miR-34a profiling, which was shown to have specificity issues later in the chapter. However, others have published data using this system and primers for miR-34a (Zauli et al. 2011; Kasinski and Slack 2012; Do et al. 2014).

Interestingly, ISH showed that miR-34a was ubiquitously expressed throughout murine and human vWAT, but with darker staining in the adipocyte nucleus. This darker nuclear staining could indicate hybridisation of the miR-34a probe with the primary miR-34a transcript, before cleavage and export from the nucleus. The dark staining within the murine epididymal tissue and blood vessels are useful positive controls. Other studies have shown the miR-34a is highly expressed in primary human endothelial cells and increases in human, atherosclerotic arteries (Ito et al. 2010; Raitoharju et al. 2011). Additionally, miR-34a is highly expressed in mouse testes, but not as highly as miR-34b and c (Dutta et al. 2007; Bao et al. 2012). Unfortunately, there was very little change in miR-34a staining intensity and localisation between non-obese and obese tissues; however, this is supported by the murine eWAT qRT-PCR data. One exception, is the observed decrease in miR-34a transcripts within 12-week-old *ob/ob* mice demonstrated by qRT-PCR, which is not reflected in the ISH staining; however, the latter is only a semi-quantitative method that would not reveal subtle differences in expression.

The decrease in 12-week-old *ob/ob* eWAT miR-34a transcript levels is surprising, as it was expected that miR-34a transcripts would increase during obesity. Additionally, this was not reflected in the WT diet-induced obesity model,

where no change in miR-34a transcripts were observed. However, the results from the diet-induced obesity model do correlate with a previous study that found a correlation between increasing BMI and miR-34a in human scWAT, but not omental vWAT (Klöting et al. 2009). Conversely, another study showed an increase in miR-34a transcripts in murine WAT during HFD-feeding, but the authors do not state which depot they used for this comparison (Fu et al. 2014). Therefore, there could be differences in miR-34a expression depending on which WAT depot is being examined. The discrepancy in eWAT miR-34a expression between *ob/ob* and diet-induced obese mice could be due to ablated leptin responses in *ob/ob* mice. However, breast cancer studies have found that leptin inhbits miR-34a expression in breast tumours from HFD-fed mice *ex vivo* and in breast cancer cell lines *in vitro*, contributing to tumour progression (Avtanski et al. 2015a; 2015b). The other possibility is that the Qiagen miScript qRT-PCR system produced some aberrant values, but when miR-34a measurement was repeated in the mouse diet-induced obesity samples, with the MicroRNA TaqMan® system, the expression profile was the same. Additionally, the RNA integrity number (RIN) values for the *ob/ob* study samples were moderate during Agilent testing, suggesting some degradation of the RNA. On the other hand, miR-34a transcripts were increased with weight gain in the iBAT and liver, of both *ob/ob* and diet-induced, obese WT mice. Curiously, the increased miR-34a transcripts within the *ob/ob* liver were only observed at 9 weeks of age, with a decrease back to WT control levels by 12 weeks of age. It is possible, that in the liver another regulatory system inhibits hepatic miR-34a expression with further weight gain. These data correlate with observations by others, showing miR-34a increases in the BAT of HFD-fed mice and in the liver of *ob/ob* and diet-induced, obese mice (Lee et al. 2010; Fu et al. 2012; Choi et al. 2013; Fu et al. 2014).

The expression of miR-34a* is not as straightforward, only following the same pattern as miR-34a in iBAT of 12-week-old *ob/ob* mice. However, miR-34a* still decreased in *ob/ob* eWAT, but only significantly in 9-week-old mice; it was significantly increased in *ob/ob* liver of 12-week-old *ob/ob* mice. In both these cases miR-34a* could counter-regulate or be regulated by its mature strand, with changes preceding and succeeding expression changes in miR-34a. There is little literature on the function of miR-34a*, with only one validated target (as far as is

known): X-linked inhibitor of apoptosis protein (XIAP) (Niederer et al. 2012). However, one study suggests that synthetic miR-34a and miR-34a* mimics work in synergy to regulate TNFα expression in primary, human monocyte-derived macrophages, with miR-34a acting indirectly (through NOTCH1) and miR-34a* directly (Guennewig et al. 2014). Additionally, the authors showed that endogenous miR-34a and 34a* were co-expressed in a ratio of 1:3-3:1, in these primary macrophages. Therefore, the expression changes in miR-34a* could be acting to enhance regulatory effects of miR-34a in *ob/ob* mouse tissues. The story in WT diet-induced obese mouse tissues is not as clear. Only once miR-34a* expression was re-examined using microRNA TaqMan® assays was it discovered that miR-34a* was also up-regulated in obese iBAT and liver tissue. However, this could be due to this method's increased sensitivity, by using a stem-loop primer with greater specificity for the target miRNA (Chen 2005). Even then, as has been shown, off-target effects with family members still occur. Therefore, miR-34a* could be acting in synergy with miR-34a in the eWAT, iBAT, and liver of obese mice. Using synthetic mimics and anti-miRs *in vivo* and in specific *in vitro* cell types could help to identify if these microRNAs co-regulate pathways during obesity.

Interestingly, the pilot OpenArray® data showed that miR-34c, 34b*, and 34c* were commonly up-regulated in the eWAT of both HFD-fed groups, which was not seen using qRT-PCR in the same samples. At the same time, miR-34a did not alter during HFD-feeding, but was still highly expressed, correlating with qRT-PCR results. This highlights some of the issues with broad screening methods, where the results cannot always be validated. The OpenArray® system relies on the same technology as qRT-PCR, bringing with it the same miRNA analysis issues. miRNA profiling can be challenging due to their small size of ~22 nucleotides, which makes it difficult to create specific PCR primers for reverse transcription and qPCR (Baker 2010; Pritchard et al. 2012). Additionally, miRNAs can be part of families that can differ by as little a one nucleotide, making it difficult to discriminate between them (Chen 2005), which has already been shown here with the miR-34 family. Further complexity is added by heterogeneity in the individual miRNA sequence between cell types and physiological states, representing isomiRs (Cloonan et al. 2011; Wyman et al. 2011). These isomiRs

mainly consist of nucleotide additions or subtractions at the 3' end of the miRNA sequence, but can also consist of nucleotide additions or subtractions at the 5' end, although these are uncommon (Chiang et al. 2010; Newman et al. 2011). Furthermore, when profiling hundreds of miRNAs miRNA-specific biases can occur, due to optimal reaction conditions varying considerably between miRNAs. These include sequence-specific differences in primer annealing and variability in GC content causing vast differences in melting temperature (T_m) (Pritchard et al. 2012). RNA-Seq using next-generation sequencing could be a viable option to get a more accurate miRNA profile, with the ability to discriminate between single nucleotide differences in miRNAs. However, this technique is not without its drawbacks too, including a high cost, a need for bioinformatic analysis to identify miRNAs, small RNA library-preparation steps can cause sequence-specific biases, inability to provide absolute quantification, and limited normalisation methods (Linsen et al. 2009; Meyer et al. 2010; Pritchard et al. 2012).

The other common increased miRNAs in the two HFD groups from the OpenArray® were: miR-135a, miR-190, miR-200b, miR-200b*, miR-200c, miR-375, and miR-429. Out of these miRNAs, only miR-200b, miR-200c, miR-375, and miR-429 have previously been shown to be dysregulated during obesity, but few have been examined in vWAT (Poy et al. 2009; Dou et al. 2013; Crépin et al. 2014). Both miR-200b and miR-429 were shown to be up-regulated in the hypothalamus of *ob/ob* mice, whereas another study showed down-regulation of the whole miR-200 (a, b, and c) family in the liver of *db/db* mice (Dou et al. 2013; Crépin et al. 2014). However, microarray analysis by the authors also showed up-regulation of miR-200c and no change in miR-429 in the same liver tissue, which could not be validated (Dou et al. 2013). In contrast, the expression of miR-200b has been observed to decrease in the eWAT of *ob/ob* mice and omental WAT from patients with obesity and T2D, but not obese non-diabetics (Oger et al. 2014).

miR-375 expression has been reported to increase in the BAT of high-fat, high-sugar (HFHS)-fed WT mice and in the serum of patients with obesity and T2D Vs. obese non-diabetics, but remain unchanged in HFHS WAT (Higuchi et al. 2015). However, this miRNA has been shown to promote white adipocyte

differentiation through suppression of extracellular-signal-regulated kinase (ERK)1/2 phosphorylation, in the 3T3-L1 pre-adipocyte cell line (Ling et al. 2011). Additionally, miR-375 increases in *ob/ob* mice pancreatic islets, and has been suggested to be pivotal for normal glucose homeostasis. miR-375 KO-*ob/ob* mice showed a severe diabetic-state, with severe reduction in β-cell mass (Poy et al. 2009). Surprisingly, miR-190, which showed the greatest change between the HFD groups, has not been previously shown to be dysregulated during obesity.

The common decreased miRNAs in the two HFD groups from the OpenArray® were miR-18a*, miR-467b, miR-706, and miR-1981. Of these, only miR-467b has been previously observed to change during obesity, decreasing in the liver of WT HFD-fed mice (Ahn et al. 2011). The authors also showed that miR-467b targets lipoprotein lipase (LPL) in a murine hepatocyte cell line. Additionally, miR-467b has been shown to be atheroprotective, reducing lipid uptake in macrophage cell lines *in vitro* and atherosclerotic plaques *in vivo*, by suppressing lipoprotein lipase (LPL) gene translation (Tian et al. 2012; 2014). Therefore, the reduced expression of miR-467b observed in the eWAT during HFD-feeding could increase adipocyte lipid uptake, by increasing LPL expression. On the other hand, miR-706 has been shown to be up-regulated by the saturated fatty acid, palmitic acid, in a mouse myoblast cell line, but reduced in combination with mono-unsaturated, oleic acid (Li et al. 2011b).

It is worth noting, that one major drawback from this pilot study OpenArray® screen is the lack of statistical analysis, due to the limited number of samples that could be examined. This makes it difficult to draw conclusions from this data, with the inability to resolve true changes from inherent noise in the system. Therefore, the common increased and decreased miRNAs within the eWAT of HFD-fed mice could be novel targets for modulating obesity co-morbidities. However, without proper statistical analysis and validation it makes it difficult to decide whether they are “true” differences that should be explored further.

In conclusion, miR-34a is ubiquitously expressed throughout murine eWAT and human omental WAT, independently of obesity. Additionally, during murine obesity miR-34a remains stationary in the eWAT, but increases in the iBAT and

liver, with a similar expression of miR-34a* observed. It has also become clear that the methods used for miRNA quantification have to be carefully examined, especially when they are in a family, to make sure an accurate reading is being made.

Chapter 4: miR-34a$^{-/-}$ Mice Are Susceptible to Diet-Induced Obesity

4.1 Introduction

The role of microRNA (miR)-34a during obesity and in particular in the inflammatory context of obesity is poorly understood. However, from the previous chapter it has become clear that miR-34a is ubiquitously expressed throughout epididymal white adipose tissue (eWAT) from murine models of obesity and omental WAT from patients with obesity. Additionally, miR-34a transcripts are increased in the liver and brown adipose tissue (BAT) of obese mice. Though miR-34a's mechanism of action in the obese adipose is poorly understood, a number of studies have implicated miR-34a in the regulation of glucose metabolism. Diabetes studies have shown that miR-34a can regulate pancreatic beta-islet cell death, induced by saturated fatty acids (FAs; e.g. palmitic acid and stearic acid) and the inflammatory cytokine interleukin (IL)-1β, by targeting the anti-apoptotic genes B cell CLL/lymphoma 2 (BCL-2) and BCL-2-like 2 (BCL-L2) (Lovis et al. 2008; Roggli et al. 2010; Lu et al. 2016). Additionally, miR-34a has been shown to mediate the age-associated decline in proliferation and increased apoptosis in human and rat *ex vivo* beta-islet cells, through direct targeting of platelet-derived growth factor receptor (PDGFR)α (Tugay et al. 2016). In terms of direct effects on metabolism, miR-34a has been shown to decrease beta-islet cell insulin secretion by blocking vesicle fusion, through targeting vesicle-associated membrane protein (VAMP)2 (Lovis et al. 2008; Roggli et al. 2010). Furthermore, miR-34a has been shown to regulate glucose metabolism in cancer cells *in vitro* by targeting the glycolytic enzymes: hexokinase (HK)1, HK2, and glucose-6-phosphate isomerase (GPI), and pyruvate dehydrogenase kinase isoform (PDK)1 (Kim et al. 2013b). This suggests that miR-34a may have a role in the regulation of adipose glucose homeostasis, warranting further investigation.

A number of studies have also explored the pathological role of miR-34a in non-alchoholic fatty liver disease (NAFLD). Studies have shown that miR-34a is up-regulated in the livers of *ob/ob* mice and diet-induced obese BALB/c mice, and inhibits hepatic: silent mating type information regulation 2, *S. cerevisiae*, homolog (SIRT)1, in a process regulated by farnesoid X receptor (FXR). miR-34a inhibition was shown to improve the HFD liver phenotype by decreasing hepatic and plasma TG levels, and gene transcripts involved in ER stress, inflammation (*tumour*

necrosis factor (*Tnf)α* and *Il6*), lipogenesis, and *Cd36*, whilst increasing β-oxidation gene transcripts and improving systemic insulin resistance (Lee et al. 2010; Choi et al. 2013). Moreover, inhibition of miR-34a by ursodeoxycholic acid reduced free-FA (FFA)-induced apoptosis in primary rat hepatocytes *in vitro*, supporting a role for miR-34a in exacerbating the progression of NAFLD (Castro et al. 2012). Furthermore, miR-34a has not only been shown to directly regulate SIRT1 transcripts in the liver, but can also inhibit SIRT1 function by targeting the rate-limiting enzyme in NAD^+ biosynthesis: Nicotinamide Phosphoribosyltransferase (NAMPT) (Choi et al. 2013). Additionally, miR-34a has been shown to inhibit the protective effects of fibroblast growth factor (FGF)19 on NAFLD development in diet-induced obese mice, by targeting the FGF receptor (FGFR)4 coreceptor β-Klotho (βKL) in hepatocytes (Fu et al. 2012). Through targeting NAMPT and βKL, miR-34a was shown to contribute to hepatic steatosis, inflammation, and impaired systemic glucose tolerance. Another study by Ding et al. suggests that miR-34a's inhibition of peroxisome proliferator-activated receptor (PPAR)α also contributes to liver steatosis (Ding et al. 2015). Therefore, these studies show that miR-34a is involved in promoting a poorer liver phenotype during rodent obesity.

The role of miR-34a in adipose tissue during obesity has been poorly investigated. However, inhibition of SIRT1 in adipocyte cell lines significantly increases expression of PPAR-ɣ and the other adipogenic markers: CCAAT-enhancer-binding protein (C/EBP)α and fatty acid binding protein (FABP)4 (Puri et al. 2012). C/EBPα has also been shown to promote miR-34a expression during granulopoiesis (Pulikkan et al. 2010). Additionally, acyl-CoA synthetase long-chain family member (ACSL)1 and 4 are validated targets of miR-34a, that are involved in triglyceride (TG) synthesis (Kaller et al. 2011; Li et al. 2011a). Interestingly, the adipokine leptin has been shown to reduce miR-34a expression in breast cancer cell lines (Avtanski et al. 2015a). This suggests that miR-34a could have a role in regulating adipocyte metabolism.

Cross-talk between metabolic tissues and the immune system during obesity have become an area of great focus. Currently, there are no studies that have looked directly at miR-34a's regulation of the inflammatory environment within

obese adipose. However, a few studies have been published that suggest miR-34a has a role in regulating inflammatory processes. In mice treated with the bacteria *Corynebacterium (C). parvum*, to induce inflammation, an upregulation in miR-34a transcripts was observed in the spleen (Mathé et al. 2012). An Ago pull-down study for miR-34a in two cancer cell lines identified the anti-inflammatory cytokine transforming growth factor (TGF)-β, FGFs, FGFRs, and the insulin receptor as potential targets of miR-34a (Lal et al. 2011). Furthermore, miR-34a has been shown to directly target the regulatory T (T_{reg}) cell chemoattractant CCL22, and inhibit TGF-β-induced CCL22 recruitment of T_{regs}, in an *in vitro* and *in vivo* portal vein tumor thrombus (PVTT) model. TGF-β and miR-34a were also shown to be part of a feedback-loop, where TGF-β inhibits miR-34a expression (Yang et al. 2012; He et al. 2015). On the contrary, lipopolysaccharide (LPS) has been shown to inhibit miR-34a, preventing CCL22 inhibition in RAW264.7 macrophages (He et al. 2015). This correlates with observations by Jiang et al. who showed that LPS-induced inflammation reduced miR-34a expression, in the same cell line (Jiang et al. 2012). The authors additionally showed that miR-34a mimics reduced LPS-induced expression of IL-6 and TNFα by targeting Notch1. In cancer cells, IL-6 signaling is inhibited by miR-34a targeting gene transcripts of the membrane-bound and soluble IL-6 receptor, with IL-6 signaling inhibiting miR-34a transcription through activation of STAT3 in a feed-back loop (Rokavec et al. 2014b; Li et al. 2015). Finally, transfection of pre-miR-34a into human hepatocytes increases expression of metalloproteinase (MMP)2 and 9, usually associated with an M2 macrophage phenotype (Meng et al. 2012). Therefore, there is conflicting evidence showing that miR-34a can regulate both inflammatory and anti-inflammatory pathways.

In summary, there are conflicting studies showing that miR-34a can regulate both inflammatory and anti-inflammatory pathways, as well as metabolic pathways. Thus, the *in vivo* effects of miR-34a deficiency on inflammatory and metabolic pathways during obesity warrants further investigation. Therefore, it is hypothesised that miR-34a has a role in regulating diet-induced obesity, through regulation of metabolic and inflammatory pathways within the adipose tissue.

4.2 Aims

- Explore the role of miR-34a during murine, diet-induced obesity using an *in vivo* miR-34a$^{-/-}$ (KO) model.

- Examine the metabolic phenotype of adipose tissue, particularly eWAT, in this *in vivo* model.

- Examine the immune phenotype of miR-34a$^{-/-}$ mice during diet-induced obesity, particularly the macrophage phenotype within eWAT.

4.3 Methods

For specific details of individual methods please refer to Chapter 2: Materials and Methods.

4.3.1 Mouse Studies

All the results in this chapter are from *in vivo* studies on 7-week-old, male, wild type (WT) or miR-34a$^{-/-}$ (B6.Cg-Mir34a^{tm1Lhe}/J) C57BL/6 mice, described in section 2.2.1. Mice were fed a normal chow or high-fat diet (HFD), ad libitum for 24 weeks. During this period, weekly weights, monthly fasting blood glucose (FBG), and glucose tolerance test (GTT) measurements, at 12 and 24 weeks, were recorded (Figure 4.1), as described in section 2.2.1.2. Glucose was administered at 2 g/kg and 1 g/kg of body weight for the week 12 and 24 GTTs, respectively.

Figure 4.1: *In vivo* miR-34a$^{-/-}$ Obesity Study Design

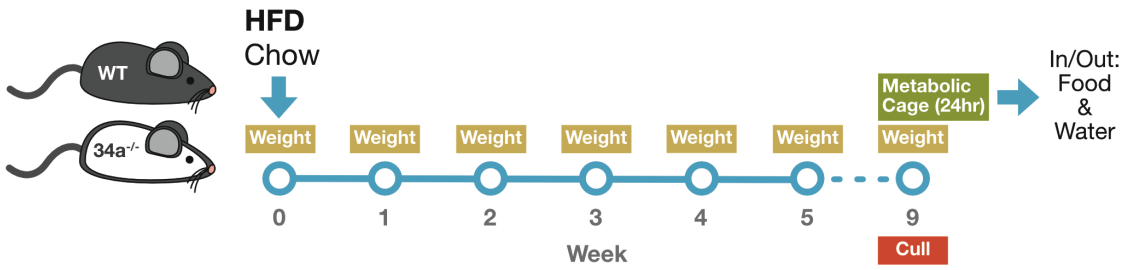

Figure 4.2: *In vivo* miR-34a$^{-/-}$ Metabolic Cage Study Design

Metabolic cage studies were carried out on miR-34a$^{-/-}$ and WT mice on chow or HFD, to monitor food and water consumption and excretion over 24 hours

(Figure 4.2), as described in section 2.2.1.3. At the end of the study, mice were euthanised by Avertin, or terminal CO_2 for the metabolic cage study, and tissues collected. Whole blood was collected by cardiac puncture, with eWAT, liver, intrascapular (i)BAT, pancreas and spleen additionally collected for further analysis. Snout-anus length and organ weight were also recorded. All the mice in the study were genotyped using tail-tip biopsies (as described in section 2.3.6) to confirm their KO and WT status (Figure 4.3).

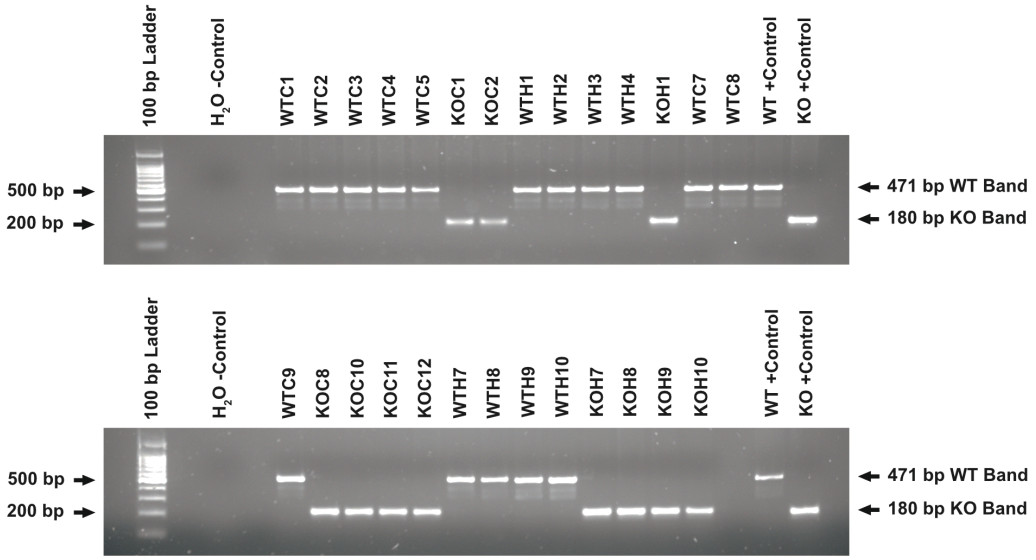

Figure 4.3: Representative Gel Images of *in vivo* miR-34a$^{-/-}$ Obesity Study Genotyping
PCR product was run on a 2% agarose gel with 0.2 µg/ml EtBr, at 85 V. WT = wild type, KO = miR-34a$^{-/-}$, C = chow, and H = HFD in the naming convention.

4.3.2 Magnetic Resonance Spectroscopy

Mouse percentage body fat was quantified using magnetic resonance spectroscopy (MRS) in terminally anesthetised mice, as described in section 2.2.1.4. This was carried out in collaboration with Dr William M. Holmes.

4.3.3 Serum Analysis

Serum was isolated from whole blood, aliquoted and stored at -80°C as described in section 2.2.3. 150 µl was used to measure serum lipid and cholesterol using the ILAB 600 clinical chemistry analyser (section 2.2.3.1). This was carried out in collaboration with Professor Muriel Caslake, who kindly granted access to the ILAB 600 and her technician Mrs Josephine Cooney. The remaining serum was used for Luminex analysis. 50 µl of serum was used for both the Mouse

Cytokine 20-Plex Panel and Mouse Adipokine Milliplex, described in section 2.2.3.2.

4.3.4 Histology

Frozen Liver sections and paraffin eWAT and pancreatic tissue sections were fixed and prepared as described in section 2.4.1. To examine tissue morphology, sections were stained following the Haematoxylin and Eosin (H&E) protocol (section 2.4.2), and liver fibrosis was examined by Masson's Trichrome staining (section 2.4.3). Images were taken of all sections with an Olympus BX41 microscope with 40X Olympus Uplan FLN Objective, except for eWAT sections, taken on an EVOS XL Core microscope with 40X Olympus Uplan FLN Objective, described in section 2.4.6. eWAT H&E images were quantified for cell area and number as described in section 2.4.7.

4.3.5 Gene Expression

Gene expression was quantified from tissues using the Qiagen reverse transcription (RT) kit and Life Technologies' Gene Expression TaqMan® qPCR system (section 2.3.4). 10ng cDNA was used for each gene expression assay and a list of the gene expression assays used are shown in Table 4.1.

Probe	Cat no.	Probe	Cat no.	Probe	Cat no.
18s rRNA	Mm03928990_g1	Cyp7a1	Mm00484150_m1	Fasn	Mm00662319_m1
Fabp4	Mm00445878_m1	Arg1	Mm00475988_m1	Cd36	Mm01135198_m1
Pparɣ	Mm01184322_m1	Pck1	Mm01247058_m1	Ccl2	Mm00441242_m1
Cebpα	Mm01265914_S1	Chi3l3	Mm00657889_mH	Lpl	Mm00434764_m1
Sirt1	Mm00490758_m1	Il-6	Mm00446190_m1	Il-10	Mm01288386_m1
Accα	Mm01304257_m1	Nos2	Mm01309897_m1	Cxcl1	Mm04207460_m1
Cpt1a	Mm01231183_m1	Retnla	Mm00445109_m1	Ucp1	Mm01244861_m1
Crot	Mm00470079_m1	TNFα	Mm00443260_g1	Col3a1	Mm01254476_m1
Hmgcr	Mm01282499_m1	Pparδ	Mm01305434_m1	Col1a1	Mm00801666_g1
Lxrα	Mm00443451	Cebpβ	Mm00843434_s1		
Srebf1	Mm00550338_m1	Pgc1α	Mm00447183_m1		

Table 4.1: List of Life Technologies TaqMan® Probes Used In This Chapter

4.3.6 Flow Cytometry

Leukocytes were isolated from the spleen and eWAT for surface marker staining and quantification by flow cytometry. eWAT leukocytes held within the stromal vascular fraction (SVF) were isolated following the steps detailed in section 2.2.2.1. Leukocytes were liberated from the spleen using a 1 ml syringe plunger and 70 μm filter (Corning: 352350). Cells were pushed through the filter into RPMI 1640 (Life Technologies: 31870-025) wash media (1% pen-strep (Life Technologies: 15140-122)) in a petri dish. The cell suspension was collected and washed with wash media, centrifuging at 478 x g for 5 minutes. Next, the cell pellet was resuspended in 2 ml Red Blood Cell Lysis Buffer (Sigma-Aldrich: R7557) for 2 minutes, before being washed again as above. Finally, the cell pellet was resuspended in 1 ml wash media.

Cells were stained and analysed as detailed in section 2.5.2, with the following antibodies (detailed in Table 2.21): F4/80-APC, CD45-APC-Cy7, CD86-PE-Cy7, CD11b-PE-Cy7, CD80-PerCP-Cy5.5, CD69-PerCP-Cy5.5, Ly-6g/Ly-6c-PerCP-Cy5.5, CD11c-FITC, CD206-PE, MHC Class II-PE, TLR2-PE, CD3-FITC, CD19-PerCP-Cy5.5, CD4-PE, CD8a-APC and CX3CR1-PE. Compensation was calibrated using single-stain controls and analysis gates were set using fluorescence minus one (FMO) controls.

4.4 Results

4.4.1 miR-34a$^{-/-}$ Mice Showed Increased Susceptibility to Diet-Induced Obesity

Observations showing ubiquitous expression of miR-34a within the eWAT and upregulation of transcripts within the liver and iBAT upon HFD-feeding (Chapter 3), prompted the induction of diet-induced obesity in miR-34a$^{-/-}$ (KO) mice. Initial observations revealed that miR-34a$^{-/-}$ mice were already heavier than WT counterparts at day 0 of the study, before HFD-feeding began (Figure 4.4A). However, the only statistically significant difference was between the HFD assigned groups (KO: 23.66 ± 0.32 g Vs. WT: 21.89 ± 0.54 g; P=0.0377) and not the chow groups (KO: 23.98 ± 0.59 g Vs. WT: 22.47 ± 0.36 g; P=0.1311). When fed HFD, miR-34a$^{-/-}$ mice were significantly heavier (9.22 ± 0.56%; P=0.0075) over the 24-week period than WT counterparts, by area under the curve (AUC) analysis (Figure 4.4B). This was not reflected in the chow groups, where miR-34a$^{-/-}$ mice were only 3.83 ± 0.35% (AUC: P>0.9999) heavier than their WT counterparts, over the same period. We did not see any difference in fasting blood glucose between HFD-fed WT and miR-34a$^{-/-}$ mice (Figure 4.4C) over the course of the study. However, both of the HFD groups showed greatly increased fasting blood glucose at week 12 onwards (P<0.0001). Additionally, GTTs were carried out at weeks 12 and 24 of the study. Initially, glucose was administered at 2g/kg body weight for the week 12 GTT, but this was reduced to 1g/kg body weight for the week 24 GTT. This was due to the higher glucose dosage frequently taking blood glucose concentrations above the threshold of the glucose meter (33.33 mmol/L) for HFD mice and long periods for blood glucose reduction. In both the week 12 and 24 GTT, no change in glucose handling was observed between WT and miR-34a$^{-/-}$ mice (Figure 4.4D-E), except between chow groups at week 12 (P=0.0271; Figure 4.4D). However, glucose clearance was significantly reduced in both WT and miR-34a$^{-/-}$ mice fed HFD, at both the week 12 (P=0.0045; Figure 4.4D) and 24 (P=0.0072; Figure 4.4E) GTT. Correlating with the lack of an observable difference in glucose handling between WT and miR-34a$^{-/-}$ mice, we did not see any beta-islet cell hyperplasia in the pancreas (Figure 4.4F).

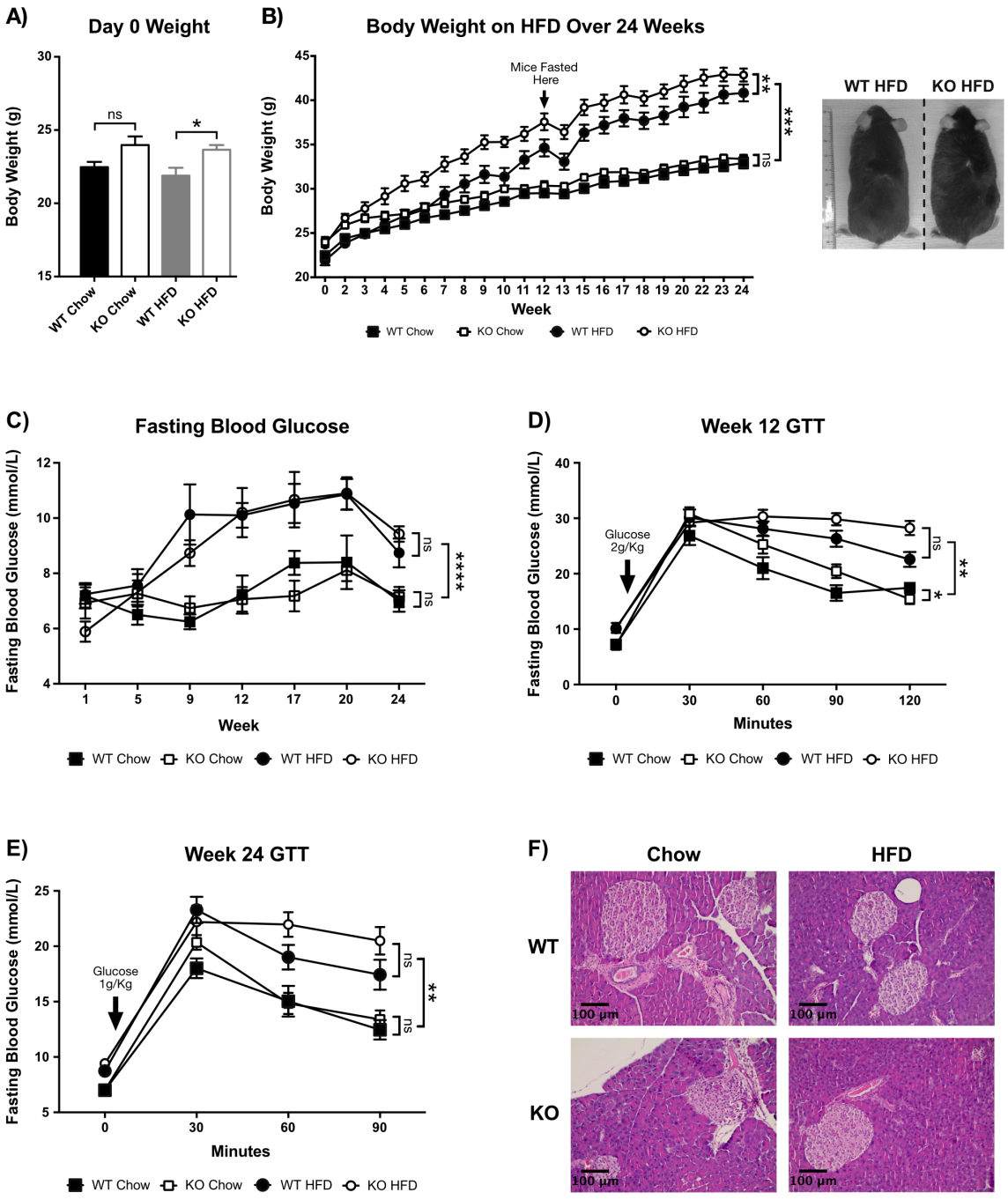

Figure 4.4: miR-34a$^{-/-}$ Mice Are More Susceptible to Diet-Induced Obesity, Without Glucose Handling Effects

(A) Starting body weight measurements at day 0 of WT and miR-34a$^{-/-}$ (KO) mice allocated to chow Vs. HFD, before diet start; n=10 for KO Chow and WT HFD, and n=9 for WT chow and KO HFD groups. (B) Body weight measurements over 24 weeks for groups in (A), including a representative image of HFD-fed WT and miR-34a$^{-/-}$ (KO) mice at week 24 of the study. (C) Monthly, fasting blood glucose measurements after a 16-18 hour fast of mice in (A); n=10 for KO Chow and WT HFD, and n=9 for WT chow and KO HFD groups. (D-E) GTT fasting blood glucose measurements following a 16-18 hour fast of mice in (A), with an I.P. injection of glucose (arrow) at 2-1 g/kg of body weight after 0 minutes, at week 12 and 24 of study; n=9 for all groups, except n=10 for WT HFD group. (F) Representative images of H&E stained pancreatic tissue at 20X from the mice in (A), at end of the study (week 24), with a 100 μm scale bar. All graphs represent mean values with SEM and statistics were calculated off AUC analysis of each replicate, except for (A). *P<0.05, **P<0.01, ***P<0.001, ****P<0.0001, ns = not significant: One-way ANOVA, with Bonferroni's multiple comparisons post-test (A-B) and Two-way ANOVA, with Sidak's multiple comparisons post-test (C-E).

Additionally, after 24 weeks the fasting serum concentration of insulin did not change between groups (Figure 4.5A), and fasting serum resistin (Figure 4.5B) only increased upon HFD-feeding in both WT (P=0.0010) and miR-34a$^{-/-}$ mice (P=0.0039). This was accompanied by no difference in fasting serum leptin (Figure 4.5C) between WT and miR-34a$^{-/-}$ mice; however, HFD feeding increased leptin levels in both groups ~3-fold (P<0.0001). Surprisingly, despite finding HFD-fed miR-34a$^{-/-}$ mice to be heavier than their WT counterparts, their total body fat percentage did not differ by MRS analysis (KO: 43.49 ± 0.68% Vs. WT: 41.69 ± 1.04%; Figure 4.5D). However, as expected, HFD-feeding significantly increased total body fat percentage in both groups (P<0.0001).

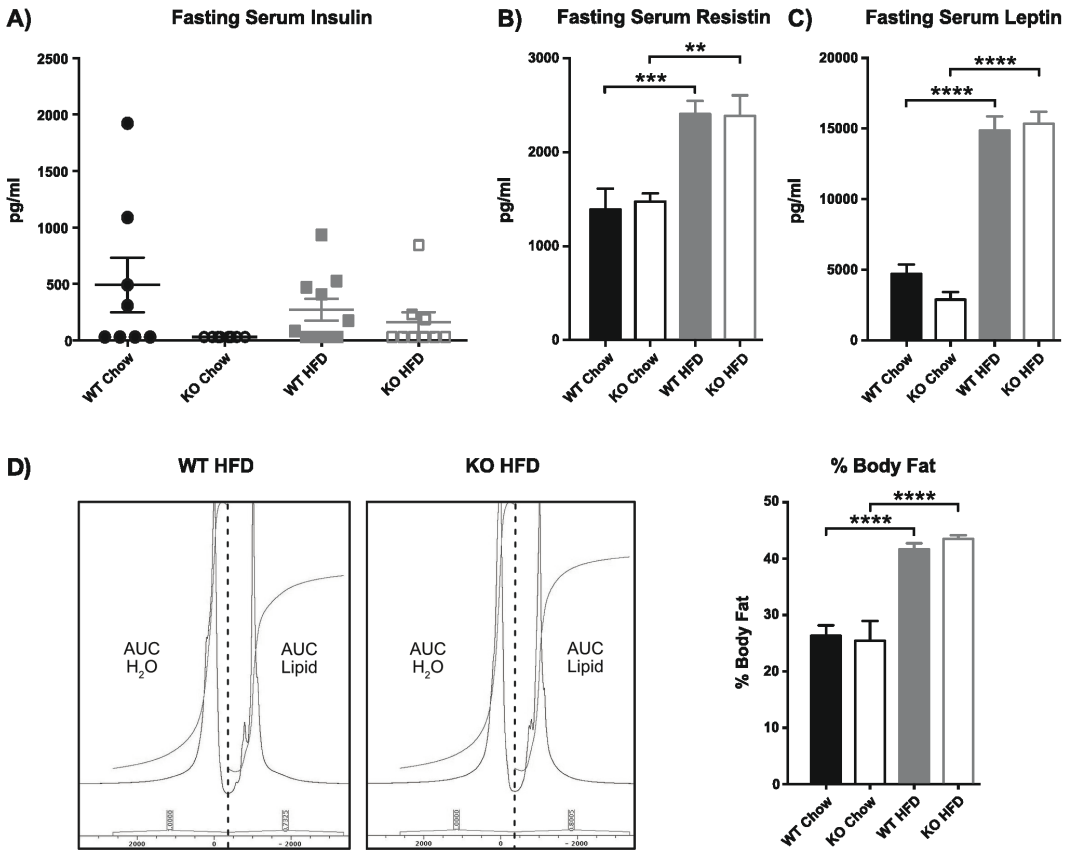

Figure 4.5: miR-34a$^{-/-}$ Mice Showed No Change in Serum Adipokines or Total Body Fat Percentage

(A-C) Adipokine luminex measurements of insulin, resistin, and leptin from fasting (16-18 hours) serum of WT and miR-34a$^{-/-}$ (KO) mice on chow Vs. HFD, after 24 weeks; n=8 for WT and KO Chow groups, n=9 for WT HFD and n=10 for KO HFD groups. (D) MRS data of the same mice as in (A-C) showing representative water (AUC_{H2O}) and lipid (AUC_{Lipid}) peaks of HFD-fed groups and quantification of all groups by AUC analysis; n=6 for WT chow and HFD, n=4 for KO HFD, and n=3 for chow HFD groups. All graphs represent mean values with SEM. **P<0.01, ***P<0.001, ****P<0.0001 One-way ANOVA, with Bonferroni's multiple comparisons post-test.

To examine whether miR-34a$^{-/-}$ mice exhibited greater hypercholesterolaemia or hyperlipidaemia than WT mice, fasting serum lipid and cholesterol levels were analysed (Table 4.2). As expected, increases in serum cholesterol and high-density lipoprotein (HDL), with little change in serum TGs, and glycerol were observed in the HFD groups (Eisinger et al. 2014). Unfortunately, there was no difference between WT and miR-34a$^{-/-}$ mice observed.

Group	Cholesterol (mmol/L)	HDL (mmol/L)	Triglycerides (mmol/L)	Free-Glycerol (mmol/L)	True TG (mmol/L)
WT Chow	1.433 (±0.14)	1.461 (±0.13)	0.266 (±0.2)	0.255 (±0.02)	0.053 (±0.01)
KO Chow	1.301 (±0.33)	1.292 (±0.29)	0.244 (±0.03)	0.241 (±0.03)	0.024 (±0.01)
Mouse (P=)	0.9115	0.7983	0.8026	0.8883	0.3191
WT HFD	3.334 (±0.25)	2.887 (±0.19)	0.229 (±0.03)	0.208 (±0.02)	0.050 (±0.01)
KO HFD	3.288 (±0.17)	2.876 (±0.11)	0.192 (±0.03)	0.204 (±0.02)	0.027 (±0.01)
Mouse (P=)	0.9881	0.9989	0.9368	0.9916	0.4317
Diet (P=)	<0.0001	<0.0001	0.4935	0.0755	0.9418

Table 4.2: Fasting Serum Lipid Measurements From miR-34a$^{-/-}$ and WT Mice During HFD-feeding
Mean serum lipid and cholesterol measurements from WT and miR-34a$^{-/-}$ mice on chow Vs. HFD for 24 weeks, following a 16-18 hour fast; high density lipoprotein (HDL), triglycerides (TG). Statistics were calculated by a Two-way ANOVA for the diet effect, with differences between WT and KO groups on each diet calculated by Sidak's multiple comparisons post-test.

4.4.2 miR-34a$^{-/-}$ Mice Show dysregulated Epididymal WAT Expansion

After 24 weeks of chow or HFD-feeding, WT and miR-34a$^{-/-}$ mice were sacrificed and tissues were collected for further analysis. During dissection it was noted that there was a large accumulation of abdominal fat in both WT and miR-34a$^{-/-}$ mice on HFD, with significant expansion of the epididymal (e)WAT (outlined; Figure 4.6A). Under closer *ex vivo* examination of the eWAT from these mice, a significant increase in HFD-fed miR-34a$^{-/-}$ eWAT weight was observed (0.61 ± 0.10 g to 1.80 ± 0.08 g: P<0.0001), which was not seen in WT eWAT (0.96 ± 0.30 g to 1.50 ± 0.14 g: P=0.1263) (Figure 4.6B). Although we did not observe any differences in liver weight between groups, histological examination of the livers by H&E staining revealed some interesting differences. Livers from miR-34a$^{-/-}$ control mice already showed signs of steatosis, which became more pronounced during HFD-feeding and was more extreme than their HFD-fed WT counterparts (Figure 4.6C).

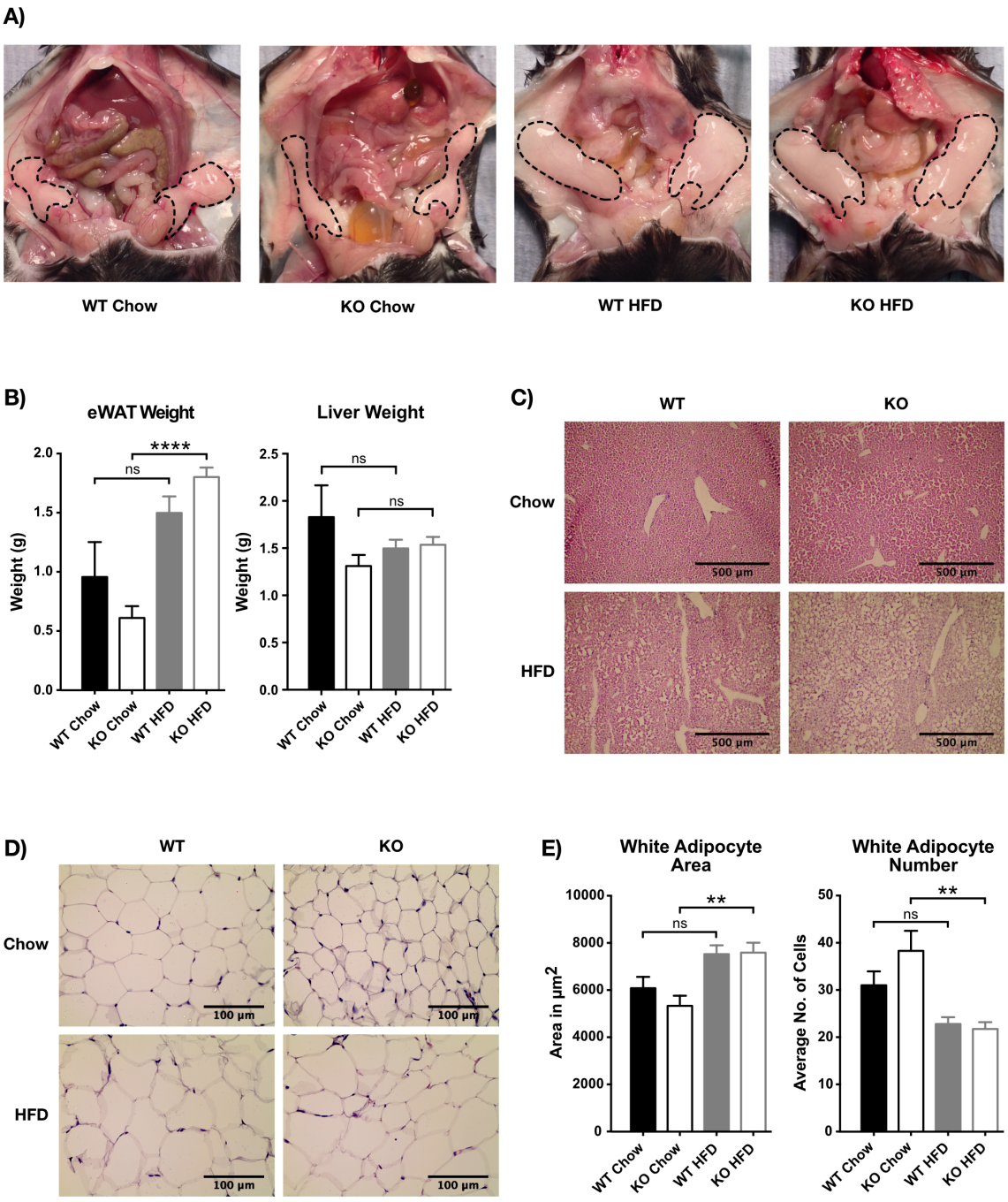

Figure 4.6: miR-34a$^{-/-}$ eWAT Showed A Greater Hypertrophic Response to HFD-Feeding
(A) Representative dissection images of WT and miR-34a$^{-/-}$ (KO) mice on chow Vs. HFD, after 24 weeks, with the epididymal (e)WAT outlined with a dashed line. (B) Weight of excised eWAT and liver from the same mice as (A); n=10 for miR-34a$^{-/-}$ (KO) chow and WT HFD, n=9 for WT chow and KO HFD. (C) Representative H&E staining of livers excised in (B) at 10X. (D) Representative H&E staining of eWAT excised in (B) at 40X. (E) Quantification of adipocyte area and number in (D), with averages taken from ≥ 5 fields per section of n=10 for KO chow and WT HFD, n=8 for WT Chow and KO HFD groups. Area measurements were converted from pixels to cm^2 using the image scale. All graphs represent mean values with SEM. **P<0.01, ****P<0.0001, ns = not significant: One-way ANOVA, with Bonferroni's multiple comparisons post-test.

Additionally, H&E staining of chow-fed miR-34a$^{-/-}$ eWAT displayed smaller and more compact adipocytes, than WT controls (Figure 4.6D). These adipocytes significantly increased in cell area (P=0.0030), with a reciprocal decrease in cell

number (P=0.0013) per field, when stressed with a HFD. These changes were less pronounced in WT epididymal adipocytes; however, miR-34a$^{-/-}$ adipocytes equaled WT levels after HFD feeding.

4.4.3 miR-34a$^{-/-}$ mice Show Basal Metabolic Gene Changes

To explore potential mechanisms for the *in vivo* and adipose phenotypes, a number of metabolic genes were profiled *ex vivo* in eWAT and iBAT of WT and miR-34a$^{-/-}$ mice on chow Vs. HFD for 24 weeks, by qRT-PCR (Figure 4.7). This included a number of cholesterol, glucose, and fatty acid metabolism genes. Interestingly, under basal conditions in miR-34a$^{-/-}$ mice (chow diet) the following genes were upregulated in eWAT, compared with WT controls: *Cd36* (P=0.0036), *3-hydroxy-3-methyl-glutaryl-CoA reductase* (*Hmgcr*; P=0.0012), *Liver X receptor (Lxr)α* (P=0.0034), *Peroxisome proliferator-activated receptor (Ppar) coactivator (Pgc)-1α* (P=0.0138), and *Fatty acid synthase* (*Fasn*; P=0.0027) (Figure 4.7A). Furthermore, *Pparγ* (P=0.0471), *Acetyl-CoA carboxylase (Acc)α* (P=0.0018), and *Fasn* (P=0.0274) transcripts decreased in miR-34a$^{-/-}$ eWAT during HFD-feeding. A number of other genes were examined in the eWAT, but they were not significantly altered in miR-34a$^{-/-}$ mice (Figure 4.7B). Given that in the previous chapter miR-34a increased in iBAT during HFD-feeding (Figure 3.10C), and the tissue's role in thermogenesis, a number of important BAT differentiation genes were examined (Figure 4.7C). Interestingly, decreased transcripts of *Cebpα* (P<0.01) and *Cebpβ* (P<0.01) were observed in both miR-34a$^{-/-}$ groups' iBAT, with increased expression of *Pgc1α* (P=0.0072) observed in miR-34a$^{-/-}$ iBAT when HFD-fed. Increased transcripts of *Pparγ* were observed in both WT (P=0.0340) and miR-34a$^{-/-}$ mice (P=0.0041) during HFD-feeding, but not between genotypes, and no change was observed in *Ucp1* or *Sirt1* transcripts. This suggests that miR-34a$^{-/-}$ mice could have a deficiency in their thermogenic processes within BAT and an imbalance in lipid handling within the visceral WAT. Additionally, metabolic genes were examined *ex vivo* in the liver of miR-34a$^{-/-}$ and WT mice on chow Vs. HFD, to look for hepatic contribution to the *in vivo* phenotype (Figure 4.8). Few changes were seen in the liver; however, basal increases in the glucose metabolism genes: *Cebpα* (P=0.0369) and *Pgc1α* (P=0.0305) were observed in miR-34a$^{-/-}$ mice on chow (Figure 4.8A).

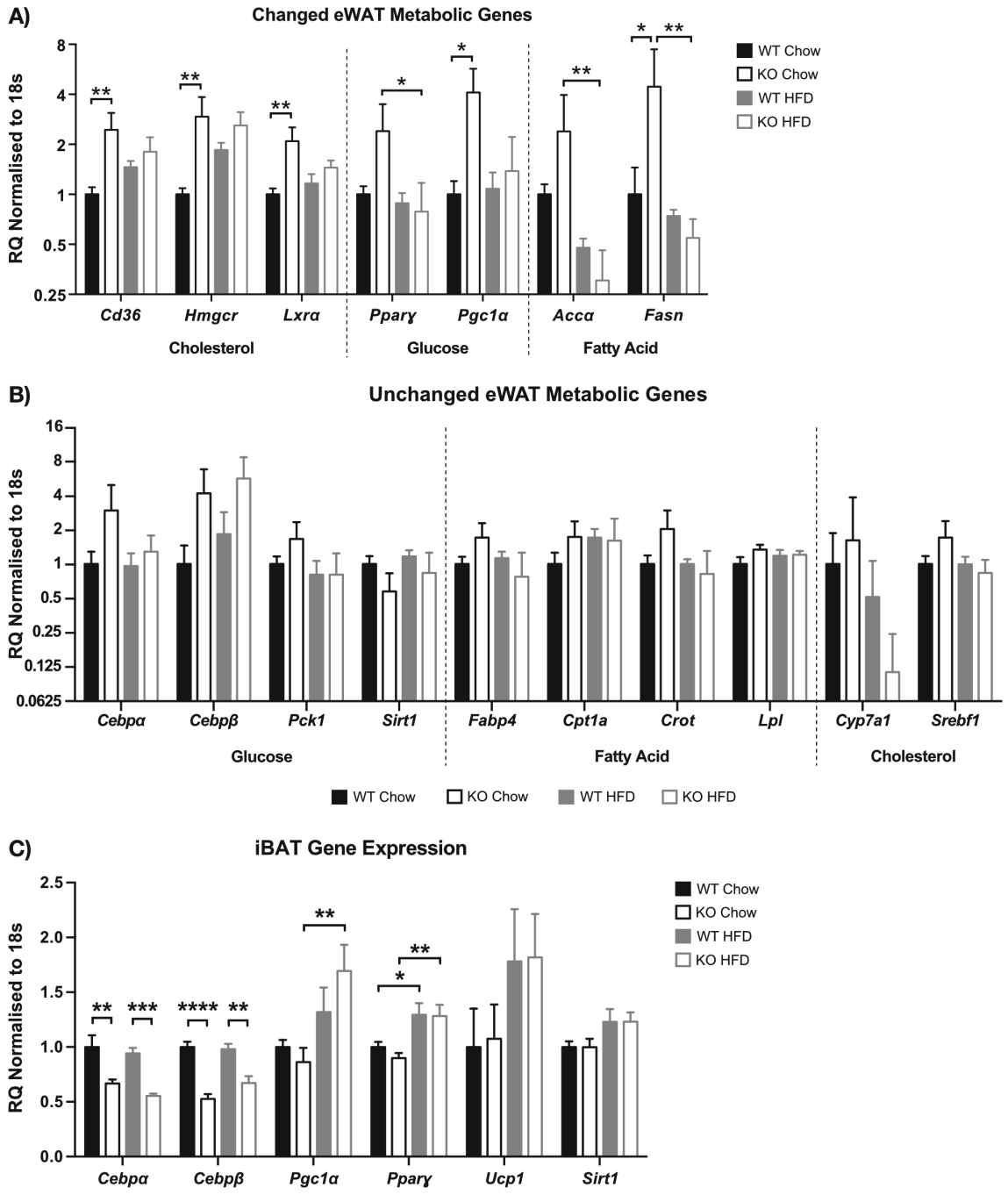

Figure 4.7: miR-34a$^{-/-}$ Adipose Tissue Metabolic Gene Changes
(A-C) qRT-PCR data of metabolic gene expression in eWAT and iBAT from WT and miR-34a$^{-/-}$ (KO) mice after 24 weeks on chow Vs. HFD, normalised to 18s rRNA; n=6 for all groups, except n=5 for KO HFD group. Dotted lines separate genes involved in glucose, fatty acid, and cholesterol metabolism. All graphs represented as relative quantification (RQ) with RQ_{min}-RQ_{max} values. *P<0.05, **P<0.01, ***P<0.001, ****P<0.0001 One-way ANOVA, with Bonferroni's multiple comparisons post-test.

Increased lipoprotein lipase (*Lpl*) transcripts were observed in both WT (P=0.0159) and miR-34a$^{-/-}$ mice (P=0.0004) when HFD-fed (Figure 4.8B). No changes were observed in the cholesterol metabolism genes examined (Figure 4.8C). This

suggests that the contribution of the liver to the *in vivo* phenotype is likely to be less than that of the adipose tissue.

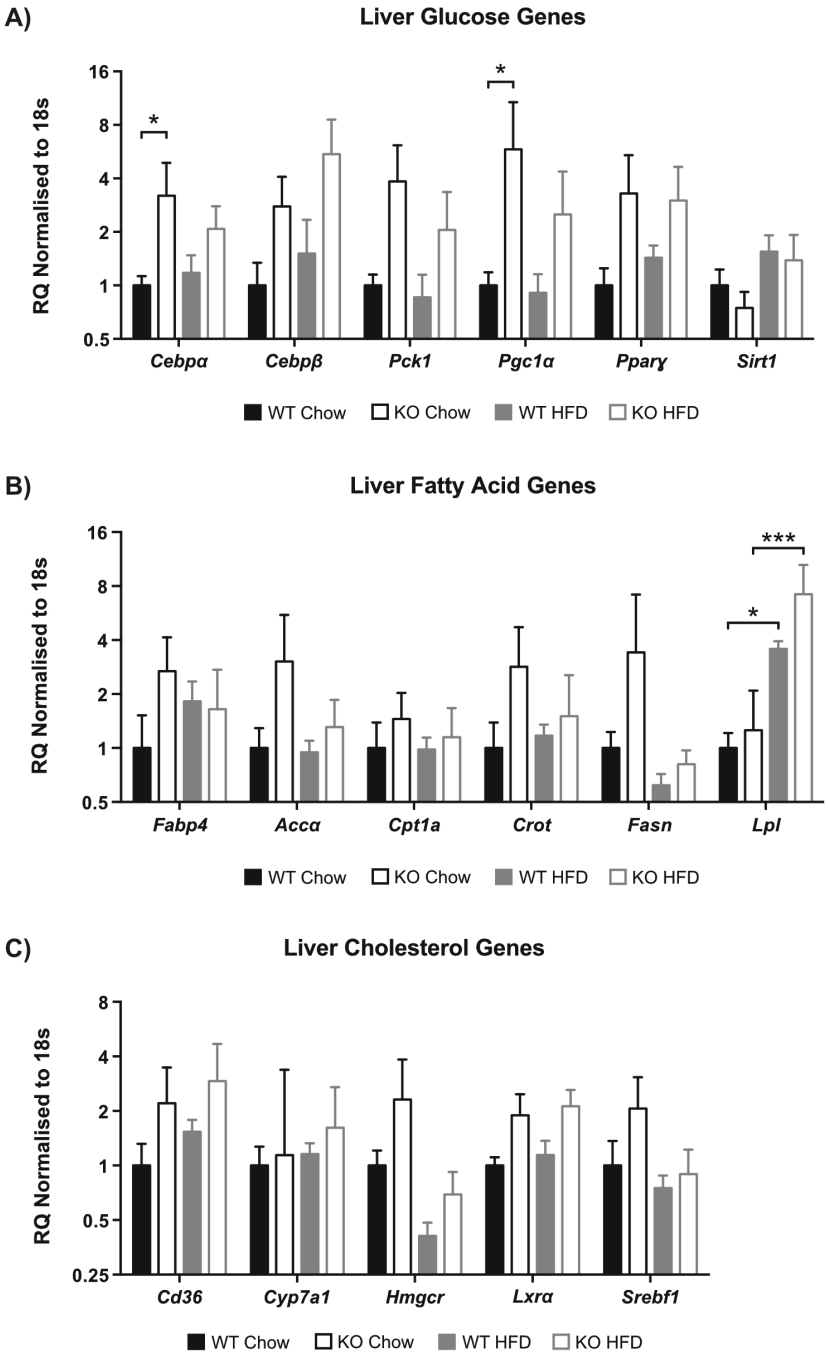

Figure 4.8: Profile of Metabolic Genes Within the miR-34a$^{-/-}$ Liver
(A-C) qRT-PCR data of metabolic gene expression in the liver from WT and miR-34a$^{-/-}$ (KO) mice after 24 weeks on chow Vs. HFD, normalised to 18s rRNA; n=6 for all groups, except n=5 for KO HFD group. All graphs represented as relative quantification (RQ) with RQ_{min}-RQ_{max} values. *P<0.05, ***P<0.001 One-way ANOVA, with Bonferroni's multiple comparisons post-test.

4.4.4 Profiling Inflammatory Markers In miR-34a$^{-/-}$ Tissues

Due to the cross-talk between the immune system and metabolism, markers of inflammation and macrophage polarisation were also explored *ex vivo* within the eWAT, liver, and serum of WT and miR-34a$^{-/-}$ mice on HFD Vs. chow diet for 24 weeks. Examination of genetic markers of macrophage polarisation within the eWAT revealed significantly higher transcripts of the M1 marker *nitric oxide synthase* (*Nos)2* (P=0.0500), in chow-fed miR-34a$^{-/-}$ mice than WT controls (Figure 4.9A). Additionally, during HFD-feeding, miR-34a$^{-/-}$ mice showed reduced transcripts of the M2 marker *resistin-like alpha* (*Retnla*), compared to HFD-fed WT (P=0.0006) and chow-fed miR-34a$^{-/-}$ mice (P=0.0023) in eWAT. Increased transcripts of the monocyte chemoattractant *CC chemokine ligand* (*Ccl)2* were observed in both WT (P=0.0111) and miR-34a$^{-/-}$ mice (P=0.0098) eWAT during HFD-feeding. There appeared to be a 2-4-fold mean basal increase in miR-34a$^{-/-}$ chow eWAT transcripts of *interlukin* (*IL)-6* (P=0.1699), *tissue necrosis factor* (*TNF)α* (P=0.0616), and *Pparδ* (P=0.0648), compared with WT chow controls; however, these were not statistically significant.

More inflammatory gene changes were seen in the livers of miR-34a$^{-/-}$ mice (Figure 4.9B). miR-34a$^{-/-}$ mice showed higher basal expression of *Pparδ* (P=0.0405) than their WT chow controls, and a decrease in arginase (*Arg)1* transcripts when HFD-fed (P=0.0229), both M2 markers (Galván-Peña and O'Neill 2014). Additionally, HFD-fed miR-34a$^{-/-}$ mice showed increased hepatic expression of the M2 marker chitinase-3-like protein (*Chi3l)3* (P=0.0315), and the M1 markers *Tnfα* (P=0.0191), and *Nos2* (P=0.0182), compared with WT HFD controls. Mirroring the expression of Ccl2 in the eWAT, hepatic expression of Ccl2 also increased in both WT (P=0.0464) and miR-34a$^{-/-}$ mice (P=0.0076) on HFD-feeding. Despite seeing increased hepatic transcripts of *Tnfα* and *Nos2*, increased hepatic fibrosis was not observed in miR-34a$^{-/-}$ mice, as assessed by Masson's Trichrome staining (Figure 4.9C). Furthermore, no change was observed in hepatic expression of the collagen genes: collagen type 1 alpha (Col1a)1 and Col3a1 (Figure 4.9D).

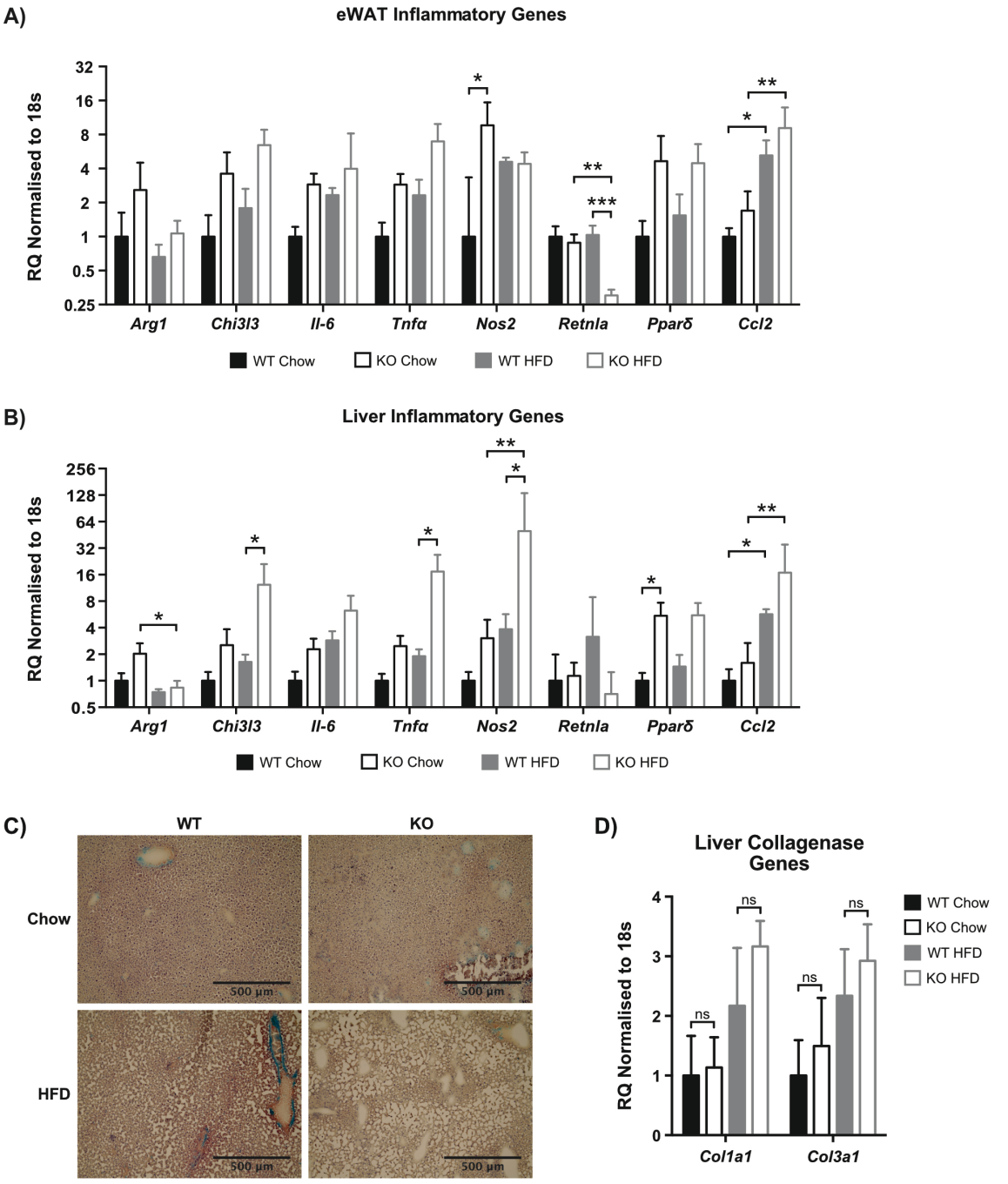

Figure 4.9: Quantification of Inflammatory Genes in eWAT and Liver From HFD-fed miR-34a$^{-/-}$ Mice

(A-B) qRT-PCR data of inflammatory gene expression in the eWAT and liver from WT and miR-34a$^{-/-}$ (KO) mice after 24 weeks on chow Vs. HFD, normalised to 18s rRNA; n=6 for all groups, except n=5 for KO HFD group. (C) Representative Masson's Trichrome staining for collagen deposition (turquoise) in frozen Liver sections from the same tissue as in (B). (D) qRT-PCR data showing collagen gene expression in the same liver tissues as in (B-C), normalised to 18s rRNA; n=6 for all groups, except n=5 for KO HFD group. All graphs represented as relative quantification (RQ) with RQ_{min}-RQ_{max} values. *P<0.05, **P<0.01, ***P<0.001, ns = not significant: One-way ANOVA, with Bonferroni's multiple comparisons post-test.

Twenty cytokines were profiled in the serum from WT and miR-34a$^{-/-}$ mice after 24 weeks on chow Vs. HFD, to investigate inflammatory proteins. The following cytokines were not detected: IL-1α, IL-2, IL-4, IL-6, IL-10, IL-13, IL-17,

TNFα, CXC chemokine ligand (CXCL)10, and vascular endothelial growth factor (VEGF). A number of other cytokines were detected within the serum, but did not change between the groups (Figure 4.10A). Interestingly, the type-2 cytokine IL-5 (P=0.0103) and T-cell chemoattractant CXCL9 (P=0.0303) were increased in serum from HFD-fed miR-34a$^{-/-}$ mice, compared to WT HFD controls (Figure 4.10B).

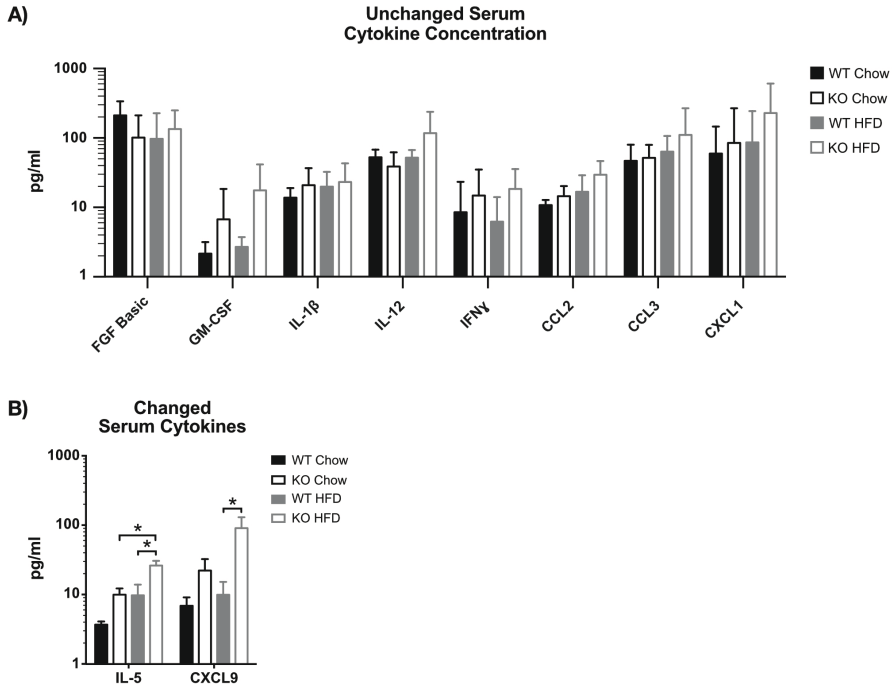

Figure 4.10: Serum Cytokine Expression in HFD-fed miR-34a$^{-/-}$ Mice.
(A) Showing Luminex cytokine data from the serum of WT and miR-34a$^{-/-}$ (KO) mice after 24 weeks on chow Vs HFD, which was not statistically different; n=5 for WT chow and KO HFD groups, and n=6 for others. (B) Showing the cytokines that were statistically changed from (A); n=5 for WT chow and KO HFD groups, and n=6 for others. Data is represented as mean values with SEM. *P<0.05 One-way ANOVA, with Bonferroni's multiple comparisons post-test.

4.4.5 *Ex vivo* Profiling of Leukocyte Phenotype in miR-34a$^{-/-}$ mice

To further explore the immune phenotype within miR-34a$^{-/-}$ mice, leukocytes were isolated from the eWAT and spleen of WT and miR-34a$^{-/-}$ mice on chow Vs. HFD for 24 weeks. The leukocytes and their phenotypic markers were quantified by flow cytometry.

4.4.5.1 eWAT Leukocytes

The leukocyte content was assessed in the eWAT, for contributions to the *in vivo* and adipose phenotype. Macrophages, lymphocytes, and neutrophils were primarily examined, as previous studies have suggested miR-34a regulates macrophage inflammatory pathways, granulopoiesis, and B cell differentiation (Pulikkan et al. 2010; Rao et al. 2010; Jiang et al. 2012). Macrophages were gated off the larger, more granular cells in forward scatter (FSC)-side scatter (SSC), which were F4/80^{+} (Figure 4.11A). These cells were also CD45^{+}, CD11b^{+}, MHCII^{+}, and CD86^{+}. This gating strategy was chosen, because adipose tissue macrophages (ATMs) accumulated lipid, making them more granular, but also increasing their auto-fluorescence (Cho et al. 2014). In general, the auto-fluorescence from WAT stromal vascular cells (SVCs) made it challenging to gate on positive populations. The markers: CD11c, CD69, CD80, CD86, CD206, major histocompatibility complex (MHC) class II, and toll-like receptor (TLR)-2 were examined on these F4/80^{+} CD45^{+} MHCII^{+} CD11b^{+} CD86^{+} cells, and representative flow cytometry plots are shown in Figure 4.11A and Figure 4.12. Quantification of these markers by percentage of positive cells and surface expression by median fluorescence intensity (MFI) did not show any differences between groups (Figure 4.13A-B). However, a lower percentage of F4/80^{+} cells was observed in the miR-34a$^{-/-}$ chow group (P=0.0078), compared with the WT chow group (KO: 69.29±5.91% Vs. WT: 90.46±4.43%), which was not seen between the HFD groups (Figure 4.11B, Figure 4.13C). Additionally, a population of F4/80^{high} cells was observed within the miR-34a$^{-/-}$ HFD group, showing significant upregulation of F4/80 surface expression (P=0.0497) from the miR-34a$^{-/-}$ chow group (Figure 4.11B, Figure 4.13C). Previous studies have found F4/80^{high} macrophages in the intestine and adipose tissue that constitutively produce the anti-inflammatory cytokine IL-10 (Bassaganya-Riera et al. 2009; Bain et al. 2013; 2014). Therefore, transcripts of *Il-10* were examined within the eWAT, and were higher in the miR-34a$^{-/-}$ HFD group than WT HFD controls (P=0.0150) and the miR-34a$^{-/-}$ chow group (P=0.0213; Figure 4.13D). *Il-10* transcripts were also examined in the liver, showing higher levels in the miR-34a$^{-/-}$ HFD group, but only in comparison to the miR-34a$^{-/-}$ chow group (P=0.0331).

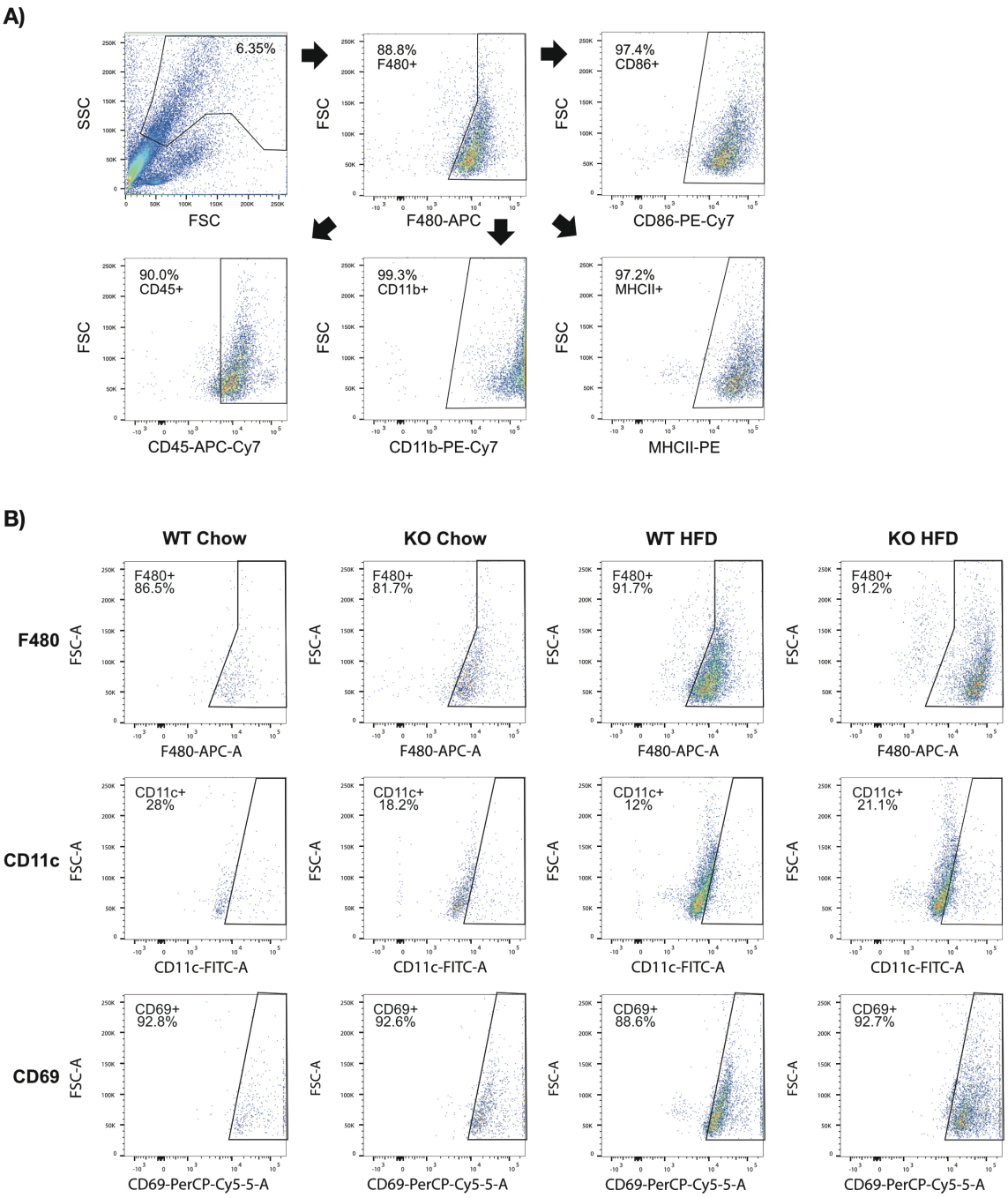

Figure 4.11: Representative Flow Cytometry Plots and Gating Strategy for eWAT Macrophages

(A) Representative flow cytometry plots of gating strategy for eWAT macrophages from week-24 of the murine WT and miR-34a$^{-/-}$ (KO), chow Vs. HFD study. The cells are shown to be F4/80^{+} CD11b^{+} CD45^{+} CD86^{+} MHCII^{+}. (B) Representative flow cytometry plots for F4/80, CD11c, and CD69 gating off F4/80^{+} cells in (A). All gates were set off FMO controls and percentages are of parent population.

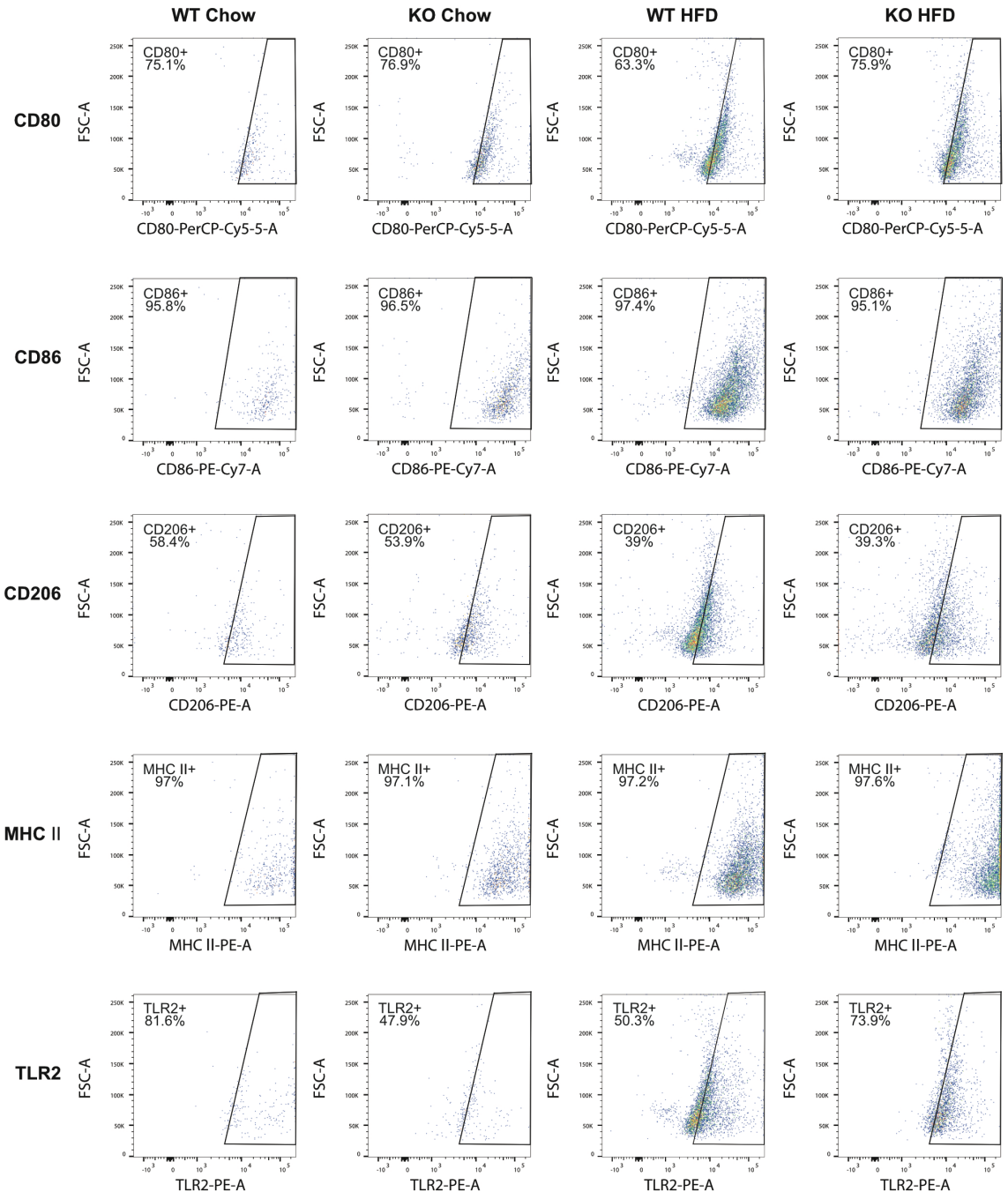

Figure 4.12: Representative Flow Cytometry Plots of eWAT Macrophage Markers, Continued
Continuation of the representative flow cytometry plots for subset markers of F4/80$^+$ macrophages shown in Figure 4.11B.

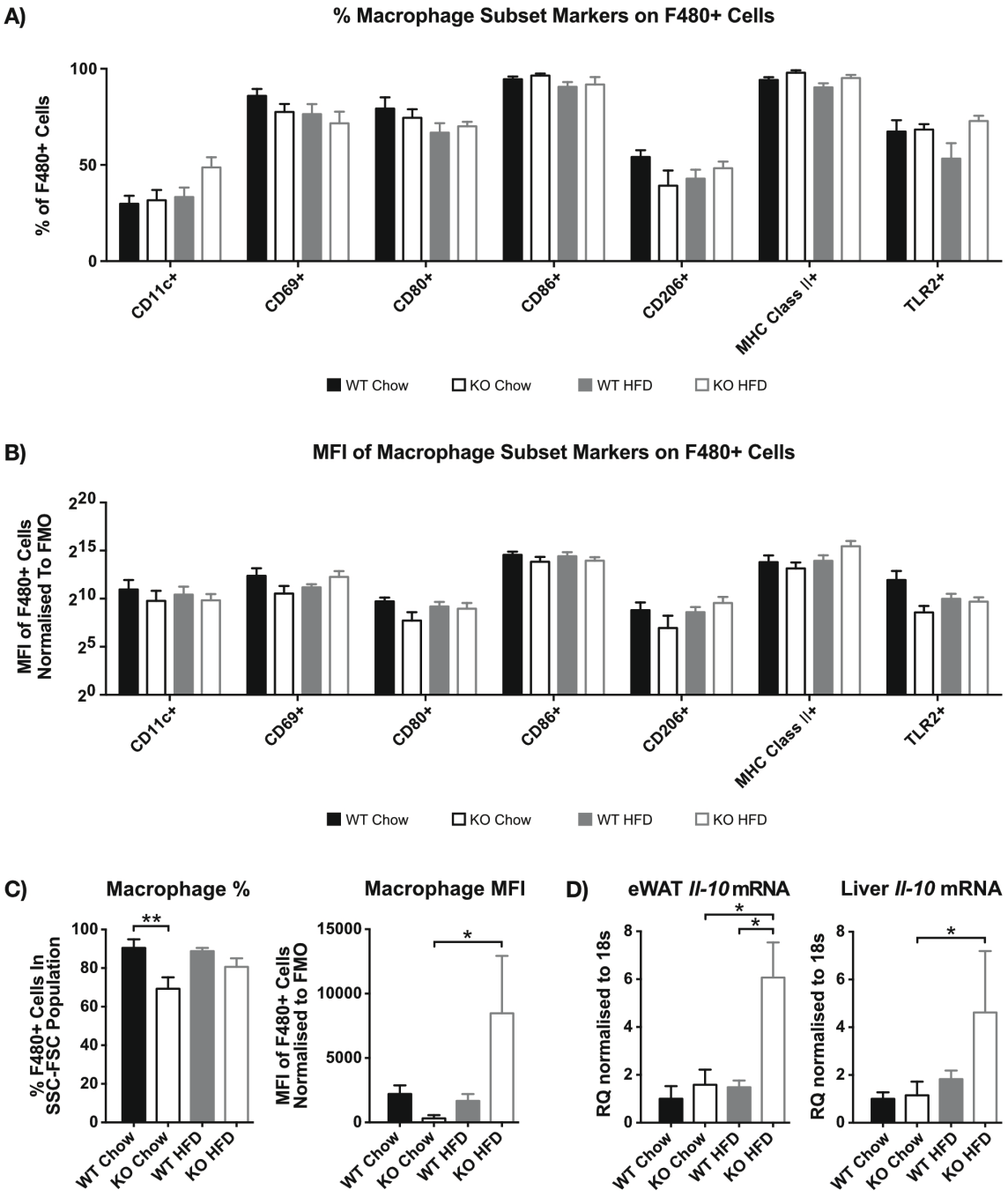

Figure 4.13: Flow Cytometry Quantification of Macrophage Markers From Cells Isolated from eWAT

(A) Quantification of macrophage subset marker expression on F4/80^{+} cells (macrophages; Figure 4.11) from *ex vivo* eWAT from WT and miR-34a$^{-/-}$ (KO) mice on week-24 of chow Vs. HFD, represented as percentage of positive cells on the F4/80^{+} population; n=9 for all, except n=10 for KO Chow. (B) Quantification of the same samples and macrophage subset markers as in (A), by Median fluorescence intensity (MFI) for surface expression. MFI is normalised to the florescence minus one (FMO) control. (C) Quantification of percentage F4/80^{+} macrophages and F4/80 MFI, normalised to FMO, in the same samples as (A). (D) qRT-PCR data from eWAT and Liver of WT and miR-34a$^{-/-}$ (KO) mice on week-24 of chow Vs. HFD, normalised to 18s rRNA expression; n=6 KO Chow and WT HFD, and n=5 WT chow and KO HFD groups. Represented as relative quantification (RQ) with RQ_{min}-RQ_{max} values. All other graphs are represented as mean values with SEM. *P<0.05, **P<0.01 One-way ANOVA, with Bonferroni's multiple comparisons post-test.

SVF lymphocytes were examined in the eWAT by gating on the smaller, least granular population in FSC-SSC and then gating on $CD3^-$ cells for B cells and $CD3^+$ cells for T cells (Figure 4.14A). B cells were identified by expression of CD19, T helper (T_H) cells by CD4 and cytotoxic T (T_C) cells by CD8, and the FSC-SSC population was shown to be $CD45^+$. Representative plots for these lymphocyte populations are shown in Figure 4.14B. Quantification of the percentage of each lymphocyte population did not show any difference between groups; however, $CD3^+$ $CD4^+$ T lymphocytes appeared to make up the highest percentage of lymphocytes present (Figure 4.15A).

Finally, neutrophils were examined in the eWAT by gating on the medium sized and granular cells in FSC-SSC, and then gating on $CD45^+$ $CD11b^+$ $F4/80^-$ $CD11c^-$ Ly6c-$Ly6g^+$ cells (Figure 4.15C). Representative flow cytometry plots for each group are shown in Figure 4.15D. Interestingly, when the percentage of these neutrophils in the FSC-SSC population was quantified, a higher percentage was observed under basal conditions in miR-$34a^{-/-}$ mice on chow (KO: 35.05±6.16% Vs. WT: 23.83±2.46%; Figure 4.15B). This decreased significantly in these mice upon HFD-feeding ($P=0.0202$), and was not observed in WT mice ($P>0.9999$).

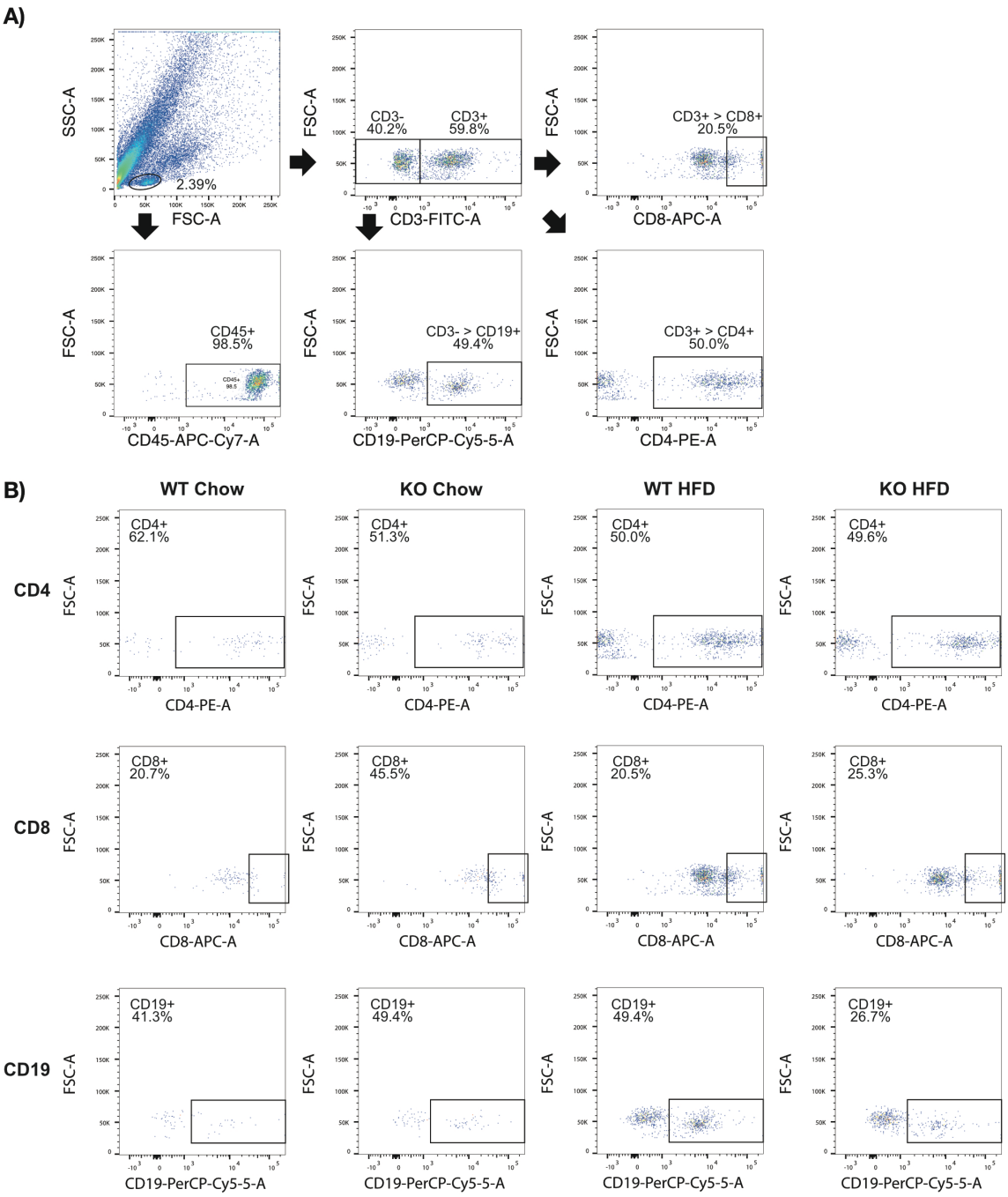

Figure 4.14: Representative Flow Cytometry Plots and Gating Strategy for eWAT Lymphocytes

(A) Representative flow cytometry plots of gating strategy for eWAT lymphocytes from week-24 of the murine WT and miR-34a$^{-/-}$ (KO), chow Vs. HFD study. The cells are shown to be CD45^{+}. (B) Representative flow cytometry plots for T helper cells (CD3^{+} CD4^{+}), cytotoxic T cells (CD3^{+} CD8^{+}), and B cells (CD3^{-} CD19^{+}), gated off populations shown in (A). All gates were set off FMO controls and percentages are of parent population.

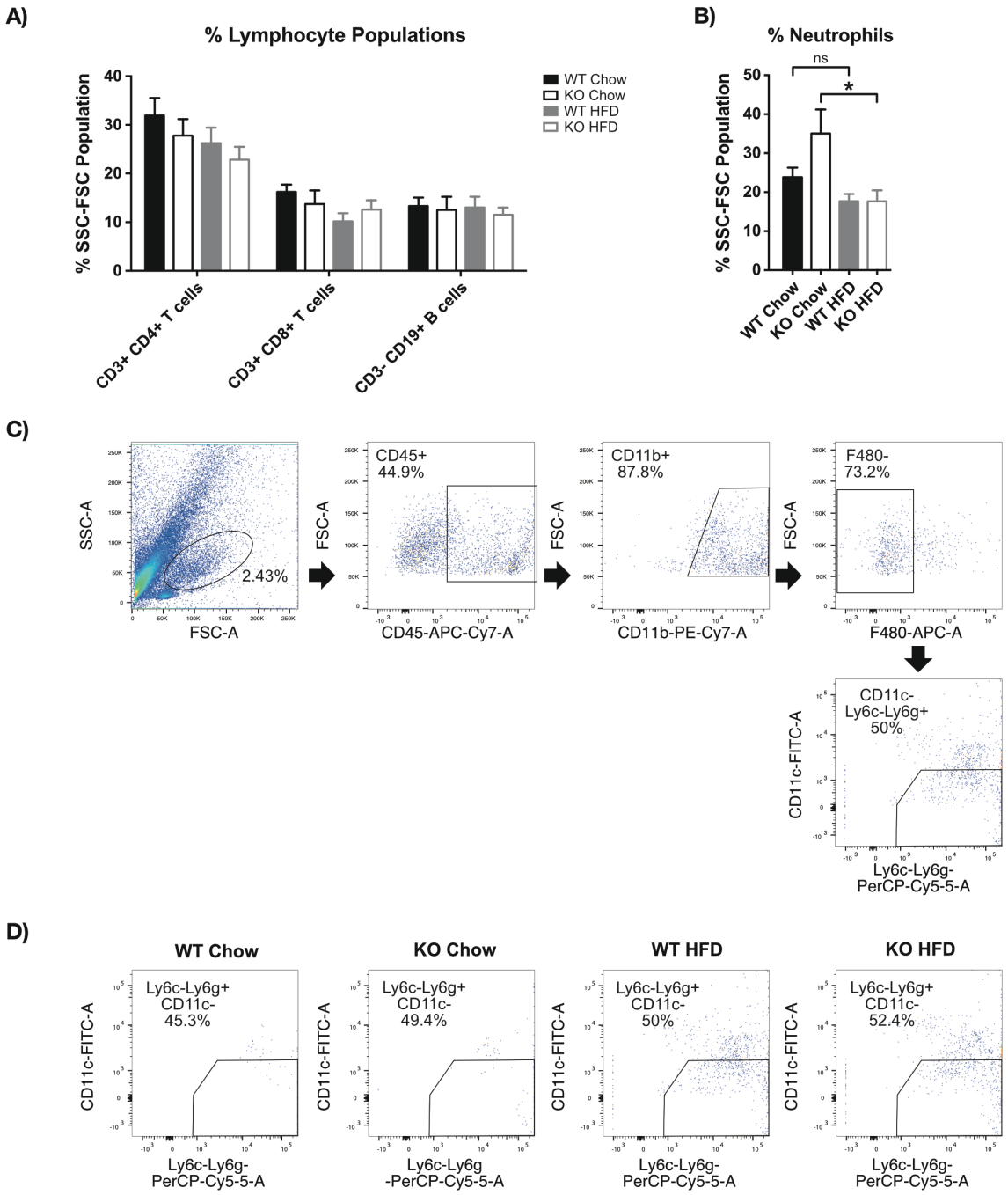

Figure 4.15: Lymphocyte and Neutrophil Quantification and Representative Flow Cytometry Plots

(A) Quantification of lymphocyte populations from the eWAT of WT and miR-34a$^{-/-}$ (KO) mice on week-24 of chow Vs. HFD, shown in Figure 4.14, represented as percentage of positive cells in the SSC-FSC population; n=9 for all, except n=10 for KO Chow. (B) Quantification of neutrophils (CD45^{+} CD11b^{+} F4/80^{-} CD11c^{-} Ly6c-Ly6g^{+}) from the same samples as (A), with gating strategy and representative plots shown in (C) and (D), respectively. Represented as percentage of positive cells in the SSC-FSC population, shown in (C). All graphs are represented as mean values with SEM. *P<0.05, ns = not significant: One-way ANOVA, with Bonferroni's multiple comparisons post-test.

4.4.5.2 Spleen Leukocytes

To assess systemic leukocyte effects in WT and miR-34a$^{-/-}$ mice on chow Vs. HFD, lymphocyte, macrophage, and neutrophil content within the spleen was examined. Lymphocytes were gated on FSC-SSC and then gated for being CD45^{+} CD3^{-} for B cells and CD45^{+} CD3^{+} for T cells. CD19+ cells were then gated off these CD45^{+} CD3^{-} cells to identify B cells. From the CD45^{+} CD3^{+} cells, CD4^{+} cells were gated to identify T_H cells and CD8^{+} cells for T_C cells (Figure 4.16A). Representative flow cytometry plots of these populations for each group are shown in Figure 4.16B. When these lymphocyte populations were quantified no change was observed in the T cell populations between groups; however, both miR-34a$^{-/-}$chow-fed (WT: 35.95±2.56% Vs. KO: 61.49±2.76% ;P=0.0002) and HFD-fed (WT: 42.62±3.57% Vs. KO: 63.66±3.33%; P=0.0005) groups exhibited a significantly higher percentage of B cells, compared to WT controls (Figure 4.17A). These B cells made up the highest proportion of overall spleen lymphocytes.

A larger FSC-SSC gate was used to gate on macrophages and neutrophils, due to the lower proportions of these cells present in the spleen, making it difficult to gate on specific populations. From this gate macrophages were identified by gating on F4/80^{+} cells (Figure 4.17C). Quantification of these F4/80^{+} cells showed no change in the percentage of these cells between groups (Figure 4.17B). Interestingly, quantification of the percentage of splenic CD45^{+} CD11b^{+} F4/80^{-} CD11c^{-} Ly6c-Ly6g^{+} neutrophils revealed a lower percentage in both miR-34a$^{-/-}$ chow-fed (WT: 9.48±1.63% Vs. KO: 2.70±0.87% ;P=0.0003) and HFD-fed (WT: 5.72±0.85% Vs. KO: 2.22±0.54%; P=0.0356) mice (Figure 4.17D). These cells were gated off the large FSC-SSC gate and were CD11b^{+} F4/80^{-} CD11c^{-} Ly6c-Ly6g^{+}. Unfortunately, the first batch of samples did not include the CD45 antibody on their staining panel; however, this was added to the staining panel of subsequent sample batches, which were shown to be CD45^{+} (Figure 4.17E). Representative flow cytometry plots of both the macrophage and neutrophil population are shown in Figure 4.18.

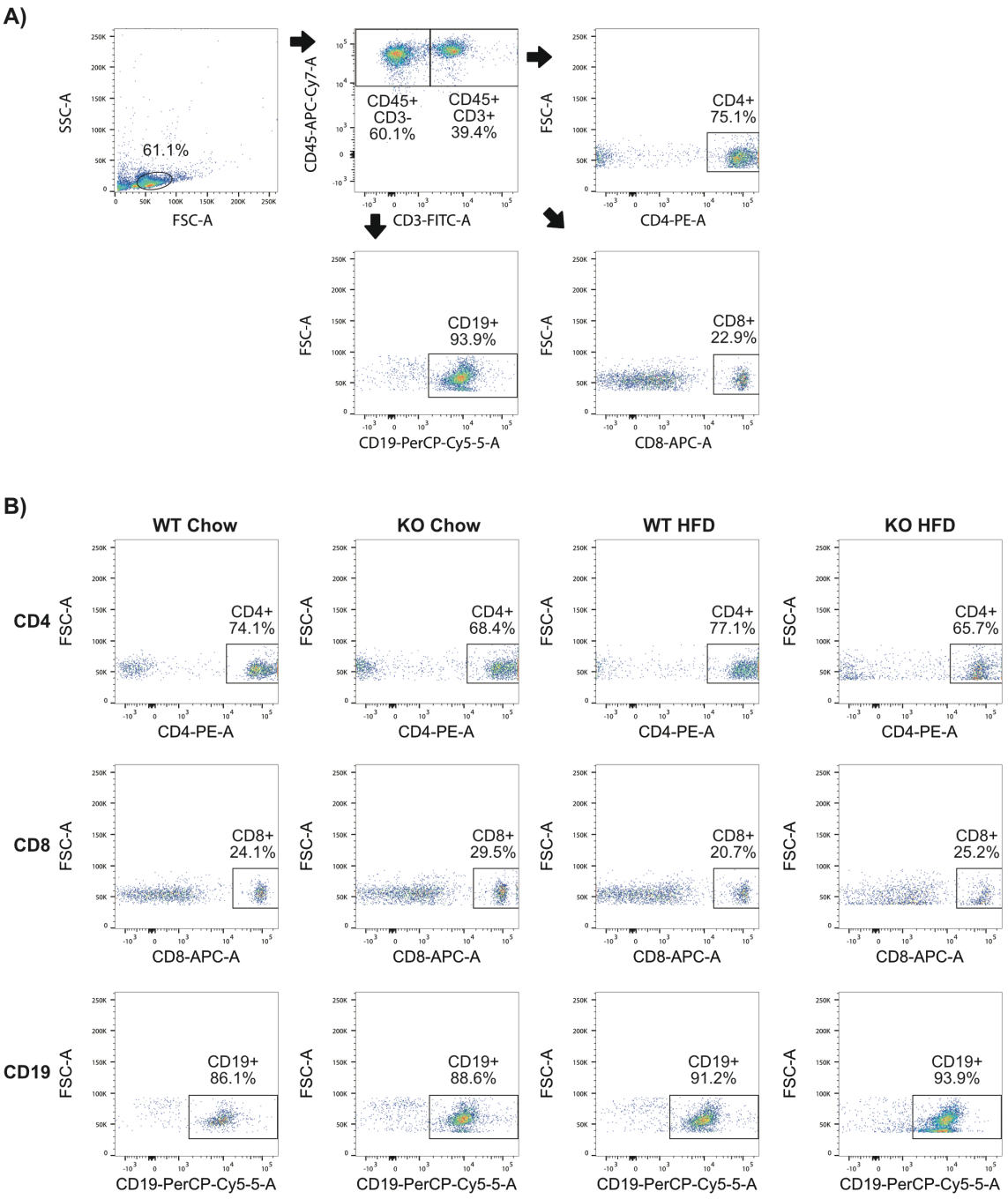

Figure 4.16: Spleen Lymphocyte Gating Strategy and Representative Flow Cytometry Plots
(A) Lymphocyte flow cytometry gating strategy for T helper cells ($CD3^+$ $CD4^+$), cytotoxic T cells ($CD3^+$ $CD8^+$), and B cells ($CD3^-$ $CD19^+$), from the spleens of WT and miR-34a$^{-/-}$ (KO) mice on week-24 of chow Vs. HFD. (B) Representative flow cytometry plots for T helper cells ($CD3^+$ $CD4^+$), T cytotoxic cells ($CD3^+$ $CD8^+$), and B cells ($CD3^-$ $CD19^+$), gated off populations shown in (A). All gates were set off FMO controls and percentages are of parent population.

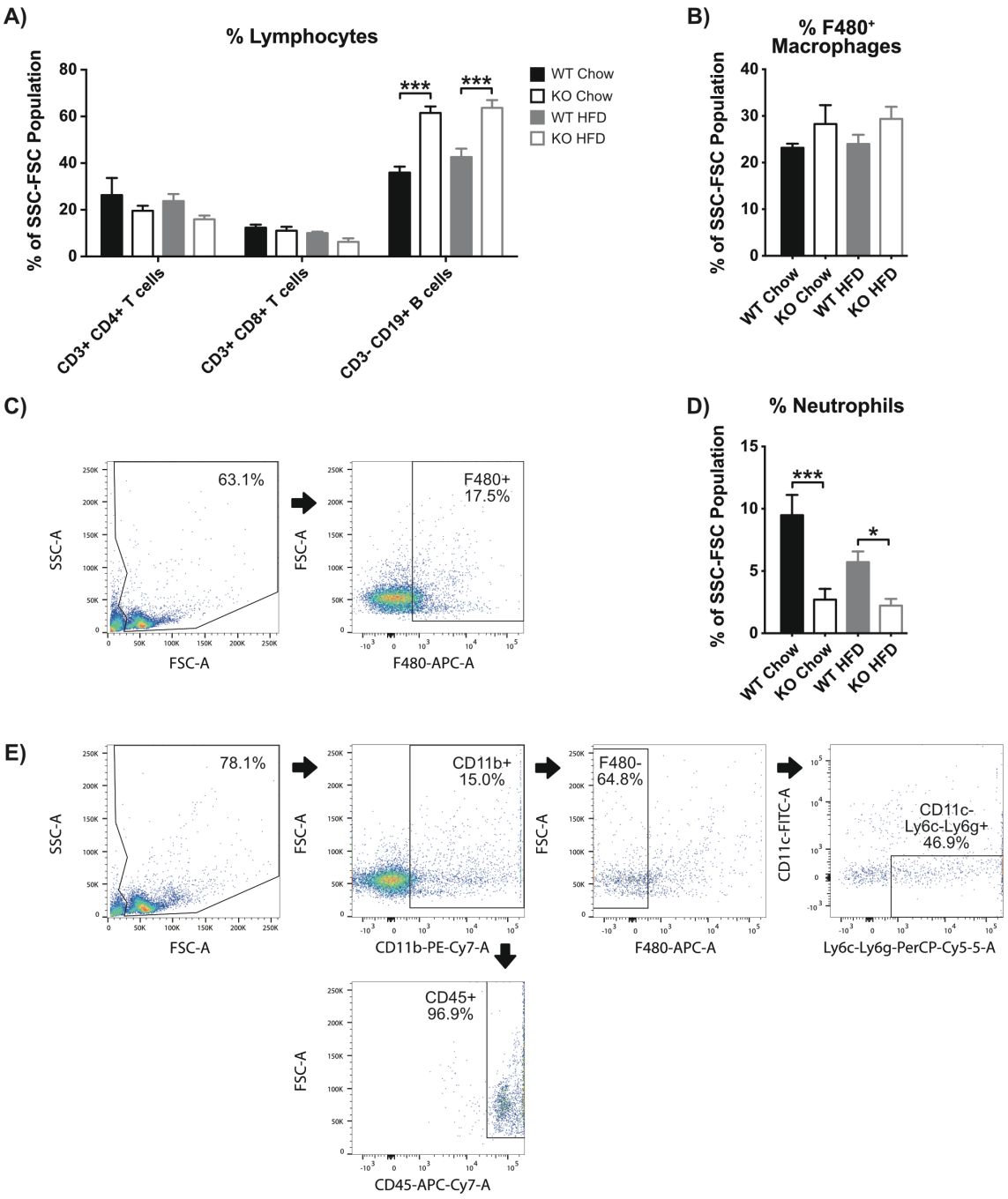

Figure 4.17: Spleen Leukocyte Quantification and Flow Cytometry Gating Strategy for Macrophages and Neutrophils

(A) Quantification of lymphocytes populations from the spleen of WT and miR-34a$^{-/-}$ (KO) mice on week-24 of chow Vs. HFD, shown in Figure 4.16, represented as percentage of positive cells in the SSC-FSC population; n=4 WT chow, n=6 WT HFD, n=7 KO HFD, and n=8 KO Chow. (B) Quantification of F4/80^{+} (macrophages) in the same samples as (A), using the gating strategy shown in (C) and percentages are of the SSC-FSC population; n=8 for all, except n=4 WT Chow and n=6 WT HFD. (D) Quantification of neutrophils (CD45^{+} CD11b^{+} F4/80^{-} CD11c^{-} Ly6c-Ly6g^{+}) from the same samples as (A), using the gating strategy shown in (E) and percentages are of the SSC-FSC population; n=8 for all, except n=4 WT Chow and n=6 WT HFD. All graphs are represented as mean values with SEM. *P<0.05, ***P<0.001 One-way ANOVA, with Bonferroni's multiple comparisons post-test.

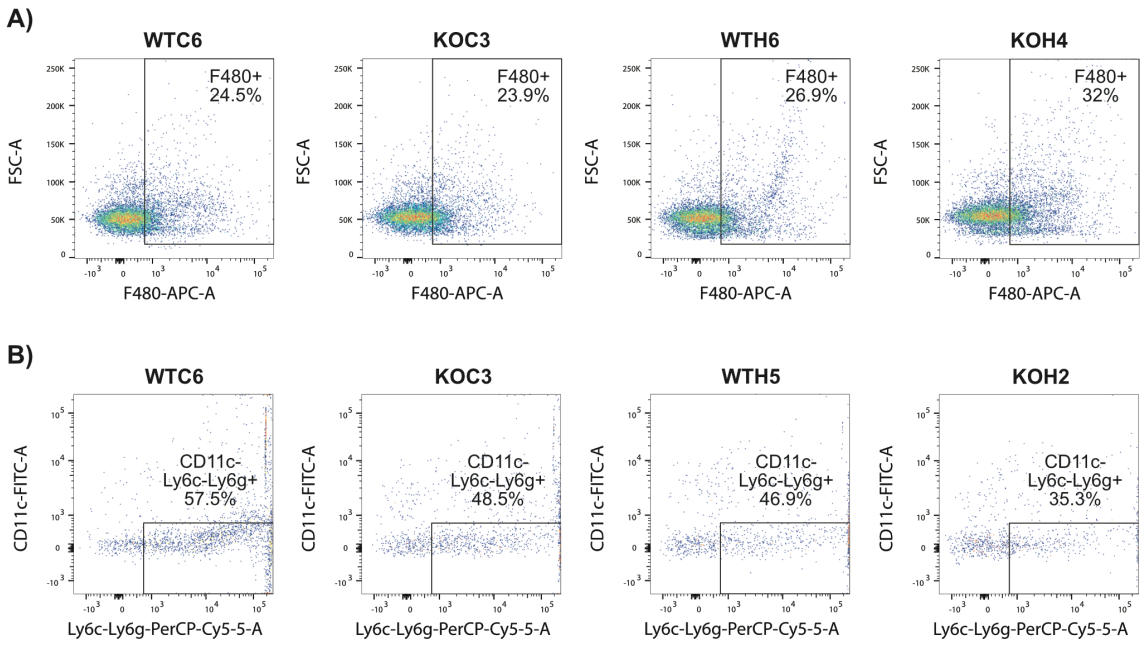

Figure 4.18: Representative Flow Cytometry plots for Splenic Macrophage and Neutrophil Populations
(A) Representative flow cytometry plots for splenic F4/80^{+} (macrophage) cells from week-24 of the murine WT and miR-34a$^{-/-}$ (KO), chow Vs. HFD study, gated as shown in Figure 4.17C. (B) Representative flow cytometry plots for splenic CD45^{+} CD11b^{+} F4/80^{-} CD11c^{-} Ly6c-Ly6g^{+} (neutrophils) cells from week-24 of the murine WT and miR-34a$^{-/-}$ (KO), chow Vs. HFD study, gated as shown in Figure 4.17E.

4.4.6 miR-34a$^{-/-}$ *in vivo* Metabolic Cage Study

The snout to anus measurement was taken for each mouse to check that differences in weight were not due to variation in length (Figure 4.19A). In both the 9-week metabolic cage study (Figure 4.2) and the 24-week diet study (Figure 4.1), there was no difference in length between groups. A metabolic cage study was conducted to check that the miR-34a$^{-/-}$ *in vivo* phenotype was not related to differences in eating and drinking behaviour. WT and miR-34a$^{-/-}$ mice on chow Vs. HFD were put in metabolic cages, after 9 weeks on each diet, for 24 hours. The 9-week time point was chosen, as HFD-fed miR-34a$^{-/-}$ mice were already 11.52% heavier (KO: 35.26±0.74 g Vs. WT: 31.62 ± 0.97 g; P=0.0043) than HFD-fed WT controls at week 9 in the 24-week study (Figure 4.4B). Examination of food and water intake and excretion did not show any differences between WT and miR-34a$^{-/-}$ mice (Figure 4.19B-C). However, opposed to the 24-week study, weekly weights of mice in the metabolic cage study showed that HFD-fed WT mice were significantly heavier than HFD-fed miR-34a$^{-/-}$ mice (WT: 36.42 ± 0.64 g Vs. KO:29.93 ± 1.65 g), by AUC analysis (P=0.0052) (Figure 4.19D). This data is in on the edge of the range for week 9 of the 24-week study (WT: 27.1-35.8 g and KO: 30.4-38.8 g), with the metabolic cage data for HFD-fed WT and miR-34a$^{-/-}$ mice

being at the high and low ends of these ranges, respectively. The mice were genotyped to confirm they were correctly assigned to each group (Figure 4.19E). Therefore, this difference with the 24-week study, may be due to the small number of mice used in the metabolic cage study.

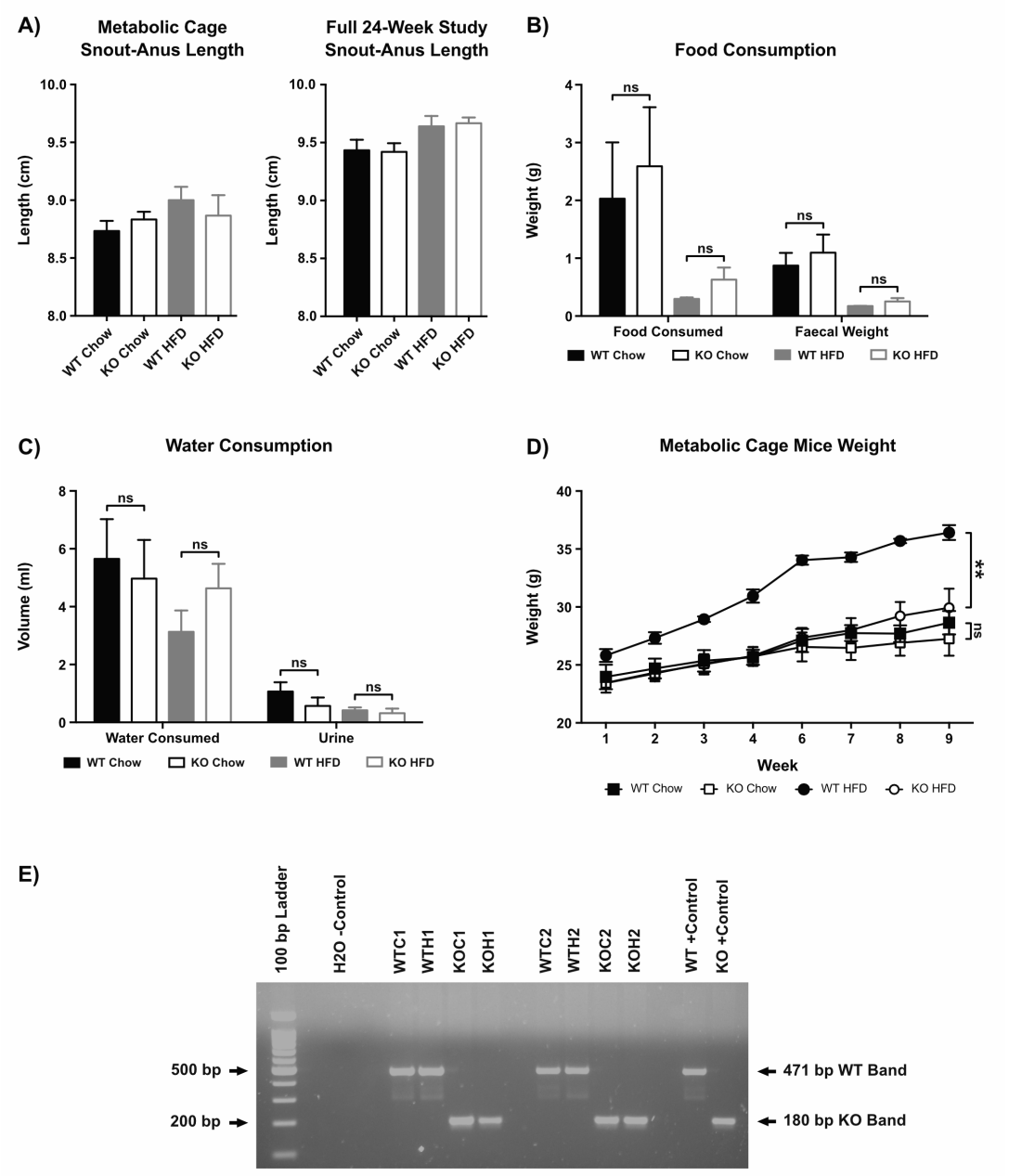

Figure 4.19: Weight Differences Between miR-34a$^{-/-}$ and WT Mice are Not Due to Differences in Food and Water Consumption

(A) Snout to anus measurements of mouse length of miR-34a$^{-/-}$ (KO) and WT mice on chow Vs. HFD at the end of a 9-week metabolic cage study (n=3) and the bigger 24-week study (n=9 for WT Chow and KO HFD, n=10 for KO Chow and WT HFD). (B) Measurements of food mass consumed and faecal mass excreted by metabolic cage mice in (A) at week 9, over a 24-hour period; n=3. (C) Measurements of water consumption and urine excretion by metabolic cage mice in (A) at week 9, over a 24-hour period; n=3. Water volume measurements were calculated off its mass, assuming: 1 g = 1 ml. (D) Body weight tracking of the metabolic cage mice in (A) over 9 weeks; n=3. Statistics were calculated off AUC analysis of each replicate. (E) Representative genotyping of metabolic cage mice in (A) at week 9, run on a 2% agarose gel with 0.2 µg/ml EtBr, at 85 V. WT = wild type, KO = miR-34a$^{-/-}$, C = chow, and H = HFD in the naming convention. All graphs represent mean values with SEM. **P<0.01, ns = not significant: One-way ANOVA, with Bonferroni's multiple comparisons post-test.

4.5 Discussion

This chapter showed that miR-34a$^{-/-}$ mice are susceptible to diet-induced obesity, with an altered *ex vivo* eWAT phenotype and altered metabolic gene profile that could contribute to miR-34a$^{-/-}$ mice's susceptibility. Additionally, changes in immune phenotype and cytokine expression were observed, which could be contributing factors. These data demonstrated that miR-34a$^{-/-}$ mice gained more weight when challenged with a HFD than WT counterparts. They also showed that miR-34a$^{-/-}$ eWAT had smaller, more numerous adipocytes, with a lower tissue mass on chow that increased to WT levels on HFD. Surprisingly, these characteristics did not alter between HFD-fed miR-34a$^{-/-}$ and WT mice, despite a clear difference in body weight. No change in liver weight was observed between HFD-fed miR-34a$^{-/-}$ and WT mice; therefore, the weight difference may be due to increased mass of other WAT depots (e.g. scWAT), BAT, or muscle tissue. The adipocytes in the eWAT may have reached their physiological limits of hypertrophy, due to the long period of HFD feeding, obscuring differences between miR-34a$^{-/-}$ and WT mice, and contributing to lipid accumulation in other tissues (DiGirolamo et al. 1998; Halberg et al. 2009). Surprisingly, MRS analysis did not reveal any difference in overall percentage body fat between HFD-fed miR-34a$^{-/-}$ and WT mice, despite a clear increase in body weight. However, whole-body MRS for body fat is a crude measurement that does not take into account muscle mass, bone mass, and overall fat distribution around the body, such as ectopic lipid distribution. Additionally, it was surprising that HFD-fed miR-34a$^{-/-}$ mice did not show increase glucose tolerance compared to their WT controls, given their clear increase in body weight. This may be due to the 16-18 hour fast used for these GTTs being too long, inducing starvation mechanisms in these mice and clouding the results. However, others routinely use overnight 12-16 hour fasts for murine GTTs (Klaman et al. 2000; Handschin et al. 2007; Wheatcroft et al. 2007; Owen et al. 2012; Higa et al. 2014), and murine starvation studies tend to use fasts ≥48 hours (Lee and Goldberg 2015; Skowronski et al. 2016). Furthermore, an increase in glucose tolerance was observed between chow and HFD groups, suggesting the assay worked. Therefore, the 16-18 hour fasting time is unlikely to have had a significant effect on the results. A shorter fast of 5-6 hours would be

more appropriate for an insulin tolerance test (ITT) (Owen et al. 2012), which is a better measurement of insulin resistance.

Metabolic gene changes within the eWAT of miR-34a$^{-/-}$ mice were examined to further explore miR-34a's regulation of adipocyte metabolism. Basal increases were observed in *Cd36, Fasn, Hmgcr, Pgc1α,* and *Lxrα* transcripts. CD36 and FAS are both involved in lipid storage by mediating FA uptake and *de novo* lipogenesis, respectively, with increased transcripts suggesting greater lipid storage (Jensen-Urstad and Semenkovich 2012). In support of this, inhibition or ablation of FAS and CD36 has been shown to increase adipocyte lipolysis (An et al. 2007; Vroegrijk et al. 2013). Furthermore, HFD-fed CD36$^{-/-}$ mice showed decreased weight gain, visceral/subcutaneous WAT mass, and eWAT adipocyte number (Vroegrijk et al. 2013). HMGCR is the rate-limiting enzyme of cholesterol biosynthesis, and is expressed in both the liver and adipocytes. Adipocyte hypertrophy within primate omental WAT has been associated with increases in total and free adipocyte cholesterol (Erol 2005; Chung et al. 2014). Contrary to these findings, viral transduction of *Pgc1α* into white adipocytes has been shown to increase *Ucp1* transcripts, mitochondrial FA oxidation genes, and mitochondrial DNA (Puigserver et al. 1998). It is surprising that *Pgc1α* transcripts were increased in the eWAT, as PGC-1α is usually lowly expressed in WAT, but this could suggest browning of the WAT. This has been previously observed by Fu et al. after miR-34a knock-down *in vivo*, with increases in WAT *Pgc1α* and *Ucp1* transcripts, mitochondrial DNA, and citrate synthase activity during murine HFD-feeding (Fu et al. 2014). LXRα's role in the metabolic regulation of adipose tissue is ambiguous, with a number of studies showing LXRα inhibits lipolysis and conflicting studies suggesting LXRα promotes lipolysis, fatty acid (FA) oxidation, and glucose uptake into adipocytes; however, there is more evidence for the latter (Dalen et al. 2003; Laffitte et al. 2003; Kalaany et al. 2005; Stenson et al. 2009; Korach-André et al. 2011; Pettersson et al. 2013; Dib et al. 2014). Therefore, this suggests that there may be an imbalance in lipolysis/FA oxidation Vs. lipid uptake/lipogenesis, which is tipped towards the latter in adipocytes of miR-34a$^{-/-}$ mice, predisposing them to weight gain when stressed with a HFD (Figure 4.20). The observed decreases in *Acca* and *Fasn* transcripts during HFD-feeding in miR-34a$^{-/-}$ eWAT, could indicate the the balance being shifted back to FA

oxidation/lipolysis to regain lipid homeostasis, by another regulatory system. The up-regulation of *Pgc1α* transcripts in miR-34a$^{-/-}$ BAT during HFD-feeding, could assist this regulatory system and compensate for the reduction observed in *c/ebpα* and *β* transcripts. Both C/EBPα and β are important transcriptional regulators of the BAT phenotype, as both C/EBPα and β transactivate UCP1, and C/EBPβ is essential for brown adipocyte differentiation and thermoregulation (Carmona et al. 2005; Kajimura et al. 2009). On the contrary, during miR-34a knock-down in HFD-fed mice, Fu et al. did not observe an increase in BAT *Pgc1α* transcripts, but showed an increase in mitochondrial DNA, and *Ucp1* and *Fabp4* transcripts (Fu et al. 2014).

It is surprising that the majority of the metabolic genes examined did not change in the eWAT and liver of WT mice when fed a HFD. In particular, a seminal paper by Vidal-Puig et al. showed that *Pparɣ* transcripts increased in the eWAT of FVB mice fed HFD for 9 weeks, which remained unchanged here (Vidal-Puig et al. 1996). However, the authors of this study did not show any change in *Pparɣ* transcripts within the liver of these mice, correlating with observations made in this chapter. On the contrary, *Pparɣ* transcripts increase in the livers of HFD-fed SV129 mice (Patsouris et al. 2006). Additionally, *Pparɣ* transcripts do not change in the eWAT of HFD-fed genetically obese UCP-DTA mice, compared to chow controls (Vidal-Puig et al. 1996). This highlights that there are strain- and model-specific differences in metabolic gene expression within these tissues (Montgomery et al. 2013). Furthermore, numerous studies on WT C57BL/6 mice (used here) show that *Pparɣ* transcript levels in the eWAT and liver remain unchanged, or decrease slightly, when fed HFD, supporting the data shown here (Wagener et al. 2010; Owen et al. 2012; Mcilroy et al. 2013; Miller et al. 2013). With regards to the other metabolic genes that remained unchanged in the eWAT and liver of HFD-fed WT mice, a number of studies on WT C57BL/6 mice confirm that there is little to no change in these genes when stressed with HFD alone (Wagener et al. 2010; Owen et al. 2012; Mcilroy et al. 2013; Miller et al. 2013; Fu et al. 2014).

Interestingly, one of the few metabolic changes observed in miR-34a$^{-/-}$ livers, apart from increased steatosis, was a basal increase in *Pgc1α* and *Cebpα* mRNA,

which was unchanged during HFD-feeding. This correlates with Fu et al. who did not see any change in hepatic *Pgc1α* mRNA during miR-34a knock-down in HFD-fed mice (Fu et al. 2014). This is further supported by another report showing decreased hepatic SIRT1-mediated deacetylation of PGC-1α during miR-34a overexpression in chow-fed mice, and increased deacetylation in anti-miR-34a treated HFD-fed mice, inhibiting and activating PGC-1α, respectively (Rodgers et al. 2008; Choi et al. 2013). With SIRT1 deacetylation of PGC-1α being shown to increase *Pgc1α* transcripts (Rodgers et al. 2005), the consistent increase in *Pgc1α* transcripts across the eWAT, BAT, and liver shown here, suggests that it is broadly regulated by miR-34a. This could be mediated through miR-34a targeting SIRT1 and fibroblast growth factor (FGF)21 receptor (FGFR1-βKL), as shown by others (Choi et al. 2013; Fu et al. 2014), or could be through direct targeting of PGC-1α gene transcripts. Given the association with obesity and the development of NAFLD, it is surprising that liver weights did not increase on HFD in either WT or miR-34a$^{-/-}$ mice (Edens et al. 2009). However, data from my group and others has shown that C57BL/6 mice (used here) fed HFD for 8 and 24 weeks show no change in liver weight, despite increases in liver TGs (Miller et al. 2013; Montgomery et al. 2013). There are stain specific differences in liver weight during HFD feeding, with C57BL/6 mice showing resistance to liver weight gain (Montgomery et al. 2013). In contrast, 8-10-week-old *ob/ob* mice show approximately a 1.7-fold increase in liver weight, compared to lean WT C57BL/6 controls (Xu et al. 2003a).

Recent discoveries showing large immune cell infiltrate into the adipose tissue during obesity (e.g. macrophages (ATMs), T cells, B cells, and neutrophils) that can modulate the metabolic functions of adipocytes, prompted examination of these leukocytes and their regulation by miR-34a. Exploration of the immune phenotype within the eWAT identified a population of F4/80^{high} CD45^{+} MHCII^{+} CD11b^{+} CD86^{+} ATMs and increased type 2 cytokines in HFD-fed miR-34a$^{-/-}$ mice. Additionally, a reduction in the percentage of F4/80^{+} ATMs was observed in chow-fed miR-34a$^{-/-}$ eWAT, but not in the spleen, suggesting a reduction in the tissue-resident ATMs under normal conditions. F4/80 is a glycoprotein that is specifically expressed on murine macrophages, and its expression increases with macrophage maturation, but the specific function of F4/80 remains ambiguous.

However, it has been suggested that F4/80 can induce $CD8^+$ T_{regs} (Lin et al. 2005; Vandenberg and Kraal 2005). Furthermore, a population of $CD45^+$ $F4/80^{high}$ $MHCII^+$ $CX3CR1^{high}$ macrophages in the colon were identified with an M2-like phenotype, showing constitutive production of IL-10, phagocytosis, and unresponsiveness to TLR stimulation (Bain et al. 2013; 2014). Previous reports have also identified a population of $F4/80^{high}$ ATMs in murine WAT, which were in equal proportions $F4/80^{low}$:$F4/80^{high}$ in obese *db/db* WAT, but there was a greater proportion of $F4/80^{high}$ ATMs in diet-induced obese WAT (Bassaganya-Riera et al. 2009; Titos et al. 2011). Bassaganya-Riera et al. showed that these $F4/80^{high}$ ATMs express higher levels of MHCII, CX3CR1, CD11c, CCR2, and PPARɣ in *db/db* mice, with increased intracellular IL-6, TNFα, CCL2, and IL-10, which increases further upon LPS-stimulation (Bassaganya-Riera et al. 2009). These reports of high IL-10 production and T_{reg} induction, support the observations made here of increased eWAT *Il-10* transcripts in HFD-fed miR-34a$^{-/-}$ mice correlating with an $F4/80^{high}$ ATM phenotype. Therefore, this could suggest that these ATMs have an M2-like phenotype. An M2 phenotype is further supported by observation of increased serum levels of the eosinophils growth and differentiation factor IL-5. Eosinophils are important for the maintenance of M2 ATMs within the WAT through the production of IL-4/13 (Wu et al. 2011; Molofsky et al. 2013). Therefore, it is possible that increased serum IL-5 could contribute to the accumulation of eosinophils in the WAT, increasing local IL-4/13 and M2 ATM polarisation. However, examination of IL-5, IL-4, IL-13, and eosinophil content in the eWAT of miR-34a$^{-/-}$ mice is needed to explore this possibility. Importantly, type-2 cytokines and M2 ATM responses have been reported to induce a protective effect from obesity and T2D, with increased insulin sensitivity, glucose uptake and anabolism in white adipocytes, but decreased body weight (Odegaard et al. 2007; Lumeng et al. 2007a; Ricardo-Gonzalez et al. 2010; Wu et al. 2011; Molofsky et al. 2013). This change in ATM phenotype may therefore be a compensatory effect, to regain metabolic homeostasis during over-nutrition in miR-34a$^{-/-}$ mice, rather than contributing to miR-34a$^{-/-}$ weight gain. Contrary to an M2 ATM phenotype, the observations by Bassaganya-Riera et al. suggest that $F4/80^{high}$ macrophages could also be M1-like, despite expressing high levels of IL-10 and PPARɣ, due to their high expression of IL-6, TNFα, CCL2, CCR2, CD11c, and MHCII (Bassaganya-Riera et al. 2009). Additionally, observations in this chapter showed

that transcripts of the M1 marker *Nos2* are increased basely in miR-34a$^{-/-}$ eWAT and the M2 marker *Retnla* is reduced in HFD-fed 34a$^{-/-}$ eWAT, compared to WT controls. Therefore, it is unclear whether miR-34a$^{-/-}$ F4/80^{high} ATMs are pro- or anti-inflammatory without additional functional data.

To explore the other branches of the immune system, lymphocyte and neutrophil content was examined in the eWAT and spleen. No change in the CD4^{+} or CD8^{+} T cell populations were observed in either the eWAT or spleen, between miR-34a$^{-/-}$ and WT mice. The current literature suggests that miR-34a enhances T cell activation *in vitro* by targeting diacylglycerol kinase (DGK)ζ (Shin et al. 2013). Additionally, it has been shown that miR-34a inhibits TGFβ-induced CCL22 recruitment of (CD4^{+} CD25^{+} FoxP3^{+}) T_{regs} in a PVTT model (Yang et al. 2012). Therefore, a change may have been observed between WT and miR-34a$^{-/-}$ T cells if functional characteristics were examined, or if there was a significant change in of adipose T_{reg} numbers. It is surprising there was no change in T cell content, given the T cell chemoattractant CXCL9 was up-regulated in HFD-fed miR-34a$^{-/-}$ serum, compared to HFD-fed WT controls. CXCL9 has been shown to be up-regulated in the serum of C57BL/6 mice after 8-12 weeks on HFD, and its release from macrophages is inhibited by adipocyte-derived adiponectin *in vitro* (Okamoto et al. 2008; Griffin et al. 2012; Vielma et al. 2013). The results in this chapter do not show an increase in serum CXCL9 during HFD-feeding; equally, diet-induced increases in the eWAT macrophage population were not observed, as seen by Weisberg et al. (Weisberg et al. 2003). This could be due to resolution of inflammation by week-24 of HFD-feeding, as previous studies have observed significant reductions in necrosis within the eWAT of C57BL/6 mice by week-20 of HFD-feeding (Strissel et al. 2007). The authors of that study also showed reductions in CD11c, CD11b, and CCL2 transcripts from week 16, and that eWAT adipocyte size peaked at week 12 of diet, decreasing at week 16 and 20.

Interestingly, despite not seeing a change in the B cell content of eWAT, splenic B cells were increased in both miR-34a$^{-/-}$ groups, compared to WT controls. This correlates with other reports exploring miR-34a's regulation of B cell differentiation. For example, miR-34a inhibits the differentiation of pro-B cells to pre-B cells by targeting the forkhead box (Fox)p1 transcription factor, causing a

reduction in the percentage of mature B Cells ($CD19^+$ IgM^+) in murine bone marrow (Rao et al. 2010). Additionally, miR-34a inhibits FOXP1-mediated malignant transformation of the low-grade, gastric mucosa-associated lymphoid tissue (MALT) B cell lymphoma to the high-grade, diffuse large B-cell lymphoma (DLBCL) *in vitro* and *in vivo* (Craig et al. 2011; 2012). Finally, miR-34a enhances transdifferentiation of murine bone marrow-derived pre-B cells into macrophage-like cells (Mac-1^+) by targeting lymphoid enhancer-binding factor (Lef)1, *in vitro* (Rodriguez-Ubreva et al. 2014). The role of B cells in obesity has not been well explored. However, B cell KO studies in mice on HFD have shown improvements in glucose handling, with reduced serum insulin levels and reduced inflammatory cytokines (Interferon (IFN)ɣ and TNFα), M1 ATM numbers, and activated $CD8^+$ T cells within the vWAT (Winer et al. 2011; DeFuria et al. 2013). However, this was not accompanied by a change in body weight. Furthermore, decreased serum IL-6, TNFα, and CCL2 was observed in HFD-fed B cell KO mice (DeFuria et al. 2013). Therefore, the increase in splenic B cells observed in miR-34a$^{-/-}$ mice may seem counterintuitive to promoting a type-2 immune response. However, a population of regulatory B cells were identified within adipose tissue that constitutively produce IL-10, with B cell-specific IL-10 deletion causing an increase in $CD8^+$ T cells, M1 macrophages, and *Tnfα*, *Il-6*, and *Ccl2* transcripts within scWAT and eWAT, during HFD-feeding (Nishimura et al. 2013). Unfortunately, the authors did not find the same population of regulatory B cells in the spleen. Therefore, it is unclear whether the increase in miR-34a$^{-/-}$ splenic B cells contributes to the increases in *Il-10* transcripts seen in the eWAT and liver. Further phenotypic characterisation of this B cell population could reveal if they have regulatory functions.

A reduction in splenic neutrophils was also observed in miR-34a$^{-/-}$ mice, with higher numbers in the eWAT of chow-fed miR-34a$^{-/-}$ mice, which reduced to WT levels on HFD-feeding. The contribution of neutrophils to obesity has been poorly studied. However, the neutrophil chemoattractants CXCL2 and CXCL8 were shown to increase in human, obese vWAT and mediate neutrophil adhesion to vWAT endothelial cells *in vitro* (Rouault et al. 2013). Additionally, *in vivo* neutrophil elastase inhibition and neutrophil-specific elastase KO (NEKO) mice conferred improved glucose handling during HFD-feeding (Talukdar et al. 2012). The authors

noted an increase in M2-like ATMs and WAT *Acca* and *Fasn* transcripts. Therefore, this reduction in systemic neutrophils could have an impact on macrophage polarisation and contribute to an M2 ATM phenotype. In support of this, another study showed that *in vivo* miR-34a overexpression increased the percentage of splenic $CD11b^{+}$ $Gr1(Ly6c\text{-}Ly6g)^{+}$ cells, which the authors suggest are myeloid-derived suppressor cells (MDSCs), but no functional data of suppressive activity is shown (Huang et al. 2014). Unfortunately, however, no reduction in eWAT neutrophils was observed in miR-34a$^{-/-}$ mice here, compared to WT.

Contrary to an anti-inflammatory phenotype in miR-34a$^{-/-}$ mice, increases in hepatic *Tnfa* and *Nos2* transcripts during HFD-feeding suggest an M1 macrophage (Kupffer cell) phenotype in the liver. However, there was also a decrease in *Arg1* and an increase in *Chi3l3* and *Il-10* transcripts upon HFD-feeding, with increased basal *Pparδ* transcripts in miR-34a$^{-/-}$ mice, suggesting an M2 macrphage phenotype. Furthermore, there was no change in liver fibrosis, suggesting an overall anti-inflammatory M2 phenotype within the liver.

Susceptibility of miR-34a$^{-/-}$ mice to weight gain was not due to differences in their length (snout-anus measurements), or differences in eating and drinking behavior during the metabolic cage study. This was further supported by no difference in serum leptin being observed in miR-34a$^{-/-}$ mice. However, this is surprising considering miR-34a$^{-/-}$ mice gained more weight on HFD than WT mice, but after 24 weeks of diet the weights of WT and miR-34a$^{-/-}$ mice start to converge. This could explain the similar leptin values for WT and miR-34a$^{-/-}$ mice at week 24. Even though the HFD groups showed high levels (approx. 15,000 pg/ml) of serum leptin, these levels remained within assay limits (max standard: 50,336 pg/ml) ruling out a quantification error. Additionally, these levels are well below those observed by others in *db/db* (approx. 125,000 pg/ml) and diet-induced obese mice (approx. 312,500 pg/ml) (Maffei et al. 1995).

Surprisingly, miR-34a$^{-/-}$ mice in the metabolic cage study showed an inverted response to HFD-feeding, compared with the 24-week HFD study, showing WT mice gained more weight than miR-34a$^{-/-}$ mice. There could be a few explanations

for this. Overall, this was an underpowered study, with only 3 mice in each group, and the data at week 9 was on the edge of the range for the same time-point in the 24-week study. Additionally, due to restrictions on equipment, the metabolic cage study was carried out in a different animal facility from the 24-week *in vivo* study. This introduced more variables into the study, with larger cage sizes, different animal technicians, smaller food bowls and a different environment. This change in environment could be associated with changes in gut microbiota, which has been shown to contribute to obesity susceptibility (Rosenbaum et al. 2015). One study showed that there were significant differences in the diversity of the gut microbiota from vendor-bought C57BL/6 mice and their in-house bred counterparts (Ussar et al. 2015). Additionally, the author of that study showed that after as little as 8 weeks in their animal facility, vendor C57BL/6 mice expressed approximately 30% of the facility-specific gut microbiota phylogeny. Finally, it was later discovered that during the metabolic cage study a malfunction caused the animal facility lighting to be on constantly, instead of on a 12-hour light/dark cycle, affecting circadian rhythm. Circadian effects in mice exposed to constant light and “jet-lagged” mice, with variable lighting conditions, have caused increases in body weight, compared to controls (Coomans et al. 2013; Oike et al. 2015).

During the course of the studies in this chapter, conflicting reports from the Kemper lab, using miRNA-targeting approaches, were published. In 2012 Fu et al. showed anti-miR-34a administration improved systemic insulin and glucose tolerance, reduced hepatic fat, and a reduction in expression of *Cyp7a1* and other cholesterol genes, in HFD-fed BALB/c mice (Fu et al. 2012). However, the authors noted increases in expression of the hepatic fatty acid oxidation genes carnitine palmitoyltransferase (*Cpt*) and medium-chain specific acyl-CoA dehydrogenase (*Mcad*), in this model. Supporting the study by Fu, Choi et al. administered anti-miR-34a to HFD-fed BALB/c mice and showed improved glucose and insulin tolerance, with a reduction in serum insulin (Choi et al. 2013). Additionally, the authors showed increased hepatic *Pparδ* and decreased *Cd36*, *TNFα*, and *Il-6* transcripts, with decreased hepatic fat. Furthermore, in 2014 Fu et al. inhibited miR-34a in the WAT and BAT of HFD-fed BALB/c mice using a lentiviral vector, and observed a reduction in body weight, vWAT (epididymal and peritoneal), inguinal scWAT, and eWAT adipocyte size, 20 days after inhibition (Fu et al.

2014). The authors also reported increased hepatic *Acca* transcripts and decreased *Fasn* and sterol regulatory element binding transcription factor (*Srebf)1* transcripts. Increased eWAT *Pparγ* and *Fabp4* transcripts, and decreased *Il-6*, *TNFα*, and *Srebf1* transcripts, were also observed in this model. Interestingly, correlating with this chapter, they observed increased *Pgc1α* transcripts in the eWAT and BAT, and decreased *Fasn* and *Acca* transcripts in eWAT of HFD mice, during miR-34a inhibition. A male C57BL/6 mouse model the authors showed a similar phenotype, with improved glucose tolerance; however, the authors did not discuss the specific tropism of the viral vector. Additionally, BALB/c mice have a greater resistance to diet-induced obesity than the C57BL/6 mice used here (Montgomery et al. 2013). Furthermore, Fu's C57BL/6 model only used a 14-week HFD-feeding protocol, in comparison to the longer 24 weeks used here. The inhibition of miR-34a was also acute in those studies, rather than the chronic deficiency seen in a KO model. In support of *in vivo* model differences, both Fu and Choi showed a decrease in serum TGs; however, Xu et al. showed the opposite in miR-34a$^{-/-}$ mice (Xu et al. 2015). Changes in serum TG were not altered in this chapter, which may be due to the reduced sensitivity of the clinical analyser, but this highlights the differences between obesity models.

In a full-body KO model, there are risks of other pathways compensating for the loss of that gene. In fact, miR-34 family KO mice do not become spontaneously tumour laden, despite the role of this family as a modulator of p53 and in tumour suppression (Concepcion et al. 2012). In this case, since miR-34a$^{-/-}$ mice still express the other miR-34 family members, they could provide compensation, as some miR-34a gene targets have also been shown to be regulated by miR-34b and c, reviewed here (Rokavec et al. 2014a). Therefore, despite the differences in models used by Kemper's group and in this chapter, the common gene changes (Notably, *Pgc1α, Acca* and *Fasn*) could indicate that they are regulated by miR-34a, with less redundancy. It has become clear that miR-34a's regulation of metabolic pathways is complex and its role is likely to vary depending on the models and treatments used, with potential cell-specific differences. To clarify the cell-specific roles of miR-34a inducible, cell/tissue-specific KO models would be invaluable. However, there are other limitations to the studies in this chapter. Only a single time point in the development of obesity

(24 weeks on HFD) was examined, at which point there may have been plateauing of responses regulated by miR-34a, with resolution of inflammation and compensatory pathways coming into effect. Physiological characteristics of metabolism were not examined (e.g. body temperature and O_2 consumption), which would give useful measurements of metabolic rate. Additionally, physical activity was not examined, which would account for differences in energy expenditure. Finally, the metabolic cage study was underpowered, suffered from inappropriate lighting, and only examined one 24-hour period for food/water consumption and excretion, with a bigger study and tighter control of environmental variables required.

In conclusion, miR-34a$^{-/-}$ mice show a susceptibility to diet-induced obesity and alterations in a number of metabolic factors within the adipose tissue and immune phenotype, which could contribute to this susceptibility. Therefore, miR-34a regulates the development of murine, diet-induced obesity in a multifactorial manner (Figure 4.20). However, more data is required to elucidate the mechanism of miR-34a in this model.

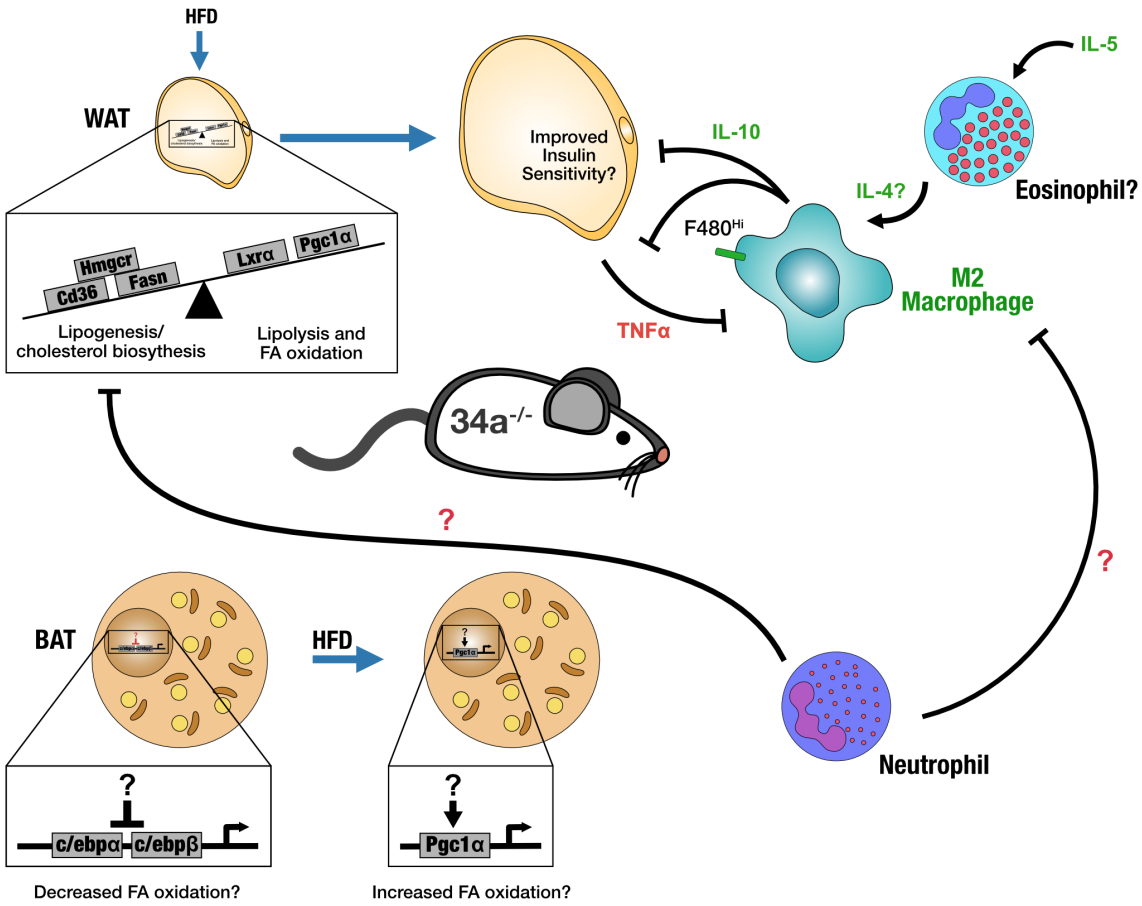

Figure 4.20: Summary of Chapter Conclusions
An imbalance in metabolic genes within the vWAT promotes a pro-hypertrophic environment under nutrient stress with a HFD. Other studies have shown that there is an increase in inflammatory cytokines within the WAT as it increases in size, polarising macrophages to an M1 phenotype (such as TNFα). Additionally, neutrophils promote an M1 macrophage phenotype and can inhibit lipogenic process; however, their reduction in miR-34a$^{-/-}$ mice could promote an M2 phenotype and contribute to adipocyte hypertrophy. Furthermore, the M2 macrophage phenotype could be promoted by increased IL-5, an eosinophil growth and differentiation factor, promoting eosinophil production of pro-M2 IL-4. IL-10 would further promote an M2 phenotype in an autocrine manner and by inhibiting inflammatory cytokine production. IL-10 could also stimulate increased insulin sensitivity in adipocytes and dampen pro-obesity processes. Finally, BAT could also contribute to this phenotype with the inhibition of key thermogenic genes pre-disposing miR-34a$^{-/-}$ mice to obesity, with the increase in *Pgc1α* transcripts being compensatory during nutrient stress with a HFD.

Chapter 5: Examining The Role of miR-34a in Macrophages *in vitro*

5.1 Introduction

From the previous chapters it has been shown that miR-34a$^{-/-}$ mice are susceptible to diet-induced obesity, with metabolic changes in the epididymal white adipose tissues (eWAT). Additionally, the adipose tissue macrophage (ATM) phenotype was altered in these mice, potentially representing a polarisation to an M2-like phenotype during obesity. Therefore, macrophages were examined further *in vitro*, to characterise the role of miR-34a in this cell type and the contribution of macrophages to the *in vivo* phenotype.

The role of miR-34a in macrophages has been poorly studied, and there are currently no studies that have examined macrophage miR-34a in the context of obesity. However, since 2010 a few studies have been published that describe functions of miR-34a in macrophages. The first paper reported that CCAAT/enhancer-binding protein (C/EBP)α transactivates miR-34a transcription allowing miR-34a to target E2F3, blocking myeloid cell differentiation during granulopoiesis in human acute myeloid leukaemia (AML) blast cells (Pulikkan et al. 2010). A paper by Jiang et al. then showed that inflammatory stimulation with lipopolysaccharide (LPS) decreased the expression of miR-34a in RAW264.7 macrophages *in vitro* (Jiang et al. 2012). Additionally, they reported that miR-34a mimics and inhibitors decreased and increased the expression of LPS-stimulated tissue necrosis factor (TNF)α and interleukin (IL)-6, respectively, in the same cells. The authors suggested these data were due to miR-34a targeting notch homolog 1, translocation-associated (NOTCH1), which can activate nuclear factor kappa-light-chain-enhancer of activated B cells (NF-κB). Another study showed a correlation between the increase in miR-34a, miR-21 and insulin-like growth factor (IGF)-1 in alveolar macrophages during murine lung fibrosis (Honeyman et al. 2013). Continuing on from Pulikkan's work, Rodriguez-Ubreva et al. showed that C/EBPα-induced transdifferentiation of pre-B cells to macrophages was aided by C/EBPα transactivating miR-34a and miR-223 transcripts, which target the transcription factor lymphoid enhancer-binding factor (Lef)1 (Rodriguez-Ubreva et al. 2014). Notably, LPS stimulation of RAW264.7 macrophages has been shown to up-regulate *Ccl22* transcripts by down-regulation of miR-34a, which directly targets *Ccl22* mRNA (He et al. 2015). A final report showed that miR-34a inhibits

apoptotic cell clearance (efferocytosis) in alveolar macrophages *in vitro*, partly through inhibition of Axl and silent mating type information regulation 2, *S. cerevisiae*, homolog (sirtuin/SIRT)1 expression, leading to a reduction in apoptotic cell binding (McCubbrey et al. 2016). Therefore, miR-34a clearly has a role in regulating inflammatory pathways in macrophages.

TNFα was one of the first inflammatory cytokines shown to increase in the WAT of obese patients, and is positively associated with insulin resistance (Hotamisligil et al. 1995). However, it is not the only inflammatory cytokine that increases in the obese WAT; IL-6, IL-1β, CC chemokine ligand (CCL)2, CXC chemokine ligand (CXCL)1/8, and others also contribute to the inflammatory environment within WAT (Gregor 2011). In mice, CXCL1 is the murine homologue of CXCL8 (IL-8) in humans, functioning as a primary inflammatory chemokine during inflammation and a chemoattractant for neutrophils. Studies have shown that serum levels of CXCL8 increase proportionally with body mass index (BMI) and waist circumference in humans (Kim et al. 2006; Utsal et al. 2012). Additionally, serum levels of CXCL1 have been reported to increase proportionately with body weight and blood glucose concentration in the obesity and type 2 diabetes (T2D) prone *db/db* mouse (Nunemaker et al. 2014). Another study showed that increased visceral adiposity from high sucrose diet feeding *in vivo*, induces increases in eWAT CXCL1 concentration, and neutrophil and mononuclear cell numbers (Oliveira et al. 2013). In humans, it has been reported that CXCL8 levels are higher in visceral WAT (vWAT), compared with subcutaneous (scWAT), in patients with obesity and it was determined that the source is not the adipocytes themselves (Bruun et al. 2004). Therefore, ATMs could be the source of the increased levels of CXCL1/8, as tissue macrophages are a major source of CXCL1 during inflammation in mice, leading to neutrophil recruitment (De Filippo et al. 2008). TNFα-induced neutrophil chemotaxis is also dependent on CXCL8 (humans) or CXCL1/2 (mice) (Smart and Casale 1994; Zhang et al. 2001). TNFα binds to the TNF receptor (TNFR)1 or 2 and activates transcription of CXCL1 through activation of NF-κB, by utilising a number of adaptor proteins that activate key signalling pathways (Ciesielski et al. 2002; Richmond 2002; Parameswaran and Patial 2010).

Therefore, it was hypothesised that miR-34a regulates inflammatory and metabolic pathways within macrophages that contribute to the inflammatory and metabolic phenotype seen *in vivo*. In this chapter, the phenotype of primary, bone marrow-derived macrophages (BMDMs) from WT and miR-34a$^{-/-}$ mice were examined in the resting state and when stimulated with TNFα. Attempts were also made to manipulate miR-34a expression in WT BMDMs using synthetic miR-34a mimics and inhibitors, to examine miR-34a's regulation of macrophage phenotype.

5.2 Aims

- Examine the expression of miR-34a in WT bone marrow-derived macrophages (BMDMs) *in vitro* under TNFα stimulation.

- Examine the phenotypic differences in BMDMs from WT and miR-34a$^{-/-}$ mice *in vitro*, with/without TNFα stimulation.

- Pharmacologically manipulate miR-34a expression in WT BMDMs *in vitro*, for gain and loss of function experiments.

5.3 Methods

For specific details of individual methods please refer to Chapter 2: Materials and Methods.

5.3.1 Bone Marrow-Derived Macrophage Culture

BMDMs were cultured from 6-8 week-old female, WT and miR-34a$^{-/-}$ mice as previously described: section 2.2.2.2. The phenotype of cultured cells was checked by flow cytometry to make sure the cells were F4/80^{+} (Figure 5.1), following the protocol outlined in section 1.5.2.

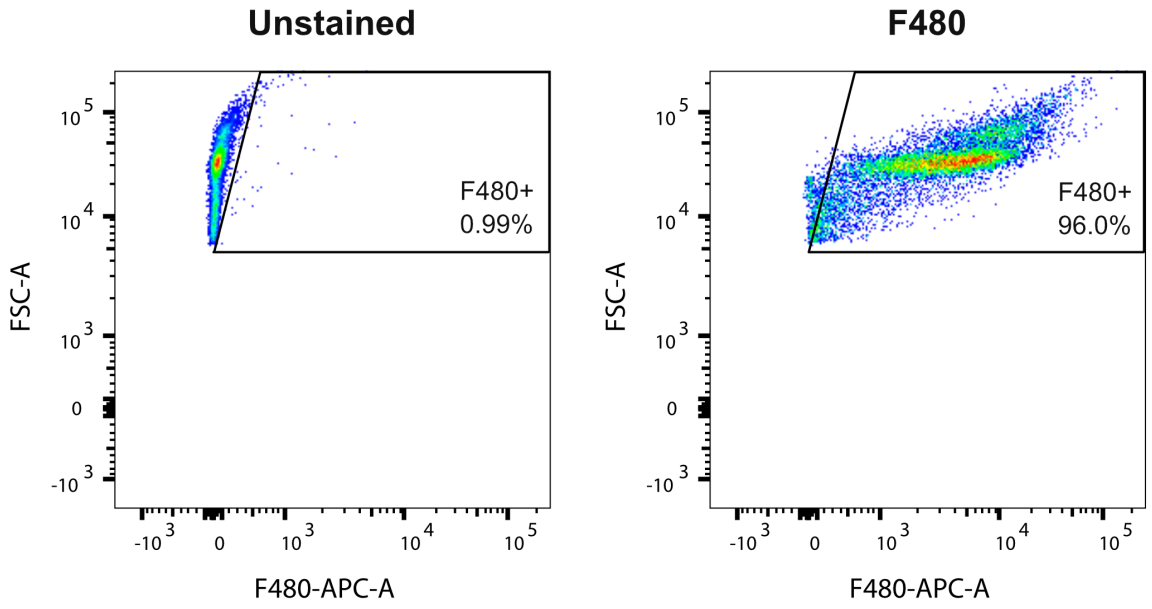

Figure 5.1: Assessment of BMDM Culture Purity by Flow Cytometry
Showing flow cytometry quantification of total F4/80 expression in *in vitro* bone marrow-derived macrophages (BMDMs) differentiated with 50 ng/ml M-CSF for 6 days, from female WT C57BL/6 mice. Gate statistic shows % F4/80^{+} cells.

5.3.2 BMDM Cytokine Stimulation

Differentiated BMDMs were plated out at 0.5x10^{6} cells/well in a 24-well culture plate or 8-well chamber slide as described in section 2.2.2.2. Once cells were distributed between wells they were stimulated with 45.45-50 ng/ml TNFα (Peprotech: 315-01A) or the same volume of complete media as a negative control, in complete media. The cells were then incubated at 37°C with 5% CO_2 for 24 hours, before RNA and supernatant collections. Supernatants were collected, leaving 20% of the volume behind to reduce the collection of dead cells, and

centrifuged at 1000 x g for 10 minutes to remove residual cells, before analysis. RNA was isolated as described in section 2.3.1.3.

5.3.3 BMDM miRNA Transfection

Differentiated BMDMs were collected and plated at $0.2x10^6$ cells/well in a 24-well culture plate, as described in section 2.2.2.2, for both miRNA mimic and anti-miR transfection. Cells were plated and incubated for 24 hours at 37°C with 5% CO_2 before transfection, except for siPORT™ transfections, where transfection took place while cells were in suspension. Three different transfection reagents were compared to identify the most efficient one, using the standard manufacturer protocol: siPORT™ NeoFX™ (Life Technologies: AM4511M), Lipofectamine® RNAiMAX (Life Technologies: 13778-150), and Lipocalyx's Viromer BLUE (VB-01LB-01) and GREEN (VG-01LB-01). At the end of the transfections cells were collected for RNA and supernatants as described in section 5.3.2, and for flow cytometry as described in section 5.3.6.

5.3.3.1 siPORT™ Transfections

The fluorescent, Dy547-labelled miRIDIAN microRNA Mimic Transfection Control (Dharmacon: CP-004500-01-05) or Qiagen's miScript mmu-miR-34a-5p mimic (MSY0000542), Anti-mmu-miR-34a-5p (MIN0000542), or Inhibitor Negative Control (1027271) were first diluted to 10 μM-0.01 nM in Opti-MEM (Life Technologies: 31985-070). The siPORT™ transfection reagent was then diluted 1:20 in Opti-MEM and incubated at room temperature for 10 minutes. Each synthetic miRNA mimic or anti-miR concentration was diluted 1:2 in the transfection reagent preparation and incubated at room temperature for 10 minutes. This was then diluted 1:5 with the cell suspension in the culture plate and incubated for 24 hours at 37°C with 5% CO_2. This made the final concentration of the synthetic miRNAs on the cells 1 μM-1 pM.

5.3.3.2 Lipofectamine® Transfections

First, the synthetic miRNAs were diluted to 2 μM-2 pM in Opti-MEM. Next, the Lipofectamine® transfection reagent was diluted 1:17.67 in Opti-MEM and the synthetic miRNA concentrations were then diluted 1:2 in the transfection reagent

preparation. This was incubated at room temperature for 10 minutes, whilst the culture media was removed from the cells. The transfection reagent-miRNA preparation was then added to each well after the time had elapsed. This made the final concentration of the synthetic miRNAs on the cells 1 μM-1 pM. Cells were incubated for 24 hours at 37°C with 5% CO_2.

5.3.3.3 Viromer Transfections

Synthetic miRNAs were diluted to 10 μM-0.01 nM in Buffer F (supplied). Next, Viromer BLUE/GREEN transfection reagents were diluted 1:90.91 in Buffer F. The synthetic miRNA concentrations were then diluted 1:10 in the transfection reagent preparation and incubated at room temperature for 10 minutes. Finally, the transfection reagent-miRNA preparation was then diluted 1:10 in the culture media on the cells. This produced a final concentration of 0.1 μM-0.1 pM for the synthetic miRNAs on the cells. Cells were incubated for 24 hours at 37°C with 5% CO_2.

5.3.4 *In situ* Hybridisation

BMDMs were grown and stimulated in chamber slides as described in section 5.3.1. The media was aspirated from each well, washed with 500 μl DPBS, and fixed in 4% PFA for 24 hours then stored in 70% ethanol at 4°C until use. Cells were stained for *in situ* hybridisation (ISH), as described in section 2.4.5.2. Images of the slides were taken with a 10 or 40X Olympus Uplan FLN objective, on an Olympus BX41 microscope with QCapture Pro 6.0 Software.

5.3.5 qRT-PCR

RNA was extracted and quantified as described in sections 2.3.1.3 and 2.3.2.1, respectively. Macrophage gene expression was quantified using the Qiagen miScript reverse transcription (RT) II kit and Life Technologies' Gene Expression TaqMan® qPCR system (section 2.3.4). 10ng cDNA was used for each gene expression assay and a list of the gene expression assays used are shown in Table 5.1.

Probe	Cat no.	Probe	Cat no.	Probe	Cat no.
18s rRNA	Mm03928990_g1	Retnla	Mm00445109_m1	Pparɣ	Mm01184322_m1
Arg1	Mm00475988_m1	Il-10	Mm01288386_m1	Accα	Mm01304257_m1
Chi3l3	Mm00657889_mH	Cxcl1	Mm04207460_m1	Fasn	Mm00662319_m1
Il-6	Mm00446190_m1	Cd36	Mm01135198_m1	Pgc1α	Mm00447183_m1
TNFα	Mm00443260_g1	Hmgcr	Mm01282499_m1	Cebpα	Mm01265914_S1
Nos2	Mm01309897_m1	Lxrα	Mm00443451		

Table 5.1: TaqMan™ Gene Expression Assays Used in This Chapter

qRT-PCR analysis of miRNA transcripts was quantified using either the Qiagen miScript system or Life Technologies' TaqMan® microRNA system, as described in section 2.3.4. For each system, Qiagen miScript primer assays or Life Technologies' TaqMan® microRNA assays were used, shown in Table 5.2.

TaqMan® microRNA		Qiagen miScript	
Primer Assay	**Cat no.**	**Primer Assay**	**Cat no.**
miR-34a	000426	Mm_miR-34a_1	MS00001428
miR-34a-3p	465771_mat	Mm_miR-34a*_1	MS00025697
miR-34b-5p	002617	Hs_RNU6B_3	MS00029204
miR-34b-3p	002618		
miR-34c	000428		
miR-34c*	002584		
U6	001973		

Table 5.2: Manufacturer Information For miRNA qRT-PCR Primer Assays

5.3.6 Flow Cytometry

Once BMDMs had been stimulated, as described in section 5.3.2, the media was discarded and cells were washed with 1 ml DPBS/well. The cells were then collected in 1 ml FACS buffer on ice, with each well being scraped with a pipette tip and flushed 4-5 times. Cells were stained and analysed as detailed in section 2.5.2, with the following antibodies (detailed in Table 2.21): F4/80-APC, CD86-PE-Cy7, CD11b-PE-Cy7, CD80-PerCP-Cy5.5, CD69-PerCP-Cy5.5, CD11c-FITC, CD206-PE, major histocompatibility complex (MHC) class II-PE, and toll-like receptor (TLR)2-PE. Compensation was set using single-stain controls and gates were set using fluorescence minus one (FMO) controls. MFI values in this chapter

were calculated as geometric mean fluorescence intensity, unless stated otherwise.

5.3.7 Supernatant Protein Analysis

BMDM supernatants were analysed using a Mouse Cytokine 20-Plex Luminex and Obesity Proteome Array, as described in section 2.2.3.2 and 2.2.3.3, respectively.

5.4 Results

5.4.1 BMDM *in vitro* Cytokine Stimulation and miR-34a Expression

One of the main inflammatory cytokines present in the obese adipose tissue is TNFα, which was shown to be up-regulated in the liver of HFD-fed miR-34a$^{-/-}$ mice, in chapter 4 (Section 4.4.4). Additionally, others have shown that miR-34a mimics reduce TNFα transcripts and protein in macrophage cell lines, during LPS-stimulation (Jiang et al. 2012). Therefore, BMDMs were stimulated with TNFα *in vitro* to assess whether this inflammatory cytokine also modulates miR-34a expression in primary macrophages (Figure 5.2).

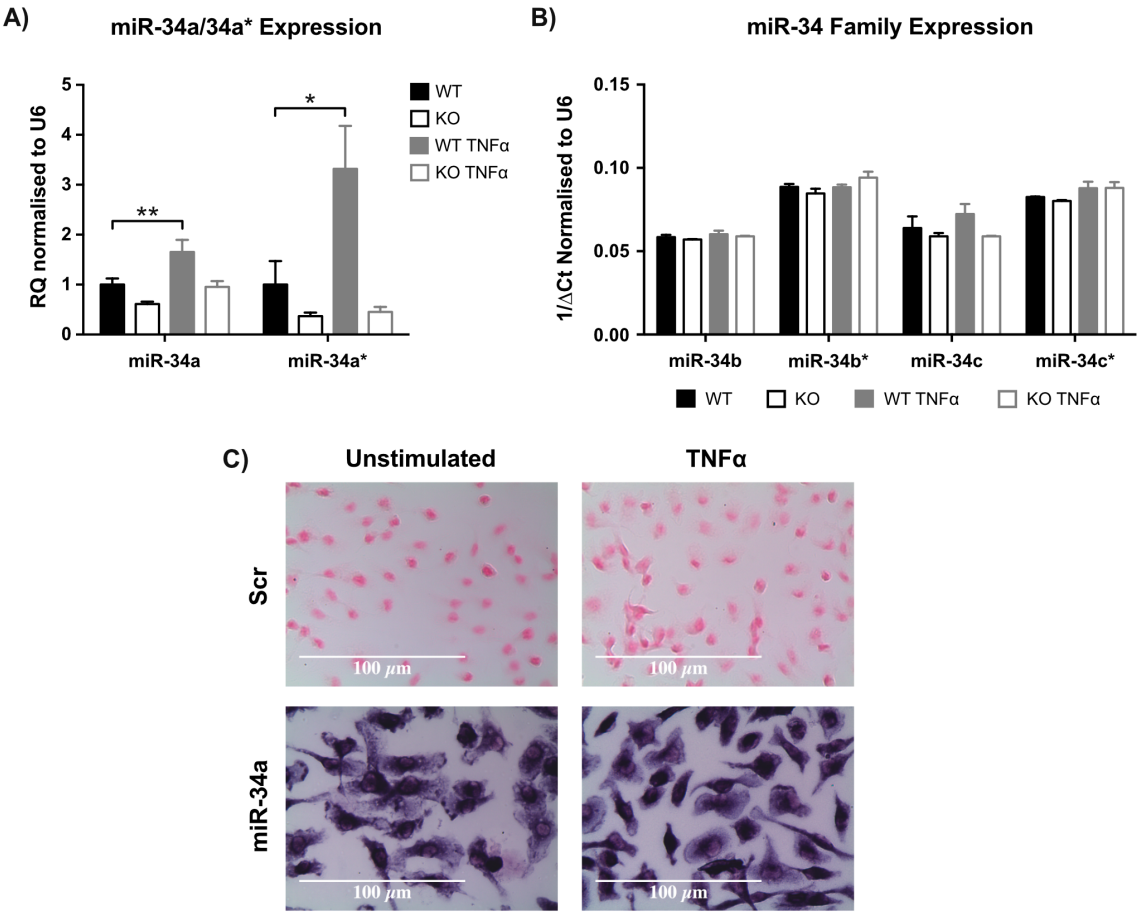

Figure 5.2: Expression of miR-34 Family in BMDMs Stimulated With TNFα
(A) Showing Taqman® qRT-PCR quantification of miR-34a and 34a* transcripts in WT and miR-34a$^{-/-}$ (KO) *in vitro* bone marrow-derived macrophages (BMDMs) ±45.45 ng/ml TNFα for 24 hours. Data is represented as relative quantification (RQ) of unstimulated WT with RQmin-RQmax values, normalised to RNU6; n=3. Statistics calculated by paired student's t-test between WT groups. (B) Taqman® qRT-PCR quantification of the other miR-34 family member transcripts in WT and KO BMDMs ±45.45ng/ml TNFα for 24 hours. Represented as 1/ΔCt, normalised to RNU6B expression, with SEM; n=3. For graphing and statistics "undetermined" values were replaced with Ct = 40, with miR-34b and 34c showing very low to no expression, with statistics calculated by One-way ANOVA, with Bonferroni's multiple comparisons post-test. (C) ISH staining for miR-34a (purple) with scramble control (pink) in the same batch of BMDMs as (A) cultured on chamber slides. *P<0.05, **P<0.01.

Interestingly, TNFα stimulation increased both miR-34a (P=0.0086) and miR-34a* (P=0.0461) transcripts in WT BMDMs, with the greatest change observed in miR-34a* (Figure 5.2A). To be confident that this was only a miR-34a/34a* effect, the other miR-34 family members' transcripts were also quantified. However, no change was observed in their transcript expression, with very low miR-34b and c transcripts detected (Figure 5.2B). Using ISH it was shown that miR-34a is highly expressed in WT BMDMs, with the darkest staining in the nuclei, but did not show the subtle increase in miR-34a expression during TNFα stimulation (Figure 5.2C).

5.4.2 Characterisation of WT and miR-34a$^{-/-}$ BMDM Phenotype *in vitro*

Next, the phenotype of BMDMs from WT and miR-34a$^{-/-}$ mice was assessed under basal conditions and with inflammatory-stimuli from TNFα, to further explore the adipose tissue macrophage (ATM) phenotype observed *ex vivo* (section 4.4.5).

5.4.2.1 Flow Cytometry Analysis of BMDM Phenotype *in vitro*

First, a number of surface markers characteristic of an M1 or M2 macrophage phenotype were assessed by flow cytometry (F4/80, CD11c, CD11b, CD206, MHC class II, TLR2, CD69, CD80, and CD86). Macrophages were gated on forward scatter (FSC)-side scatter (SSC) by selecting the larger cells, which compose the majority of the cells in the sample (Figure 5.3A). A population of F4/80^{+} cells were then selected from this FSC-SSC population, and all other markers were then gated from this F4/80^{+} population. Across all of the groups, over 96% of the cells in the FSC-SSC population were F4/80^{+} (Figure 5.3B and Figure 5.5A). No shift in F4/80 surface expression was observed between the groups, by comparing MFI (Figure 5.3B and Figure 5.5B). Additionally, examination of the other markers on these F4/80^{+} cells did not reveal any differences between WT and miR-34a$^{-/-}$ BMDMs (Figure 5.3B, Figure 5.4, and Figure 5.5C-D). However, during TNFα stimulation in both WT and miR-34a$^{-/-}$ BMDMs there were noticeable positive shifts in fluorescence intensity for TLR2, MHC class II, CD86, and CD69 (Figure 5.3B and Figure 5.4). Quantification of these changes revealed that in WT BMDMs there was a significant increase in the percentage of TLR2^{+} cells during TNFα stimulation (P=0.0352), which was not

observed in miR-34a$^{-/-}$ BMDMs (P=0.0989), with no change in MFI seen in either (Figure 5.5C-D).

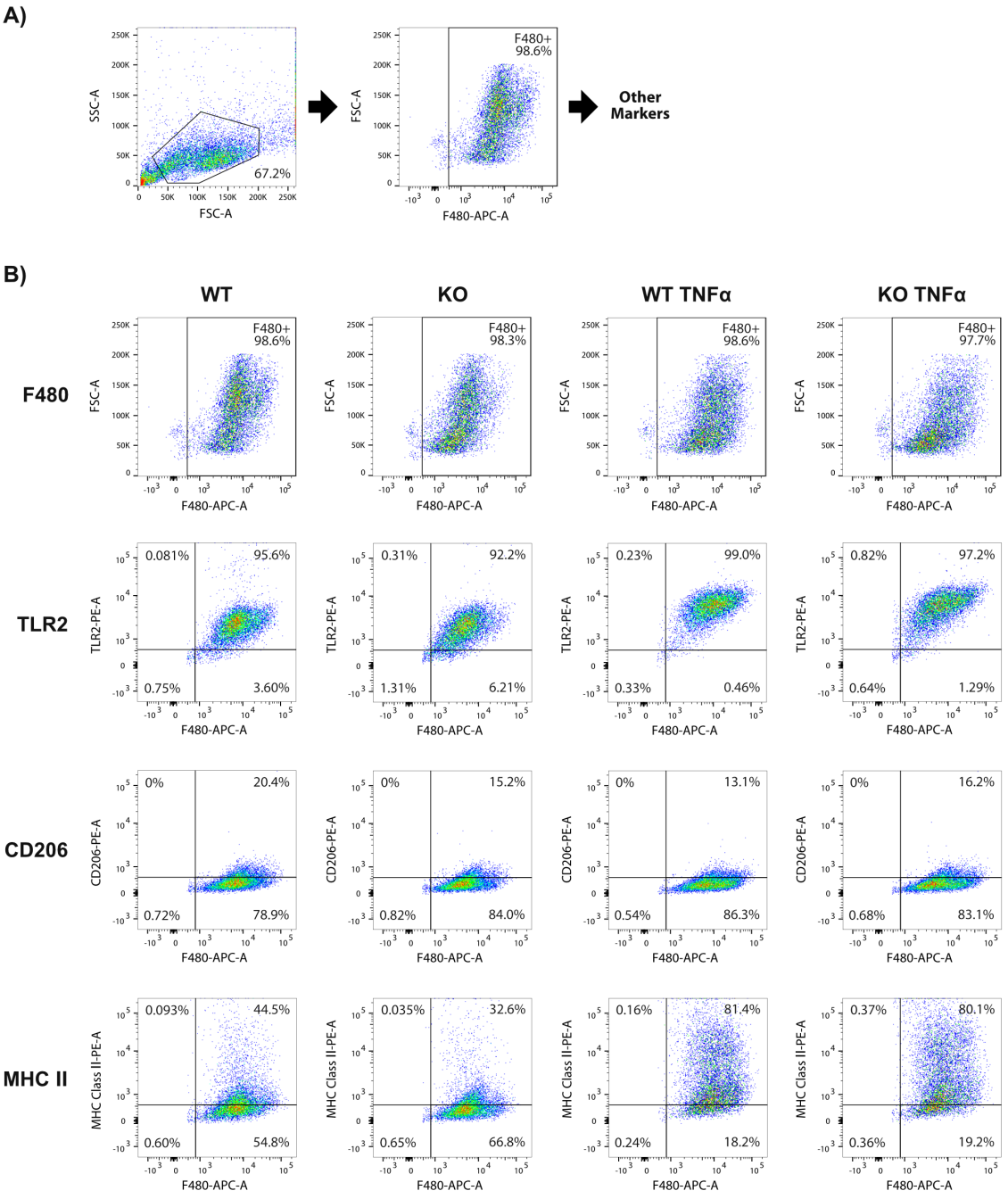

Figure 5.3: Gating Strategy and Representative Flow Cytometry Plots for Macrophage Markers on WT and miR-34a$^{-/-}$ BMDMs Stimulated With TNFα
(A) Showing the flow cytometry gating strategy for BMDMs from WT and miR-34a$^{-/-}$ (KO) mice stimulated with ±45.45 ng/ml TNFα *in vitro* for 24 hours. (B) Showing the representative flow cytometry plots of F4/80, TLR2, CD206, and major histocompatability complex (MHC) class II for each group in (A). All gates were set off FMO controls and percentages are of parent population.

On the other hand, the percentage of MHC class II^{+} cells were significantly increased in both WT (P=0.0048) and miR-34a$^{-/-}$ BMDMs (P=0.0029) with TNFα

stimulation, which was also reflected in MFI analysis (P=0.0303 and 0.0054, respectively). For CD86, a significant increase was only observed in the percentage of WT BMDMs positive for CD86, when stimulated with TNFα (P=0.0400). Unfortunately, statistical analysis could not be performed on the CD69 data, as only two data points were collected. However, cumulatively these data suggest that TNFα stimulation successfully polarised the BMDMs to an M1 phenotype.

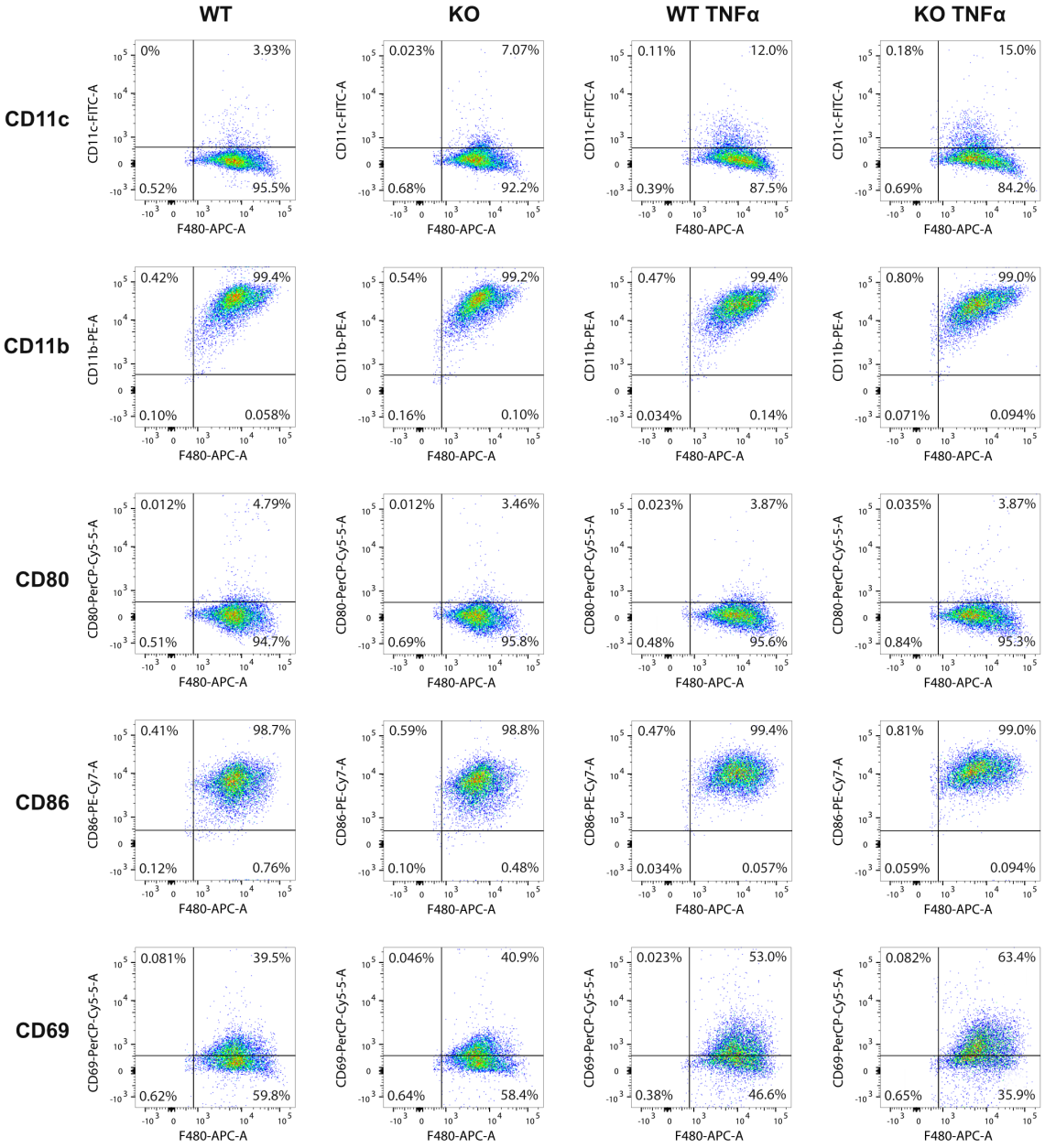

Figure 5.4: Representative Flow Cytometry Plots for Macrophage Markers on WT and miR-34a$^{-/-}$ BMDMs Stimulated With TNFα, Continued
Continuation of the representative flow cytometry plots for macrophage markers on F4/80^{+} cells shown in Figure 5.3B.

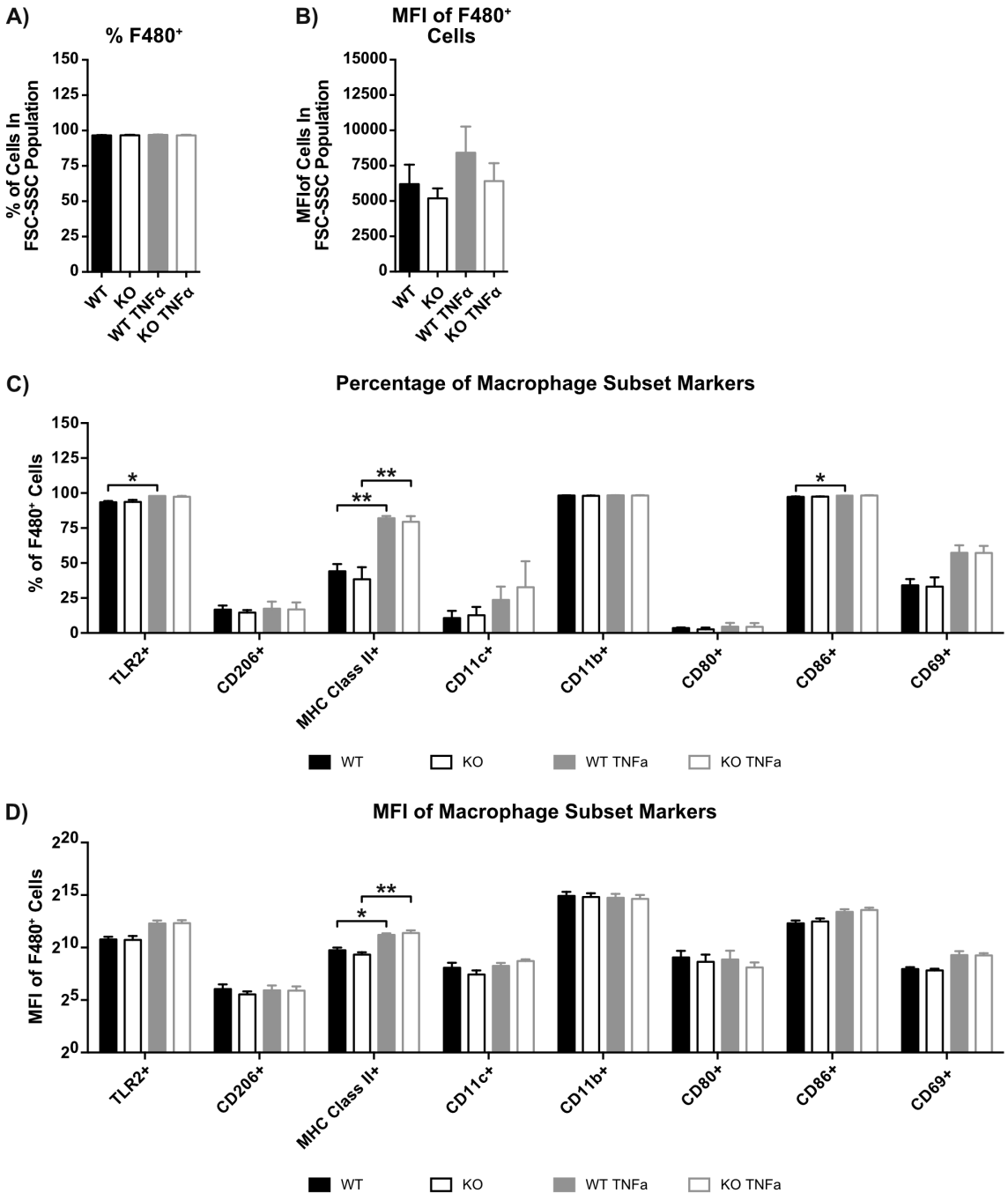

Figure 5.5: Flow Cytometry Quantification of Macrophage Markers on WT and miR-34a$^{-/-}$ BMDMs Stimulated With TNFα

(A-B) Quantification of the percentage of cells positive for and geometric mean florescence intensity (MFI) of F4/80 expression on BMDMs from WT and miR-34a$^{-/-}$ (KO) mice stimulated with ±45.45 ng/ml TNFα *in vitro* for 24 hours, as represented in Figure 5.3; n=3, with the mean of 4 technical replicates for each. (C-D) Quantification of the percentage of cells positive for and MFI of macrophage makers on the same F4/80^{+} population shown in (A-B), and represented in Figure 5.3 and Figure 5.4; n=3 for all except CD69: n=2 and CD11c KO TNFα: n=2. Data is represented as mean values normalised to the FMO control, with SEM. *P<0.05, **P<0.01 One-way ANOVA, with Bonferroni's multiple comparisons post-test.

5.4.2.2 Gene Expression Analysis of BMDM Phenotype *in vitro*

To further characterise the phenotype of macrophages from miR-34a$^{-/-}$ mice *in vitro*, a number of M1/M2 polarisation marker genes (M1: *Nos2*; M2: *Arg1*, *Chi3l3*, *Retnla*, and *Il-10*) were examined by qRT-PCR in WT and miR-34a$^{-/-}$

BMDMs stimulated with ±TNFα. No difference was observed in these polarisation markers between WT and miR-34a$^{-/-}$ BMDMs (Figure 5.6A). However, typical of an M1 phenotype, an increase in *nitric oxide synthase (Nos)2* (P<0.0001), and a decrease in *resistin-like alpha (Retnla)* (WT: P=0.0027; KO: P=0.0036) and *interleukin (Il)-10* (P<0.0001), was observed in both WT and miR-34a$^{-/-}$ BMDMs stimulated with TNFα (Lawrence and Natoli 2011). No expression change was observed in *chitinase 3-like 3 (Chi3l3)* and, atypically, *Arginase (Arg)1* increased (P=0.0104) in WT BMDMs stimulated with TNFα. Additionally, *Tnfα* and *Il-6* gene expression was examined in these samples, but a full data set (n=3) was only obtained for some of the groups, only allowing statistical analysis between the groups indicated (Figure 5.6D). In both the TNFα-stimulated groups it appears that there was an up-regulation of both *Tnfα* and *Il-6* transcripts in the BMDMs; however, this could only be supported statistically in WT BMDMs for *Tnfα* (P=0.0002) and KO BMDMs for *Il-6* (P=0.0011). These data support the suggestion that TNFα-stimulation successfully induced an M1 phenotype in the BMDMs, but does not show any differences between WT and miR-34a$^{-/-}$ BMDMs.

A number of metabolic genes were found to be altered in miR-34a$^{-/-}$ eWAT *ex vivo* (*Cd36*, *3-hydroxy-3-methylglutaryl-CoA reductase* (*Hmgcr)*, *liver X receptor* (*Lxr)α*, *peroxisome proliferator-activated receptor* (*Ppar)ɣ*, *acetyl-CoA carboxylase* (*Acc)α*, *fatty acid synthase* (*Fasn)*, *PPAR gamma coactivator* (*Pgc)1α*, and *Cebpα*) in chapter 4 (section 4.4.3). Therefore, these genes were also examined in BMDMs to see if these changes could be attributed to differences in the tissue macrophages. However, no differences in these genes' transcript expression were observed between WT and miR-34a$^{-/-}$ BMDMs, except for *Pgc1α* transcripts (Figure 5.6B-C). miR-34a$^{-/-}$ BMDMs showed higher basal transcript expression of *Pgc1α*, compared to WT (P=0.0024), which decreased back to WT levels when stimulated with TNFα (P=0.0139) (Figure 5.6C). In both WT and miR-34a$^{-/-}$ BMDMs, increases were observed in *Hmgcr* (WT: P=0.0085; KO: P=0.0305) and *Lxrα* (WT: P=0.0005; KO: P=0.0001) when stimulated with TNFα (Figure 5.6B). Additionally, decreases in *Pparɣ* (P<0.0001), *Fasn* (WT: P=0.0198; KO: P=0.0068), and *Cebpα* (WT: P=0.0112; KO: P=0.0707) transcripts were observed in both genotypes when stimulated with TNFα (Figure 5.6B-C). These data suggest that *Pgc1α* gene expression is dysregulated in miR-34a$^{-/-}$ macrophages.

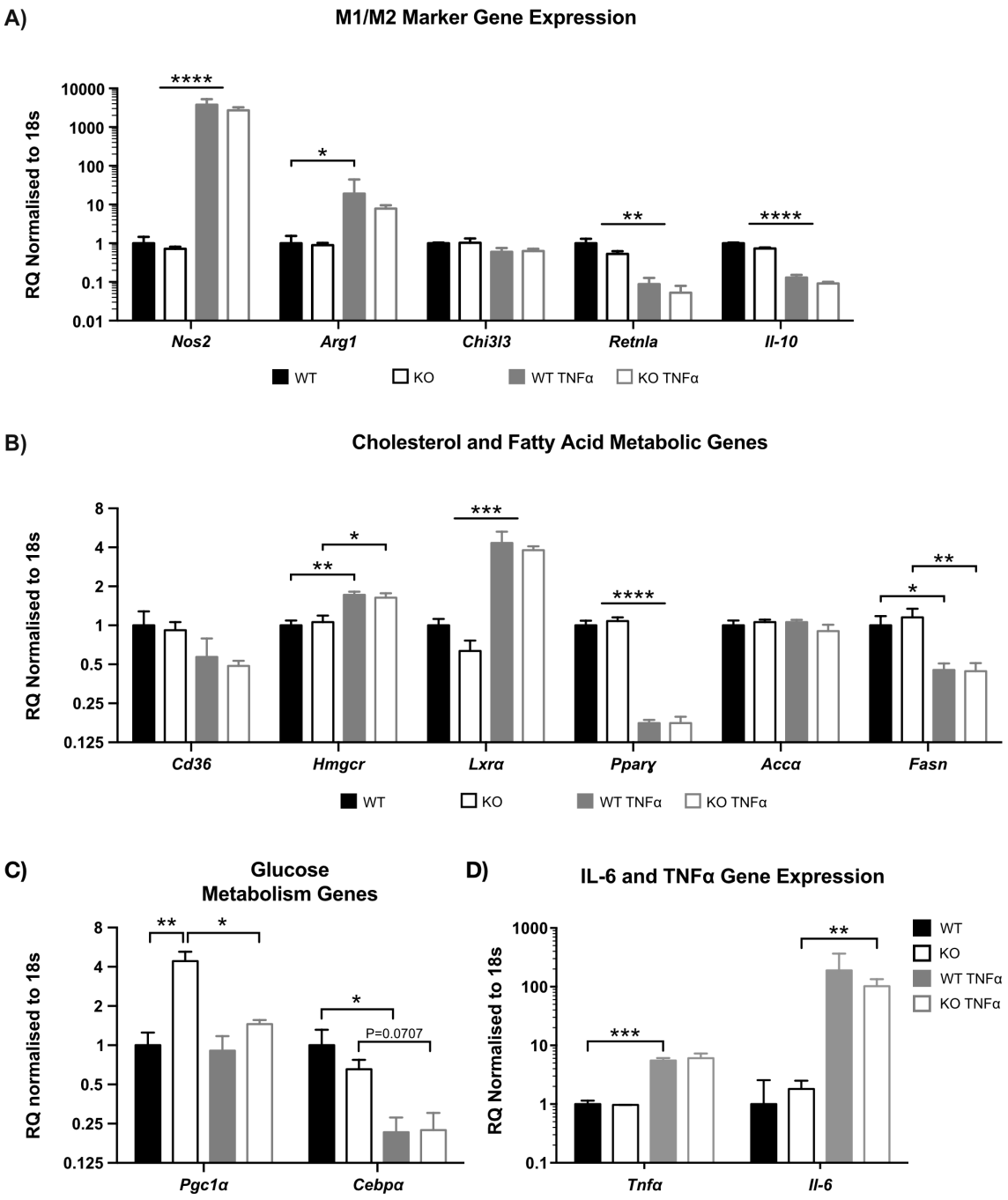

Figure 5.6: Gene Expression Changes Between WT and miR-34a$^{-/-}$ BMDMs Stimulated With TNFα

(A) Showing qRT-PCR gene expression of macrophage phenotype markers in WT and miR-34a$^{-/-}$ (KO) BMDMs stimulated with ±45.45 ng/ml TNFα *in vitro* for 24 hours; n=3. (B-C) Showing qRT-PCR gene expression of specific metabolic genes, previously found to be altered in KO epididymal white adipose tissue (eWAT), in the same samples as (A); n=3. (D) Preliminary qRT-PCR gene expression of *Il-6* and *Tnfα* in the same samples as (A); n=3 for all, except *Il-6* WT: n=2 and *Tnfα* KO: n=2. For all graphs, data is represented as relative quantification (RQ) of WT samples, normalised to 18s rRNA, with RQmax and RQmin values. *P<0.05, **P<0.01, ***P<0.001, ****P<0.0001 One-way ANOVA, with Bonferroni's multiple comparisons post-test. A single line for statistics = both WT and KO have the same statistical value when stimulated with TNFα.

5.4.2.3 Profiling Secreted Proteins from BMDMs *in vitro*

Finally, secreted cytokines and adipokines were analysed in the supernatants from *in vitro* WT and miR-34a$^{-/-}$ BMDM cultures, to characterise functional aspects of these cells. Out of the screen of 20 cytokines in the supernatants of BMDMs using Luminex, 14 were detected: vascular endothelial growth factor (VEGF), basic fibroblast growth factor (FGF Basic), IL-1β, IL-2, IL-5, IL-6, IL-10, IL-12, TNFα, CCL2, CCL3, CXCL9, CXCL10, and CXCL1 (Figure 5.7). For the majority of these, no difference in abundance was detected between WT and miR-34a$^{-/-}$ BMDMs (Figure 5.7A). However, it was noticed that CXCL1's up-regulation response to TNFα stimulation was ablated in miR-34a$^{-/-}$ BMDMs. WT BMDMs stimulated with TNFα showed a higher supernatant concentration than unstimulated WT (P=0.0470) and TNFα-stimulated miR-34a$^{-/-}$ BMDMs (P=0.0470) (Figure 5.7B). Additionally, transcripts of *Cxcl1* followed that same trend, with TNFα-stimulated WT BMDMs showing more transcripts than unstimulated WT (P=0.0300) and TNFα-stimulated (P=0.0168) miR-34a$^{-/-}$ BMDMs. As expected, some of the other cytokines increased in both genotypes following TNFα stimulation: IL-1β (WT: P=0.2253; KO: P=0.0089), IL-2 (WT: P=0.0260; KO: P=0.0437), IL-5 (WT: P=0.0036; KO: P=0.0017), IL-12 (P<0.0001), TNFα (WT: P=0.0013; KO: P=0.0010), CCL2 (WT: P=0.0238; KO: P=0.0085), CCL3 (WT: P=0.0082; KO: P=0.0035), CXCL9 (WT: P=0.0113; KO: P=0.0205), and CXCL10 (WT: P=0.0024; KO: P=0.0023). These data suggest that TNFα regulation of CXCL1 expression is dysregulated in miR-34a$^{-/-}$ BMDMs.

To further characterise the obesity proteome of miR-34a$^{-/-}$ BMDMs, a Mouse Obesity Proteome Array was used to analyse the supernatant adipokines from WT and miR-34a$^{-/-}$ BMDMs ±TNFα (Figure 5.8). Each kit only supplied 4 membranes; therefore, the supernatants from 3 independent cultures were pooled together for each group. The array can detect 38 murine adipokines, but of these only 18 were detectable above background levels: adiponectin, endocan, hepatocyte growth factor (HGF), intracellular adhesion molecule (ICAM)-1, insulin-like growth factor (IGF)-I, IL-6, IL-10, leptin, leukaemia inhibitory factor (LIF), lipocalin-2, CCL2, macrophage colony-stimulating factor (M-CSF), pentraxin 3, pref-1, CCL5, serpin E1, TNFα, and VEGF (Figure 5.8B). However, there were few obvious differences

between WT and miR-34a$^{-/-}$ BMDMs. The main adipokines that appear to be altered were: CCL2 and CCL5 (Figure 5.8B). The array showed that a lower concentration of CCL2 was produced in miR-34a$^{-/-}$ BMDMs in response to TNFα stimulation than WT. Additionally, it appeared that unstimulated miR-34a$^{-/-}$ BMDMs produced more CCL5 than WT, but less when stimulated with TNFα. Overall the main differences observed were between unstimulated and TNFα-stimulated cells.

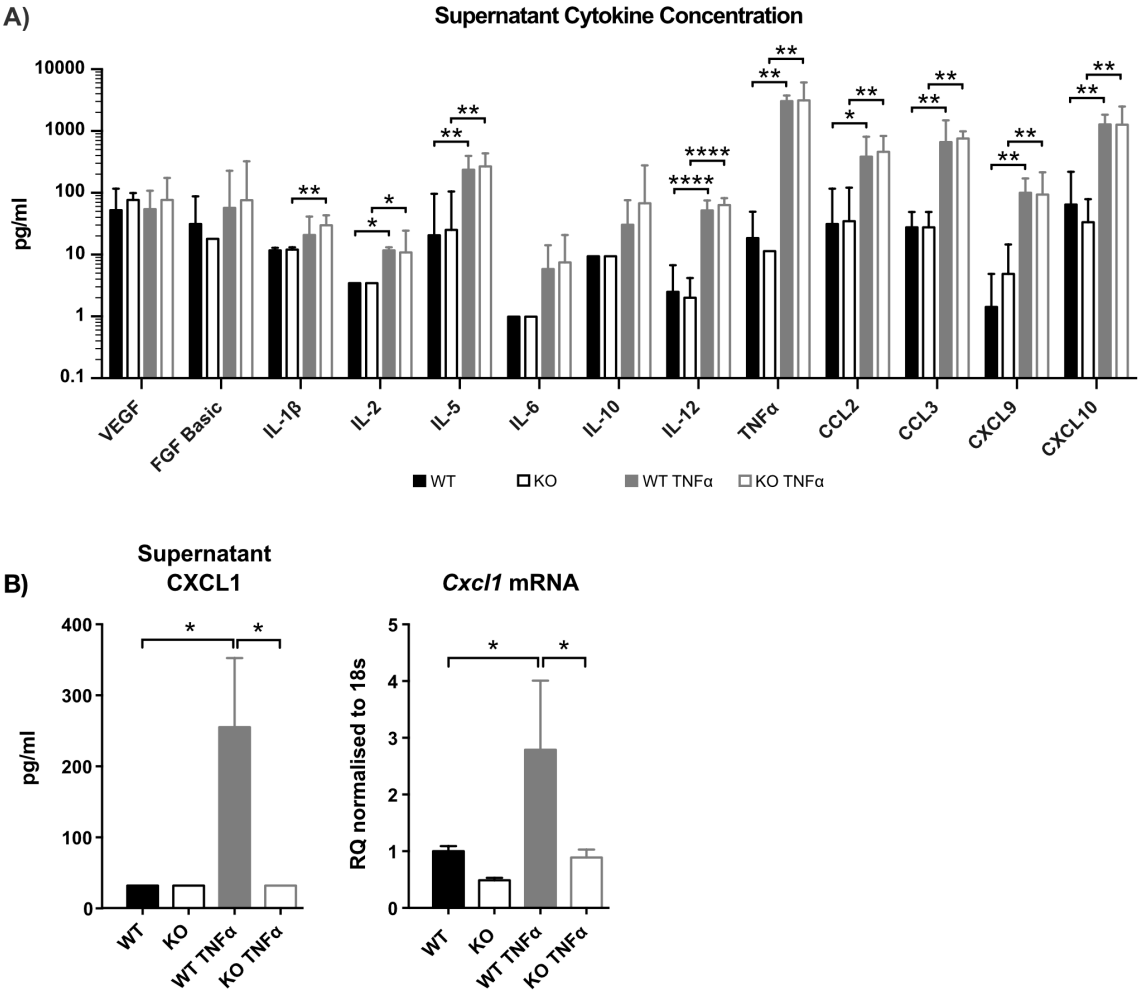

Figure 5.7: WT and miR-34a$^{-/-}$ BMDM Supernatant Cytokine Luminex Results
(A) Luminex data, showing the detectable cytokines present in the supernatants of *in vitro* WT and miR-34a$^{-/-}$ BMDMs stimulated with ±45.45 ng/ml TNFα for 24 hours; n=3. (B) Showing the cytokine Luminex data for CXCL1 in the same samples as (A), and qRT-PCR data for *Cxcl1* transcript expression in the corresponding cellular RNA samples; n=3. qRT-PCR data is represented as relative quantification (RQ) of the WT samples, normalised to 18s rRNA, with RQmin-RQmax values. Luminex data is represented as mean values with SEM. *P<0.05, **P<0.01, ****P<0.0001 One-way ANOVA, with Bonferroni's multiple comparisons post-test.

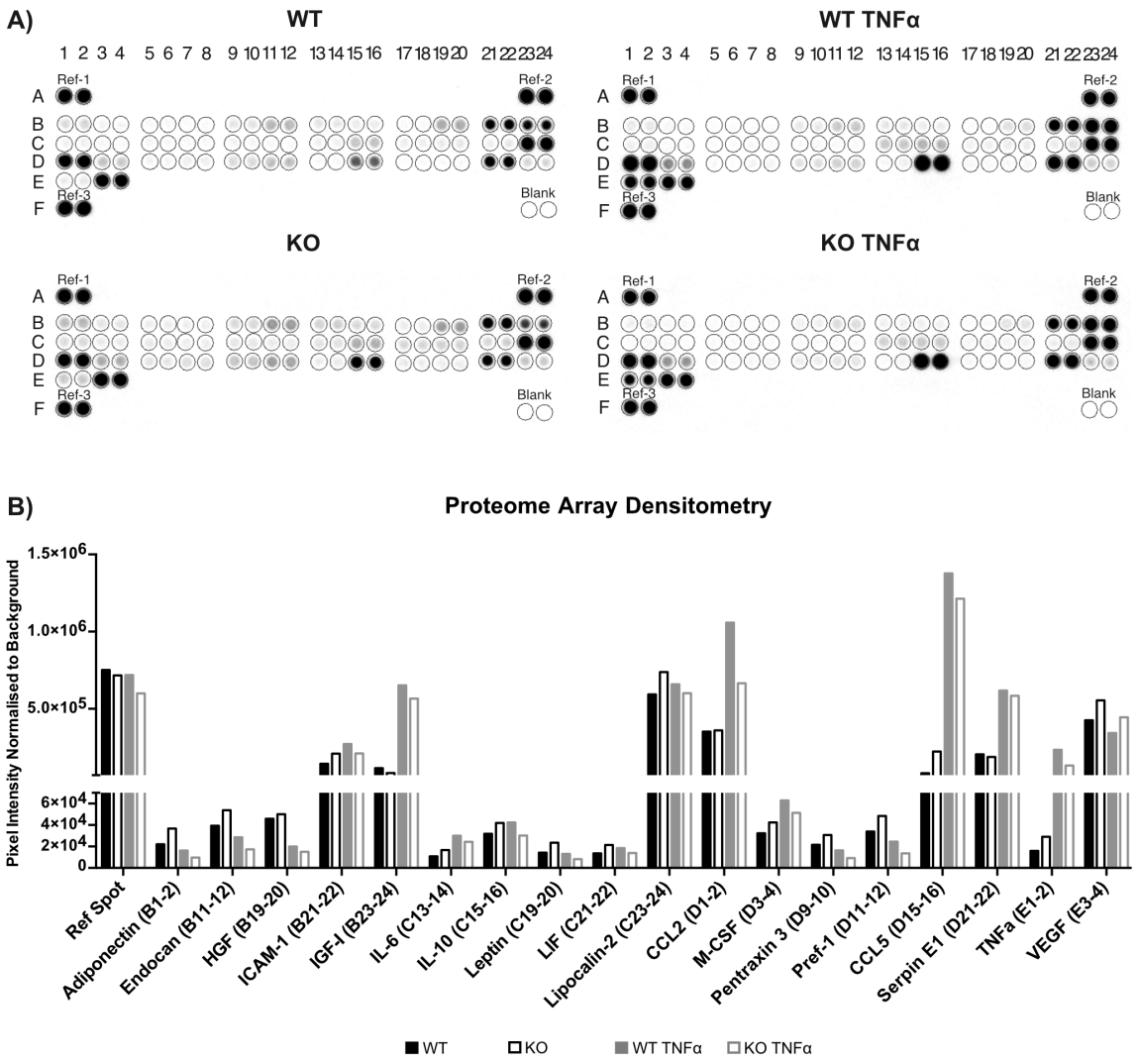

Figure 5.8: WT and miR-34a-/- BMDM Supernatant Obesity Proteome Array Results
Showing the results from a Mouse Obesity Adipokine Array on the *in vitro* supernatants from WT and miR-34a$^{-/-}$ (KO) BMDMs stimulated with ±45.45 ng/ml TNFα for 24 hours. (A) Shows the array membranes after development, which were quantified by densitometry (B). (B) Shows densitometry quantification of the detectable proteins, above the threshold of the WT TNFα signal, which has been normalised to the background spots (Blank) for each membrane. For each group the supernatants from 3 independent cultures were pooled together, and the quantification is represented as an average of the technical duplicate spots/adipokine, or 6 spots for the positive reference control. The x-axis labels for (B) contain the grid number for each spot shown in (A).

5.4.3 *in vitro* Manipulation of miR-34a in WT BMDMs

To further explore whether the differences observed in miR-34a$^{-/-}$ BMDMs were regulated by miR-34a, synthetic miR-34a mimic and anti-miR-34a transfections were carried out on WT BMDMs.

5.4.3.1 Transfection Optimisation

First, 4 transfection systems and a number of anti-miR/mimic concentrations were trialed in WT BMDMs to find the optimum transfection conditions. The

transfection efficiencies of siPORT™, Lipofectamine® RNAiMAX, Viromer BLUE, and Viromer GREEN were examined using flow cytometry and a fluorescent mimic (Dy-547), which emitted a signal in the phycoerythrin (PE) channel (Figure 5.9A-B). Due to differences in the manufacturer protocols for the transfection systems, the highest concentration of mimic was 1 μM for siPORT™ and Lipofectamine®, and 0.1 μM for the Viromer System. Despite this, both Viromer BLUE and GREEN showed more efficient transfection at 0.1 μM than siPORT™ and Lipofectamine® at 1 and 0.1 μM. Viromer BLUE outperformed the other transfections agents at 0.1 μM, showing transfection of 20.58% of the cells in the culture, compared with only 6.47% for Viromer GREEN and 4.13-4.19% for siPORT™ and Lipofectamine®. Curiously, Viromer GREEN was more efficient than Viromer BLUE at the lower concentration of 0.01 μM, but not at lower concentrations. To check that Viromer BLUE still showed the highest transfection efficiency at the transcript level, Qiagen's miR-34a-mimic was transfected into WT BMDMs at the 3 highest concentrations with the same transfection systems (Figure 5.9C). At both 0.1 and 0.01 μM of mimic, Viromer BLUE showed the highest up-regulation of miR-34a transcripts. Therefore, Viromer BLUE with a mimic concentration of 0.1 μM was chosen as the optimal conditions for transfection.

Using Viromer BLUE, a number of concentrations of Qiagen's anti-miR-34a (25-200 nM) were examined in WT BMDMs to identify the optimal concentration for knock-down of miR-34a (Figure 5.9D). Transcripts of both miR-34a's mature and star strand were examined to check that only the mature strand was altered. Unfortunately, none of the anti-miR concentrations produced knock-down of miR-34a. Therefore, only the mimic transfection experiments were taken forward.

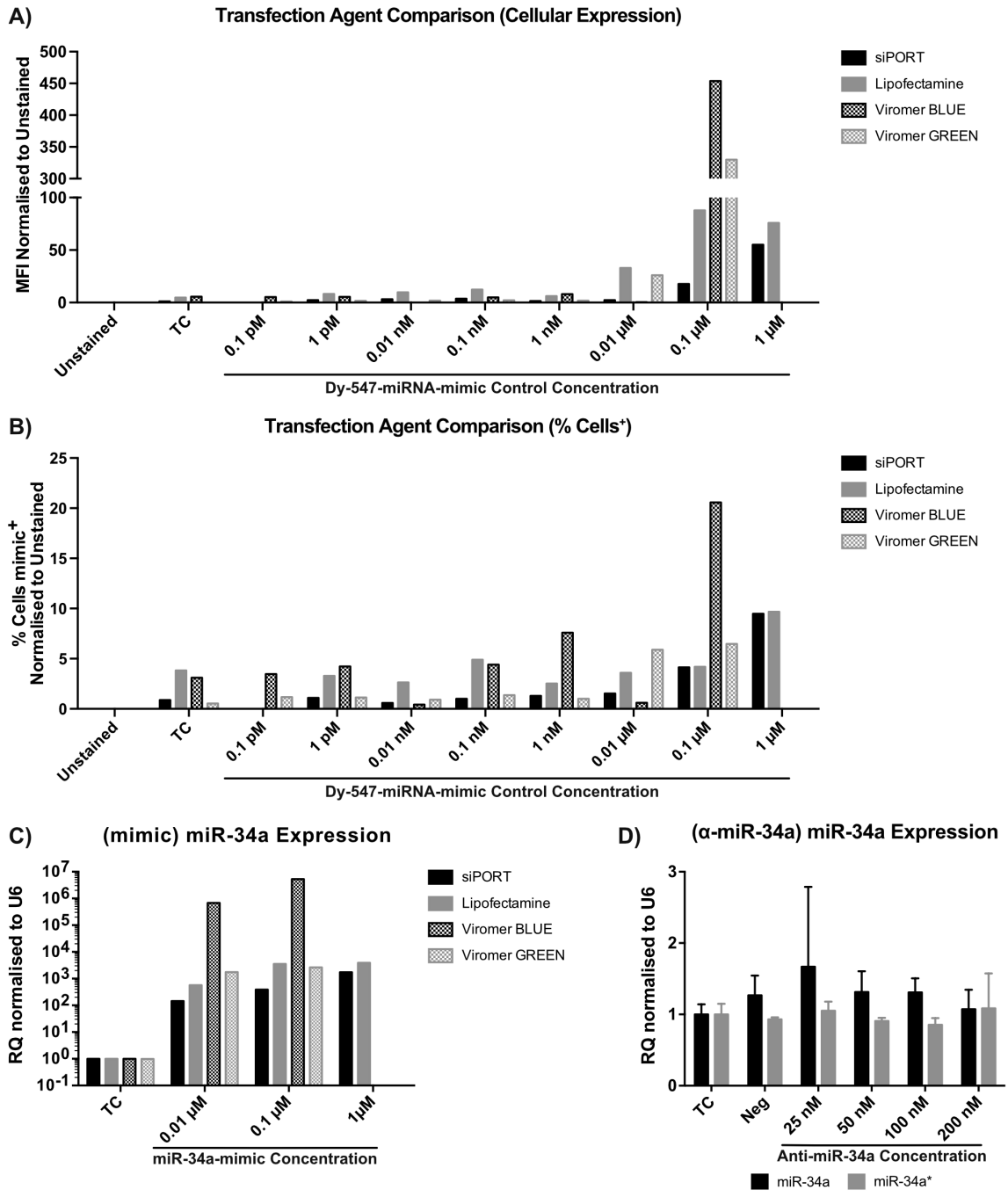

Figure 5.9: Transfection Optimisation in WT BMDMs
(A-B) A comparison of the transfection efficiencies of 4 different transfection agents: siPORT, Lipofectamine RNAiMAX, Viromer BLUE, and Viromer GREEN. Showing flow cytometry data quantifying the cellular expression of (A; mean fluorescence intensity (MFI)) and the percentage of cells positive for (B) the fluorescent control mimic: Dy-547-miRNA-mimic, following a 24-hour transfection into WT BMDMs at a concentration of 1 μM-1 pM for siPORT and Lipofectamin, and 0.1 μM-0.1 pM for the Viromers; n=1. Data is normalised to the unstained control and TC = transfection control (everything minus mimic). (C) qRT-PCR data quantifying the expression of the Qiagen miR-34a-mimic into WT BMDMs at the highest concentrations in the same experiment as (A-B), using the Qiagen SYBR Green miScript miR-34a primer assay; n=1. (D) qRT-PCR data examining the endogenous expression of miR-34a and miR-34a* in WT BMDMs, using Qiagen SYBR Green miScript primer assays, following a 24-hour transfection of the Qiagen anti-miR-34a into the cells; n=2. qRT-PCR data is represented as relative quantification (RQ) of TC, normalised to RNU6B, with RQmax and RQmin values for error bars. Neg = Qiagen Negative Control RNA.

5.4.3.2 WT BMDM miR-34a Mimic Transfections *in vitro*

WT BMDMs were transfected with Qiagen's miR-34a-mimic in unstimulated and TNFα-stimulated conditions, to simulate inflammatory conditions and to investigate whether miR-34a enhances the pro-inflammatory actions of TNFα. The whole miR-34 family was quantified by qRT-PCR after transfection to check that only miR-34a was up-regulated and that TNFα stimulation did not interfere with transfection (Figure 5.10). Only miR-34a was observed to increase following miR-34a-mimic transfection (Figure 5.10A-F). Increased miR-34a transcripts were observed in both unstimulated (ΔCt: 3.4±0.1; P=0.0011) and TNFα-stimulated (ΔCt: 2.63±0.6; P=0.0019) BMDMs over the negative control (Unstimulated ΔCt: 12.3±0.26, TNFα ΔCt: 11.3±0.23) (Figure 5.10A).

Next, transcripts of macrophage polarisation markers (M1: *Nos2*, *Il-6*, and *Tnfa*; M2: *Arg1* and *Chi3l3*) were examined in the miR-34a-mimic transfected BMDMs ±TNFα (Figure 5.11). *Retnla* was also examined, but no usable data was obtained. Unfortunately, no changes were observed in the transcript expression of these genes when transfected with miR-34a-mimic. Interestingly, it appeared that the transfection process itself had a small pro-inflammatory effect, increasing transcripts of *Nos2* and *Il-6* (Figure 5.11C-D). Notably, there was a lot of variability between replicates in the TNFα stimulated samples. An increase in sample size is required to get a clearer picture of any differences and draw proper conclusions. Finally, the supernatants from these cells were screened for changes in cytokine secretion (Figure 5.12). However, no changes were observed in cytokine secretion from WT BMDMs when transfected with miR-34a-mimic, with or without TNFα. Additionally, no changes were seen in CXCL1 secretion.

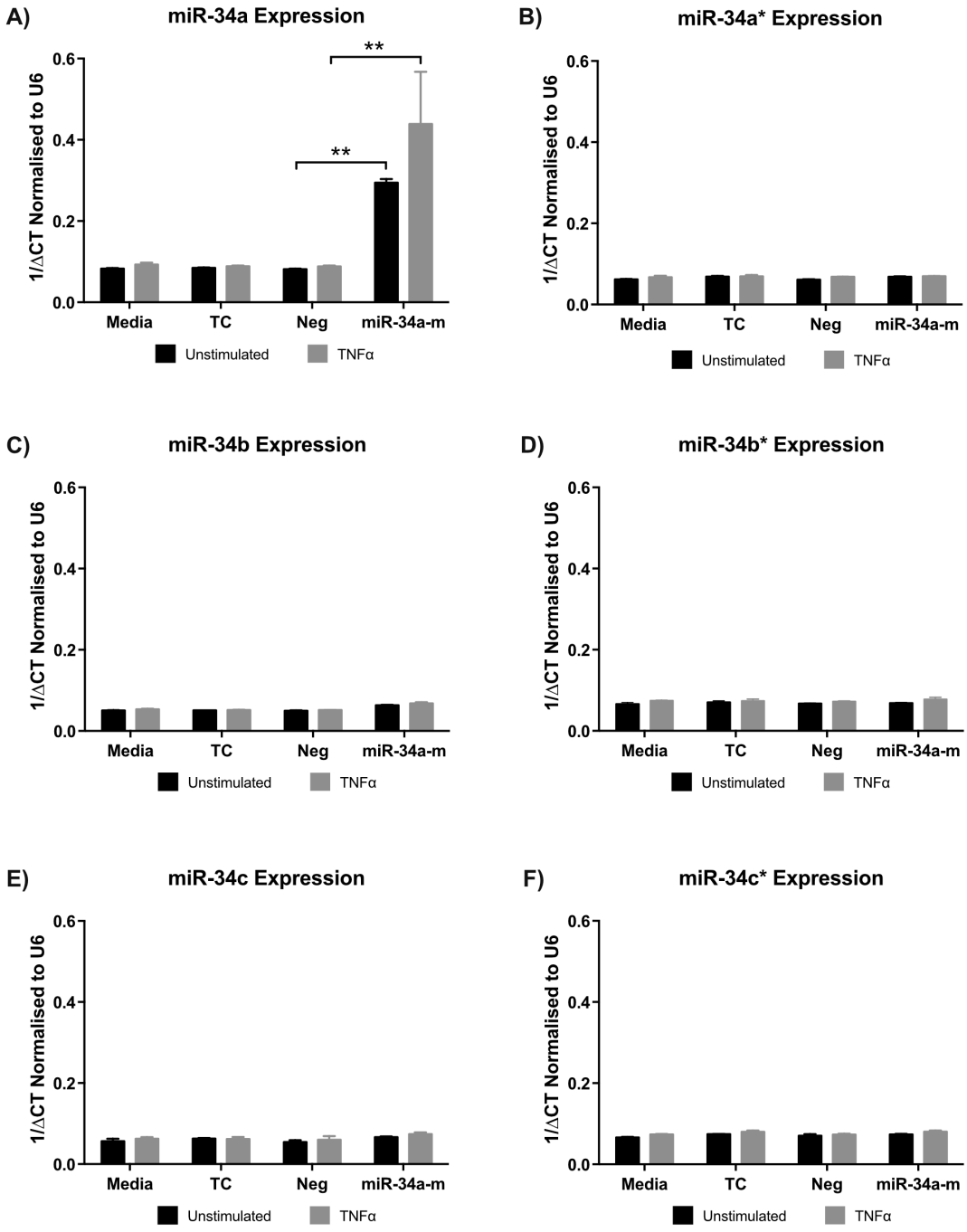

Figure 5.10: Transcript Expression of The miR-34 Family In miR-34a-mimic Transfected WT BMDMs

(A-F) TaqMan® qRT-PCR data quantifying the transcripts expression of the whole miR-34 family in WT BMDMs, after a 24-hour transfection of 0.02 μM Qiagen miR-34a-mimic (miR-34a-m) ±50 ng/ml TNFα for the same period. Controls: TC = transfection solution only, Neg = Qiagen Negative Control RNA. Data is represented as mean values of 1/ΔCt with SEM; n=3. During 1/ΔCt calculations "Undetermined" values were replaced with Ct = 40 for graphing and statistics for miR-34b and miR-34c. **P<0.01 paired Student's t-test between mimic and neg bars.

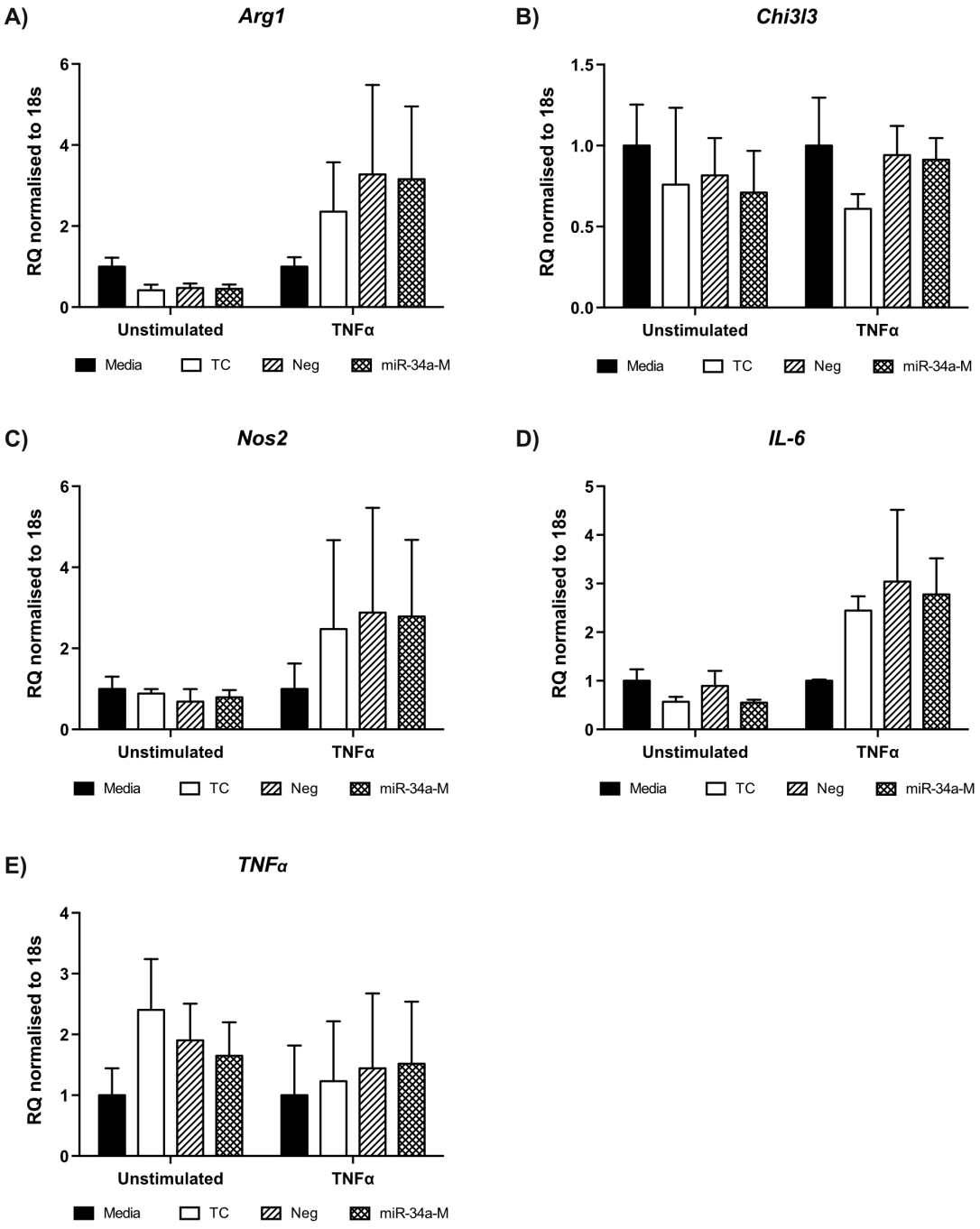

Figure 5.11: Transcripts Expression of M1/M2 Marker Genes in miR-34a-mimic Transfected WT BMDMs

(A-E) qRT-PCR data quantifying the transcript expression of a number of macrophage polarisation markers in WT BMDMs, after a 24-hour transfection of 0.02 μM Qiagen miR-34a-mimic (miR-34a-m) ±50 ng/ml TNFα for the same period. Controls: TC = transfection solution only, Neg = Qiagen Negative Control RNA. Data is represented as relative quantification (RQ) of "media" samples, normalised to 18s rRNA, with RQmin and RQmax values; n=3. Paired Student's t-test between mimic and neg bars.

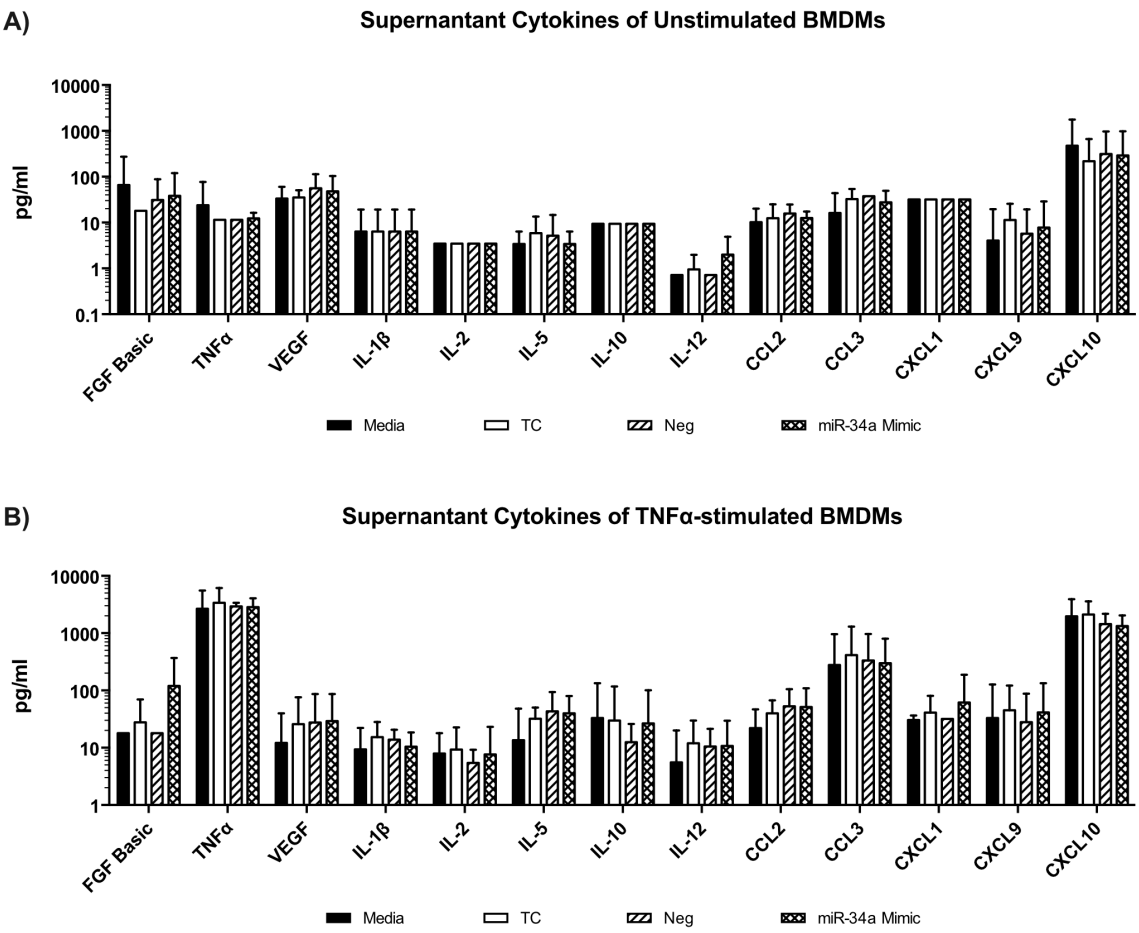

Figure 5.12: Supernatant Cytokine Luminex Results from miR-34a-mimic Transfected WT BMDMs

(A-B) Showing Luminex quantification of cytokines in the supernatants of WT BMDMs, after a 24-hour transfection of 0.02 μM Qiagen miR-34a-mimic (miR-34a-m) ±50 ng/ml TNFα for the same period. Controls: TC = transfection solution only, Neg = Qiagen Negative Control RNA. Data is represented as mean values with SEM; n=3. Paired Student's t-test between mimic and neg bars.

5.5 Discussion

This chapter has focused on using *in vitro* macrophages to model the miR-34a$^{-/-}$ macrophage phenotype observed in ATMs *in vivo* in chapter 4, to further dissect the role of miR-34a in macrophages specifically. Unfortunately, many of the parameters examined did not reveal differences between primary WT and miR-34a$^{-/-}$ BMDMs. This could reflect the complex environment within the obese WAT that is not appropriately replicated in this *in vitro* model. However, miR-34a was shown to be ubiquitously expressed throughout WT BMDMs and up-regulated by direct TNFα-stimulation, along with miR-34a*. Additionally, miR-34a$^{-/-}$ BMDMs showed an ablated CXCL1 response to TNFα-stimulation, further suggesting miR-34a regulates aspects of TNFα signalling. Finally, correlating with eWAT observations from chapter 4, miR-34a$^{-/-}$ BMDMs showed higher transcripts of *Pgc1α* in unstimulated cells.

The ISH data in this chapter showed that miR-34a is highly expressed within WT BMDMs, with highest expression appearing in the nuclei. This greater nuclear staining could be a result of the miR-34a ISH probe hybridising with the primary miR-34a transcript. Additionally, the observations made here of increased miR-34a transcripts in WT BMDMs upon stimulation with TNFα, connect with Jiang and colleagues' observations of miR-34a mimics reducing TNFα transcript and protein expression, suggesting that miR-34a counter-regulates TNFα (Jiang et al. 2012). However, these results are contrary to Jiang and colleagues' observations that LPS stimulation decreases miR-34a expression, this is likely due to the different signalling pathways involved. It is curious that miR-34a$^{-/-}$ BMDMs did not show increased transcript or protein levels of TNFα if miR-34a does inhibit TNFα expression. However, under resting conditions there should be little to no TNFα and the process of stimulating BMDMs with TNFα to produce a pro-inflammatory phenotype could obscure differences in expression by saturating the system (Vila-del Sol et al. 2008). Another inflammatory stimulus, such as interferon (IFN)ɣ, IL-6, or free-fatty acids may be interesting to explore.

It was disappointing that the miR-34a mimic transfection experiments did not show a reduction in TNFα transcripts and protein, as had been observed

previously with LPS stimulation (Jiang et al. 2012). This could be due to the lower 20 nM concentration of mimic used, due to the low stock volume of mimic, or the 24-hour transfection incubations, compared to the 100 nM concentration and 36-hour incubation used by Jiang et al. However, at 10 and 20 nM concentrations, a significant increase in miR-34a transcripts was still detected in WT BMDMs. It is possible that the mimic is not being loaded into RISC and is therefore non-functional. A previous paper reported that, although qRT-PCR identified a >1000 fold increase in miR-200a following a 48-hour transfection of 60 nM miR-200a-mimic, argonaute immunoprecipitation (IP) showed that the amount loaded into RISC was >1 order of magnitude lower (Thomson et al. 2013). This brings into question the reliability of qRT-PCR in determining transfection efficiency. The authors also showed that most of the miRNA mimic transfected using liposome-based methods, such as those explored here, formed cytoplasmic aggregates that did not associated with argonaute proteins. However, the Viromer system is advertised featuring a novel endosome escape mechanism to aid cytosolic delivery. Even if the mature miRNA mimic does escape the endosome, there is no guarantee that it will act in the same manner as endogenous miRNA. Post-transcriptional modifications of the miRNA sequence produce different isomiRs, which vary between cell type and physiological states, and are thought to have differences in specific mRNA targeting (Cloonan et al. 2011; Wyman et al. 2011; Tan et al. 2014). One way to get around this problem is to transfect cells with a synthetic pri-miRNA that will be endogenously processed, but then there is the issue of potential functional effects from the star-strand. Even the pri-miRNA has to be designed carefully, with both the nucleotide sequence and secondary RNA structure determining how it is processed (van den Berg et al. 2016).

Using effective mimics and anti-miRs should be useful tools to identify whether miR-34a and/or miR-34a* are responsible for the phenotype observed in miR-34a$^{-/-}$ mice and BMDMs, as both are deleted in these models. It is of particular importance, as it has been previously shown that synthetic miR-34a and miR-34a* can both inhibit LPS-induced TNFα secretion in primary human macrophages (Guennewig et al. 2014). However, as highlighted above, the mimic experiments did not produce any detectable changes in WT BMDMs and anti-miR-34a did not produce any knock-down of endogenous miR-34a, as quantified by qRT-PCR.

There could be a number of reasons why inhibition was not observed. Anti-miRs face the same *in vitro* delivery problems as mentioned above for mimics, with the majority of the anti-miR potentially forming cytosolic aggregates and not binding to the target miRNA in RISC, limiting miRNA inhibition (Thomson et al. 2013). The anti-miRs and mimics may have also been engulfed by the macrophages during transfection, causing them to be stuck in a phagosome. The chemistry of the anti-miRs is another important factor in determining the fate of the target miRNA, with low affinity oligonucleotides, such as 2'-O-methyl (2'-O-Me) modified anti-miRs, promoting miRNA degradation, and high affinity oligonucleotides, such as locked nucleic acid (LNA)-modified anti-miRs, promoting miRNA sequestration (Stenvang et al. 2012). The Qiagen anti-miR-34a is a 2'-O-Me modified RNA oligo, so should therefore promote degradation of endogenous miR-34a. However, the anti-miRs are designed to bind to a specific miRNA sequence, which does not take into account the different isomiRs of that miRNA; this means that the efficiency of knock-down could vary between different cell types. Using anti-miRs composed of "tiny" LNA, which target the seed sequence of the miRNA, could account for this, as the seed sequence does not tend to change between the different isomiRs (Obad et al. 2011). However, both miR-34a and miR-34c share the same seed sequence, meaning that the tiny LNA would likely also inhibit miR-34c (Rokavec et al. 2014a). Furthermore, all the current anti-miR technologies are prone to off-target effects with miRNA family members (Li and Rana 2014). Another reason why no inhibition of miR-34a was detected may be because miR quantity was determined by qRT-PCR. It has been shown that anti-miR in the samples can inhibit the qPCR reaction and give false readings of miRNA reduction (Stenvang et al. 2012; Thomson et al. 2013). However, if this was the case, then a reduction would have likely been seen by qRT-PCR at one of the concentrations trialed. It is conceivable that there could have been separation of the low affinity, 2'-O-Me modified Qiagen anti-miR-34a from endogenous miR-34a during RNA extraction, allowing miR-34a to still be detected, masking inhibition. Due to the potential interference from measuring knock-down directly, the qRT-PCR method should have been accompanied by measurement of transcription and protein levels of known miR-34a targets, such as: SIRT1 and NOTCH1, or use of a miRNA luciferase or GFP reporter (Yamakuchi et al. 2008; Jiang et al. 2012). Using a miRNA sponge or specific deletion of only the mature strand of miR-34a through

Clustered regularly-interspaced short palindromic repeats (CRISPR) technology *in vitro* are other methods that could be employed.

Interestingly, an ablated CXCL1 response was observed in miR-34a$^{-/-}$ BMDMs when stimulated with TNFα. These data further suggest that miR-34a has a role in regulating TNFα signalling. There are currently no studies that have examined miR-34a's regulation of CXCL1. However, miRWalk (http://zmf.umm.uni-heidelberg.de/apps/zmf/mirwalk2/) was used to examine the predicted targets of miR-34a in the miRWalk and TargetScan databases (generated by Dr Ashley Miller), and *CXCL1* was identified as a predicted target in humans, but not mice, in the miRWalk database (Dweep and Gretz 2015). Additionally, CXCL1's receptor *Cxcr2/CXCR2* was also a predicted target in both mice and humans in miRWalk, although, if *Cxcl1* was directly targeted by miR-34a then an increase in expression rather than a decrease would be expected in miR-34a$^{-/-}$ BMDMs. Therefore, miR-34a targeting regulatory processes prior to *Cxcl1* transcription seem more likely. In fact, the *TNFα-induced protein (TNFAIP)1, 3,* and *8-like (8L)2* genes were identified as predicted targets from human miRWalk. These genes regulate TNFα signalling and NF-κB activity, with TNFAIP1 being shown to induce NF-κB activity, and TNFAIP3 and TNFAIP8L2 inhibiting NF-κB activity, in cancer models (Zhang et al. 2014; Zou et al. 2014; Zhang et al. 2015). Additionally, a number of papers have suggested a regulatory axis between miR-34a and NF-κB. Li et al. reported that NF-κB can directly up-regulate miR-34a expression in cancer cells by binding the p65 subunit to the gene promoter at the third kb site, but gene expression is dependent on the expression of the known miR-34a inducer, p53 (Li et al. 2012). However, p53-independent up-regulation of miR-34a transcripts by NF-κB in a germinal-centre-derived B cell lymphoma cell line have also been reported (Forte et al. 2012). Additionally, miR-34a has been shown to activate NF-κB through inhibition of SIRT1, a well-known miR-34a target, increasing acetylation of the p65 subunit (Yamakuchi et al. 2008; Tan et al. 2012; Zhang et al. 2012). Therefore, in miR-34a$^{-/-}$ BMDMs, SIRT1 may be inhibiting NF-κB, preventing up-regulation of *Cxcl1* transcription during TNFR signalling. In fact, SIRT1 has been shown to inhibit NF-κB by directly binding and deacetylating the RelA/p65 subunit at lysine 310, blocking TNFα-induced gene expression through NF-κB (Yeung et al. 2004). In this case we would expect to see a reduction in *Tnfα*

transcription in miR-34a$^{-/-}$ BMDMs, as the NF-κB p65 subunit is required for *Tnfα* gene expression, and has previously been shown to be suppressed by increase SIRT1 expression in THP1 macrophages (Liu et al. 2000; 2011b). The lack of change in *Tnfα* transcription in miR-34a$^{-/-}$ BMDMs could suggest a different miR-34a target is involved, residual NF-κB signalling, or a compensatory pathway.

Interestingly, SIRT1 has been shown to increase PGC1α activity through direct deacetylation and also deacetylation of liver kinase (LK)B1, triggering 5' adenosine monophosphate-activated protein kinase (AMPK) activation, which subsequently phosphorylates PGC1α (Rodgers et al. 2005; Lan et al. 2008; Canto and Auwerx 2009). This could explain why miR-34a$^{-/-}$ BMDMs have increased basal levels of *Pgc1α* transcripts. Additionally, *PGC1α* is a predicted target of miR-34a in humans using miRWalk. Accordingly, the increase in *Pgc1α* transcripts in miR-34a$^{-/-}$ BMDMs could be a direct effect of miR-34a deletion. One report showed that *PGC1α* overexpression in human aortic smooth muscle and endothelial cells reduced TNFα-induced NF-κB signalling, *CCL2* and *vascular cell adhesion molecule (VCAM)-1* transcripts, and reactive oxygen species (ROS) production (Kim et al. 2007a). Additionally, Eisele et al. reported that PGC1α can inhibit NF-κB signalling by reducing the phosphorylation of the RelA/p65 subunit, through reduced phosphorylation of Akt, and promoting *Pparα* transcription in a mouse skeletal muscle cell line *in vitro* (Eisele et al. 2013). The authors reported that PGC1α overexpression reduced *Il-6*, *Tnfα*, and *Ccl3* transcripts induced by TNFα, TLR activation, and free-fatty acids (FFAs). However, the authors also showed that basal *Tnfα* transcripts were not affected and did not completely reduce to basal levels under 10 ng/ml TNFα stimulation. Additionally, the authors noted that PGC1α only reduced TNFα-mediated phosphorylation of RelA/p65 by approximately 50%. Therefore, the lack of reduction in *Tnfα* transcription observed in miR-34a$^{-/-}$ BMDMs, could be due to residual NF-κB signalling and the use of approximately 5 times the TNFα concentration employed by Eisele et al. It has also been reported that TNFα-induced NF-κB and p38 mitogen-activated protein kinase (p38 MAPK) pathways can down-regulate PGC1α expression in cardiac cells, which has been shown to be mediated by physical association of the NF-κB subunit RelA/p65 with PGC1α (Palomer et al. 2009; Alvarez-Guardia et al. 2010). This in turn, could explain the down-regulation of *Pgc1α* transcripts observed in

TNFα-stimulated miR-34a$^{-/-}$ BMDMs. Finally, muscle-specific PGC1α KO mice showed increased *Tnfα*, *Il-6,* and *Cd68* transcripts in skeletal muscle (Handschin et al. 2007). Conversely, miR-34a has been suggested to target NOTCH1, which can activate NF-κB by phosphorylation of the NF-κB subunit p50, reducing LPS-induced TNFα and IL-6 expression (Palaga et al. 2008; Jiang et al. 2012). However, this effect may be dependent on TLR stimulation, not explored here. It would be interesting to explore whether PGC1α is a direct target of miR-34a, which is not currently known. Additionally, exploration of the NF-κB pathway and SIRT1 expression would be useful to elucidate miR-34a's mechanism controlling CXCL1 expression.

Disappointingly, the same F4/80^{high} macrophage phenotype was not observed in TNFα-stimulated miR-34a$^{-/-}$ BMDMs *in vitro* as that observed in HFD-fed miR-34a$^{-/-}$ mice *ex vivo* (section 4.4.5.1). The phenotype may have been lost *in vitro* by not using an appropriate or single stimulus, along with macrophage polarisation *in vitro,* producing artificial M1 or M2 phenotypes that are at opposite ends of a spectrum of macrophage phenotypes. The inflammatory environment within the adipose tissue is complex and a number of stimuli may be required to induce this phenotype, such as FFAs. On the other hand, an anti-inflammatory cytokine such as IL-10 or IL-4 may be more appropriate, since *Il-10* eWAT transcripts and serum IL-5 were increased in HFD-fed miR-34a$^{-/-}$ mice. Using WAT-conditioned media from obese WAT could be a way to mimic this complex inflammatory environment *in vitro*. Both WT and miR-34a$^{-/-}$ BMDMs were successfully polarised to an M1 phenotype by TNFα stimulation using the parameters examined, with the only exception being the increase in *Arg1* transcripts. However, it has been previously shown that IFNɣ and TNFα stimulation of murine BMDMs *in vitro*, for 24 hours, induced moderate expression of *Arg1* transcripts (Munder et al. 1999). Unfortunately, except for the changes in *Pgc1α* transcripts and CXCL1, no other changes were observed between WT and miR-34a$^{-/-}$ BMDMs. It did appear that there were differences in CCL2 and CCL5 from the proteome array; however, these changes were not observed in the Luminex data, bringing their validity into question, as Luminex is a more reliable quantitative method. Using Luminex technology to profile the cytokine environment of eWAT from HFD-fed miR-34a$^{-/-}$ mice, with validation by enzyme-linked

immunosorbent assay (ELISA), could be useful to identify more appropriate stimuli for future *in vitro* BMDM experiments. Finally, out of the metabolic genes profiled in WT Vs. miR-34a$^{-/-}$ BMDMs, which were altered in eWAT *ex vivo* (section 4.4.3), only *Pgc1α* transcripts were changed. This suggests that the changes in *Cd36*, *Hmgcr*, *Lxrα*, *Pparγ*, *Accα*, *Fasn*, and *Cebpα* could be specific to the eWAT adipocytes and not tissue macrophages.

In conclusion, miR-34a appears to regulate aspects of TNFα signalling in BMDMs, potentially through targeting of SIRT1 and/or PGC1α, which inhibit the RelA/p65 subunit of NF-κB (Figure 5.13). However, miR-34a's mechanism of regulation needs to be further explored to identify specific targets and signalling pathways. Additionally, the tools used to manipulate miR-34a expression need to be carefully and critically assessed.

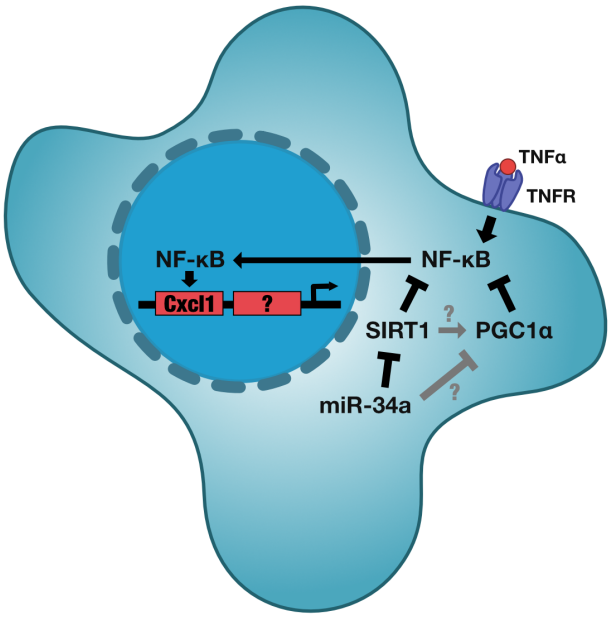

Figure 5.13: Theoretical Mechanism for miR-34a's Regulation of TNFα Signalling in Macrophages

Chapter 6: Examining the Role of miR-34a in Adipocytes *in vitro*

6.1 Introduction

In previous chapters, the *in vivo* functions of miR-34a (Chapter 4) and miR-34a's function in macrophages *in vitro* (Chapter 5) were explored. This chapter continues the exploration into cell-specific functions of miR-34a in white and brown adipocytes using primary cultures from murine epididymal white adipose tissue (eWAT) and intrascapular brown adipose tissue (iBAT), respectively. In Chapter 4 it was observed that there were a number of metabolic genes altered in the eWAT and iBAT from miR-34a$^{-/-}$ mice, along with phenotypic differences in the eWAT showing smaller, more numerous adipocytes on chow. Specifically, *cluster of differentiation* (*Cd)36*, *3-hydroxy-3-methyl-glutaryl-CoA reductase (Hmgcr)*, *Liver X receptor (Lxr)α*, *peroxisome proliferator-activated receptor (PPAR)ɣ coactivator (Pgc)1α*, *Acetyl-CoA carboxylase (Acc)α*, and *Fatty acid synthase (Fasn)* transcripts were altered in the eWAT and *CCAAT/enhancer binding protein* (*Cebp)α*, *Cebpβ*, and *Pgc1α* transcripts in iBAT.

It has previously been shown by microarray that miR-34a is one of a number of miRNAs up-regulated in mature, human subcutaneous adipocytes following *in vitro* differentiation (Ortega et al. 2010). Furthermore, miR-34a has also been suggested to inhibit beige/brite and brown adipose formation *in vivo* during murine diet-induced obesity through fibroblast growth factor (FGF)21 (Fu et al. 2014). Sirtuin (silent mating type information regulation 2, *S. Cerevisiae*, homolog) 1 (SIRT1) is a well-studied target of miR-34a and has been shown to inhibit white adipocyte adipogenesis *in vivo* and *in vitro*, likely through repression of *(PPAR)ɣ*, which has been shown to directly associate with, and be deacetylated by, SIRT1 (Han et al. 2010; Mayoral et al. 2015; Kim et al. 2015b). However, SIRT1 overexpression increases thermogenesis in BAT *in vivo* and brown adipocytes *in vitro*, but does not affect brown adipocyte differentiation (Boutant et al. 2015). The increased *Pgc1α* transcripts observed in high fat diet (HFD)-fed miR-34a$^{-/-}$ iBAT (section 4.4.3) is of particular interest, as alterations in expression of this protein can contribute to obesity by changing mitochondrial biogenesis and uncoupling protein 1 (UCP1) expression, affecting thermogenesis. When PGC1α was first described, it was shown that ectopic expression in 3T3-F442A white pre-adipocytes was sufficient to induce brown adipocyte differentiation with UCP1,

respiratory chain enzymes, and mitochondrial DNA (Puigserver et al. 1998). Therefore, miR-34a could regulate white and/or brown adipocyte differentiation and function.

To investigate the role of miR-34a in adipocyte differentiation, primary cells were cultured from WT and miR-34a$^{-/-}$ mice. A number of metabolic genes, phenotypic characteristics, and functional attributes were then examined. It was hypothesised that miR-34a regulates the differentiation of white and brown adipocytes, and also thermogenesis in brown adipocytes, which contributes to the *in vivo* phenotype of miR-34a$^{-/-}$ mice.

6.2 Aims

- Characterise the phenotype of white and brown pre-adipocytes from WT mice over the time-course of differentiation to validate the *in vitro* model.

- Quantify miR-34a expression in WT white and brown pre-adipocytes over the time-course of differentiation *in vitro*, and examine miR-34a's regulation of differentiation using miR-34a$^{-/-}$ cells.

- Explore functional characteristics of mature WT and miR-34a$^{-/-}$ white and brown adipocytes *in vitro*, by examining lipid content, mitochondrial content, and the secretome.

6.3 Methods

For specific details on individual methods please refer to Chapter 2: Materials and Methods.

6.3.1 *In vitro* Adipocyte Culture

Primary adipocytes were grown as outlined in section 2.2.2.1, following a similar protocol to that used by Professor Barbara Cannon's group (Walden et al. 2009). Pre-adipocytes in the stromal vascular fraction (SVF) were isolated from the eWAT and iBAT from WT and miR-34a$^{-/-}$ mice. These pre-adipocytes were cultured at a density of 1x10^{6} cells/well in 8-well chamber slides for 8 days, with 1 µM Rosiglitazone-supplemented complete media; this was replaced every second day (Figure 6.1).

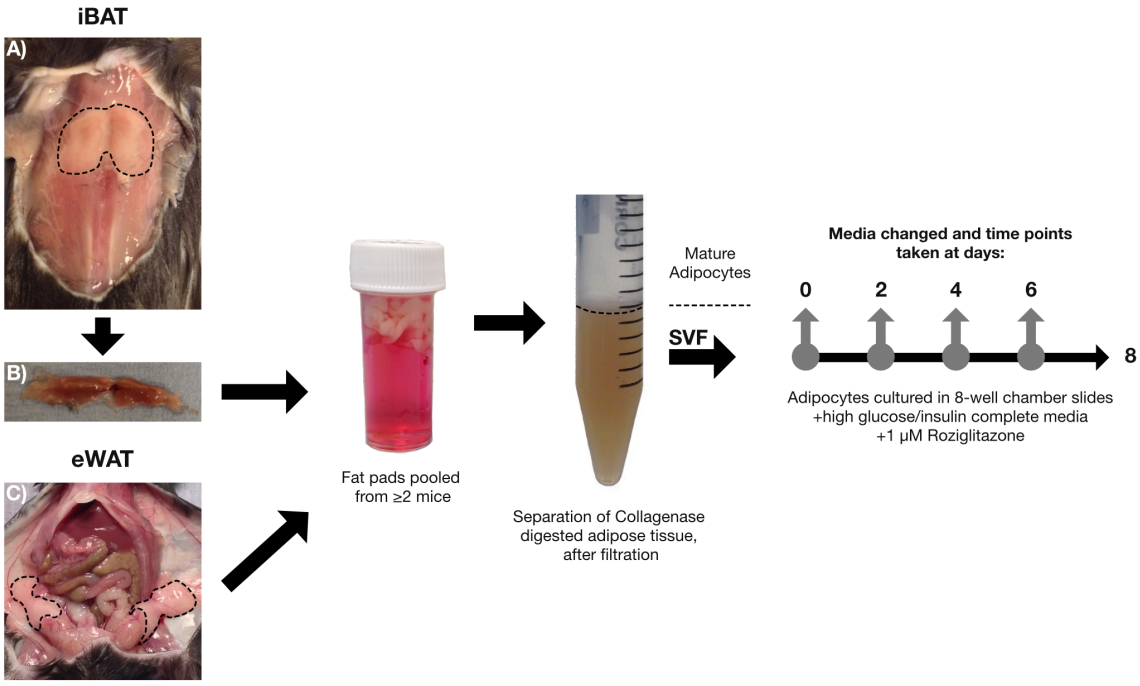

Figure 6.1: Diagram of the *in vitro* Primary Pre-Adipocyte Differentiation Protocol
Anatomical locations of Intrascapular brown adipose tissue (iBAT (A); isolated BAT (B)) and epididymal white adipose tissue (eWAT; (C)) are outlined in the pictures.

When supernatants were collected, only 50% of the media was replaced on these days to allow the cytokines etc. to accumulate. The purity of the cultures was assessed using Flow Cytometry (section 6.3.5) to examine the percentage of

contaminating immune cells ($CD45^+$) and vascular endothelial cells ($CD31^+$) (Figure 6.2). The viability and differentiation of the pre-adipocytes was assessed by quantifying numerous gene transcripts and microscopy, described in 6.4.1.

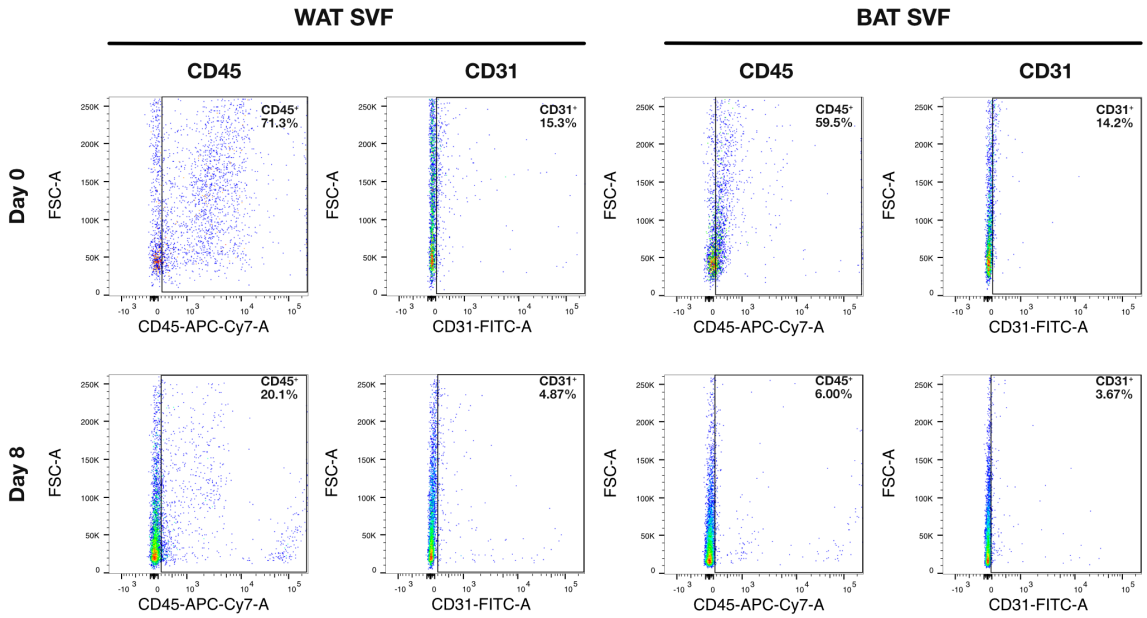

Figure 6.2: Representative Flow Cytometry Plots Showing *in vitro* Adipocyte Culture Purity
Representative flow cytometry plots examining the expression of $CD45^+$ (immune cells) and $CD31^+$ (vascular endothelial cells) cells at day 0 and 8 of white (WAT SVF) and brown (BAT SVF) pre-adipocyte differentiation; n=3. Gates for $CD45^+$ and $CD31^+$ cells constituted the large "cells" gate on SSC-FSC. Statistics are all percentages of the parent gate.

6.3.1.1 Adipocyte Stimulations

To examine brown adipocyte phenotype at day 8, cells were stimulated with/without 0.1 μM noradrenaline for 4 hours, then cells were collected for RNA isolation and the gene expression of *Ucp1* and *Pgc1α* was quantified, as described in section 6.3.4. For quantifying lipid and mitochondrial content in brown adipocytes, cells were stimulated with/without 0.1 μM noradrenaline for 20 hours, and lipid and mitochondrial content were quantified by flow cytometry, as described in section 5.3.6.

6.3.2 Histology

Adipocytes were stained for lipid using Oil Red "O" (ORO) as described in section 2.4.4. Adipocytes at the day 0 time-point were incubated for 2 hours on the chamber slides before they were fixed, to allow attachment. Images of the stained

cells were taken using an Olympus BX41 microscope, with 10, 40, and 100X Olympus Uplan FLN Objective, and QCapture Pro 6.0 Software (section 2.4.6). Lipid content in Adipocyte ORO images was quantified using Fiji 2 software as described in section 2.4.7.

6.3.3 Confocal Microscopy

Lipid and mitochondrial content in adipocytes was stained using BODIPY 493/503 and MitoTracker Deep Red FM, respectively, as described in section 2.6. Images were taken on a Zeiss LSM 510 Meta Confocal Microscope, with 40X and 63X objective lenses.

6.3.4 qRT-PCR

RNA was extracted and quantified as described in sections 2.3.1.3 and 2.3.2.1, respectively. Adipocyte gene expression was quantified using the Qiagen miScript reverse transcription (RT) II kit and Life Technologies' Gene Expression TaqMan® qPCR system (section 2.3.4). 10ng cDNA was used for each gene expression assay and a list of the gene expression assays used are shown in Table 5.1.

Probe	Cat no.	Probe	Cat no.
18s rRNA	Mm03928990_g1	Pparɣ	Mm01184322_m1
Ucp1	Mm01244861_m1	Accα	Mm01304257_m1
Fabp4	Mm00445878_m1	Fasn	Mm00662319_m1
Cd36	Mm01135198_m1	Pgc1α	Mm00447183_m1
Hmgcr	Mm01282499_m1	Cebpα	Mm01265914_S1
Lxrα	Mm00443451	Cebpβ	Mm00843434_s1

Table 6.1: TaqMan™ Gene Expression Assays Used in This Chapter

miRNA transcripts were quantified by qRT-PCR using Life Technologies' TaqMan® microRNA system, as described in section 2.3.4. For the microRNA system, Life Technologies' TaqMan® microRNA assays were used, shown in Table 3.2.

TaqMan® microRNA	
Primer Assay	**Cat no.**
miR-34a	000426
miR-34a-3p	465771_mat
miR-34b-5p	002617
miR-34b-3p	002618
miR-34c	000428
miR-34c*	002584
U6	001973

Table 6.2: Manufacturer Information for miRNA qRT-PCR Primer Assays

6.3.5 Flow Cytometry

During collection of adipocytes for flow cytometry analysis, media was removed from the wells and 500 μl Trypsin-EDTA (Life Technologies: 15400054) solution, diluted 1:10 in DPBS, was added to each well and incubated for 5-10 minutes at 37°C. After the incubation time had elapsed, each well was flushed 4-5 times to remove cells and any residual cells were scraped with a pipette tip to remove them. Technical repeats were pooled and the cell suspension was diluted in DPBS and centrifuged at 510 x g for 5 minutes, before re-suspending the pellet in 1 ml FACS Buffer. Cells were stained and analysed, as detailed in section 2.5.2, with the following antibodies (detailed in Table 2.21): CD45-APC-Cy7 and CD31-FITC, or with BODIPY 493/503 and MitoTracker Deep Red FM to stain cellular lipid and mitochondria content, respectively. Compensation was set using single-stain controls and gates were set using fluorescence minus one (FMO) controls. MFI values in this chapter were calculated as geometric mean fluorescence intensity, unless stated otherwise.

6.3.6 Supernatant Protein Analysis

Adipocyte supernatants were analysed using a Mouse Adipokine Milliplex and Obesity Proteome Array, as described in section 2.2.3.2 and 2.2.3.3, respectively. Supernatant samples were centrifuged at 1000 x g for 5 minutes to pellet debris and the supernatant was used in the assay. 200 μl of supernatant from each independent repeat was pooled together for white (n=3) and brown (n=4) adipocyte cultures for analysis by the Obesity Proteome Array.

6.4 Results

6.4.1 Characterisation of *in vitro* Murine Pre-Adipocyte Differentiation

Firstly, the *in vitro* differentiation of both murine, primary white and brown pre-adipocytes was assessed histologically and genetically to ensure they had differentiated appropriately. The culture protocol was the same for both white and brown pre-adipocytes, using high glucose and insulin complete media supplemented with the PPARɣ agonist Rosiglitazone, as PPARɣ is required for differentiation of both of these cell types (Barak et al. 1999; Rosen et al. 1999). This protocol was the standard group protocol for growing these cells *in vitro*, and they were cultured to maturity over 8 days.

6.4.1.1 *in vitro* White Pre-Adipocytes

To check that the *in vitro* white pre-adipocytes were differentiating properly, cells were taken off at day 0, 2, 4, 6, and 8, and stained for lipid using Oil Red "O" (ORO) and examined histologically. On examination it was observed that day 0 and 2 cells showed low to no lipid vacuoles, but these became visible at day 4 and a steady increase in cytosolic lipid was observed over days 6 to 8 (Figure 6.3A). Quantification of the ORO staining showed that the pre-adipocytes had accumulated a significant quantity of lipid by day 6 ($P=0.0081$) and 8 ($P=0.0003$) of differentiation, relative to day 0 (Figure 6.3B). It was also noted that the pre-adipocytes showed a stellate, fibroblast-like morphology at day 2 of differentiation, which disappeared over days 4 to 6 as the cells rounded out (Figure 6.3A). This correlated with an approximately 5.9-fold increase in *ectodermal-neural cortex (Enc)1* transcripts ($P=0.0002$), which is known to be important in cytoskeletal reorganisation during pre-adipocyte differentiation (Zhao et al. 2000) (Figure 6.3C). This peak in *Enc1* transcripts, which decreased back to basal levels by day 4, preceded the increase in the other pre-adipocyte differentiation markers: *fatty acid binding protein* (*Fabp)4*, *Cebpα*, and *Pparɣ*. The expression of these genes peaked at day 6 with an approximate 7.1, 4.8, and 2.8-fold increase in *Fabp4* ($P<0.0001$), *Cebpα* ($P<0.0001$), and *Pparɣ* ($P<0.0051$), respectively.

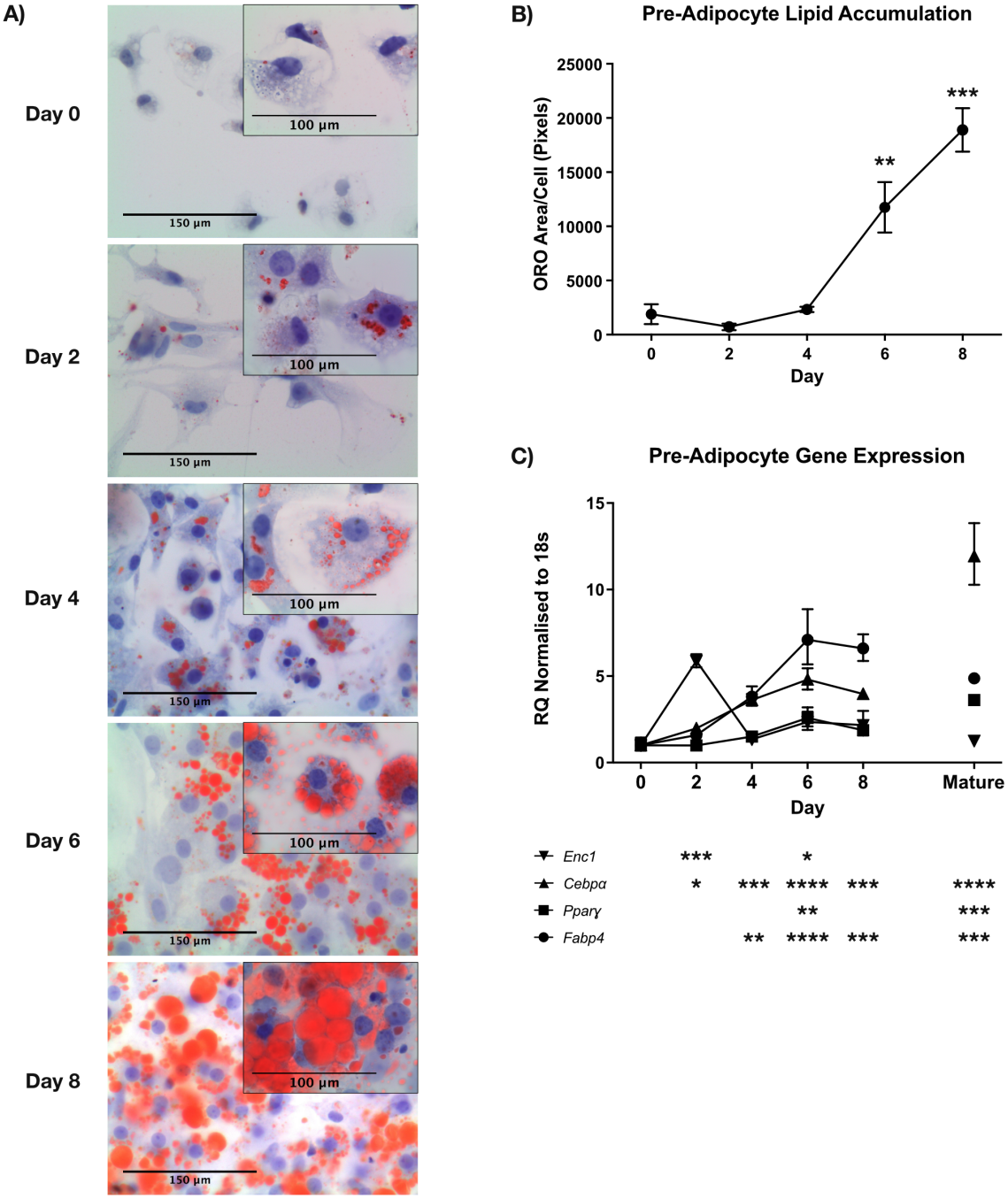

Figure 6.3: Primary White Pre-Adipocyte Differentiation Profile
(A) Representative oil red "O" (ORO) images of white pre-adipocytes as they differentiate over 8 days, showing the lipid (red) accumulation in these cells *in vitro*. Images were taken at 40X, with 100X insert; n=3. (B) Quantification of ORO staining in (A) from ≥5 random fields/section from n=3/time-point using Fiji analysis software and custom batch-processing JavaScript, normalised to cell number/section. Data is represented as mean values with SEM (C) qRT-PCR analysis of key gene expression over white pre-adipocyte differentiation, as in (A), compared with *ex vivo* "mature" adipocytes separated from the SVF during pre-adipocyte separation. Data is represented as relative change (RQ) over day 0, normalised to 18s rRNA, with RQ_{min}-RQ_{max} values; n=3. All statistics were compared to day 0; *P<0.05, **P<0.01, ***P<0.001, ****P<0.0001, One-way ANOVA, with Dunnett's multiple comparison post-test.

This correlated nicely with the peak in lipid content observed at day 6 (Figure 6.3A-B). Interestingly, at day 8 there was a slight decrease in *Fabp4* (P=0.0001),

Cebpα (P<0.0002), and *Pparɣ* (P=0.0556) expression, and a 2.4-fold increase was seen in *Enc1* (P=0.0331) at day 6 (Figure 6.3C). The gene expression levels of *Fabp4, Cebpα,* and *Pparɣ* in day 6 and 8 pre-adipocytes did not match that seen in the *ex vivo* mature adipocytes, showing a 4.9- (P=0.0004), 11.9- (P<0.0001), and 3.6 (P=0.0006)-fold increase, respectively, over day 0 pre-adipocyte levels. However, these data show that the white pre-adipocytes have successfully differentiated into mature adipocytes by day 8 of culture.

6.4.1.2 *in vitro* Brown Pre-Adipocytes

The primary brown pre-adipocytes were more challenging to culture *in vitro*, than the white pre-adipocytes. Being thermosensitive cells they did not respond well to being outside of the incubator for long periods, tending to detaching into the supernatant. Frequently the pre-adipocytes would detach during changing of media, so this was done gently to limit the amount of loss, and cells were carefully taken in/out of the incubator. Despite these challenges, the brown pre-adipocytes were cultured successfully. To assess their differentiation histologically, time-points at day 0, 2, 4, 6, and 8 were taken and they were stained with ORO to examine lipid droplets. Unlike the white pre-adipocytes, the brown pre-adipocytes did not show signs of lipid droplets until day 6, but most of the lipid droplets did not develop until day 8 (Figure 6.4). These lipid droplets were generally small and spread out through the cytoplasm, in between other granular structures, which are likely to be the dense mitochondria characteristic of these cells. The granular cytoplasm of these cells can been seen in the 100X images (Figure 6.4 Right). The majority of the pre-adipocytes also showed a stellate morphology up to day 6, rounding out by day 8. However, there were numerous cells that still showed a stellate morphology with no lipid droplets at day 8.

To further assess the differentiation of the *in vitro* brown pre-adipocytes genetically, the expression of *Pgc1α*, *Ucp1*, *Fabp4*, *Cebpα*, *Cebpβ*, and *Pparɣ* was quantified over the 8-day differentiation using qRT-PCR (Figure 6.5). *Pgc1α* is essential for the thermogenic functions of brown adipocytes (Puigserver et al. 1998).

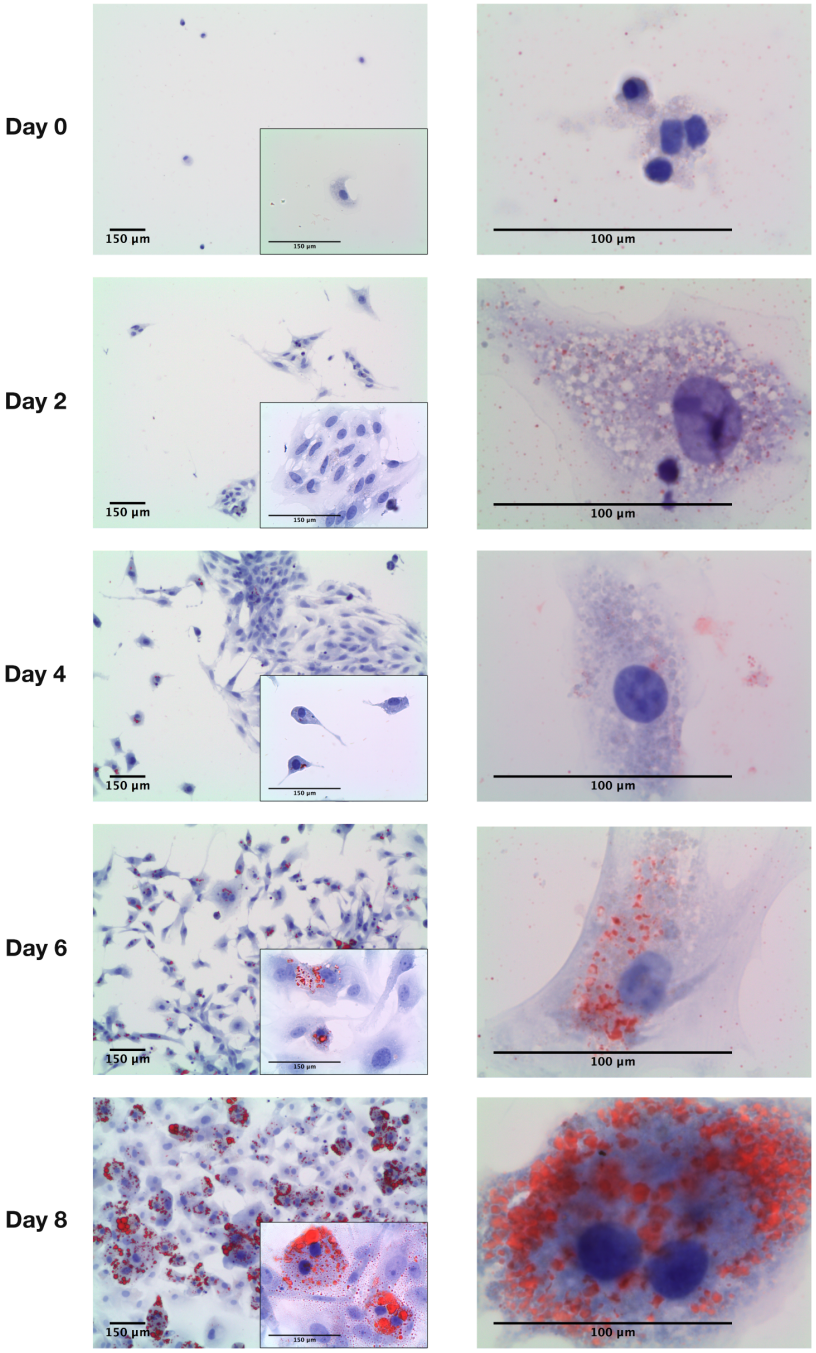

Figure 6.4: Representative Oil Red "O" Images of Brown Pre-Adipocyte Differentiation
Representative oil red "O" (ORO) images of lipid (red) accumulation in brown pre-adipocytes over differentiation for 8 days *in vitro*. (Left) shows 10X images with a 40X insert from the same field and (Right) shows 100X images from a different culture; n=2.

During brown pre-adipocyte differentiation *Pgc1α* transcripts were up-regulated by day 2 (P=0.0101) and continued to increase over day 4 (P=0.0028) and 6 (P=0.0003), before decreasing slightly at day 8 (P=0.0015) (Figure 6.5A). Interestingly, *Ucp1* transcripts decreased over differentiation, showing significantly reduced transcripts by day 8 (P=0.0178) (Figure 6.5B), despite Pgc1α previously

being shown to increase *Ucp1* transcripts (Puigserver et al. 1998). However, they were still highly expressed: day 0 = ΔCt 11.47±1.08 to day 8 = ΔCt 15.16±0.31 (18s rRNA: Ct 16.08±0.31).

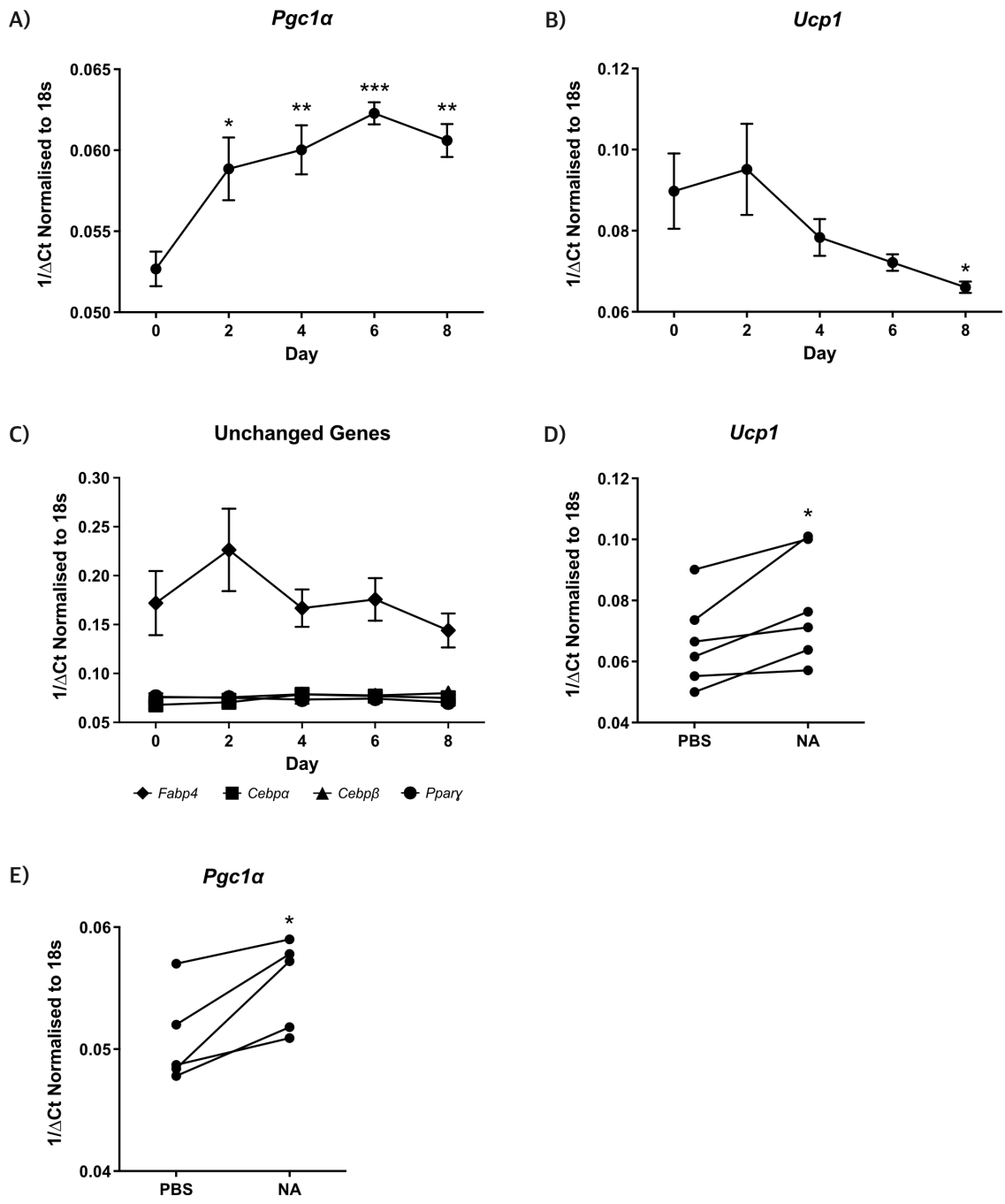

Figure 6.5: Genetic Markers of Brown Pre-Adipocyte Differentiation
(A-C) qRT-PCR data showing the change in transcript expression of *Pgc1α* (A) and *Ucp1* (B), and the static expression of *Fabp4*, *Cebpα*, *Cebpβ*, and *Pparγ* (C), over the 8-day brown pre-adipocyte differentiation *in vitro*; n=4. (D-E) qRT-PCR data showing the expression of *Ucp1* (D) and *Pgc1α* (E) in day 8 brown pre-adipocytes during beta-adrenergic stimulation with 0.1 μM noradrenaline (NA), or PBS control, for 4 hours *in vitro*; n=5-6. All data is represented as 1/ΔCt values normalised to 18s rRNA, with SEM. *P<0.05, **P<0.01, ***P<0.001, One-way ANOVA, with Dunnett's multiple comparison post-test (A-C), and paired Student's t test (D-E).

Analysis of *Fabp4*, *Cebpα*, *Cebpβ*, and *Pparγ* transcripts showed that their levels were not changed over differentiation (Figure 6.5C), but were already highly expressed on day 0: *Fabp4* = ΔCt 6.39±1.02, *Cebpα* = ΔCt 14.80±0.61, *Cebpβ* = ΔCt 13.34±0.72, and *Pparγ* = ΔCt 13.21±0.58 (18s rRNA: Ct 15.46±0.24), corresponding to previous reports of rosiglitazone-induced differentiation (Petrovic et al. 2008). Finally, to check the differentiated pre-adipocytes were responsive to beta-adrenergic stimulation, day 8 pre-adipocytes were stimulated with noradrenaline for 4 hours and the transcript expression of *Ucp1* and *Pgc1α* was quantified by qRT-PCR (Figure 6.5D-E). Both of these genes are known to increase in mature brown adipocytes when stimulated with noradrenaline (Petrovic et al. 2010). It was observed that noradrenaline stimulation increased both *Ucp1* (P=0.0219) and *Pgc1α* (P=0.0226) transcripts in day 8 pre-adipocytes (Figure 6.5D-E). However, there was a large amount of variability in expression between biological replicates at basal levels and when stimulated. Additionally, low RNA yields were produced from these cultures. These data indicate that the brown pre-adipocytes are differentiating successfully, but that perhaps the culture conditions produce a variable quantity of mature brown adipocytes. Therefore, only cultures where WT brown pre-adipocytes successfully upregulated *Ucp1* under noradrenaline stimulation, were used for downstream analysis.

6.4.2 Investigating the Role of miR-34a During *in vitro* Adipocyte Differentiation

The data from Chapter 4 showing phenotypic differences in eWAT (section 4.4.2) and metabolic gene expression differences in both eWAT and iBAT (section 4.4.3) between WT and miR-34a$^{-/-}$ mice, prompted further investigation of white and brown adipocytes *in vitro*. Particularly, these data suggested that miR-34a may have a role during white and brown adipocyte differentiation. To investigate this, the transcript expression of the miR-34 family and key differentiation genes was examined during white and brown pre-adipocyte differentiation in primary WT and miR-34a$^{-/-}$ pre-adipocytes.

6.4.2.1 White Pre-Adipocyte Differentiation

First, the transcript expression of the miR-34 family members were quantified by qRT-PCR over the 8-day *in vitro* white pre-adipocyte differentiation protocol, at days 0, 2, 4, 6, and 8 (Figure 6.6A-B). It was observed that miR-34a transcripts were increased by day 4 (P=0.1195) of differentiation, which remained elevated at days 6 (P=0.1296) and 8 (P=0.0330), but was only statistically significant at day 8 (Figure 6.6A). Examination of the other miR-34 family members showed that transcripts of both miR-34b* and 34c* began to increase at day 2 (34b*: P=0.0107; 34c*: P=0.0464), peaking at day 4 (34b*: P=0.0109; 34c*: P=0.0135) of differentiation, before decreasing over day 6 and 8 (Figure 6.6B).

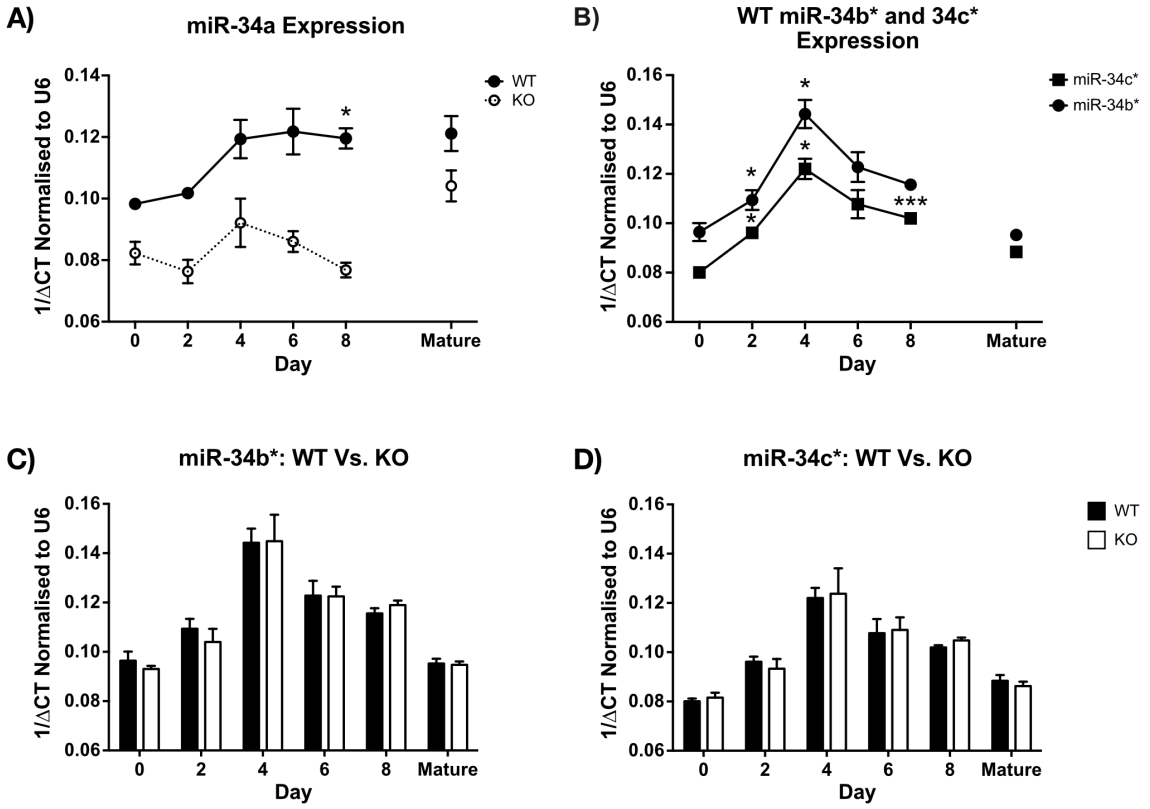

Figure 6.6: miR-34 Family Expression During White Pre-Adipocyte Differentiation *in vitro*
(A-B) qRT-PCR quantification of the miR-34 family transcripts (34a, 34b* and 34c*) over the 8-day differentiation of WT white pre-adipocytes *in vitro*, compared with the "mature" adipocyte fraction from SVF separation. Quantification of miR-34a in miR-34a$^{-/-}$ (KO) white pre-adipocytes is included as a negative control in (A). The other family members were also examined (34a*, 34b and 34c), but no/low detectable transcripts of these miRNAs were observed; n=3 and statistics were calculated compared to day 0. (C-D) qRT-PCR data comparing miR-34b* (C) and 34c* (D) transcripts between WT and KO white pre-adipocytes over differentiation, as in (A-B); n=3. All data is represented as 1/ΔCt values, normalised to RNU6B, with SEM. *P<0.05, ***P<0.001, One-way ANOVA, with Dunnett's multiple comparison post-test (A-B), and Two-way ANOVA, with Bonferroni's multiple comparison post-test (C-D).

miR-34a*, 34b, and 34c were also examined, but they showed very low to no detectable transcripts over differentiation. Because both miR-34b* and 34c* peaked at day 4 as miR-34a expression was increasing, before falling off, this could indicate that these miRNAs are regulated by miR-34a.

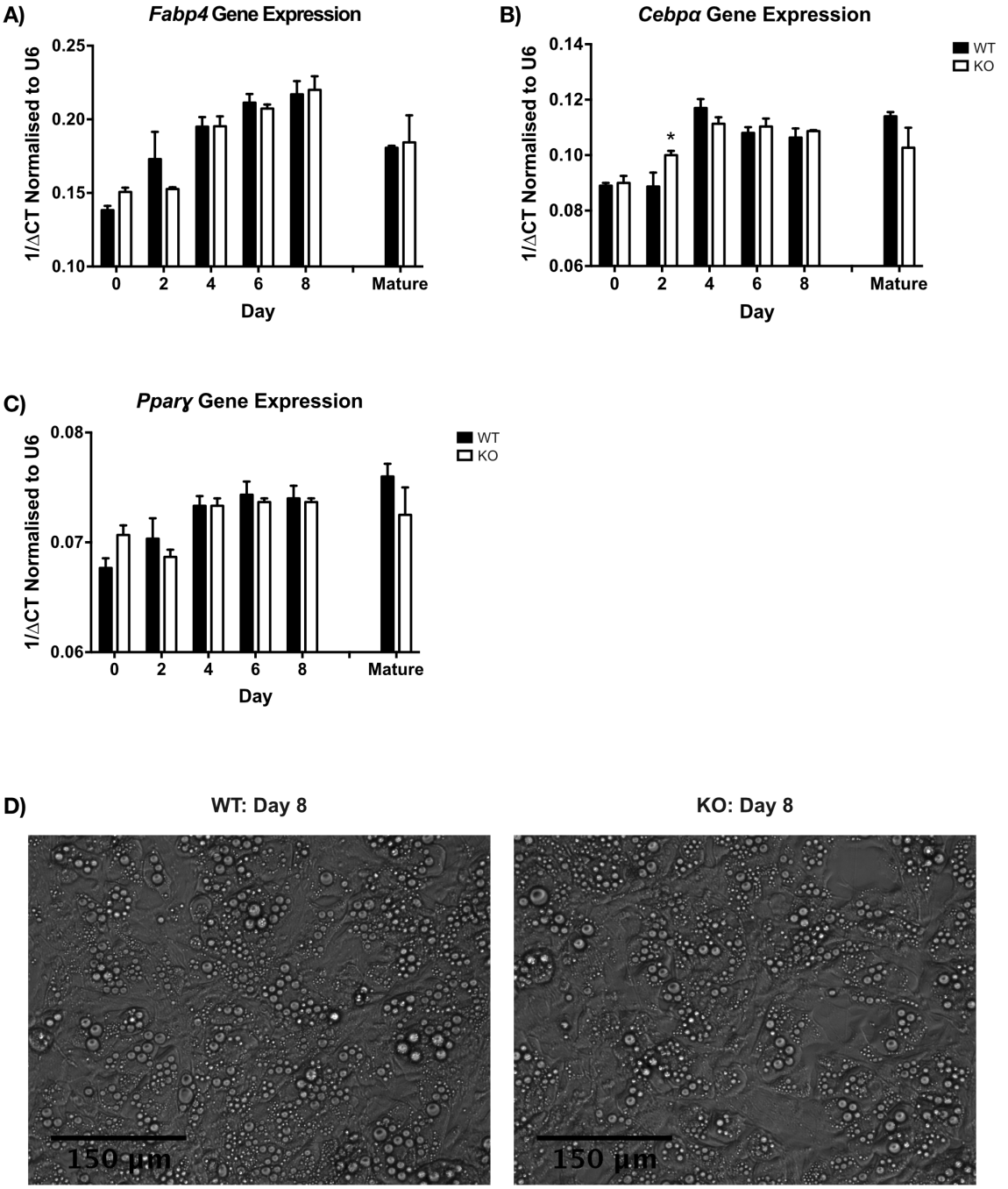

Figure 6.7: Comparison of Differentiation Markers in WT and miR-34a$^{-/-}$ White Pre-Adipocyte *in vitro*

(A-C) qRT-PCR data comparing differentiation marker expression between WT and miR-34a$^{-/-}$ (KO) white pre-adipocytes over the 8-day differentiation *in vitro*, compared with the "mature" adipocyte fraction from SVF separation; n=3. (D) Representative 20X light microscope, phase-contrast images of WT (left) and KO (right) white pre-adipocytes at day 8 of differentiation. qRT-PCR Data is represented as 1/ΔCt values, normalised to 18s rRNA, with SEM. Two-way ANOVA, with Bonferroni's multiple comparison post-test.

Therefore, the transcript expression of miR-34b* and 34c* in white pre-adipocytes were examined in the absence of miR-34a, using miR-34a$^{-/-}$ pre-adipocytes. However, no differences in expression were seen for either miR-34b* or 34c* between WT and miR-34a$^{-/-}$ white pre-adipocytes over differentiation (Figure 6.6C-D). Overall, these data indicate that miR-34a, 34b*, and 34c* could contribute to the regulation of white pre-adipocyte differentiation.

Next, to explore whether miR-34a regulates key white adipocyte differentiation genes, the transcript expression of *Fabp4*, *Cebpa*, and *Pparɣ* were examined in WT and miR-34a$^{-/-}$ white pre-adipocytes over differentiation (Figure 6.7A-C). However, no differences were observed between WT and miR-34a$^{-/-}$ white pre-adipocytes over differentiation, except for a small increase in *Cebpa* (P=0.0396) at day 2 of differentiation in miR-34a$^{-/-}$ white pre-adipocytes (Figure 6.7B).

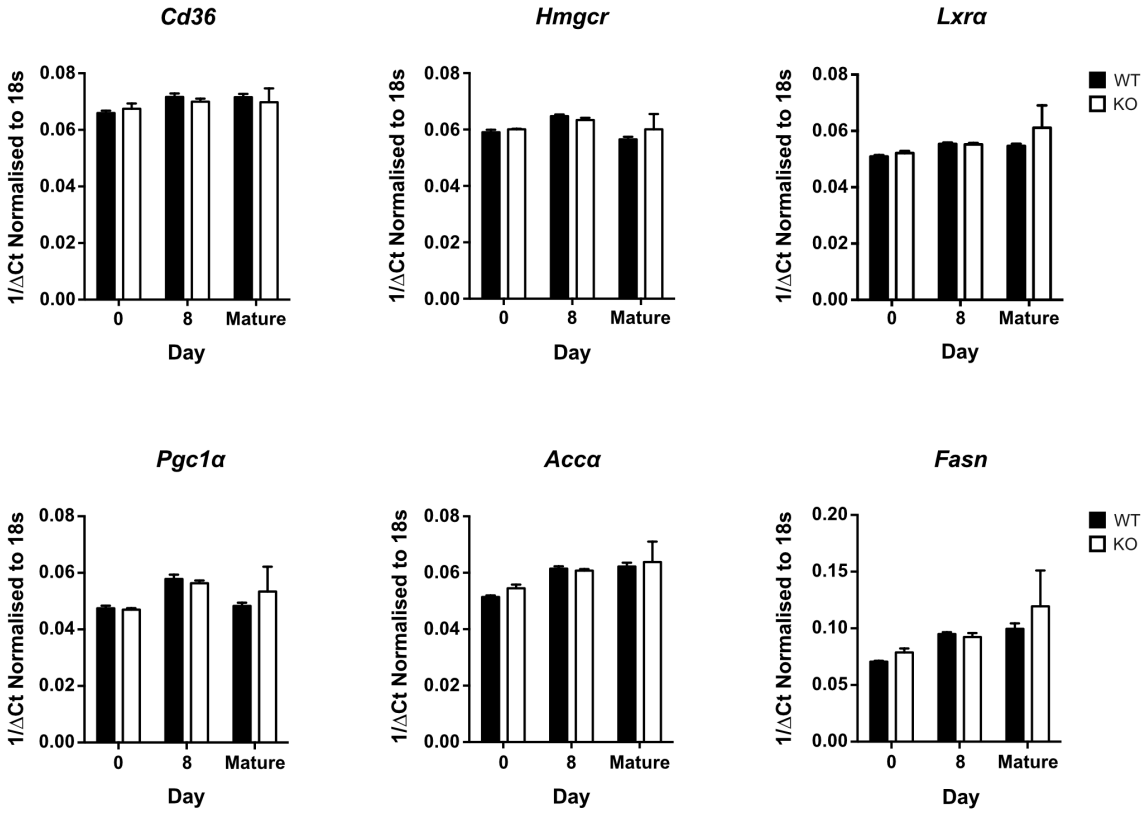

Figure 6.8: Examination of Altered miR-34a$^{-/-}$ eWAT Genes During White Pre-Adipocyte Differentiation *in vitro*
Showing qRT-PCR data comparing the expression of various metabolic genes between WT and miR-34a$^{-/-}$ (KO) white pre-adipocytes over differentiation *in vitro*, in day 0 and 8 pre-adipocytes, and in the "mature" adipocyte fraction from SVF separation; n=3. Data is represented as 1/ΔCt values, normalised to 18s rRNA, with SEM. Two-way ANOVA, with Bonferroni's multiple comparison post-test.

Furthermore, no phenotypic differences were identified between WT and miR-34a$^{-/-}$ white pre-adipocytes over differentiation, in culture (Figure 6.7D).

Finally, the transcript expression of *Cd36*, *Hmgcr*, *Lxra*, *Pgc1a*, *Acca*, and *Fasn* were examined in WT and miR-34a$^{-/-}$ white pre-adipocytes *in vitro* (Figure 6.8), due to their altered expression in miR-34a$^{-/-}$ eWAT *ex vivo* (section 4.4.3). These genes were examined at day 0 and 8 of differentiation, and in the mature adipocytes isolated from the mature fraction during SVF separation. No differences in any of these genes were observed between WT and miR-34a$^{-/-}$ white pre-adipocytes (Figure 6.8). These data suggest that miR-34a does not regulate the metabolic genes examined, at least at the transcript level, during white pre-adipocyte differentiation.

6.4.2.2 Brown Pre-Adipocyte Differentiation

Transcript expression of the miR-34 family was first examined during WT brown pre-adipocytes differentiation *in vitro*. Examination of miR-34a expression showed that there were no statistically significant changes over brown pre-adipocytes differentiation, even though there appeared to be an increase in miR-34a expression at day 8 (ΔCt 8.69±0.36 Vs. Day 0: ΔCt 11.74±0.49; P=0.1846) (Figure 6.9A). Looking at the other miR-34 family members it was observed that both miR-34b* and 34c* increased over differentiation (Figure 6.9B). miR-34b* was significantly increased at day 4 (P=0.0305), with both miR-34b* and 34c* further increasing by day 6 (34b*: P=0.0022; 34c*: P=0.0224) and 8 (34b*: P=0.0006; 34c*: P=0.0089). Expression of miR-34a*, 34b, and 34c was also examined, but no transcripts were detectable during differentiation. To determine whether there was regulation of miR-34b* and 34c* by miR-34a over the period of differentiation, their transcript expression was examined in the absence of miR-34a using miR-34a$^{-/-}$ pre-adipocytes (Figure 6.9C-D). However, there were no differences in transcript expression observed between WT and miR-34a$^{-/-}$ pre-adipocytes, for either miR-34b* or 34c*, over differentiation. These data suggest that miR-34b* and 34c* could contribute to the regulation of brown pre-adipocyte differentiation.

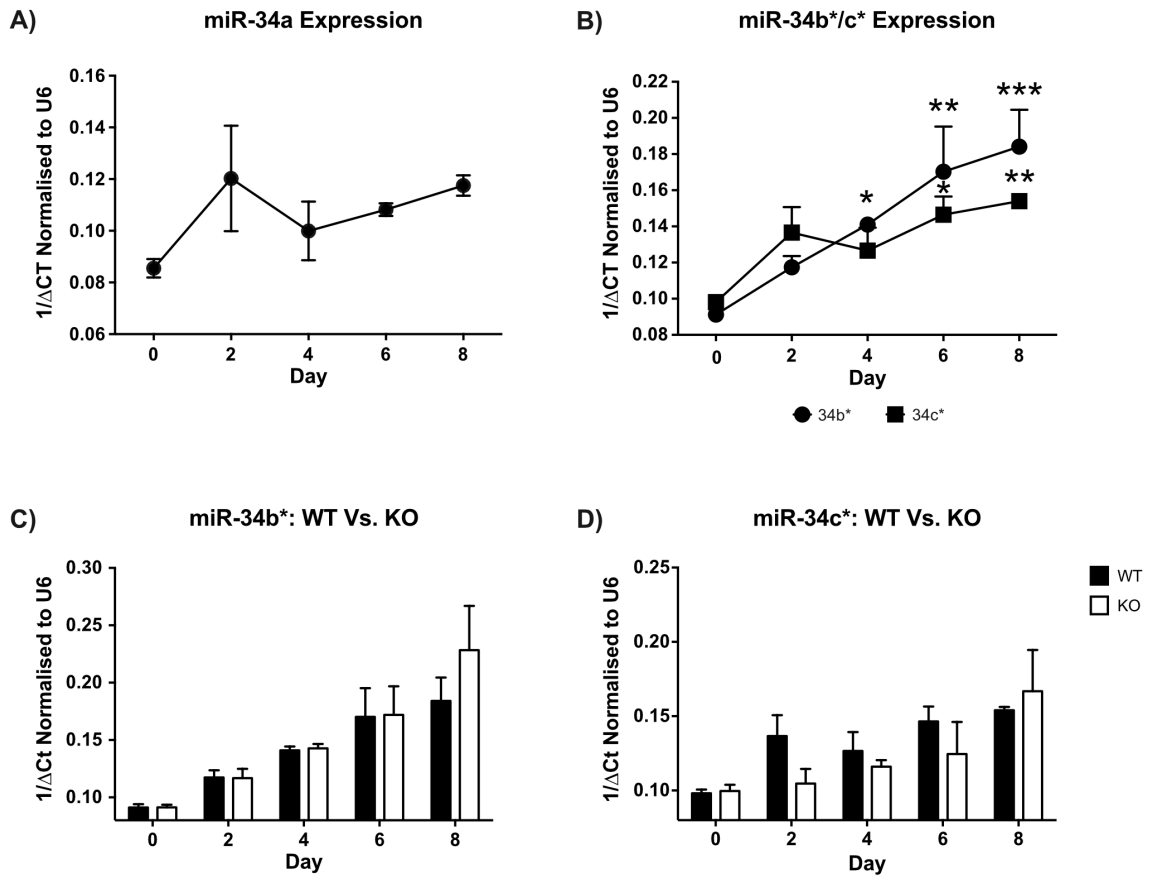

Figure 6.9: miR-34 Family Expression Over Brown Adipocyte Differentiation *in vitro*
(A-B) qRT-PCR quantification of the miR-34 family transcripts (34a, 34b* and 34c*) over the 8-day differentiation of WT brown pre-adipocytes *in vitro*. The other family members were also examined (34a*, 34b and 34c), but no transcripts of these miRNAs, or miR-34a in miR-34a$^{-/-}$ (KO) brown pre-adipocytes, were detected; n=3 and statistics were calculated compared to day 0. (C-D) qRT-PCR data comparing miR-34b* (C) and 34c* (D) transcripts between WT and KO brown pre-adipocytes over differentiation, as in (A-B); n=3. All data is represented as 1/ΔCt values, normalised to RNU6B, with SEM. *P<0.05, **P<0.01, ***P<0.001, One-way ANOVA, with Dunnett's multiple comparison post-test (A-B), and Two-way ANOVA, with Bonferroni's multiple comparison post-test (C-D).

Next, transcript expression of the brown adipocyte differentiation genes: *Pgc1α*, *Ucp1*, *Cebpα*, *Cebpβ*, and *Pparγ* was quantified by qRT-PCR in WT and miR-34a$^{-/-}$ brown pre-adipocytes during differentiation, to determine if they were regulated by miR-34a (Figure 6.10A-E). No expression differences were observed between WT and miR-34a$^{-/-}$ pre-adipocytes during differentiation, for these genes. Furthermore, the transcript expression of *Pgc1α* and *Ucp1* was functionally assessed in both of these cell types at day 8, under beta-adrenergic stimulation with noradrenaline to simulate physiological signals of thermogenic activation (Figure 6.10F). However, there was no statistical differences observed in *Pgc1α* and *Ucp1* transcript expression, between WT and miR-34a$^{-/-}$ brown pre-adipocytes. Even though it appeared that miR-34a$^{-/-}$ pre-adipocytes were not as

responsive as WT pre-adipocytes to noradrenaline stimulation of *Pgc1α* (WT: ΔCt 19.50±0.73 > 17.85±0.61; KO: ΔCt 17.69±1.03 > 17.40±0.81) and *Ucp1* (WT: ΔCt 15.23±1.91 > 12.17±1.39; KO: ΔCt 13.35±2.50 > 13.49±1.41) expression, which were already highly expressed.

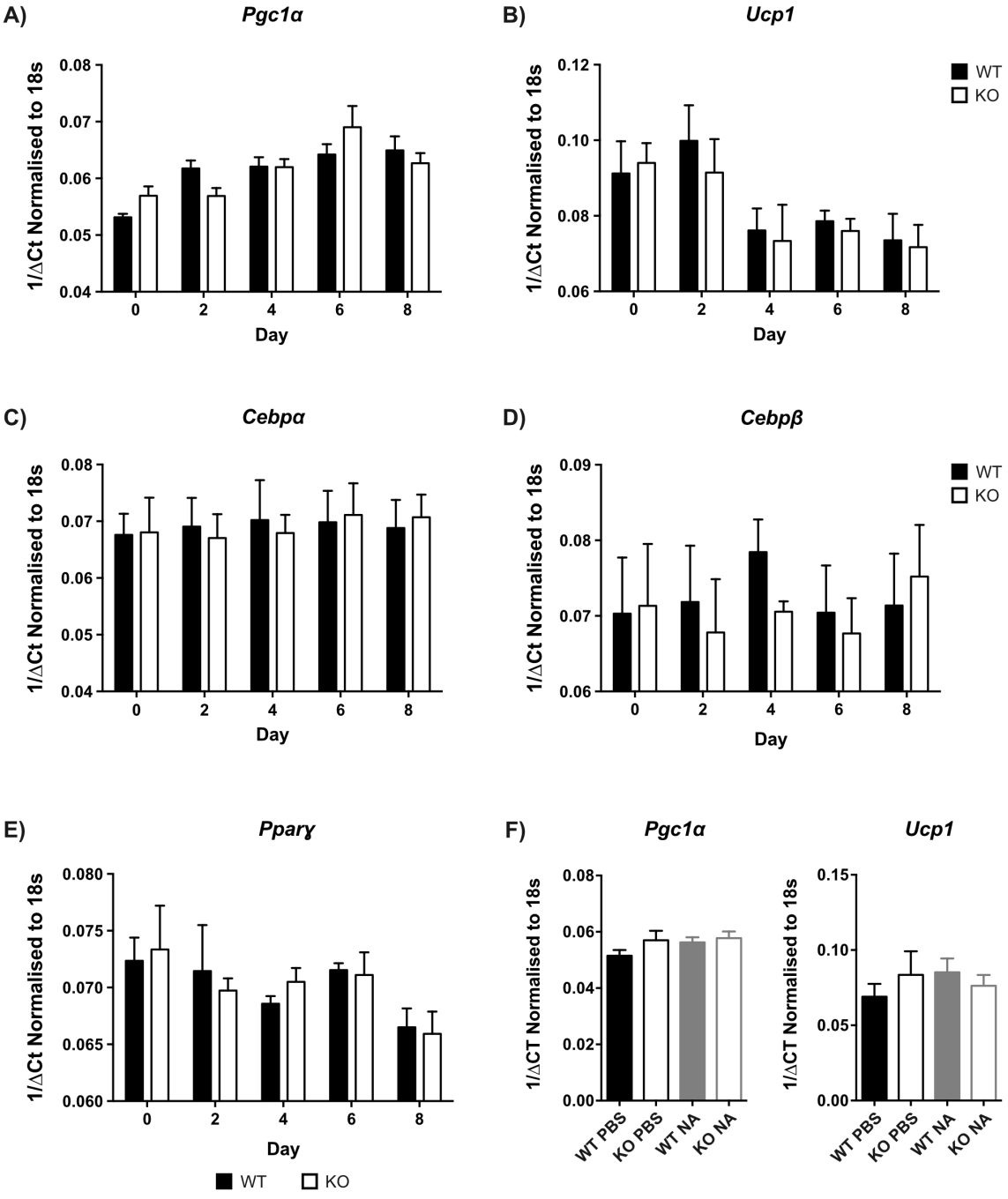

Figure 6.10: Comparison of Differentiation Markers in WT and miR-34a$^{-/-}$ Brown Pre-Adipocytes *in vitro*

(A-E) qRT-PCR data comparing differentiation marker expression between WT and miR-34a$^{-/-}$ (KO) brown pre-adipocytes over the 8-day differentiation *in vitro*; n=3-4. (F) qRT-PCR data comparing the expression of *Pgc1α* and *Ucp1* between WT and KO brown pre-adipocytes at day 8 of differentiation, after a 4-hour stimulation with 0.1μM Noradrenaline (NA) or PBS control; n=4. Data is represented as 1/ΔCt values, normalised to 18s rRNA, with SEM. Two-way ANOVA, with Bonferroni's multiple comparison post-test (A-E), and One-way ANOVA, with Bonferroni's multiple comparison post-test (F).

Finally, no differences in morphology were observed between WT and miR-34a$^{-/-}$ brown pre-adipocytes during differentiation (Figure 6.11). These data indicate that miR-34a does not regulate the metabolic genes examined at the transcript level during brown pre-adipocyte differentiation, but does not conclusively show that *Pgc1a* and *Ucp1* transcripts are not regulated by miR-34a under beta-adrenergic stimulation.

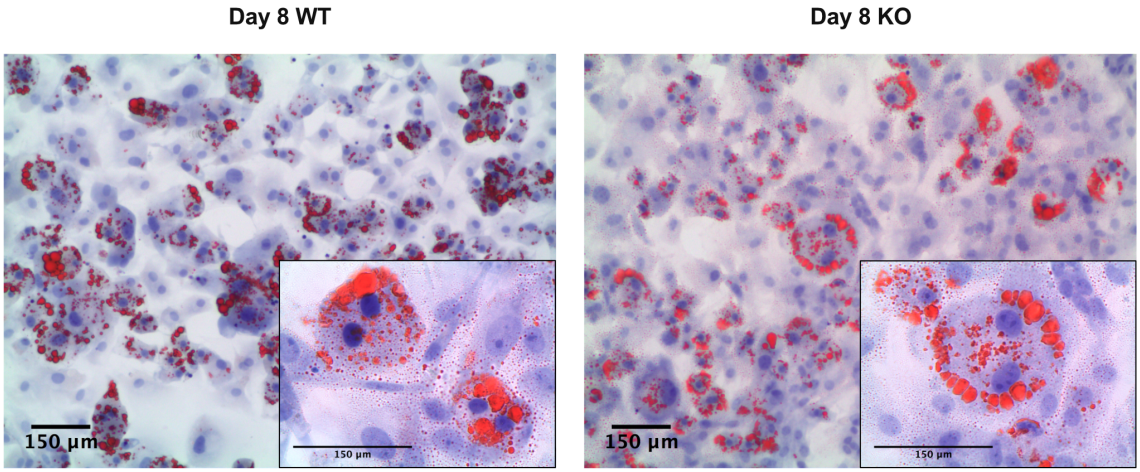

Figure 6.11: *in vitro* WT and miR-34a$^{-/-}$ Brown Pre-Adipocyte Phenotype At Day 8
Representative 10X image of oil red "O" (ORO) lipid (red) staining of WT and miR-34a$^{-/-}$ (KO) brown pre-adipocytes, at day 8 of *in vitro* differentiation, with 40X insert.

6.4.3 Exploring Functional Characteristics of WT and miR-34a$^{-/-}$ Adipocytes *in vitro*

To further explore differences between WT and miR-34a$^{-/-}$ pre-adipocytes *in vitro*, functional studies were undertaken. These explored the possibility that if *Pgc1a* is regulated by miR-34a there could be differences in brown adipocyte mitochondrial biogenesis, and that differences in white adipocyte lipid uptake could explain the *ex vivo* eWAT phenotype in miR-34a$^{-/-}$ mice (section 4.4.2). Additionally, various adipokines were profiled to see if changes in the secretome could contribute to the immune and metabolic phenotypes *ex vivo*.

6.4.3.1 Adipocyte Lipid and Mitochondria Content

To examine the lipid and mitochondrial content of adipocytes the fluorescent dyes BODIPY 493/503 and MitoTracker Deep Red FM were used, respectively. Both of these dyes have been used by others to examine lipid and mitochondria in

adipocytes (Wilson-Fritch et al. 2004; Koh et al. 2009; Nishimura et al. 2009; Sato et al. 2014).

6.4.3.1.1 MitoTracker and BODIPY Method Optimisation

First, confocal microscopy was used to examine the cellular structures that were stained by MitoTracker and BODIPY in day-8 WT white and brown pre-adipocytes *in vitro*, using various dye concentrations (Figure 6.12 and Figure 6.13). It was observed that a MitoTracker concentration of 100 nM produced faint staining in both white and brown pre-adipocytes, with a concentration of 200 nM producing better results (Figure 6.12). However, it was also noticed that, in white pre-adipocytes, MitoTracker brightly stained circular structures within the cells' cytosol, which resembled the large lipid droplets found in these cells. The rest of the cytosol showed lower levels of staining. In brown pre-adipocytes, MitoTracker staining was evenly distributed throughout the cytosol, showing a network of structures, presumably mitochondria.

To confirm that MitoTracker was staining the lipid droplets in white pre-adipocytes and check that only lipid droplets were stained by BODIPY, two concentrations of BODIPY were tested (10-100 ng/ml) whilst co-stained with MitoTracker (Figure 6.13). A concentration of 10 ng/ml was sufficient to stain the large lipid droplets of white pre-adipocytes, but not high enough to get a clear images of the small lipid droplets in brown pre-adipocytes. On the other hand, 100 ng/ml was sufficient to get a clear image of the small lipid droplets in brown pre-adipocytes, but too high for white pre-adipocytes, showing intense staining of the whole cell. Under the appropriate staining conditions, there were distinct structures stained by both BODIPY and MitoTracker in both cell types, without overlap. However, MitoTracker still stained circular structures within the cytosol of white pre-adipocytes, but notably less than when MitoTracker was used alone. In the brown pre-adipocytes stained with 100 ng/ml BODIPY, the small lipid droplets could be seen surrounded by the MitoTracker-stained structures, as expected for mitochondria and lipid droplets in brown adipocytes.

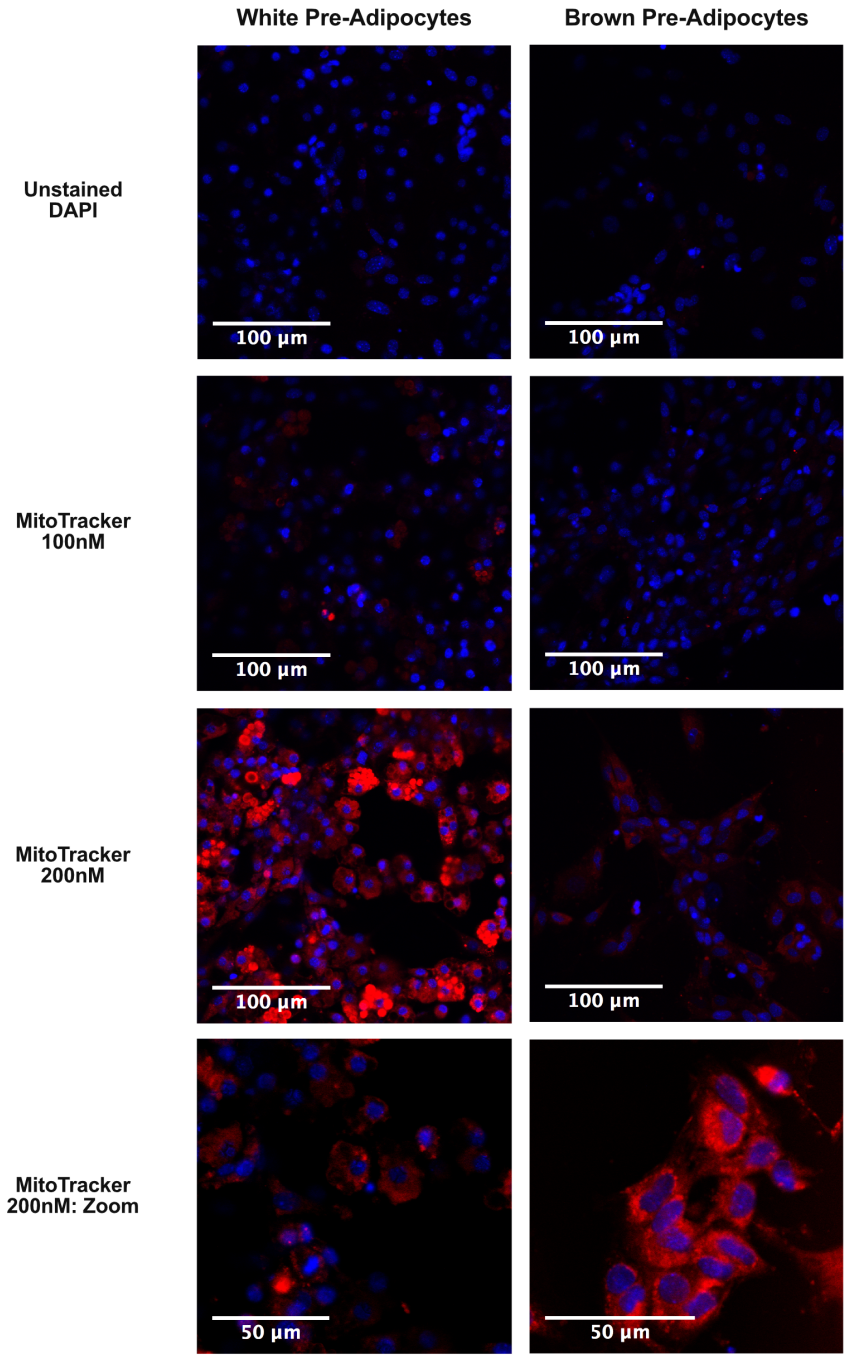

Figure 6.12: Confocal Images of MitoTracker Staining Optimisation in Pre-Adipocytes
Showing 40X confocal images of fluorescent MitoTracker Deep Red FM (red) staining optimisation in WT white and brown pre-adipocytes at day 8 of *in vitro* differentiation, with DAPI nuclei staining (blue). Laser voltages and images adjustments were set using the unstained DAPI control.

Next, MitoTracker was titrated (50, 100, and 200 nM) and analysed by flow cytometry in day 8 white and brown pre-adipocytes to find the optimal concentration with least spectral overlap (Figure 6.14). MitoTracker is detectable in the allophycocyanin (APC) channel using flow cytometry.

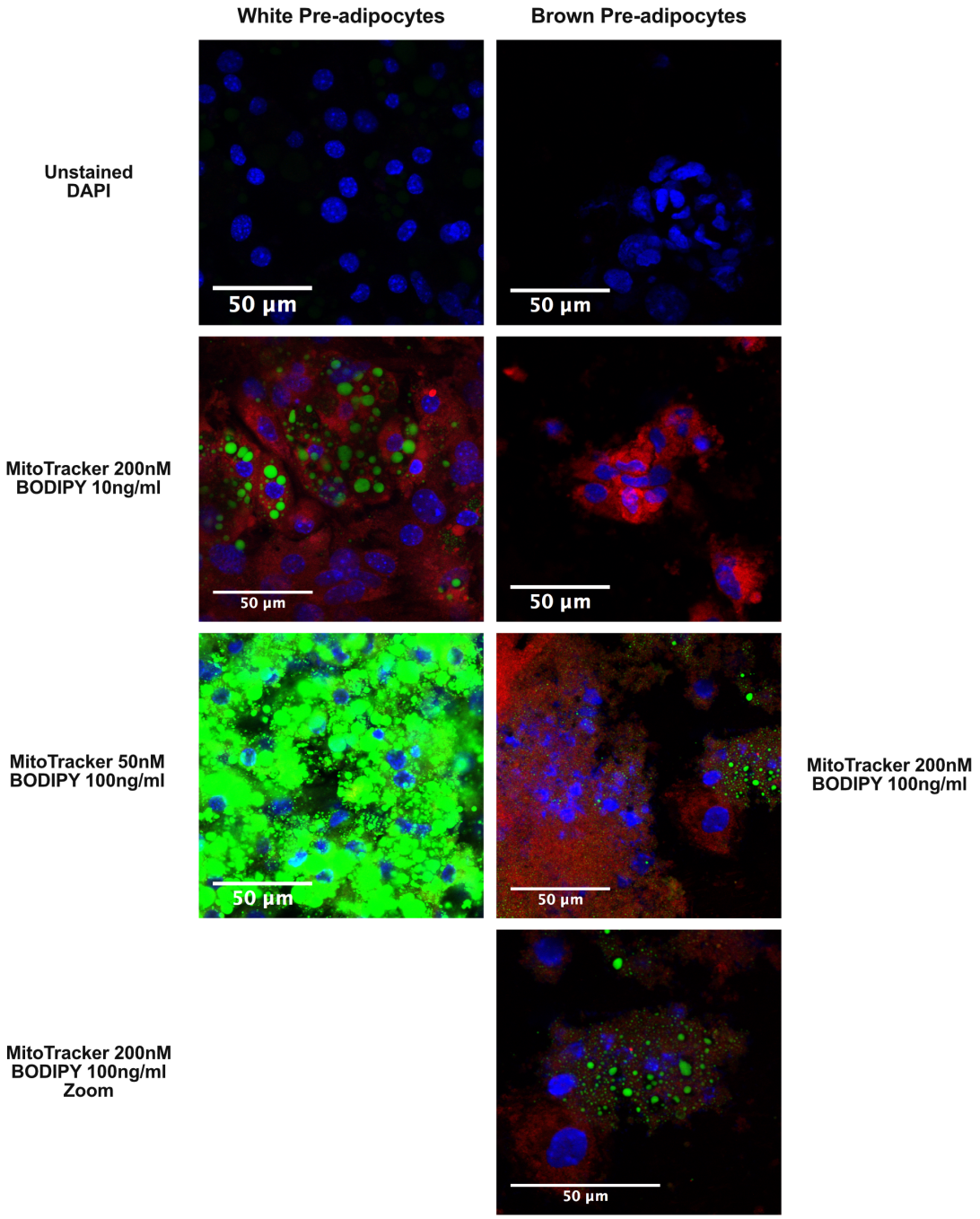

Figure 6.13: Confocal Images of BODIPY Staining Optimisation in Pre-Adipocytes
Showing 63X confocal images of fluorescent BODIPY 493/503 (green) staining optimisation with 200nM MitoTracker Deep Red FM (red) staining (except where indicated) in WT white and brown pre-adipocytes at day 8 of *in vitro* differentiation, with DAPI nuclei staining (blue). Laser voltages and image adjustments were set using the unstained DAPI control.

The 200 nM concentration for both white and brown pre-adipocytes showed the greatest spectral separation from the unstained population; however, it was also noted that there was a large amount of bleeding into the APC-Cy7 channel. This was greatly reduced using 50 nM MitoTracker, which did not show as good separation from the unstained population, but still allowed approximately 99% of

positive cells to be identified. Interestingly, at all of the concentrations examined, white pre-adipocytes showed a greater MitoTracker MFI than brown pre-adipocytes, suggesting greater mitochondrial content. However, with the confocal microscopy observations of MitoTracker staining in white pre-adipocytes, this suggests that non-mitochondrial structures are being detected in these cells. Therefore, these data suggest that a 50 nM concentration of MitoTracker is optimal to analyse mitochondrial content in brown, but not white pre-adipocytes, by flow cytometry. Additionally, they suggest that a low concentration of BODIPY is sufficient to specifically label lipid in both white and brown pre-adipocytes.

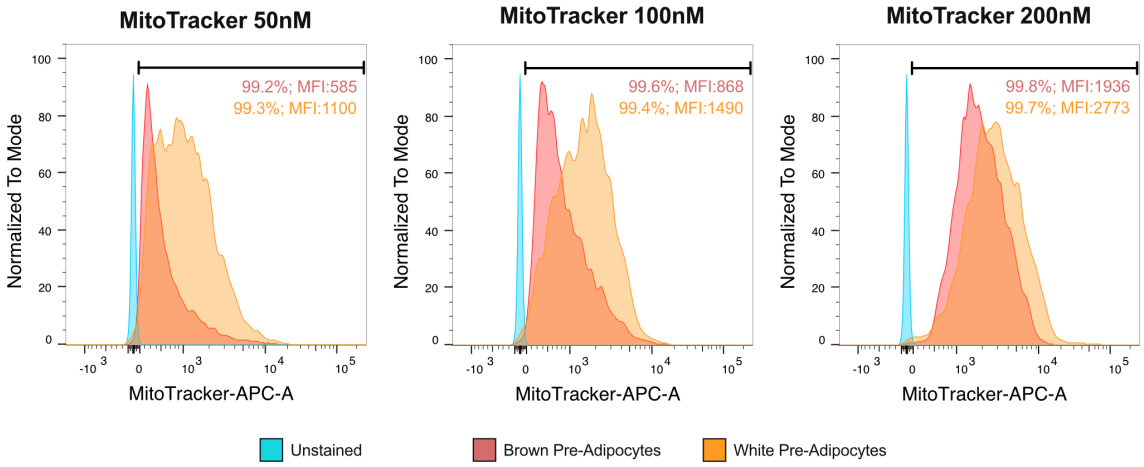

Figure 6.14: Flow Cytometry Quantification of MitoTracker Titration in Pre-Adipocytes
Showing flow cytometry quantification of titration of different staining concentrations (50, 100, and 200 nM) of MitoTracker Deep Red FM (APC) on WT white and brown pre-adipocytes at day 8 of *in vitro* differentation; n=1. Gates were set off unstained and statistics are represented as percentage of parent populations and geometric mean fluorescence intensity (MFI).

6.4.3.1.2 Flow Cytometry Quantification of Adipocyte Lipid and Mitochondria Content

Differences in lipid and mitochondrial content between day 8 WT and miR-34a$^{-/-}$ white and brown pre-adipocytes were quantified by flow cytometry using BODIPY and MitoTracker, respectively (Figure 6.15). Mitochondrial content was only quantified in brown pre-adipocytes, due to the issues with MitoTracker in white pre-adipocytes, described above (section 6.4.3.1.1). Additionally, brown pre-adipocytes were stimulated with noradrenaline to drive mitochondrial biogenesis and increase thermogenesis.

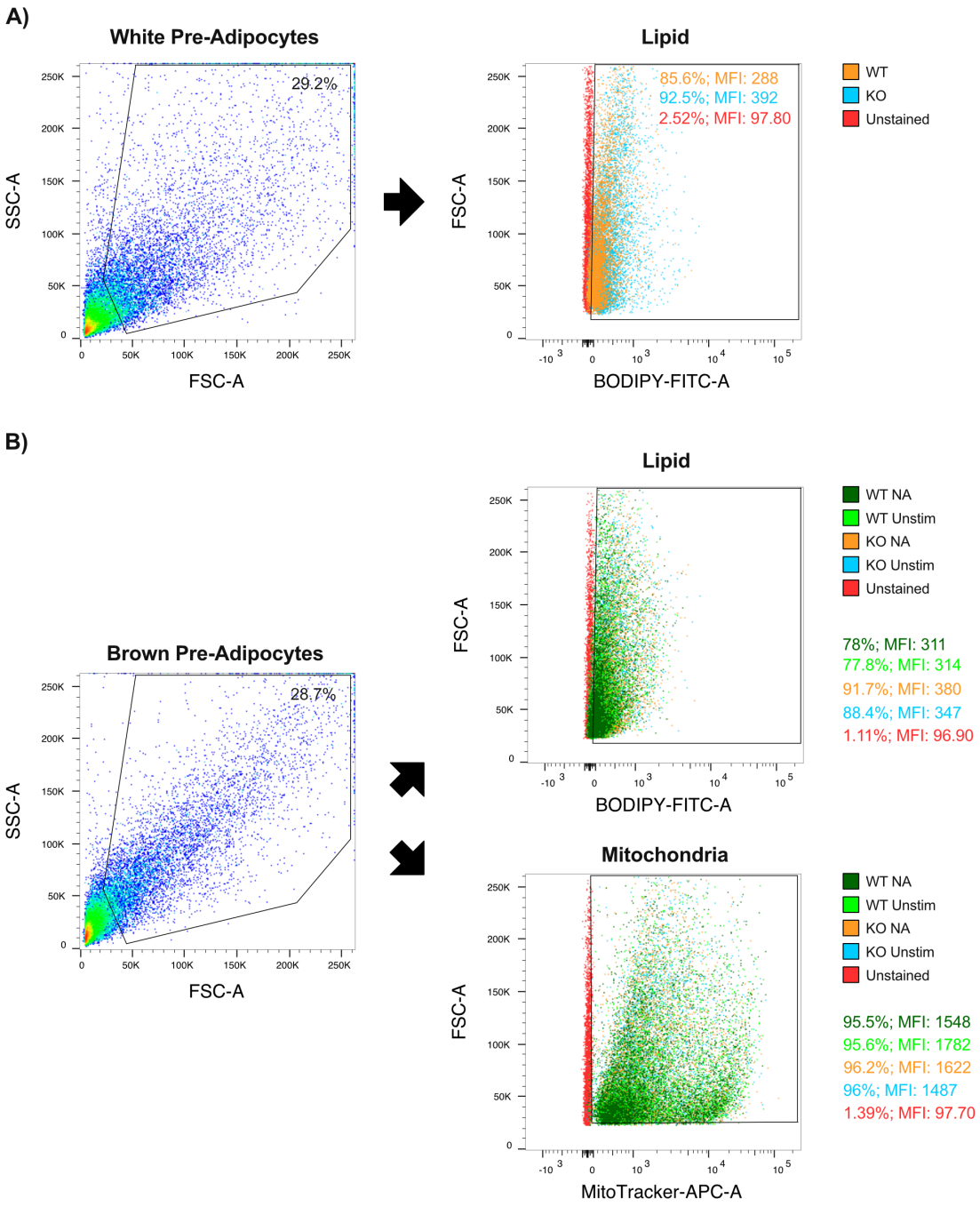

Figure 6.15: Representative Dot-Plot Overlays of Flow Cytometry Quantification of Lipid and Mitochondria Content in Pre-Adipocytes

(A) Representative flow cytometry plots of lipid+ (0.1 μg/ml BODIPY 493/503) cells gated off the SSC-FSC population, of WT and miR-34a$^{-/-}$ (KO) day 8 white pre-adipocytes *in vitro*; 1 replicate representative of n=3. (B) Representative flow cytometry plots of lipid+ (0.1 μg/ml BODIPY 493/503) and mitochondria+ (50 μg/ml MitoTracker Deep Red FM) cells gated off the SSC-FSC population, of WT and miR-34a$^{-/-}$ (KO) day 8 brown pre-adipocytes stimulated for 4 hours ±0.1 μM Noradrenaline (NA) or PBS control (Unstim) *in vitro*; 1 replicate representative of n=3. Gates were set off FMO or unstained controls and statistics are represented as percentages of parent populations and geometric mean fluorescence intensity (MFI) values.

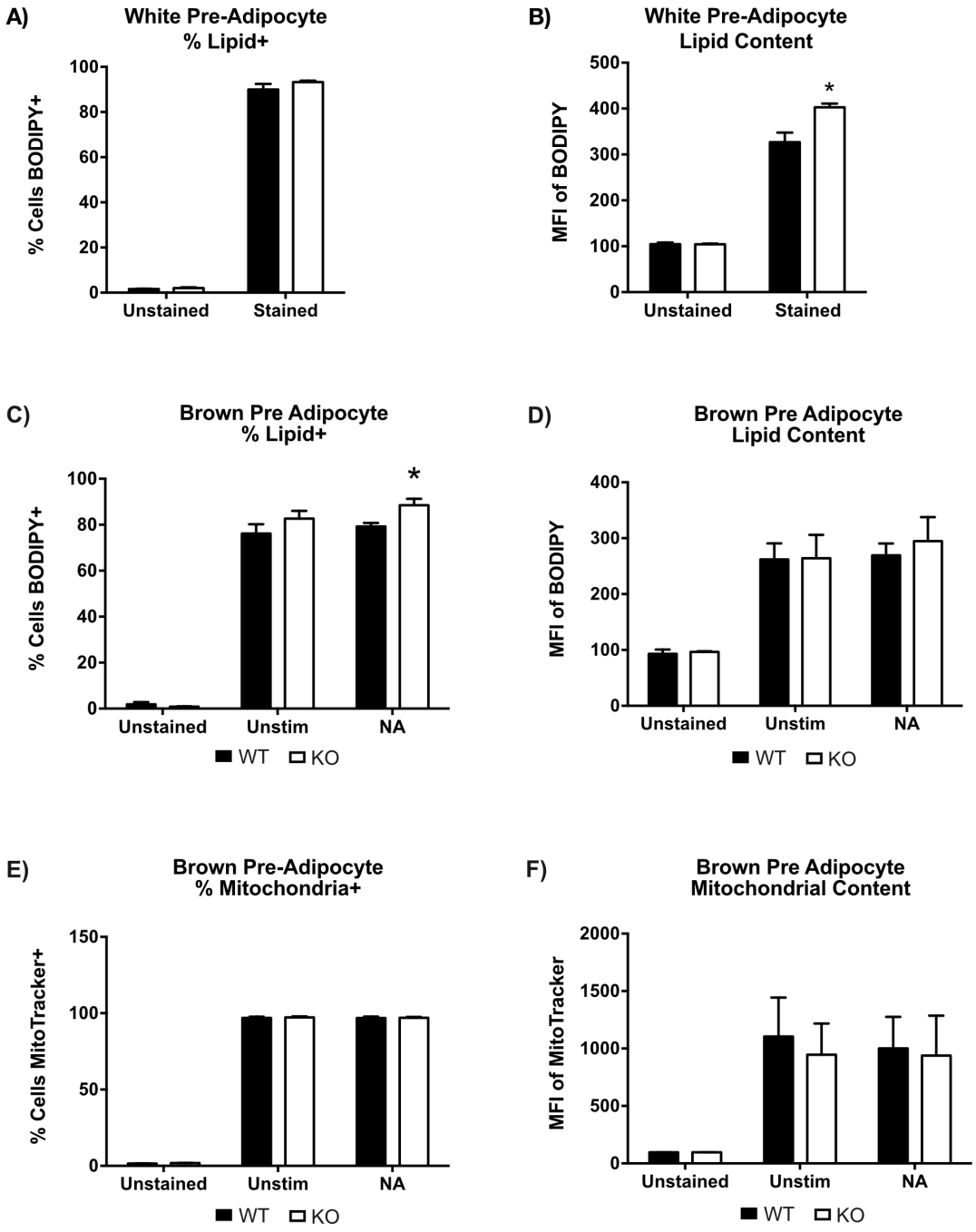

Figure 6.16: Flow Cytometry Quantification of Lipid and Mitochondrial Content in Pre-Adipocytes

(A-B) flow cytometry quantification of lipid in WT and miR-34a$^{-/-}$ (KO) day 8 white pre-adipocytes *in vitro*, using 0.1 μg/ml BODIPY 493/503 as in Figure 6.15A, and represented as percentage positive cells (A) and content using geometric mean fluorescence intensity (MFI; B); n=3. (C-F) flow cytometry quantification of lipid and mitochondria content in WT and KO day 8 brown pre-adipocytes stimulated for 4 hours ±0.1 μM Noradrenaline (NA) or PBS control (Unstim) *in vitro*, using 0.1 μg/ml BODIPY 493/503 (lipid) and 50 nM MitoTracker Deep Red FM (mitochondria) as in Figure 6.15B. Data is represented as percentage positive cells (C, E) and content using MFI (D, F); n=3. All graphs represent mean values with SEM. *P<0.05, unpaired student's t-test between WT and KO.

In white pre-adipocytes no difference was observed in the percentage of lipid positive cells, but an increase in lipid content (MFI) of 24.2±7.52% (P=0.0280) was

seen in miR-34a$^{-/-}$ white pre-adipocytes, compared to WT (Figure 6.15A and Figure 6.16A-B). In contrast, miR-34a$^{-/-}$ brown pre-adipocytes stimulated with noradrenaline showed an 11.67±3.09% increase in the percentage of lipid positive cells (P=0.0445), compared to noradrenaline-stimulated WT cells (Figure 6.15B and Figure 6.16C). This difference was not observed in unstimulated cells and no difference was seen in the cellular lipid content between miR-34a$^{-/-}$ and WT brown pre-adipocytes (Figure 6.16C-D). Finally, mitochondrial content was examined in brown pre-adipocytes; however, no differences were seen in either the percentage positive or cellular content of mitochondria between miR-34a$^{-/-}$ and WT cells (Figure 6.15B and Figure 6.16E-F). These data suggest that miR-34a$^{-/-}$ white and brown pre-adipocytes store more lipid than their WT counterparts.

6.4.3.2 Characterising Pre-Adipocyte Supernatant Adipokines

To examine the adipokines secreted by WT and miR-34a$^{-/-}$ white and brown pre-adipocytes *in vitro*, supernatants from these cells were analysed using Luminex for insulin, leptin, and resistin, and an obesity proteome array. During white pre-adipocyte differentiation it was observed that miR-34a$^{-/-}$ cells had increased supernatant levels of leptin at day 0 (P=0.0458) and lower levels at day 6 (P=0.0009), compared to WT (Figure 6.17A). Additionally, miR-34a$^{-/-}$ cells showed decreased supernatant levels of insulin at day 2 (P=0.0041) of white pre-adipocyte differentiation, compared to WT (Figure 6.17B). In both WT and miR-34a$^{-/-}$ white pre-adipocytes, resistin was observed to increase over differentiation from day 4-8, but no differences were seen between WT and miR-34a$^{-/-}$ cells (Figure 6.17C). At day 8 of brown pre-adipocyte differentiation no differences in insulin, leptin, or resistin were observed between WT and miR-34a$^{-/-}$ cells (Figure 6.17D).

Further examination of supernatant adipokines by an obesity proteome array showed few differences between WT and miR-34a$^{-/-}$ white and brown pre-adipocytes at day 8 of differentiation (Figure 6.18). The array profiled 38 murine adipokines, but only the ones detectable above the background signal are shown. In white pre-adipocytes a small decrease in insulin-like growth factor-binding protein (IGFBP)-3 and -5 were observed in miR-34a$^{-/-}$ cells (Figure 6.18B). Furthermore, in brown pre-adipocytes a decrease in IGFBP-2 and increase in

adiponectin was observed in miR-34a$^{-/-}$ cells (Figure 6.18C). These data suggest that there could be some adipokine differences between WT and miR-34a$^{-/-}$ pre-adipocytes.

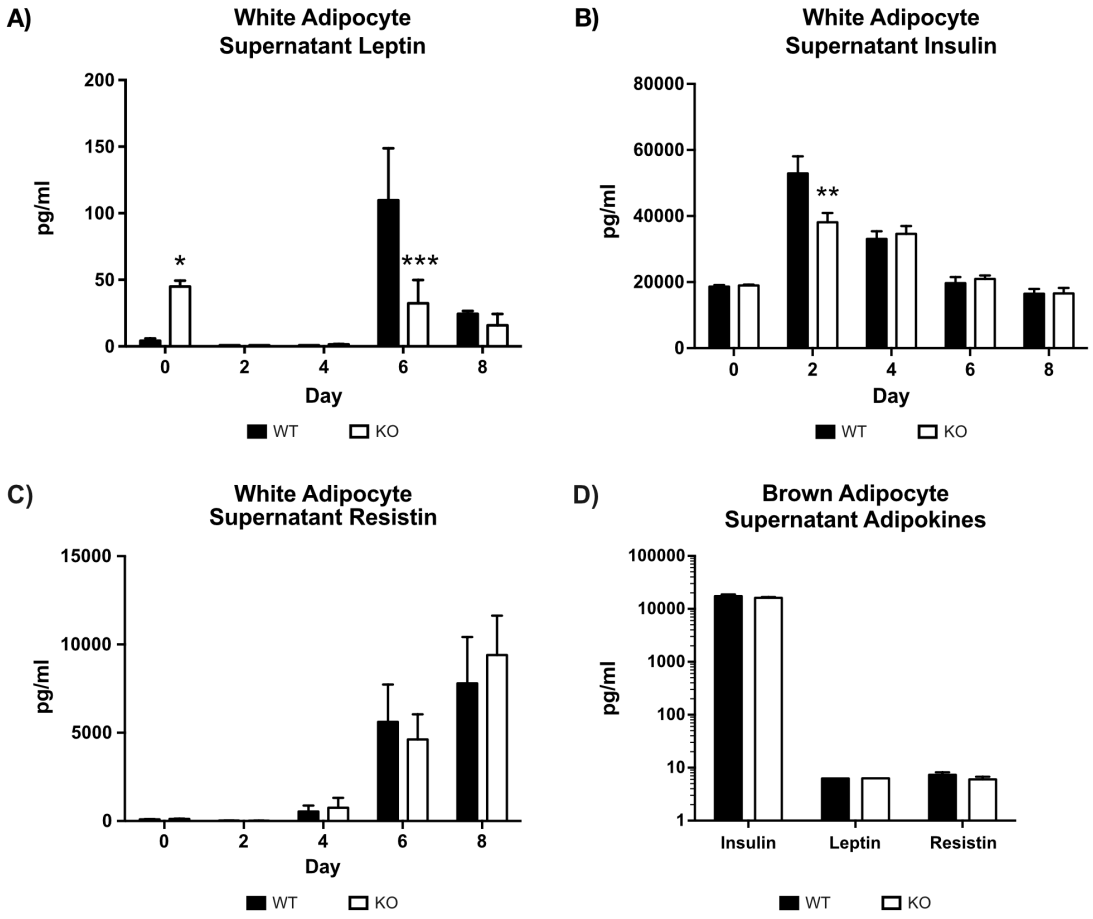

Figure 6.17: Luminex Quantification of Supernatant Adipokines During Pre-Adipocyte Differentiation

(A-C) Adipokine Milliplex Quantification of adipokines in supernatants from WT and miR-34a$^{-/-}$ (KO) white pre-adipocytes at day 0-8 of differentiation *in vitro*; n=3. (D) Adipokine Milliplex Quantification of adipokines in supernatants from WT and KO brown pre-adipocytes at day 8 of differentiation *in vitro*; n=4. All data is represented as mean values with SEM. *P<0.05, **P<0.01, ***P<0.001, Two-way ANOVA, with Bonferronni's multiple comparisons post-test (A-C), and unpaired student's t-test between WT and KO (D).

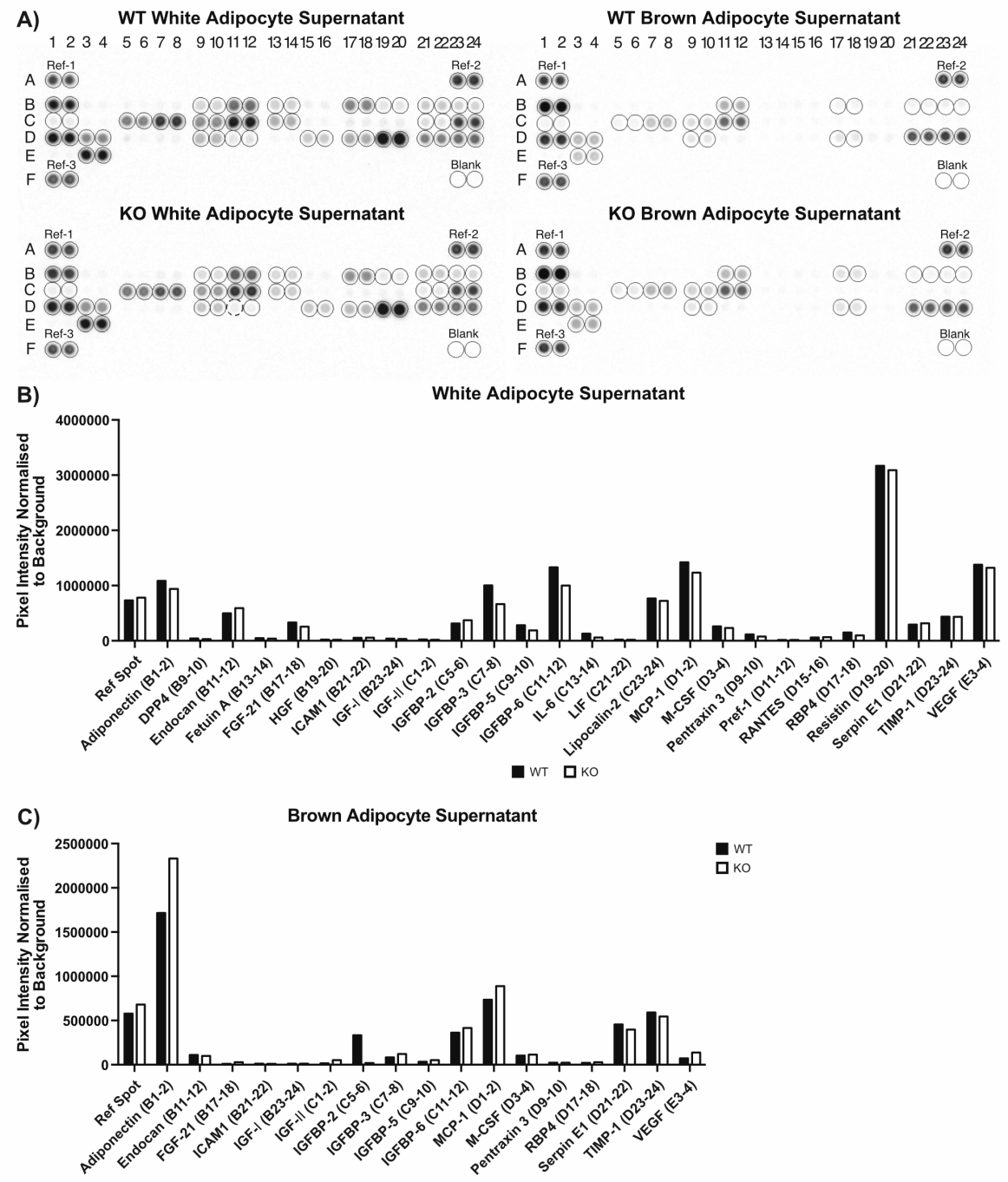

Figure 6.18: Obesity Proteome Array Analysis of Adipokines in Day 8 Pre-Adipocytes
(A) Showing the developed array membranes from a Mouse Obesity Adipokine Array on supernatants from WT and miR-34a-/- (KO) white (left) and brown (right) pre-adipocytes at day 8 of differentiation *in vitro*. For each group the supernatants from 3 (white) or 4 (brown) independent cultures were pooled together. These membranes were quantified by densitometry for white (B) and brown (C) pre-adipocytes, with normalisation to the background spots (Blank) for each membrane. Quantified data is represented as the mean of 2 spots per adipokine, or 6 spots for the positive control reference, and the x-axis labels for (B and C) contain the grid number for each spot shown in (A).

6.5 Discussion

In this chapter an *in vitro* model of murine white and brown adipocyte differentiation was used to explore whether miR-34a regulates adipocyte differentiation and function, which could contribute to the *in vivo/ex vivo* phenotype of miR-34a$^{-/-}$ mice (chapter 4). It was shown that miR-34a does increase over white, but not brown, pre-adipocyte differentiation, with miR-34b* and 34c* also increasing in both. However, miR-34a$^{-/-}$ white and brown pre-adipocytes did not show any deficiency in differentiation, using the characteristics examined. Nonetheless, day 8 miR-34a$^{-/-}$ white pre-adipocytes were observed to have greater lipid content. Additionally, differences in supernatant leptin, insulin, and IGFBP-3 and 6 were observed in miR-34a$^{-/-}$ white pre-adipocytes, with differences in adiponectin and IGFBP-2 observed in miR-34a$^{-/-}$ brown pre-adipocytes.

The data in this chapter showing an increase in miR-34a transcripts over the time-course of WT white pre-adipocyte differentiation correlates with a previous study, showing that miR-34a increases in mature human subcutaneous adipocytes, following *in vitro* differentiation (Ortega et al. 2010). Additionally, a recent publication showed that miR-34a overexpression reduced proliferation and differentiation of primary, human white adipose derived stem cells (ADSCs) into adipocytes by regulating senescence and cell cycle progression (Park et al. 2015). The authors additionally noted that miR-34a overexpression during adipogenesis reduces PPARɣ and adiponectin gene transcripts, but not supernatant adiponectin protein, with increases in the CC chemokine ligand (CCL)2, CCL5, CXC chemokine ligand (CXCL)8, and interleukin (IL)-6 protein in supernatants. Therefore, the increase in miR-34a transcripts observed here at day 4-8 of white pre-adipocyte differentiation could be acting as a negative regulator of adipogenesis, limiting further differentiation and proliferation. In fact, a correlation was observed between the statistically significant up-regulation of miR-34a at day 8 (Figure 6.6A) and a reduction in *Fabp4*, *Cebpa*, and *Pparɣ* transcripts (Figure 6.3C). However, if this were the case, then an increase in these genes would be expected in miR-34a$^{-/-}$ white pre-adipocytes, which was not observed. Only a small increase was seen in *Cebpa* transcripts at day 2 of differentiation. However, there could still be post-transcriptional differences in these genes' protein products.

There is also the possibility that there is redundancy in the control of adipogenesis through miR-34b* and 34c*, both shown to increase during white pre-adipocyte differentiation, but not regulated by miR-34a. Neither of these miRNAs have been previously shown to increase during white pre-adipocyte differentiation. However, miR-34c has been shown to increase in 3T3-L1 pre-adipocytes at day 9 of differentiation, which is after terminal differentiation and lies outside the time period examined here, but not at day 1, 2, or 5 (Kajimoto et al. 2006). The authors also observed no change in differentiation markers using a miR-34c anti-miR. Additionally, another study found that miR-34c did not change in primary, murine white pre-adipocytes over a 7-day differentiation (Keller et al. 2011). These studies support the observations made here of undetectable miR-34c transcripts over the 8-day white pre-adipocyte differentiation. Because miR-34c inhibition had no effect on differentiation markers, Kajimoto et al. proposed that it could be involved in mature adipocyte functions, but not differentiation (Kajimoto et al. 2006). The same could be true for miR-34a, with no detectable difference in differentiation between WT and miR-34a$^{-/-}$ white pre-adipocytes.

Therefore, the increased lipid content observed in day 8 miR-34a$^{-/-}$ white pre-adipocytes could be the result of dysregulation of mature lipid handling processes. There are numerous possible pathways that could be dysregulated in these cells. These include:

1) Increased uptake of free fatty acids (FFAs) into the adipocytes. However, no change was observed in *Cd36* transcripts, one of the major FA transporters in adipocytes (Coburn et al. 2000). The FA transport proteins (FATP1-6), particularly FATP1, are also important for adipocyte sequestration of FFAs (Wu et al. 2006). The FATPs were not examined here, but increases in these proteins' expression could contribute to increased cellular lipid.

2) Increased FA synthesis. ACCα catalyses the first committed and rate-limiting step of *de novo* FA synthesis, with inhibition of ACCα being shown to reduce lipid accumulation in differentiating 3T3-L1 adipocytes *in vitro* (Levert et al. 2002). However, no change was observed in *Accα* transcripts

in miR-34a$^{-/-}$ white pre-adipocytes. Additionally, *Fasn* transcripts were not altered; this is a key enzyme for *de novo* FA synthesis, with its inhibition in differentiating 3T3-L1 adipocytes reducing lipid accumulation (Liu et al. 2004). Other enzymatic steps exist that could also be affected.

3) Increases in esterification of FAs into triglycerides (TGs) for storage in the lipid droplet could be responsible, as the BODIPY dye has been shown to primarily stain the cytosolic, hydrophobic neutral lipids, such as TGs in the lipid droplet (Gocze and Freeman 1994). The acyl-CoA:glycerol-3-phosphate acyltransferase (GPAT) enzymes catalyse the first, rate-limiting step of *de novo* TG synthesis, which involves acyl-CoA-dependant acetylation of glycerol-3-phosphate (G3P). Two GPAT isoforms are highly expressed in adipose tissue: GPAT3-4, and knock-down of both of these isoforms in differentiating 3T3-L1 adipocytes diminish lipid droplet formation by day 8 *in vitro*, with individual knock-down of GPAT3 showing the greatest reduction over GPAT4 (Shan et al. 2010).

4) Decreased mitochondrial activity/catabolic metabolism. However, examination of *Pgc1α* transcripts reveals no differences in miR-34a$^{-/-}$ white pre-adipocytes. Unfortunately, MitoTracker was not a reliable method for determining mitochondrial content in white pre-adipocytes, as this could have provided useful data. Furthermore, the reduction in supernatant leptin at day 6 of miR-34a$^{-/-}$ white pre-adipocyte differentiation could suggest a reduction in lipolysis, as it has been shown that *in vitro* administration of leptin to mature adipocytes isolated from lean and *ob/ob* mice increases lipolysis in these cells (Fruhbeck 1997). This reduction in catabolic metabolism could be further enhanced by the reduction observed in IGFBP-3 and 6. IGFBP-6 is expressed at extremely low levels in serum and is unlikely to play a major physiological role (Russo et al. 2015). However, IGFBP-3 (the most abundant IGFBP) has been shown to inhibit insulin-mediated glucose uptake in 3T3-L1 adipocytes (Chan et al. 2005; Kim et al. 2007b), and dihydroxyacetone phosphate (DHAP) produced during glycolysis is needed for TG synthesis in adipose. This reduction could also contribute to the reduced insulin concentration in miR-34a$^{-/-}$ white pre-

adipocyte supernatants at day 2 of differentiation, suggesting these cells may be more insulin sensitive. However, because the proteome data for IGFBP-3 and 6 is from pooled replicates, there is no statistical support for these observations, making it difficult to determine if they are real changes. Additionally, the small changes in these IGFBPs may not actually be physiologically relevant. It is clear that there are many possible pathways miR-34a could regulate in white adipocytes that affect their lipid content, which need to be explored further before a mechanism can be elucidated.

It was interesting that the transcript levels of *Cd36*, *Hmgcr*, *Lxra*, *Pgc1a*, and *Fasn* were not altered in miR-34a$^{-/-}$ white pre-adipocytes (day 0-8) or the *ex vivo* mature adipocytes separated from the SVF, given the higher basal levels observed in chow-fed miR-34a$^{-/-}$ mouse eWAT *ex vivo* (section 4.4.3). However, this *in vitro* model may not be truly reflective of the eWAT adipocyte population *in vivo*. For one, there was a large age difference between the mice used for the *in vitro* culture (usually 6 weeks of age) and those at the end of the miR-34a$^{-/-}$ high-fat diet (HFD) *in vivo* study (31 weeks of age). Additionally, mature primary pre-adipocytes (day 8) *in vitro* show smaller lipid droplets than those *in viv*o and the *ex vivo* mature adipocytes are cells intermediate in size that are less than 70 μm (filtration step), with a high enough lipid content to allow them to float to the top of the SVF. Therefore, they represent a more homogenous adipocyte population than those *in vivo*. These basal gene differences may only occur in the larger adipocytes, which are undergoing greater metabolic stress. In differentiated pre-adipocytes differences may also be obscured by rosiglitazone, which has been shown to increase mitochondrial biogenesis and fatty acid oxidation enzymes in mature 3T3-L1 adipocytes (Wilson-Fritch et al. 2003). Additionally, rosiglitazone has been shown to increase fatty acid oxidation proteins, mitochondrial biogenesis, fatty acid oxidation, oxygen consumption, and *Pgc1a* transcripts in white adipocytes isolated from the eWAT of rosiglitazone-treated *ob/ob* mice (Wilson-Fritch et al. 2004). This could push the adipocytes towards catabolic over anabolic metabolic processes, which could be regulated by miR-34a. Furthermore, there is evidence that rosiglitazone induces a brown adipocyte-like “brite” phenotype in white adipocytes, inducing expression of UCP1 (Petrovic et al. 2010). This may also explain why the SVF *ex vivo* mature adipocyte gene

expression levels did not fully match those of the *in vitro* differentiated pre-adipocytes, along with a more variable *in vivo* environment. Culturing the pre-adipocytes with rosiglitazone during the initiation of differentiation, followed by culture with rosiglitazone-free maintenance media, or a rosiglitazone-free differentiation could be a better alternative.

There are limited studies examining miRNA regulation of brown adipocyte differentiation, but miR-155 is an example of a miRNA that negatively regulates brown adipocyte differentiation and decreases over the time-course of differentiation (Chen et al. 2013). In this chapter, miR-34a transcripts levels did not change over the time-course of differentiation in WT brown pre-adipocytes. It has not been previously reported whether miR-34a transcript levels change over brown pre-adipocyte differentiation *in vitro*, but it is surprising, given the *ex vivo* observations, that transcripts of both *Cebpα* and *Cebpβ* were decreased in iBAT from miR-34a$^{-/-}$ mice (section 4.4.3). However, a previous report suggests that miR-34a is an inhibitor of beige/brite and brown adipose formation, showing miR-34a inhibition in mice with established diet-induced obesity increases the transcript levels of *Ucp1*, *PR domain containing* (*Prdm)16*, *Fabp4*, and mitochondrial DNA in BAT (Fu et al. 2014). Although Fu et al. did not look directly at differentiation in brown adipocytes, this study does suggest that, under normal differentiation, miR-34a may not be expected to increase in brown adipocytes. Despite this, both miR-34b* and 34c* levels increased during brown pre-adipocyte differentiation, suggesting that they may regulate differentiation in these cells. There are currently no publications examining these miRNAs in brown adipocytes, although, one publication showed that miR-34c transcript levels were increased at the end of primary, murine brown pre-adipocyte differentiation, using qRT-PCR (Keller et al. 2011). However, its authors caution that these results were the opposite to their microarray data on the same samples, which showed a decrease. Even though the authors observed conflicting results from their quantification methods, it is curious that no miR-34c was detected here. This could be explained by differences in culture conditions, as Keller et al. did not use a *Pparγ* agonist, such as rosiglitazone used here, which could affect expression of miR-34c.

With the lack of change in miR-34a expression during brown pre-adipocyte differentiation, it is not surprising that miR-34a$^{-/-}$ brown pre-adipocytes did not show any differences in the differentiation markers examined. However, it is surprising that no differences were seen in the transcript levels of *Cebpα* and *Cebpβ*, (as mentioned above) and *Pgc1α* under noradrenaline stimulation, as *Pgc1α* transcripts were upregulated in the iBAT of miR-34a$^{-/-}$ mice when fed a HFD, not observed in WT (section 4.4.3). However, the *in vivo* stimulus increasing *Pgc1α* transcript expression may be something other than beta-adrenergic stimulation, e.g. thyroid hormone, FGF21, or natriuretic peptides (de Jesus et al. 2001; Hondares et al. 2010; Bordicchia et al. 2012). It was noted that day 8 miR-34a$^{-/-}$ brown pre-adipocytes already had higher levels of *Pgc1α* and *Ucp1* transcripts than WT, but not to a statistically significant degree. With only n=4 these studies were likely underpowered, especially with the high degree of variability between cultures, which could obscure biological changes. Additionally, chronic rosiglitazone treatment has been shown to upregulate both PGC1α and UCP1 in brown adipocytes, which can limit the stimulatory effect of noradrenaline (Petrovic et al. 2008). The authors showed that this was only the case with *Ucp1* transcripts in mature, day-7 brown pre-adipocytes, whereas *Pgc1α* transcripts could still be further enhanced by acute noradrenaline stimulation. It is curious that here Ucp1 transcripts decreased over differentiation, when they have previously been shown to increase with chronic rosiglitazone treatment (Petrovic et al. 2008). Primary murine brown pre-adipocytes differentiated without a *Pparγ* agonist, or acute noradrenaline stimulation, with *Ucp1* transcripts undetectable until stimulated with noradrenaline (Rehnmark et al. 1990). Therefore, the high level of *Ucp1* transcripts detected during differentiation, despite their decrease, still suggests stimulation by rosiglitazone, but also perhaps desensitisation to rosiglitazone over time. One of the major issues with this culture system is its poor efficiency and low yield, which could also be due to the large seeding density making the cells over-confluent. Therefore, more optimisation of this differentiation protocol is required to produce more consistent results with a higher yield of fully differentiated cells, perhaps in a rosiglitazone-free culture.

Interestingly, despite the issues with the culture system, an upregulation of adiponectin and downregulation of IGFBP-2 transcription was observed in the

supernatants from day 8 miR-34a$^{-/-}$ brown pre-adipocytes, compared with WT. Adiponectin administration has been shown to reduce thermogenesis in adiponectin KO mice *in vivo*, reducing iBAT expression of UCP1 and PGC1α, and also UCP1 expression in brown pre-adipocytes cultured from adiponectin KO mice *in vitro* (Qiao et al. 2014). However, to observe these effects *in vivo* the authors had to increase serum levels of adiponectin 10-12-fold, so the small increase in supernatant adiponectin observed in miR-34a$^{-/-}$ brown pre-adipocytes here, may not be physiologically relevant, especially since BAT is substantially smaller than other adipose depots that also produce adiponectin. Although there could be autocrine stimulation of the brown adipocytes, no change in *Ucp1* transcripts was observed in miR-34a$^{-/-}$ brown pre-adipocytes. Murine over-expression of IGFBP-2 *in vivo* reduced diet-induced weight gain, WAT and BAT mass, liver mass, visceral adiposity, and glucose intolerance, and inhibited 3T3-L1 adipocyte differentiation *in vitro* (Wheatcroft et al. 2007). Therefore, the reduction seen in supernatant IGFBP-2 from day 8 miR-34a$^{-/-}$ brown pre-adipocytes could promote increased white adipocyte differentiation and overall adiposity *in vivo*. However, the small amount that is produced in WT cells begs the question of whether this minor change would have a physiological affect. There could be local effects on the brown adipocytes themselves, but no change in differentiation was observed here. However, Wheatcroft et al. showed that the inhibitory effect is lost *in vitro* when insulin in present in the culture medium. Despite not seeing any difference in the mitochondria content of day 8 miR-34a$^{-/-}$ brown pre-adipocytes, this does not mean that the activity of these mitochondrial are the same. Further investigations are required to fully characterise the metabolic parameters of miR-34a$^{-/-}$ brown pre-adipocytes, such as quantification of citrate synthase activity, heat production, and measurement of cellular oxygen consumption to examine the metabolic activity of the mitochondria. Furthermore, the gene/protein expression of mitochondrial respiratory chain genes could be examined.

In conclusion, the function of miR-34a in white and brown adipocytes still remains elusive. However, it seems that miR-34a does not control adipogenesis in these *in vitro* models, but instead appears to regulate TG accumulation in white adipocytes. Additionally, there may be novel roles for the passenger strands miR-34b* and 34c* in regulating adipogenesis. Further studies are required to fully

elucidate miR-34a's function in white adipocytes and brown adipocytes, with greater refinements to the differentiation protocols for both of these cell types required.

Chapter 7: General Discussion and Conclusion

In the introduction of this thesis, obesity was shown to be a complex disease that combines metabolic dysfunction and chronic, low-grade inflammation that contributes to the development of numerous diseases, including CVDs and T2D. Additionally, it was clearly shown that adipose tissue plays an important role in the pathology of obesity, with its distribution around the body being an important factor in determining whether individuals with obesity are metabolically healthy or unhealthy. This stemmed from Dr Vague's observations that android obesity, with adipose tissue mostly distributed on the trunk of the body, was a greater risk factor for CVD and T2D development than gynoid obesity, where more was situated on the hips and thighs (Vague 1956). Subsequent studies showed that this association is related to the increased volume of VAT, which is strongly associated with increased systemic inflammation (Pou et al. 2007; Rosito et al. 2008; Preis et al. 2010; Tadros et al. 2010; Liu et al. 2010a; 2010b; 2011a). The VAT itself has been shown to be more hypertrophic, prone to lipolysis, and have greater levels of inflammation than SAT, at least peripheral SAT (Arner 1997; Ibrahim 2010). During obesity, the adipose tissue rapidly expands through hypertrophy with fibrosis and limited angiogenesis, this causes reduced oxygen permeation into the tissue, resulting in a hypoxic core with necrotic adipocytes that release their lipid droplets (Sun et al. 2011). The hypertrophic adipocytes become insulin resistant leading to increased lipolysis, and also generate ROS thereby increasing inflammation. The increased free lipids within the tissue can then stimulate bystander adipocytes through TLR4 to release numerous inflammatory cytokines (e.g. TNFα and IL-6), chemokines (e.g. CCL2), and adipokines (e.g. leptin and resistin) that promote tissue inflammation and insulin resistance (Shoelson et al. 2006; Sun et al. 2013). The secretion of CCL2 from adipocytes recruits inflammatory monocytes to the adipose tissue that differentiate into M1-polarised ATMs ($F4/80^+$ $CD11b^+$ $CD11c^+$ $CCR2^+$) that cluster around dying adipocytes in CLSs and further promote tissue inflammation, insulin resistance, and metabolic dysfunction (Weisberg et al. 2006; Lumeng et al. 2007a). Other immune cells have also been shown to be recruited to the obese adipose, exacerbating inflammation, including T_H1 cells, T_c cells, B cells, and neutrophils (Talukdar et al. 2012; Kraakman et al. 2014). Therefore, macrophages and adipocytes clearly have a major role in adipose inflammation, but the regulation of their inflammatory functions and the connection with metabolism in this context remain poorly

defined. MicroRNAs “fine tune” the regulation of disease mechanisms involved in CVDs and obesity, showing both protective and causal functions. In both macrophages and adipocytes, miRNAs contribute to adipose inflammation through regulation of inflammatory and metabolic processes in both of these cell types, but the current literature is limited (Zhuang et al. 2012; Kim et al. 2013a; Lien et al. 2014; Lorente-Cebrián et al. 2014). This PhD project aimed to address the role of miR-34a in regulating adipose inflammation.

The studies in this thesis are the first to report that miR-34a is involved in the regulation of inflammatory and metabolic pathways in adipose macrophages during obesity. Additionally, they are the first to report that miR-34a is ubiquitously expressed throughout human and murine vWAT during obesity, and that miR-34a$^{-/-}$ mice are more susceptible to weight gain when challenged with a HFD, accompanied by alterations in white adipocyte phenotype and metabolic gene expression in WAT and BAT. Previous reports suggested that miR-34a inhibition would have beneficial effects on metabolic profile (section 1.3.4.3); however, the opposite was observed in miR-34a$^{-/-}$ mice, which were heavier than WT controls and gained more weight when challenged with a HFD, suggesting they were more susceptible to weight gain. miR-34a$^{-/-}$ eWAT showed smaller, more numerous adipocytes, with a lower tissue mass on chow that increased to WT levels on HFD. Surprisingly, there was no difference in these characteristics between HFD-fed miR-34a$^{-/-}$ and WT mice, despite a clear difference in body weight. With the lack of change in eWAT and liver mass, this suggests there could be increases in the mass of other WAT depots (e.g. scWAT), BAT, or muscle tissue.

Pgc1α mRNA was commonly up-regulated in all of the *ex vivo* miR-34$^{-/-}$ tissues examined and *in vitro* BMDMs, suggesting that it could be broadly regulated by miR-34a in these tissues. In fact, the well-known miR-34a target SIRT1 can increase PGC1α activity through direct deacetylation and activation of AMPK (Rodgers et al. 2005; Lan et al. 2008; Canto and Auwerx 2009). Whilst carrying out studies for this thesis, others showed that miR-34a could increase PGC1α activity. This was shown to be mediated through miR-34a inhibition of SIRT1 gene translation and FGF21 signaling, by targeting βKL and FGFR1 gene transcripts, in HFD-fed murine eWAT and 3T3L1 adipocytes, thereby promoting

adipose browning (Fu et al. 2014). Correlating with our results, the authors observed increased levels of *Pgc1α* transcripts in eWAT and BAT after lentiviral-mediated inhibition of miR-34a in WAT and BAT of male, HFD-fed BALB/c and C57BL/6 mice. However, they also observed a reduction in body weight, and visceral (epidiymal and peritoneal) and subcutaneous WAT, with improved glucose tolerance. Additionally, earlier studies showed that anti-miR-34a administration to HFD-fed mice improved systemic glucose tolerance, insulin tolerance, and liver phenotype (Fu et al. 2012; Choi et al. 2013). These studies all used acute miR-34a inhibition in established murine obesity, which is milder than the 24-week HFD-feeding used here. Therefore, these differences with our model are probably due to compensatory effects of using a full-body KO. Due to PGC1α's induction of oxidative metabolism, it seems paradoxical that miR-34a ablation causes an up-regulation in *Pgc1α* transcripts, but at the same time promotes weight gain. However, full-body *Pgc1α* KO mice were shown to lose weight, rather than gain weight as expected, and skeletal muscle-specific murine Pgc1α over-expression (MPGC-1α TG) caused muscle adipose accumulation, atrophy, and decreased ATP synthesis and content, indicative of mitochondrial respiratory uncoupling (Lin et al. 2004; Miura et al. 2006). This is linked to increased FA oxidation (Clapham et al. 2000).

It may seem counterproductive that the miR-34a$^{-/-}$ eWAT showed basal increases in genes involved in lipid uptake: *Cd36, de novo* lipogenesis: *Fasn*, and cholesterol biosynthesis: *Hmgcr* (An et al. 2007; Vroegrijk et al. 2013; Chung et al. 2014). However, MPGC-1α TGs show increased expression of *Cd36* and *Fasn*, with *Fasn* expression driven by PGC1α's increase in *Lxrα* expression, and increased intracellular lipid (Summermatter et al. 2010). The authors suggest that this response "refuels" the cell's lipid stores for continued FA oxidation. Additionally, the buildup of malonyl-CoA during *de novo* lipogenesis inhibits the rate-limiting enzyme of FA oxidation, carnitine palmitoyl transferase-1 (CPT-1), inhibiting FA oxidation and preserving the lipogenic state (Rutkowski et al. 2015). LXRα is also known to transcriptionally repress the expression of UCP1, through blocking of PPARγ/PGC1α binding to the UCP1 promoter, which would inhibit the browning process observed by Fu et al. (Wang et al. 2008; Fu et al. 2014). Therefore, there may be an imbalance in lipolysis/FA oxidation Vs. lipid

uptake/lipogenesis, pushing metabolism towards the latter in adipocytes of miR-34a$^{-/-}$ mice, due to chronic PGC1α up-regulation, and predisposing these mice to weight gain when stressed with a HFD. This could explain why miR-34a$^{-/-}$ mice are heavier before HFD-feeding. In fact, when MPGC-1α TGs were fed HFD they developed insulin resistance and were not protected from diet-induced obesity, showing increased lipid uptake and increased expression of lipogenic genes, including *Cd36*, in skeletal muscle (Choi et al. 2008). As observed here, the authors also saw no change in resting serum insulin, triglycerides, cholesterol, glucose, and FFAs. The increased lipid content observed in mature *in vitro* miR-34a$^{-/-}$ white adipocytes supports this metabolic imbalance. Additionally, the increase in WT adipocyte miR-34a over the time-course of differentiation suggests that miR-34a may regulate these processes in mature adipocytes, due to the lack of change in differentiation markers in miR-34a$^{-/-}$ white adipocytes.

The decreases in *Pparɣ*, *Fasn,* and *Accα* eWAT transcript levels upon HFD-feeding in miR-34a$^{-/-}$ mice could be evidence of the balance being shifted back to FA oxidation to regain lipid homeostasis by other regulatory systems. This could be assisted by the up-regulation of *Pgc-1α* mRNA in HFD-fed miR-34a$^{-/-}$ BAT, compensating for the reduced *c/ebpα* and *β* mRNA, as both c/EBPα and β transactivate UCP1, and c/EBPβ is essential for brown adipocyte differentiation and thermoregulation (Carmona et al. 2005; Kajimura et al. 2009). Unfortunately, we did not see these differences in brown adipocytes *in vitro* with beta-adrenergic stimulation, but other stimuli could be involved *in vivo*. Furthermore, PGC1α is a predicted target of miR-34a in humans, but not mice, according to miRWalk (Dweep and Gretz 2015). Therefore, the *in vivo* phenotype of miR-34a$^{-/-}$ mice could be attributed to PGC1α being a direct target of miR-34a, or an indirect target through SIRT1/FGFR1/βKL, with dysregulation of PGC1α potentially causing mitochondrial dysfunction.

This thesis showed that miR-34a$^{-/-}$ ATMs have an altered phenotype and deficiency in inflammatory TNFα responses *in vitro*. Flow cytometric analysis identified F4/80^{high} CD45^{+} MHCII^{+} CD11b^{+} CD86^{+} macrophages within the eWAT of HFD-fed miR-34a$^{-/-}$ mice and a reduced F4/80^{+} macrophage population in chow-fed miR-34a$^{-/-}$ mice. F4/80 is a glycoprotein specific for murine macrophages, its

expression increases as macrophages mature, but its specific function remains unknown. However, Lin et al. showed that F4/80 has a role in generating $CD8^+$ regulatory T-cells (Lin et al. 2005). Additionally, Bain et al. identified a population of M2-like macrophages in the colon that were $CD45^+$ $F480^{high}$ $MHCII^+$ $CX3CR1^{high}$ and showed constitutive production of IL-10, phagocytosis, and unresponsiveness to TLR stimulation (Bain et al. 2013; 2014). Furthermore, $F4/80^{high}$ ATMs have previously been observed in murine WAT, showing equal proportions of $F4/80^{low}$:$F4/80^{high}$ ATMs in obese *db/db* WAT and greater proportions of $F4/80^{high}$ ATMs in diet-induced obese WAT (Bassaganya-Riera et al. 2009; Titos et al. 2011). Bassaganya-Riera et al. showed that these $F4/80^{high}$ ATMs express higher levels of MHCII, CX3CR1, CD11c, CCR2, and PPARɣ in *db/db* mice, with increased intracellular IL-6, TNFα, CCL2, and IL-10, which rise further upon LPS-stimulation (Bassaganya-Riera et al. 2009). These reports support the observations shown here of increased *Il-10* mRNA in HFD-fed miR-34a$^{-/-}$ eWAT, correlating with the ATM $F4/80^{high}$ phenotype. This increase in Il-10 suggests an M2-like phenotype. Additionally, the *in vitro* data showed ablated up-regulation of CXCL1 in TNFα stimulated miR-34a$^{-/-}$ BMDMs, suggesting a deficiency in TNFα signaling. Furthermore, the up-regulation of miR-34a transcripts in TNFα stimulated BMDMs, supports the possibility of miR-34a regulating the TNFα pathway. This has been previously suggested by Jiang et al. with contradictory results using LPS-stimulated RAW264.7 macrophages that show miR-34a inhibits TNFα expression by targeting the NF-κB p50-subunit activator NOTCH1 (Jiang et al. 2012). However, here *Pgc1α* was up-regulated in unstimulated miR-34a$^{-/-}$ *in vitro* macrophages, which others have shown represses TNFα-induced pro-inflammatory cytokine production by reducing RelA/p65 phosphorylation and inhibiting NF-κB signalling in murine skeletal muscle (Eisele et al. 2013). The up-regulation of *Pgc1α* transcripts could also indicate a switch to oxidative metabolism, a hallmark of M2 macrophages (Kauppinen et al. 2013; Kelly and O'Neill 2015). Paradoxically, Bassaganya-Riera et al. suggested that $F4/80^{high}$ macrophages are M1-like, despite expressing high levels of IL-10 and PPARɣ. Additionally, in this thesis miR-34a$^{-/-}$ eWAT transcript levels of the M2 marker *Retnla* (HFD-fed) were reduced while those of the M1 marker *Nos2* (chow-fed) were increased. Therefore, it is unclear whether miR-34a$^{-/-}$ macrophages have a

pro- or anti-inflammatory phenotype, but their phenotype could be altered by dysregulation of PGC1α.

Systemically, characteristics of a type-2 immune response in miR-34a$^{-/-}$ mice was observed, with increased serum IL-5 protein during HFD-feeding and a reduction in splenic neutrophils shown in both miR-34a$^{-/-}$ groups. IL-5 is a growth and differentiation factor for eosinophils, which can maintain an M2 ATM phenotype through IL-4/13 production (Wu et al. 2011; Molofsky et al. 2013). Therefore, this increase in IL-5 could promote/indicate greater eosinophil infiltration into the HFD-fed miR-34a$^{-/-}$ eWAT, which could promote an M2 ATM phenotype. Interestingly, neutrophil-specific elastase KO (NEKO) mice have increased M2-like ATMs and increased transcript levels of *Acca* and *Fasn* within WAT (Talukdar et al. 2012). Although, we did not see the same decrease in eWAT neutrophils, previous murine obesity studies showed that serum levels of CXCL1 increased proportionally with body weight and blood glucose concentration, with accompanying increases in eWAT CXCL1 concentration, neutrophil content, and mononuclear cells (Oliveira et al. 2013; Nunemaker et al. 2014). Therefore, reduced production of CXCL1 from macrophages in miR-34a$^{-/-}$ mice may contribute to reduced neutrophil recruitment to other tissues by tissue resident macrophages in, for example, the spleen, the WAT surrounding the pancreas, or the pancreas itself, reducing inflammation (Böni-Schnetzler et al. 2008). Importantly, a type 2 immune response has been reported to promote increased insulin sensitivity, glucose uptake and anabolism in white adipocytes, but also an overall protective effect from obesity and T2D (Lumeng et al. 2007a; Ricardo-Gonzalez et al. 2010; Molofsky et al. 2013). Therefore, a type-2 immune response in HFD-fed miR-34a$^{-/-}$ mice may be initiated as a compensatory effect during over-nutrition, to regain metabolic homeostasis.

It is worth noting that one limitation of these studies is the focus on male mice. Despite men having an increased risk of CVD than women, the UK statistics show comparable levels of obesity in adult men and women (Townsend et al. 2015). Therefore, examination of these metabolic and inflammatory pathways in both genders would be more representative of the human population. Additionally, the patient samples examined in chapter 3 were mainly from female participants

and *in vitro* BMDM cultures in chapter 5 used monocytes from female mice. This makes it more difficult to reliably compare data from these studies and those carried out on male mice, as there are known metabolic and physiological differences between males and females (Mauvais-Jarvis 2015). These differences may affect miR-34a's function, showing different responses upon manipulation in males and females. However, male mice were used due to the relative ease of eWAT isolation, which provides a large abdominal visceral adipose depot, not found in females (Cinti 2005). The male distribution of adipose tissue also has a greater association with cardiovascular and T2D risk (section 1.1.4). Additionally, male mice show less variance in their metabolic responses than females, due to their menstrual cycle. Unfortunately, due to slow breeding of miR-34a$^{-/-}$ mice, the remaining female mice were used for *in vitro* BMDM experiments. However, because the monocytes isolated from these female mice were differentiated in an artificial environment, the sex differences are probably limited.

In summary, this thesis has demonstrated that miR-34a regulates the development of diet-induced obesity in mice, with miR-34a-/- mice showing a susceptibility to weight gain, likely through dysregulation of PGC1α (Figure 7.1). It is clear that the role of miR-34a in metabolism is complex and likely to vary depending on the context of treatment and model, with potentially contrasting roles in different cell types. miRNAs' fine-tuning of gene expression results in subtle changes in protein synthesis, making it complex to follow up in vivo observations with complete mechanistic data in vitro, as seen here. However, this thesis has highlighted that chronic miR-34a inhibition, as a treatment for obesity, may have undesirable metabolic and immuno-regulatory consequences. Further research is required to fully elucidate the metabolic and inflammatory pathways regulated by miR-34a. In particular, further investigations are required to:

1) Determine whether PGC1α gene transcripts are direct targets of miR-34a and/or whether miR-34a regulates PGC1α expression through SIRT1.

2) Further explore the miR-34a$^{-/-}$ macrophage phenotype with functional assays to determine pro- or anti-inflammatory functions and the interaction between these macrophages and adipocytes.

3) Examine whether miR-34a regulates adipose eosinophil recruitment and IL-4/13 production.

4) Examine further functional metabolic characteristics of adipocytes, e.g. oxygen consumption, FA/glucose uptake, thermogenesis, and mitochondrial complex protein activity and expression.

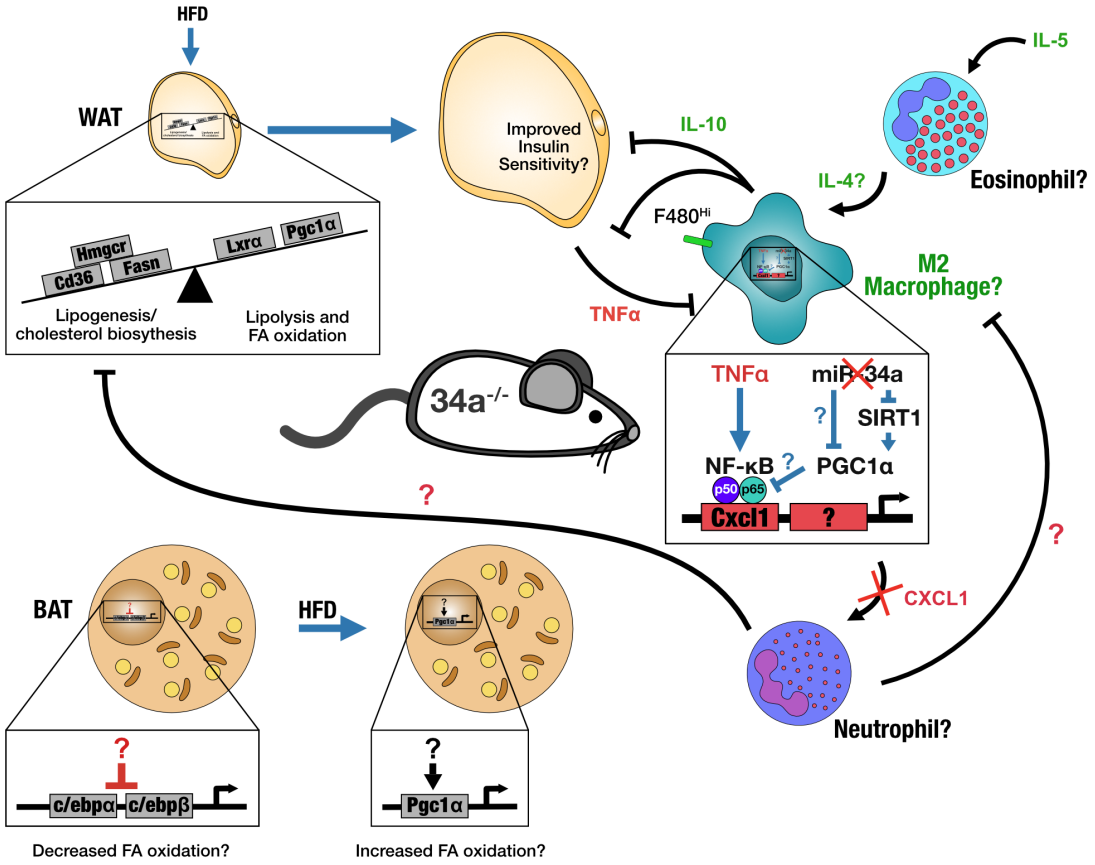

Figure 7.1: Theoretical Mechanism in miR-34a$^{-/-}$ Mice Predisposing them to Obesity
The imbalance in WAT metabolic genes caused by chronic over-expression of PGC1*α* and mitochondrial dysfunction promotes lipid uptake/storage and weight gain when stressed with a HFD. As the tissue increases in size there is an increase in inflammatory cytokines, such as TNF*α*, which polarize macrophages to an M1 phenotype. However, the KO macrophages are unresponsive to TNF*α* induction of CXCL1 and possibly other pro-M1 genes, through over-expression of PGC1*α* inhibiting the NF-B subunit p65, suggesting an M2 phenotype. This inhibits the recruitment of neutrophils which could promote an M1 phenotype and inhibit lipogenic processes. The M2 phenotype is further promoted by IL-5, which can induce eosinophils to produce pro-M2 IL-4. IL-10 likely produced by macrophages can then stimulate adipocytes to be more insulin sensitive and dampen inflammatory processes, reducing pro-obesity processes. Inhibition of key thermogenic genes in BAT pre-disposes the mice to obesity development, with over compensation by the induction of PGC1*α* during HFD-feeding.

List of References

Abente EJ, Subramanian M, Ramachandran V, Najafi-Shoushtari SH. MicroRNAs in obesity-associated disorders. Arch Biochem Biophys. 2016 Jan 1;589:108–19.

Agostini M, Knight RA. miR-34: from bench to bedside. Oncotarget. 2014 Feb 28;5(4):872–81.

Ahmed K, Tunaru S, Tang C, Müller M, Gille A, Sassmann A, et al. An autocrine lactate loop mediates insulin-dependent inhibition of lipolysis through GPR81. Cell Metab. 2010 Apr 7;11(4):311–9.

Ahn J, Lee H, Chung CH, Ha T. High fat diet induced downregulation of microRNA-467b increased lipoprotein lipase in hepatic steatosis. Biochemical and Biophysical Research Communications. Elsevier Inc; 2011 Nov 4;414(4):664–9.

Alberti KGMM, Eckel RH, Grundy SM, Zimmet PZ, Cleeman JI, Donato KA, et al. Harmonizing the metabolic syndrome: a joint interim statement of the International Diabetes Federation Task Force on Epidemiology and Prevention; National Heart, Lung, and Blood Institute; American Heart Association; World Heart Federation; International Atherosclerosis Society; and International Association for the Study of Obesity. Circulation. 2009. pp. 1640–5.

Albrink MJ, Meigs JW. Interrelationship Between Skinfold Thickness Serum Lipids and Blood Sugar in Normal Men. Am J Clin Nutr. 1964;15(5):255–&.

Allison DB, Kaprio J, Korkeila M, Koskenvuo M, Neale MC, Hayakawa K. The heritability of body mass index among an international sample of monozygotic twins reared apart. Int J Obes Relat Metab Disord. 1996 Jun;20(6):501–6.

Alvarez-Guardia D, Palomer X, Coll T, Davidson MM, Chan TO, Feldman AM, et al. The p65 subunit of NF-kappaB binds to PGC-1alpha, linking inflammation and metabolic disturbances in cardiac cells. Cardiovasc Res. 2010 Aug 1;87(3):449–58.

An Z, Wang H, Song P, Zhang M, Geng X, Zou M-H. Nicotine-induced activation of AMP-activated protein kinase inhibits fatty acid synthase in 3T3L1 adipocytes: a role for oxidant stress. J Biol Chem. 2007 Sep 14;282(37):26793–801.

Arner P. Regional adipocity in man. Journal of Endocrinology. 1997;155(2):191–2.

Artis D, Spits H. The biology of innate lymphoid cells. Nature. 2015 Jan 14;517(7534):293–301.

Aryal B, Rotllan N, Fernández-Hernando C. Noncoding RNAs and atherosclerosis. Curr Atheroscler Rep. 2014 Apr 30;16(5):407–7.

Avogaro P, Crepaldi G, Enzi G, Tiengo A. Associazione di iperlipemia, diabete mellito e obesita' di medio grado. Acta Diabetologica Latina. 1967;4(4):572–90.

Avtanski DB, Nagalingam A, Bonner MY, Arbiser JL, Saxena NK, Sharma D. Honokiol activates LKB1-miR-34a axis and antagonizes the oncogenic actions of leptin in breast cancer. Oncotarget. 2015a Oct 6;6(30):29947–62.

Avtanski DB, Nagalingam A, Kuppusamy P, Bonner MY, Arbiser JL, Saxena NK, et al. Honokiol abrogates leptin-induced tumor progression by inhibiting Wnt1-MTA1-β-catenin signaling axis in a microRNA-34a dependent manner. Oncotarget. 2015b Jun 30;6(18):16396–410.

Baigent C, Keech A, Kearney PM, Blackwell L, Buck G, Pollicino C, et al. Efficacy and safety of cholesterol-lowering treatment: prospective meta-analysis of data from 90 056 participants in 14 randomised trials of statins. The Lancet. 2005;366(9493):1267–78.

Bain CC, Bravo-Blas A, Scott CL, Gomez Perdiguero E, Geissmann F, Henri S, et al. Constant

replenishment from circulating monocytes maintains the macrophage pool in the intestine of adult mice. Nat Immunol. 2014 Aug 24;15(10):929–37.

Bain CC, Scott CL, Uronen-Hansson H, Gudjonsson S, Jansson O, Grip O, et al. Resident and pro-inflammatory macrophages in the colon represent alternative context-dependent fates of the same Ly6Chi monocyte precursors. Mucosal Immunol. 2013 May;6(3):498–510.

Baker M. MicroRNA profiling: separating signal from noise. Nat Meth. 2010 Sep;7(9):687–92.

Balkau B, Deanfield JE, Després J-P, Bassand J-P, Fox KAA, Smith SC, et al. International Day for the Evaluation of Abdominal Obesity (IDEA): a study of waist circumference, cardiovascular disease, and diabetes mellitus in 168,000 primary care patients in 63 countries. Circulation. 2007 Oct 23;116(17):1942–51.

Bao J, Li D, Wang L, Wu J, Hu Y, Wang Z, et al. MicroRNA-449 and microRNA-34b/c function redundantly in murine testes by targeting E2F transcription factor-retinoblastoma protein (E2F-pRb) pathway. Journal of Biological Chemistry. 2012 Jun 22;287(26):21686–98.

Barak Y, Nelson MC, Ong ES, Jones YZ, Ruiz-Lozano P, Chien KR, et al. PPAR gamma is required for placental, cardiac, and adipose tissue development. Mol Cell. 1999 Oct;4(4):585–95.

Bartelt A, Bruns OT, Reimer R, Hohenberg H, Ittrich H, Peldschus K, et al. Brown adipose tissue activity controls triglyceride clearance. Nat Med. 2011 Feb;17(2):200–5.

Bassaganya-Riera J, Misyak S, Guri AJ, Hontecillas R. PPAR gamma is highly expressed in F4/80(hi) adipose tissue macrophages and dampens adipose-tissue inflammation. Cellular Immunology. 2009;258(2):138–46.

Bean MK, Stewart K, Olbrisch ME. Obesity in America: Implications for Clinical and Health Psychologists. J Clin Psychol Med Settings. 2008 Aug 7;15(3):214–24.

Berry GJ, Budgeon LR, Cooper TK, Christensen ND, Waldner H. The type 1 diabetes resistance locus B10 Idd9.3 mediates impaired B-cell lymphopoiesis and implicates microRNA-34a in diabetes protection. Eur J Immunol. 2014 Jun;44(6):1716–27.

Bertola A, Ciucci T, Rousseau D, Bourlier V, Duffaut C, Bonnafous S, et al. Identification of adipose tissue dendritic cells correlated with obesity-associated insulin-resistance and inducing Th17 responses in mice and patients. Diabetes. 2012 Sep;61(9):2238–47.

Bénézech C, Luu N-T, Walker JA, Kruglov AA, Loo Y, Nakamura K, et al. Inflammation-induced formation of fat-associated lymphoid clusters. Nat Immunol. 2015 Jun 29;16(8):819–28.

Bierhaus A, Humpert PM, Morcos M, Wendt T, Chavakis T, Arnold B, et al. Understanding RAGE, the receptor for advanced glycation end products. J Mol Med. 2005 Aug 24;83(11):876–86.

Bird IM. Extraction of RNA from cells and tissue. Methods Mol Med. New Jersey: Humana Press; 2005;108:139–48.

Bird L. Macrophages: Lipids and stress — a deadly duo. Nature Publishing Group. Nature Publishing Group; 2010 Dec 1;10(12):809–9.

Blair D, Habicht JP, Sims EA, Sylwester D, Abraham S. Evidence for an increased risk for hypertension with centrally located body fat and the effect of race and sex on this risk. Am J Epidemiol. 1984 Apr;119(4):526–40.

Bommer GT, Gerin I, Feng Y, Kaczorowski AJ, Kuick R, Love RE, et al. p53-mediated activation of miRNA34 candidate tumor-suppressor genes. Current Biology. 2007 Aug 7;17(15):1298–307.

Boon RA, Iekushi K, Lechner S, Seeger T, Fischer A, Heydt S, et al. MicroRNA-34a regulates cardiac ageing and function. Nature Publishing Group; 2013 Feb 20;:1–5.

Bordicchia M, Liu D, Amri E-Z, Ailhaud G, Dessì-Fulgheri P, Zhang C, et al. Cardiac natriuretic peptides act via p38 MAPK to induce the brown fat thermogenic program in mouse and human adipocytes. J Clin Invest. 2012 Mar 1;122(3):1022–36.

Bourgeois F, Alexiu A, Lemonnier D. Dietary-induced obesity: effect of dietary fats on adipose tissue cellularity in mice. Br J Nutr. 1983 Jan;49(1):17–26.

Boutant M, Joffraud M, Kulkarni SS, García-Casarrubios E, García-Roves PM, Ratajczak J, et al. SIRT1 enhances glucose tolerance by potentiating brown adipose tissue function. Mol Metab. 2015 Feb;4(2):118–31.

Böni-Schnetzler M, Ehses JA, Faulenbach M, Donath MY. Insulitis in type 2 diabetes. Diabetes Obes Metab. 2008 Nov;10 Suppl 4:201–4.

Brestoff JR, Kim BS, Saenz SA, Stine RR, Monticelli LA, Sonnenberg GF, et al. Group 2 innate lymphoid cells promote beiging of white adipose tissue and limit obesity. Nature. Nature Publishing Group; 2014 Dec 22;:1–17.

Bruun JM, Lihn AS, Madan AK, Pedersen SB, Schiøtt KM, Fain JN, et al. Higher production of IL-8 in visceral vs. subcutaneous adipose tissue. Implication of nonadipose cells in adipose tissue. Am J Physiol Endocrinol Metab. 2004 Jan;286(1):E8–13.

Caescu CI, Guo X, Tesfa L, Bhagat TD, Verma A, Zheng D, et al. Colony stimulating factor-1 receptor signaling networks inhibit mouse macrophage inflammatory responses by induction of microRNA-21. Blood. 2015 Feb 19;125(8):e1–13.

Calkin AC, Tontonoz P. Transcriptional integration of metabolism by the nuclear sterol-activated receptors LXR and FXR. Nat Rev Mol Cell Biol. 2012 Mar 14.

Cancello R, Tordjman J, Poitou C, Guilhem G, Bouillot JL, Hugol D, et al. Increased infiltration of macrophages in omental adipose tissue is associated with marked hepatic lesions in morbid human obesity. Diabetes. 2006 Jun;55(6):1554–61.

Cannon B, Nedergaard J. The biochemistry of an inefficient tissue: brown adipose tissue. Essays Biochem. 1985;20:110–64.

Cannon B, Nedergaard J. Brown adipose tissue: function and physiological significance. Physiol Rev. 2004 Jan;84(1):277–359.

Cannon B, Nedergaard J. Cell biology: Neither brown nor white. Nature. 2012a Aug 16;:286–7.

Cannon B, Nedergaard J. Yes, even human brown fat is on fire! J Clin Invest. 2012b Feb;122(2):486–9.

Cannon CP, Blazing MA, Giugliano RP, McCagg A, White JA, Theroux P, et al. Ezetimibe Added to Statin Therapy after Acute Coronary Syndromes. N Engl J Med. 2015 Jun 18;372(25):2387–97.

Canto C, Auwerx J. PGC-1α, SIRT1 and AMPK, an energy sensing network that controls energy expenditure. Curr Opin Lipidol. 2009 Apr;20(2):98–105.

Carmona MC, Hondares E, Rodríguez de la Concepción ML, Rodríguez-Sureda V, Peinado-Onsurbe J, Poli V, et al. Defective thermoregulation, impaired lipid metabolism, but preserved adrenergic induction of gene expression in brown fat of mice lacking C/EBPbeta. 2005 Jul 1;389(Pt 1):47–56.

Caruso P, Dempsie Y, Stevens HC, McDonald RA, Long L, Lu R, et al. A role for miR-145 in pulmonary arterial hypertension: evidence from mouse models and patient samples. Circulation Research. 2012 Jul 20;111(3):290–300.

Castro RE, Ferreira DMS, Afonso MB, Borralho PM, Machado MV, Cortez-Pinto H, et al. miR-

34a/SIRT1/p53 is suppressed by ursodeoxycholic acid in the rat liver and activated by disease severity in human non-alcoholic fatty liver disease. J Hepatol. 2012 Aug 15;58:119–25.

Cermelli S, Ruggieri A, Marrero JA, Ioannou GN, Beretta L. Circulating microRNAs in patients with chronic hepatitis C and non-alcoholic fatty liver disease. PLoS ONE. 2011 Jan 1;6(8):e23937–7.

Chan SSY, Twigg SM, Firth SM, Baxter RC. Insulin-like growth factor binding protein-3 leads to insulin resistance in adipocytes. J Clin Endocrinol Metab. 2005 Dec;90(12):6588–95.

Chen C. Real-time quantification of microRNAs by stem-loop RT-PCR. Nucleic Acids Res. 2005 Nov 27;33(20):e179–9.

Chen Y, Siegel F, Kipschull S, Haas B, Fröhlich H, Meister G, et al. miR-155 regulates differentiation of brown and beige adipocytes via a bistable circuit. Nat Comms. Nature Publishing Group; 2013;4:1769–13.

Cheung O, Puri P, Eicken C, Contos MJ, Mirshahi F, Maher JW, et al. Nonalcoholic steatohepatitis is associated with altered hepatic MicroRNA expression. Hepatology. 2008 Aug 5;48(6):1810–20.

Chiang HR, Schoenfeld LW, Ruby JG, Auyeung VC, Spies N, Baek D, et al. Mammalian microRNAs: experimental evaluation of novel and previously annotated genes. Genes Dev. 2010 May 15;24(10):992–1009.

Cho KW, Morris DL, Lumeng CN. Flow cytometry analyses of adipose tissue macrophages. Methods Enzymol. 2014 Jan 1;537:297–314.

Choi CS, Befroy DE, Codella R, Kim S, Reznick RM, Hwang Y-J, et al. Paradoxical effects of increased expression of PGC-1alpha on muscle mitochondrial function and insulin-stimulated muscle glucose metabolism. Proceedings of the National Academy of Sciences. 2008 Dec 16;105(50):19926–31.

Choi S-E, Fu T, Seok S, Kim DH, Yu E, Lee K-W, et al. Elevated microRNA-34a in obesity reduces NAD+ levels and SIRT1 activity by directly targeting NAMPT. Aging Cell. 2013 Dec;12(6):1062–72.

Chomczynski P, Sacchi N. The single-step method of RNA isolation by acid guanidinium thiocyanate-phenol-chloroform extraction: twenty-something years on. Nature Protocols. 2006;1(2):581–5.

Chung S, Cuffe H, Marshall SM, McDaniel AL, Ha J-H, Kavanagh K, et al. Dietary cholesterol promotes adipocyte hypertrophy and adipose tissue inflammation in visceral, but not in subcutaneous, fat in monkeys. Arteriosclerosis, Thrombosis, and Vascular Biology. 2014 Sep;34(9):1880–7.

Ciesielski CJ, Andreakos E, Foxwell BMJ, Feldmann M. TNFalpha-induced macrophage chemokine secretion is more dependent on NF-kappaB expression than lipopolysaccharides-induced macrophage chemokine secretion. Eur J Immunol. 2002 Jul;32(7):2037–45.

Cinti S. The adipose organ. Prostaglandins, Leukotrienes and Essential Fatty Acids. 2005 Jul;73(1):9–15.

Cinti S, Mitchell G, Barbatelli G, Murano I, Ceresi E, Faloia E, et al. Adipocyte death defines macrophage localization and function in adipose tissue of obese mice and humans. The Journal of Lipid Research. 2005 Nov;46(11):2347–55.

Clapham JC, Arch JR, Chapman H, Haynes A, Lister C, Moore GB, et al. Mice overexpressing human uncoupling protein-3 in skeletal muscle are hyperphagic and lean. Nature. 2000 Jul 27;406(6794):415–8.

Cloonan N, Wani S, Xu Q, Gu J, Lea K, Heater S, et al. MicroRNAs and their isomiRs function cooperatively to target common biological pathways. Genome Biol. 2011;12(12):R126.

Coburn CT, Knapp FF, Febbraio M, Beets AL, Silverstein RL, Abumrad NA. Defective uptake and utilization of long chain fatty acids in muscle and adipose tissues of CD36 knockout mice. J Biol Chem. 2000 Oct 20;275(42):32523–9.

Coleman DL. Obese and diabetes: two mutant genes causing diabetes-obesity syndromes in mice. Diabetologia. 1978 Mar;14(3):141–8.

Coleman DL, Hummel KP. Studies with the mutation, diabetes, in the mouse. Diabetologia. 1967 Apr;3(2):238–48.

Coleman R. Enzymes of triacylglycerol synthesis and their regulation. Progress in Lipid Research. 2004 Mar;43(2):134–76.

Concepcion CP, Han Y-C, Mu P, Bonetti C, Yao E, D'Andrea A, et al. Intact p53-dependent responses in miR-34-deficient mice. Grimes HL, editor. PLoS Genet. 2012;8(7):e1002797.

Coomans CP, van den Berg SAA, Houben T, van Klinken JB, van den Berg R, Pronk ACM, et al. Detrimental effects of constant light exposure and high-fat diet on circadian energy metabolism and insulin sensitivity. The FASEB Journal. 2013 Apr;27(4):1721–32.

Coste A, Louet JF, Lagouge M, Lerin C, Antal MC, Meziane H, et al. The genetic ablation of SRC-3 protects against obesity and improves insulin sensitivity by reducing the acetylation of PGC-1. Proceedings of the National Academy of Sciences. 2008 Oct 30;105(44):17187–92.

Craig VJ, Cogliatti SB, Imig J, Renner C, Neuenschwander S, Rehrauer H, et al. Myc-mediated repression of microRNA-34a promotes high-grade transformation of B-cell lymphoma by dysregulation of FoxP1. Blood. 2011 Jun 9;117(23):6227–36.

Craig VJ, Tzankov A, Flori M, Schmid CA, Bader AG, ller AMU. Systemic microRNA-34a delivery induces apoptosis and abrogates growth of diffuse large B-cell lymphoma in vivo. Leukemia. Nature Publishing Group; 2012 May 15;26(11):2421–4.

Crépin D, Benomar Y, Riffault L, Amine H, Gertler A, Taouis M. The over-expression of miR-200a in the hypothalamus of ob/ob mice is linked to leptin and insulin signaling impairment. Molecular and Cellular Endocrinology. 2014 Mar 25;384(1-2):1–11.

Cristancho AG, Lazar MA. Forming functional fat: a growing understanding of adipocyte differentiation. Nature Publishing Group; 2011 Sep 28;12(11):722–34.

Curat CA, Miranville A, Sengenès C, Diehl M, Tonus C, Busse R, et al. From blood monocytes to adipose tissue-resident macrophages: induction of diapedesis by human mature adipocytes. Diabetes. 2004 May;53(5):1285–92.

Dalen KT, Ulven SM, Bamberg K, Gustafsson J-A, Nebb HI. Expression of the insulin-responsive glucose transporter GLUT4 in adipocytes is dependent on liver X receptor alpha. J Biol Chem. 2003 Nov 28;278(48):48283–91.

De Filippo K, Henderson RB, Laschinger M, Hogg N. Neutrophil chemokines KC and macrophage-inflammatory protein-2 are newly synthesized by tissue macrophages using distinct TLR signaling pathways. J Immunol. 2008 Mar 15;180(6):4308–15.

de Jesus LA, Carvalho SD, Ribeiro MO, Schneider M, Kim S-W, Harney JW, et al. The type 2 iodothyronine deiodinase is essential for adaptive thermogenesis in brown adipose tissue. J Clin Invest. 2001 Nov 1;108(9):1379–85.

de Koning L, Merchant AT, Pogue J, Anand SS. Waist circumference and waist-to-hip ratio as predictors of cardiovascular events: meta-regression analysis of prospective studies. Eur Heart J. 2007 Apr;28(7):850–6.

DeFuria J, Belkina AC, Jagannathan-Bogdan M, Snyder-Cappione J, Carr JD, Nersesova YR, et al. B cells promote inflammation in obesity and type 2 diabetes through regulation of T-cell function and an inflammatory cytokine profile. Proceedings of the National Academy of Sciences. 2013 Mar 26;110(13):5133–8.

Deng J, Liu S, Zou L, Xu C, Geng B, Xu G. Lipolysis response to endoplasmic reticulum stress in adipose cells. Journal of Biological Chemistry. 2012 Feb 24;287(9):6240–9.

Deng L, Blanco FJ, Stevens H, Lu R, Caudrillier A, McBride M, et al. MicroRNA-143 Activation Regulates Smooth Muscle and Endothelial Cell Crosstalk in Pulmonary Arterial Hypertension. Circulation Research. 2015 Oct 23;117(10):870–83.

Dentin R, Pégorier J-P, Benhamed F, Foufelle F, Ferré P, Fauveau V, et al. Hepatic glucokinase is required for the synergistic action of ChREBP and SREBP-1c on glycolytic and lipogenic gene expression. J Biol Chem. 2004 May 7;279(19):20314–26.

Després J-P. Body fat distribution and risk of cardiovascular disease: an update. Circulation. 2012 Sep 4;126(10):1301–13.

Després J-P, Lemieux I. Abdominal obesity and metabolic syndrome. Nature. 2006 Dec 14;444(7121):881–7.

Després J-P, Lemieux I, Bergeron J, Pibarot P, Mathieu P, Larose E, et al. Abdominal obesity and the metabolic syndrome: contribution to global cardiometabolic risk. Arteriosclerosis, Thrombosis, and Vascular Biology. 2008 Jun;28(6):1039–49.

Dib L, Bugge A, Collins S. LXRα fuels fatty acid-stimulated oxygen consumption in white adipocytes. The Journal of Lipid Research. 2014 Feb;55(2):247–57.

DiGirolamo M, Fine JB, Tagra K, Rossmanith R. Qualitative regional differences in adipose tissue growth and cellularity in male Wistar rats fed ad libitum. Am J Physiol. 1998 May;274(5 Pt 2):R1460–7.

Ding J, Li M, Wan X, Jin X, Chen S, Yu C, et al. Effect of miR-34a in regulating steatosis by targeting PPARα expression in nonalcoholic fatty liver disease. Sci Rep. 2015;5:13729.

Do MT, Kim HG, Choi JH, Jeong HG. Metformin induces microRNA-34a to downregulate the Sirt1/Pgc-1α/Nrf2 pathway, leading to increased susceptibility of wild-type p53 cancer cells to oxidative stress and therapeutic agents. Free Radic Biol Med. Elsevier; 2014 Jul 2;:1–14.

Donath MY, Shoelson SE. Type 2 diabetes as an inflammatory disease. Nature Publishing Group. Nature Publishing Group; 2011 Jan 14;11(2):98–107.

Dou L, Zhao T, Wang L, Huang X, Jiao J, Gao D, et al. miR-200s contribute to interleukin-6 (IL-6)-induced insulin resistance in hepatocytes. Journal of Biological Chemistry. 2013 Aug 2;288(31):22596–606.

Dutta KK, Zhong Y, Liu Y-T, Yamada T, Akatsuka S, Hu Q, et al. Association of microRNA-34a overexpression with proliferation is cell type-dependent. Cancer Sci. 2007 Dec;98(12):1845–52.

Dweep H, Gretz N. miRWalk2.0: a comprehensive atlas of microRNA-target interactions. Nat Meth. Nature Publishing Group; 2015 Aug 1;12(8):697–7.

Edens MA, Kuipers F, Stolk RP. Non-alcoholic fatty liver disease is associated with cardiovascular disease risk markers. Obes Rev. 2009 Jul;10(4):412–9.

Eisele PS, Salatino S, Sobek J, Hottiger MO, Handschin C. The peroxisome proliferator-activated receptor coactivator 1 / (PGC-1) coactivators repress the transcriptional activity of NF- B in skeletal muscle cells. Journal of Biological Chemistry. 2013;288(9):6589–9.

Eisinger K, Liebisch G, Schmitz G, Aslanidis C, Krautbauer S, Buechler C. Lipidomic analysis of serum from high fat diet induced obese mice. IJMS. 2014;15(2):2991–3002.

Elbers JM, Asscheman H, Seidell JC, Gooren LJ. Effects of sex steroid hormones on regional fat depots as assessed by magnetic resonance imaging in transsexuals. Am J Physiol. 1999 Feb;276(2 Pt 1):E317–25.

Elbers JM, Asscheman H, Seidell JC, Megens JA, Gooren LJ. Long-term testosterone administration increases visceral fat in female to male transsexuals. J Clin Endocrinol Metab. 1997 Jul;82(7):2044–7.

Elbers JMH, Giltay EJ, Teerlink T, Scheffer PG, Asscheman H, Seidell JC, et al. Effects of sex steroids on components of the insulin resistance syndrome in transsexual subjects. Clin Endocrinol (Oxf). 2003 May;58(5):562–71.

Erol A. The role of fat tissue in the cholesterol lowering and the pleiotropic effects of statins--statins activate the generation of metabolically more capable adipocytes. Med Hypotheses. 2005;64(1):69–73.

Esau C, Davis S, Murray SF, Yu XX, Pandey SK, Pear M, et al. miR-122 regulation of lipid metabolism revealed by in vivo antisense targeting. Cell Metab. 2006 Feb;3(2):87–98.

Essandoh K, Li Y, Huo J, Fan G-C. Mirna-Mediated Macrophage Polarization and its Potential Role in the Regulation of Inflammatory Response. SHOCK. 2016 Mar;:1–37.

Fabricatore AN, Wadden TA. Treatment of obesity: an overview. Clinical Diabetes. 2003;21(2):67–72.

Fantuzzi G. Adipose tissue, adipokines, and inflammation. J Allergy Clin Immunol. 2005 May;115(5):911–9–quiz920.

Feldman R, Sender AJ, Siegelaub AB. Difference in diabetic and nondiabetic fat distribution patterns by skinfold measurements. Diabetes. 1969 Jul;18(7):478–86.

Feuerer M, Herrero L, Cipolletta D, Naaz A, Wong J, Nayer A, et al. Lean, but not obese, fat is enriched for a unique population of regulatory T cells that affect metabolic parameters. Nat Med. 2009 Aug;15(8):930–9.

Forte E, Salinas RE, Chang C, Zhou T, Linnstaedt SD, Gottwein E, et al. The Epstein-Barr virus (EBV)-induced tumor suppressor microRNA MiR-34a is growth promoting in EBV-infected B cells. J Virol. 2012 Jun;86(12):6889–98.

Franckhauser S, Muñoz S, Pujol A, Casellas A, Riu E, Otaegui P, et al. Increased fatty acid re-esterification by PEPCK overexpression in adipose tissue leads to obesity without insulin resistance. Diabetes. 2002 Mar;51(3):624–30.

Freedland ES. Role of a critical visceral adipose tissue threshold (CVATT) in metabolic syndrome: implications for controlling dietary carbohydrates: a review. Nutr Metab (Lond). 2004 Nov 5;1(1):12.

Friedman JM. Leptin, leptin receptors and the control of body weight. Eur J Med Res. 1997 Jan;2(1):7–13.

Frontini A, Cinti S. Distribution and development of brown adipocytes in the murine and human adipose organ. Cell Metab. 2010 Apr 7;11(4):253–6.

Fruhbeck GEA. In Vitro Lipolytic Effect of Leptin on Mouse Adipocytes: Evidence for a Possible Autocrine/Paracrine Role of Leptin. 1997 Nov 18;:1–5.

Fu T, Choi S-E, Kim DH, Seok S, Suino-Powell KM, Xu HE, et al. Aberrantly elevated microRNA-34a in obesity attenuates hepatic responses to FGF19 by targeting a membrane coreceptor β-

Klotho. Proceedings of the National Academy of Sciences. 2012 Oct 2;109(40):16137–42.

Fu T, Seok S, Choi S, Huang Z, Suino-Powell K, Xu HE, et al. MicroRNA 34a inhibits beige and brown fat formation in obesity in part by suppressing adipocyte fibroblast growth factor 21 signaling and SIRT1 function. Mol Cell Biol. American Society for Microbiology; 2014 Nov 15;34(22):4130–42.

Gaillard R. Maternal obesity during pregnancy and cardiovascular development and disease in the offspring. Eur J Epidemiol. 2015 Nov;30(11):1141–52.

Galic S, Oakhill JS, Steinberg GR. Adipose tissue as an endocrine organ. Molecular and Cellular Endocrinology. 2010 Mar;316(2):129–39.

Galván-Peña S, O'Neill LAJ. Metabolic reprograming in macrophage polarization. Front Immunol. 2014;5:420.

Gao C-L, Zhu C, Zhao Y-P, Chen X-H, Ji C-B, Zhang C-M, et al. Mitochondrial dysfunction is induced by high levels of glucose and free fatty acids in 3T3-L1 adipocytes. Molecular and Cellular Endocrinology. Elsevier Ireland Ltd; 2010 May 14;320(1-2):25–33.

Garrison RJ, Wilson PW, Castelli WP, Feinleib M, Kannel WB, McNamara PM. Obesity and lipoprotein cholesterol in the Framingham offspring study. Metab Clin Exp. 1980 Oct;29(11):1053–60.

Ghoorah K, Campbell P, Kent A, Maznyczka A, Kunadian V. Obesity and cardiovascular outcomes: a review. European Heart Journal: Acute Cardiovascular Care. 2016 Jan 15;5(1):77–85.

Gocze PM, Freeman DA. Factors underlying the variability of lipid droplet fluorescence in MA-10 Leydig tumor cells. Cytometry. 1994 Oct 1;17(2):151–8.

Grant JS, Morecroft I, Dempsie Y, van Rooij E, Maclean MR, Baker AH. Transient but not genetic loss of miR-451 is protective in the development of pulmonary arterial hypertension. Pulmonary Circulation. 2013 Dec;3(4):840–50.

Green H, Meuth M. An established pre-adipose cell line and its differentiation in culture. Cell. 1974 Oct;3(2):127–33.

Gregor M. Inflammatory Mechanisms in Obesity - Annual Review of Immunology, 29(1):415. Annu Rev Immunol. 2011.

Griffin TM, Huebner JL, Kraus VB, Yan Z, Guilak F. Induction of osteoarthritis and metabolic inflammation by a very high-fat diet in mice: effects of short-term exercise. Arthritis Rheum. 2012 Feb;64(2):443–53.

Grueter CE, van Rooij E, Johnson BA, DeLeon SM, Sutherland LB, Qi X, et al. A cardiac microRNA governs systemic energy homeostasis by regulation of MED13. Cell. 2012 Apr 27;149(3):671–83.

Guennewig B, Roos M, Dogar AM, Gebert LFR, Zagalak JA, Vongrad V, et al. Synthetic pre-microRNAs reveal dual-strand activity of miR-34a on TNF-α. RNA. 2014 Jan;20(1):61–75.

Guh DP, Zhang W, Bansback N, Amarsi Z, Birmingham CL, Anis AH. The incidence of co-morbidities related to obesity and overweight: a systematic review and meta-analysis. BMC Public Health. 2009;9:88.

Ha M, Kim VN. Regulation of microRNA biogenesis. Nature Publishing Group. Nature Publishing Group; 2014 Jul 16;15(8):509–24.

Haase J, Weyer U, Immig K, Klöting N, Blüher M, Eilers J, et al. Local proliferation of macrophages in adipose tissue during obesity-induced inflammation. Diabetologia. 2014 Mar;57(3):562–71.

Halberg N, Khan T, Trujillo ME, Wernstedt-Asterholm I, Attie AD, Sherwani S, et al. Hypoxia-inducible factor 1alpha induces fibrosis and insulin resistance in white adipose tissue. Mol Cell Biol. 2009 Aug;29(16):4467–83.

Haller H. [Epidermiology and associated risk factors of hyperlipoproteinemia]. Z Gesamte Inn Med. 1977 Apr 15;32(8):124–8.

Hams E, Locksley RM, McKenzie ANJ, Fallon PG. Cutting Edge: IL-25 Elicits Innate Lymphoid Type 2 and Type II NKT Cells That Regulate Obesity in Mice. 2013 Dec 1;191(11):5349–53.

Han L, Zhou R, Niu J, McNutt MA, Wang P, Tong T. SIRT1 is regulated by a PPAR{γ}-SIRT1 negative feedback loop associated with senescence. Nucleic Acids Res. 2010 Nov;38(21):7458–71.

Handschin C, Choi CS, Chin S, Kim S, Kawamori D, Kurpad AJ, et al. Abnormal glucose homeostasis in skeletal muscle-specific PGC-1alpha knockout mice reveals skeletal muscle-pancreatic beta cell crosstalk. J Clin Invest. 2007 Nov;117(11):3463–74.

Hariri N, Thibault L. High-fat diet-induced obesity in animal models. Nutr Res Rev. 2010 Dec;23(2):270–99.

Harms M, Seale P. Brown and beige fat: development, function and therapeutic potential. Nat Med. 2013 Oct;19(10):1252–63.

Haslam D. Obesity: a medical history. Obes Rev. 2007 Mar;8 Suppl 1:31–6.

Haslam D. The history of obesity. Clinical Obesity. 2011 Aug;1(4-6):189–97.

He L, He X, Lim LP, de Stanchina E, Xuan Z, Liang Y, et al. A microRNA component of the p53 tumour suppressor network. 2007 Jun 6;447(7148):1130–4.

He M, Song G, Yu Y, Jin Q, Bian Z. LPS-miR-34a-CCL22 axis contributes to regulatory T cell recruitment in periapical lesions. Biochemical and Biophysical Research Communications. Elsevier Ltd; 2015 May 8;460(3):733–40.

Heinemann A, Zhao F, Pechlivanis S, Eberle J, Steinle A, Diederichs S, et al. Tumor suppressive microRNAs miR-34a/c control cancer cell expression of ULBP2, a stress-induced ligand of the natural killer cell receptor NKG2D. Cancer Res. 2012 Jan 15;72(2):460–71.

Herman MA, Peroni OD, Villoria J, Schön MR, Abumrad NA, Blüher M, et al. A novel ChREBP isoform in adipose tissue regulates systemic glucose metabolism. Nature. Nature Publishing Group; 2012 Apr 10;484(7394):333–8.

Higa TS, Spinola AV, Fonseca-Alaniz MH. Comparison between cafeteria and high-fat diets in the induction of metabolic dysfunction in mice. International journal of …. 2014.

Higuchi C, Nakatsuka A, Eguchi J, Teshigawara S, Kanzaki M, Katayama A, et al. Identification of circulating miR-101, miR-375 and miR-802 as biomarkers for type 2 diabetes. Metab Clin Exp. 2015 Apr;64(4):489–97.

Higuchi R, Dollinger G, Walsh PS, Griffith R. Simultaneous Amplification and Detection of Specific DNA Sequences. Bio/Technology. Nature Publishing Group; 1992;10(4):413–7.

Higuchi R, Fockler C, Dollinger G, Watson R. Kinetic PCR analysis: real-time monitoring of DNA amplification reactions. Biotechnology (NY). 1993 Sep;11(9):1026–30.

Hirsch J, Batchelor B. Adipose tissue cellularity in human obesity. Clin Endocrinol Metab. 1976 Jul;5(2):299–311.

Hoggard N, Agouni A, Mody N, Delibegovic M. Serum levels of RBP4 and adipose tissue levels of PTP1B are increased in obese men resident in northeast Scotland without associated changes

in ER stress response genes. Int J Gen Med. 2012 Jan 1;5:403–11.

Holland WL, Summers SA. Sphingolipids, insulin resistance, and metabolic disease: new insights from in vivo manipulation of sphingolipid metabolism. Endocr Rev. 2008 Jun;29(4):381–402.

Hondares E, Rosell M, Diaz-Delfin J, Olmos Y, Monsalve M, Iglesias R, et al. Peroxisome Proliferator-activated Receptor (PPAR) Induces PPAR Coactivator 1 (PGC-1) Gene Expression and Contributes to Thermogenic Activation of Brown Fat: INVOLVEMENT OF PRDM16. J Biol Chem. 2011 Dec 9;286(50):43112–22.

Hondares E, Rosell M, Gonzalez FJ, Giralt M, Iglesias R, Villarroya F. Hepatic FGF21 expression is induced at birth via PPARalpha in response to milk intake and contributes to thermogenic activation of neonatal brown fat. Cell Metab. 2010 Mar 3;11(3):206–12.

Honeyman L, Bazett M, Tomko TG, Haston CK. MicroRNA profiling implicates the insulin-like growth factor pathway in bleomycin-induced pulmonary fibrosis in mice. Fibrogenesis Tissue Repair. 2013;6(1):16.

Horton JD, Goldstein JL, Brown MS. SREBPs: activators of the complete program of cholesterol and fatty acid synthesis in the liver. J Clin Invest. 2002 May 1;109(9):1125–31.

Hotamisligil GS, Arner P, Caro JF, Atkinson RL, Spiegelman BM. Increased adipose tissue expression of tumor necrosis factor-alpha in human obesity and insulin resistance. J Clin Invest. 1995 May;95(5):2409–15.

Hotamisligil GS, Shargill NS, Spiegelman BM. Adipose expression of tumor necrosis factor-alpha: direct role in obesity-linked insulin resistance. Science. 1993 Jan 1;259(5091):87–91.

Huang A, Zhang H, Chen S, Xia F, Yang Y, Dong F, et al. miR-34a expands myeloid-derived suppressor cells via apoptosis inhibition. Experimental Cell Research. 2014 Aug 15;326(2):259–66.

Hummel KP, Dickie MM, Coleman DL. Diabetes, a new mutafton in the mouse. Science. 1966;153(3740):1127–8.

Ibrahim MM. Subcutaneous and visceral adipose tissue: structural and functional differences. Obes Rev. 2010 Jan;11(1):11–8.

Iekushi K, Seeger F, Assmus B, Zeiher AM, Dimmeler S. Regulation of cardiac microRNAs by bone marrow mononuclear cell therapy in myocardial infarction. Circulation. 2012 Apr 10;125(14):1765–73–S1–7.

Ikonen E. Cellular cholesterol trafficking and compartmentalization. Nat Rev Mol Cell Biol. 2008 Feb;9(2):125–38.

Ingalls AM, Dickie MM, Snell GD. Obese, a new mutation in the house mouse. J Hered. 1950 Dec;41(12):317–8.

Ingelsson E, Massaro JM, Sutherland P, Jacques PF, Levy D, D'Agostino RB, et al. Contemporary trends in dyslipidemia in the Framingham Heart Study. Arch Intern Med. 2009 Feb 9;169(3):279–86.

Ito T, Yagi S, Yamakuchi M. MicroRNA-34a regulation of endothelial senescence. Biochemical and Biophysical Research Communications. 2010 Aug;398(4):735–40.

Jarcho JA, Keaney JF. Proof That Lower Is Better--LDL Cholesterol and IMPROVE-IT. N Engl J Med. 2015 Jun 18;372(25):2448–50.

Jensen-Urstad APL, Semenkovich CF. Fatty acid synthase and liver triglyceride metabolism: housekeeper or messenger? Biochim Biophys Acta. 2012 May;1821(5):747–53.

Jiang P, Liu R, Zheng Y, Liu X, Chang L, Xiong S, et al. MiR-34a inhibits lipopolysaccharide-induced inflammatory response through targeting Notch1 in murine macrophages. Experimental Cell Research. 2012 Jun;318(10):1175–84.

Jo J, Gavrilova O, Pack S, Jou W, Mullen S, Sumner AE, et al. Hypertrophy and/or Hyperplasia: Dynamics of Adipose Tissue Growth. PLoS Comput Biol. Public Library of Science; 2009 Mar;5(3):e1000324.

Joe AWB, Yi L, Even Y, Vogl AW, Rossi FMV. Depot-Specific Differences in Adipogenic Progenitor Abundance and Proliferative Response to High-Fat Diet. Stem Cells. Wiley Subscription Services, Inc., A Wiley Company; 2009 Oct;27(10):2563–70.

Jung M, Schaefer A, Steiner I, Kempkensteffen C, Stephan C, Erbersdobler A, et al. Robust MicroRNA Stability in Degraded RNA Preparations from Human Tissue and Cell Samples. Clinical Chemistry. 2010 May 28;56(6):998–1006.

Kahn R, Buse J, Ferrannini E, Stern M, American Diabetes Association, European Association for the Study of Diabetes. The metabolic syndrome: time for a critical appraisal: joint statement from the American Diabetes Association and the European Association for the Study of Diabetes. Diabetes Care. 2005 Sep;28(9):2289–304.

Kajimoto K, Naraba H, Iwai N. MicroRNA and 3T3-L1 pre-adipocyte differentiation. RNA. 2006 Sep;12(9):1626–32.

Kajimura S, Seale P, Kubota K, Lunsford E, Frangioni JV, Gygi SP, et al. Initiation of myoblast to brown fat switch by a PRDM16-C/EBP-beta transcriptional complex. 2009 Aug 27;460(7259):1154–8.

Kajimura S, Seale P, Tomaru T, Erdjument-Bromage H, Cooper MP, Ruas JL, et al. Regulation of the brown and white fat gene programs through a PRDM16/CtBP transcriptional complex. Genes Dev. 2008 May 15;22(10):1397–409.

Kalaany NY, Gauthier KC, Zavacki AM, Mammen PPA, Kitazume T, Peterson JA, et al. LXRs regulate the balance between fat storage and oxidation. Cell Metab. 2005 Apr;1(4):231–44.

Kaller M, Liffers S-T, Oeljeklaus S, Kuhlmann K, Röh S, Hoffmann R, et al. Genome-wide characterization of miR-34a induced changes in protein and mRNA expression by a combined pulsed SILAC and microarray analysis. Mol Cell Proteomics. 2011 Aug;10(8):M111.010462.

Kannel WB. Lipids, diabetes, and coronary heart disease: insights from the Framingham Study. Am Heart J. 1985 Nov;110(5):1100–7.

Kasinski AL, Slack FJ. miRNA-34 prevents cancer initiation and progression in a therapeutically resistant K-ras and p53-induced mouse model of lung adenocarcinoma. Cancer Res. 2012 Nov 1;72(21):5576–87.

Kauppinen A, Suuronen T, Ojala J, Kaarniranta K, Salminen A. Antagonistic crosstalk between NF-κB and SIRT1 in the regulation of inflammation and metabolic disorders. Cell Signal. 2013 Oct;25(10):1939–48.

Keller P, Gburcik V, Petrovic N, Gallagher IJ, Nedergaard J, Cannon B, et al. Gene-chip studies of adipogenesis-regulated microRNAs in mouse primary adipocytes and human obesity. BMC Endocrine Disorders. BioMed Central Ltd; 2011 Mar 22;11(1):7.

Kelly B, O'Neill LA. Metabolic reprogramming in macrophages and dendritic cells in innate immunity. Cell Res. Nature Publishing Group; 2015 Jun 5;25(7):771–84.

Kern PA, Saghizadeh M, Ong JM, Bosch RJ, Deem R, Simsolo RB. The expression of tumor necrosis factor in human adipose tissue. Regulation by obesity, weight loss, and relationship to lipoprotein lipase. J Clin Invest. 1995 May 1;95(5):2111–9.

Khvorova A, Reynolds A, Jayasena SD. Functional siRNAs and miRNAs exhibit strand bias. Cell. 2003 Oct 17;115(2):209–16.

Kim C, Lee H, Cho YM, Kwon O-J, Kim W, Lee EK. TNFα-induced miR-130 resulted in adipocyte dysfunction during obesity-related inflammation. FEBS Letters. Federation of European Biochemical Societies; 2013a Nov 29;587(23):3853–8.

Kim C-S, Park H-S, Kawada T, Kim J-H, Lim D, Hubbard NE, et al. Circulating levels of MCP-1 and IL-8 are elevated in human obese subjects and associated with obesity-related parameters. Int J Obes Relat Metab Disord. 2006 Sep;30(9):1347–55.

Kim H-J, Park K-G, Yoo E-K, Kim Y-H, Kim Y-N, Kim H-S, et al. Effects of PGC-1α on TNF-α–Induced MCP-1 and VCAM-1 Expression and NF-κB Activation in Human Aortic Smooth Muscle and Endothelial Cells. Antioxidants & Redox Signaling. 2007a Mar;9(3):301–7.

Kim H-R, Roe J-S, Lee J-E, Cho E-J, Youn H-D. p53 regulates glucose metabolism by miR-34a. Biochemical and Biophysical Research Communications. 2013b Jul 25;437(2):225–31.

Kim HS, Ali O, Shim M, Lee K-W, Vuguin P, Muzumdar R, et al. Insulin-like growth factor binding protein-3 induces insulin resistance in adipocytes in vitro and in rats in vivo. Pediatr Res. 2007b Feb;61(2):159–64.

Kim JI, Huh JY, Sohn JH, Choe SS, Lee YS, Lim CY, et al. Lipid-overloaded enlarged adipocytes provoke insulin resistance independent of inflammation. Mol Cell Biol. 2015a May;35(10):1686–99.

Kim SC, Kim YH, Son SW, Moon E-Y, Pyo S, Um SH. Fisetin induces Sirt1 expression while inhibiting early adipogenesis in 3T3-L1 cells. Biochemical and Biophysical Research Communications. 2015b Nov 27;467(4):638–44.

Kim SH, Després J-P, Koh KK. Obesity and cardiovascular disease: friend or foe? Eur Heart J. 2015c Dec 18;:ehv509–11.

Kir S, Beddow SA, Samuel VT, Miller P, Previs SF, Suino-Powell K, et al. FGF19 as a Postprandial, Insulin-Independent Activator of Hepatic Protein and Glycogen Synthesis. Science. 2011 Mar 24;331(6024):1621–4.

Kissebah AH, Vydelingum N, Murray R, Evans DJ, Hartz AJ, Kalkhoff RK, et al. Relation of Body-Fat Distribution to Metabolic Complications of Obesity. J Clin Endocrinol Metab. 1982;54(2):254–60.

Klaman LD, Boss O, Peroni OD, Kim JK, Martino JL, Zabolotny JM, et al. Increased energy expenditure, decreased adiposity, and tissue-specific insulin sensitivity in protein-tyrosine phosphatase 1B-deficient mice. Mol Cell Biol. 2000 Aug;20(15):5479–89.

Klaus S, Ely M, Encke D, Heldmaier G. Functional assessment of white and brown adipocyte development and energy metabolism in cell culture. Dissociation of terminal differentiation and thermogenesis in brown adipocytes. Journal of Cell Science. 1995 Sep 30;108 (Pt 10):3171–80.

Klöting N, Berthold S, Kovacs P, Schön MR, Fasshauer M, Ruschke K, et al. MicroRNA expression in human omental and subcutaneous adipose tissue. PLoS ONE. 2009;4(3):e4699.

Koh YJ, Park B-H, Park J-H, Han J, Lee I-K, Park JW, et al. Activation of PPARγ induces profound multilocularization of adipocytes in adult mouse white adipose tissues. Exp Mol Med. 2009;41(12):880.

Kong L, Zhu J, Han W, Jiang X, Xu M, Zhao Y, et al. Significance of serum microRNAs in pre-diabetes and newly diagnosed type 2 diabetes: a clinical study. Acta Diabetol. 2011 Mar;48(1):61–9.

Korach-André M, Archer A, Gabbi C, Barros RP, Pedrelli M, Steffensen KR, et al. Liver X receptors regulate de novo lipogenesis in a tissue-specific manner in C57BL/6 female mice. AJP: Endocrinology and Metabolism. 2011 Jul;301(1):E210–22.

Kovanen PT, Nikkilä EA, Miettinen TA. Regulation of cholesterol synthesis and storage in fat cells. The Journal of Lipid Research. 1975 May;16(3):211–23.

Kozomara A, Griffiths-Jones S. miRBase: annotating high confidence microRNAs using deep sequencing data. Nucleic Acids Res. 2013 Dec 28;42(D1):D68–D73.

Kraakman MJ, Murphy AJ, Jandeleit-Dahm K, Kammoun HL. Macrophage polarization in obesity and type 2 diabetes: weighing down our understanding of macrophage function? Front Immunol. 2014;5(1):470.

Krotkiewski M, Björntorp P, Sjostrom L, Smith U. Impact of Obesity on Metabolism in Men and Women - Importance of Regional Adipose-Tissue Distribution. J Clin Invest. 1983;72(3):1150–62.

Kubista M, Andrade JM, Bengtsson M, Forootan A, Jonák J, Lind K, et al. The real-time polymerase chain reaction. Molecular Aspects of Medicine. 2006 Apr;27(2-3):95–125.

Kubota N, Terauchi Y, Miki H, Tamemoto H, Yamauchi T, Komeda K, et al. PPAR gamma mediates high-fat diet-induced adipocyte hypertrophy and insulin resistance. Mol Cell. 1999 Oct;4(4):597–609.

Kurowska-Stolarska M, Alivernini S, Ballantine LE, Asquith DL, Millar NL, Gilchrist DS, et al. MicroRNA-155 as a proinflammatory regulator in clinical and experimental arthritis. Proceedings of the National Academy of Sciences. 2011 Jul 5;108(27):11193–8.

Kusminski CM, Scherer PE. Mitochondrial dysfunction in white adipose tissue. Trends Endocrinol Metab. 2012 Sep;23(9):435–43.

Laffitte BA, Chao LC, Li J, Walczak R, Hummasti S, Joseph SB, et al. Activation of liver X receptor improves glucose tolerance through coordinate regulation of glucose metabolism in liver and adipose tissue. Proc Natl Acad Sci USA. 2003 Apr 29;100(9):5419–24.

Lafontan M. Advances in adipose tissue metabolism. Int J Obes Relat Metab Disord. 2008 Dec;32:S39–S51.

Lafontan M, Langin D. Lipolysis and lipid mobilization in human adipose tissue. Progress in Lipid Research. Elsevier Ltd; 2009 Sep 1;48(5):275–97.

Lal A, Thomas MP, Altschuler G, Navarro F, O'Day E, Li XL, et al. Capture of MicroRNA–Bound mRNAs Identifies the Tumor Suppressor miR-34a as a Regulator of Growth Factor Signaling. McManus MT, editor. PLoS Genet. 2011 Nov 10;7(11):e1002363.

Lan F, Cacicedo JM, Ruderman N, Ido Y. SIRT1 modulation of the acetylation status, cytosolic localization, and activity of LKB1. Possible role in AMP-activated protein kinase activation. J Biol Chem. American Society for Biochemistry and Molecular Biology; 2008 Oct 10;283(41):27628–35.

Langin D, Arner P. Importance of TNFα and neutral lipases in human adipose tissue lipolysis. Trends in Endocrinology & Metabolism. 2006 Oct;17(8):314–20.

Lapidus L, Bengtsson C, Larsson BO, Pennert K. Distribution of adipose tissue and risk of cardiovascular disease and death: a 12 year follow up of participants in the population study of women in Gothenburg, …. BMJ. 1984;289(6454):1257–61.

Larsson B, Svardsudd K, Welin L, Wilhelmsen L, Björntorp P, Tibblin G. Abdominal adipose tissue distribution, obesity, and risk of cardiovascular disease and death: 13 year follow up of participants in the study of men born in 1913. Br Med J (Clin Res Ed). 1984 May

12;288(6428):1401–4.

Lau NC, Lim LP, Weinstein EG, Bartel DP. An Abundant Class of Tiny RNAs with Probable Regulatory Roles in Caenorhabditis elegans. Science. 2001 Oct;294(5):858–62.

Lawrence T, Natoli G. Transcriptional regulation of macrophage polarization: enabling diversity with identity. Nature Reviews Immunology. Nature Publishing Group; 2011 Nov 1;11(11):750–61.

Lee D, Goldberg AL. Muscle wasting in fasting requires activation of NF-κB and inhibition of AKT/mTOR by the protein acetylase, GCN5. J Biol Chem. 2015 Oct 29;:jbc.M115.685164–12.

Lee J, Padhye A, Sharma A, Song G, Miao J, Mo YY, et al. A Pathway Involving Farnesoid X Receptor and Small Heterodimer Partner Positively Regulates Hepatic Sirtuin 1 Levels via MicroRNA-34a Inhibition. Journal of Biological Chemistry. 2010 Apr 16;285(17):12604–11.

Lee M-W, Odegaard JI, Mukundan L, Qiu Y, Molofsky AB, Nussbaum JC, et al. Activated Type 2 Innate Lymphoid Cells Regulate Beige Fat Biogenesis. Cell. Elsevier Inc; 2014 Dec 23;160(1-2):1–14.

Lee R, Feinbaum R. The C. elegans heterochronic gene lin-4 encodes small RNAs with antisense complementarity to lin-14. Cell. 1993.

Lemieux S, s JPD, Moorjani S, Nadeau A, riault GT, Prud'homme D, et al. Are gender differences in cardiovascular disease risk factors explained by the level of visceral adipose tissue? Diabetologia. 1994;37(8):757–64.

Levert KL, Waldrop GL, Stephens JM. A biotin analog inhibits acetyl-CoA carboxylase activity and adipogenesis. J Biol Chem. 2002 May 10;277(19):16347–50.

Li H, Rokavec M, Hermeking H. Soluble IL6R represents a miR-34a target: potential implications for the recently identified IL-6R/STAT3/miR-34a feed-back loop. Oncotarget. 2015 Jun 2;6(17):14026–32.

Li J, Wang K, Chen X, Meng H, Song M, Wang Y, et al. Transcriptional activation of microRNA-34a by NF-kappa B in human esophageal cancer cells. BMC Mol Biol. 2012;13(1):4.

Li P, Lu M, Nguyen MTA, Bae EJ, Chapman J, Feng D, et al. Functional heterogeneity of CD11c-positive adipose tissue macrophages in diet-induced obese mice. Journal of Biological Chemistry. 2010 May 14;285(20):15333–45.

Li S, Chen X, Zhang H, Liang X, Xiang Y, Yu C, et al. Differential expression of microRNAs in mouse liver under aberrant energy metabolic status. The Journal of Lipid Research. 2009 Sep;50(9):1756–65.

Li W-Q, Chen C, Xu M-D, Guo J, Li Y-M, Xia Q-M, et al. The rno-miR-34 family is upregulated and targets ACSL1 in dimethylnitrosamine-induced hepatic fibrosis in rats. FEBS Journal. 2011a Apr 1;278(9):1522–32.

Li Z, Rana TM. Therapeutic targeting of microRNAs: current status and future challenges. Nat Rev Drug Discov. Nature Publishing Group; 2014 Jul 11;13(8):622–38.

Li Z-Y, Na H-M, Peng G, Pu J, Liu P. Alteration of microRNA expression correlates to fatty acid-mediated insulin resistance in mouse myoblasts. Mol Biosyst. 2011b Mar;7(3):871–7.

Libby P, Ridker PM, Hansson GK. Progress and challenges in translating the biology of atherosclerosis. Nature. 2011;473(7347):317–25.

Lien G-S, Liu J-F, Chien M-H, Hsu W-T, Chang T-H, Ku C-C, et al. The ability to suppress macrophage-mediated inflammation in orbital fat stem cells is controlled by miR-671-5p. Stem Cell Res Ther. 2014;5(4):97.

Lin H-H, Faunce DE, Stacey M, Terajewicz A, Nakamura T, Zhang-Hoover J, et al. The macrophage F4/80 receptor is required for the induction of antigen-specific efferent regulatory T cells in peripheral tolerance. J Exp Med. 2005 May 16;201(10):1615–25.

Lin J, Wu P-H, Tarr PT, Lindenberg KS, St-Pierre J, Zhang C-Y, et al. Defects in adaptive energy metabolism with CNS-linked hyperactivity in PGC-1alpha null mice. Cell. 2004 Oct 1;119(1):121–35.

Ling H-Y, Wen G-B, Feng S-D, Tuo Q-H, Ou H-S, Yao CH, et al. MicroRNA-375 promotes 3T3-L1 adipocyte differentiation through modulation of extracellular signal-regulated kinase signalling. Clin Exp Pharmacol P. 2011 Apr;38(4):239–46.

Linsen SEV, de Wit E, Janssens G, Heater S, Chapman L, Parkin RK, et al. Limitations and possibilities of small RNA digital gene expression profiling. Nat Meth. Nature Publishing Group; 2009 Jul 1;6(7):474–6.

Lissner L, Björkelund C, Heitmann BL, Seidell JC, Bengtsson C. Larger hip circumference independently predicts health and longevity in a Swedish female cohort. Obes Res. 2001 Oct;9(10):644–6.

Liu H, Sidiropoulos P, Song G, Pagliari LJ, Birrer MJ, Stein B, et al. TNF-alpha gene expression in macrophages: regulation by NF-kappa B is independent of c-Jun or C/EBP beta. J Immunol. 2000 Apr 15;164(8):4277–85.

Liu J, Fox CS, Hickson D, Bidulescu A, Carr JJ, Taylor HA. Fatty liver, abdominal visceral fat, and cardiometabolic risk factors: the Jackson Heart Study. Arteriosclerosis, Thrombosis, and Vascular Biology. 2011a Nov;31(11):2715–22.

Liu J, Fox CS, Hickson D, Sarpong D, Ekunwe L, May WD, et al. Pericardial adipose tissue, atherosclerosis, and cardiovascular disease risk factors: the Jackson heart study. Diabetes Care. 2010a Jul;33(7):1635–9.

Liu J, Fox CS, Hickson DA, May WD, Hairston KG, Carr JJ, et al. Impact of abdominal visceral and subcutaneous adipose tissue on cardiometabolic risk factors: the Jackson Heart Study. J Clin Endocrinol Metab. 2010b Dec;95(12):5419–26.

Liu L-H, Wang X-K, Hu Y-D, Kang J-L, Wang L-L, Li S. Effects of a fatty acid synthase inhibitor on adipocyte differentiation of mouse 3T3-L1 cells. Acta Pharmacol Sin. 2004 Aug;25(8):1052–7.

Liu TF, Yoza BK, Gazzar El M, Vachharajani VT, McCall CE. NAD+-dependent SIRT1 deacetylase participates in epigenetic reprogramming during endotoxin tolerance. Journal of Biological Chemistry. American Society for Biochemistry and Molecular Biology; 2011b Mar 18;286(11):9856–64.

Llewellyn C, Wardle J. Behavioral susceptibility to obesity: Gene–environment interplay in the development of weight. Physiology & Behavior. Elsevier Inc; 2015 Dec 1;152(Part B):494–501.

Lorente-Cebrián S, Mejhert N, Kulyté A, Laurencikiene J, Åström G, Hedén P, et al. MicroRNAs regulate human adipocyte lipolysis: effects of miR-145 are linked to TNF-α. PLoS ONE. 2014;9(1):e86800.

Lovis P, Roggli E, Laybutt DR, Gattesco S, Yang J-Y, Widmann C, et al. Alterations in microRNA expression contribute to fatty acid-induced pancreatic beta-cell dysfunction. Diabetes. 2008 Oct;57(10):2728–36.

Lu H, Hao L, Li S, Lin S, Lv L, Chen Y, et al. Elevated circulating stearic acid leads to a major lipotoxic effect on mouse pancreatic beta cells in hyperlipidaemia via a miR-34a-5p-mediated PERK/p53-dependent pathway. Diabetologia. Diabetologia; 2016 May 3;:1–11.

Lumeng CN, Bodzin JL, Saltiel AR. Obesity induces a phenotypic switch in adipose tissue macrophage polarization. J Clin Invest. 2007a Jan;117(1):175–84.

Lumeng CN, DelProposto JB, Westcott DJ, Saltiel AR. Phenotypic Switching of Adipose Tissue Macrophages With Obesity Is Generated by Spatiotemporal Differences in Macrophage Subtypes. Diabetes. 2008 Dec 1;57(12):3239–46.

Lumeng CN, Deyoung SM, Bodzin JL, Saltiel AR. Increased inflammatory properties of adipose tissue macrophages recruited during diet-induced obesity. Diabetes. 2007b Jan;56(1):16–23.

Lutz TA, Woods SC. Overview of animal models of obesity. Curr Protoc Pharmacol. 2012 Sep;Chapter 5:Unit5.61.

Lynch L, Nowak M, Varghese B, Clark J, Hogan AE, Toxavidis V, et al. Adipose tissue invariant NKT cells protect against diet-induced obesity and metabolic disorder through regulatory cytokine production. Immunity. 2012 Sep 21;37(3):574–87.

Lynch L, O'Shea D, Winter DC, Geoghegan J, Doherty DG, O'Farrelly C. Invariant NKT cells and CD1d(+) cells amass in human omentum and are depleted in patients with cancer and obesity. Eur J Immunol. 2009 Jul;39(7):1893–901.

Maffei M, Halaas J, Ravussin E, Pratley RE, Lee GH, Zhang Y, et al. Leptin levels in human and rodent: Measurement of plasma leptin and ob RNA in obese and weight-reduced subjects. Nat Med. 1995;1(11):1155–61.

Maron DJ, Fazio S, Linton MF. Current perspectives on statins. Circulation. 2000 Jan 18;101(2):207–13.

Martinez-Nunez RT, Louafi F, Sanchez-Elsner T. The interleukin 13 (IL-13) pathway in human macrophages is modulated by microRNA-155 via direct targeting of interleukin 13 receptor alpha1 (IL13Ralpha1). Journal of Biological Chemistry. 2011 Jan 21;286(3):1786–94.

Mathé E, Nguyen GH, Funamizu N, He P, Moake M, Croce CM, et al. Inflammation regulates microRNA expression in cooperation with p53 and nitric oxide. 2012 Aug 1;131(3):760–5.

Matthias A, Ohlson KB, Fredriksson JM, Jacobsson A, Nedergaard J, Cannon B. Thermogenic responses in brown fat cells are fully UCP1-dependent. UCP2 or UCP3 do not substitute for UCP1 in adrenergically or fatty scid-induced thermogenesis. J Biol Chem. 2000 Aug 18;275(33):25073–81.

Mauvais-Jarvis F. Sex differences in metabolic homeostasis, diabetes, and obesity. Biology of Sex Differences. Biology of Sex Differences; 2015 Aug 11;:1–9.

Mayer J, Bates MW, Dickie MM. Hereditary diabetes in genetically obese mice. Science. 1951 Jun 29;113(2948):746–7.

Mayoral R, Osborn O, McNelis J, Johnson AM, Oh DY, Izquierdo CL, et al. Adipocyte SIRT1 knockout promotes PPARγ activity, adipogenesis and insulin sensitivity in chronic-HFD and obesity. Mol Metab. 2015 May;4(5):378–91.

Mazzola N. Review of current and emerging therapies in type 2 diabetes mellitus. Am J Manag Care. 2012 Jan;18(1 Suppl):S17–26.

Mårin P, Andersson B, Ottosson M, Olbe L, Chowdhury B, Kvist H, et al. The morphology and metabolism of intraabdominal adipose tissue in men. Metab Clin Exp. 1992 Nov;41(11):1242–8.

McCubbrey AL, Nelson JD, Stolberg VR, Blakely PK, McCloskey L, Janssen WJ, et al. MicroRNA-34a Negatively Regulates Efferocytosis by Tissue Macrophages in Part via SIRT1. J Immunol. 2016 Feb 1;196(3):1366–75.

McDonald RA, Halliday CA, Miller AM, Diver LA, Dakin RS, Montgomery J, et al. Reducing In-Stent Restenosis: Therapeutic Manipulation of miRNA in Vascular Remodeling and Inflammation. Journal of the American College of Cardiology. 2015 Jun 2;65(21):2314–27.

McDonald RA, White KM, Wu J, Cooley BC, Robertson KE, Halliday CA, et al. miRNA-21 is dysregulated in response to vein grafting in multiple models and genetic ablation in mice attenuates neointima formation. Eur Heart J. 2013 Jun;34(22):1636–43.

McGill HC, McMahan CA, Herderick EE, Zieske AW, Malcom GT, Tracy RE, et al. Obesity accelerates the progression of coronary atherosclerosis in young men. Circulation. 2002 Jun 11;105(23):2712–8.

McGregor RA, Choi MS. microRNAs in the regulation of adipogenesis and obesity. Curr Mol Med. 2011 Jun;11(4):304–16.

Mcilroy GD, Delibegovic M, Owen C, Stoney PN, Shearer KD, McCaffery PJ, et al. Fenretinide treatment prevents diet-induced obesity in association with major alterations in retinoid homeostatic gene expression in adipose, liver, and hypothalamus. Diabetes. 2013 Mar;62(3):825–36.

Meng F, Glaser SS, Francis H, Yang F, Han Y, Stokes A, et al. Epigenetic regulation of miR-34a expression in alcoholic liver injury. 2012 Sep;181(3):804–17.

Meyer SU, Pfaffl MW, Ulbrich SE. Normalization strategies for microRNA profiling experiments: a “normal” way to a hidden layer of complexity? Biotechnol Lett. 2010 Aug 12;32(12):1777–88.

Miller AM, Asquith DL, Hueber AJ, Anderson LA, Holmes WM, McKenzie AN, et al. Interleukin-33 induces protective effects in adipose tissue inflammation during obesity in mice. 2010 Sep 3;107(5):650–8.

Miller AM, Gilchrist DS, Nijjar J, Araldi E, Ramirez CM, Lavery CA, et al. MiR-155 Has a Protective Role in the Development of Non-Alcoholic Hepatosteatosis in Mice. Federici M, editor. PLoS ONE. 2013 Aug 21;8(8):e72324.

Misra A, Vikram NK. Clinical and pathophysiological consequences of abdominal adiposity and abdominal adipose tissue depots. Nutrition. 2003 May;19(5):457–66.

Miura S, Tomitsuka E, Kamei Y, Yamazaki T, Kai Y, Tamura M, et al. Overexpression of peroxisome proliferator-activated receptor gamma co-activator-1alpha leads to muscle atrophy with depletion of ATP. The American Journal of Pathology. 2006 Oct;169(4):1129–39.

Molenaar EA, Hwang S-J, Vasan RS, Grobbee DE, Meigs JB, D'Agostino RB, et al. Burden and rates of treatment and control of cardiovascular disease risk factors in obesity: the Framingham Heart Study. Diabetes Care. 2008 Jul;31(7):1367–72.

Molofsky AB, Nussbaum JC, Liang H-E, Van Dyken SJ, Cheng LE, Mohapatra A, et al. Innate lymphoid type 2 cells sustain visceral adipose tissue eosinophils and alternatively activated macrophages. J Exp Med. 2013 Mar 11;210(3):535–49.

Montgomery MK, Hallahan NL, Brown SH, Liu M, Mitchell TW, Cooney GJ, et al. Mouse strain-dependent variation in obesity and glucose homeostasis in response to high-fat feeding. Diabetologia. 2013 May;56(5):1129–39.

Moreno-Navarrete JM, Fernández-Real JM. Adipocyte differentiation. Adipose tissue biology. 2012;:17–38.

Moro K, Yamada T, Tanabe M, Takeuchi T, Ikawa T, Kawamoto H, et al. Innate production of TH2 cytokines by adipose tissue-associated c-Kit+Sca-1+ lymphoid cells. Nature. Nature Publishing Group; 2010 Jan 18;463(7280):540–4.

Munder M, Eichmann K, Morán JM, Centeno F, Soler G, Modolell M. Th1/Th2-regulated expression of arginase isoforms in murine macrophages and dendritic cells. J Immunol. 1999 Oct 1;163(7):3771–7.

Nedergaard J, Bengtsson T, Cannon B. Unexpected evidence for active brown adipose tissue in

adult humans. Am J Physiol Endocrinol Metab. 2007 Aug;293(2):E444–52.

Newman MA, Mani V, Hammond SM. Deep sequencing of microRNA precursors reveals extensive 3' end modification. RNA. 2011 Oct;17(10):1795–803.

Nguyen KD, Qiu Y, Cui X, Goh YPS, Mwangi J, David T, et al. Alternatively activated macrophages produce catecholamines to sustain adaptive thermogenesis. Nature Publishing Group; 2011 Nov 21;480(7375):104–8.

Nguyen MTA, Favelyukis S, Nguyen A-K, Reichart D, Scott PA, Jenn A, et al. A subpopulation of macrophages infiltrates hypertrophic adipose tissue and is activated by free fatty acids via Toll-like receptors 2 and 4 and JNK-dependent pathways. J Biol Chem. 2007 Nov 30;282(48):35279–92.

Niederer F, Trenkmann M, Ospelt C, Karouzakis E, Neidhart M, Stanczyk J, et al. Down-regulation of microRNA-34a* in rheumatoid arthritis synovial fibroblasts promotes apoptosis resistance. Arthritis Rheum. 2012 Jun;64(6):1771–9.

Nishimura S, Manabe I, Nagasaki M, Eto K, Yamashita H, Ohsugi M, et al. CD8+ effector T cells contribute to macrophage recruitment and adipose tissue inflammation in obesity. Nature Publishing Group; 2009 Jul 26;:1–8.

Nishimura S, Manabe I, Nagasaki M, Seo K, Yamashita H, Hosoya Y, et al. In vivo imaging in mice reveals local cell dynamics and inflammation in obese adipose tissue. J Clin Invest. 2008 Jan 17;:1–12.

Nishimura S, Manabe I, Takaki S, Nagasaki M, Otsu M, Yamashita H, et al. Short Article. Cell Metab. Elsevier Inc; 2013 Nov 5;18(5):759–66.

Nolan T, Hands RE, Bustin SA. Quantification of mRNA using real-time RT-PCR. Nature Protocols. 2006;1(3):1559–82.

Nunemaker CS, Chung HG, Verrilli GM, Corbin KL, Upadhye A, Sharma PR. Increased serum CXCL1 and CXCL5 are linked to obesity, hyperglycemia, and impaired islet function. J Endocrinol. 2014 Aug;222(2):267–76.

O'Connell RM, Taganov KD, Boldin MP, Cheng G, Baltimore D. MicroRNA-155 is induced during the macrophage inflammatory response. Proc Natl Acad Sci USA. 2007 Jan 30;104(5):1604–9.

Obad S, Santos dos CO, Petri A, Heidenblad M, Broom O, Ruse C, et al. Silencing of microRNA families by seed-targeting tiny LNAs. Nat Genet. 2011 Mar 20;43(4):371–8.

Odegaard JI, Ricardo-Gonzalez RR, Goforth MH, Morel CR, Subramanian V, Mukundan L, et al. Macrophage-specific PPARgamma controls alternative activation and improves insulin resistance. Nature. 2007 Jun 28;447(7148):1116–20.

Oger F, Gheeraert C, Mogilenko D, Benomar Y, Molendi-Coste O, Bouchaert E, et al. Cell-specific dysregulation of microRNA expression in obese white adipose tissue. J Clin Endocrinol Metab. 2014 Aug;99(8):2821–33.

Ohlson LO, Larsson B, Svardsudd K, Welin L, Eriksson H, Wilhelmsen L, et al. The Influence of Body Fat Distribution on the Incidence of Diabetes Mellitus: 13.5 Years of Follow-up of the Participants in the Study of Men Born in 1913. Diabetes. 1985;34(10):1055–8.

Oike H, Sakurai M, Ippoushi K, Kobori M. Time-fixed feeding prevents obesity induced by chronic advances of light/dark cycles in mouse models of jet-lag/shift work. Biochemical and Biophysical Research Communications. 2015 Sep 25;465(3):556–61.

Okamoto Y, Folco EJ, Minami M, Wara AK, Feinberg MW, Sukhova GK, et al. Adiponectin inhibits the production of CXC receptor 3 chemokine ligands in macrophages and reduces T-

lymphocyte recruitment in atherogenesis. Circulation Research. 2008 Feb 1;102(2):218–25.

Oliveira MC, Menezes-Garcia Z, Henriques MCC, Soriani FM, Pinho V, Faria AMC, et al. Acute and sustained inflammation and metabolic dysfunction induced by high refined carbohydrate-containing diet in mice. Obesity (Silver Spring). 2013 Sep;21(9):E396–406.

Ortega FJ, Moreno-Navarrete JM, Pardo G, Sabater M, Hummel M, Ferrer A, et al. MiRNA expression profile of human subcutaneous adipose and during adipocyte differentiation. Wang Y, editor. PLoS ONE. 2010 Jan 1;5(2):e9022–2.

Osman OS, Selway JL, Kępczyńska MA, Stocker CJ, O'Dowd JF, Cawthorne MA, et al. A novel automated image analysis method for accurate adipocyte quantification. Adipocyte. 2013 Jul 1;2(3):160–4.

Ou J, Tu H, Shan B, Luk A, DeBose-Boyd RA, Bashmakov Y, et al. Unsaturated fatty acids inhibit transcription of the sterol regulatory element-binding protein-1c (SREBP-1c) gene by antagonizing ligand-dependent activation of the LXR. Proc Natl Acad Sci USA. 2001 May 22;98(11):6027–32.

Owen C, Czopek A, Agouni A, Grant L, Judson R, Lees EK, et al. Adipocyte-specific protein tyrosine phosphatase 1B deletion increases lipogenesis, adipocyte cell size and is a minor regulator of glucose homeostasis. Saez ME, editor. PLoS ONE. 2012;7(2):e32700.

Palaga T, Buranaruk C, Rengpipat S, Fauq AH, Golde TE, Kaufmann SHE, et al. Notch signaling is activated by TLR stimulation and regulates macrophage functions. Eur J Immunol. 2008 Jan;38(1):174–83.

Palomer X, Alvarez-Guardia D, Rodríguez-Calvo R, Coll T, Laguna JC, Davidson MM, et al. TNF-alpha reduces PGC-1alpha expression through NF-kappaB and p38 MAPK leading to increased glucose oxidation in a human cardiac cell model. Cardiovasc Res. 2009 Mar 1;81(4):703–12.

Parameswaran N, Patial S. Tumor necrosis factor-α signaling in macrophages. Crit Rev Eukaryot Gene Expr. 2010;20(2):87–103.

Park H, Park H, Pak H-J, Yang D-Y, Kim Y-H, Choi W-J, et al. miR-34a inhibits differentiation of human adipose tissue-derived stem cells by regulating cell cycle and senescence induction. Differentiation. Elsevier; 2015 Dec 8;:1–10.

Pasquinelli AE, Reinhart BJ, Slack F, Martindale MQ, Kuroda MI, Maller B, et al. Conservation of the sequence and temporal expression of let-7 heterochronic regulatory RNA. Nature. 2000 Nov 2;408(6808):86–9.

Patsouris D, Reddy JK, Müller M, Kersten S. Peroxisome Proliferator-Activated Receptor α Mediates the Effects of High-Fat Diet on Hepatic Gene Expression. Endocrinology. 2006 Mar;147(3):1508–16.

Pedersen SB, Hansen PS, Lund S, Andersen PH, Odgaard A, Richelsen B. Identification of oestrogen receptors and oestrogen receptor mRNA in human adipose tissue. Eur J Clin Invest. 1996 Apr;26(4):262–9.

Petrovic N, Shabalina IG, Timmons JA, Cannon B, Nedergaard J. Thermogenically competent nonadrenergic recruitment in brown preadipocytes by a PPARgamma agonist. Am J Physiol Endocrinol Metab. 2008 Aug;295(2):E287–96.

Petrovic N, Walden TB, Shabalina IG, Timmons JA, Cannon B, Nedergaard J. Chronic peroxisome proliferator-activated receptor gamma (PPARgamma) activation of epididymally derived white adipocyte cultures reveals a population of thermogenically competent, UCP1-containing adipocytes molecularly distinct from classic brown adipocytes. Journal of Biological Chemistry. 2010 Mar 5;285(10):7153–64.

Pettersson AML, Stenson BM, Lorente-Cebrián S, Andersson DP, Mejhert N, Krätzel J, et al. LXR is a negative regulator of glucose uptake in human adipocytes. Diabetologia. 2013 Sep;56(9):2044–54.

Pfaffl MW. A new mathematical model for relative quantification in real-time RT-PCR. Nucleic Acids Res. 2001 May 1;29(9):e45.

Pou KM, Massaro JM, Hoffmann U, Vasan RS, Maurovich-Horvat P, Larson MG, et al. Visceral and subcutaneous adipose tissue volumes are cross-sectionally related to markers of inflammation and oxidative stress: the Framingham Heart Study. Circulation. 2007 Sep 11;116(11):1234–41.

Pouliot MC, Despres JP, Lemieux S, Moorjani S, Bouchard C, Tremblay A, et al. Waist Circumference and Abdominal Sagittal Diameter - Best Simple Anthropometric Indexes of Abdominal Visceral Adipose-Tissue Accumulation and Related Cardiovascular Risk in Men and Women. The American Journal of Cardiology. 1994;73(7):460–8.

Poy MN, Hausser J, Trajkovski M, Braun M, Collins S, Rorsman P, et al. miR-375 maintains normal pancreatic alpha- and beta-cell mass. Proceedings of the National Academy of Sciences. 2009 Apr 7;106(14):5813–8.

Preis SR, Massaro JM, Robins SJ, Hoffmann U, Vasan RS, Irlbeck T, et al. Abdominal subcutaneous and visceral adipose tissue and insulin resistance in the Framingham heart study. Obesity (Silver Spring). 2010 Nov;18(11):2191–8.

Prins JB, O'Rahilly S. Regulation of adipose cell number in man. Clin Sci. 1997 Jan;92(1):3–11.

Pritchard CC, Cheng HH, Tewari M. MicroRNA profiling: approaches and considerations. Nature Publishing Group; 2012 May 1;:1–12.

Puigserver P, Wu Z, Park CW, Graves R, Wright M, Spiegelman BM. A cold-inducible coactivator of nuclear receptors linked to adaptive thermogenesis. Cell. 1998 Mar 20;92(6):829–39.

Pulikkan JA, Peramangalam PS, Dengler V, Ho PA, Preudhomme C, Meshinchi S, et al. C/EBPα regulated microRNA-34a targets E2F3 during granulopoiesis and is down-regulated in AML with CEBPA mutations. Blood. 2010 Dec 16;116(25):5638–49.

Puri N, Sodhi K, Haarstad M, Kim DH, Bohinc S, Foglio E, et al. Heme induced oxidative stress attenuates sirtuin1 and enhances adipogenesis in mesenchymal stem cells and mouse pre-adipocytes. J Cell Biochem. 2012;:n/a–n/a.

Qiao L, Yoo HS, Bosco C, Lee B, Feng G-S, Schaack J, et al. Adiponectin reduces thermogenesis by inhibiting brown adipose tissue activation in mice. Diabetologia. 2014 Feb 16;57(5):1027–36.

Qiu Y, Nguyen KD, Odegaard JI, Cui X, Tian X, Locksley RM, et al. Eosinophils and type 2 cytokine signaling in macrophages orchestrate development of functional beige fat. Cell. 2014 Jun 5;157(6):1292–308.

Raitoharju E, Lyytikäinen L-P, Levula M, Oksala N, Mennander A, Tarkka M, et al. miR-21, miR-210, miR-34a, and miR-146a/b are up-regulated in human atherosclerotic plaques in the Tampere Vascular Study. Atherosclerosis. 2011 Nov;219(1):211–7.

Ramkhelawon B, Hennessy EJ, nager MELME, Ray TD, Sheedy FJ, Hutchison S, et al. Netrin1 promotes adipose tissue macrophage retention and insulin resistance in obesity. Nature Publishing Group; 2014 Mar 2;20(4):377–84.

Rankin W, Wittert G. Anti-obesity drugs. Curr Opin Lipidol. 2015 Dec;26(6):536–43.

Rao DS, O'Connell RM, Chaudhuri AA, Garcia-Flores Y, Geiger TL, Baltimore D. MicroRNA-34a perturbs B lymphocyte development by repressing the forkhead box transcription factor Foxp1. Immunity. 2010 Jul 23;33(1):48–59.

Rayner KJ, Esau CC, Hussain FN, McDaniel AL, Marshall SM, van Gils JM, et al. Inhibition of miR-33a/b in non-human primates raises plasma HDL and lowers VLDL triglycerides. 2011 Oct 20;478(7369):404–7.

Reaven GM. Banting lecture 1988. Role of insulin resistance in human disease. Diabetes. 1988 Dec;37(12):1595–607.

Rebuffé-Scrive M, Lundholm K, Björntorp P. Glucocorticoid hormone binding to human adipose tissue. Eur J Clin Invest. 1985 Oct;15(5):267–71.

Rehnmark S, Antonson P, Xanthopoulos KG, Jacobsson A. Differential adrenergic regulation of C/EBP alpha and C/EBP beta in brown adipose tissue. FEBS Letters. 1993 Mar 8;318(3):235–41.

Rehnmark S, Néchad M, Herron D, Cannon B, Nedergaard J. Alpha- and beta-adrenergic induction of the expression of the uncoupling protein thermogenin in brown adipocytes differentiated in culture. J Biol Chem. 1990 Sep 25;265(27):16464–71.

Reiner Z, Catapano AL, De Backer G, Graham I, Taskinen M-R, Wiklund O, et al. ESC/EAS Guidelines for the management of dyslipidaemias: the Task Force for the management of dyslipidaemias of the European Society of Cardiology (ESC) and the European Atherosclerosis Society (EAS). Eur Heart J. 2011 Jun 30;32(14):1769–818.

Reinhart BJ, Slack FJ, Basson M, Pasquinelli AE, Bettinger JC, Rougvie AE, et al. The 21-nucleotide let-7 RNA regulates developmental timing in Caenorhabditis elegans. Nature. 2000 Feb 24;403(6772):901–6.

Reynolds CM, McGillicuddy FC, Harford KA, Finucane OM, Mills KHG, Roche HM. Dietary saturated fatty acids prime the NLRP3 inflammasome via TLR4 in dendritic cells-implications for diet-induced insulin resistance. Mol Nutr Food Res. 2012 Jun 15;56(8):1212–22.

Ricardo-Gonzalez RR, Red Eagle A, Odegaard JI, Jouihan H, Morel CR, Heredia JE, et al. IL-4/STAT6 immune axis regulates peripheral nutrient metabolism and insulin sensitivity. Proceedings of the National Academy of Sciences. 2010 Dec 28;107(52):22617–22.

Richmond A. NF-κB, chemokine gene transcription and tumour growth. Nature Reviews Immunology. 2002 Sep;2(9):664–74.

Robertson S, MacKenzie SM, Alvarez-Madrazo S, Diver LA, Lin J, Stewart PM, et al. MicroRNA-24 is a novel regulator of aldosterone and cortisol production in the human adrenal cortex. Hypertension. 2013 Sep;62(3):572–8.

Rodeheffer MS, Birsoy K, Friedman JM. Identification of white adipocyte progenitor cells in vivo. Cell. 2008 Oct 17;135(2):240–9.

Rodgers JT, Lerin C, Gerhart-Hines Z, Puigserver P. Metabolic adaptations through the PGC-1α and SIRT1 pathways. FEBS Letters. 2008 Jan;582(1):46–53.

Rodgers JT, Lerin C, Haas W, Gygi SP, Spiegelman BM, Puigserver P. Nutrient control of glucose homeostasis through a complex of PGC-1alpha and SIRT1. 2005 Mar 3;434(7029):113–8.

Rodriguez-Ubreva J, Ciudad L, van Oevelen C, Parra M, Graf T, Ballestar E. C/EBPa-Mediated Activation of miR-34a and miR-223 Inhibits Lef1 Expression to Achieve Efficient Reprogramming into Macrophages. 2014 Jan 13.

Roggli E, Britan A, Gattesco S, Lin-Marq N, Abderrahmani A, Meda P, et al. Involvement of MicroRNAs in the Cytotoxic Effects Exerted by Proinflammatory Cytokines on Pancreatic -Cells. Diabetes. 2010 Mar 29;59(4):978–86.

Rojas LBA, Gomes MB. Metformin: an old but still the best treatment for type 2 diabetes. Diabetol Metab Syndr. 2013 Jan 1;5(1):6–6.

Rokavec M, Li H, Jiang L, Hermeking H. The p53/miR-34 axis in development and disease. J Mol Cell Biol. 2014a Jun;6(3):214–30.

Rokavec M, Öner MG, Li H, Jackstadt R, Jiang L, Lodygin D, et al. IL-6R/STAT3/miR-34a feedback loop promotes EMT-mediated colorectal cancer invasion and metastasis. J Clin Invest. 2014b Apr;124(4):1853–67.

Rosen ED, Sarraf P, Troy AE, Bradwin G, Moore K, Milstone DS, et al. PPAR gamma is required for the differentiation of adipose tissue in vivo and in vitro. Mol Cell. 1999 Oct;4(4):611–7.

Rosenbaum M, Knight R, Leibel RL. The gut microbiota in human energy homeostasis and obesity. Trends Endocrinol Metab. 2015 Sep;26(9):493–501.

Rosenthal N, Brown S. The mouse ascending: perspectives for human-disease models. Nat Cell Biol. 2007 Sep;9(9):993–9.

Rosito GA, Massaro JM, Hoffmann U, Ruberg FL, Mahabadi AA, Vasan RS, et al. Pericardial fat, visceral abdominal fat, cardiovascular disease risk factors, and vascular calcification in a community-based sample: the Framingham Heart Study. Circulation. 2008 Feb 5;117(5):605–13.

Rothwell NJ, Stock MJ. A role for brown adipose tissue in diet-induced thermogenesis. Nature. 1979 Sep 6;281(5726):31–5.

Rouault C, Pellegrinelli V, Schilch R, Cotillard A, Poitou C, Tordjman J, et al. Roles of chemokine ligand-2 (CXCL2) and neutrophils in influencing endothelial cell function and inflammation of human adipose tissue. Endocrinology. 2013 Mar;154(3):1069–79.

Rousset S, Alves-Guerra M-C, Mozo J, Miroux B, Cassard-Doulcier A-M, Bouillaud F, et al. The biology of mitochondrial uncoupling proteins. Diabetes. 2004 Feb;53 Suppl 1:S130–5.

Russo VC, Azar WJ, Yau SW, Sabin MA, Werther GA. IGFBP-2: The dark horse in metabolism and cancer. Cytokine & growth factor reviews. Elsevier Ltd; 2015 Jun 1;26(3):329–46.

Rutkowski JM, Stern JH, Scherer PE. Beyond the cell: The cell biology of fat expansion. The Journal of Cell Biology. 2015 Mar 2;208(5):501–12.

Saiki RK, Scharf S, Faloona F, Mullis KB, Horn GT, Erlich HA, et al. Enzymatic amplification of beta-globin genomic sequences and restriction site analysis for diagnosis of sickle cell anemia. Science. 1985 Dec 20;230(4732):1350–4.

Sam S, Haffner S, Davidson MH, D'Agostino RB, Feinstein S, Kondos G, et al. Relation of abdominal fat depots to systemic markers of inflammation in type 2 diabetes. Diabetes Care. 2009 May;32(5):932–7.

Samuel VT, Liu Z-X, Qu X, Elder BD, Bilz S, Befroy D, et al. Mechanism of hepatic insulin resistance in non-alcoholic fatty liver disease. J Biol Chem. 2004 Jul 30;279(31):32345–53.

Saponaro C, Gaggini M, Carli F, Gastaldelli A. The Subtle Balance between Lipolysis and Lipogenesis: A Critical Point in Metabolic Homeostasis. Nutrients. 2015 Dec;7(12):9453–74.

Saris WHM, Blair SN, van Baak MA, Eaton SB, Davies PSW, Di Pietro L, et al. How much physical activity is enough to prevent unhealthy weight gain? Outcome of the IASO 1st Stock Conference and consensus statement. Obes Rev. 2003. pp. 101–14.

Sato MK, Toda M, Inomata N, Maruyama H, Okamatsu-Ogura Y, Arai F, et al. Temperature Changes in Brown Adipocytes Detected with a Bimaterial Microcantilever. Biophysj. Biophysical Society; 2014 Jun 3;106(11):2458–64.

Sazanov LA. A giant molecular proton pump: structure and mechanism of respiratory complex I. Nature Publishing Group. Nature Publishing Group; 2015 May 20;16(6):375–88.

Schwarz DS, Hutvágner G, Du T, Xu Z, Aronin N, Zamore PD. Asymmetry in the assembly of the RNAi enzyme complex. Cell. 2003 Oct 17;115(2):199–208.

Seale P, Bjork B, Yang W, Kajimura S, Chin S, Kuang S, et al. PRDM16 controls a brown fat/skeletal muscle switch. Nature. 2008 Aug 21;454(7207):961–7.

Seeger T, Fischer A, Muhly-Reinholz M, Zeiher AM, Dimmeler S. Long-term inhibition of miR-21 leads to reduction of obesity in db/db mice. Obesity (Silver Spring). 2014 Aug 20.

Sellers RS, Clifford CB, Treuting PM, Brayton C. Immunological Variation Between Inbred Laboratory Mouse Strains: Points to Consider in Phenotyping Genetically Immunomodified Mice. Veterinary Pathology. 2012 Jan 3;49(1):32–43.

Shan D, Li J-L, Wu L, Li D, Hurov J, Tobin JF, et al. GPAT3 and GPAT4 are regulated by insulin-stimulated phosphorylation and play distinct roles in adipogenesis. The Journal of Lipid Research. 2010 Jul;51(7):1971–81.

Shaul ME, Bennett G, Strissel KJ, Greenberg AS, Obin MS. Dynamic, M2-like remodeling phenotypes of CD11c+ adipose tissue macrophages during high-fat diet--induced obesity in mice. Diabetes. 2010 May;59(5):1171–81.

Shi H, Kokoeva MV, Inouye K, Tzameli I, Yin H, Flier JS. TLR4 links innate immunity and fatty acid–induced insulin resistance. J Clin Invest. 2006 Nov 1;116(11):3015–25.

Shimano H, Yahagi N, Amemiya-Kudo M, Hasty AH, Osuga J, Tamura Y, et al. Sterol regulatory element-binding protein-1 as a key transcription factor for nutritional induction of lipogenic enzyme genes. J Biol Chem. 1999 Dec 10;274(50):35832–9.

Shin J, Xie D, Zhong X-P. MicroRNA-34a enhances T cell activation by targeting diacylglycerol kinase ζ. Houtman JCD, editor. PLoS ONE. 2013;8(10):e77983.

Shoelson SE, Herrero L, Naaz A. Obesity, inflammation, and insulin resistance. Gastroenterology. 2007 May;132(6):2169–80.

Shoelson SE, Lee J, Goldfine AB. Inflammation and insulin resistance. J Clin Invest. 2006 Jul;116(7):1793–801.

Singer P. [Diagnosis of primary hyperlipoproteinemias]. Z Gesamte Inn Med. 1977 Apr 15;32(8):128contd.

Skowronski MT, Skowronska A, Rojek A, Oklinski MK, Nielsen S. Prolonged Starvation Causes Up-Regulation of AQP1 in Adipose Tissue Capillaries of AQP7 Knock-Out Mice. IJMS. 2016 Jul 22;17(7).

Smart SJ, Casale TB. TNF-alpha-induced transendothelial neutrophil migration is IL-8 dependent. Am J Physiol. 1994 Mar;266(3 Pt 1):L238–45.

Solinas G, Borén J, Dulloo AG. De novo lipogenesis in metabolic homeostasis: More friend than foe? Mol Metab. 2015 May;4(5):367–77.

Stanhope KL. Sugar consumption, metabolic disease and obesity: The state of the controversy. Critical Reviews in Clinical Laboratory Sciences. 2015 Aug 17;53(1):52–67.

Stenson BM, Rydén M, Steffensen KR, Wåhlén K, Pettersson AT, Jocken JW, et al. Activation of liver X receptor regulates substrate oxidation in white adipocytes. Endocrinology. 2009 Sep;150(9):4104–13.

Stenvang J, Petri A, Lindow M, Obad S, Kauppinen S. Inhibition of microRNA function by antimiR oligonucleotides. Silence. BioMed Central Ltd; 2012 Jan 9;3(1):1.

Stern MP, Haffner SM. Body fat distribution and hyperinsulinemia as risk factors for diabetes and

cardiovascular disease. Arteriosclerosis. 1986 Mar;6(2):123–30.

Stevens HC, Deng L, Grant JS, Pinel K, Thomas M, Morrell NW, et al. Regulation and function of miR-214 in pulmonary arterial hypertension. Pulmonary Circulation. 2016 Mar;6(1):109–17.

Stöckli J, Fazakerley DJ, James DE. GLUT4 exocytosis. Journal of Cell Science. 2011 Dec 15;124(Pt 24):4147–59.

Strålfors P, Björgell P, Belfrage P. Hormonal regulation of hormone-sensitive lipase in intact adipocytes: identification of phosphorylated sites and effects on the phosphorylation by lipolytic hormones and insulin. Proc Natl Acad Sci USA. 1984 Jun;81(11):3317–21.

Strissel KJ, Stancheva Z, Miyoshi H, Perfield JW, DeFuria J, Jick Z, et al. Adipocyte Death, Adipose Tissue Remodeling, and Obesity Complications. Diabetes. 2007 Sep 5;56(12):2910–8.

Sturley SL, Hussain MM. Lipid droplet formation on opposing sides of the endoplasmic reticulum. The Journal of Lipid Research. 2012 Sep;53(9):1800–10.

Su S, Zhao Q, He C, Huang D, Liu J, Chen F, et al. miR-142-5p and miR-130a-3p are regulated by IL-4 and IL-13 and control profibrogenic macrophage program. Nat Comms. 2015;6:8523.

Suganami T, Nishida J, Ogawa Y. A paracrine loop between adipocytes and macrophages aggravates inflammatory changes: role of free fatty acids and tumor necrosis factor alpha. Arteriosclerosis, Thrombosis, and Vascular Biology. 2005 Oct;25(10):2062–8.

Summermatter S, Baum O, Santos G, Hoppeler H, Handschin C. Peroxisome proliferator-activated receptor {gamma} coactivator 1{alpha} (PGC-1{alpha}) promotes skeletal muscle lipid refueling in vivo by activating de novo lipogenesis and the pentose phosphate pathway. Journal of Biological Chemistry. 2010 Oct 22;285(43):32793–800.

Sun K, Kusminski CM, Scherer PE. Adipose tissue remodeling and obesity. 2011 Jun 1;121(6):2094–101.

Sun K, Tordjman J, Clément K, Scherer PE. Fibrosis and adipose tissue dysfunction. Cell Metab. 2013 Oct 1;18(4):470–7.

Svane MS, Madsbad S. Bariatric surgery - effects on obesity and related co-morbidities. Curr Diabetes Rev. 2014 May;10(3):208–14.

Swinburn BA, Sacks G, Hall KD, McPherson K, Finegood DT, Moodie ML, et al. The global obesity pandemic: shaped by global drivers and local environments. The Lancet. 2011 Aug;378(9793):804–14.

Sørensen TI, Price RA, Stunkard AJ, Schulsinger F. Genetics of obesity in adult adoptees and their biological siblings. BMJ. 1989 Jan 14;298(6666):87–90.

Tadros TM, Massaro JM, Rosito GA, Hoffmann U, Vasan RS, Larson MG, et al. Pericardial fat volume correlates with inflammatory markers: the Framingham Heart Study. Obesity (Silver Spring). 2010 May;18(5):1039–45.

Takahashi M, Ikemoto S, Ezaki O. Effect of the fat/carbohydrate ratio in the diet on obesity and oral glucose tolerance in C57BL/6J mice. J Nutr Sci Vitaminol. 1999 Oct;45(5):583–93.

Talukdar S, Oh DY, Bandyopadhyay G, Li D, Xu J, McNelis J, et al. Neutrophils mediate insulin resistance in mice fed a high-fat diet through secreted elastase. Nat Med. 2012 Sep;18(9):1407–12.

Tan GC, Chan E, Molnar A, Sarkar R, Alexieva D, Isa IM, et al. 5' isomiR variation is of functional and evolutionary importance. Nucleic Acids Res. 2014 Aug;42(14):9424–35.

Tan J, Fan L, Mao JJ, Chen B, Zheng L, Zhang T, et al. Restoration of miR-34a in p53 deficient cells unexpectedly promotes the cell survival by increasing NFκB activity. J Cell Biochem. 2012 Sep;113(9):2903–8.

Tang W, Zeve D, Suh JM, Bosnakovski D, Kyba M, Hammer RE, et al. White fat progenitor cells reside in the adipose vasculature. Science. American Association for the Advancement of Science; 2008 Oct 24;322(5901):583–6.

Tankó LB, Bagger YZ, Alexandersen P, Larsen PJ, Christiansen C. Central and peripheral fat mass have contrasting effect on the progression of aortic calcification in postmenopausal women. Eur Heart J. 2003a Aug;24(16):1531–7.

Tankó LB, Bagger YZ, Alexandersen P, Larsen PJ, Christiansen C. Peripheral adiposity exhibits an independent dominant antiatherogenic effect in elderly women. Circulation. 2003b Apr 1;107(12):1626–31.

Tartaglia LA, Dembski M, Weng X, Deng N. Identification and expression cloning of a leptin receptor, OB-R. Cell. 1995;83(7):1263–71.

Tervahauta M, Pekkanen J, Kivinen P, Stengård J, Jauhiainen M, Ehnholm C, et al. Prevalence of coronary heart disease and associated risk factors among elderly Finnish men in the Seven Countries Study. Atherosclerosis. 1993 Dec;104(1-2):47–59.

The Scottish Government. The Scottish Health Survey 2014: Volume 1: Main Report. 2015 Sep 22;1:1–315. Available from: http://www.gov.scot/Publications/2015/09/6648/downloads

Thomson DW, Bracken CP, Szubert JM, Goodall GJ. On measuring miRNAs after transient transfection of mimics or antisense inhibitors. PLoS ONE. 2013;8(1):e55214.

Tian G-P, Chen W-J, He P-P, Tang S-L, Zhao G-J, Lv Y-C, et al. MicroRNA-467b targets LPL gene in RAW 264.7 macrophages and attenuates lipid accumulation and proinflammatory cytokine secretion. Biochimie. Elsevier Masson SAS; 2012 Dec 1;94(12):2749–55.

Tian G-P, Tang Y-Y, He P-P, Lv Y-C, Ouyang X-P, Zhao G-J, et al. The effects of miR-467b on lipoprotein lipase (LPL) expression, pro-inflammatory cytokine, lipid levels and atherosclerotic lesions in apolipoprotein E knockout mice. Biochemical and Biophysical Research Communications. Elsevier Inc; 2014 Jan 10;443(2):428–34.

Tilg H, Moschen AR. Adipocytokines: mediators linking adipose tissue, inflammation and immunity. Nature Reviews Immunology. 2006 Sep 22;6(10):772–83.

Titos E, Rius B, González-Périz A, López-Vicario C, Morán-Salvador E, Martínez-Clemente M, et al. Resolvin D1 and its precursor docosahexaenoic acid promote resolution of adipose tissue inflammation by eliciting macrophage polarization toward an M2-like phenotype. J Immunol. 2011 Nov 15;187(10):5408–18.

Tordjman J, Chauvet G, Quette J, Beale EG, Forest C, Antoine B. Thiazolidinediones block fatty acid release by inducing glyceroneogenesis in fat cells. J Biol Chem. 2003 May 23;278(21):18785–90.

Townsend N, Bhatnagar P, Wilkins E, Wickramasinghe K, Rayner M. Cardiovascular Disease Statistics 2015. British Heart Foundation: London. 2015 Jan 1;:1–75.

Tugay K, Guay C, Marques AC, Allagnat F, Locke JM, Harries LW, et al. Role of microRNAs in the age-associated decline of pancreatic beta cell function in rat islets. Diabetologia. 2016 Jan;59(1):161–9.

Uldry M, Yang W, St-Pierre J, Lin J, Seale P, Spiegelman BM. Complementary action of the PGC-1 coactivators in mitochondrial biogenesis and brown fat differentiation. Cell Metab. 2006 May;3(5):333–41.

Ussar S, Griffin NW, Bezy O, Fujisaka S, Vienberg S, Softic S, et al. Interactions between Gut Microbiota, Host Genetics and Diet Modulate the Predisposition to Obesity and Metabolic Syndrome. Cell Metab. 2015 Sep 1;22(3):516–30.

Utsal L, Tillmann V, Zilmer M, Mäestu J, Purge P, Jürimäe J, et al. Elevated Serum IL-6, IL-8, MCP-1, CRP, and IFN-? Levels in 10- to 11-Year-Old Boys with Increased BMI. Horm Res Paediatr. 2012;78(1):31–9.

Vague J. The degree of masculine differentiation of obesities: a factor determining predisposition to diabetes, atherosclerosis, gout, and uric calculous disease. Am J Clin Nutr. 1956 Jan;4(1):20–34.

van den Berg FT, Rossi JJ, Arbuthnot P, Weinberg MS. Design of Effective Primary MicroRNA Mimics With Different Basal Stem Conformations. Mol Ther Nucleic Acids. 2016;5:e278.

van der Klaauw AA, Farooqi IS. The hunger genes: pathways to obesity. Cell. 2015 Mar 26;161(1):119–32.

van Harmelen V, Skurk T, Röhrig K, Lee Y-M, Halbleib M, Aprath-Husmann I, et al. Effect of BMI and age on adipose tissue cellularity and differentiation capacity in women. Int J Obes Relat Metab Disord. 2003 Aug;27(8):889–95.

van Rooij E, Sutherland LB, Liu N, Williams AH, McAnally J, Gerard RD, et al. A signature pattern of stress-responsive microRNAs that can evoke cardiac hypertrophy and heart failure. Proc Natl Acad Sci USA. 2006 Nov 28;103(48):18255–60.

Vandenberg T, Kraal G. A function for the macrophage F4/80 molecule in tolerance induction. 2005 Oct;26(10):506–9.

Varbo A, Benn M, Smith GD, Timpson NJ, Tybjaerg-Hansen A, Nordestgaard BG. Remnant cholesterol, low-density lipoprotein cholesterol, and blood pressure as mediators from obesity to ischemic heart disease. Circulation Research. 2015 Feb 13;116(4):665–73.

Vazquez G, Duval S, Jacobs DR, Silventoinen K. Comparison of body mass index, waist circumference, and waist/hip ratio in predicting incident diabetes: a meta-analysis. Epidemiol Rev. 2007;29:115–28.

Vidal-Puig A, Jimenez-Liñan M, Lowell BB, Hamann A, Hu E, Spiegelman B, et al. Regulation of PPAR gamma gene expression by nutrition and obesity in rodents. J Clin Invest. 1996 Jun 1;97(11):2553–61.

Vielma SA, Klein RL, Levingston CA, Young MRI. Adipocytes as immune regulatory cells. International Immunopharmacology. Elsevier B.V; 2013 Jun 1;16(2):224–31.

Vila-del Sol V, Punzón C, Fresno M. IFN-gamma-induced TNF-alpha expression is regulated by interferon regulatory factors 1 and 8 in mouse macrophages. J Immunol. 2008 Oct 1;181(7):4461–70.

Vomelová I, Vanícková Z, Sedo A. Methods of RNA purification. All ways (should) lead to Rome. Folia Biol (Praha). 2009;55(6):243–51.

Vroegrijk IOCM, van Klinken JB, van Diepen JA, van den Berg SAA, Febbraio M, Steinbusch LKM, et al. CD36 is important for adipocyte recruitment and affects lipolysis. Obesity. 2013 May 29;21(10):2037–45.

Wagener A, Goessling HF, Schmitt AO, Mauel S, Gruber AD, Reinhardt R, et al. Genetic and diet effects on Ppar-α and Ppar-γ signaling pathways in the Berlin Fat Mouse Inbred line with genetic predisposition for obesity. Lipids Health Dis. 2010;9(1):99–10.

Walden TB, Timmons JA, Keller P, Nedergaard J, Cannon B. Distinct expression of muscle-specific microRNAs (myomirs) in brown adipocytes. J Cell Physiol. 2009 Feb;218(2):444–9.

Wang H, Zhang Y, Yehuda-Shnaidman E, Medvedev AV, Kumar N, Daniel KW, et al. Liver X receptor alpha is a transcriptional repressor of the uncoupling protein 1 gene and the brown fat phenotype. Mol Cell Biol. 2008 Apr;28(7):2187–200.

Wang QA, Tao C, Gupta RK, Scherer PE. Tracking adipogenesis during white adipose tissue development, expansion and regeneration. Nature Publishing Group; 2013 Sep 1;19(10):1338–44.

Wang Z, Brandt S, Medeiros A, Wang S, Wu H, Dent A, et al. MicroRNA 21 is a homeostatic regulator of macrophage polarization and prevents prostaglandin E2-mediated M2 generation. PLoS ONE. 2015;10(2):e0115855.

Wardle J, Carnell S, Haworth CM, Plomin R. Evidence for a strong genetic influence on childhood adiposity despite the force of the obesogenic environment. Am J Clin Nutr. 2008 Feb;87(2):398–404.

Wareham N. Physical activity and obesity prevention. Obes Rev. 2007 Mar;8 Suppl 1:109–14.

Way JM, Harrington WW, Brown KK, Gottschalk WK, Sundseth SS, Mansfield TA, et al. Comprehensive messenger ribonucleic acid profiling reveals that peroxisome proliferator-activated receptor gamma activation has coordinate effects on gene expression in multiple insulin-sensitive tissues. Endocrinology. 2001 Mar;142(3):1269–77.

Weisberg SP, Hunter D, Huber R, Lemieux J, Slaymaker S, Vaddi K, et al. CCR2 modulates inflammatory and metabolic effects of high-fat feeding. 2006 Jan;116(1):115–24.

Weisberg SP, McCann D, Desai M, Rosenbaum M, Leibel RL, Ferrante AW. Obesity is associated with macrophage accumulation in adipose tissue. J Clin Invest. 2003 Dec;112(12):1796–808.

Welch C, Chen Y, Stallings RL. MicroRNA-34a functions as a potential tumor suppressor by inducing apoptosis in neuroblastoma cells. Oncogene. 2007 Jul 26;26(34):5017–22.

Weng W, Wang M, Xie S, Long Y, Li F, Sun F, et al. YY1-C/EBPα-miR34a regulatory circuitry is involved in renal cell carcinoma progression. Oncol Rep. 2014 Apr;31(4):1921–7.

Wentworth JM, Naselli G, Brown WA, Doyle L, Phipson B, Smyth GK, et al. Pro-inflammatory CD11c+CD206+ adipose tissue macrophages are associated with insulin resistance in human obesity. Diabetes. 2010 Jul;59(7):1648–56.

Wheatcroft SB, Kearney MT, Shah AM, Ezzat VA, Miell JR, Modo M, et al. IGF-binding protein-2 protects against the development of obesity and insulin resistance. Diabetes. 2007 Feb;56(2):285–94.

Wightman B, Ha I, Ruvkun G. Posttranscriptional regulation of the heterochronic gene lin-14 by lin-4 mediates temporal pattern formation in C. elegans. Cell. 1993 Dec 3;75(5):855–62.

Wilson-Fritch L, Burkart A, Bell G, Mendelson K, Leszyk J, Nicoloro S, et al. Mitochondrial biogenesis and remodeling during adipogenesis and in response to the insulin sensitizer rosiglitazone. 2003 Feb;23(3):1085–94.

Wilson-Fritch L, Nicoloro S, Chouinard M, Lazar MA, Chui PC, Leszyk J, et al. Mitochondrial remodeling in adipose tissue associated with obesity and treatment with rosiglitazone. 2004 Nov;114(9):1281–9.

Winer DA, Winer S, Shen L, Wadia PP, Yantha J, Paltser G, et al. B cells promote insulin resistance through modulation of T cells and production of pathogenic IgG antibodies. Nat Med. 2011 Apr 17;17(5):610–7.

Winer S, Chan Y, Paltser G, Truong D, Tsui H, Bahrami J, et al. Normalization of obesity-associated insulin resistance through immunotherapy. Nat Med. Nature Publishing Group; 2009 Jul 26;:1–10.

World Health Organization. Waist circumference and waist-hip ratio: report of a WHO expert consultation. 2011;:1–39. Available from: http://www.who.int/nutrition/publications/obesity/WHO_report_waistcircumference_and_waisthip_ratio/en/

Wronska A, Kmiec Z. Structural and biochemical characteristics of various white adipose tissue depots. Acta Physiol. 2012 Feb 1;205(2):194–208.

Wu D, Molofsky AB, Liang H-E, Ricardo-Gonzalez RR, Jouihan HA, Bando JK, et al. Eosinophils sustain adipose alternatively activated macrophages associated with glucose homeostasis. Science. 2011 Apr 8;332(6026):243–7.

Wu Q, Ortegon AM, Tsang B, Doege H, Feingold KR, Stahl A. FATP1 is an insulin-sensitive fatty acid transporter involved in diet-induced obesity. Mol Cell Biol. 2006 May;26(9):3455–67.

Wyman SK, Knouf EC, Parkin RK, Fritz BR, Lin DW, Dennis LM, et al. Post-transcriptional generation of miRNA variants by multiple nucleotidyl transferases contributes to miRNA transcriptome complexity. Genome Res. 2011 Sep;21(9):1450–61.

Xie H, Lim B, Lodish HF. MicroRNAs induced during adipogenesis that accelerate fat cell development are downregulated in obesity. Diabetes. 2009 May;58(5):1050–7.

Xu A, Wang Y, Keshaw H, Xu LY, Lam KSL, Cooper GJS. The fat-derived hormone adiponectin alleviates alcoholic and nonalcoholic fatty liver diseases in mice. J Clin Invest. 2003a Jul;112(1):91–100.

Xu F, Kang Y, Zhang H, Piao Z, Yin H, Diao R, et al. Akt1-mediated regulation of macrophage polarization in a murine model of Staphylococcus aureus pulmonary infection. J Infect Dis. 2013 Aug 1;208(3):528–38.

Xu H, Barnes GT, Yang Q, Tan G, Yang D, Chou CJ, et al. Chronic inflammation in fat plays a crucial role in the development of obesity-related insulin resistance. 2003b Dec 15;112(12):1821–30.

Xu Q, Seeger FH, Castillo J, Iekushi K, Boon RA, Farcas R, et al. Micro-RNA-34a contributes to the impaired function of bone marrow-derived mononuclear cells from patients with cardiovascular disease. Journal of the American College of Cardiology. 2012 Jun 5;59(23):2107–17.

Xu Y, Zalzala M, Xu J, Li Y, Yin L, Zhang Y. A metabolic stress-inducible miR-34a-HNF4α pathway regulates lipid and lipoprotein metabolism. Nat Comms. 2015;6:7466.

Xue W, Dahlman JE, Tammela T, Khan OF, Sood S, Dave A, et al. Small RNA combination therapy for lung cancer. Proceedings of the National Academy of Sciences. 2014 Aug 26;111(34):E3553–61.

Yamada H, Suzuki K, Ichino N, Ando Y, Sawada A, Osakabe K, et al. Associations between circulating microRNAs (miR-21, miR-34a, miR-122 and miR-451) and non-alcoholic fatty liver. Clin Chim Acta. 2013 Sep 22;424:99–103.

Yamakuchi M, Ferlito M, Lowenstein CJ. miR-34a repression of SIRT1 regulates apoptosis. Proceedings of the National Academy of Sciences. 2008 Sep 9;105(36):13421–6.

Yamamura S, Saini S, Majid S, Hirata H, Ueno K, Chang I, et al. MicroRNA-34a suppresses malignant transformation by targeting c-Myc transcriptional complexes in human renal cell carcinoma. Carcinogenesis. 2012 Feb;33(2):294–300.

Yang P, Li Q-J, Feng Y, Zhang Y, Markowitz GJ, Ning S, et al. TGF-β-miR-34a-CCL22 signaling-induced Treg cell recruitment promotes venous metastases of HBV-positive hepatocellular carcinoma. 2012 Sep 11;22(3):291–303.

Yang Q, Graham TE, Mody N, Preitner F, Peroni OD, Zabolotny JM, et al. Serum retinol binding protein 4 contributes to insulin resistance in obesity and type 2 diabetes. Nature. 2005 Jul 21;436(7049):356–62.

Yang Y, Cheng H-W, Qiu Y, Dupee D, Noonan M, Lin Y-D, et al. MicroRNA-34a Plays a Key Role in Cardiac Repair and Regeneration Following Myocardial Infarction. Circulation Research. 2015 Aug 14;117(5):450–9.

Yeung F, Hoberg JE, Ramsey CS, Keller MD, Jones DR, Frye RA, et al. Modulation of NF-kappaB-dependent transcription and cell survival by the SIRT1 deacetylase. EMBO J. EMBO Press; 2004 Jun 16;23(12):2369–80.

Zauli G, Voltan R, di Iasio MG, Bosco R, Melloni E, Sana ME, et al. miR-34a induces the downregulation of both E2F1 and B-Myb oncogenes in leukemic cells. 2011 May 1;17(9):2712–24.

Zhang C-L, Wang C, Yan W-J, Gao R, Li Y-H, Zhou X-H. Knockdown of TNFAIP1 inhibits growth and induces apoptosis in osteosarcoma cells through inhibition of the nuclear factor-κB pathway. Oncol Rep. 2014 Jun 25;:1–7.

Zhang H-S, Chen X-Y, Wu T-C, Sang W-W, Ruan Z. MiR-34a is involved in Tat-induced HIV-1 long terminal repeat (LTR) transactivation through the SIRT1/NFκB pathway. FEBS Letters. 2012 Nov 30;586(23):4203–7.

Zhang XW, Wang Y, Liu Q, Thorlacius H. Redundant function of macrophage inflammatory protein-2 and KC in tumor necrosis factor-α-induced extravasation of neutrophils in vivo. European Journal of Pharmacology. 2001;427(3):277–83.

Zhang Y, Proenca R, Maffei M, Barone M, Leopold L, Friedman JM. Positional cloning of the mouse obese gene and its human homologue. Nature. 1994 Dec 1;372(6505):425–32.

Zhang YH, Yan HQ, Wang F, Wang YY, Jiang YN, Wang YN, et al. TIPE2 inhibits TNF-α-induced hepatocellular carcinoma cell metastasis via Erk1/2 downregulation and NF-κB activation. Int J Oncol. 2015 Jan 1;46(1):254–64.

Zhao L, Gregoire F, Sul HS. Transient induction of ENC-1, a Kelch-related actin-binding protein, is required for adipocyte differentiation. J Biol Chem. 2000 Jun 2;275(22):16845–50.

Zhao Y, Samal E, Srivastava D. Serum response factor regulates a muscle-specific microRNA that targets Hand2 during cardiogenesis. 2005 Jul 14;436(7048):214–20.

Zhou J, Wang K-C, Wu W, Subramaniam S, Shyy JY-J, Chiu J-J, et al. MicroRNA-21 targets peroxisome proliferators-activated receptor-alpha in an autoregulatory loop to modulate flow-induced endothelial inflammation. Proceedings of the National Academy of Sciences. 2011 Jun 21;108(25):10355–60.

Zhu H, Leung SW. Identification of microRNA biomarkers in type 2 diabetes: a meta-analysis of controlled profiling studies. Diabetologia. 2015 Feb 13;58(5):900–11.

Zhuang G, Meng C, Guo X, Cheruku PS, Shi L, Xu H, et al. A novel regulator of macrophage activation: miR-223 in obesity-associated adipose tissue inflammation. Circulation. 2012 Jun 12;125(23):2892–903.

Zou X-L, Pei D-A, Yan J-Z, Xu G, Wu P. A20 Overexpression Inhibits Lipopolysaccharide-Induced NF-κB Activation, TRAF6 and CD40 Expression in Rat Peritoneal Mesothelial Cells. IJMS. 2014 Apr;15(4):6592–608.